GWRI/2010-TR1

Georgia Water Resources Institute | Georgia Institute of Technology

Climate Variability and Change Assessment for the ACF River Basin, Southeast US

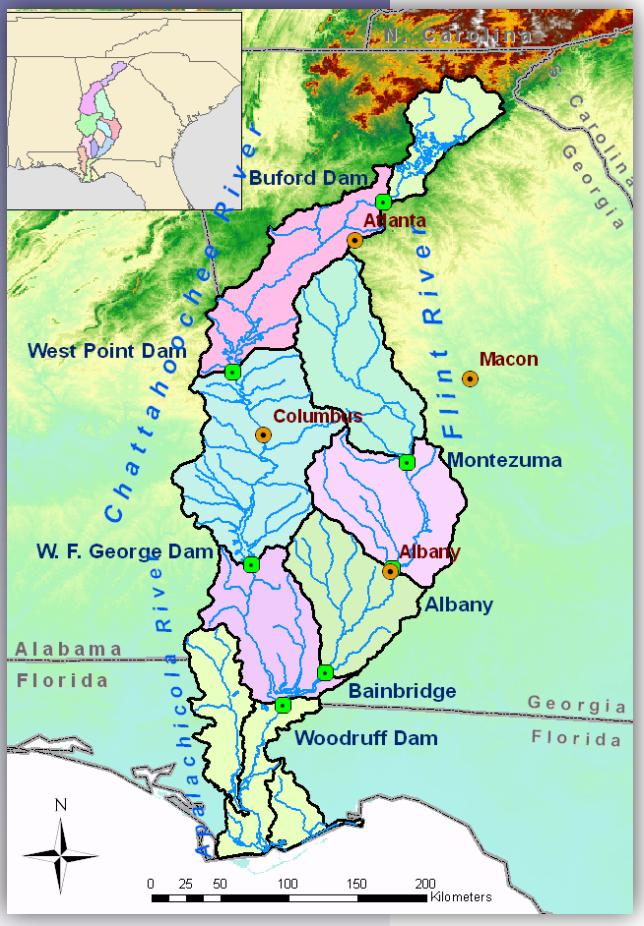

Developed by

Aris Georgakakos, **Feng Zhang**, and **Huaming Yao**

Georgia Water Resources Institute
Georgia Institute of Technology

Sponsored by

NOAA
Climate Prediction Program for the Americas

Georgia DNR/EPD

Georgia Water Resources Institute
State Water Resources Research Program

August 2010

Climate Variability and Change Assessment for the ACF River Basin, Southeast US

Developed by

Aris Georgakakos, Feng Zhang, and **Huaming Yao**

Georgia Water Resources Institute
Georgia Institute of Technology

Sponsored by

NOAA
Climate Prediction Program for the Americas

Georgia DNR/EPD

and

Georgia Water Resources Institute
State Water Resources Research Program

August 2010

Acknowledgements

The ACF Climate Change Assessment study and associated reports were developed by the Georgia Water Resources Institute (GWRI) at the Georgia Institute of Technology with support from *(1)* the National Oceanic and Atmospheric Administration, Office of Global Programs, Climate Prediction Program for the Americas (CPPA; NOAA contract No. NA06OAR4310073), *(2)* the Georgia Department of Natural Resources, Environmental Protection Division (Georgia EPD contract No. 761-70091), and *(3)* the State Water Institute Program administered by USGS.

We wish to thank Nancy Beller-Simms of the NOAA CPPA Program for her administrative support, oversight, encouragement, and patience. We also wish to thank Dr. Carol Couch and Mr. Allen Barnes, Georgia EPD Directors, and their technical and policy advisors (Dr. Wei Zeng and Mr. Nap Caldwell) for their support and cooperation during this project. Our hope is that the new tools and knowledge developed herein will have a positive impact on the management of the ACF river basin and will contribute to an amicable resolution of the outstanding water sharing issues.

Aris Georgakakos
GWRI Director and Georgia Tech Professor
Atlanta, August 8, 2010

Disclaimer

Report Citation

This report should be cited as follows:

Georgakakos, A., F. Zhang, and H. Yao, 2010: Climate Variability and Change Assessment for the ACF River Basin, Southeast US. Georgia Water Resources Institute (GWRI) Technical Report No. GWRI/2010-TR1, Georgia Institute of Technology, Atlanta, Georgia, USA, 321 pp.

Contents

Executive Summary

The southeast US has historically enjoyed abundant water resources, with past issues mostly associated with flooding due to hurricane-induced tropical storms. However, recent decades ushered in rapid population and water demand increases, unsustainable agricultural expansion, severe droughts with devastating socioeconomic impacts, crawling urbanization, widespread river pollution, endangered ecosystems, and litigious transboundary water disputes. These challenges are exemplified in the Apalachicola-Chattahoochee-Flint (ACF) River Basin shared by Alabama, Georgia, and Florida, which is the geographic focus of this study.

The study objective is to develop a clear understanding of the impacts associated with climate change and to generate reliable data and information to support the on-going regional water resources planning and management efforts. Toward meeting this objective, the study undertakes *(1)* development of an integrated (climate-hydrology-water resources) modeling system; *(2)* assessment of the historical ACF response; and *(3)* assessment of the projected ACF response under various GCM scenarios, demand scenarios, and regulation policies. The study was sponsored by NOAA, Georgia DNR/EPD, and USGS.

An assessment of the historical 1901-2009 period shows that the ACF exhibits increasing potential evapotranspiration and drier soil moisture and runoff trends. Basin assessments with future climate and demand scenarios indicate that drier soil moisture and runoff trends will continue with critical implications for agriculture and water management. Severe floods are also expected to intensify. Under current regulation practices, climate and demand change will adversely impact lake levels, water supply reliability, energy generation, and ecological flows. The study demonstrates that there is a critical need for flexible technical and institutional measures to mitigate and adapt to simultaneous climate, demand, and land use change, with adaptive management being a particularly effective mitigation strategy.

Chapter 1

Overview of the ACF Assessment Process and Study

1.1 Study Scope and Approach

The southeast US has historically enjoyed abundant water resources, with past issues mostly associated with flooding due to hurricane-induced tropical storms. Such vulnerabilities continue to exist, but recent decades ushered in rapid population and water demand increases, unsustainable agricultural expansion, severe droughts with devastating socioeconomic impacts, crawling urbanization, widespread river pollution, endangered ecosystems, and litigious transboundary water disputes. These challenges are exemplified in the Apalachicola-Chattahoochee-Flint (ACF) River Basin (**Figure 1.1**) shared by Alabama, Georgia, and Florida, which provides a wealth of water resources, environmental, ecological, energy, and socio-economic benefits and services, and is the geographic focus of this study.

The study objective is to develop a clear understanding of the impacts associated with climate change and to generate reliable data and information to support the on-going regional water resources planning and management efforts. Toward meeting this objective, the study undertakes *(1)* development of an integrated (climate-hydrology-water resources) modeling system; *(2)* assessment of the historical ACF response; and *(3)* assessment of the projected ACF response under various GCM scenarios, demand scenarios, and regulation policies.

Figure 1.2 illustrates the integrated modeling framework comprising three main components: *(1)* processing of general circulation model (GCM) scenarios for bias correction and downscaling (**climate component**); *(2)* developing physically based conceptual models for all ACF sub-watersheds (**hydrology component**); and *(3)* representing all ACF regulation infrastructure and water uses within an adaptive river and reservoir regulation and assessment model (**water**

resources component). Research contributions include new methods for *(i)* consistent temperature-precipitation downscaling; *(ii)* physically based watershed modeling with data driven functional relationships and parameters; and *(iii)* improved river basin management methods with full consideration of system uncertainty.

1.2 Report Organization

The ACF assessment study is described in two volumes. The current volume is the main study report and includes six chapters. Chapter 2 provides background information on the historical ACF climate, hydrology, and water uses. Chapter 3 discusses the development of a new downscaling method and its application to generating temperature, precipitation, and potential evapotranspiration scenarios over the main ACF watersheds. Additional results and comparisons pertaining to this chapter are included in Appendix A. Chapter 4 describes the development of watershed models for all ACF watersheds and their use in characterizing the hydrologic ACF response under historical and future climate scenarios. Chapter 5 focuses on water resources assessments under climate and demand change, and Chapter 6 summarizes the main study findings. Lastly, Volume II provides an in-depth technical presentation of the decision support system used in the water resources assessments described in Chapter 5.

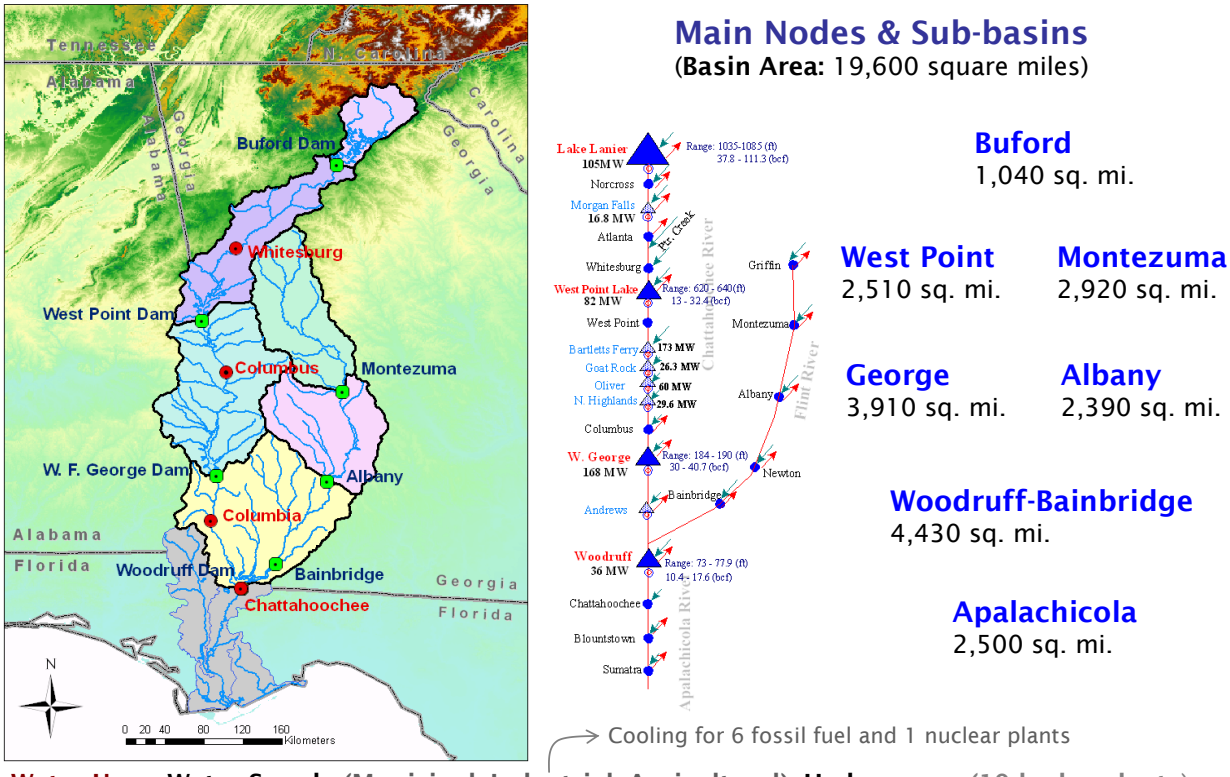

Figure 1.1: A schematic of the ACF River Basin, Infrastructure, and Water Uses

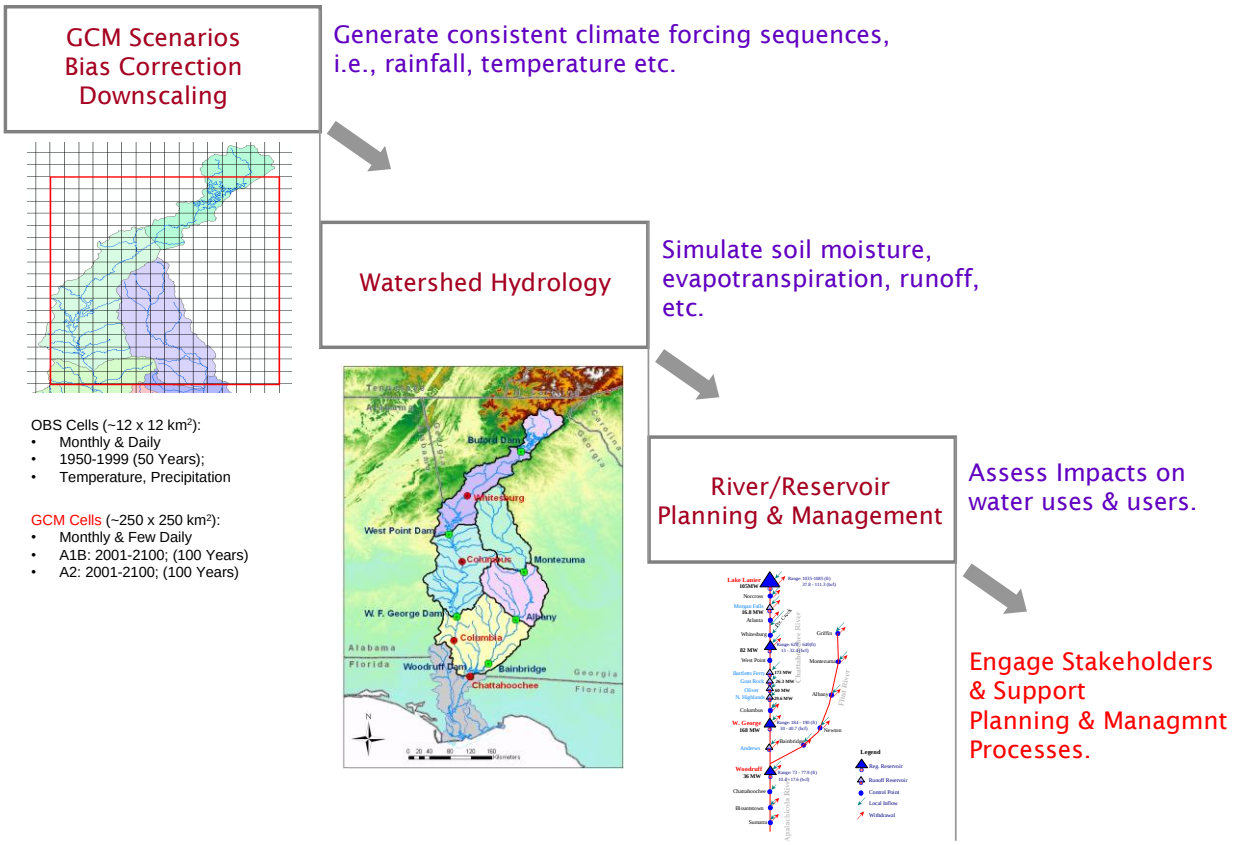

Figure 1.2: Integrated Modeling Framework

Chapter 2

ACF River System: Historical Climate, Hydrology, and Water Uses

2.1 ACF River Basin

The Apalachicola-Chattahoochee-Flint (ACF) river system (**Figure 2.1**) is located in the southeast US. The ACF begins from north Georgia and flows into the Gulf of Mexico, near Apalachicola, Florida. The total ACF drainage area is 19,600 square miles.

The Chattahoochee River originates in the Blue Ridge Mountains of the Appalachian Highlands in northeast Georgia, and flows southwesterly for 120 miles and then southerly along the Georgia - Alabama border for another 200 miles. The Chattahoochee drainage basin is 8,770 square miles. The Flint originates south of Atlanta and flows in a southerly direction toward the Coastal Plain where it joins the Chattahoochee River at Lake Seminole. The Flint River drainage basin is 8,460 square miles. The releases from Lake Seminole enter the Apalachicola River which lies in the Coastal Plain over its entire length of 108 miles and flows south across northwest Florida to the Apalachicola Bay. The Apalachicola River drainage basin is 2,370 square miles.

The Chattahoochee flows are highly regulated by a series of federal and private reservoirs. The federal reservoirs operate for multiple purposes, including flood control, water supply, hydropower, navigation, water quality, recreation, and aquatic life protection, while the private reservoirs are power facilities. The Flint and Apalachicola Rivers are largely unregulated.

Based on the locations of major storage projects and the geography of the basin, this study distinguishes eight sub-basins: *(1)* the Chattahoochee headwater reach extending up to and including Lake Lanier and Buford Dam; *(2)* the Chattahoochee reach from Lake Lanier up to and including West Point Lake and Dam; *(3)* the Middle Chattahoochee reach from West Point up to

and including Lake Walter F. George and Dam; *(4)* the Lower Chattahoochee reach from Lake W.F. George up to and including Lake Seminole and Jim Woodruff Lock and Dam; *(5)* the Flint headwater reach up to Montezuma; *(6)* the Flint reach from Montezuma up to Albany; *(7)* the Flint reach from Albany to Bainbridge; and *(8)* the Apalachicola River reach. **Table 2.1** summarizes general characteristics of the ACF sub-basins.

Table 2.1: General Characteristics of the ACF Sub-basins

ACF Sub-basins	Latitude (Centroid)	Longitude (Centroid)	Area (km^2)	Mean Elevation (m)	Min. Elevation (m)	Max. Elevation (m)
Buford	34°31’	-83°48’	2694	454	320	1250
West Point	33°40’	-84°44’	5189	270	137	455
George	32°20’	-85°01’	4787	143	46	396
Woodruff	31°13’	-84°58’	2141	64	22	167
Montezuma	32°55’	-84°24’	4507	213	85	394
Albany	32°01’	-84°11’	2605	115	53	235
Bainbridge	31°25’	-84°24’	1875	72	23	173
Apalachicola	30°21’	-85°08’	2121	59	1	128

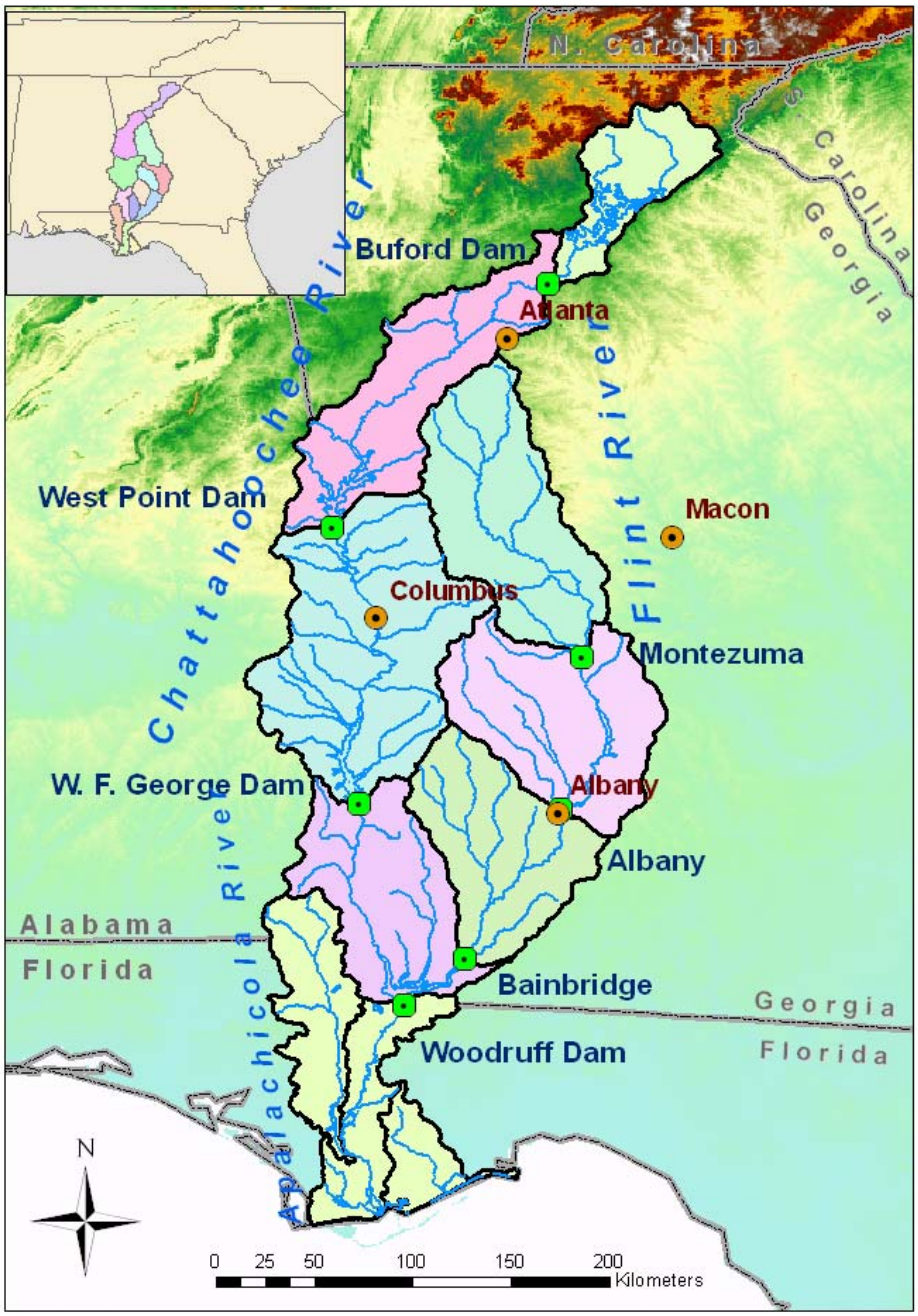

Figure 2.1: The Apalachicola-Chattahoochee-Flint (ACF) River System

2.2 Historical Climate and Hydrology

The ACF river basin has a warm, humid, and temperate climate, typical of the subtropics, with mild winters and hot summers. The Atlantic Ocean on the east coast of Georgia and the mountain region to the north impact the state climate, including the ACF basin. The basin experiences all four seasons, with monthly temperature varying from 39°F (4°C) in the winter to 76°F (25°C) in the summer. The average annual precipitation over Georgia is 50 inches (1,250 mm). Spatially, annual precipitation varies from 45 inches (1,100 mm) in central Georgia to approximately 75 inches (1,900 mm) in the northeast corner of the state.

Water in Georgia originates mainly as rainfall and occasionally as snow or sleet. Over the long term, approximately 70 percent of Georgia's precipitation becomes evapotranspiration (ET), while the remaining 30 percent becomes runoff and streamflow. These percentages vary seasonally and by watershed location, with ET being higher during summer and at lower latitudes.

Geological conditions play a key role in shaping watershed soil type, hydrology, and stream morphology. The rivers and streams emanating from the Blue Ridge Mountains of north Georgia (upper Chattahoochee River) are generally steep, fast-flowing, cold, and clear. In the Piedmont (middle Chattahoochee and upper Flint Rivers), rivers are slower because of the flatter, rolling topography. Rivers and streams below the fall line (Apalachicola and lower Chattahoochee and Flint Rivers) exhibit varying degrees of aquifer interactions. Lime sinks, sinkholes, and springs are common in this part of the ACF basin.

2.2.1 Precipitation

The mechanisms of Georgia's precipitation vary from season to season. Frontal storms are common during winter, spring, and fall, while convective storms dominate during summer.

Hurricane-induced tropical storms are also common during the hurricane season from June to November. Strong El Niño years tend to be wetter than normal, while La Niña years are drier. Overall, annual precipitation varies by as much as 40 percent of the long term mean.

The left and middle plots in **Figure 2.2** show the seasonal (DJF, MAM, JJA, and SON) precipitation climatology over Georgia and the ACF basin, based on historical data from 01/1950 to 12/1999. The figures show that the northeastern ACF region (Blue Ridge) receives much more precipitation than the rest of the basin, except during summer and fall when southern Apalachicola in Florida is impacted by tropical cyclones and summer thunderstorms. The Blue Ridge Mountains have the most frequent snowfall in Georgia, although snowfall is less than other regions of the Appalachian Mountains.

The right plot in **Figure 2.2** shows the monthly precipitation climatology by sub-basin. The figure shows that all basins exhibit a similar monthly precipitation pattern with highs in March and July and lows in October. The July high and October low become more pronounced for watersheds in lower latitudes. The Buford watershed, extending in the Blue Ridge Mountains, receives the highest precipitation amounts in all months.

Figure 2.3 shows the historical monthly average precipitation sequences from 1901 to 2002 for all ACF watersheds. The corresponding two-year moving average sequences are also plotted in the same figures. Historically, severe droughts occur with an average frequency of 8-12 years and last for 2 - 5 years.

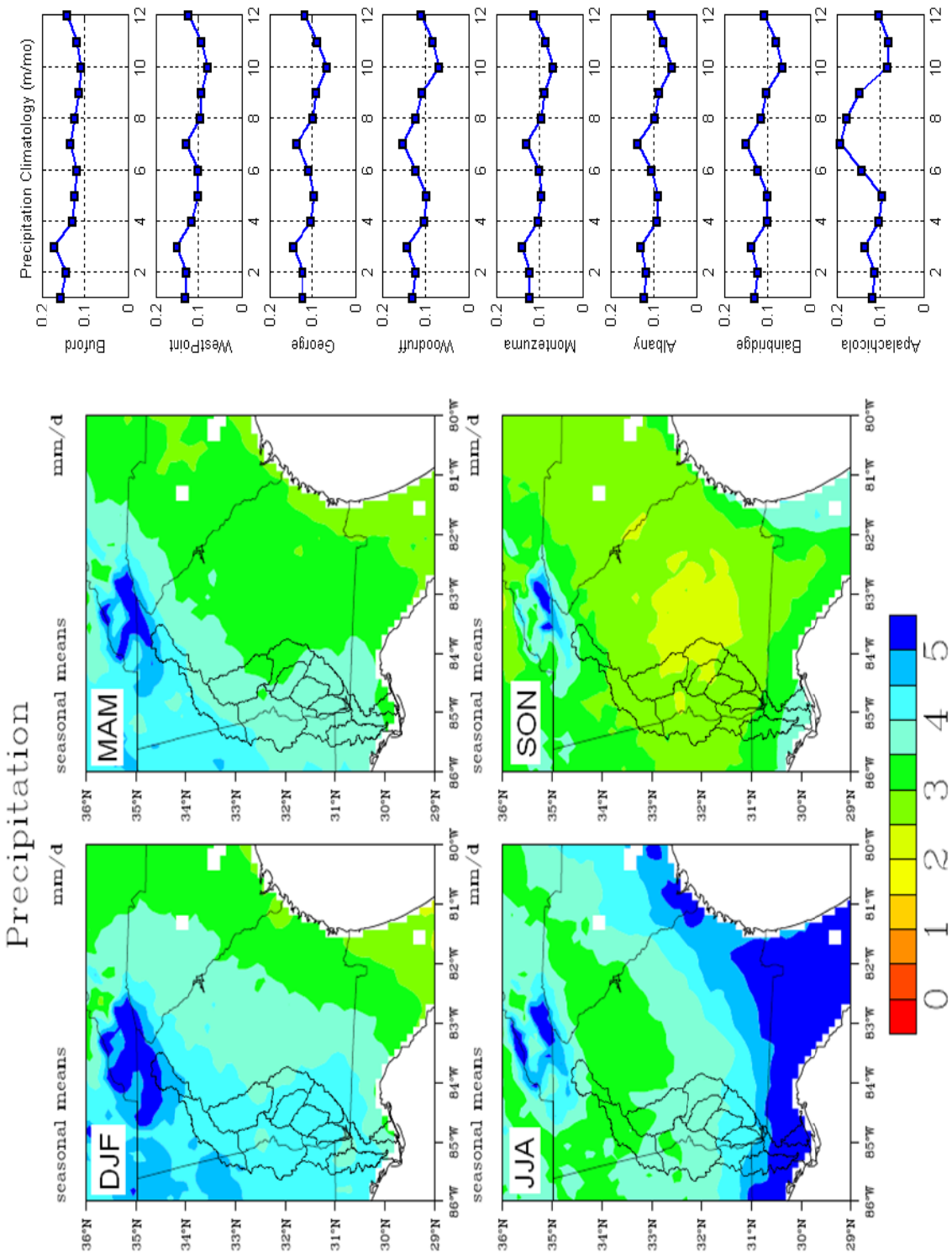

Figure 2.2: Precipitation Climatology for ACF Sub-basins: Left and Middle Seasonal Climatology Map; Right Watershed Climatology

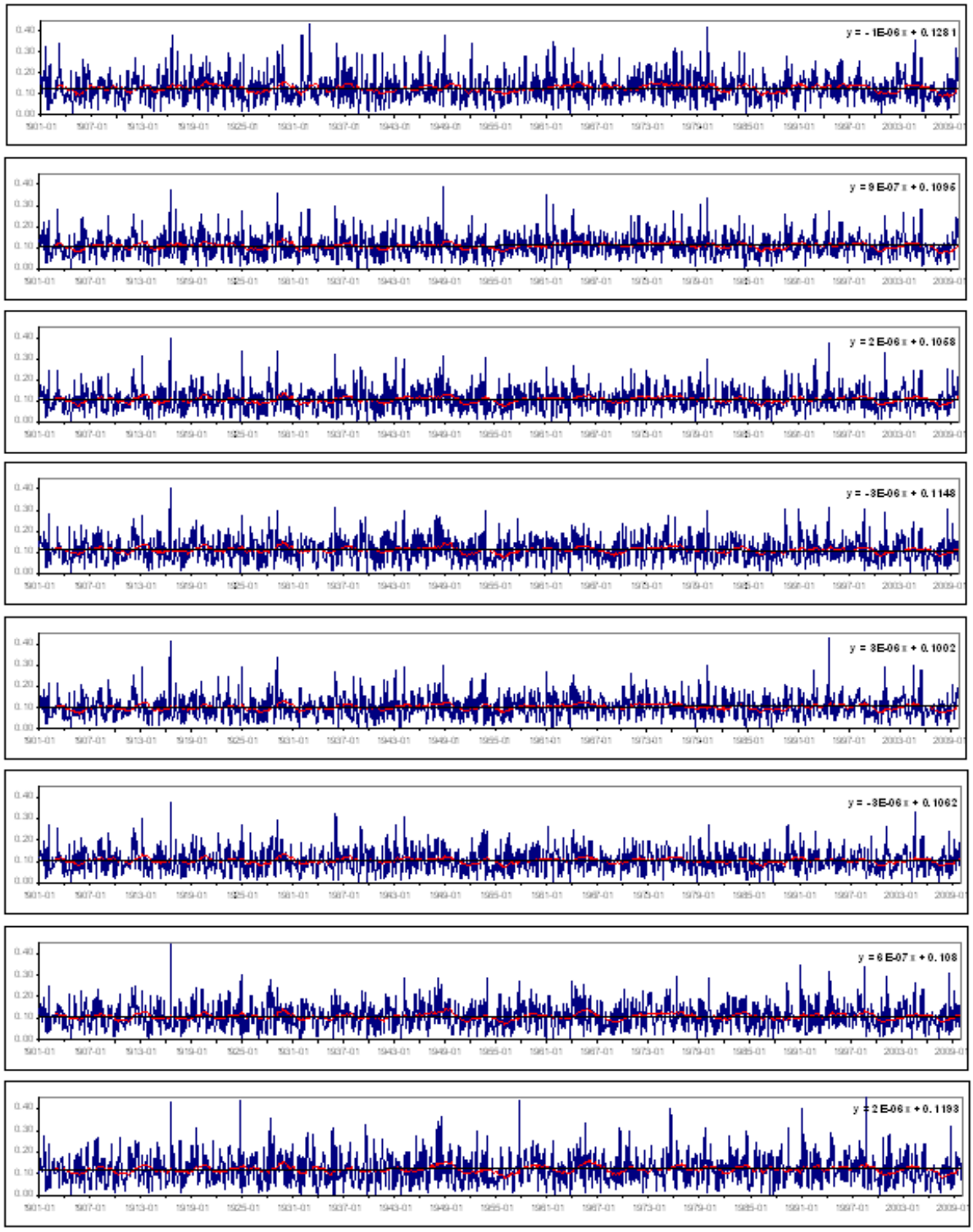

Figure 2.3: Monthly Precipitation Sequences for the ACF Sub-basins: Buford, West Point, George, Woodruff, Montezuma, Albany, and Bainbridge (from top to bottom).

2.2.2 Temperature and Potential Evapotranspiration (PET)

ACF temperature exhibits temporal and spatial variations due to regional geographic and climatic features. **Figure 2.4** shows the ACF seasonal temperature climatology (DJF, MAM, JJA, and SON) based on the historical data from 01/1950 to 12/1999. Seasonal average temperature variations of 3 to 6 degrees are observed from north to south, with the northeastern region being colder due to the orography. The right plot in **Figure 2.4** shows the monthly temperature climatology of the eight ACF sub-basins. All sub-basins exhibit similar patterns. The hottest months are July and August with temperatures varying from 22^{o}C to 28^{o}C, while the two coldest months are December and January with temperatures varying from 4^{o}C to 10^{o}C.

The historical monthly temperature sequences from 1901 to 2009 and the corresponding two-year moving average sequences for all sub-basins are shown in **Figure 2.5**. No significant long term trends are observed.

Potential evapotranspiration demand (PET) is the amount of water that *could* be evaporated from open water surfaces and transpired by vegetation assuming unlimited water supply. PET measures the ability of the lower atmosphere to transport moisture away from the land surface. For short temporal scales, PET is highly variable, with highest rates occurring on warm, dry, and windy days, and lowest rates on cold, wet, and calm days. However, PET is considerably less variable for longer time scales (e.g., months).

Many methods exist for estimating PET, based on different assumptions, requirements, and regional climate specifications (Grismer, 2002). PET calculation techniques include temperature based methods (Thornthwaite , 1948, Hamon, 1963, and Hargreaves-Samani, 1985),

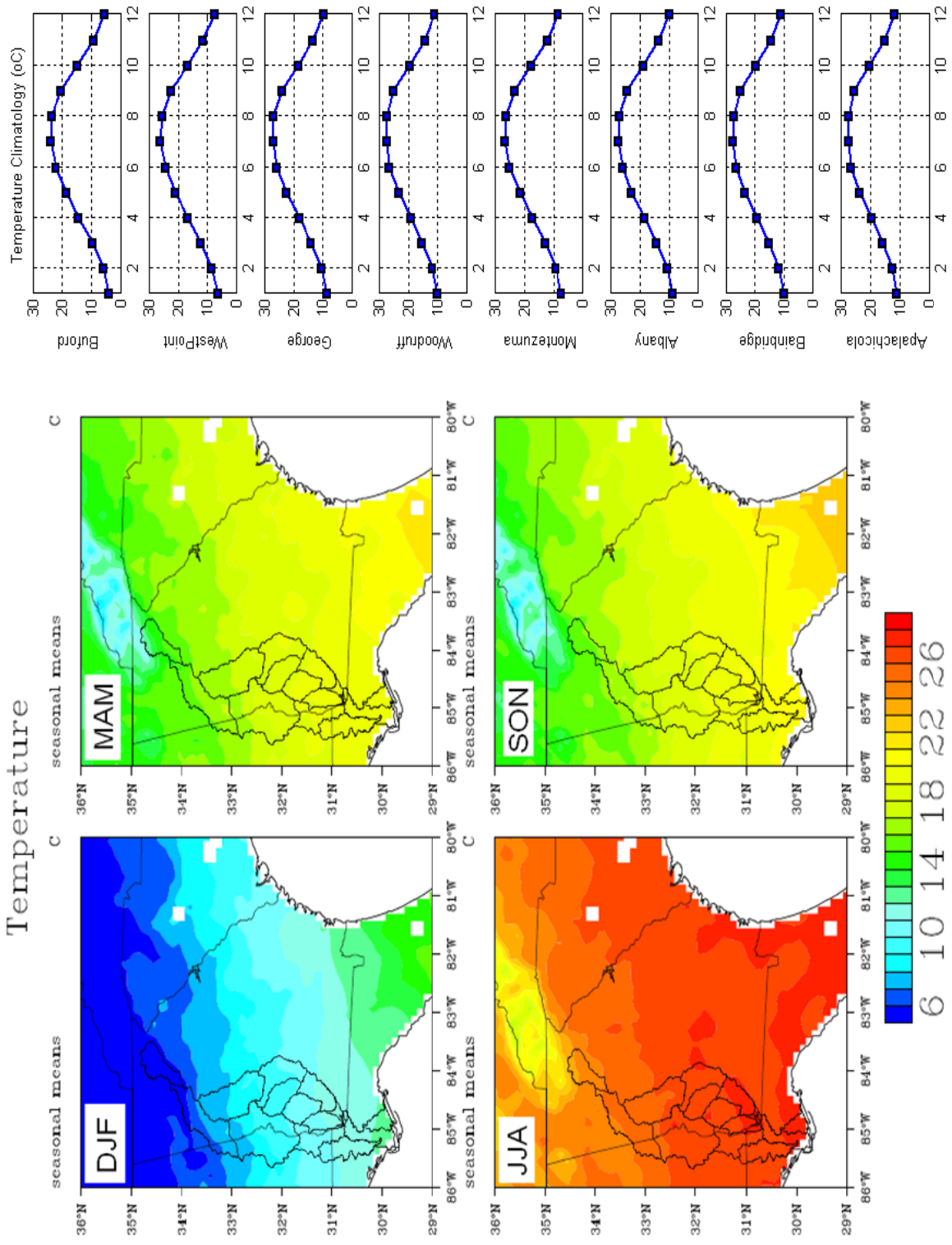

Figure 2.4: Temperature Climatology for ACF Sub-basins: Seasonal Climatology Shown on the Left and Middle Maps; Monthly Climatology Shown on the Right Plots.

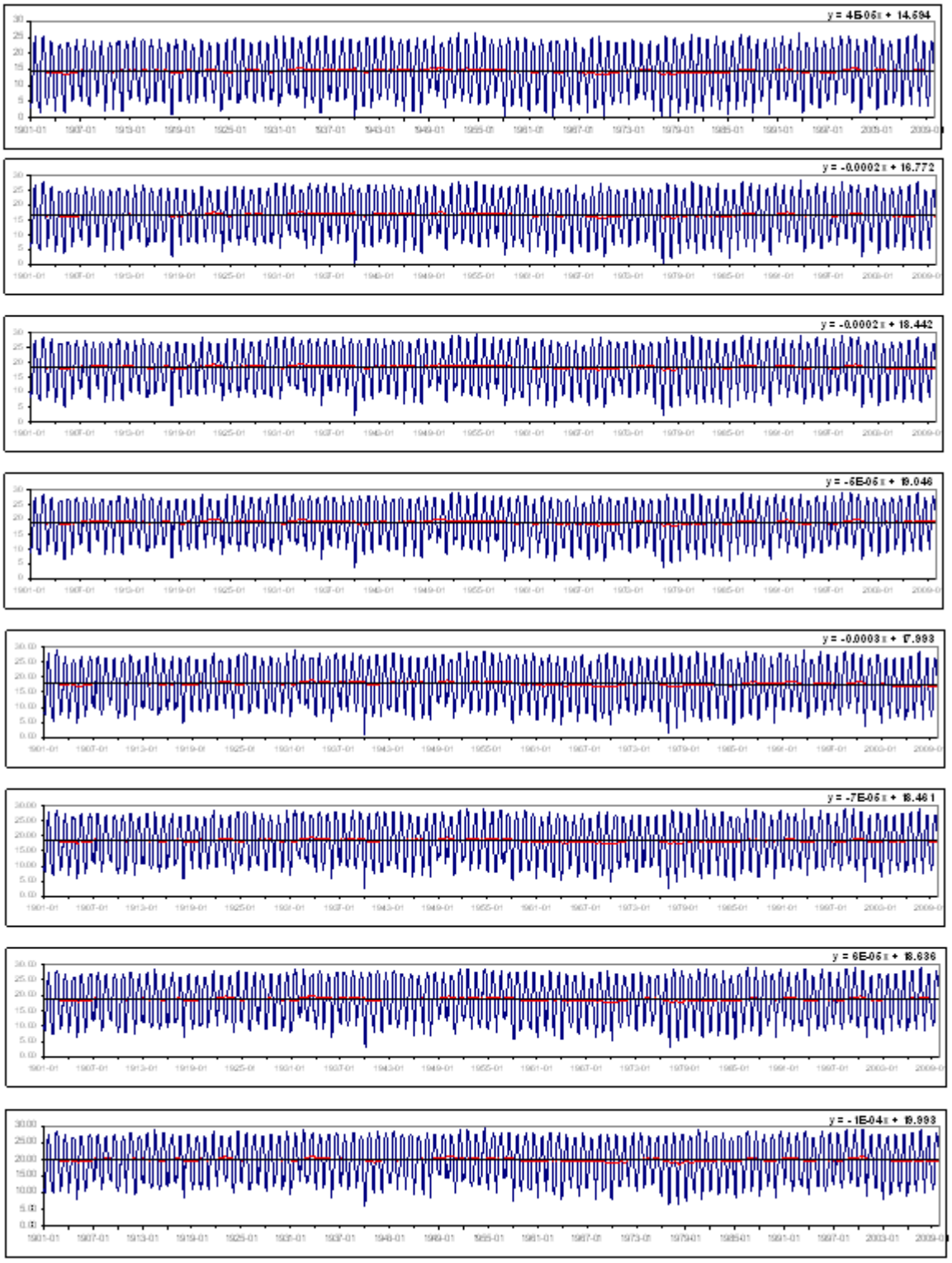

Figure 2.5: Monthly Temperature Sequences for the ACF Sub-basins: (From Top to Bottom) Buford, West Point, George, Woodruff, Montezuma, Albany, Bainbridge, and Apalachicola

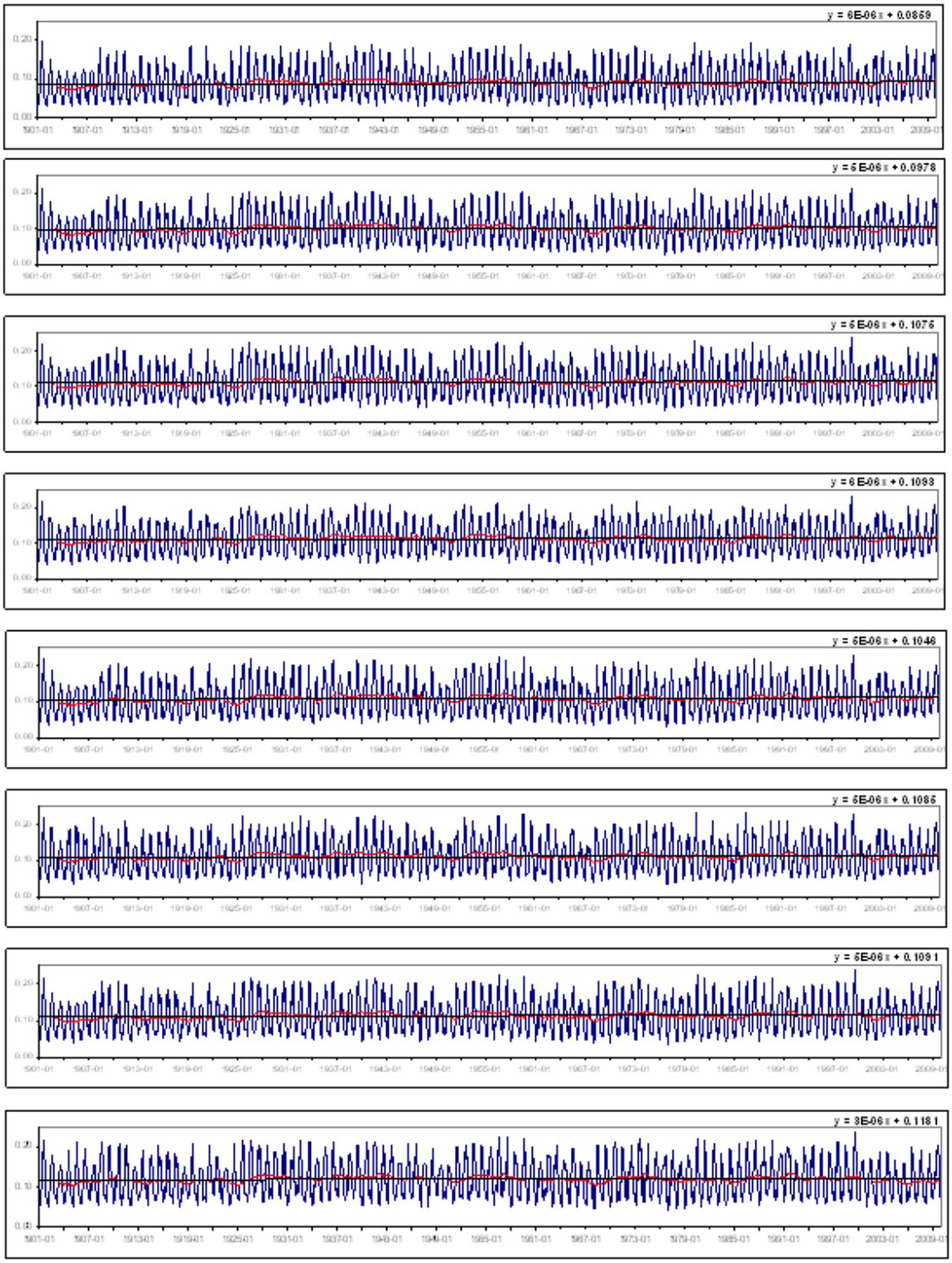

Figure 2.6: Monthly PET Sequences (Hamon) for ACF Sub-basins: Buford, West Point, George, Woodruff, Montezuma, Albany, Bainbridge, and Apalachicola (from top to bottom).

Radiation-based methods (Turc 1961, Makkink, 1957, and Priestley-Taylor, 1972), and combination methods (Penman, 1948). In a comparative investigation of several *monthly* PET methods, Lu (2005) concluded that the Priestley-Taylor, Turc, and Hamon methods are suitable for watershed-scale applications in the southeastern United States.

This study also carried out a comparison of three methods: Hamon, 1963, Priestley-Taylor, 1972, and the PET estimates of the NCEP Regional Climate Model (Juang et al, 1997). All methods are based on grid data obtained from the NCEP Re-analysis Dataset I (Kalnay et al., 1996). The NCEP/NCAR Reanalysis 1 project is using a state-of-the-art analysis/forecast system to perform data assimilation using data from 1948 to the present. It has 4-time daily, daily, and monthly reanalysis data on a global grid (~50km horizontal) including 17 pressure levels and 28 sigma levels. In addition, the methods use data on air temperature at 2 meters, net longwave radiation, and net shortwave radiation. The grid data are spatially aggregated into four sub-basins: Buford, West Point, George, and Woodruff.

The formulas used in the PET calculation are included below.

- Hamon Method:

$$PET = 0.1651 \;\; Ld \;\; RHOSAT \;\; KPEC \qquad (2.1)$$

PET: daily PET (mm/day);

Ld: daytime length (i.e., time from sunrise to sunset in multiples of 12 hours);

RHOSAT: saturated vapor density (g/m^3) at the daily mean air temperature (*T*);

$$RHOSAT = 216.7 \;\; ESAT / (T + 273.3) \qquad (2.2)$$

$$ESAT = 6.108 \;\; \exp(17.26939 \;\; T / (T + 237.3)) \qquad (2.3)$$

T: daily mean air temperature (^oC);

ESAT: saturated vapor pressure (mb) at the given *T*;

KPEC: calibration coefficient, set to 1.2 in this study;

Thus, the only input data needed for the Hamon method is "*Air Temperature at 2 meters*".

- Priestley-Taylor (1972) Method:

$$\lambda\ PET = \alpha \frac{\Delta}{\Delta + \gamma}\left(R_n - G\right) \tag{2.4a}$$

$$\lambda = 2.501 - 0.002361T \tag{2.4b}$$

$$\Delta = 0.200\left(0.00738T + 0.8072\right)^7 - 0.000116 \tag{2.4c}$$

PET: daily PET (mm/day);

λ: is the latent heat of vaporization (MJ/kg);

T: is the daily mean air temperature (^{o}C);

α: calibration constant, set to 1.26 is this study;

Δ: slope of the saturation vapor pressure temperature curve;

γ: psychrometric constant modified by the ration of canopy resistance to atmospheric resistance (kPa/^{o}C);

$$\gamma = \frac{c_p p}{0.622\lambda} \tag{2.5}$$

$$p = 101.3 - 0.01055 \tag{2.6}$$

c_p: constant pressure (kJ/kg/^{o}C), which is 1.013 kJ/kg/^{o}C;

p: atmospheric pressure (kPa), where EL is the elevation (m);

R_n: net radiation (long wave radiation plus short wave radiation, MJ/m^2/day);

G: heat flux density to the ground (MJ/m^2/day);

The input datasets needed for Priestley-Taylor method is "Air Temperature at 2 meters", "Net longwave radiation", and "Net shortwave radiation".

- NCEP Re-analysis:

The NCEP re-analysis dataset also provides the potential evaporation rate for each cell in the grid. This rate is obtained by the NCEP regional models. The NCEP evaporation rate is expressed in energy flux units, W/m^2, and unit conversion is needed to make it comparable to the other two methods. Namely,

$$\lambda\ PET = 0.0864\ \ PRT \qquad (2.7)$$

where *PRT* is the energy flux obtained from the NCEP re-analysis, and λ is the latent heat of vaporization (MJ/kg) defined above.

The above three methods were applied to the four sub-basins of the Chattahoochee River. The Hamon and Priestly-Taylor method results are highly correlated (**Table 2.2**). The generated monthly PET sequences for the seven watersheds from 1901 to 2009 using the Hamon method are shown in **Figure 2.6**. The Hammon method is selected for use in this study due to *(1)* its generally reliable performance and *(2)* the applicability in future climate assessments. PET values are lowest in the basin headwaters, gradually increasing at the downstream watersheds near the warmer Gulf coast. Actual evapotranspiration (ET) depends on several other factors such as soil type, vegetation cover, and land use, among others, and will be estimated by the hydrologic models to be discussed later in this report.

Table 2.2: Correlation Coefficients

	Hamon-PT	Hamon-NCEP	PT-NCEP
Buford	0.84	0.69	0.85
West Point	0.84	0.62	0.82
George	0.82	0.56	0.79
Woodruff	0.79	0.67	0.63

2.2.3 Unimpaired Inflow and Watershed Runoff

Unimpaired flows are the river flows that would have been observed in the absence of human water use and regulation. The unimpaired flow sequences used in this study were initially developed by the U.S. Army Corps of Engineers (USACE) as part of the ACF Comprehensive Study for the period from 1939 to 1993. This dataset was extended to 2001 by USACE Mobile District in September 2003. A further extension to 2007 was carried out recently by the Georgia EPD as part of the Georgia Water Plan. **Figure 2.7** shows the incremental unimpaired flows for each ACF watershed. (This data is used for the calibration of the hydrologic watershed models to be discussed at a later section.) The monthly unimpaired flows for all ACF watersheds, except Woodruff, exhibit mild decreasing trends during the abovementioned periods. Woodruff's calculated unimpaired flow data, provided by USACE, increase about 53% on average after 1963, which suggests that there are significant errors in flow data of Woodruff watershed.

Watershed runoff is influenced by several factors (including catchment size, location, slope, soil type, vegetation, land use, and time scale). Runoff coefficient is defined as the percentage of precipitation that appears as runoff over a certain time period. **Figure 2.8** shows 12-month moving average runoff coefficient sequences and their linear trends. Except for Woodruff, all watersheds show decreasing trends over the observed periods from 1939 to 2003. **Figure 2.9** shows the long term runoff coefficient for each ACF sub-basin, computed by dividing the average incremental unimpaired flow values by the corresponding average precipitation. The figure shows that the runoff coefficient decreases from north to south. However, for Woodruff and Apalachicola, the runoff coefficients are abnormally high compared to the other watersheds. These are mainly due to groundwater recharge in this region.

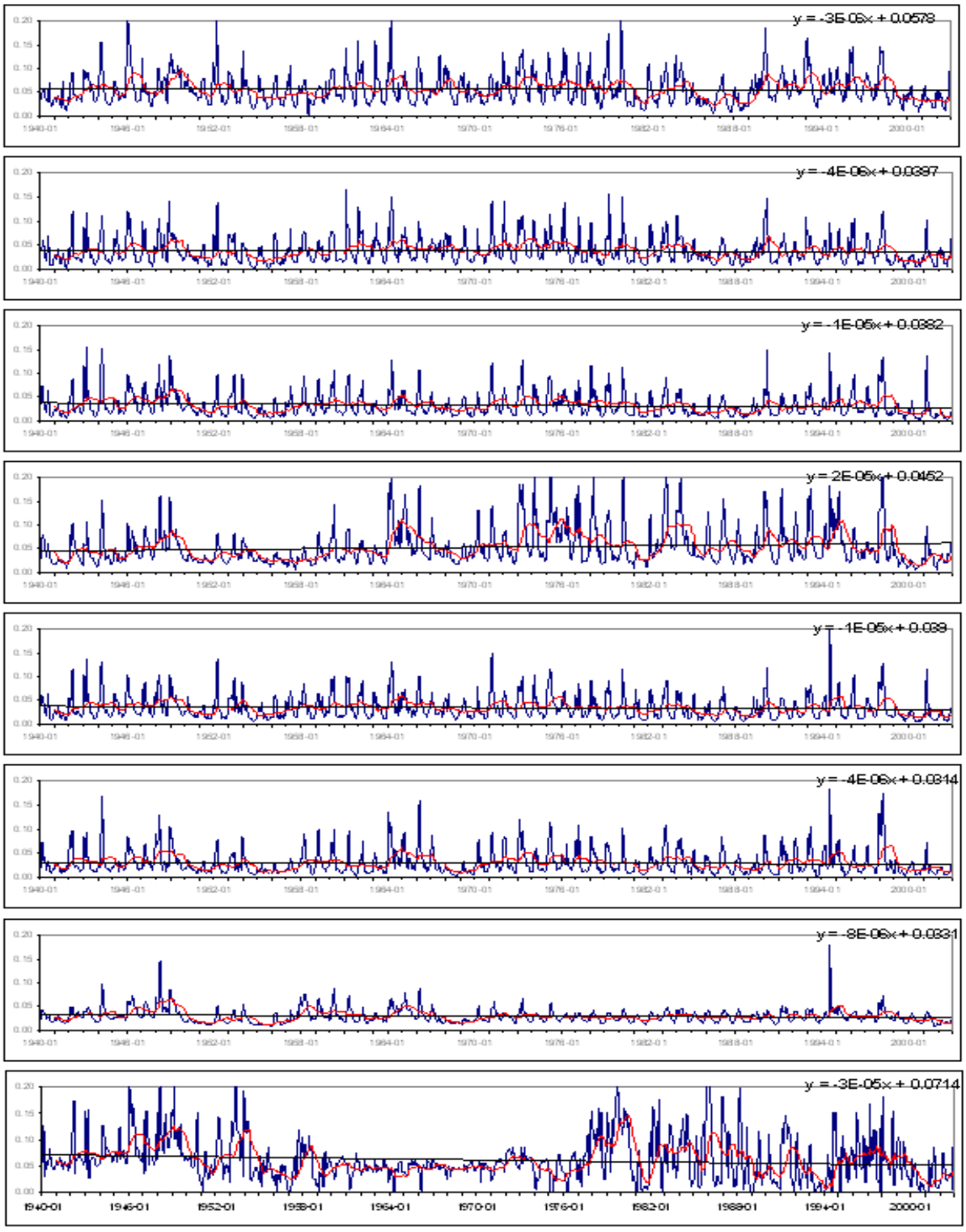

Figure 2.7: Monthly Flow Sequences for ACF Sub-basins: Buford, West Point, W.F. George, Woodruff, Montezuma, Albany, and Bainbridge (from top to bottom).

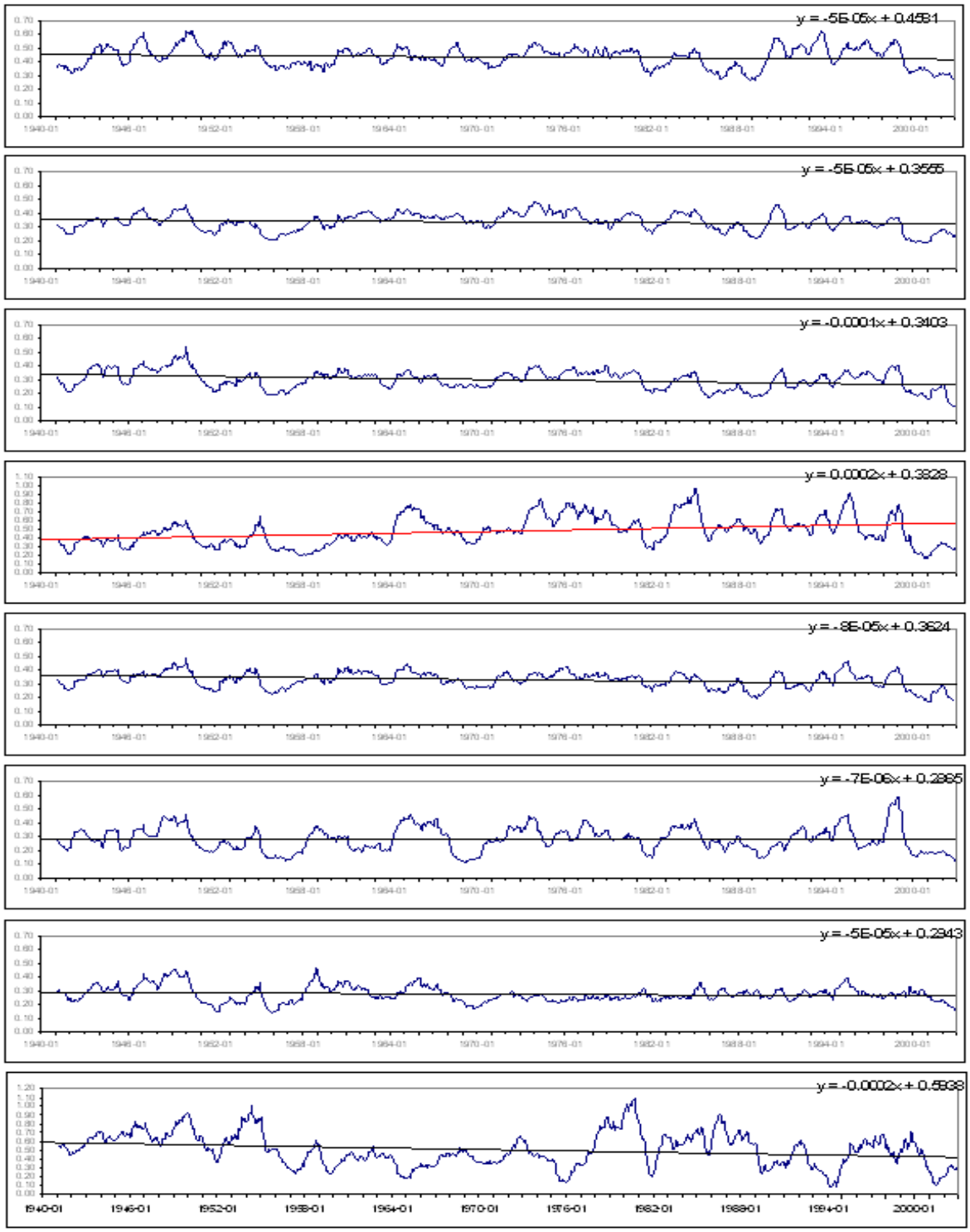

Figure 2.8: Monthly Runoff Coefficients for ACF Sub-basins: (From top to bottom) Buford, West Point, George, Woodruff, Montezuma, Albany, Bainbridge, and Apalachicola.

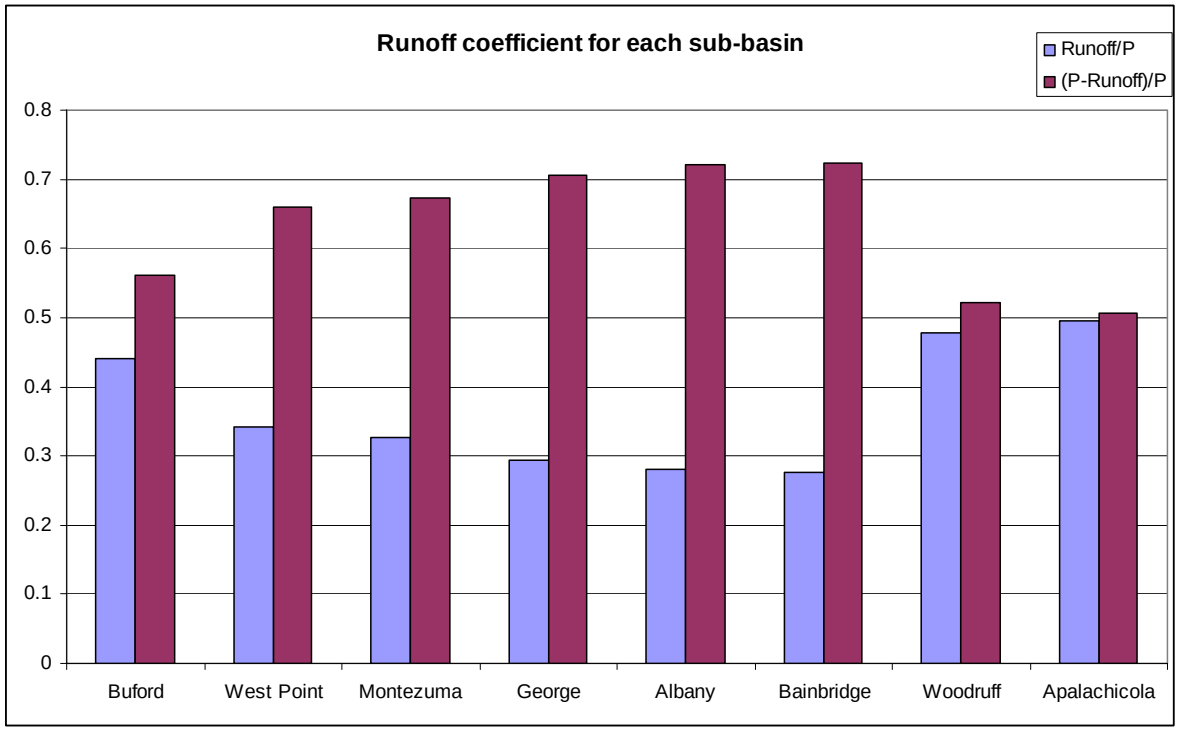

Figure 2.9: Average Runoff Coefficient by ACF Sub-basin.

2.2.4 Groundwater

Groundwater is a substantial water resource especially for southern Georgia, where the agriculture irrigations rely heavily on groundwater storages. The fall line runs across Georgia and ACF basin northeastward from Columbus to Augusta. It separates Upper Coastal Plain sedimentary rocks to the south from Piedmont crystalline rocks to the north. This leads to a clear separation of groundwater systems between north and south part of Georgia.

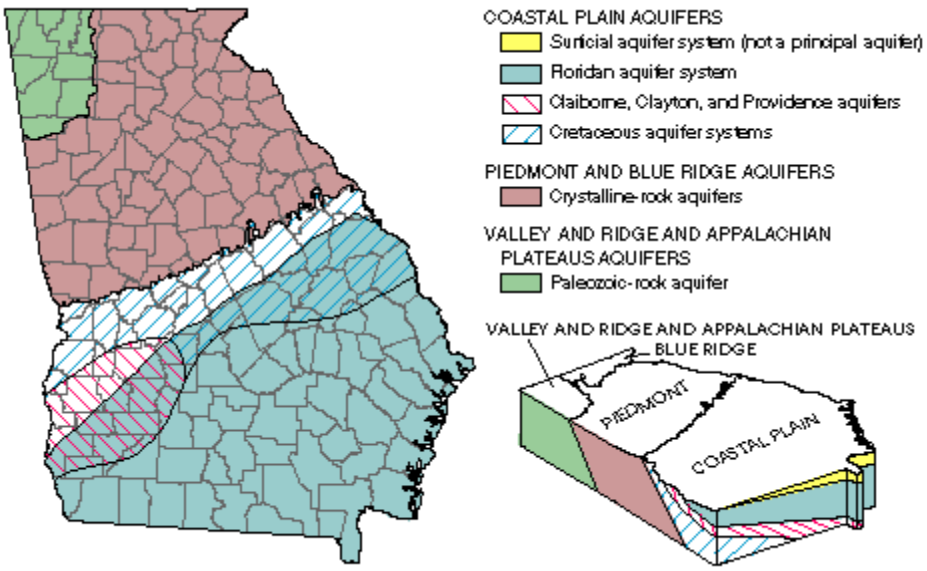

Figure 2.10: Principal Aquifers, Areas of Use, and Physiographic Provinces

Groundwater storage in the Blue Ridge and Piedmont regions is limited by shallow depth to bedrock and limited porosity in the bedrock. Most groundwater is stored in the saprolite and takes only a few months on average to reach the nearest stream. In the Coastal Plain, groundwater is more readily available because the bedrock can store more water.

- The Upper Floridan Aquifers underline most of south Georgia. In most places, the Upper Floridan Aquifer is confined by clay layers and it is shallow and productive. In the lower Flint River basin in south Georgia, the aquifer is semiconfined, and it is primarily used for agricultural pumping.
- The Claiborne and Cretaceous Aquifers in south Georgia consist of sands and gravels deposited on ancient beaches and are not as productive as the Upper Floridan Aquifers.
- The Valley and Ridge (Paleozoic Rock) Aquifers consist of limestones underlying the valleys. These aquifers are generally very productive.

- The Piedmont and Blue Ridge Aquifers are crystalline rock aquifers and they consist of bedrock overlain by unconsolidated material called regolith. Groundwater can be obtained from either regolith or fractures in the rock, with high yield.

The interaction between the surface and the groundwater in the basin is incorporated in the hydrologic model presented in Chapter 4.

2.3 Land Uses, Water Uses, and Challenges

2.3.1 Land Cover and Use

The land cover and land use of the ACF watersheds is constantly being modified due to the rapidly increasing population and economy.

The Georgia Land Use Trends (GLUT) project, completed by the Natural Resources Spatial Analysis Laboratory, University of Georgia, provides higher resolution historical land cover maps for Georgia (Kramer, Conroy, et al., 2004). The maps were produced from Landsat TM imagery with a spatial resolution of 30x20m. The following land cover types are distinguished for 1974, 1985, 1991 and 2005:

- Beaches/Dunes/Mud
- Quarries/Strip Mines/Rock Outcrops
- Open Water
- Low Intensity Urban
- High Intensity Urban
- Clearcut/Sparse
- Deciduous Forest
- Evergreen Forest
- Mixed Forest

- Row Crops/Pasture
- Forested Wetland (salt water)
- Frorested Wetland (freshwater)
- Non-forested Wetland

Table 2.3 shows the percentages of the above land use types aggregated into seven ACF sub-basins within the state of Georgia. The high and low intensity urban percentages increase from 1974 consistently for all sub-basins and almost doubled from 1991 to 2005. At the same time, the forest and wetland percentages have decreased. The percentage of clear cut area also shows an increasing trend for most sub-basins, with the headwater sub-basins (Buford, West Point, and Montezuma) changing the most.

Table 2.3: Land Use Percentages for the ACF Sub-basins for 1974, 1985, 1991 and 2005

1974												
Watershed	BEACH/DUNES/ MUD	OPEN WATER	LOW; URBAN	HIGH; URBAN	CLEAR CUT	ROCK OUTCROP	FOREST (DECIDUOUS)	FOREST (EVERGREEN)	FOREST (MIXED)	ROW CROP	WETLAND (FORESTED)	WETLAND (NON-FORESTED)
BUFORD	0.0007	0.0534	0.0447	0.0049	0.0186	0.0001	0.5268	0.1881	0.0208	0.1381	0.0039	0.0000
WEST POINT	0.0000	0.0064	0.0899	0.0235	0.0414	0.0005	0.3856	0.2444	0.0105	0.1591	0.0384	0.0003
MONTEZUMA	0.0000	0.0054	0.0325	0.0071	0.0352	0.0012	0.3273	0.2603	0.0298	0.2031	0.0981	0.0001
GEORGE	0.0002	0.0225	0.0282	0.0040	0.0408	0.0001	0.3297	0.3304	0.0457	0.1312	0.0670	0.0001
ALBANY	0.0000	0.0075	0.0199	0.0022	0.0375	0.0005	0.1154	0.2045	0.0363	0.4514	0.1244	0.0003
BAINBRIDGE	0.0000	0.0031	0.0226	0.0028	0.0273	0.0002	0.0702	0.2048	0.0257	0.4987	0.1434	0.0012
WOODRUFF	0.0000	0.0262	0.0167	0.0012	0.0190	0.0000	0.0787	0.1938	0.0147	0.5351	0.1141	0.0004
1985												
Watershed	BEACH/DUNES/ MUD	OPEN WATER	LOW; URBAN	HIGH; URBAN	CLEAR CUT	ROCK OUTCROP	FOREST (DECIDUOUS)	FOREST (EVERGREEN)	FOREST (MIXED)	ROW CROP	WETLAND (FORESTED)	WETLAND (NON-FORESTED)
BUFORD	0.0006	0.0559	0.0539	0.0061	0.0156	0.0002	0.5390	0.1448	0.0244	0.1552	0.0043	0.0000
WEST POINT	0.0000	0.0190	0.1417	0.0294	0.0778	0.0007	0.3149	0.2225	0.0283	0.1301	0.0355	0.0001
MONTEZUMA	0.0000	0.0049	0.0420	0.0083	0.0935	0.0017	0.3000	0.2169	0.0381	0.1933	0.1013	0.0000
GEORGE	0.0001	0.0241	0.0370	0.0048	0.0917	0.0002	0.2677	0.3413	0.0569	0.1009	0.0752	0.0000
ALBANY	0.0000	0.0083	0.0231	0.0026	0.0630	0.0003	0.0885	0.2367	0.0170	0.4303	0.1297	0.0004
BAINBRIDGE	0.0000	0.0042	0.0263	0.0034	0.0470	0.0000	0.0495	0.2418	0.0152	0.4702	0.1410	0.0016
WOODRUFF	0.0002	0.0245	0.0189	0.0019	0.0567	0.0000	0.0528	0.2294	0.0116	0.4842	0.1193	0.0004
1991												
Watershed	BEACH/DUNES/ MUD	OPEN WATER	LOW; URBAN	HIGH; URBAN	CLEAR CUT	ROCK OUTCROP	FOREST (DECIDUOUS)	FOREST (EVERGREEN)	FOREST (MIXED)	ROW CROP	WETLAND (FORESTED)	WETLAND (NON-FORESTED)
BUFORD	0.0009	0.0620	0.0582	0.0060	0.0205	0.0005	0.5052	0.1682	0.0260	0.1490	0.0036	0.0000
WEST POINT	0.0007	0.0255	0.1519	0.0336	0.0539	0.0011	0.2972	0.2704	0.0235	0.1091	0.0331	0.0001
MONTEZUMA	0.0005	0.0093	0.0508	0.0092	0.1243	0.0013	0.2200	0.2825	0.0310	0.1767	0.0940	0.0001
GEORGE	0.0004	0.0261	0.0399	0.0060	0.1131	0.0006	0.2677	0.3393	0.0517	0.0865	0.0679	0.0006
ALBANY	0.0000	0.0108	0.0274	0.0025	0.0838	0.0004	0.1239	0.2119	0.0220	0.3834	0.1330	0.0007
BAINBRIDGE	0.0001	0.0074	0.0313	0.0036	0.0757	0.0001	0.0880	0.2015	0.0309	0.4156	0.1430	0.0027
WOODRUFF	0.0003	0.0289	0.0235	0.0018	0.0893	0.0000	0.0753	0.1963	0.0206	0.4464	0.1140	0.0036
2005												
Watershed	BEACH/DUNES/ MUD	OPEN WATER	LOW; URBAN	HIGH; URBAN	CLEAR CUT	ROCK OUTCROP	FOREST (DECIDUOUS)	FOREST (EVERGREEN)	FOREST (MIXED)	ROW CROP	WETLAND (FORESTED)	WETLAND (NON-FORESTED)
BUFORD	0.0000	0.0641	0.1114	0.0134	0.0393	0.0006	0.4648	0.1006	0.0563	0.1463	0.0030	0.0001
WEST POINT	0.0000	0.0270	0.2263	0.0657	0.0851	0.0016	0.2272	0.2203	0.0099	0.1038	0.0331	0.0000
MONTEZUMA	0.0001	0.0118	0.0851	0.0183	0.0894	0.0017	0.1907	0.2974	0.0339	0.1854	0.0858	0.0004
GEORGE	0.0000	0.0274	0.0645	0.0120	0.0994	0.0009	0.2498	0.2903	0.0874	0.1094	0.0585	0.0004
ALBANY	0.0001	0.0134	0.0484	0.0040	0.0823	0.0005	0.1037	0.2131	0.0439	0.3872	0.1011	0.0023
BAINBRIDGE	0.0000	0.0095	0.0538	0.0056	0.0489	0.0002	0.0932	0.2012	0.0456	0.4251	0.1145	0.0025
WOODRUFF	0.0000	0.0313	0.0417	0.0031	0.0391	0.0000	0.0905	0.1882	0.0606	0.4465	0.0977	0.0014

2.3.2 Water Uses

The principle ACF **water uses** include:

Irrigation: Irrigation is a major use in the southern ACF watersheds and is estimated at 533.28 million gallons per day (mgd) from May to October, and 70.32 mgd from November to April.

Municipal and Industrial Water Supply: Municipal and industrial uses approximately require 294.82 mgd from May to October, and 194.31 mgd from November to April. Most of the municipal water use takes place in the upper Chattahoochee basin.

Thermoelectric: The ACF river basin houses six fossil fuel and one nuclear plants. The average cooling water requirements for these plants amount to 129.63 mgd from May to October and 98.73 mgd from November to April. Most of these withdrawals return to the river.

Navigation: The ACF River System is navigable from the mouth of the Apalachicola in Florida up to Columbus, Georgia, and is used for the transportation of construction materials. The economic significance of this activity is gradually waning, but it continues to require the maintenance of navigation drafts (and sustained reservoir releases) for certain weeks in late summer. Channel and port navigability is facilitated by annual dredging operations (U.S. Army Corps of Engineers—USACE).

Hydropower: The ACF river basin includes four federal and five private hydropower facilities. The energy and power from the federal projects (with a total installed capacity of 368.7 MW) is marketed to cooperatives and municipalities by the South East Power Administration (SEPA) as dependable capacity and primary energy. The private facilities are owned and operated by Southern Services and have 276.1 MW total installed capacity.

River and Estuary Ecology: The basin sustains rich ecosystems, the most important of which is the ecosystem of the Apalachicola Bay. This ecosystem presently supports 131 freshwater and estuarine fish species and serves as a nursery for many significant Gulf of Mexico species (e.g., the Gulf sturgeon, oysters, etc.). River and estuary ecology depend on historical hydrological conditions under which they have evolved. Such conditions include magnitude, variability, frequency, and persistence of floods, droughts, and normal periods. The biological productivity of the bay is strongly influenced by the amount, timing, and duration of the freshwater inflow. The Apalachicola River provides the essential nutrients that form the base for the food web in the Bay. Any alteration of flow in the watershed disrupts the nutrient inputs of the ecosystem. Extreme hydrologic activity associated with hurricanes (e.g., hurricane Elena in 1985) also has severe effects on oyster reefs in the Apalachicola Bay. However, developing a comprehensive understanding of the linkages between river hydrology, estuarine salinity, and fish ecology is an on-going effort. Such understanding is critical for the development of a sound instream flow policy for ecosystem protection and sustainability. As an interim policy in Georgia, the monthly 7Q10 flow statistic (representing the minimum seven day average flow with a return period of 10 years) is used as a minimum instream flow requirement. At the Chattahoochee gage in Florida, the minimum monthly 7Q10 statistic occurs in October and amounts to 5,000 cfs.

Recreation: The ACF lakes are major recreation sites generating significant economic benefits for the local economy. According to USACE, in 2003 Lake Lanier registered 7,666,160 visitor days for a total economic benefit of 146.59 million dollars. In the same year, Lake West Point registered 2,264,600 visitor days and 37.47 million dollars. Apalachicola Bay is a major eco-tourism attraction in Florida. Florida's tourism is valued at $73 billion per year.

The percent return of the surface water withdrawals varies by water use, with thermoelectric withdrawals returning more than 90% and irrigation less than 10%. The ACF groundwater aquifers are primarily pumped for irrigation but also for domestic and industrial water supply (e.g., pulp and paper industries in the lower ACF). Groundwater provides approximately 62% of the region's irrigation water.

2.3.3 Water Resources Management Challenges

Despite its many environmental and economic benefits, the ACF river basin faces serious **water resources challenges**:

Rapid population and demand growth: Georgia's population is 8.5 million people and growing at nearly 25% (or 1.5-2 million people) every 10 years. The most rapid population growth occurs in Atlanta and surrounding districts where more than five million Georgians currently reside. Atlanta's average water demand (now approximately 0.8 bgd) rises by 0.2 – 0.25 bgd per decade, while its water supply depends on a single source: the 1,040 square mile Lake Lanier watershed, with the distinction of being the *smallest* watershed supplying a major US metropolitan area. Current water supplies are estimated at 0.933 bgd and are expected to last until 2020. The urgency of this fast approaching date is anxiously felt in the Atlanta Metro Area and at the Georgia Governor's Office. Among the water augmentation strategies being considered are water conservation, reclamation, inter-basin transfer, and construction of new reservoirs, but none has emerged as a long term viable solution. Nearly half of Atlanta's water withdrawals return to the Chattahoochee River through a combined sewage system. However, return flow carries various pollutants, in spite of the applied treatment. Impaired water quality remains a serious concern for the downstream City of LaGrange, West Point Lake, and other water users to the south.

Agricultural and Irrigation Expansion: Georgia and the southeast US experienced a very rapid growth in irrigated acreage from the mid seventies through the early eighties. This expansion occurred primarily in the south where approximately 1.5 million acres are currently under irrigation. Agriculture is a key component of the region's economy, with top ranked national production in peanuts, cotton, corn, soybeans, and nursery products. However, irrigation is stressing surface and groundwater resources. The impacts are particularly intense during droughts when irrigation quadruples relative to a normal year.

Climate Variability and Droughts: Severe droughts occur in Georgia and the southeast US every 8 to 12 years and last for 2 to 4 years. Most notable recent droughts took place in 1980-1981, 1986-1988, 1998-2002, and 2007-2009, with devastating economic consequences for several industries. Severe droughts reduce natural inflow (and water supplies) by as much as 50% of normal. Thus, while on average, Georgia's water resources are abundant, water demands in several regions have become unsustainable during droughts.

Climate Change: **C**limate change is only beginning to draw the attention of planning and management agencies. Mitigation strategies and adaptive management are not currently considered.

Legal and Institutional Shortcomings: These mainly fall under the following categories:

- Conflicts between federal laws (e.g., Endangered Species Act) and state priorities;
- Lack of coordination among state and federal agencies;
- Failure to agree on an ACF water sharing compact among Alabama, Florida, and Georgia, despite more than two-decades of negotiations;
- Outdated federal project authorizations and water control procedures; and
- Ineffective stakeholder participation in planning and management processes.

Chapter 3

Downscaling Procedures and Climate Assessments

3.1 IPCC Climate Scenarios

The Intergovernmental Panel on Climate Change (IPCC) was set up jointly by the World Meteorological Organization and the United Nations Environment Program to promote the scientific understanding of climate change causes and impacts (IPCC, 2007). To date, IPCC has produced four assessment reports (in 1990, 1995, 2001 and 2007) which are referenced widely by scientists in a wide range of disciplines.

The IPCC reports are based on the results and findings of many climate research programs and experiments. One such program is the World Climate Research Program (WCRP) Coupled Model Intercomparison Project Phase Three (CMIP3), carried out under the Program for Climate Model Diagnosis and Intercomparison (PCMDI). This program produced an array of climate change computational experiments under past, projected, or idealized CO_2 emission scenarios, three of which are used in this study (**Table 3.1**).

The first experiment, 20CM3, represents the 20th century historical emission scenarios, and serves as a baseline case illustrating the way in which climate models simulate the historical climate. The other two experiments pertain to projected climate changes in the 21st century and are a subset of the IPCC Special Report on Emission Scenarios (SRES; Nakićenović and Swart, 2000). These experiments are the SRESA1B and SRESA2, respectively based on medium and high emission scenarios, as described below (Nakicenovic and Swart, 2000):

*"The **A1** storyline and scenario family describes a future world of very rapid economic growth, global population that peaks in mid-century and declines thereafter, and the rapid introduction of new and more efficient technologies. Major underlying themes are convergence*

among regions, capacity building, and increased cultural and social interactions, with a substantial reduction in regional differences in per capita income. ***A1B*** *scenarios represent a balance across all energy sources.*

The ***A2*** *storyline and scenario family describes a very heterogeneous world. The underlying theme is self-reliance and preservation of local identities. Fertility patterns across regions converge very slowly, which results in continuously increasing global population. Economic development is primarily regionally oriented and per capita economic growth and technological changes are more fragmented and slower than in other storylines."*

Table 3.1: PCMDI Experiments used in this study

Experiment Name	**Monthly Data**	**Features**
20C3M Experiment (climate of the 20th Century)	~1850 – present	Baseline run (historical emissions).
SRES A2 Experiment	present – 2100	Use the end of the 20C3M run as its initial condition.
SRES A1B Experiment (720 ppm stabilization)	present – 2200 or present– (2300)	Impose SRES A1B conditions, initialize with conditions from the end of the 20C3M simulation, and run to 2100. After 2100, hold concentrations fixed and continue the simulation to 2200. Extend one member of the ensemble for an additional 100 years (to 2300), continuing to hold concentrations fixed.

General circulation models (GCMs) are scientific tools used to assess the future global climate response associated with various greenhouse gas emission scenarios (IPCC WGI, 2007). The GCMs represent (through a large system of partial differential equations) the coupled atmospheric and oceanic processes currently understood to govern the Earth's climate. Climate scenarios are generated by the numerical integration of the underlying equations over space and time. **Table 3.2** lists 13 different GCMs, selected scenarios from which (corresponding to emission scenarios 20CM3, SRESA2, and SRESA1B) are utilized in this study. In this table,

under atmospheric resolution, T is the horizontal resolution and L is the vertical resolution in numbers of vertical layers. Oceanic resolution is provided in degrees (horizontal resolution) and numbers of vertical layers (L: vertical resolution). The latter is not reported for all models.

Table 3.2: Summary of GCMs used in this study

Model	Contributor	Atm. Resolution	Ocean Resolution
BCCR-BCM2.0, Norway	Bjerknes Centre for Climate Research	T63L31	1.5 ^{o} x1.5 ^{o}, L31
CGCM3.1(T63), Canada	Canadian Centre for Climate Modeling and Analysis	T63L31	1.4 ^{o} x0.9 ^{o}, L29
CNRM-CM3, France	Centre National de Recherches Meteorologiques	T63L45	2.0 ^{o} x1.2 ^{o}
CSIRO-Mk3.5, Australia	CSIRO, Australia	T63L18	1.875^{o} x0.84^{o}
ECHAM5/MPI-OM, Germany	Max Planck Institute for Meteorology	T63L31	1.5 ^{o} x1.5 ^{o}, L40
GFDL-CM2.1, USA	Geophysical Fluid Dynamics Laboratory, NOAA	2.5^{o}x2.5^{o}	1^{o} x1^{o}
GISS-AOM, USA	NASA Goddard Institute for Space Studies	4^{o} x3^{o}, 12L	4^{o} x3^{o}, L16
MIROC3.2(hires), Japan	CCSR/NIES/FRCGC, Japan	T105L56	0.28^{o} x0.19^{o}, L47
CCSM3, USA	National Center for Atmospheric Research (NCAR),	T85L26	1.125 ^{o} x(0.27^{o} - 1.0^{o}) , L40
PCM, USA	NCAR, NSF, DOE, NASA, NOAA	T42L26	1.125^{o} x0.469^{o} , L40
UKMO-HadCM3, UK	Hadley Centre for Climate Prediction and Research	2.75^{o} x2.75^{o}	1.25^{o} x1.25^{o}
MIUB ECHO-G, Germany/Korea	Meteorological Institute of the University of Bonn	T30L19	T42
INM-CM3.0, Russia	Institute for Numerical Mathematics	N.A.	N.A.

3.2 Historical and GCM Data Sources

Historical climatic data are used to assess and adjust GCM outputs, to establish regional spatial relationships, and to calibrate hydrologic models. The historical data are derived from three

observational climatic datasets: *(1)* CRU TS2.0 monthly dataset with resolution of 1/2 degree from 1901 to 2002 (Mitchell et al., 2005; http://www.cru.uea.ac.uk/cru/data/); *(2)* monthly and daily gridded meteorological data at 1/8 degree spatial resolution from 1950 to 1999 (Maurer et al., 2002; http://www.engr.scu.edu/~emaurer/data.shtml); and *(3)* PRISM monthly dataset at 4km spatial resolution from 1901 to 2009 (Daly, 1994; http://www.prism.oregonstate.edu/).

Monthly temperature and precipitation data of all GCM models were downloaded from the Earth System Grid (http://www.earthsystemgrid.org/). The Earth System Grid (ESG) acts as a data distribution center for large scale data and analysis results, including IPCC experiment outputs.

In general, GCMs were designed to run on global scales (**Figure 3.1**, blue lines) at relatively low spatial resolutions (~100x100 km^2 to ~250x250 km^2). However, the observational grids usually have much higher spatial resolution. A comparison of GCM and observational data resolutions is shown in **Figure 3.1**, where the CGCM3.1 (Canadian Centre for Climate Modeling and Analysis) grid is superimposed on the observational data grid over the southeastern US.

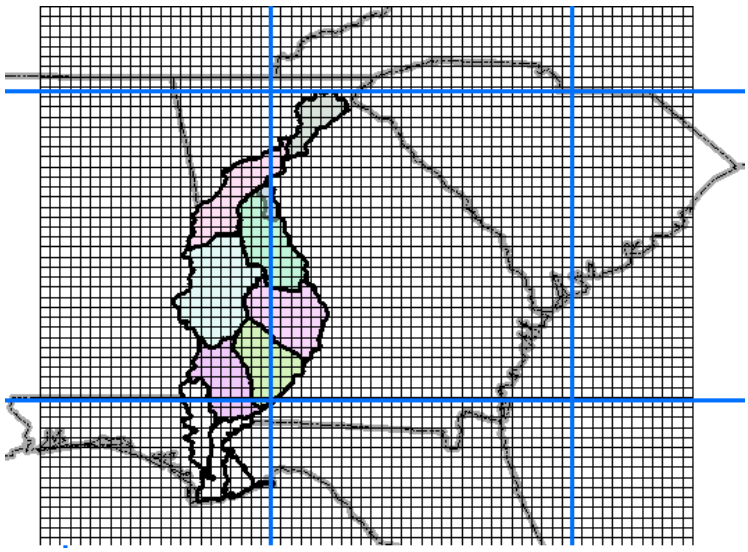

Figure 3.1: Spatial Resolutions of the Canadian GCM3.1 (blue) and Observational Data Sets (OBS—black) over the Southeastern US

Because of their coarse spatial resolution, GCM outputs are usually inadequate to capture the spatial variability at regional or local scales necessary for hydrological applications. Xu (1999) shows that predicting runoff directly from GCM outputs is over-simplified and ignores the lateral transfer of water between grid cells within the land phase. This conclusion is corroborated by the large uncertainties arising from using different models driven by the same scenarios (Tebaldi, 2005; Mitchell and Hulme, 1999; Mujumdar and Ghosh, 2008). The purpose of downscaling procedures to be discussed next is to construct climate scenarios at more application-relevant spatial (and temporal) scales.

3.3 Downscaling Methods

3.3.1 Literature Review

Downscaling methods can be distinguished in two main categories: *(1)* dynamic downscaling and *(2)* statistical downscaling methods. Fowler and Blenkinsop (2007), Wilby and Wigley (1997), and Xu (1999) provide thorough reviews on many existing downscaling methods.

In dynamic downscaling, a regional climate model (RCM) is used to model the target region at finer scales bounded by larger GCM nodes (Miller et al., 1999; Xue et al., 2007). The results of RCMs still depend on the validity and skill of the overriding GCM. Mearns et al. (2003a) outlined the advantages and disadvantages of using RCMs and provided guidance on the use of their outputs. Generally, RCMs provide high resolution climatic fields spatially and globally consistent with GCM scenarios. However, these results inherit the biases of the driving global models and are computationally expensive.

The North American Regional Climate Change Assessment Program (NARCCAP) is among the most notable dynamic downscaling research efforts and provides valuable online datasets (http://www.narccap.ucar.edu/) This program investigates the uncertainties of regional scale projections of GCM outputs, and generates high resolution scenarios for regional climate impact assessments. Although NARCCAP provides a very important source of dynamically downscaled regional climatic scenarios, there are only a few simulations available to date. These simulations correspond only to SRES A2 emissions scenario and are generated for selected time horizons (1971-2000; 2041-2070) due to their heavy computational requirements. Regarding the latter, it takes approximately 36 hours to complete a 30-day simulation using a RCM (e.g., MM5 or WRF) over an area of 90,000 km^2 with 30 x 30 km spatial resolution on a 2.1GHz dual core personal computer. Thus, the currently available results are not sufficient for comprehensive climate change impact assessments, but are used in this study to compare the skill of statistical versus dynamic downscaling methods. Lastly, it is unclear whether the uncertainties surrounding *dynamic* downscaling methods are not comparable to those of the more computationally efficient *statistical* downscaling methods.

Statistical downscaling does not depend on GCM boundary conditions and can be used to downscale climatic variables without the full set of climatic fields at the coarse level. Statistical downscaling is based on relationships between low resolution GCM outputs and associated higher resolution observations over the same historical period. These statistical relationships are then used to infer the observations on finer grids at future times when only GCM outputs are available. Examples of statistical downscaling methods include changing factor methods (Beniston et al., 2003), regression methods (Huth, 1999), weather typing schemes (Vrac, 2007),

weather generators (Wilks and Wilby, 1999), bias correction and spatial disaggregation (BCSD; Wood et al., 2004), and constructed analogues (CA, Hidalgo et al., 2008; van den Dool, 1994).

Wood et al. (2004) proposed a two-step statistical downscaling method to address bias correction and spatial disaggregation (BCSD). In the first step, GCM biases are adjusted through a quantile mapping technique individually for temperature and precipitation. The spatial disaggregation step translates adjusted GCM data on climate model resolutions to a basin-relevant resolution (observational resolution) by using interpolated spatial factors. The spatial interpolation method is a modified version of inverse-distance-squared interpolation developed by Shepard (1984). As will be seen, such interpolation tends to generate homogenous factor maps.

BCSD is a very efficient statistical downscaling technique for climate change assessments. One BCSD disadvantage, however, is that it generates more homogenous downscaled fields than the observed fields. This results from the use of cell-by-cell spatial interpolation factors, and marginal, not joint, variable distributions in the quantile mapping process. Furthermore, while the temperature shift-removing procedure enables the bias-correction step without extrapolation, it also makes the assumption that future temperature distributions remain similar to those of the historical run. However, the extreme future temperature distributions (either high or low) are most likely to change outside the historical range.

Hidalgo et al. (2008) proposed the constructed analogues (CA) technique. This method essentially makes no bias corrections, but rather relates model-simulated variables to observed variables, using relationships established during historical periods when observations are available. These relationships are established through multiple regression analysis. Maurer and

Hidalgo (2008) stated that the CA method may need a bias correction step before deriving the regression relationships. Furthermore, long term observed historical climatic fields on higher resolution grids are required to build statistical relationships with GCM outputs. Such observations are not readily available.

The performance of downscaling methods vary across seasons, stations, and indices (Fowler and Blenkinsop, 2007). Many researchers have concluded that the accuracy of statistical downscaling methods has a geographical and seasonal component (Huth, 1999).

Overall, downscaled sequences must meet several criteria to be useful in regional water resources assessments:

- First, the downscaled sequences should be consistent with historical observations.
- Second, the downscaled sequences should capture climatic mean and variability trends.
- Third, spatial and temporal correlations and interdependencies between the atmospheric fields that largely drive hydrological processes should be represented.
- Lastly, to ensure that hydrological assessments at different temporal scales (e.g., annually, monthly, and daily) using the same downscaled products are consistent, the smoothness of these products across these time scales should be ensured.

These criteria formed the guiding principles for a new statistical downscaling method discussed next.

3.3.2 Joint Variable Spatial Downscaling (JVSD) Method

JVSD aims to produce high resolution gridded hydrological datasets suitable for regional watershed modeling and assessments. The method is applicable to multiple atmospheric fields, but it is presented herein for the downscaling of GCM precipitation and temperature, as these two variables represent the principle atmospheric forcing that drives monthly watershed response.

JVSD conceptually follows the general approach introduced by Wood et al., 2004 (Bias Correction and Spatial Downscaling—BCSD), with several new features. First, instead of removing and replacing the variable long term trends before and after the bias correction step, JVSD uses a differencing process to create stationary time series and joint frequency distributions (for temperature and precipitation) between GCM control and future runs. Bias correction is then based on quantile-to-quantile mapping of these stationary frequency distributions. The bias corrected sequences are recovered by inverting the differenced series. For spatial disaggregation, JVSD also uses the historical analogue approach. However, historical analogues are identified simultaneously for all atmospheric fields being downscaled, and for all GCM cells that cover the assessment region. This feature ensures the temporal and spatial coherence of the downscaled climatic fields. Finally, a technique to expand the range of the historical analogues is implemented to handle future data values that fall outside the historical range.

JVSD is implemented as shown in **Figure 3.2** as a two step process: bias correction and spatial downscaling

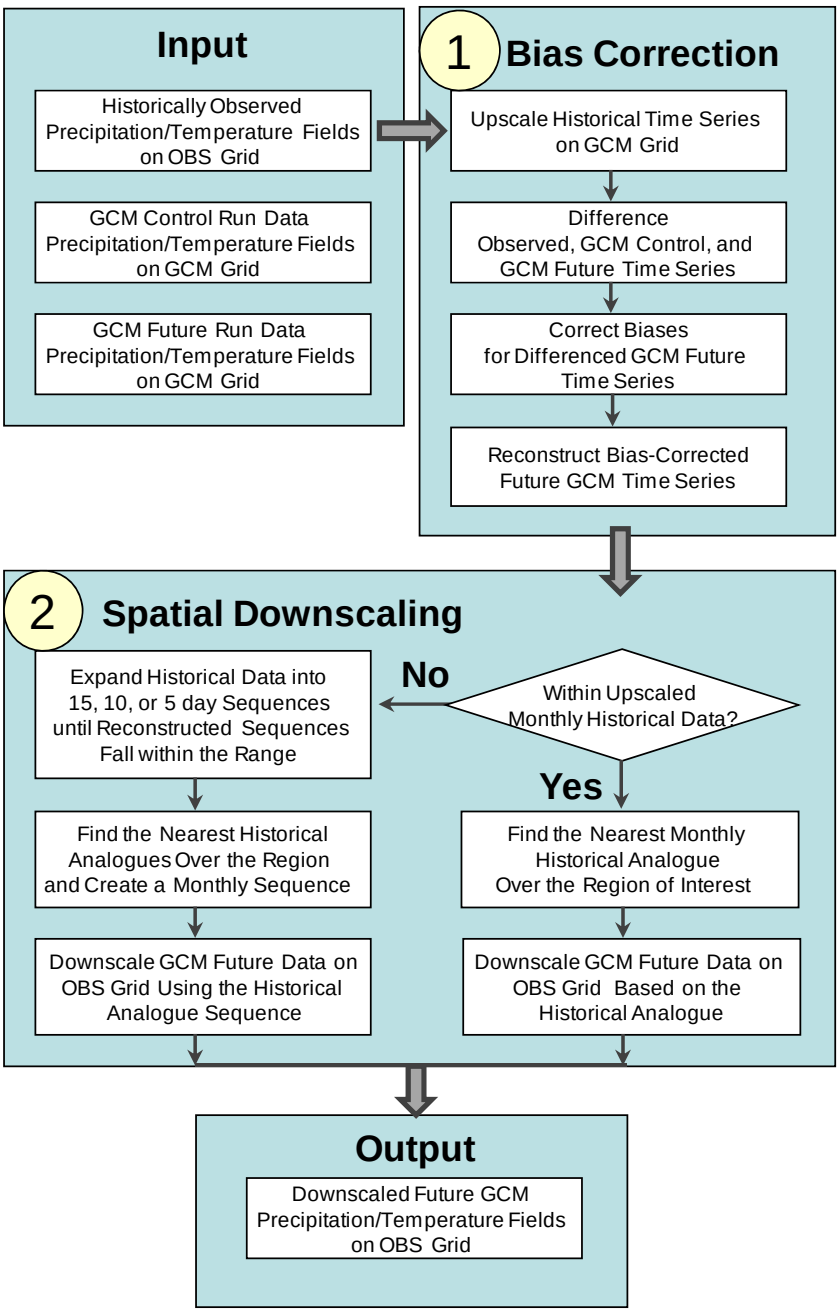

Figure 3.2: Joint Variable Spatial Downscaling (JVSD) Method Flow Chart

3.3.3 Bias Correction

GCM outputs contain significant biases that must be corrected before any meaningful assessment can be carried out. **Figure 3.3** compares the frequency distributions of GCM simulated (CGCM3.1, run1) temperature and precipitation versus observed values aggregated over the

same ACF cell for the historical period 1950-1999. Biases exist not only in the mean of these distributions but throughout the distributional range, and are uneven at different quantiles.

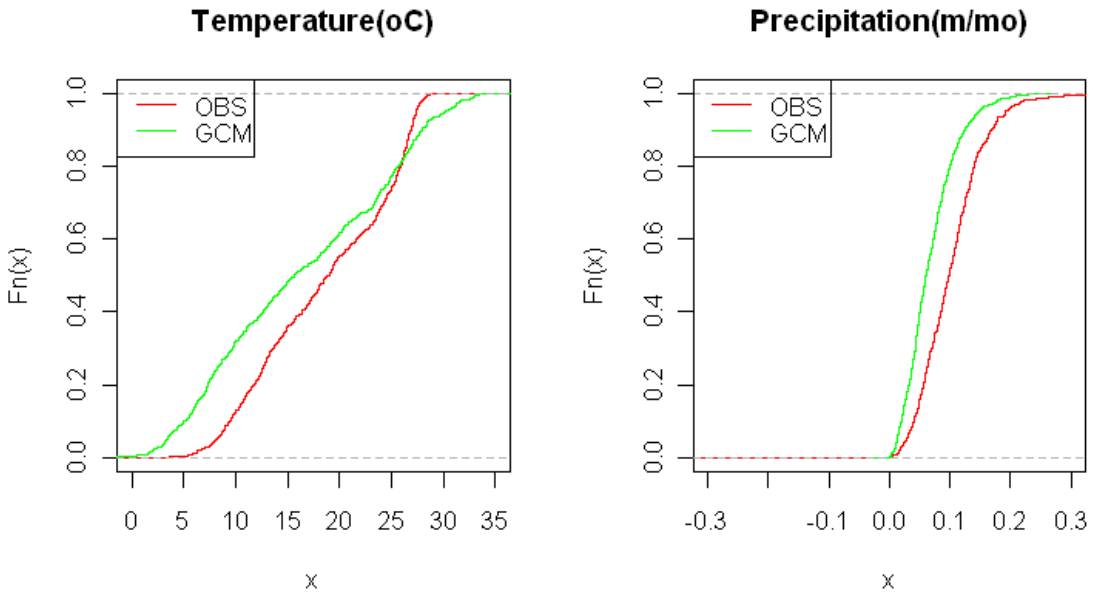

Figure 3.3: Typical Frequency Curves of GCM Simulated and Observed Variables

The JVSD bias correction process is presented using the following notation:

- TS1 and TS2: Monthly precipitation and temperature time series of GCM *future* runs on individual GCM grids:

$$TS1: \quad P\_GCM_t \quad (t = 1,2,\cdots,NF_{month})$$
$$TS2: \quad T\_GCM_t \quad (t = 1,2,\cdots,NF_{month})$$

where, NF_{month} is the length of the monthly time series.

- TS3 and TS4: Monthly precipitation and temperature time series of GCM *control* runs on individual GCM grids. GCM control runs correspond to a historical (control) time period, such as the entire 20th Century or some portion of it.

$$TS3: \quad P\_\mathrm{CON}_t \quad (t = 1,2,\cdots,\mathrm{NC}_{\mathrm{month}})$$

$$TS4: \quad T\_\mathrm{CON}_t \quad (t = 1,2,\cdots,\mathrm{NC}_{\mathrm{month}})$$

where $\mathrm{NC}_{\mathrm{month}}$ is the length of the monthly time series.

- DTS5 and DTS6: Daily *observed* precipitation and temperature time series on individual observational scale grids:

$$DTS5: \quad P\_\mathrm{OBS}_{td} \quad (td = 1,2,\cdots,\mathrm{NO}_{\mathrm{day}})$$

$$DTS6: \quad T\_\mathrm{OBS}_{td} \quad (td = 1,2,\cdots,\mathrm{NO}_{\mathrm{day}})$$

where $\mathrm{NO}_{\mathrm{day}}$ is the length of the daily observed time series.

Step 1: Upscaling

DTS5 and DTS6 are aggregated into two new monthly sequences TS5 and TS6 over the GCM spatial resolution grids. The aggregation process can be represented as shown below:

$$TS5: \quad P\_\mathrm{OBS}_t = \Delta_P^{d_t}\left(P\_\mathrm{OBS}_{td}\right)_t \quad (t = 1,2,\cdots,\mathrm{NC}_{\mathrm{month}}) \qquad (3.1a)$$

$$TS6: \quad T\_\mathrm{OBS}_t = \Delta_P^{d_t}\left(T\_\mathrm{OBS}_{td}\right)_t \quad (t = 1,2,\cdots,\mathrm{NC}_{\mathrm{month}}) \qquad (3.1b)$$

where

d_t is the number of days in month t;

P is the number of observational cells falling into a GCM cell;

Δ_P^d is the upscaling operator in space and time.

The upscaling operator Δ_P^d first performs spatial upscaling over each GCM cell and then performs temporal upscaling to monthly time scales. The *spatial* upscaling operator, $\Delta_P\left(TS_i; i \in A_P\right)$, corresponding to a GCM cell P which includes A_P observational cells, is defined by:

$$\Delta_P\left(TS_i; i \in A_P\right) = \frac{\sum_{i \in A_P}\left(TS_i\right)}{P} \qquad (3.2)$$

Other spatial aggregation schemes such as spatial interpolation and kriging (Drignei, 2009) may also be used in this step. The concept of spatial upscaling of observational fields is illustrated in **Figure 3.4**.

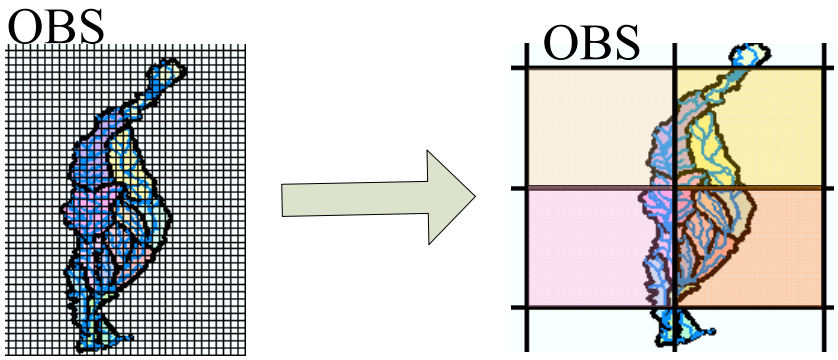

Figure 3.4: Schematic of Spatial Upscaling, From Observational Scale Grids (OBS) to GCM Scale Grids (GCM); Colored Area – Watersheds

The *temporal* upscaling operator, $\Delta^{d_t}\left(TS\right)_t$, for a month t with d_t days is defined by:

$$\Delta^{d_t}\left(TS\right)_t = \frac{\sum_{i=1}^{d_t} TS_i}{d_t} \qquad (3.3)$$

Step 2: Differencing

Differencing aims to remove seasonalities and deterministic trends, and create stationary time series. Differencing can be applied at various lags and orders. For example, a 12-month differencing process applied to the monthly time series (*TS1*, *TS2*, *TS3*, *TS4*, *TS5*, and *TS6*) on each GCM cell can be expressed as shown below:

$$TS1': \quad SP\_GCM_t = \nabla_{12}(P\_GCM_t) \quad (t = 1,2,\cdots, NF_{month})$$

$$TS2': \quad ST\_GCM_t = \nabla_{12}(T\_GCM_t) \quad (t = 1,2,\cdots, NF_{month})$$

$$TS3': \quad SP\_CON_t = \nabla_{12}(P\_CON_t) \quad (t = 1,2,\cdots, NC_{month})$$

$$TS4': \quad ST\_CON_t = \nabla_{12}(T\_CON_t) \quad (t = 1,2,\cdots, NC_{month})$$

$$TS5': \quad SP\_OBS_t = \nabla_{12}(P\_OBS_t) \quad (t = 1,2,\cdots, NC_{month})$$

$$TS6': \quad ST\_OBS_t = \nabla_{12}(T\_OBS_t) \quad (t = 1,2,\cdots, NC_{month})$$

where the differencing operator ∇_D with lag D is defined as

$$\nabla_D(TS_t) = TS_t - TS_{t-D} \tag{3.4}$$

For D = 12 months, the operator simply subtracts the series values one year apart (**Figure 3.5**). If trends persist, higher order differencing may also be used.

The effect of 12-month differencing of GCM temperature and precipitation outputs is shown on **Figure 3.6**. The top plots of this figure show contour lines of the joint empirical temperature-precipitation frequency curve of the control (CON) and future runs (from the Canadian GCM—CGCM3.1/ run1). Future runs are divided into the first 50-year period (FUT1) from 2000 to 2049, and the second 50-year period (FUT2) from 2050 to 2099. Thus, all sample sizes (i.e., CON, FUT1, and FUT2) are 50-year long. The plots support the following observations:

(1) The joint frequency distributions of temperature and precipitation are different in the control and future runs; and

(2) The relationship of the joint frequency distributions (of control versus future data) is different in the first versus the second 50-year period, indicating that the joint frequency distribution is non-stationary.

These differences and nonstationarities bias the results of all existing downscaling methods that are commonly based on quantile-to-quantile mapping of these or the associated marginal statistics.

On the other hand, the bottom two plots of **Figure 3.6** show the joint frequency distribution (of temperature and precipitation) after a 12-month differencing of the original sequences. These plots clearly show that the differenced sequences exhibit very good correspondence between control and future runs, in both future periods. Thus, the joint statistics of the 12-month differenced series are stationary and can serve as pivotal quantities for the quantile-to-quantile bias correction process. This result and conclusion holds for all 13 GCMs available through IPCC.

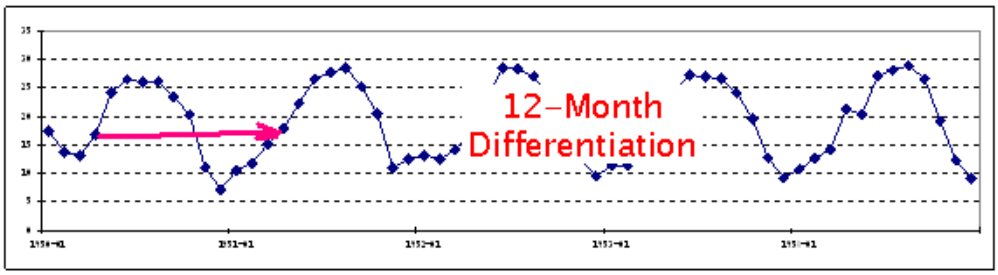

Figure 3.5: Example of Twelve-Month Differencing of the Original Time Series

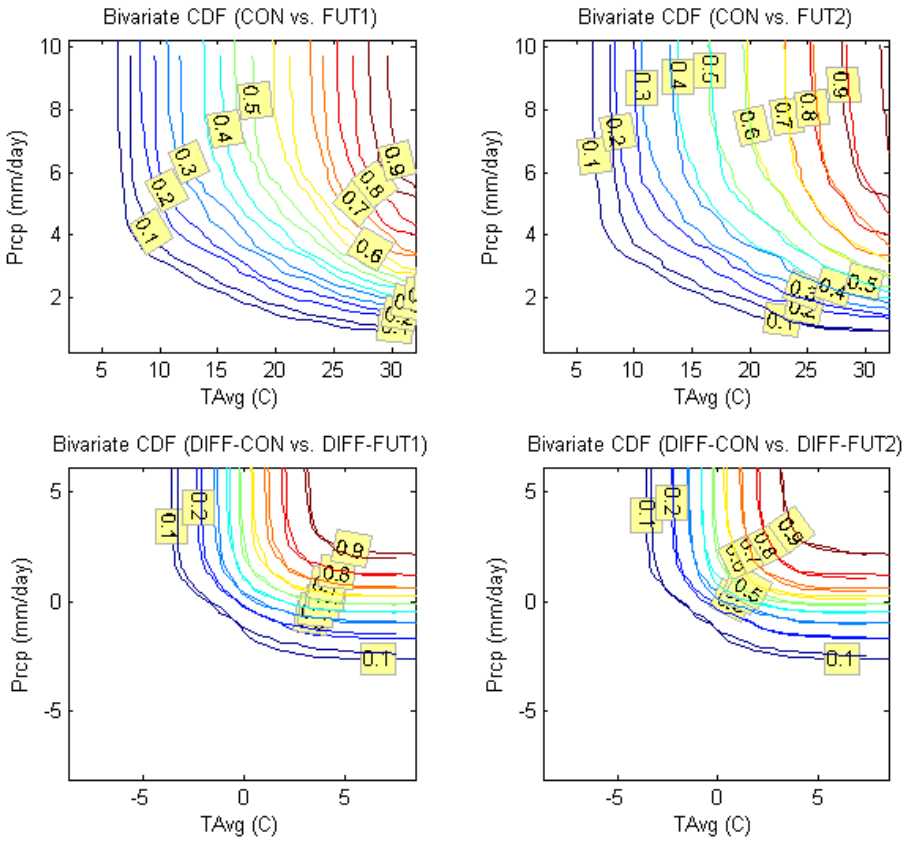

Figure 3.6: Bivariate Empirical Cumulative Distribution Frequency Curves for Original (Top) and Differenced (Bottom) Time Series of Temperature and Precipitation

Step 3: Joint Frequency Mapping

In keeping with the previous discussion, the bias correction process consists of *(1)* creating a differenced series of future temperature and precipitation; (2) finding the joint frequency of the contemporaneous differenced data values; *(3)* assuming that this joint frequency is the same in the future differenced series as it is in the control differenced series; and *(4)* mapping each joint frequency point of the GCM Control distribution to a corresponding point on the joint frequency distribution of the observed differenced series (OBS). The last step is illustrated on **Figure 3.7**. The schematic shows two corresponding pairs of GCM and OBS joint iso-probability curves, and the nearest neighbor mapping of a GCM point to a point on the corresponding OBS iso-probability contour. The nearest neighbor is the one which minimizes the Euclidean distance between the GCM point and all points on the OBS frequency contour.

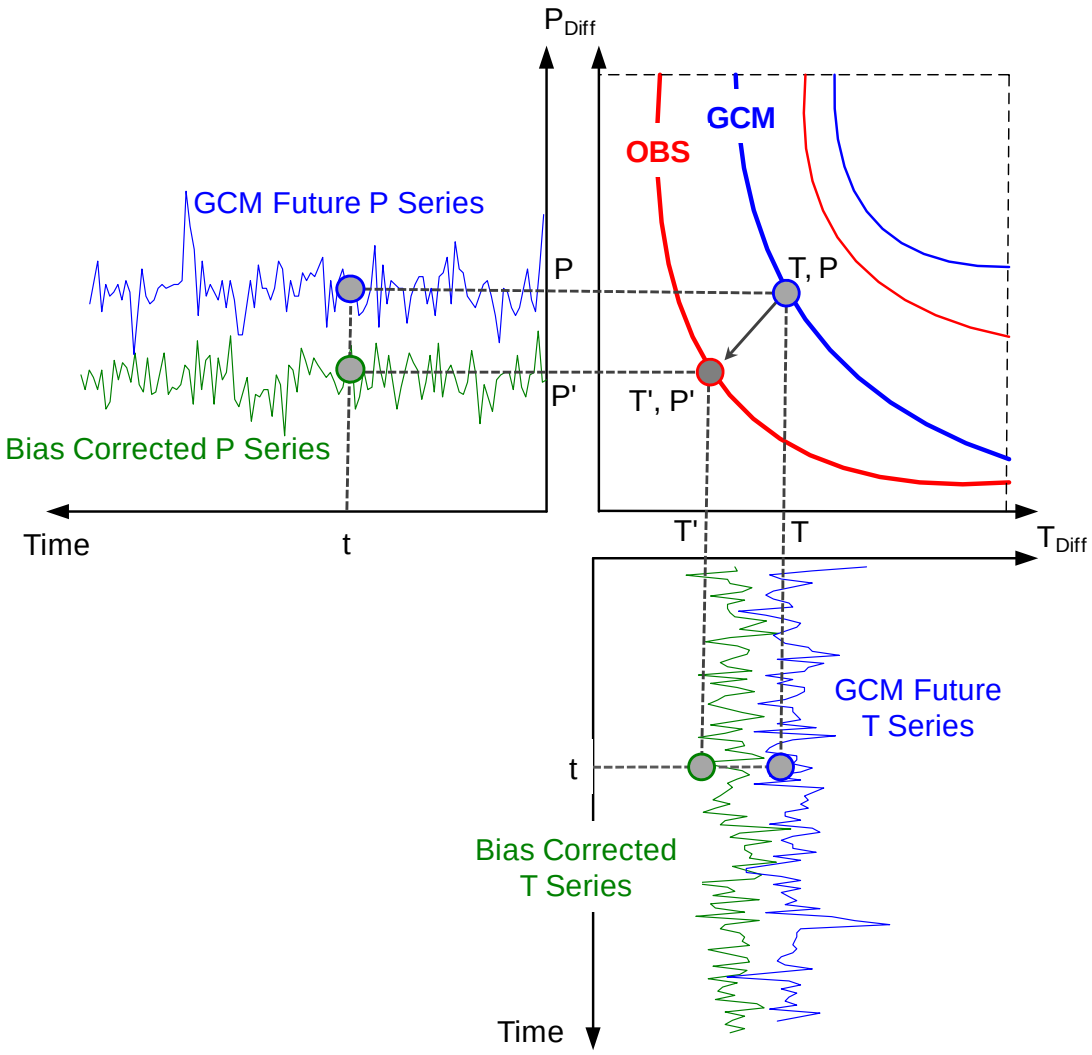

Figure 3.7: Joint Frequency Distribution Mapping

Step 4: Series Reconstruction

The bias corrected monthly temperature and precipitation series for each GCM cell (denoted *TS7* and *TS8*) are obtained by inverting the differencing operation on the bias corrected series:

$$TS7:\ P\_C_t = (\nabla_D)^{-1}(SP\_C_t) = SP\_C_t + SP\_C_{t\text{-}D} \quad (t = 1,2,\cdots,NF_{month}) \quad (3.5a)$$

$$TS8:\ T\_C_t = (\nabla_D)^{-1}(ST\_C_t) = ST\_C_t + ST\_C_{t\text{-}D} \quad (t = 1,2,\cdots,NF_{month}) \quad (3.5b)$$

3.3.4 Spatial Downscaling

The JVSD spatial downscaling component is based on matching the bias-corrected temperature and precipitation patterns with similar observed patterns (historical analogues) over the assessment region (e.g., river basin). This process has the following distinguishing features compared to existing methods:

(1) Pattern matching is performed *simultaneously* for temperature and precipitation fields;

(2) Pattern matching is performed *simultaneously* for all GCM cells that cover the region of interest (e.g., river basin), thus maintaining the climatic coherence of the temperature and precipitation fields;

(3) Future temperature and precipitation fields that fall outside the historical range are accommodated by expanding the range of historical analogues as described in the following section.

The spatial downscaling procedure is summarized below.

Step 5: Data Range Adequacy Test

In this step, the monthly temperature and precipitation values of the relevant GCM cells are checked to determine if they fall within the historical observed range of the monthly values. If they fall within the historical range, the downscaling process continues to Step 7; otherwise, the process continues to Step 6.

Step 6: Historical Analogue Range Expansion

This step is invoked when the future GCM patterns fall outside the historical range, a case particularly relevant to a changing climate. To expand the historical analogue range, upscaling of the historical data in Step 4 is performed for several periods smaller than a month, e.g., d = 15, 10, 5, or 1 days. Because these periods entail fewer days than those in a month, their averages are

expected to exhibit higher (than monthly) variability and a wider data range. This process aims to identify the largest interval *d* which generates historical analogues containing the future T and P values. The data range expansion is carried out for the calendar month to be downscaled, but if this is not sufficient and further expansion is necessary, it includes 15 days from the previous and following months.

The process is illustrated in **Figure 3.8**. In the top plot, the maximum and minimum historical monthly precipitation averaged over 30, 10, 5, and 1 days are plotted in solid lines, and the corresponding standard deviations in dashed lines. In the bottom plot, the same quantities are plotted for the historical temperature. These plots show the data range expansion as the averaging interval decreases.

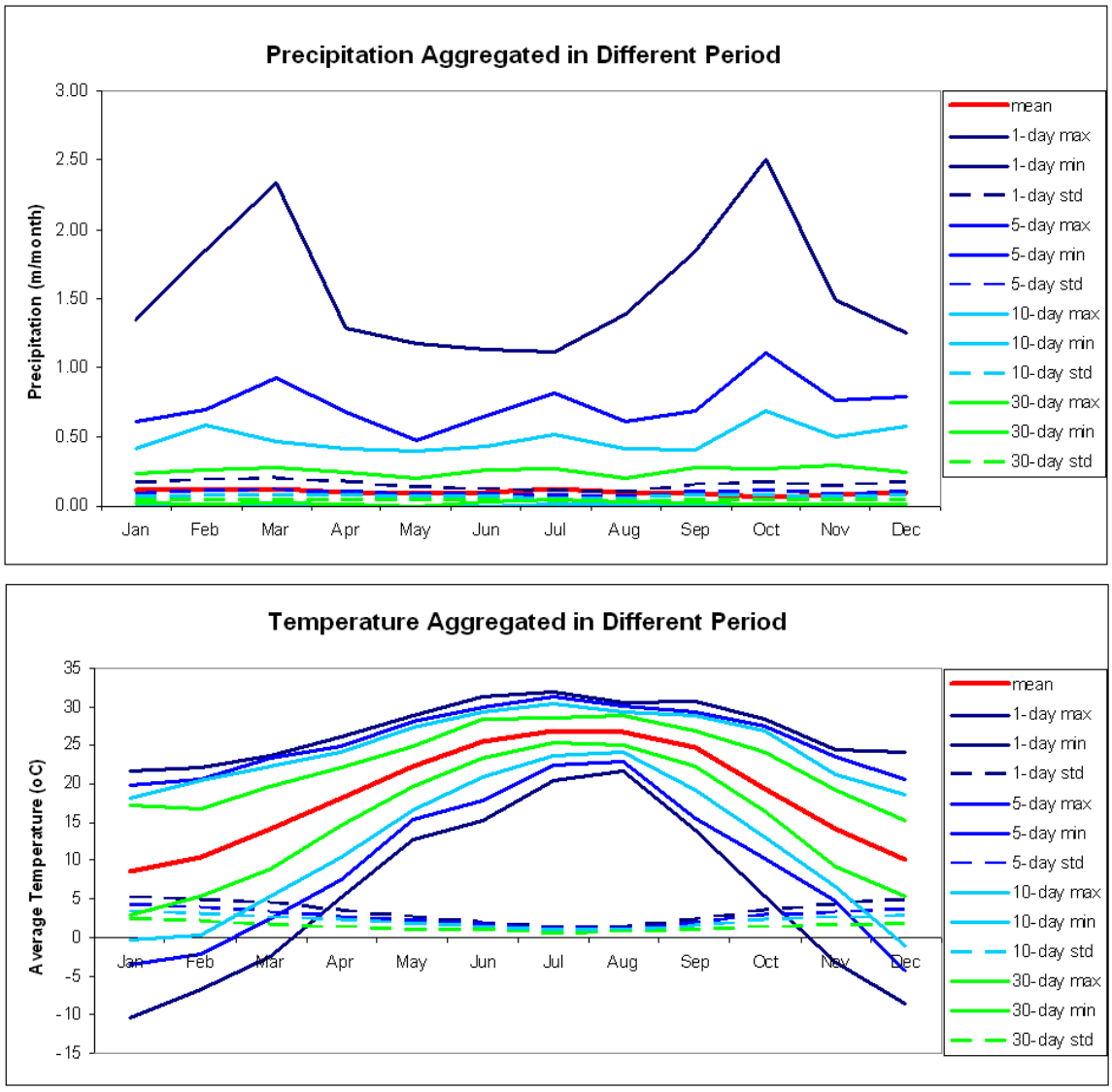

Figure 3.8: Data Range Expansion Example

Step 7: Historical Analogue Matching

Next, the nearest point (OBS_P_i, OBS_T_i) in the historical sequences *TS5* and *TS6* to a particular point (GCM_P_i, GCM_T_i) in the future GCM sequences *TS7* and *TS8* is determined by minimizing the Euclidean distance:

$$R^2 = \sum_{i \in A} \alpha (OBS\_P_i - GCM\_P_i)^2 + \beta (OBS\_T_i - GCM\_T_i)^2 \qquad (3.6)$$

where *A* is the set of cells that cover the region (basin) of interest; α and β are weighting coefficients if one wishes to emphasize matching one of the variable over the other; and *i* is the cell index on the GCM grid.

Once the nearest historical analogue point is identified, the T-P values can be spatially downscaled based on the historical T-P values over the observational cells. The downscaled temperature and precipitation sequences are denoted *TS9* and *TS10*:

$$\begin{Bmatrix} TS9 \\ TS10 \end{Bmatrix} : \begin{Bmatrix} P\_\mathrm{DS_t} \\ T\_\mathrm{DS_t} \end{Bmatrix} = Nearest\ Historical\ Analogue \begin{Bmatrix} P\_OBS_j \\ T\_OBS_j \end{Bmatrix} \quad (\mathrm{t} = 1,2,\cdots,\mathrm{NF_{month}})$$

where *j* is the cell index of the observational (high resolution) grid.

Step 8: Temporal Downscaling

Daily (or other duration) temperature and precipitation sequences *DTS9* and *DTS10* can now be constructed by suitable temporal upscaling of the historical analogue fields. If the nearest historical analogue was found from the monthly historical observed fields, then, the downscaled daily sequences are directly extracted from the corresponding month. On the other hand, if the nearest historical analogue required expansion of the historical range (using the process outlined in Step 6), then, the downscaled daily sequences are constructed by assembling several nearest historical analogues the total duration of which equals one month.

3.3.5 Comparisons and Assessments

In this section, JVSD is first evaluated by comparison with observed historical data and other statistical and dynamic downscaling methods.

3.3.5.1 Climatology Comparison

The climatology maps of precipitation and temperature in the ACF basin region are shown in **Figures 3.9** to **3.16**. The results presented here are from the Canadian model CGCM3.1, run1. Results from all other GCMs are included in Appendix A. **Figures 3.9** through **3.12** show JVSD climatology results, and **Figures 3.13** though **3.16** show BCSD climatology results. Monthly precipitation and temperature data are aggregated by seasons (DJF, MAM, JJA, and SON) for three periods: *(1)* 01/1950 to 12/1999 using both observations as well as data from the CMIP pilot project called 20th Century Climate in Coupled Models (20CM3); *(2)* from 01/2000 to 12/2049 for A1B scenarios, and *(3)* from 01/2050 to 12/2099 for A1B and A2 scenarios. The first column is constructed from observed, high resolution data from the 1/8 degree spatial resolution dataset (Maurer et al., 2002) for the period 1950-1999. The second column shows results from JVSD using coarse resolution GCM data from the 20CM3 experiments (1950-1999) as input. The third (2000-2049) and fourth columns (2050-2099) are also generated by JVSD with input from the A1B or A2 GCM scenario results.

A comparison of the first two columns in these figures shows that JVSD results compare favorably with observed high resolution data in that they reproduce fairly well the seasonal spatial temperature and precipitation distributions. Furthermore, the results in columns 3 and 4 support the following comments:

(1) Temperature exhibits increasing trends over the ACF basin for all seasons and all A1B and A2 scenarios; The A2 temperature increases are more significant in the 2050 – 2099 time period and the northern part of the ACF Basin, e.g., the Buford watershed. The most pronounced temperature increase is projected to happen in late spring and early summer (April to July);

(2) The most significant precipitation changes occur in the summer and fall in the north part of Georgia and the ACF basin, where precipitation experiences declining trends and higher spatial variability; There are no salient precipitation changes in the southern ACF watersheds, except in July when all ACF watersheds are expected to receive less precipitation in both A1B and A2 scenarios.

Figures 3.13 through **3.16** show similar climatology results from the BCSD downscaling method. As can be seen by the first two columns of these figures, BCSD generally performs well, showing similar overall trends for seasonal temperature and precipitation as those of the observed data and JVSD. However, the following differences are noted between the two methods:

(1) The BCSD precipitation fields exhibit less spatial variability than those generated by JVSD. The reasons for this difference have already been discussed.

(2) BCSD predicts that the highest temperature increases will occur during late spring and early summer as does JVSD. However, summer temperature increases (July and August) are higher under BCSD than under JVSD.

(3) BCSD predicts milder precipitation changes than JVSD for all ACF watersheds. The most likely reason for this difference is that JVSD downscales simultaneously precipitation and temperature while BCSD operates on the individual variables.

Temperature and precipitation climatologies for the six ACF sub-basins are also plotted in **Figures 3.17** to **3.18**. All sub-basins show increasing temperature trends, with higher increases occurring in the summer months. Precipitation is projected to increase during winter and decrease during summer for most watersheds. The Buford watershed in the upper Chattahoochee experiences the most marked changes.

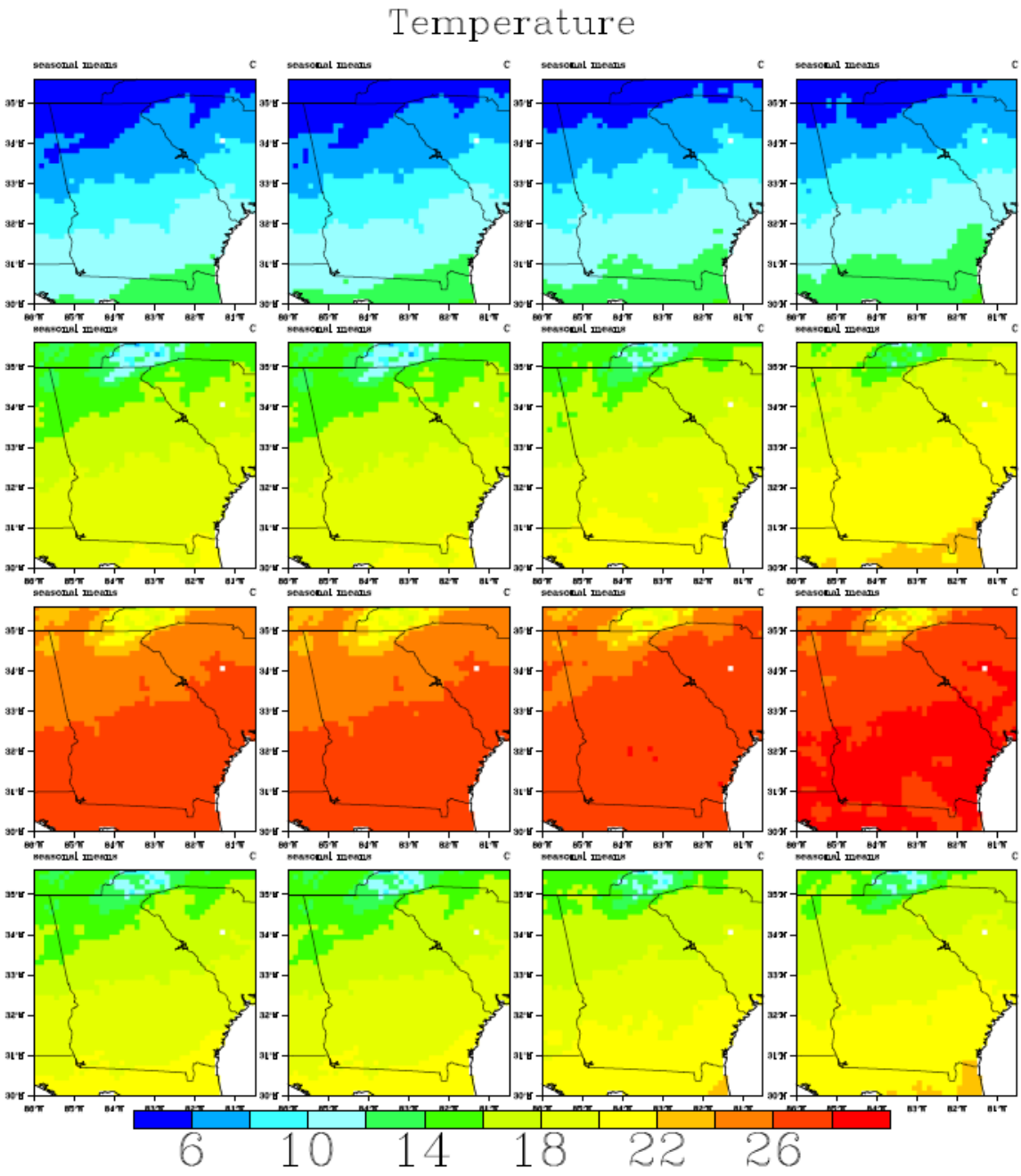

Figure 3.9: Spatial temperature distributions over the ACF basin and the southeast US. Monthly temperature fields are aggregated by season (DJF, MAM, JJA, SON). The columns depict observations for the period 01/1950 - 12/1999 (Column 1); JVSD downscaled data using input from the 20CM3 experiment for the period 01/1950 - 12/1999 (Column 2); JVSD downscaled data using input from the CGCM3.1-run1 A1B Scenario for the period 01/2000-12/2049 (Column 3); and JVSD downscaled data using input from the CGCM3.1-run1A1B Scenario for the period 01/2050-12/2099 (Column 4).

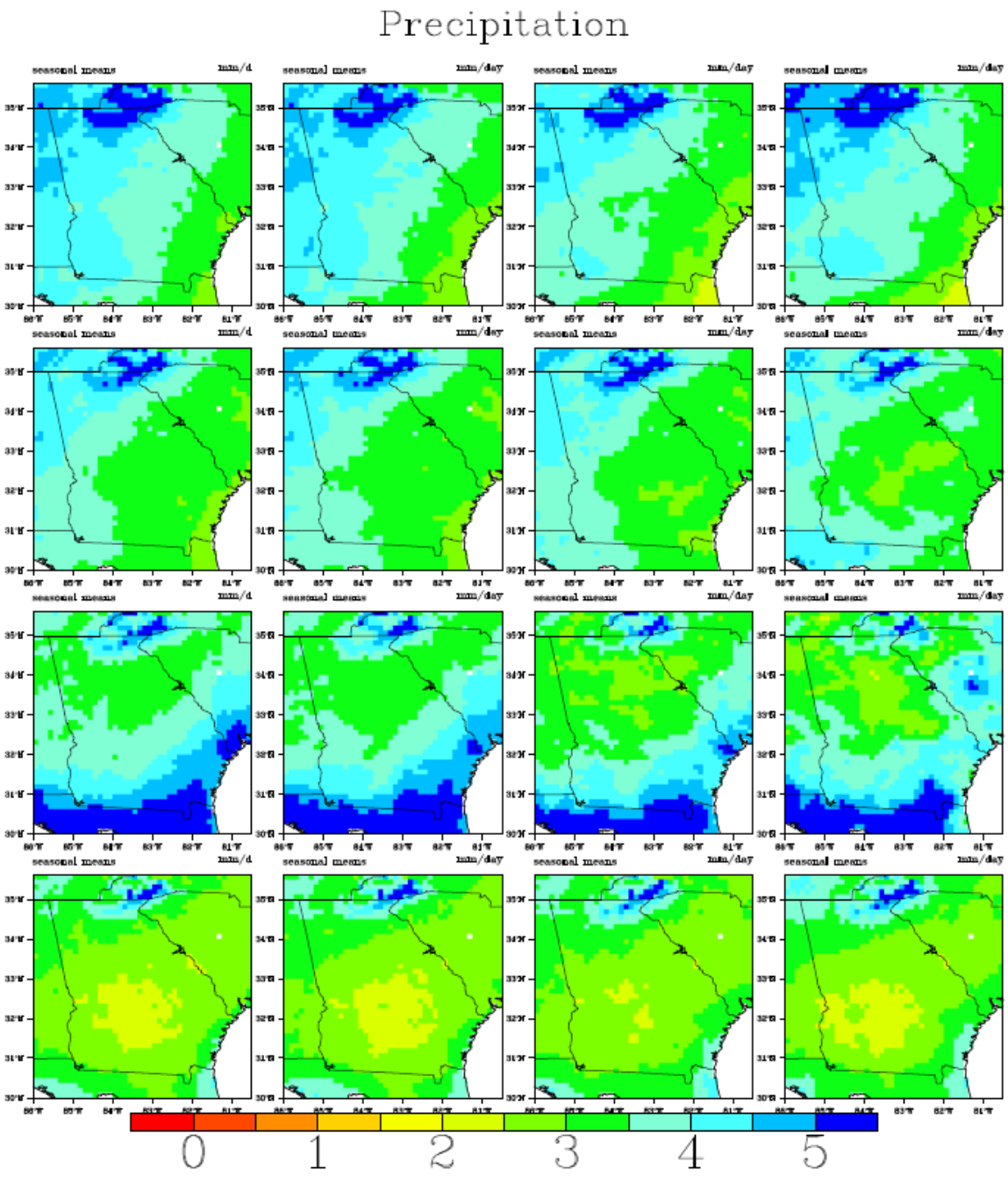

Figure 3.10: Spatial precipitation distributions over the ACF basin and the southeast US. Monthly precipitation fields are aggregated by season (DJF, MAM, JJA, SON). The columns depict observations for the period 01/1950 - 12/1999 (Column 1); JVSD downscaled data using input from the 20CM3 experiment for the period 01/1950 - 12/1999 (Column 2); JVSD downscaled data using input from the CGCM3.1-run1A1B Scenario for the period 01/2000-12/2049 (Column 3); and JVSD downscaled data using input from the CGCM3.1-run1 A1B Scenario for the period 01/2050-12/2099 (Column 4).

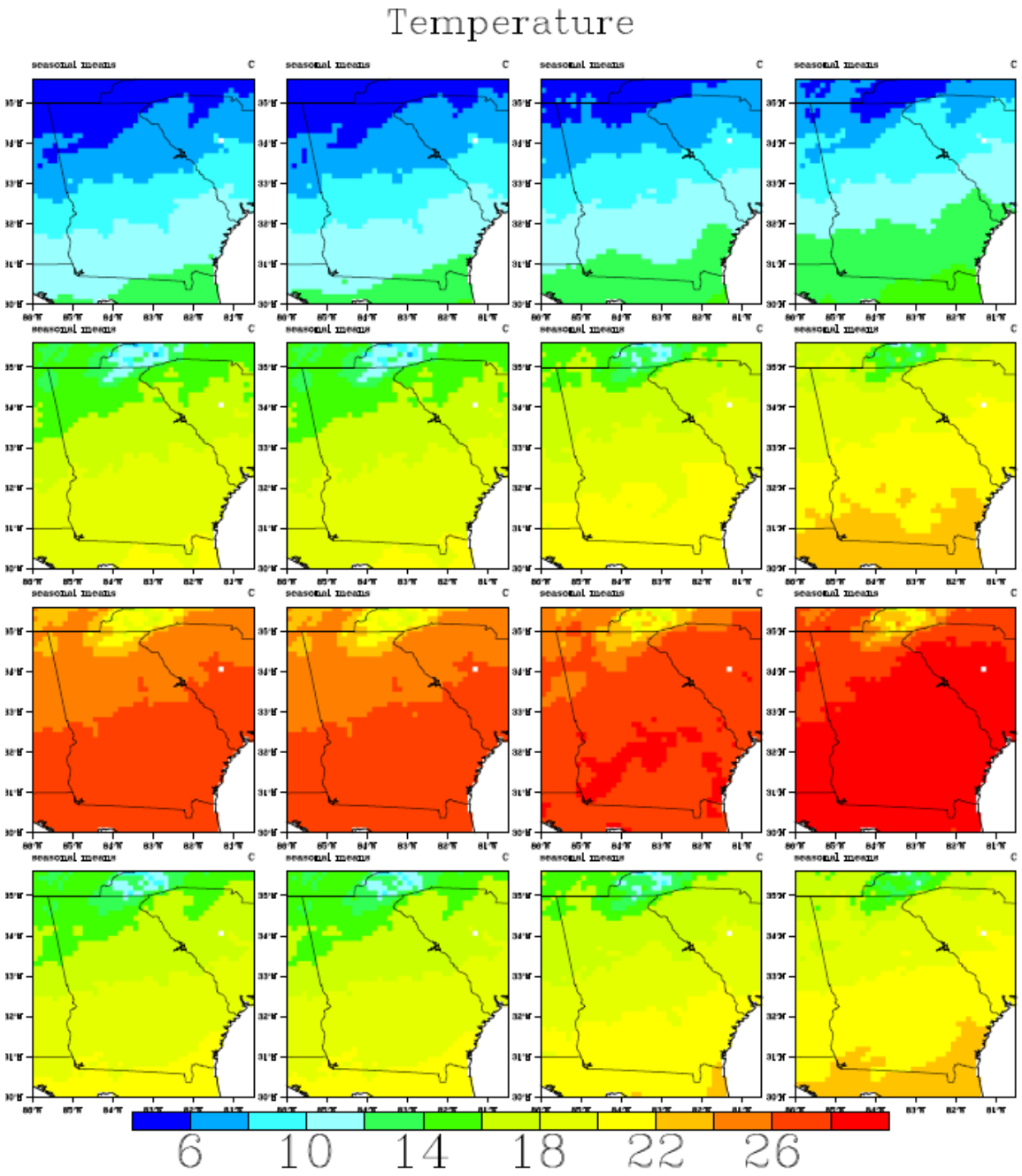

Figure 3.11: Spatial temperature distributions over the ACF basin and the southeast US. Monthly temperature fields are aggregated by season (DJF, MAM, JJA, SON). The columns depict observations for the period 01/1950 - 12/1999 (Column 1); JVSD downscaled data using input from the 20CM3 experiment for the period 01/1950 - 12/1999 (Column 2); JVSD downscaled data using input from the CGCM3.1-run1A2 Scenario for the period 01/2000-12/2049 (Column 3); and JVSD downscaled data using input from the CGCM3.1-run1A2 Scenario for the period 01/2050-12/2099 (Column 4).

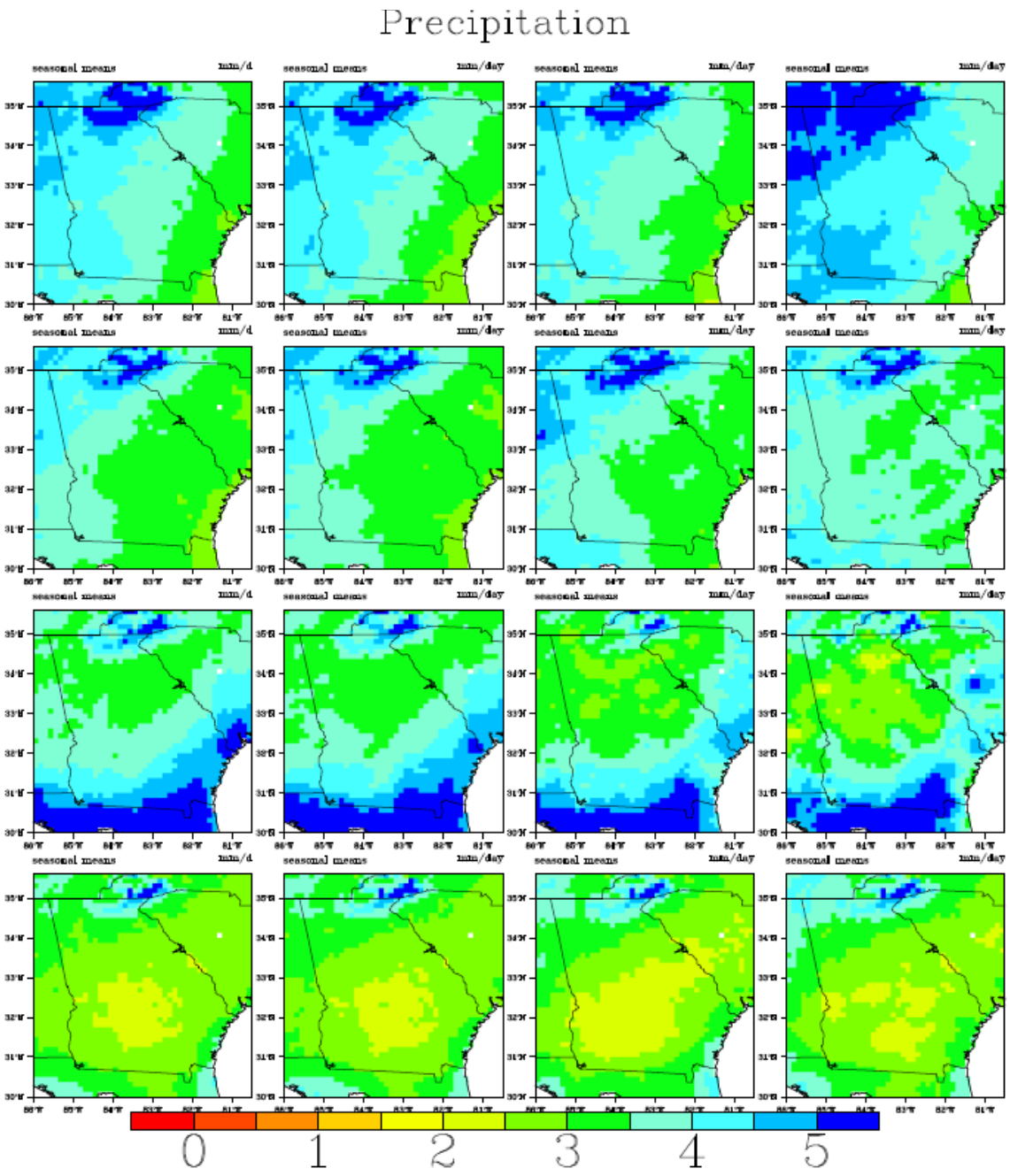

Figure 3.12: Spatial precipitation distributions over the ACF basin and the southeast US. Monthly precipitation fields are aggregated by season (DJF, MAM, JJA, SON). The columns depict observations for the period 01/1950 - 12/1999 (Column 1); JVSD downscaled data using input from the 20CM3 experiment for the period 01/1950 - 12/1999 (Column 2); JVSD downscaled data using input from the CGCM3.1-run1A2 Scenario for the period 01/2000-12/2049 (Column 3); and JVSD downscaled data using input from the CGCM3.1-run1A2 Scenario for the period 01/2050-12/2099 (Column 4).

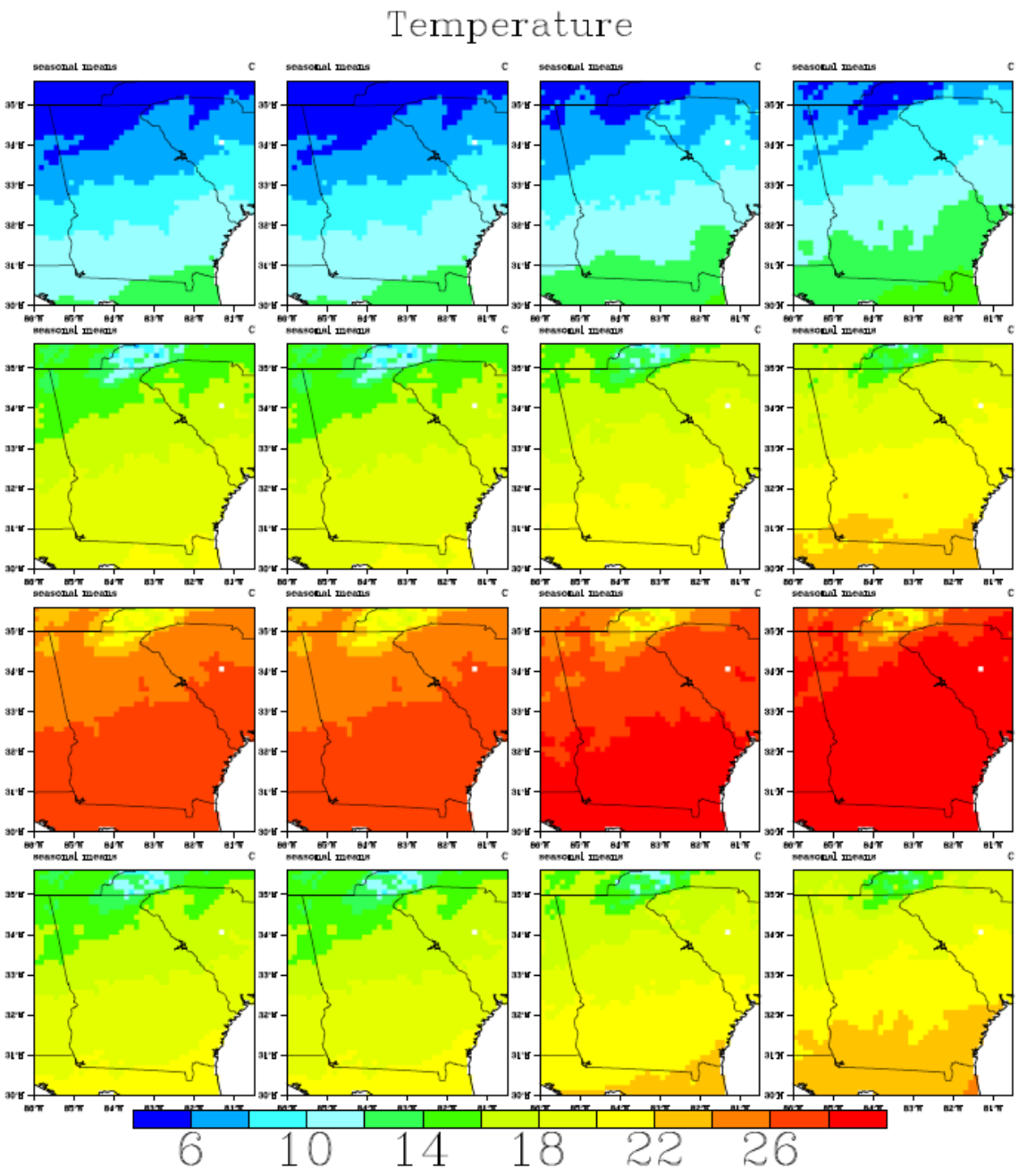

Figure 3.13: Spatial temperature distributions over the ACF basin and the southeast US. Monthly temperature fields are aggregated by season (DJF, MAM, JJA, SON). The columns depict observations for the period 01/1950 - 12/1999 (Column 1); BCSD downscaled data using input from the 20CM3 experiment for the period 01/1950 - 12/1999 (Column 2); BCSD downscaled data using input from the CGCM3.1-run1 A1B Scenario for the period 01/2000-12/2049 (Column 3); and BCSD downscaled data using input from the CGCM3.1-run1 A1B Scenario for the period 01/2050-12/2099 (Column 4).

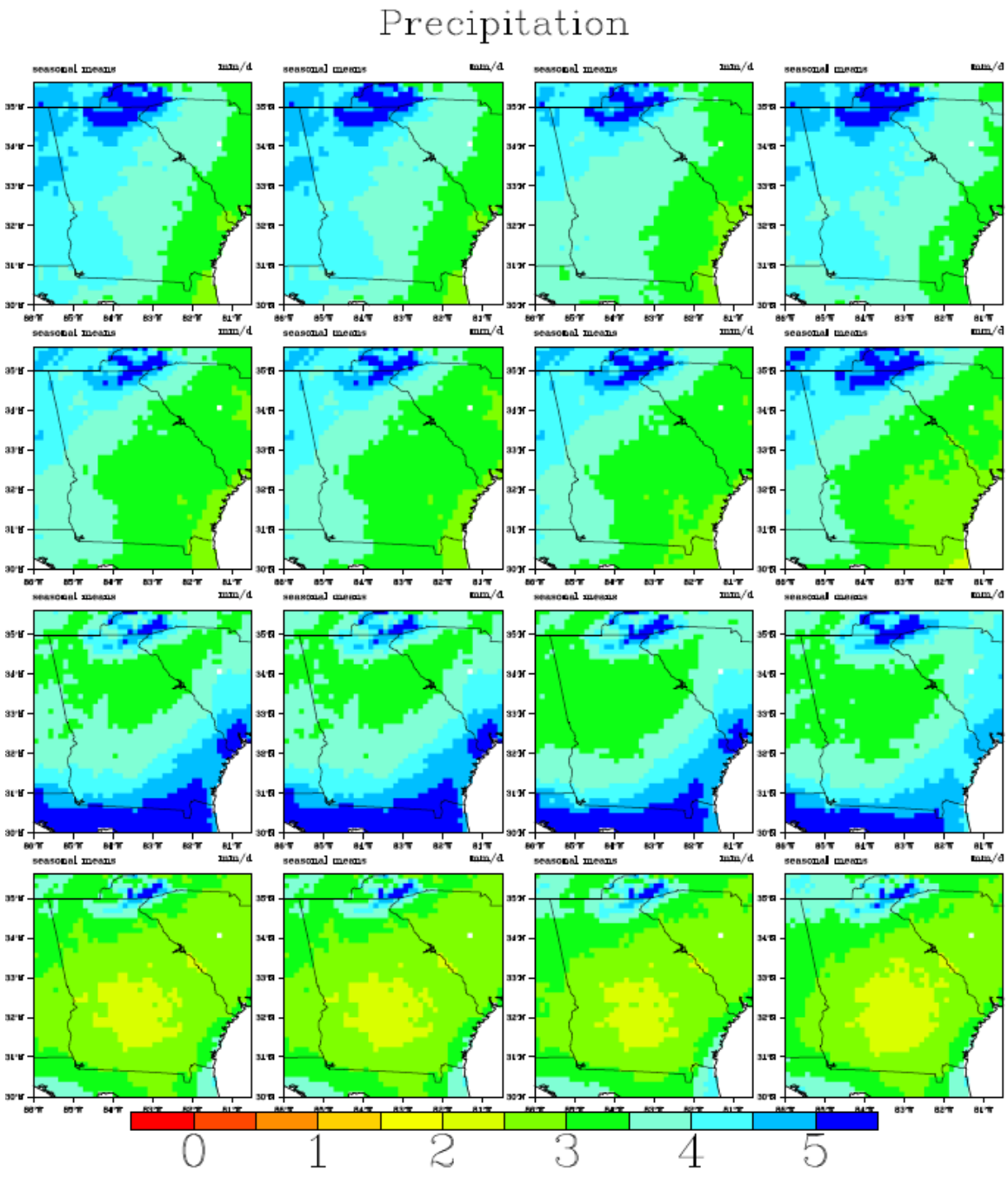

Figure 3.14: Spatial precipitation distributions over the ACF basin and the southeast US. Monthly precipitation fields are aggregated by season (DJF, MAM, JJA, SON). The columns depict observations for the period 01/1950 - 12/1999 (Column 1); BCSD downscaled data using input from the 20CM3 experiment for the period 01/1950 - 12/1999 (Column 2); BCSD downscaled data using input from the CGCM3.1-run1A1B Scenario for the period 01/2000-12/2049 (Column 3); and BCSD downscaled data using input from the CGCM3.1-run1A1B Scenario for the period 01/2050-12/2099 (Column 4).

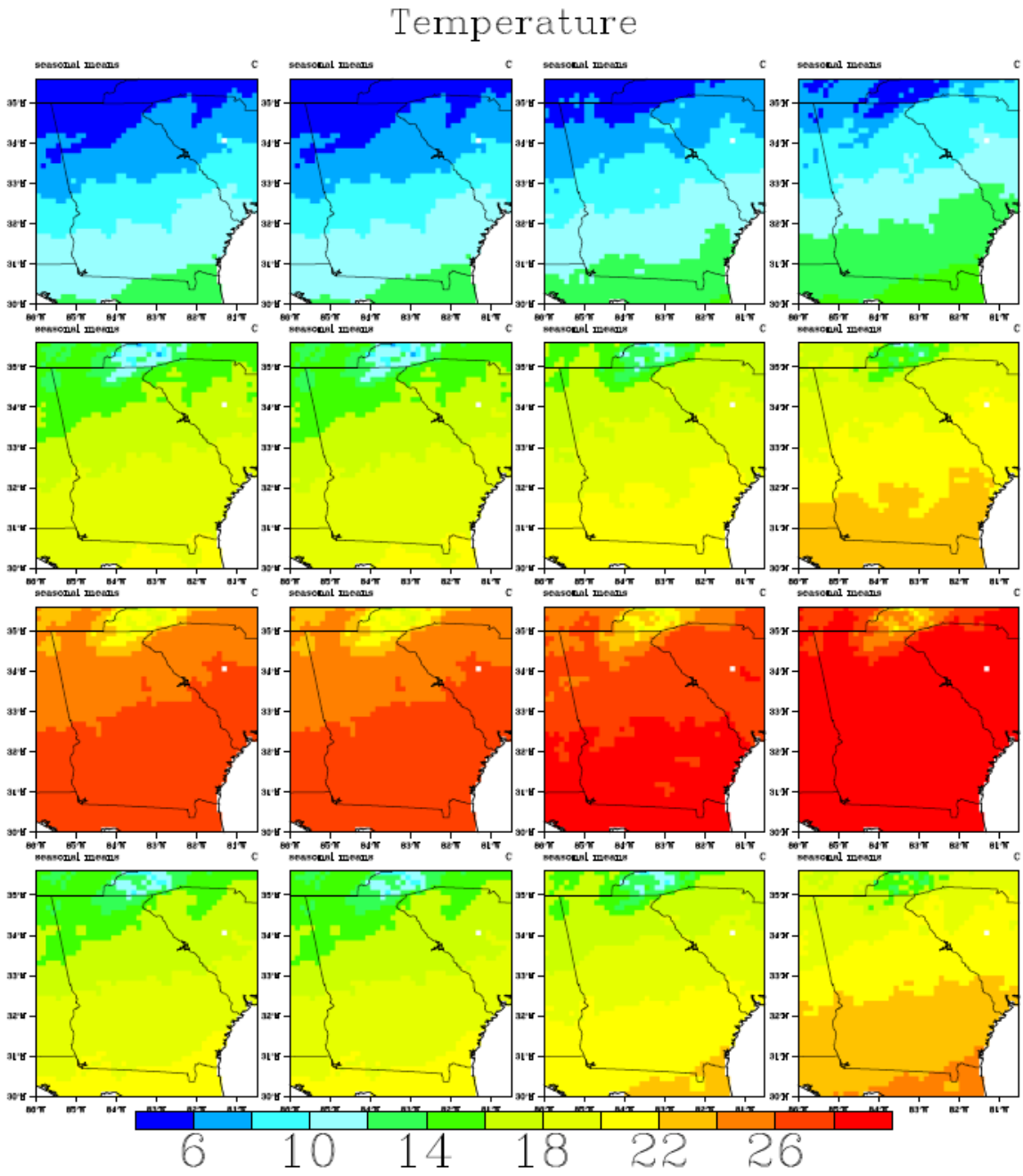

Figure 3.15: Spatial temperature distributions over the ACF basin and the southeast US. Monthly temperature fields are aggregated by season (DJF, MAM, JJA, SON). The columns depict observations for the period 01/1950 - 12/1999 (Column 1); BCSD downscaled data using input from the 20CM3 experiment for the period 01/1950 - 12/1999 (Column 2); BCSD downscaled data using input from the CGCM3.1-run1 A2 Scenario for the period 01/2000-12/2049 (Column 3); and BCSD downscaled data using input from the CGCM3.1-run1 A2 Scenario for the period 01/2050-12/2099 (Column 4).

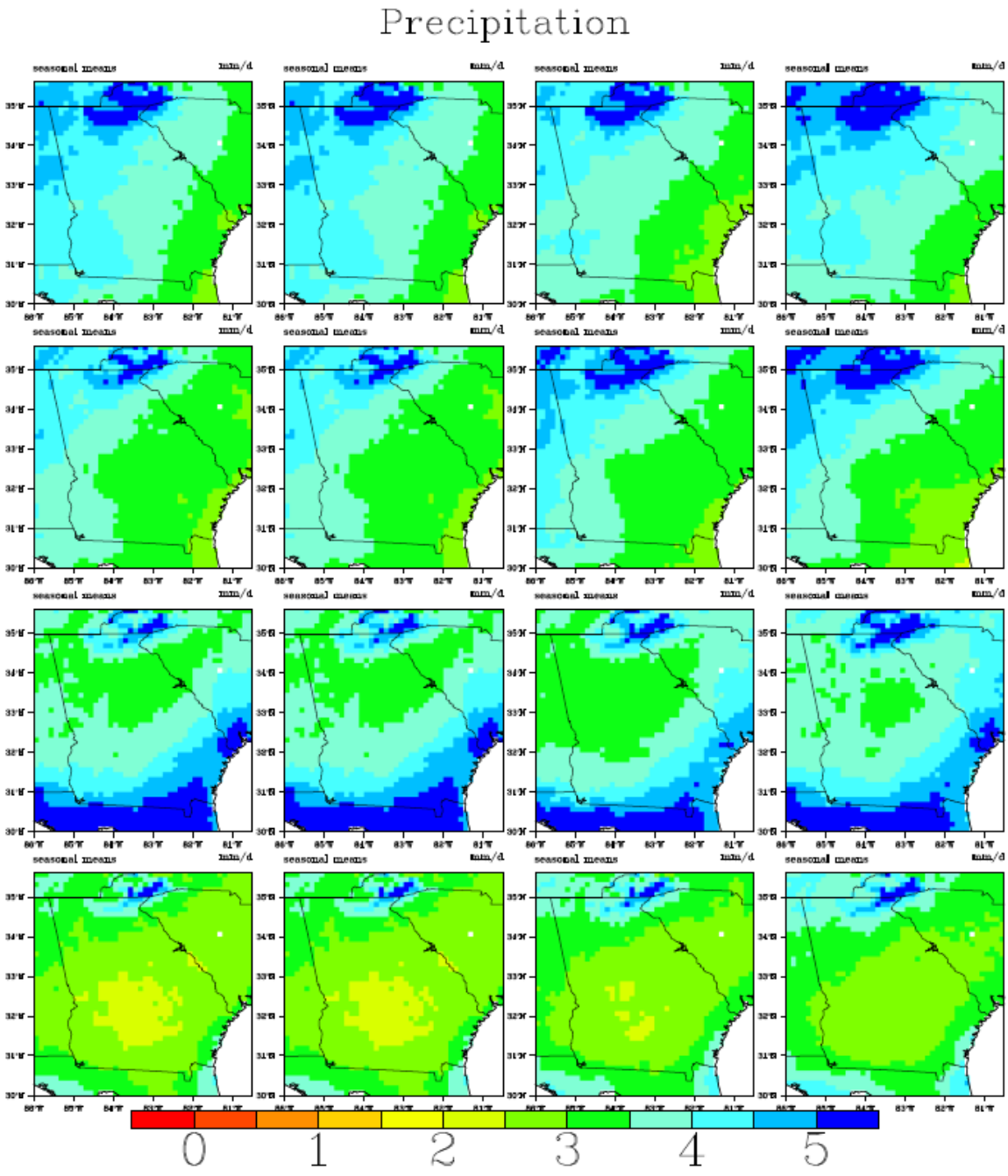

Figure 3.16: Spatial precipitation distributions over the ACF basin and the southeast US. Monthly precipitation fields are aggregated by season (DJF, MAM, JJA, SON). The columns depict observations for the period 01/1950 - 12/1999 (Column 1); BCSD downscaled data using input from the 20CM3 experiment for the period 01/1950 - 12/1999 (Column 2); BCSD downscaled data using input from the CGCM3.1-run1A2 Scenario for the period 01/2000-12/2049 (Column 3); and BCSD downscaled data using input from the CGCM3.1-run1A2 Scenario for the period 01/2050-12/2099 (Column 4).

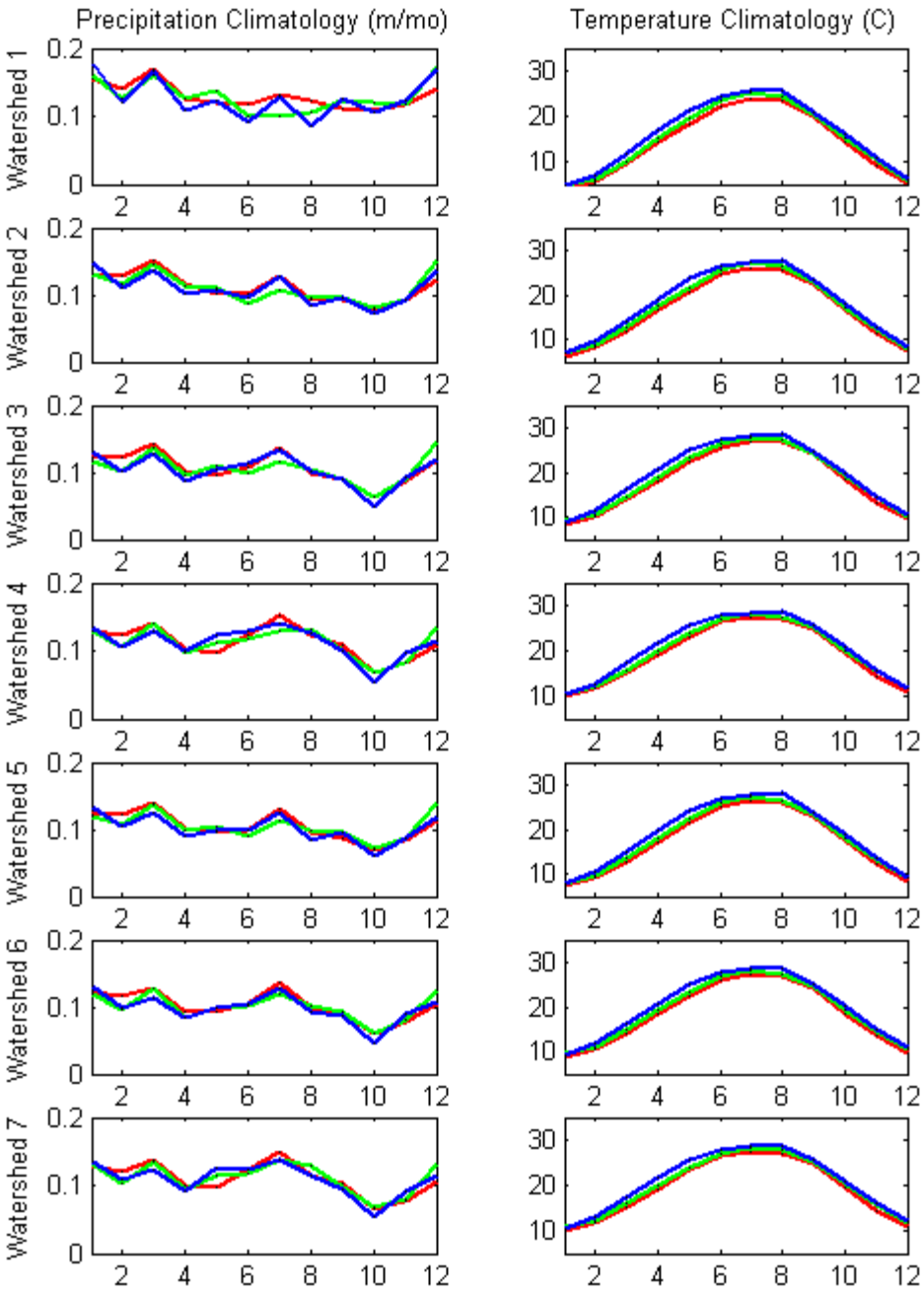

Figure 3.17a: Climatologies of spatially aggregated precipitation and temperature for seven ACF watersheds: *(1)* Buford, *(2)* West Point, *(3)* George, *(4)* Woodruff, *(5)* Montezuma, *(6)* Albany, and *(7)* Bainbridge; Lines in Red–Observations (1950-1999); Green–JVSD downscaled (2000- 2049); Blue–JVSD downscaled (2050-2099) under A1B Scenarios.

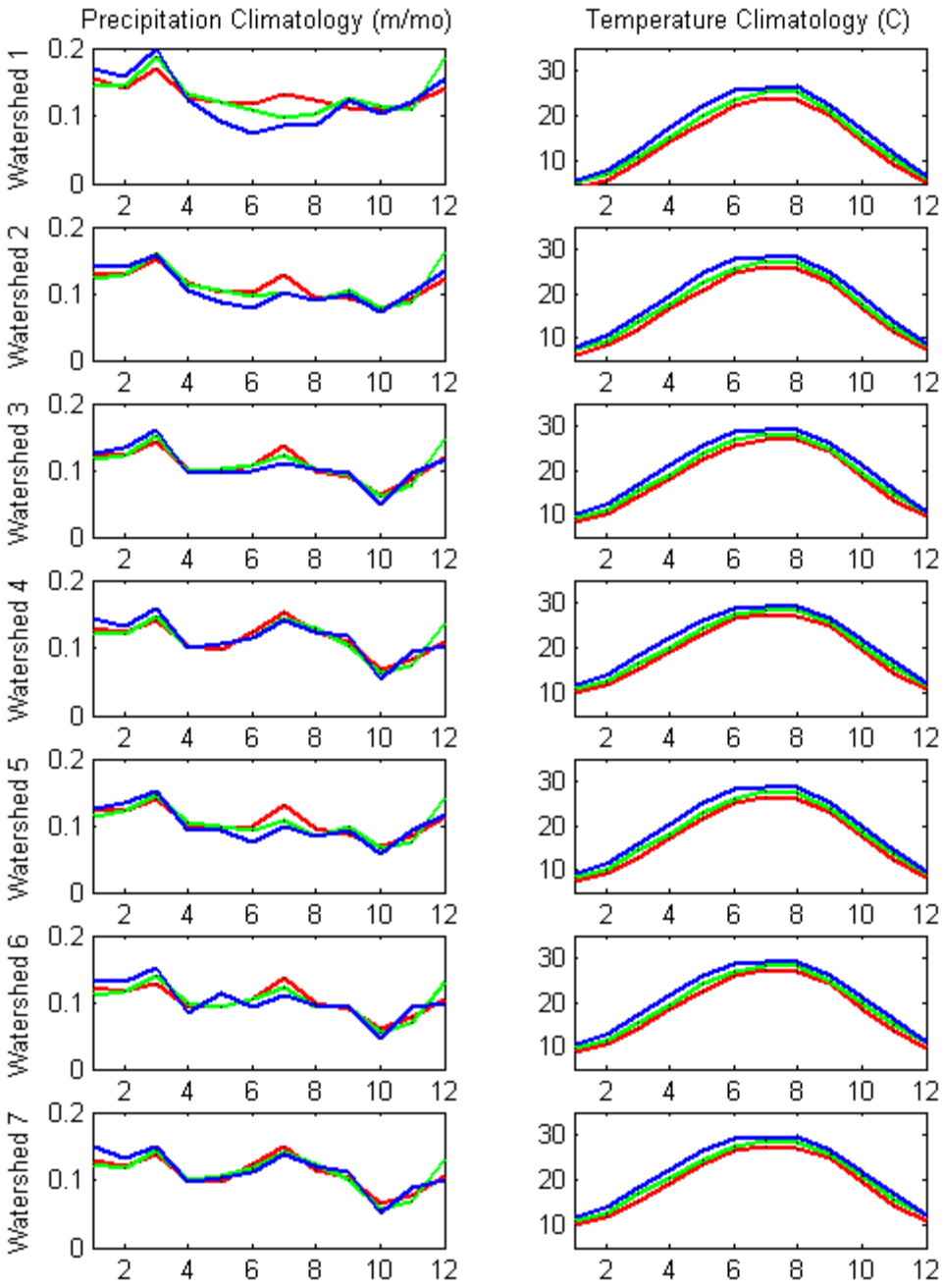

Figure 3.17b: Climatologies of spatially aggregated precipitation and temperature for seven ACF watersheds: *(1)* Buford, *(2)* West Point, *(3)* George, *(4)* Woodruff, *(5)* Montezuma, *(6)* Albany, and *(7)* Bainbridge; Lines in Red–Observations (1950-1999); Green–JVSD downscaled (2000- 2049); Blue–JVSD downscaled (2050-2099) under A2 Scenarios.

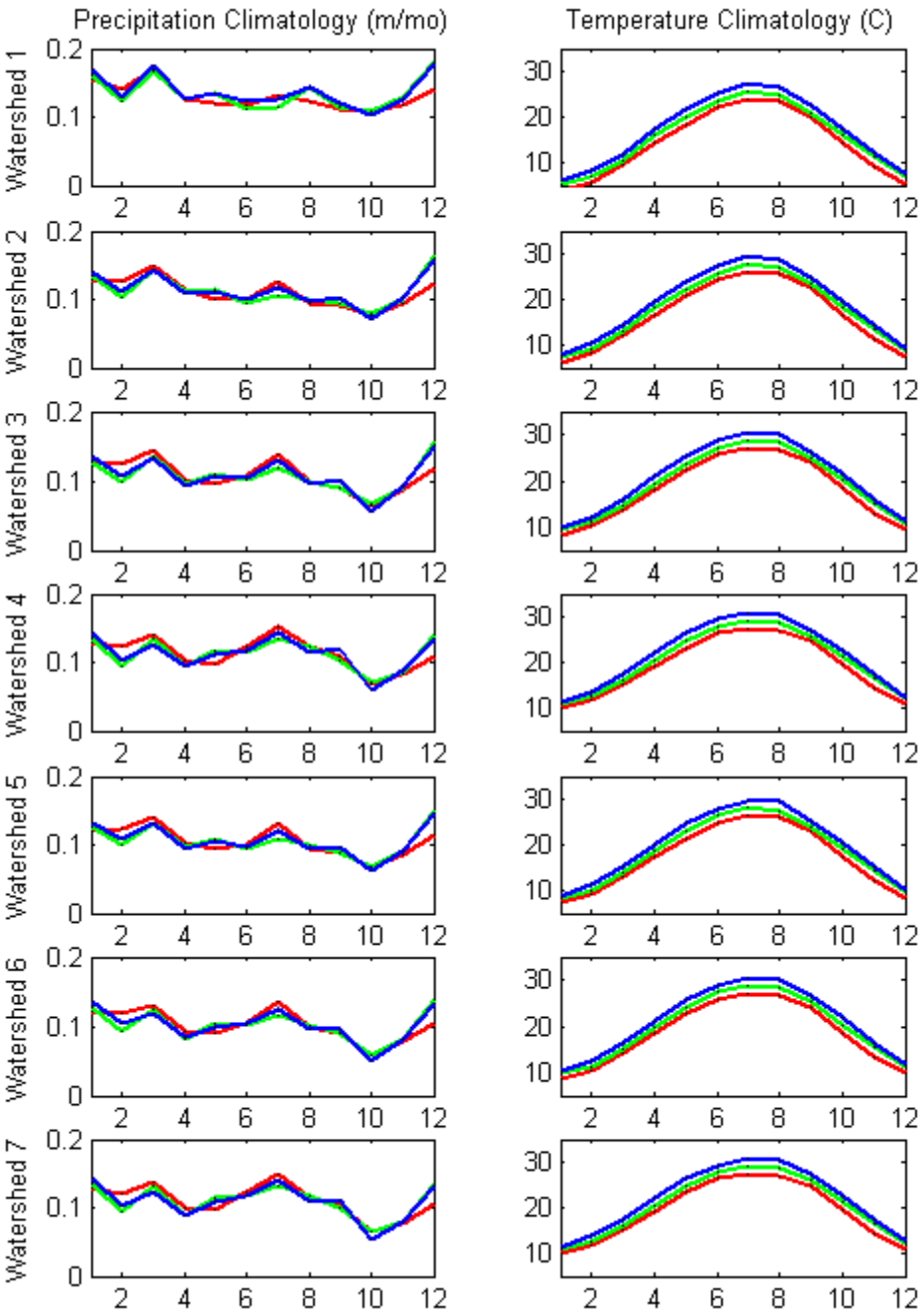

Figure 3.18a: Climatologies of spatially aggregated precipitation and temperature for seven ACF watersheds: *(1)* Buford, *(2)* West Point, *(3)* George, *(4)* Woodruff, *(5)* Montezuma, *(6)* Albany, and *(7)* Bainbridge; Lines in Red–Observations (1950-1999); Green–BCSD downscaled (2000-2049); Blue–BCSD downscaled (2050-2099) under A1B Scenarios

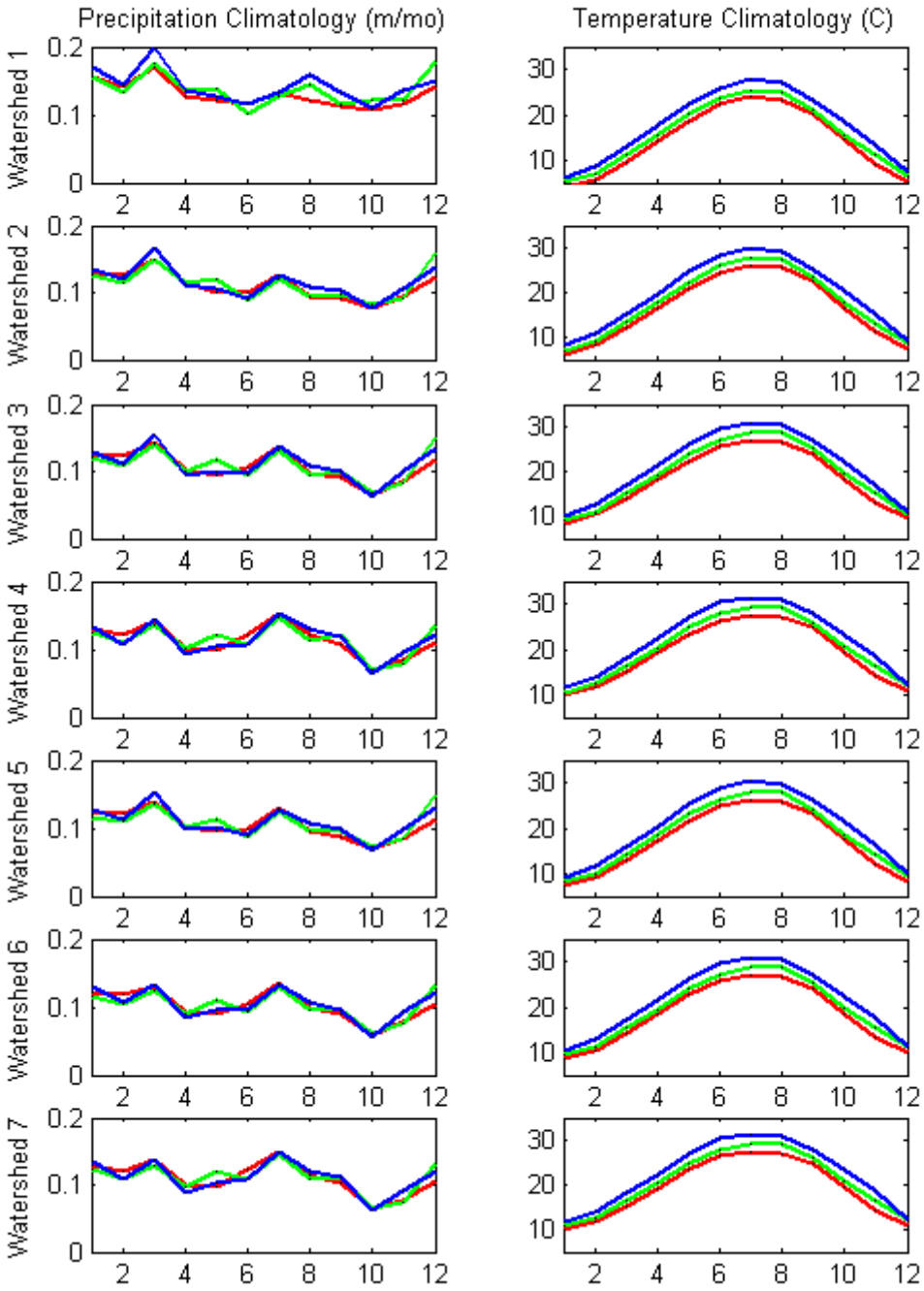

Figure 3.18b: Climatologies of spatially aggregated precipitation and temperature for seven ACF watersheds: *(1)* Buford, *(2)* West Point, *(3)* George, *(4)* Woodruff, *(5)* Montezuma, *(6)* Albany, and *(7)* Bainbridge; Lines in Red–Observations (1950-1999); Green–BCSD downscaled (2000- 2049); Blue–BCSD downscaled (2050-2099) under A2 Scenarios

3.3.5.2 Seasonal Joint CDF and Coefficients of Variability Comparisons

First, the reliability of the seasonal joint temperature and precipitation CDFs is assessed for each watershed over the historical period 01/1950 - 12/1999 (control period). The CDFs are constructed for three datasets: *(1)* historical observational data (Maurer et al., 2002); *(2)* JVSD downscaled data; and *(3)* BCSD downscaled data (Wood et al., 2004). The results (**Figures 3.19** to **3.20**) show that JVSD represents well the joint relationships over the entire frequency and data value ranges. On the other hand, BCSD exhibits various shortcoming especially in the low and high frequencies and extreme values.

Second, the seasonal coefficient of variability (CV) for each watershed is computed and compared for both the observational and downscaled datasets. The seasonal watershed CV is the spatial mean of the seasonal coefficient of variability. The seasonal coefficient of variability at a particular grid cell is defined as the ratio of the standard deviation of the cell seasonal values to the mean seasonal value. Then, the watershed CV is obtained as the spatial mean of all seasonal CVs over all watershed grid cells. **Table 3.3** shows that the JVSD watershed CVs are more representative of the historical CVs than the BCSD CVs, especially for watershed precipitation. It also shows (as in the first test) that BCSD underestimates precipitation variability within each watershed.

Table 3.3: Watershed coefficient of variability (CV) in seasonal precipitation and temperature for the ACF watersheds

Watershed	**Season**	**Precipitation**			**Temperature**		
		OBS	JVSD	BCSD	OBS	JVSD	BCSD
Buford	DJF	0.447	0.449	0.358	0.514	0.465	0.511
	MAM	0.510	0.515	0.379	0.191	0.198	0.188
	JJA	0.561	0.546	0.388	0.090	0.146	0.087
	SON	0.553	0.561	0.456	0.442	0.432	0.440
West Point	DJF	0.446	0.453	0.389	0.379	0.344	0.389

	MAM	0.534	0.531	0.442	0.169	0.176	0.442
	JJA	0.524	0.506	0.422	0.078	0.129	0.422
	SON	0.612	0.616	0.544	0.358	0.345	0.544
George	DJF	0.455	0.467	0.411	0.298	0.270	0.411
	MAM	0.552	0.538	0.464	0.153	0.159	0.464
	JJA	0.556	0.525	0.438	0.064	0.112	0.438
	SON	0.689	0.703	0.592	0.301	0.289	0.592
Woodruff	DJF	0.474	0.463	0.432	0.260	0.463	0.432
	MAM	0.577	0.533	0.493	0.138	0.533	0.493
	JJA	0.539	0.497	0.439	0.054	0.497	0.439
	SON	0.692	0.686	0.616	0.267	0.686	0.616
Montezuma	DJF	0.461	0.479	0.396	0.329	0.304	0.329
	MAM	0.526	0.522	0.442	0.159	0.166	0.158
	JJA	0.569	0.539	0.425	0.073	0.122	0.071
	SON	0.645	0.660	0.425	0.327	0.316	0.326
Bainbridge	DJF	0.486	0.480	0.561	0.274	0.251	0.268
	MAM	0.553	0.530	0.422	0.142	0.147	0.141
	JJA	0.547	0.496	0.467	0.059	0.106	0.056
	SON	0.708	0.703	0.596	0.279	0.269	0.277

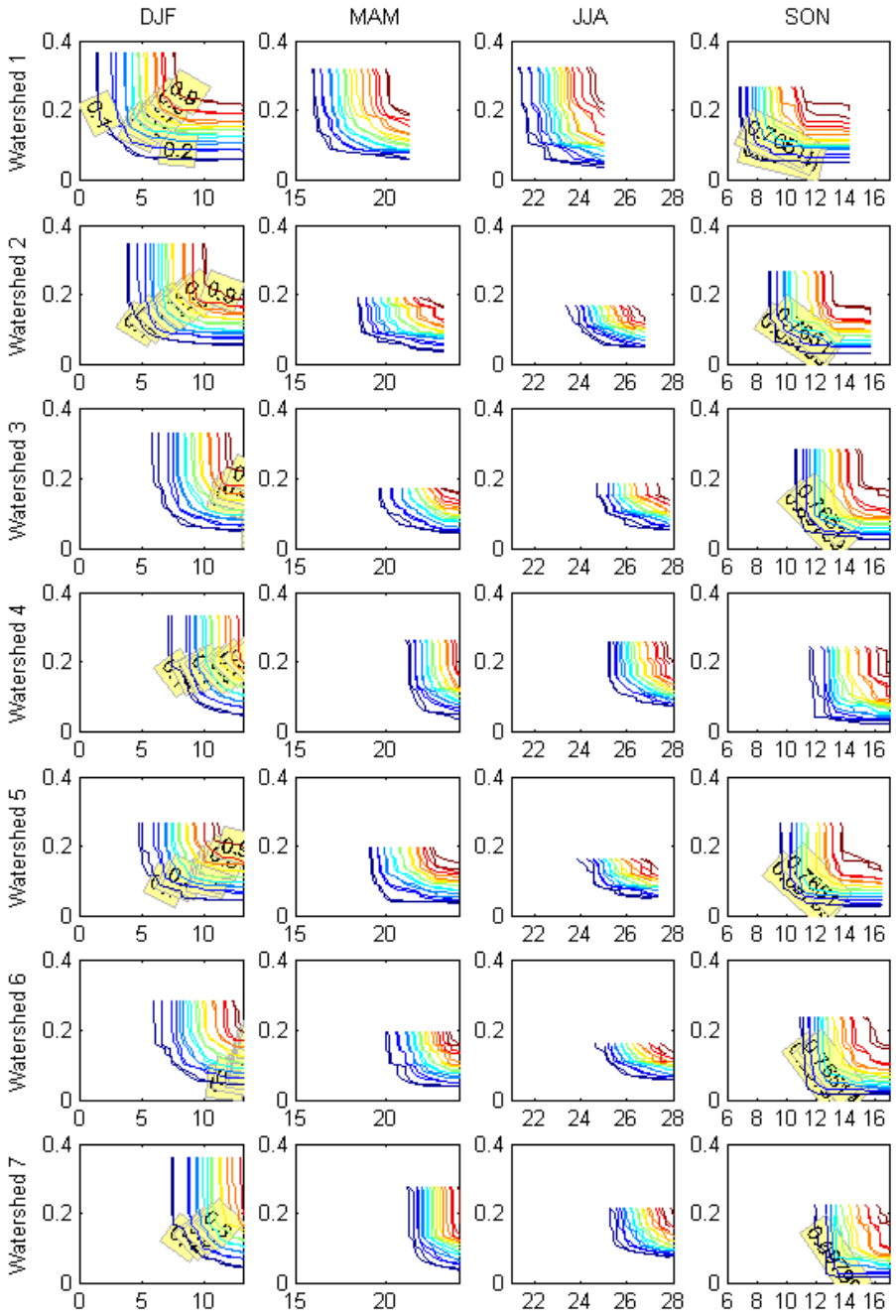

Figure 3.19: Joint CDFs of precipitation and temperature for each watershed and season corresponding to OBS and JVSD data: *(1)* Buford, *(2)* West Point, *(3)* George, *(4)* Woodruff, *(5)* Montezuma, *(6)* Albany, and *(7)* Bainbridge

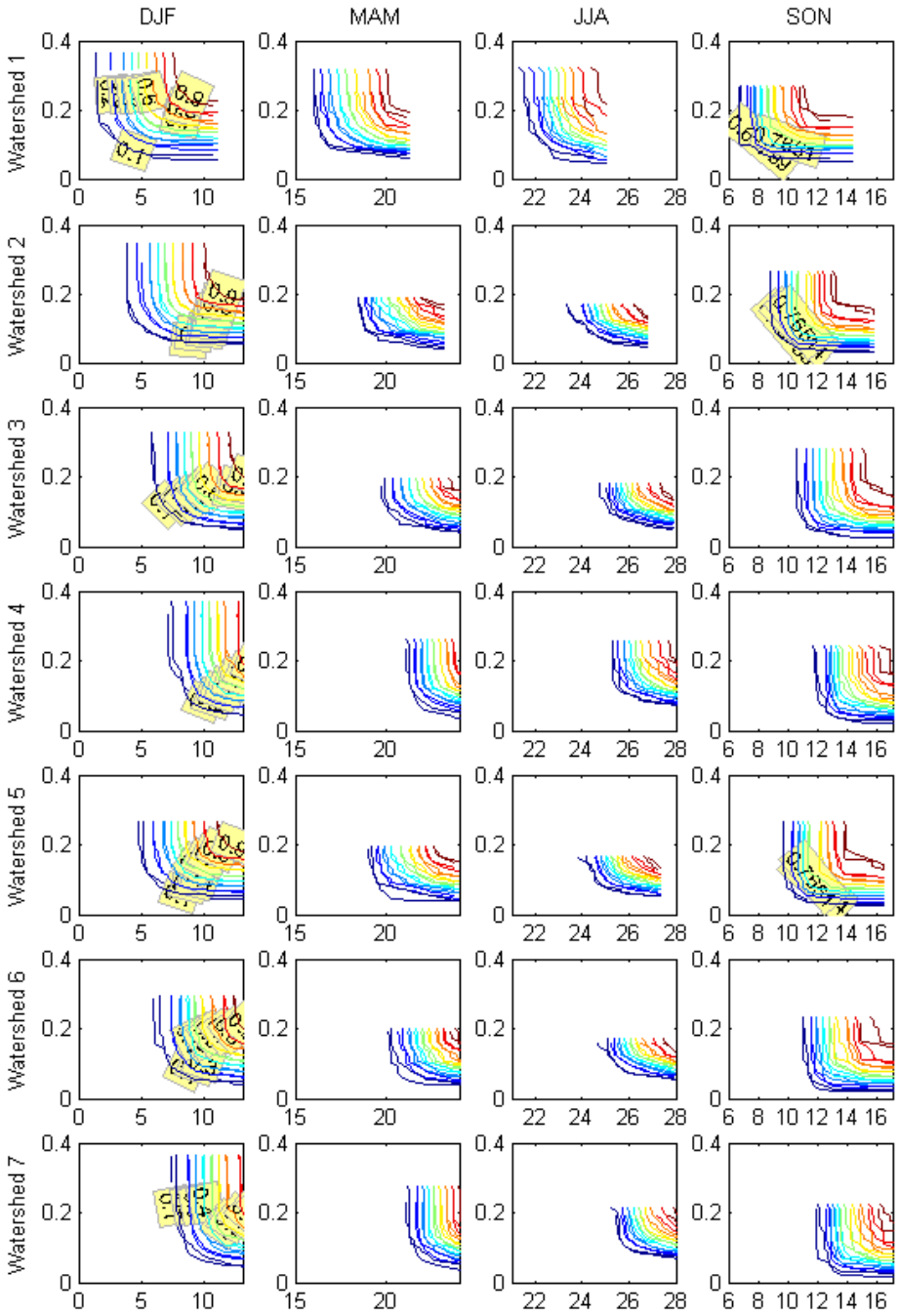

Figure 3.20: Joint CDFs of precipitation and temperature for each watershed and season corresponding to OBS and BCSD data: *(1)* Buford, *(2)* West Point, *(3)* George, *(4)* Woodruff, *(5)* Montezuma, *(6)* Albany, and *(7)* Bainbridge

3.3.5.3 Spatial (Inter-Grid Variability) Comparison

Many descriptive statistics exist to characterize the spatial patterns of gridded data including the covariance matrix (measurement of spatial dispersion), mean correlation coefficient (measurement of spatial correlation), and Ripley's K and L functions (measurements of spatial homogeneity of point data). This section examines the distribution of the pair-wise correlation between any two grid points within a watershed (Gissila et al., 2004).

Box-plots of the pair-wise correlation coefficients across the ACF watersheds are shown in **Figure 3.21**. As shown, the temperature field (second row of plots in **Figure 3.21**) exhibits high grid point correlations (greater than 0.99), indicating that the monthly temperatures are highly homogeneous within each watershed. Both JVSD and BCSD reproduce this homogeneity, but BCSD's correlation distributions are overly concentrated in comparison to the historical and JVSD distributions.

With respect to precipitation (first row of plots in **Figure 3.21**), the historical correlation distributions vary between 0.75 and 0.9. The plots show that the JVSD distributions match very closely the historical statistics, while BCSD exhibits a significant bias toward homogeneity. While this distributional bias is not as critical with respect to temperature, misrepresenting the spatial precipitation variability is a more serious weakness, especially if hydrologic assessments are based on distributed watershed models. The plots also show that the southern ACF watersheds, i.e., those that are situated below the fall line, have much larger inter-grid precipitation variability than the two northern watersheds (Buford and West Point).

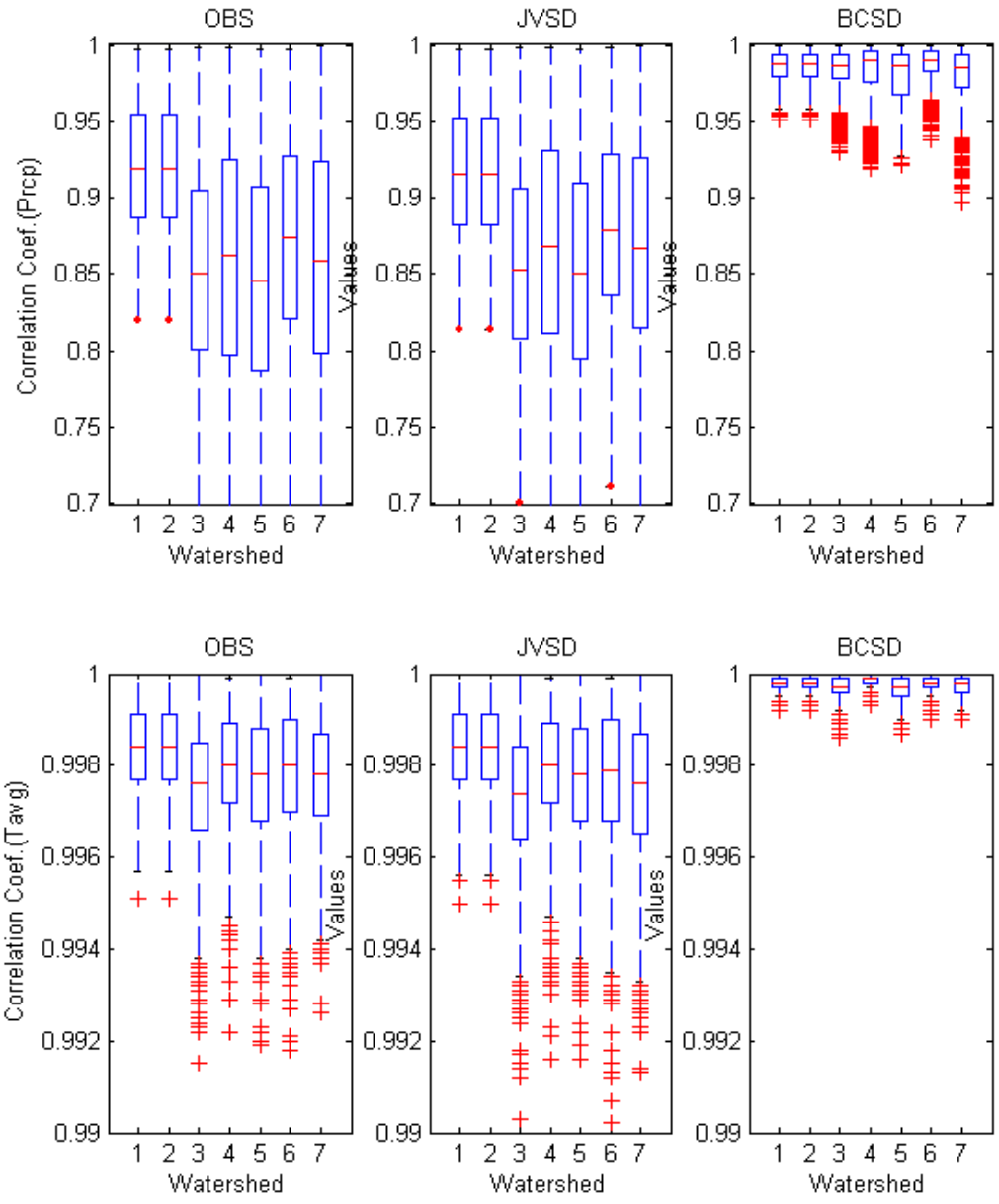

Figure 3.21: Box-plots of the pair-wise correlation coefficients across the ACF sub-basins: *(1)*Buford, *(2)* West Point, *(3)* George, *(4)* Woodruff, *(5)* Montezuma, *(6)*Albany, and *(7)* Bainbridge

3.3.5.4 Comparison with Dynamic Downscaling Methods

In this section, JVSD and BCSD are compared with the dynamic downscaling methods used in the North American Regional Climate Change Assessment Program (NARCCAP).

High resolution climate scenarios have been produced by NARCCAP using regional climate models (RCMs). The RCMs are nested within coupled Atmospheric-Ocean GCMs for the historical period 1971-2000 and for the future period 2041-2070 (NARCCAP, 2010). Several RCM/GCM combinations have been run and some of the products are available through the ESG (Earth System Grid; http://www.earthsystemgrid.org/) data distribution center. In the comparison presented herein, we select the results from one typical RCM/GCM combination corresponding to the Canadian GCM3 run4 data (cccma_cgcm3_1 sresa2, Run 4).

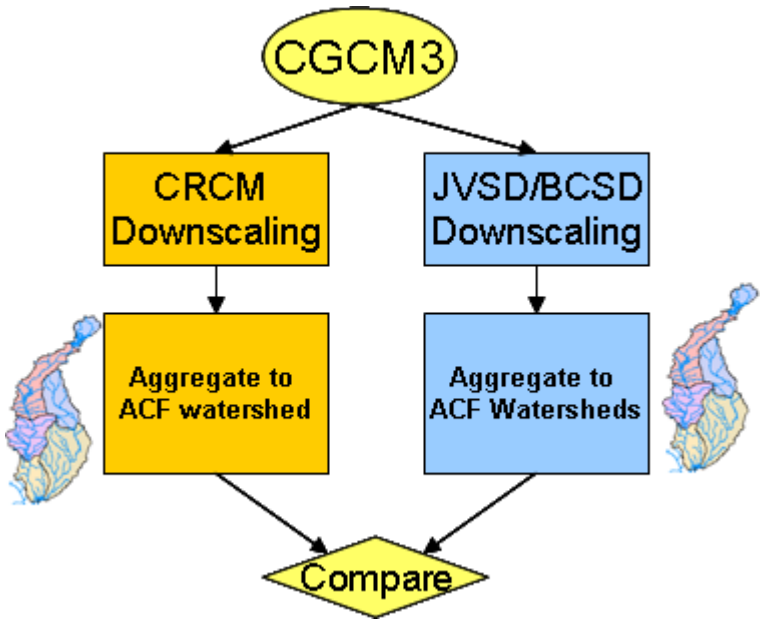

Figure 3.22: Comparison Process of JVSD with Dynamic Downscaling Methods from the NARCCAP Dataset (CRCM/CGCM3) for the Future Period 2041-2070

As illustrated in **Figure 3.22**, the results from CGCM3/SRESA2/RUN4 were downscaled using JVSD, BCSD, and CRCM/CGCM3 dynamic methods. The resulting precipitation and

temperature fields are aggregated over the ACF watersheds, and comparisons are made among these aggregated time series.

It is noted that the CGCM3 experiment provides boundary conditions for the CRCM run (Randel, 2007) without any bias corrections. Therefore, the downscaled data inherit the original GCM biases. To account for this inconsistency, JVSD was implemented and compared with CGCM3 with and without bias correction.

The comparisons of temperature and precipitation time series for the ACF watersheds are respectively shown in **Figures 3.23** and **3.24**. As indicated, the overall appearance of all downscaled time series is reasonably compatible. Conspicuously significant differences exist only for a few points. To better understand their differences, if any, the data values are expressed in frequency curves (**Figures 3.25** and **3.26**). The graphs comprising these figures correspond to the ACF watersheds and include four curves corresponding to the dynamically downscaled data (blue line), BCSD downscaled data (pink line), JVSD downscaled data without bias correction (cyan line), and JVSD downscaled data with bias correction (green line). Temperature comparisons are shown on **Figure 3.25**, and precipitation on **Figure 3.26**.

First, these comparisons show that the "No Bias Correction" JVSD version is very close to the dynamic downscaling method for both precipitation and temperature, thus supporting JVSD's applicability in the southeast US.

Second, the full JVSD (with bias correction) exhibits significant differences compared to the dynamic downscaling results for both temperature and precipitation. In light of the good correspondence of the observed data and JVSD results, dynamic downscaling without some form of bias correction would not be suitable for hydrologic assessments.

Third, BCSD and JVSD (the bias correction version) are fairly consistent with respect to temperature, but exhibit significant differences with respect to precipitation. The differences corroborate the findings of the previous comparisons indicating a BCSD tendency to generate less variable data, both temporally and spatially.

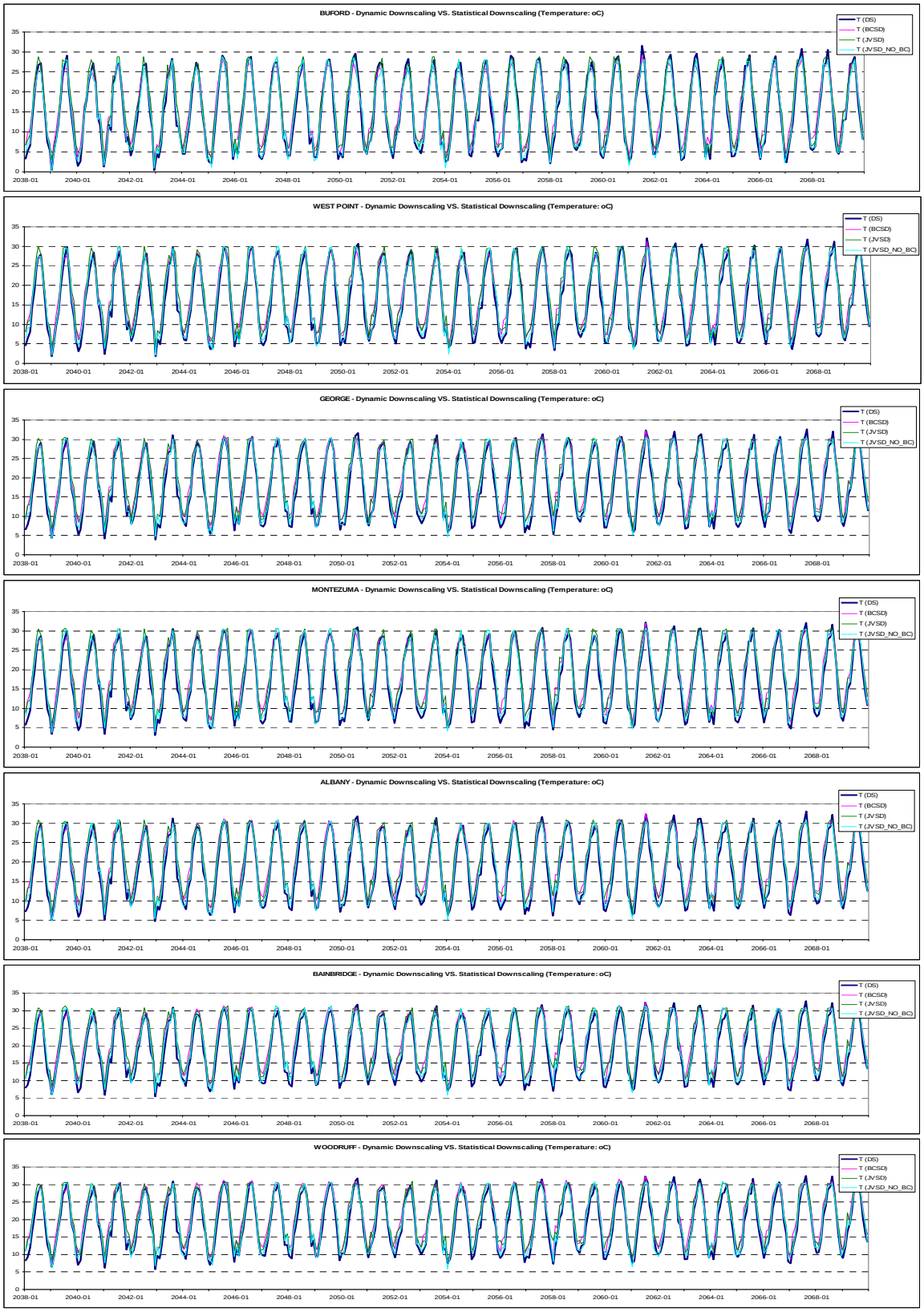

Figure 3.23: Comparisons of Downscaled Temperature Series for ACF Watersheds based on NARCCAP Methods, BCSD, JVSD with no bias correction, and JVSD with bias correction

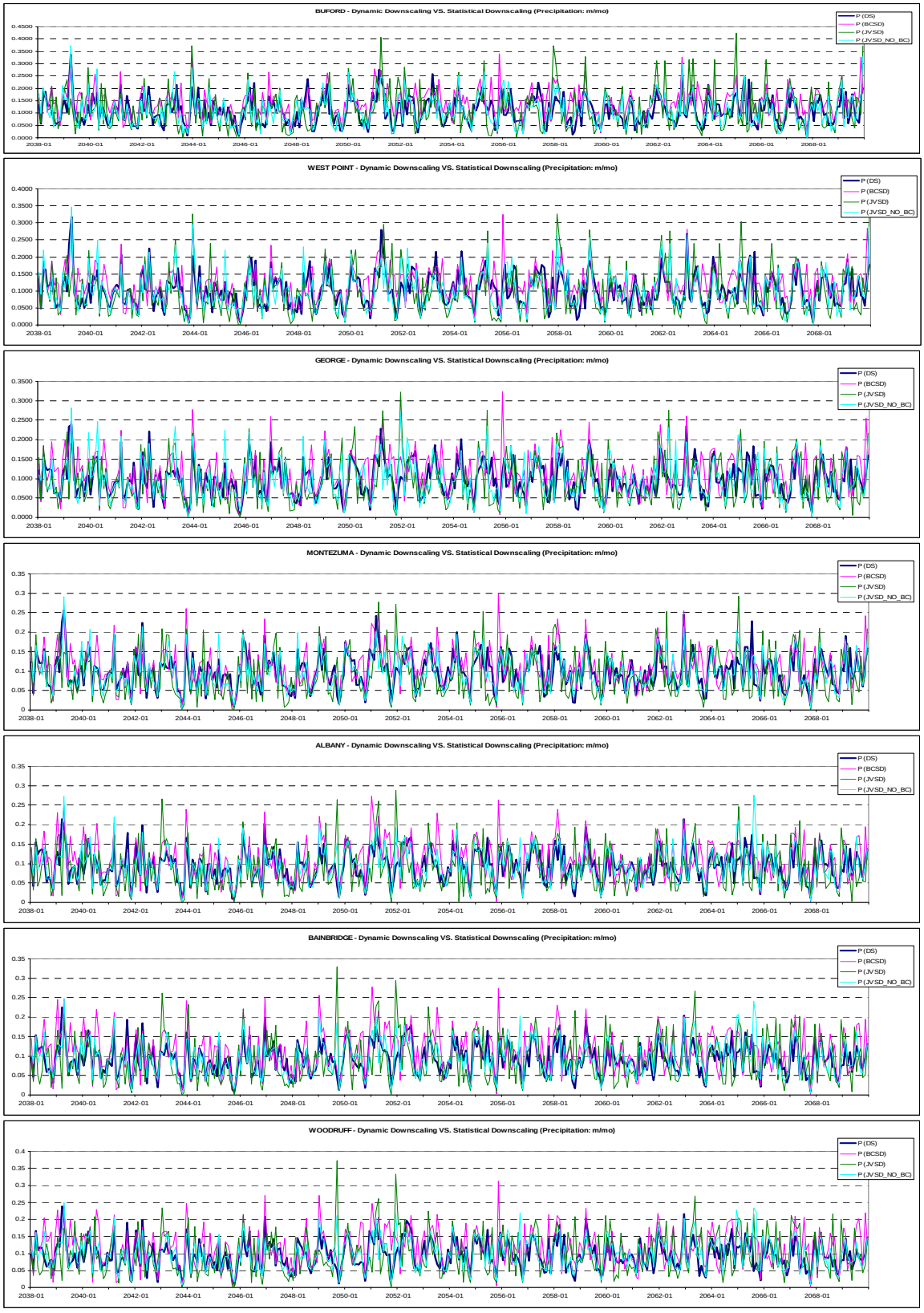

Figure 3.24: Comparisons of Downscaled Precipitation Series for the ACF Watersheds based on NARCCAP Methods, BCSD, JVSD without bias correction, and JVSD with bias correction

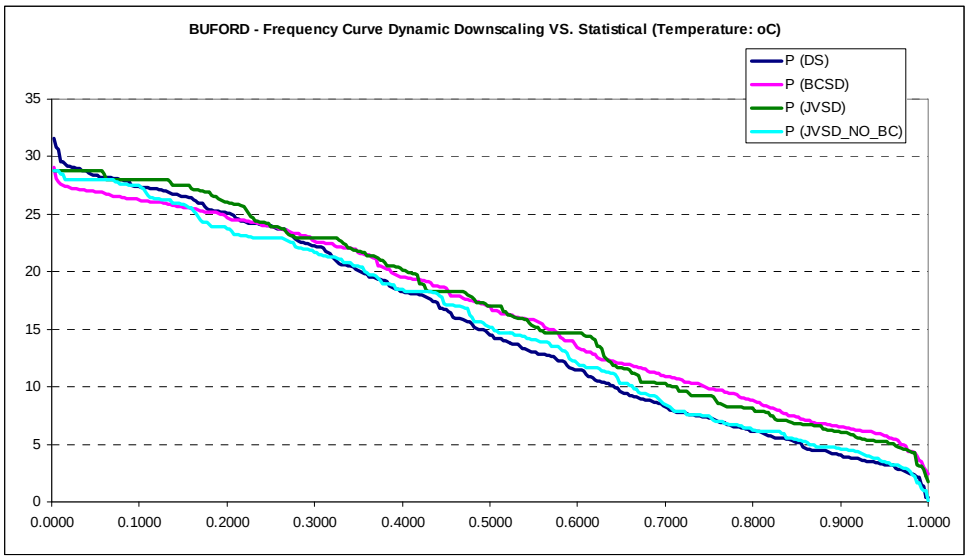
BUFORD - Frequency Curve Dynamic Downscaling VS. Statistical (Temperature: oC)
P (DS)
P (BCSD)
P (JVSD)
P (JVSD_NO_BC)
35
30
25
20
15
10
5
0
0.0000
0.1000
0.2000
0.3000
0.4000
0.5000
0.6000
0.7000
0.8000
0.9000
1.0000

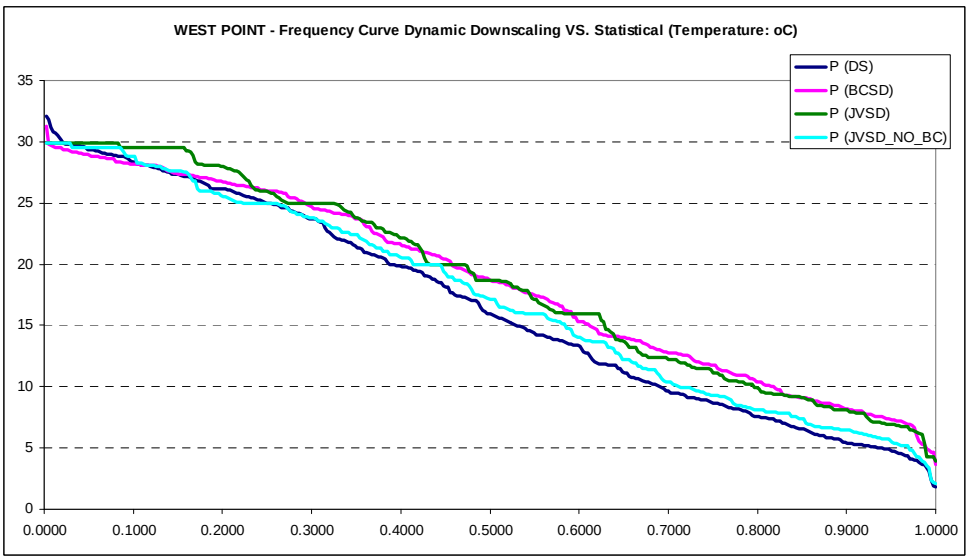
WEST POINT - Frequency Curve Dynamic Downscaling VS. Statistical (Temperature: oC)
P (DS)
P (BCSD)
P (JVSD)
P (JVSD_NO_BC)
35
30
25
20
15
10
5
0
0.0000
0.1000
0.2000
0.3000
0.4000
0.5000
0.6000
0.7000
0.8000
0.9000
1.0000

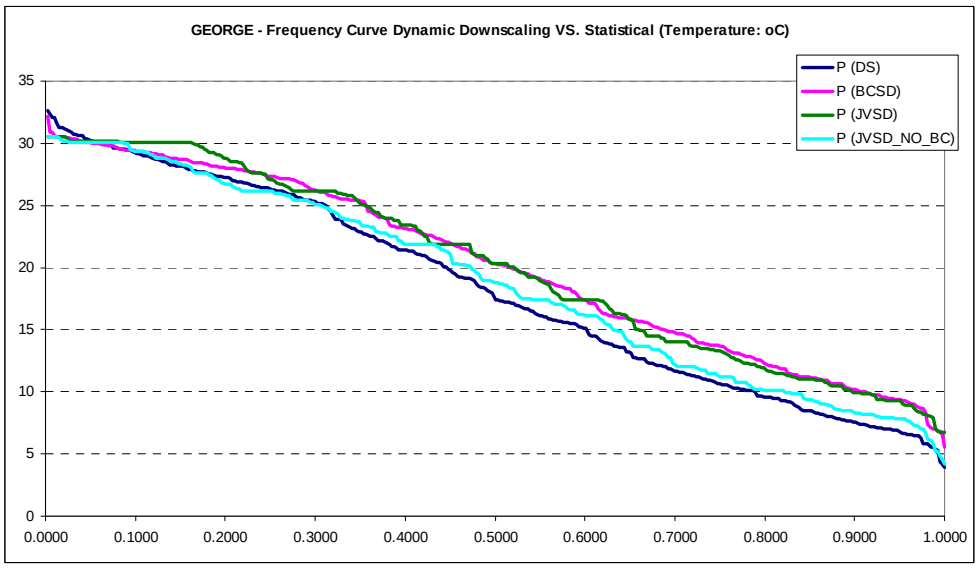
GEORGE - Frequency Curve Dynamic Downscaling VS. Statistical (Temperature: oC)
P (DS)
P (BCSD)
P (JVSD)
P (JVSD_NO_BC)
35
30
25
20
15
10
5
0
0.0000
0.1000
0.2000
0.3000
0.4000
0.5000
0.6000
0.7000
0.8000
0.9000
1.0000

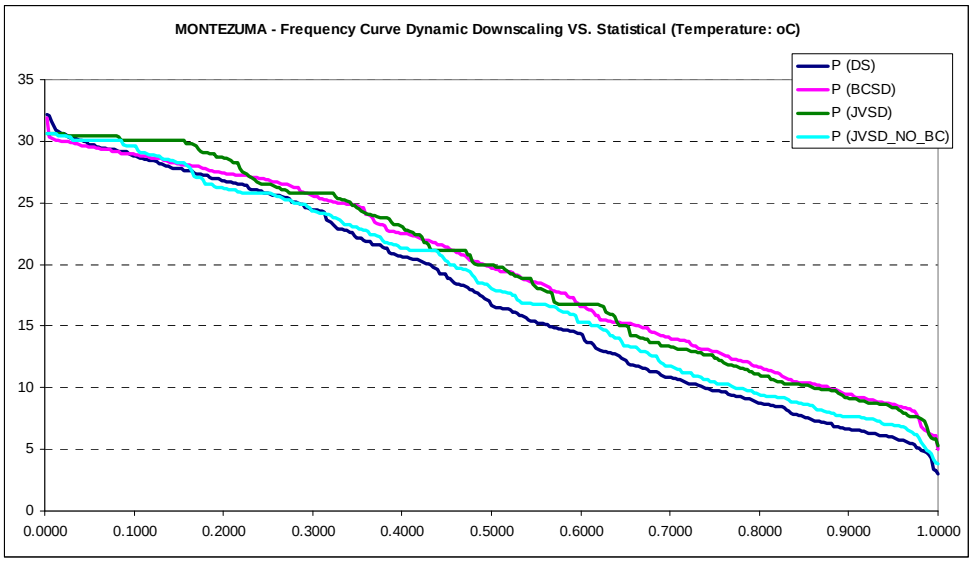
MONTEZUMA - Frequency Curve Dynamic Downscaling VS. Statistical (Temperature: oC)
P (DS)
P (BCSD)
P (JVSD)
P (JVSD_NO_BC)
35
30
25
20
15
10
5
0
0.0000
0.1000
0.2000
0.3000
0.4000
0.5000
0.6000
0.7000
0.8000
0.9000
1.0000

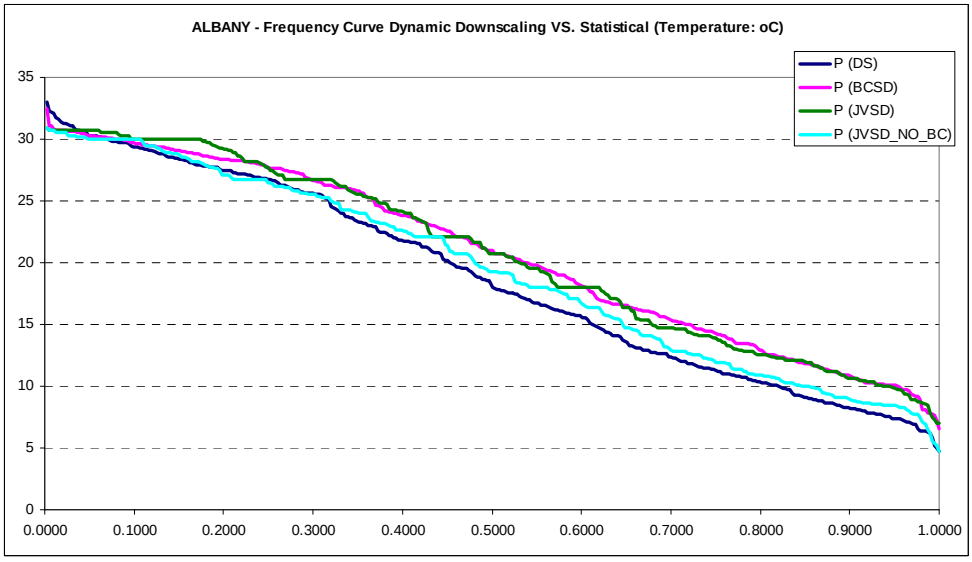
ALBANY - Frequency Curve Dynamic Downscaling VS. Statistical (Temperature: oC)
P (DS)
P (BCSD)
P (JVSD)
P (JVSD_NO_BC)
35
30
25
20
15
10
5
0
0.0000
0.1000
0.2000
0.3000
0.4000
0.5000
0.6000
0.7000
0.8000
0.9000
1.0000

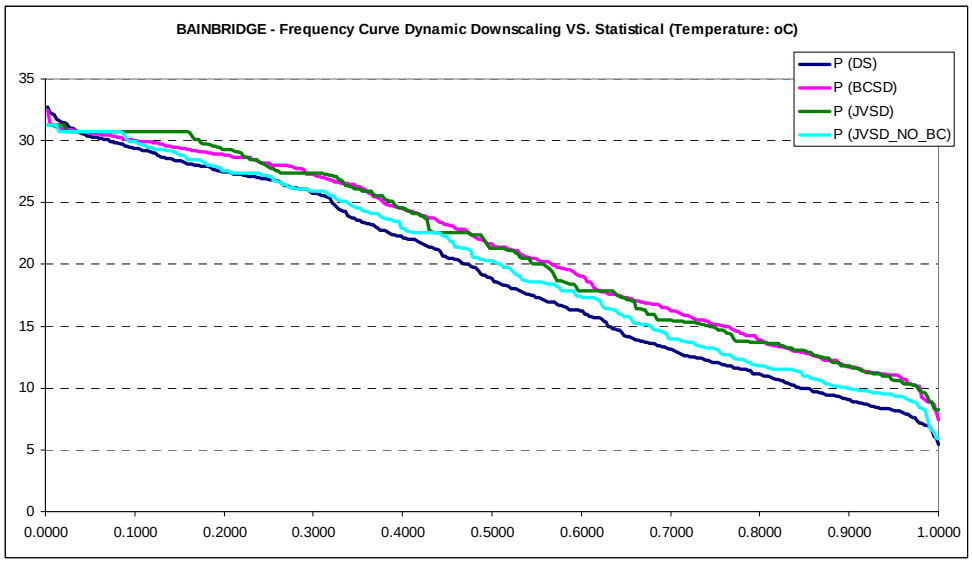
BAINBRIDGE - Frequency Curve Dynamic Downscaling VS. Statistical (Temperature: oC)
P (DS)
P (BCSD)
P (JVSD)
P (JVSD_NO_BC)
35
30
25
20
15
10
5
0
0.0000
0.1000
0.2000
0.3000
0.4000
0.5000
0.6000
0.7000
0.8000
0.9000
1.0000

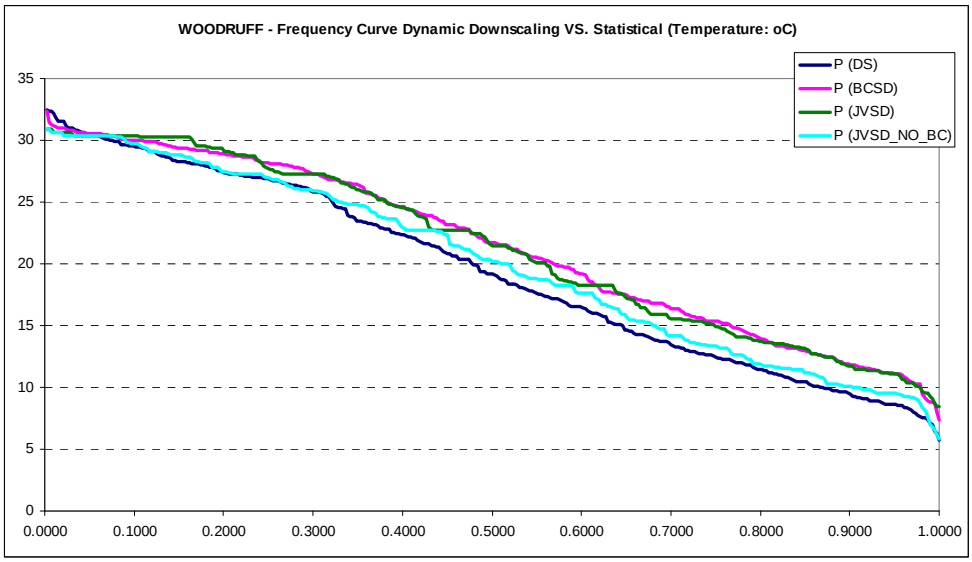

Figure 3.25: Comparisons of Downscaled Temperature Frequencies for ACF Watersheds based on NARCCAP Methods, BCSD, JVSD with no bias correction, and JVSD with bias correction

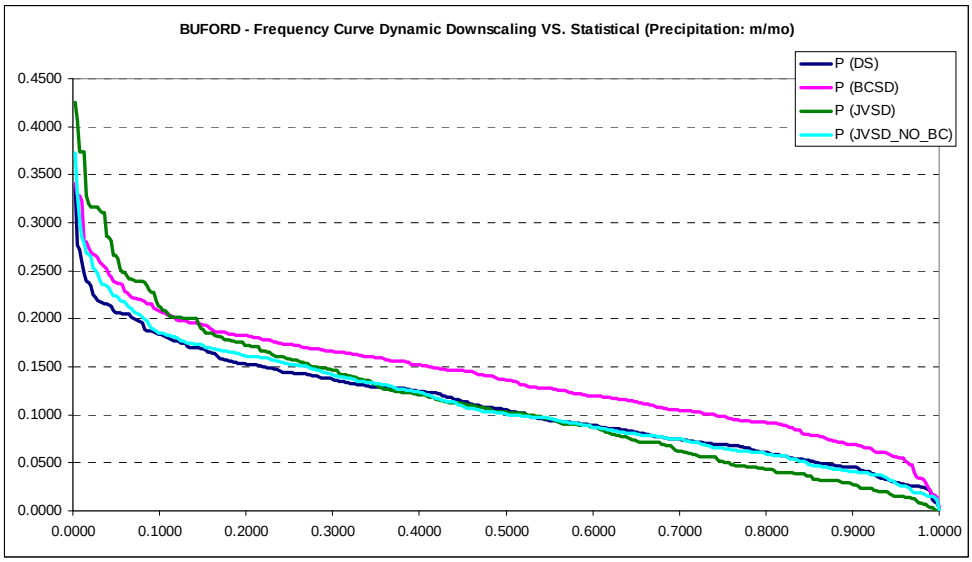
BUFORD - Frequency Curve Dynamic Downscaling VS. Statistical (Precipitation: m/mo)
P (DS)
P (BCSD)
P (JVSD)
P (JVSD_NO_BC)
0.4500
0.4000
0.3500
0.3000
0.2500
0.2000
0.1500
0.1000
0.0500
0.0000
0.0000
0.1000
0.2000
0.3000
0.4000
0.5000
0.6000
0.7000
0.8000
0.9000
1.0000

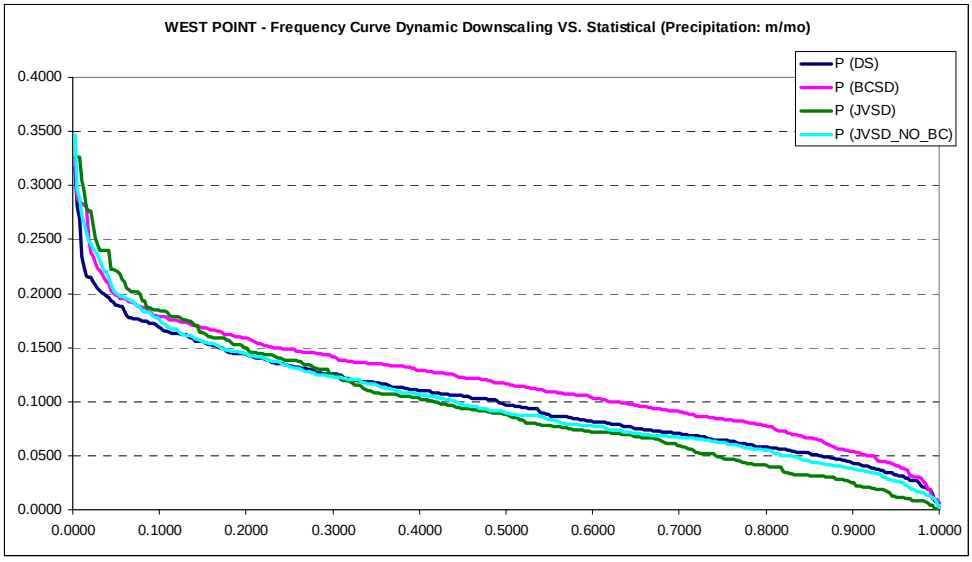
WEST POINT - Frequency Curve Dynamic Downscaling VS. Statistical (Precipitation: m/mo)
P (DS)
P (BCSD)
P (JVSD)
P (JVSD_NO_BC)
0.4000
0.3500
0.3000
0.2500
0.2000
0.1500
0.1000
0.0500
0.0000
0.0000
0.1000
0.2000
0.3000
0.4000
0.5000
0.6000
0.7000
0.8000
0.9000
1.0000

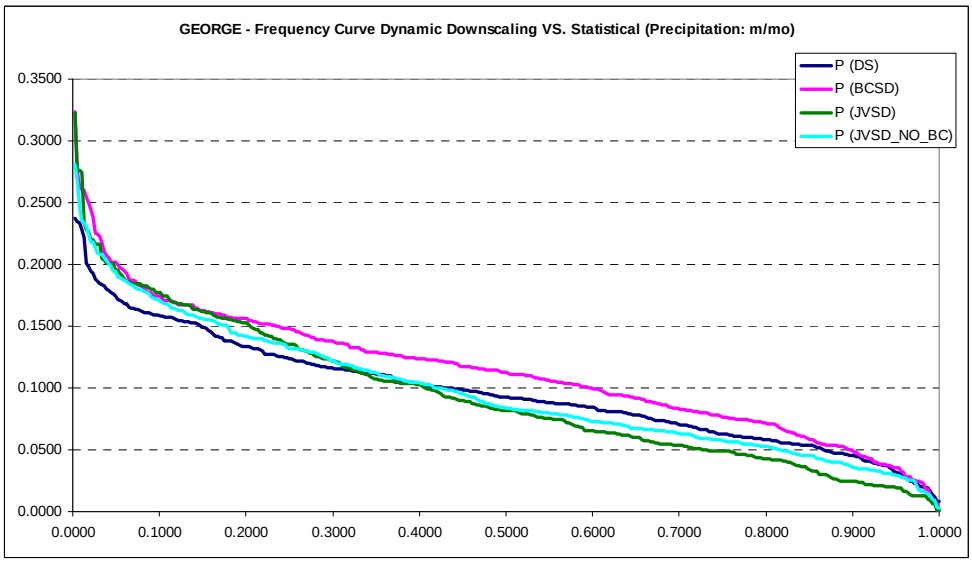
GEORGE - Frequency Curve Dynamic Downscaling VS. Statistical (Precipitation: m/mo)
P (DS)
P (BCSD)
P (JVSD)
P (JVSD_NO_BC)
0.3500
0.3000
0.2500
0.2000
0.1500
0.1000
0.0500
0.0000
0.0000
0.1000
0.2000
0.3000
0.4000
0.5000
0.6000
0.7000
0.8000
0.9000
1.0000

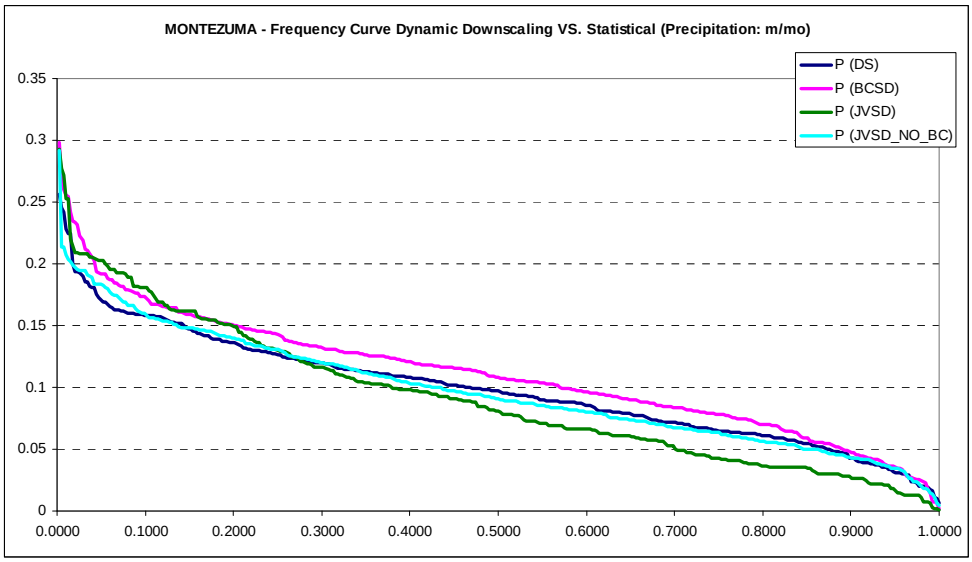
MONTEZUMA - Frequency Curve Dynamic Downscaling VS. Statistical (Precipitation: m/mo)
P (DS)
P (BCSD)
P (JVSD)
P (JVSD_NO_BC)
0.35
0.3
0.25
0.2
0.15
0.1
0.05
0
0.0000
0.1000
0.2000
0.3000
0.4000
0.5000
0.6000
0.7000
0.8000
0.9000
1.0000

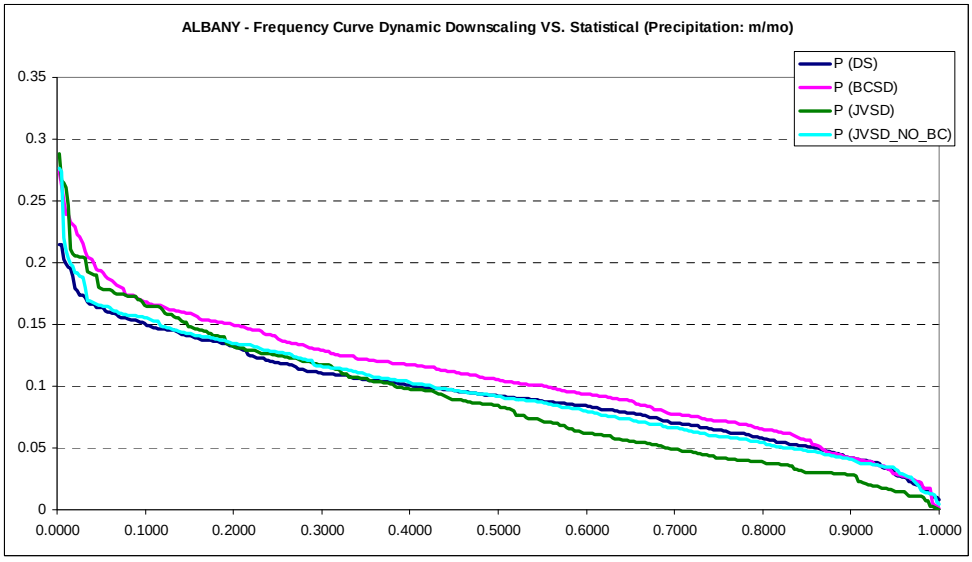
ALBANY - Frequency Curve Dynamic Downscaling VS. Statistical (Precipitation: m/mo)
P (DS)
P (BCSD)
P (JVSD)
P (JVSD_NO_BC)
0.35
0.3
0.25
0.2
0.15
0.1
0.05
0
0.0000
0.1000
0.2000
0.3000
0.4000
0.5000
0.6000
0.7000
0.8000
0.9000
1.0000

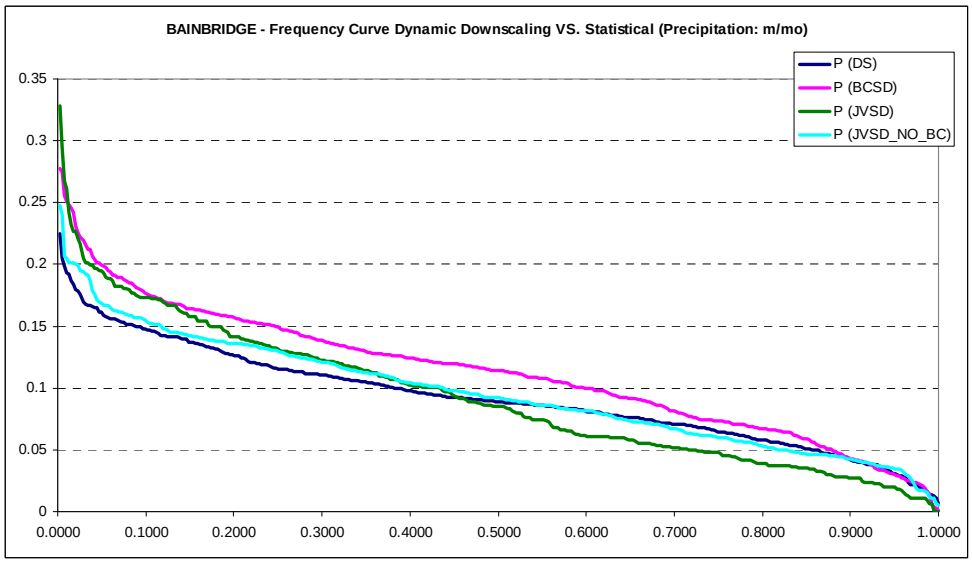
BAINBRIDGE - Frequency Curve Dynamic Downscaling VS. Statistical (Precipitation: m/mo)
P (DS)
P (BCSD)
P (JVSD)
P (JVSD_NO_BC)
0.35
0.3
0.25
0.2
0.15
0.1
0.05
0
0.0000
0.1000
0.2000
0.3000
0.4000
0.5000
0.6000
0.7000
0.8000
0.9000
1.0000

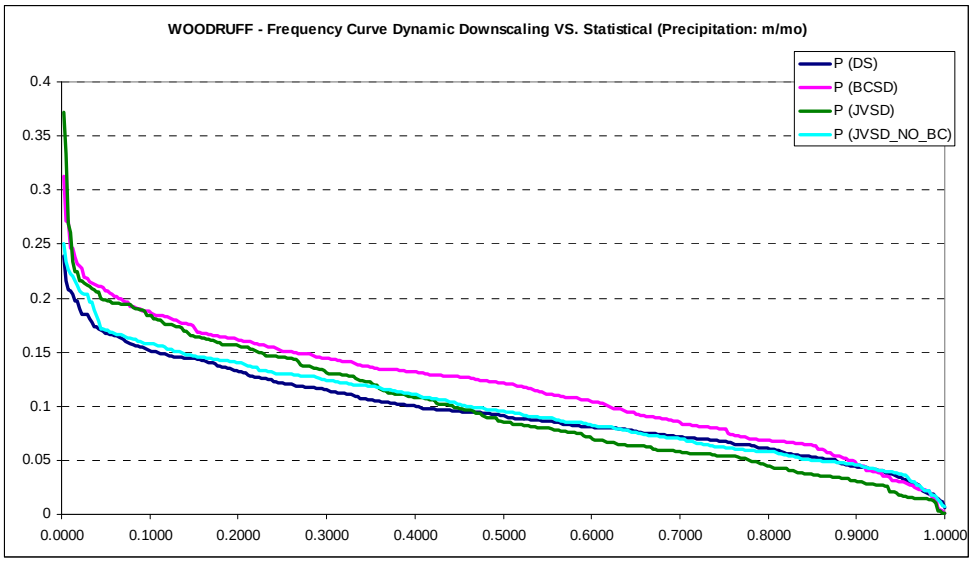

Figure 3.26: Comparisons of Downscaled Precipitation Frequencies for ACF Watersheds based on NARCCAP Methods, BCSD, JVSD with no bias correction, and JVSD with bias correction

3.4 Climate Assessments Based on Downscaled Scenarios

Using the new downscaling method, the temperature and precipitation of all A1B and A2 IPCC scenarios were downscaled for the ACF river basin region. The resulting temperature sequences for each ACF watershed were converted into potential evapotranspiration demand (Hammon PET method, Chapter 2) and are used together with the associated precipitation sequences as the basis of the assessments. These sequences are expressed in the form of frequency curves for the historical (1900-1999) and future time series (2000-2099) and are plotted for every watershed in **Figure 3.27** (A1B) and **Figure 3.28** (A2). The figures support the following comments:

(1) Both A1B and A2 scenarios exhibit increasing average PET for all ACF watersheds. Such increases intensify for watersheds in lower latitudes.

(2) PET increases are uneven across the frequency distribution, with high PET values experiencing considerably higher increases than the average or low PET values.

(3) Average precipitation changes over the ACF basin are insignificant. However, both distribution tails show significant changes, with high precipitation values exhibiting significant increases and low precipitation values exhibiting significant decreases. Namely, while the precipitation mean appears to stay comparable to the historical level, both extremes (floods and droughts) are expected to intensify; Combining this and previous findings, most ACF watersheds are likely to experience wetter winters (especially the watersheds in the upper Chattahoochee—Buford and West Point) and hotter summers (especially the watersheds in the Flint River—Montezuma and Albany) with more extreme floods and droughts possible;

(4) The A2 scenarios changes are more significant than those of A1B; and

(5) The differences among the GCM scenarios indicate large uncertainties associated with long-range climate simulations. It is thus important that hydrologic and water resources assessments be carried out for multiple scenarios and the results interpreted from an ensemble perspective. Such assessments are taken up in the following chapters.

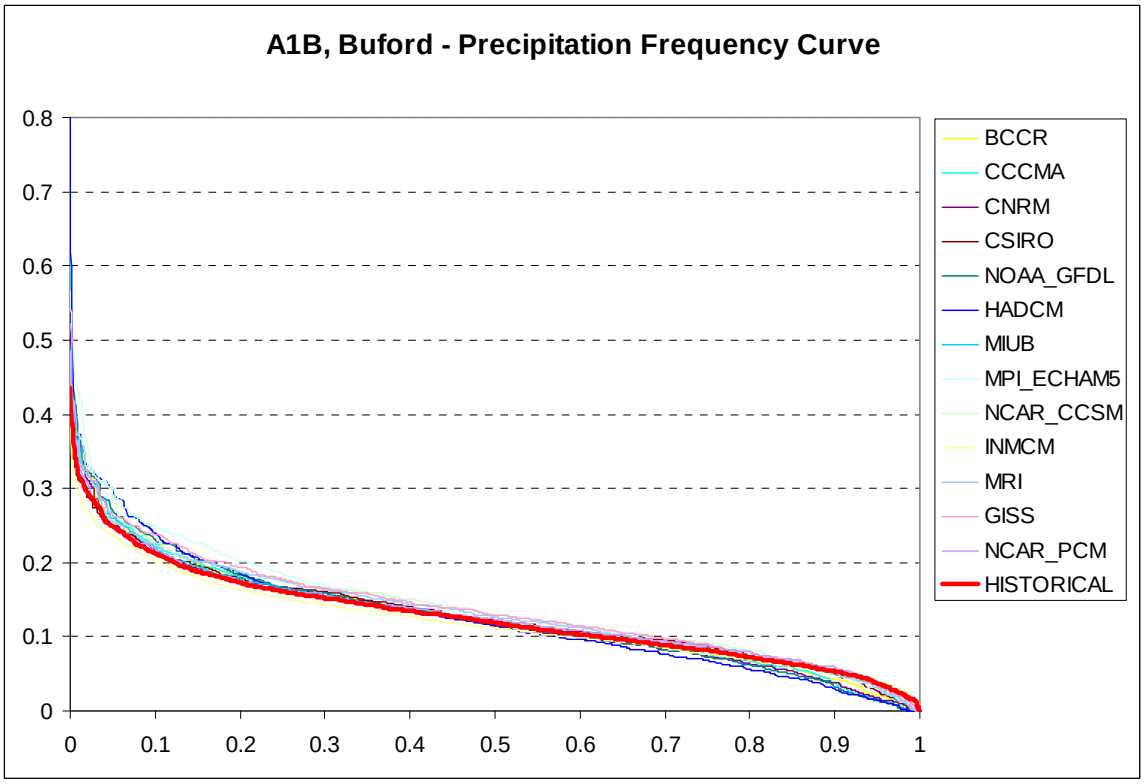
A1B, Buford - Precipitation Frequency Curve
0.8
0.7
0.6
0.5
0.4
0.3
0.2
0.1
0
0
0.1
0.2
0.3
0.4
0.5
0.6
0.7
0.8
0.9
1
BCCR
CCCMA
CNRM
CSIRO
NOAA_GFDL
HADCM
MIUB
MPI_ECHAM5
NCAR_CCSM
INMCM
MRI
GISS
NCAR_PCM
HISTORICAL

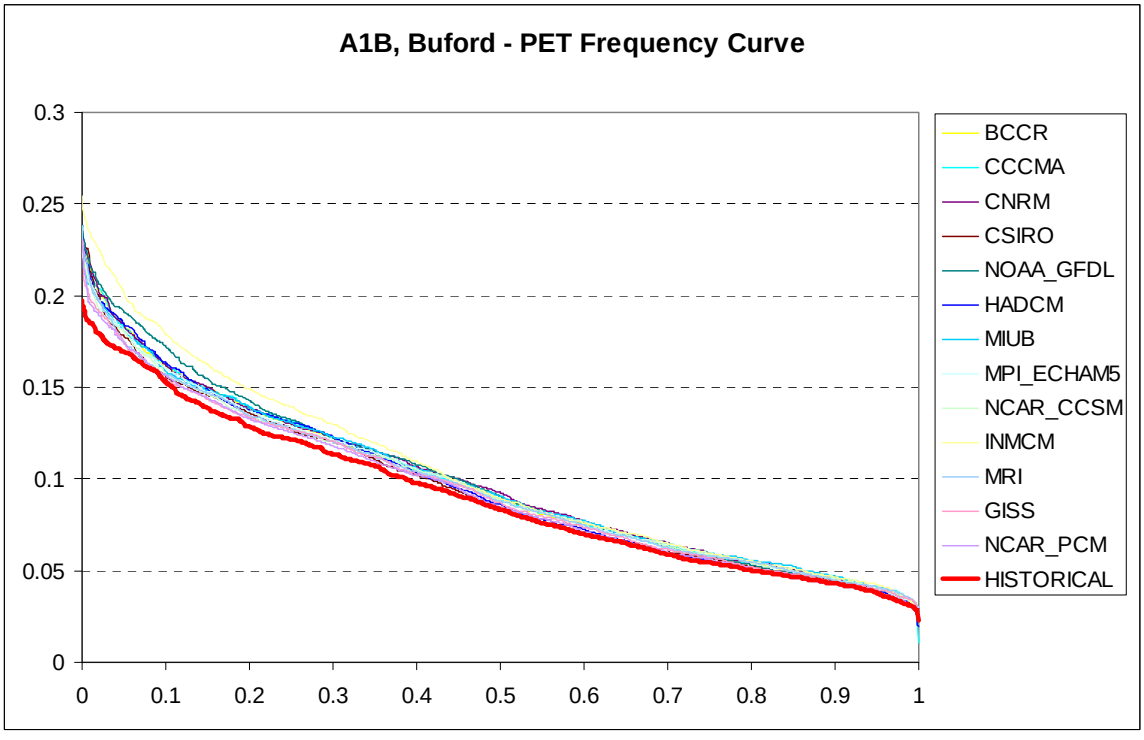
A1B, Buford - PET Frequency Curve
0.3
0.25
0.2
0.15
0.1
0.05
0
0
0.1
0.2
0.3
0.4
0.5
0.6
0.7
0.8
0.9
1
BCCR
CCCMA
CNRM
CSIRO
NOAA_GFDL
HADCM
MIUB
MPI_ECHAM5
NCAR_CCSM
INMCM
MRI
GISS
NCAR_PCM
HISTORICAL

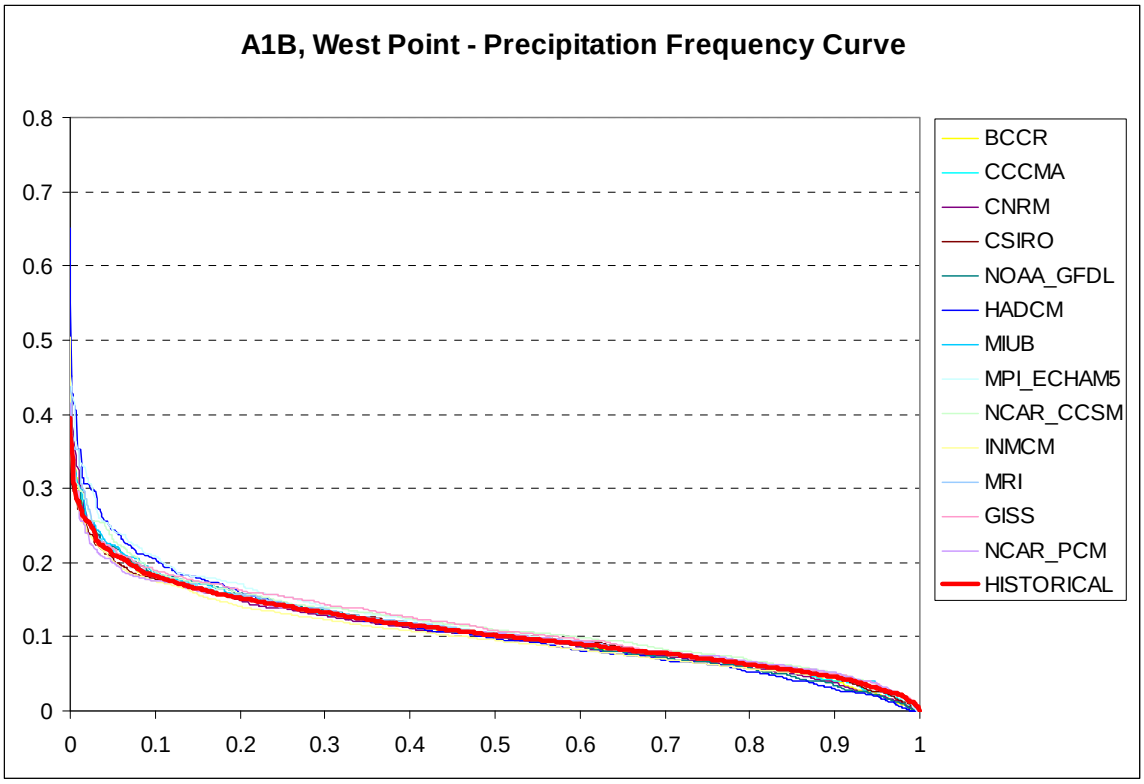
A1B, West Point - Precipitation Frequency Curve
0.8
0.7
0.6
0.5
0.4
0.3
0.2
0.1
0
0
0.1
0.2
0.3
0.4
0.5
0.6
0.7
0.8
0.9
1
BCCR
CCCMA
CNRM
CSIRO
NOAA_GFDL
HADCM
MIUB
MPI_ECHAM5
NCAR_CCSM
INMCM
MRI
GISS
NCAR_PCM
HISTORICAL

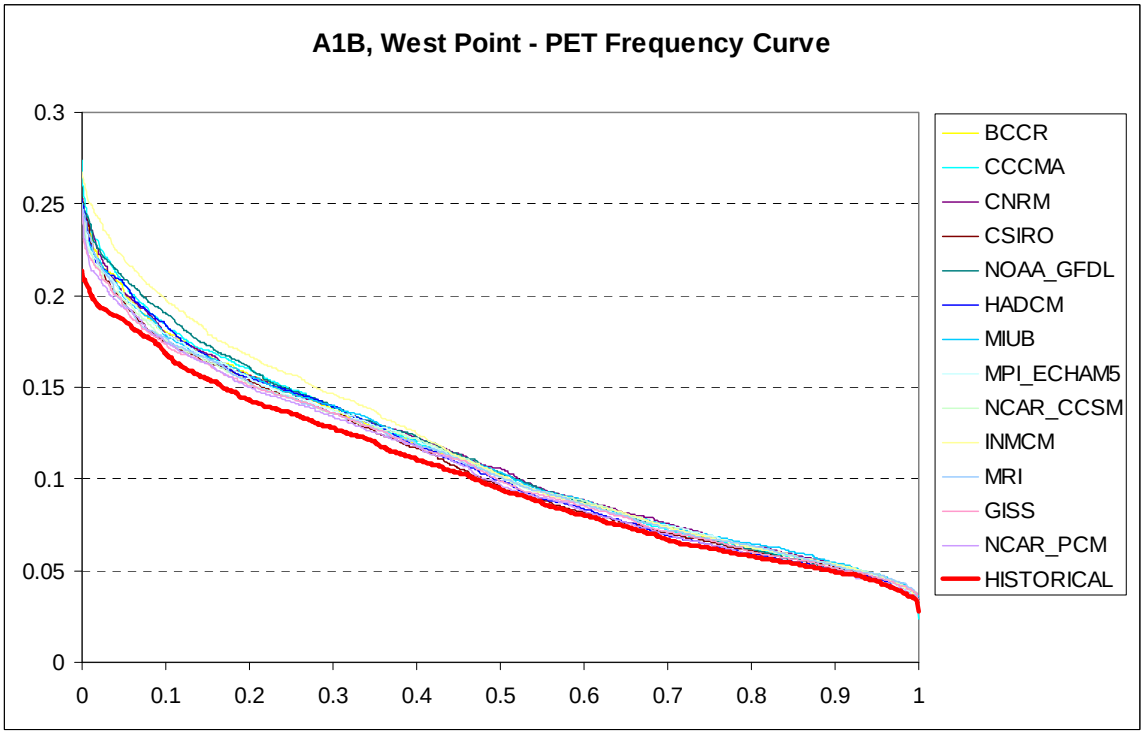
A1B, West Point - PET Frequency Curve
0.3
0.25
0.2
0.15
0.1
0.05
0
0
0.1
0.2
0.3
0.4
0.5
0.6
0.7
0.8
0.9
1
BCCR
CCCMA
CNRM
CSIRO
NOAA_GFDL
HADCM
MIUB
MPI_ECHAM5
NCAR_CCSM
INMCM
MRI
GISS
NCAR_PCM
HISTORICAL

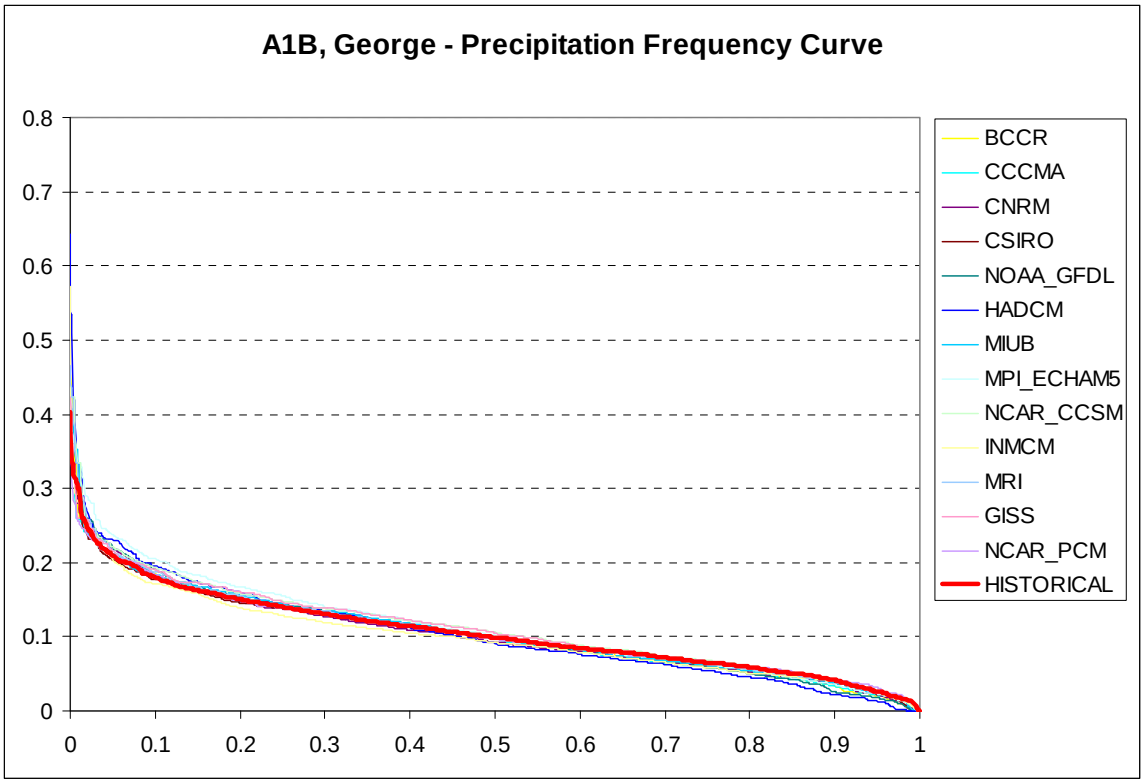
A1B, George - Precipitation Frequency Curve
0.8
0.7
0.6
0.5
0.4
0.3
0.2
0.1
0
0
0.1
0.2
0.3
0.4
0.5
0.6
0.7
0.8
0.9
1
BCCR
CCCMA
CNRM
CSIRO
NOAA_GFDL
HADCM
MIUB
MPI_ECHAM5
NCAR_CCSM
INMCM
MRI
GISS
NCAR_PCM
HISTORICAL

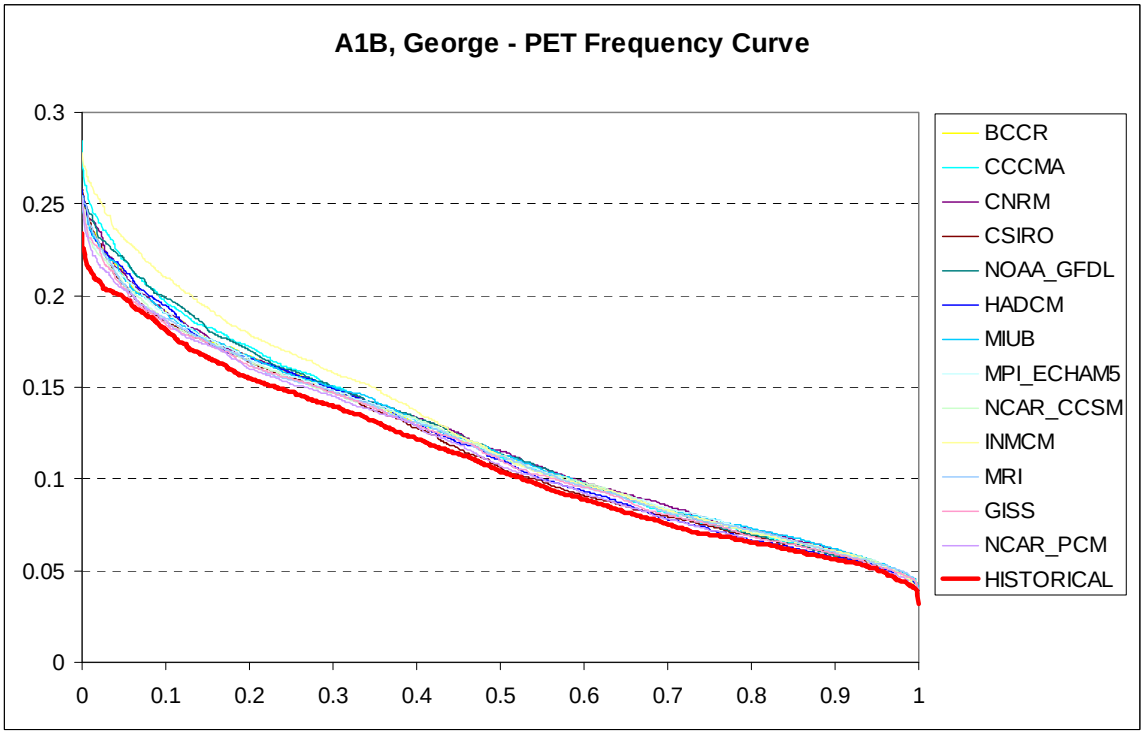
A1B, George - PET Frequency Curve
0.3
0.25
0.2
0.15
0.1
0.05
0
0
0.1
0.2
0.3
0.4
0.5
0.6
0.7
0.8
0.9
1
BCCR
CCCMA
CNRM
CSIRO
NOAA_GFDL
HADCM
MIUB
MPI_ECHAM5
NCAR_CCSM
INMCM
MRI
GISS
NCAR_PCM
HISTORICAL

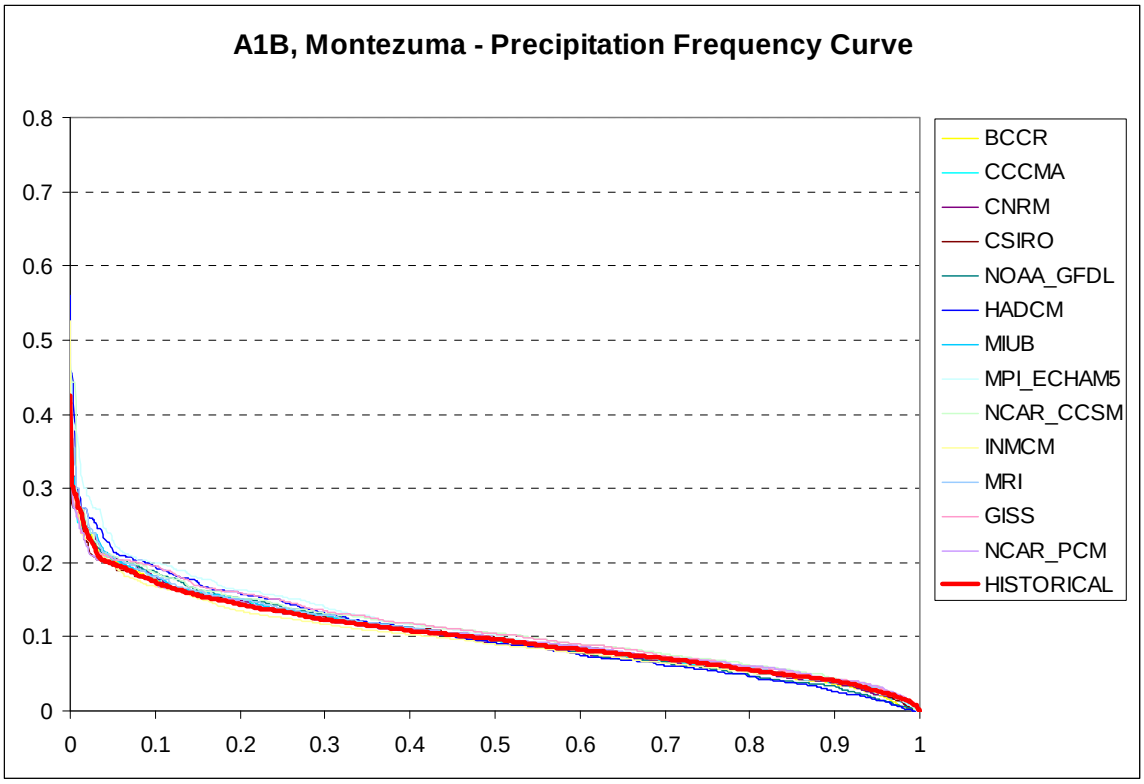
A1B, Montezuma - Precipitation Frequency Curve
0.8
0.7
0.6
0.5
0.4
0.3
0.2
0.1
0
0
0.1
0.2
0.3
0.4
0.5
0.6
0.7
0.8
0.9
1
BCCR
CCCMA
CNRM
CSIRO
NOAA_GFDL
HADCM
MIUB
MPI_ECHAM5
NCAR_CCSM
INMCM
MRI
GISS
NCAR_PCM
HISTORICAL

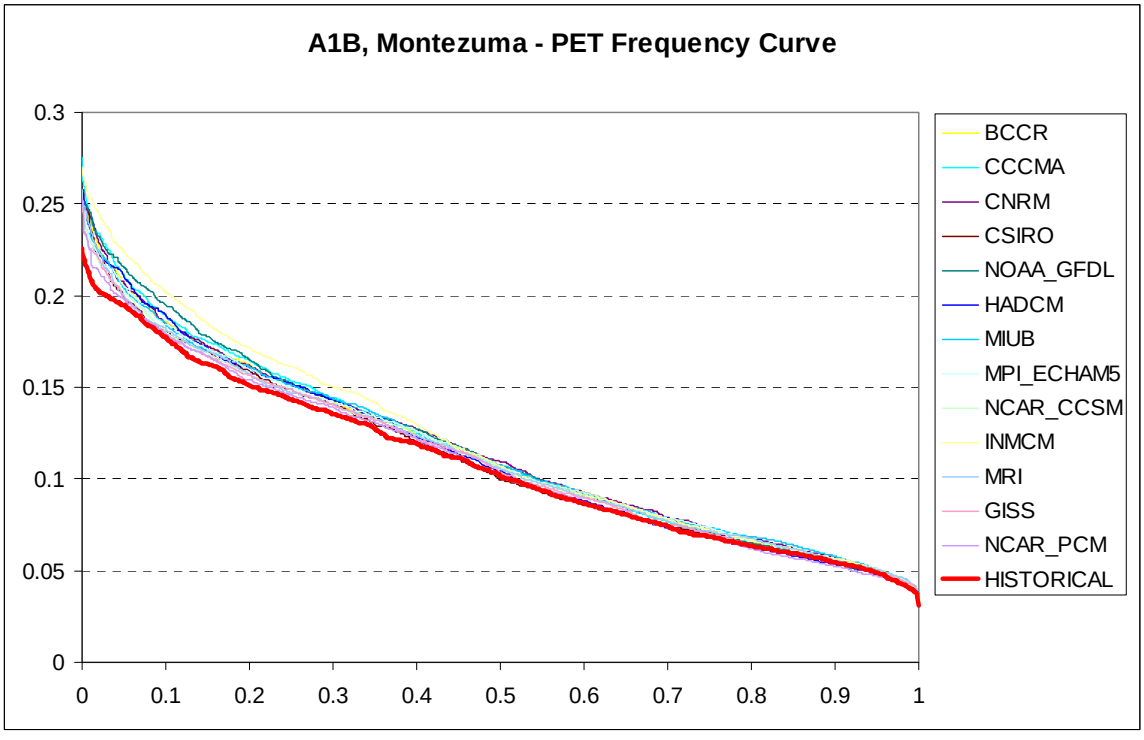
A1B, Montezuma - PET Frequency Curve
0.3
0.25
0.2
0.15
0.1
0.05
0
0
0.1
0.2
0.3
0.4
0.5
0.6
0.7
0.8
0.9
1
BCCR
CCCMA
CNRM
CSIRO
NOAA_GFDL
HADCM
MIUB
MPI_ECHAM5
NCAR_CCSM
INMCM
MRI
GISS
NCAR_PCM
HISTORICAL

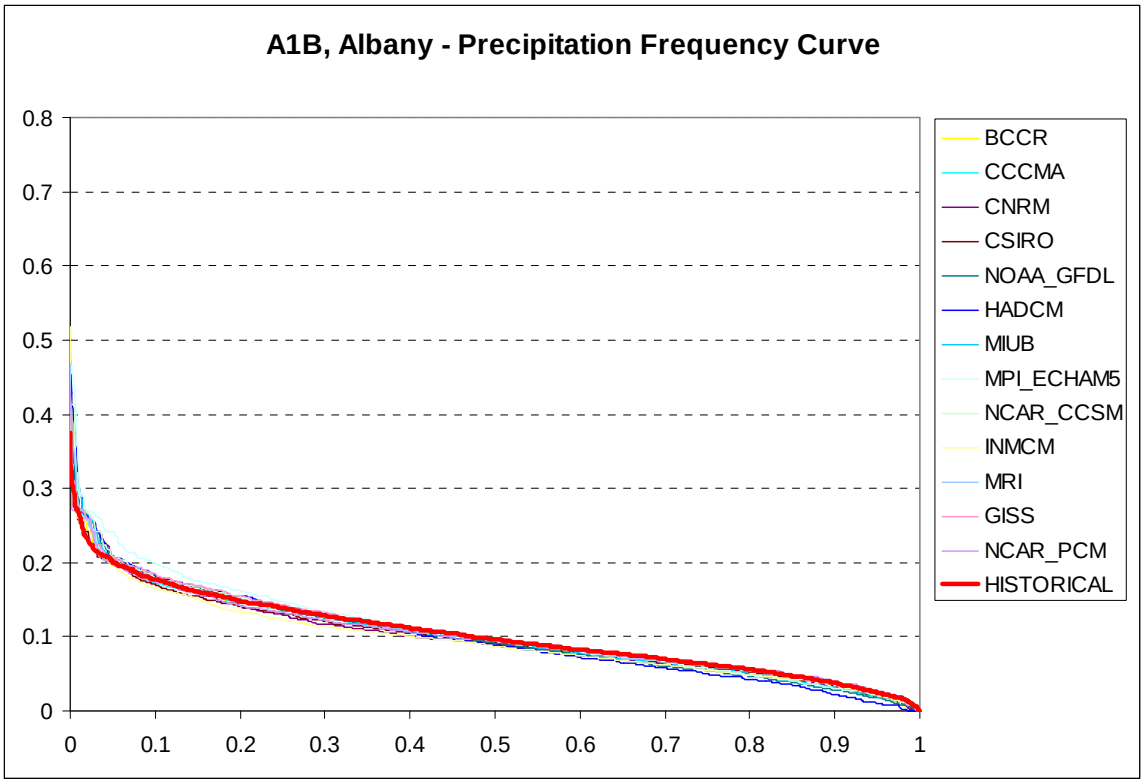
A1B, Albany - Precipitation Frequency Curve
0.8
0.7
0.6
0.5
0.4
0.3
0.2
0.1
0
0
0.1
0.2
0.3
0.4
0.5
0.6
0.7
0.8
0.9
1
BCCR
CCCMA
CNRM
CSIRO
NOAA_GFDL
HADCM
MIUB
MPI_ECHAM5
NCAR_CCSM
INMCM
MRI
GISS
NCAR_PCM
HISTORICAL

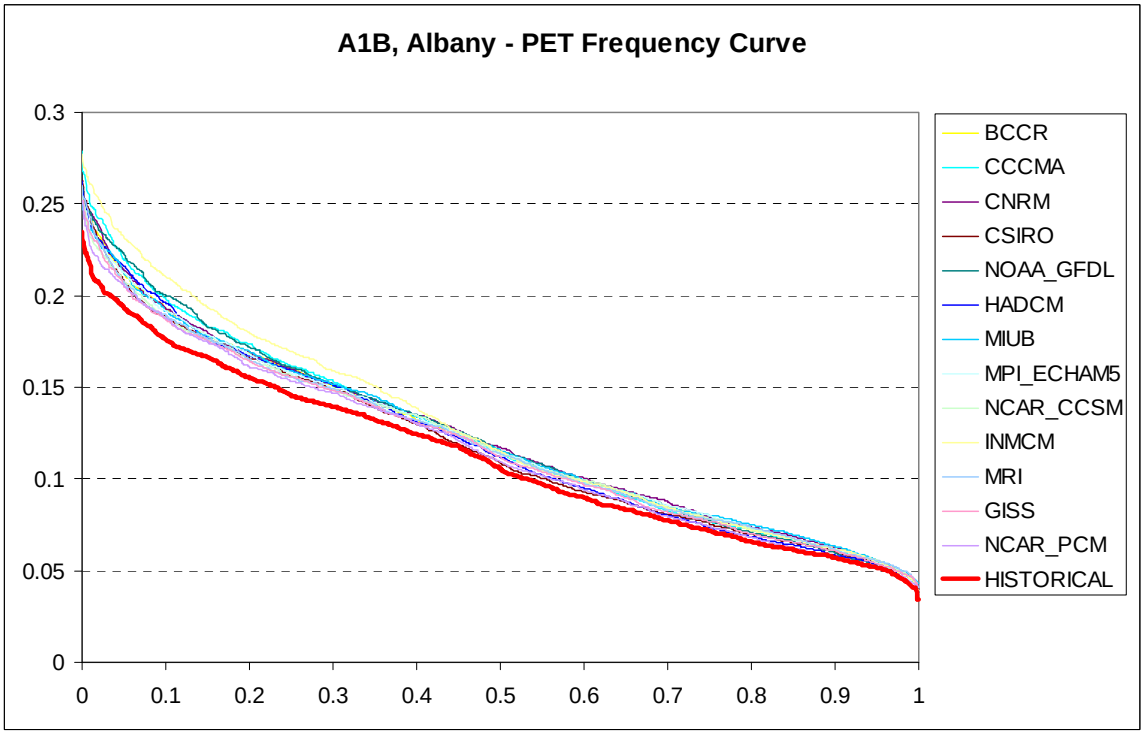
A1B, Albany - PET Frequency Curve
0.3
0.25
0.2
0.15
0.1
0.05
0
0
0.1
0.2
0.3
0.4
0.5
0.6
0.7
0.8
0.9
1
BCCR
CCCMA
CNRM
CSIRO
NOAA_GFDL
HADCM
MIUB
MPI_ECHAM5
NCAR_CCSM
INMCM
MRI
GISS
NCAR_PCM
HISTORICAL

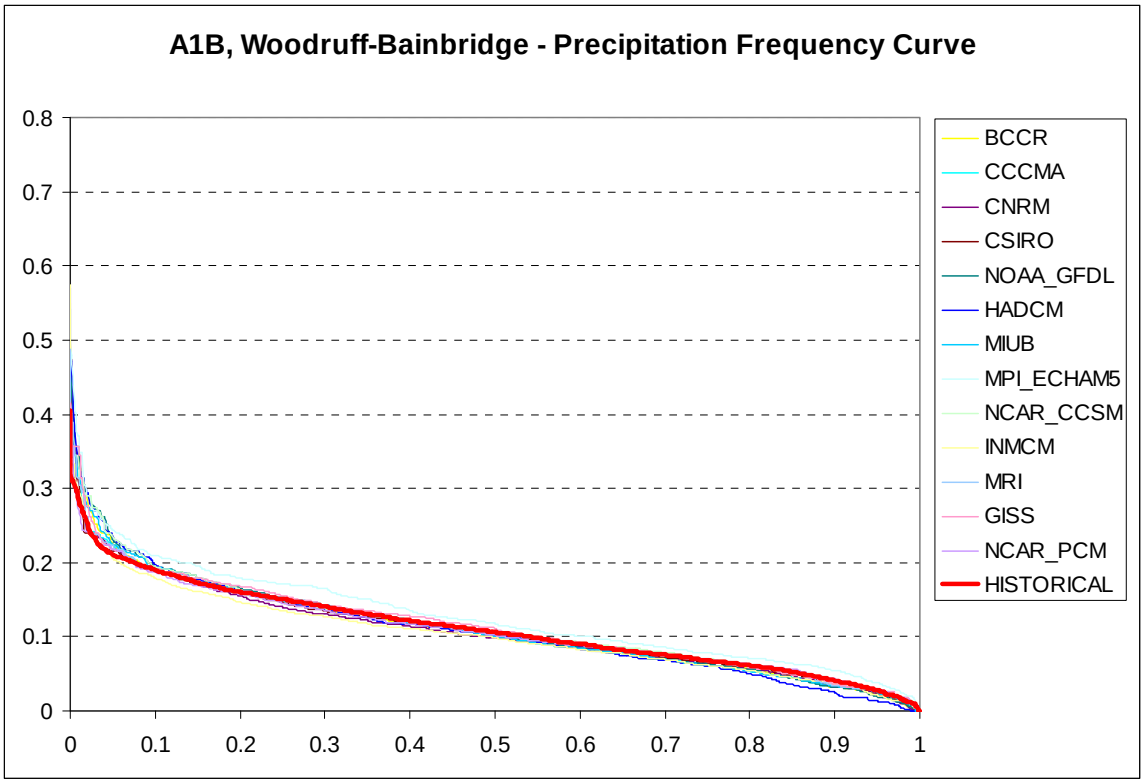

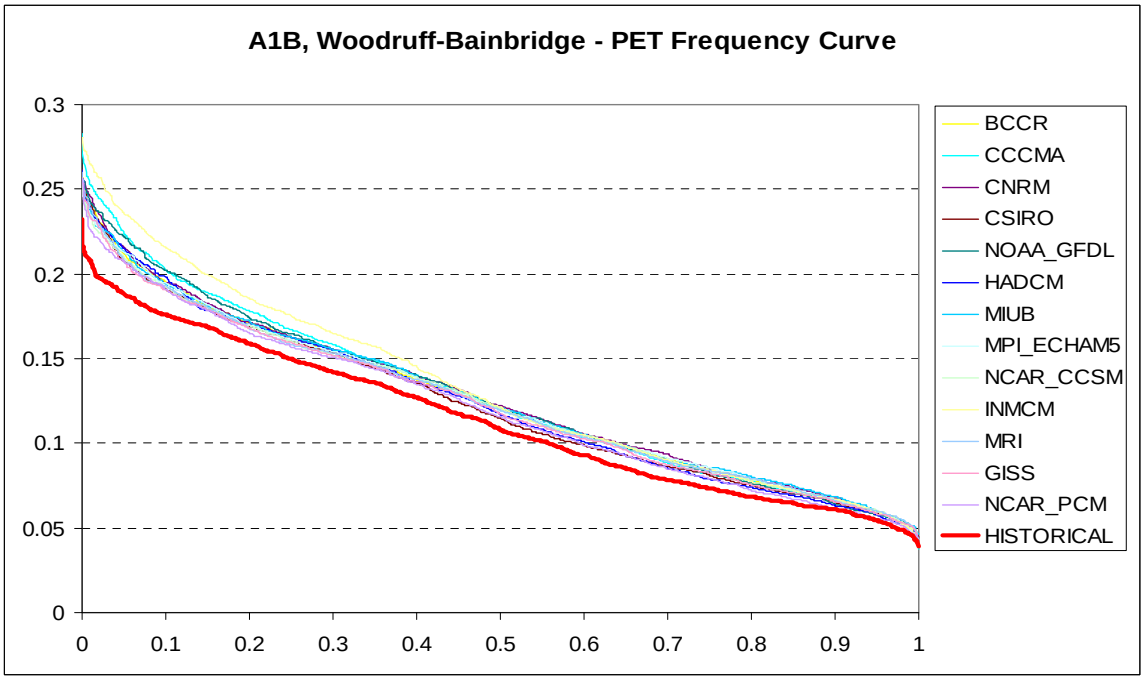

Figure 3.27: Frequency Curves of Precipitation and PET Sequences for A1B Scenarios

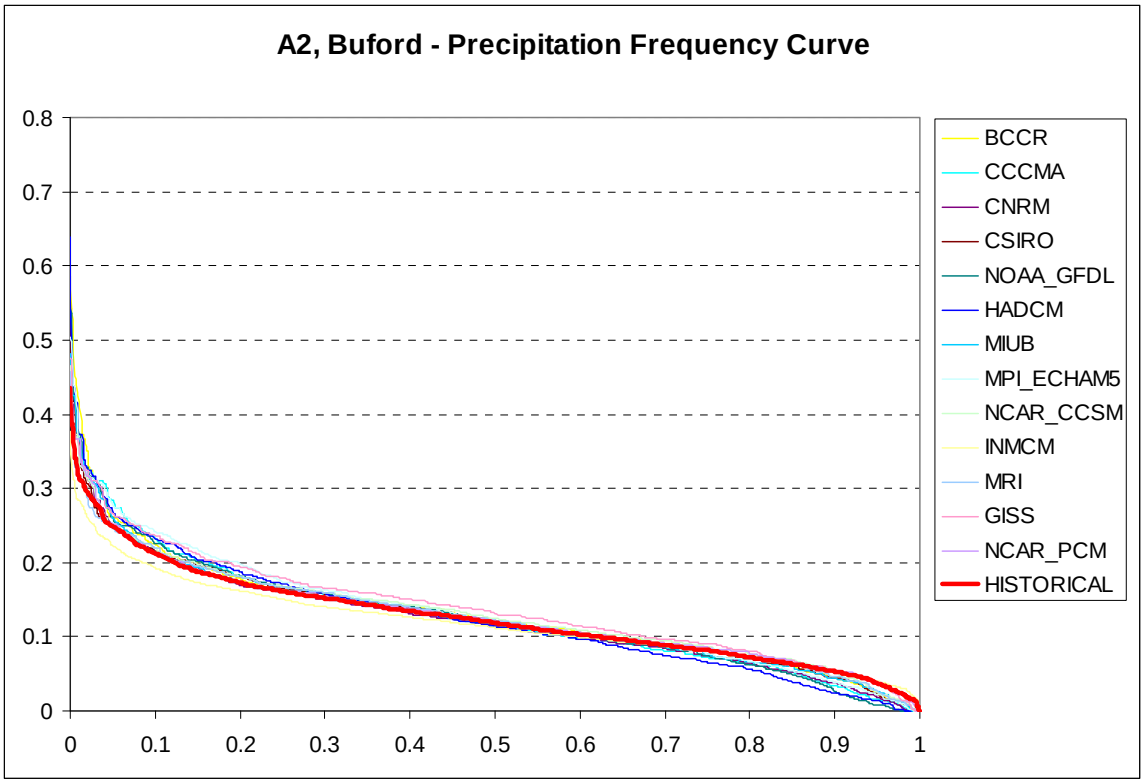
A2, Buford - Precipitation Frequency Curve
0.8
0.7
0.6
0.5
0.4
0.3
0.2
0.1
0
0
0.1
0.2
0.3
0.4
0.5
0.6
0.7
0.8
0.9
1
BCCR
CCCMA
CNRM
CSIRO
NOAA_GFDL
HADCM
MIUB
MPI_ECHAM5
NCAR_CCSM
INMCM
MRI
GISS
NCAR_PCM
HISTORICAL

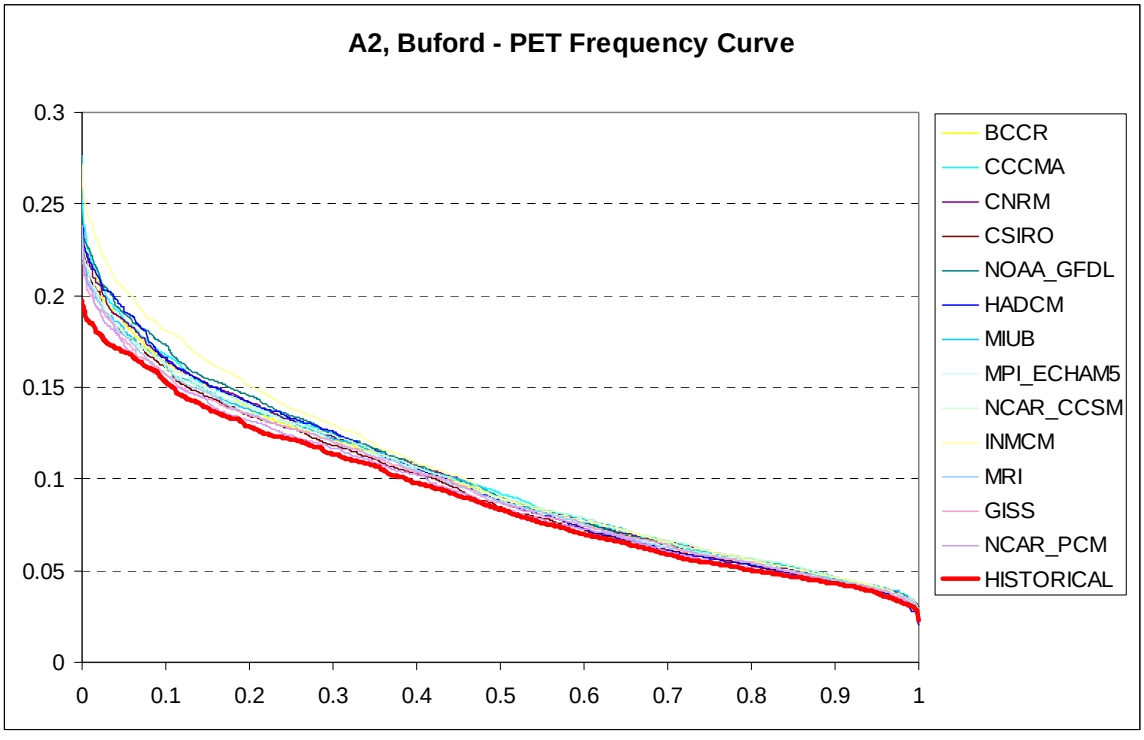
A2, Buford - PET Frequency Curve
0.3
0.25
0.2
0.15
0.1
0.05
0
0
0.1
0.2
0.3
0.4
0.5
0.6
0.7
0.8
0.9
1
BCCR
CCCMA
CNRM
CSIRO
NOAA_GFDL
HADCM
MIUB
MPI_ECHAM5
NCAR_CCSM
INMCM
MRI
GISS
NCAR_PCM
HISTORICAL

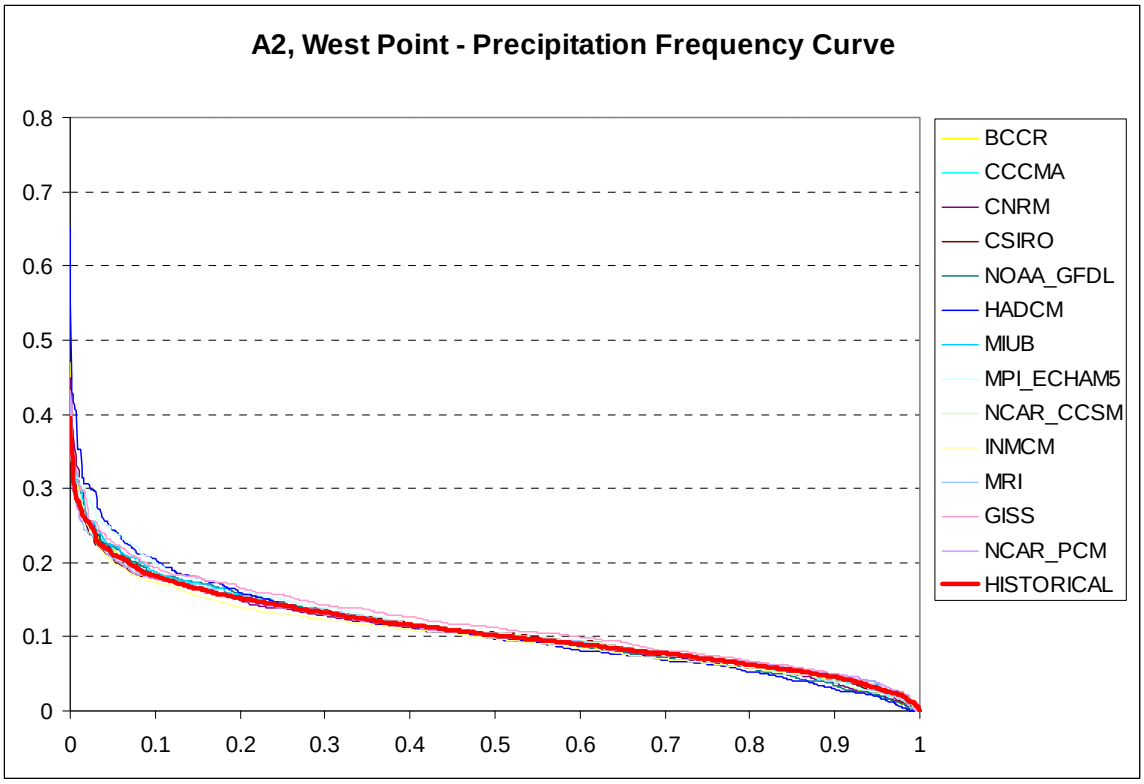
A2, West Point - Precipitation Frequency Curve
0.8
0.7
0.6
0.5
0.4
0.3
0.2
0.1
0
0
0.1
0.2
0.3
0.4
0.5
0.6
0.7
0.8
0.9
1
BCCR
CCCMA
CNRM
CSIRO
NOAA_GFDL
HADCM
MIUB
MPI_ECHAM5
NCAR_CCSM
INMCM
MRI
GISS
NCAR_PCM
HISTORICAL

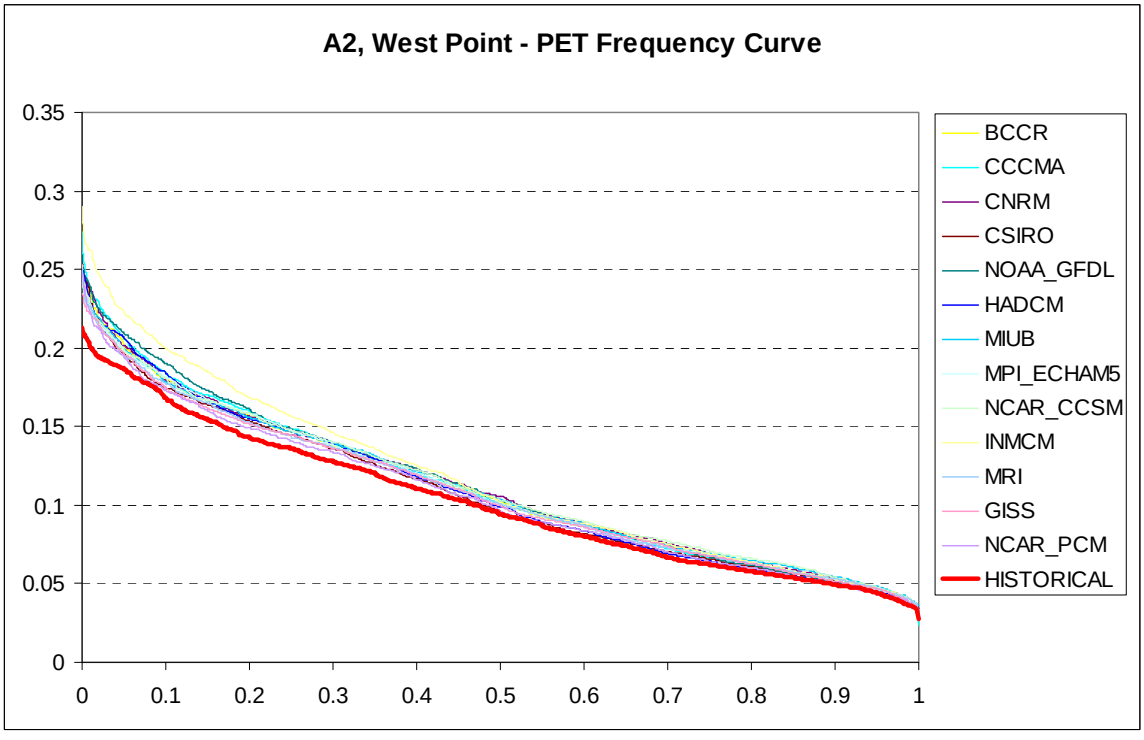
A2, West Point - PET Frequency Curve
0.35
0.3
0.25
0.2
0.15
0.1
0.05
0
0
0.1
0.2
0.3
0.4
0.5
0.6
0.7
0.8
0.9
1
BCCR
CCCMA
CNRM
CSIRO
NOAA_GFDL
HADCM
MIUB
MPI_ECHAM5
NCAR_CCSM
INMCM
MRI
GISS
NCAR_PCM
HISTORICAL

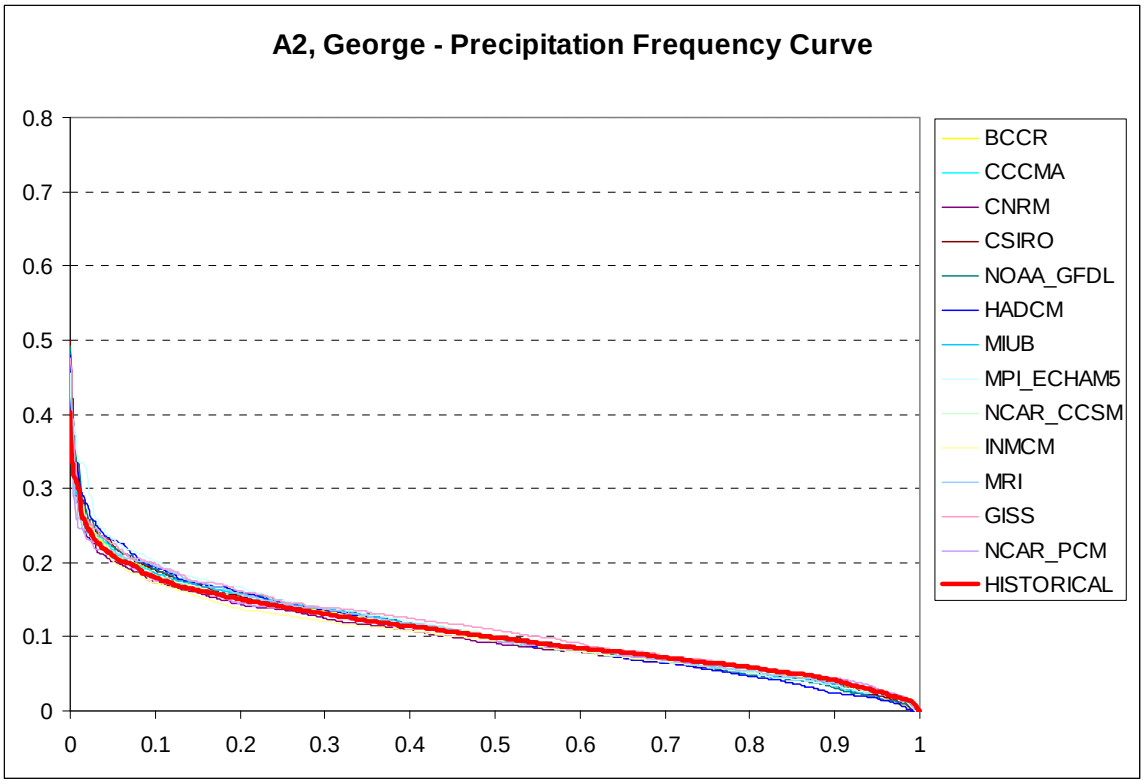
A2, George - Precipitation Frequency Curve
0.8
0.7
0.6
0.5
0.4
0.3
0.2
0.1
0
0
0.1
0.2
0.3
0.4
0.5
0.6
0.7
0.8
0.9
1
BCCR
CCCMA
CNRM
CSIRO
NOAA_GFDL
HADCM
MIUB
MPI_ECHAM5
NCAR_CCSM
INMCM
MRI
GISS
NCAR_PCM
HISTORICAL

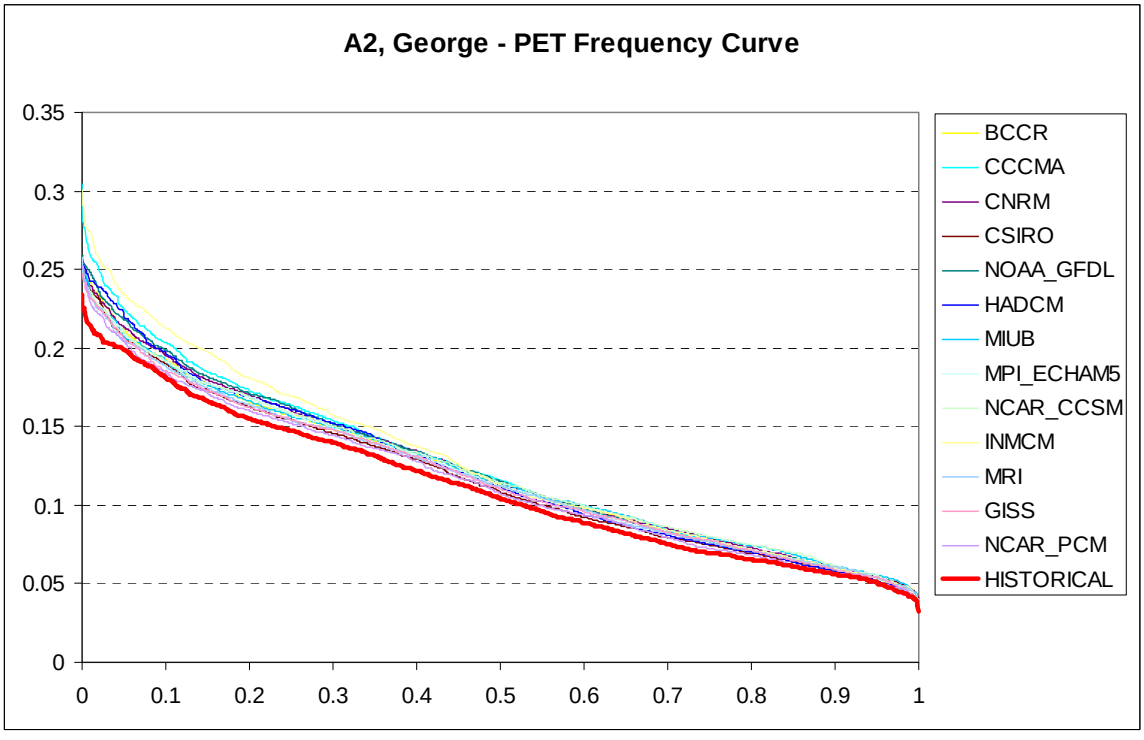
A2, George - PET Frequency Curve
0.35
0.3
0.25
0.2
0.15
0.1
0.05
0
0
0.1
0.2
0.3
0.4
0.5
0.6
0.7
0.8
0.9
1
BCCR
CCCMA
CNRM
CSIRO
NOAA_GFDL
HADCM
MIUB
MPI_ECHAM5
NCAR_CCSM
INMCM
MRI
GISS
NCAR_PCM
HISTORICAL

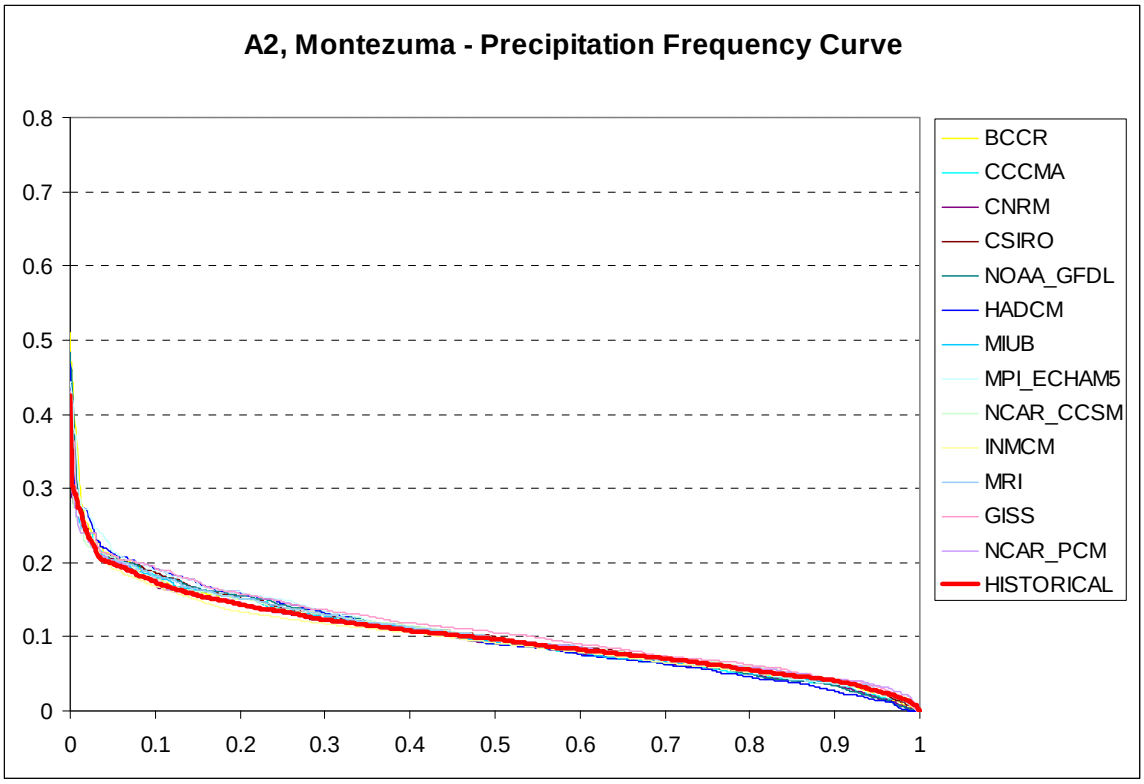
A2, Montezuma - Precipitation Frequency Curve
0.8
0.7
0.6
0.5
0.4
0.3
0.2
0.1
0
0
0.1
0.2
0.3
0.4
0.5
0.6
0.7
0.8
0.9
1
BCCR
CCCMA
CNRM
CSIRO
NOAA_GFDL
HADCM
MIUB
MPI_ECHAM5
NCAR_CCSM
INMCM
MRI
GISS
NCAR_PCM
HISTORICAL

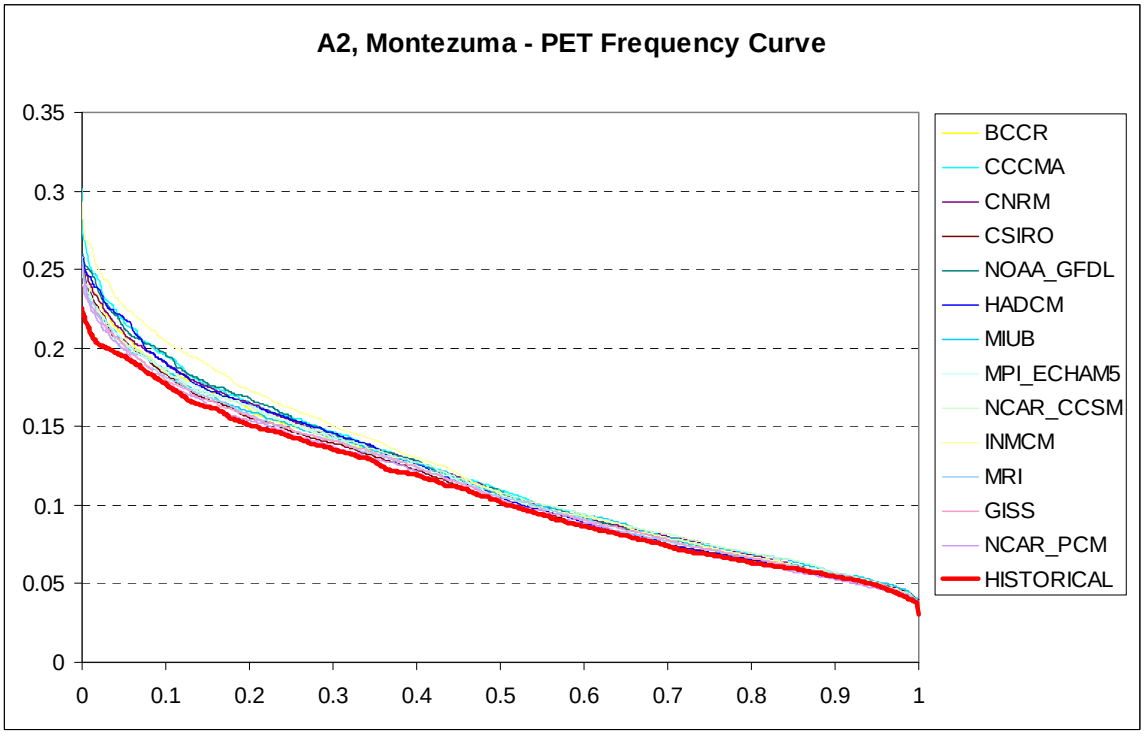
A2, Montezuma - PET Frequency Curve
0.35
0.3
0.25
0.2
0.15
0.1
0.05
0
0
0.1
0.2
0.3
0.4
0.5
0.6
0.7
0.8
0.9
1
BCCR
CCCMA
CNRM
CSIRO
NOAA_GFDL
HADCM
MIUB
MPI_ECHAM5
NCAR_CCSM
INMCM
MRI
GISS
NCAR_PCM
HISTORICAL

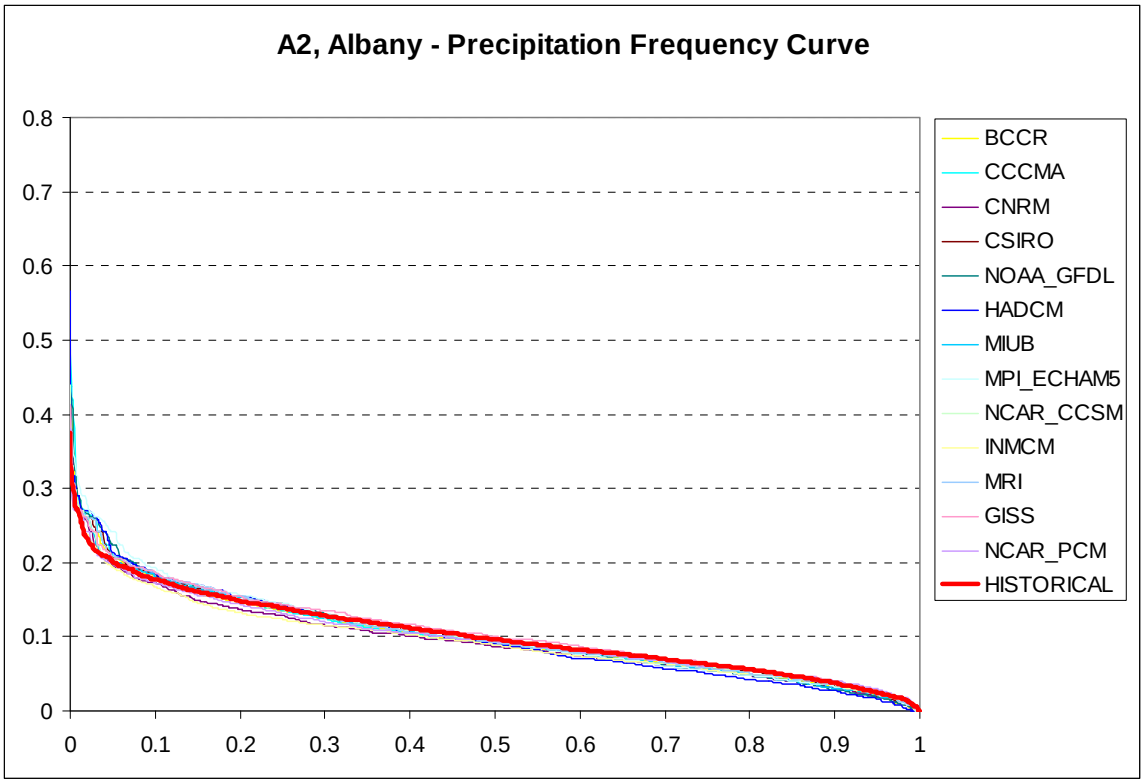
A2, Albany - Precipitation Frequency Curve
0.8
0.7
0.6
0.5
0.4
0.3
0.2
0.1
0
0
0.1
0.2
0.3
0.4
0.5
0.6
0.7
0.8
0.9
1
BCCR
CCCMA
CNRM
CSIRO
NOAA_GFDL
HADCM
MIUB
MPI_ECHAM5
NCAR_CCSM
INMCM
MRI
GISS
NCAR_PCM
HISTORICAL

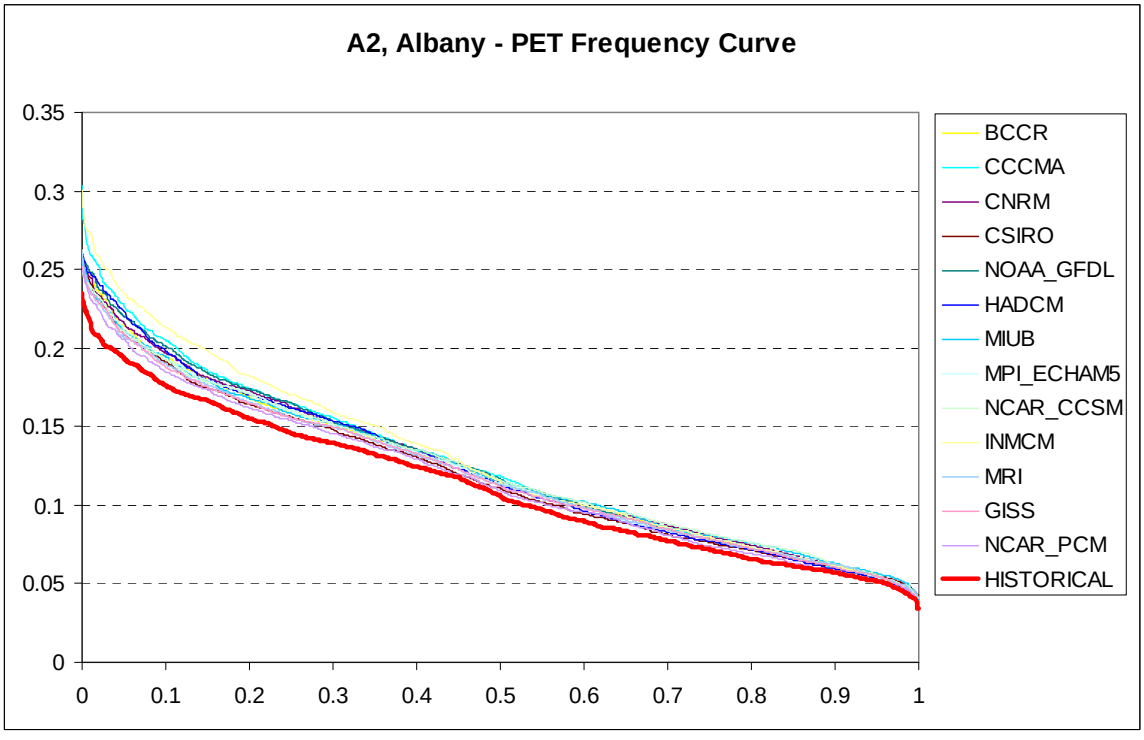
A2, Albany - PET Frequency Curve
0.35
0.3
0.25
0.2
0.15
0.1
0.05
0
0
0.1
0.2
0.3
0.4
0.5
0.6
0.7
0.8
0.9
1
BCCR
CCCMA
CNRM
CSIRO
NOAA_GFDL
HADCM
MIUB
MPI_ECHAM5
NCAR_CCSM
INMCM
MRI
GISS
NCAR_PCM
HISTORICAL

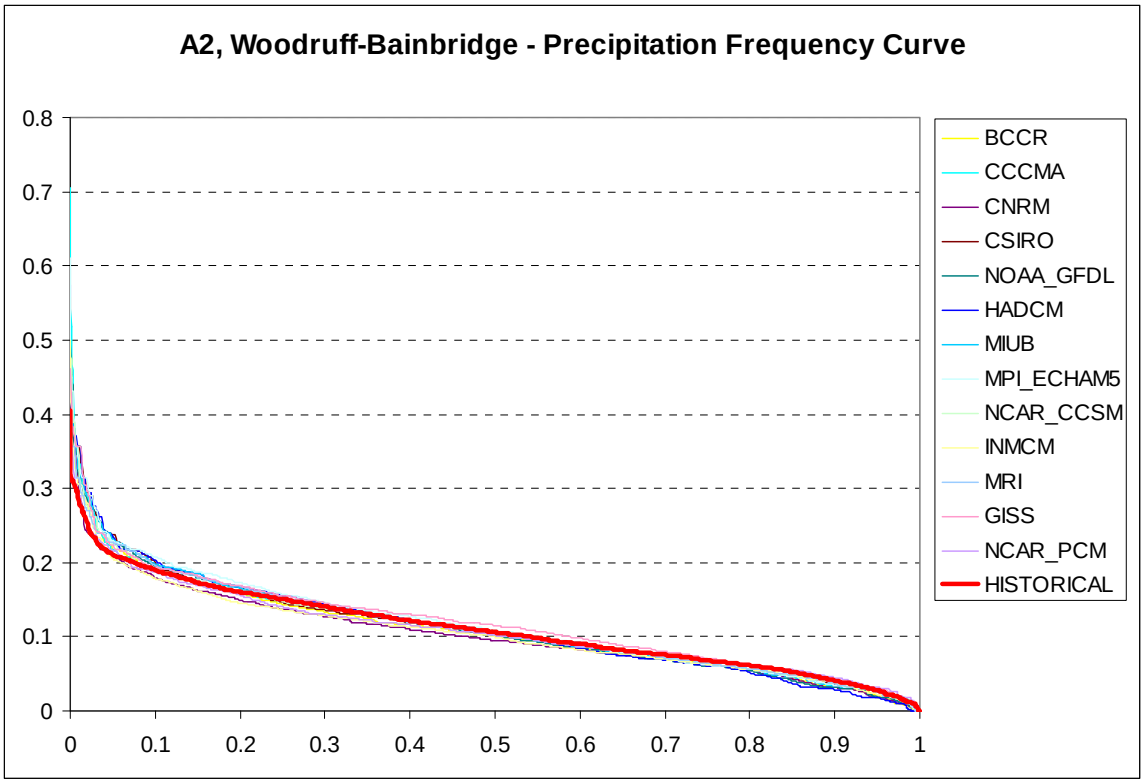

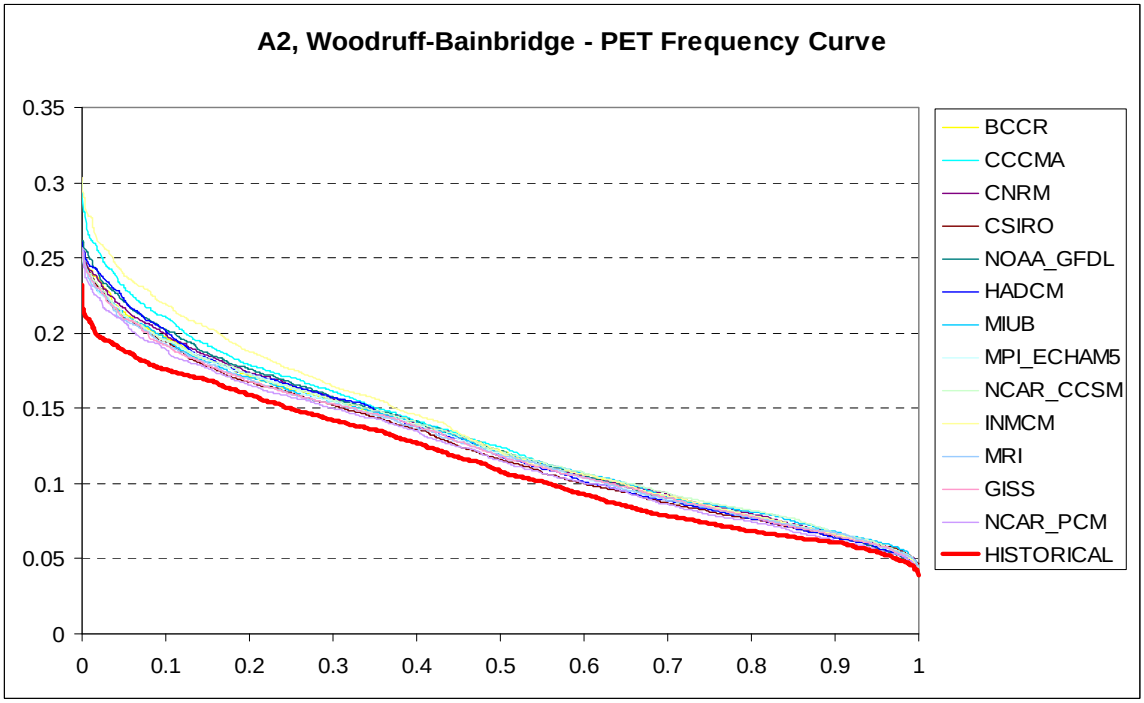

Figure 3.28: Frequency Curves of Precipitation and PET Sequences for A2 scenarios

Chapter 4

Hydrologic Assessments

4.1 Introduction

This chapter describes the hydrologic component of the integrated climate assessment. This component utilizes the downscaled precipitation and potential evapotranspiration sequences and quantifies the corresponding ACF watershed response in terms of watershed evapotranspiration, soil moisture, and runoff.

Toward this goal, the study utilizes a new conceptual hydrologic model which simulates the important hydrologic processes operating at monthly time scales. The model formulation, parameter calibration, and testing is described next. The use of the model in historical and future climate assessments for the ACF River Basin follows.

4.2 Watershed Model

4.2.1 Literature Review

Watershed models have been developed since the 1940s for applications ranging from streamflow forecasting (e.g., Thornwaite, 1948; Thornwaite and Mather, 1955; Alley, 1985; Xu and Vandwiele, 1995; Georgakakos and Baumer, 1996; and Mohseni and Stefan, 1998), simulation of land hydrological processes (e.g., Liang et al., 1994; Arnold, 2005; Vieux, 2001; Koren et al., 2004; and Carpenter and Georgakakos, 2004), and, most recently, climate change assessments (Lettenmaier and Rind, 1992; Stamm et al., 1994; Conway, 1998; Wood et al., 2004; Maurer, 2007; and Yao and Georgakakos, 2001).

The basis of all hydrologic models is the simulation of the relevant water flux processes over the watershed including rainfall, evapotranspiration, infiltration, percolation, soil moisture storage, and runoff. The models can be generally distinguished as conceptual or physically

based, depending on the way they represent these processes. The physically-based models generally represent hydrological systems by small scale hill-slope drainage or channel storage elements. Such schemes generally result in a large number of model parameters, and pose calibration challenges. Discussions of parameter optimization schemes and the issues associated with over-parameterization problems can be found in Duan et al., 1994; Gupta and Sorooshian, 1998; Yapo et al., 1998; Duan et al., 2007; Wagener et al., 2009; and Apostolopoulos and Georgakakos, 1997.

Conceptual models comprise a number of lumped storage elements which involve a limited number of parameters and are relatively easier to calibrate. It has been shown that increasing the number of parameters in a conceptual model can potentially increase model skill. However, there are also concerns of data over-fitting if the number of parameters becomes large.

The storage-release relationships are the core components for any conceptual hydrologic model. Although linear storage-release forms (e.g., Wood, 1992) have been broadly used before, there is increasing interest in developing nonlinear storage-release relationships (e.g., Amorocho, 1963, 1967; Wittenberg, 1999; Mishra et al., 2003; Brutsaert, 2005; and Botter, 2009). For instance, Wittenberg (1999) developed deterministic nonlinear reservoir algorithms extended for separation of baseflow from daily river discharges of 14 stations in the upper Weser and Ilmenau basins in Germany. Botter (2009) developed a series analytical stochastic solution for runoff variability by using different forms of nonlinearity, including concave/convex power and hyperbolic forms. These functional forms are pre-selected based on prior model calibration experience. Young (1993, 1998, 1999, and 2003) calls such models hypothetic-deductive, which implies that certain structural assumptions are made first, and then the associated parameters are estimated using various methods.

Alternatively, the inductive approach infers the functional model forms and associated parameters directly from data, the aim being to keep the model order and complexity minimal while achieving maximal statistical significance. A recent example of such an approach is provided by Kirchner (2009) for two headwater catchments of the Severn and Wye rivers at Plynlimon, Wales. In that study, each catchment is represented by a single storage element. The discharge from the single storage is determined by the storage alone and the storage-release function is estimated from an analysis of stream fluctuations. The catchment sensitivity to changes in storage is estimated by identifying times when the precipitation and evapotranspiration are relatively small. In cross validation, the Nash-Sutcliffe (N-S) efficiencies for the two watersheds were found to range from 0.82 to 0.94. This N-S efficiency range is compatible with a 4-parameter model. Kirchner's modeling scheme can be improved by adding more components into the model structure (i.e., a second storage element) that would expand the applicability of such models to larger spatial and temporal scales. However, such extensions complicate the underlying function and parameter identification process.

The model developed in this study extends Kirchner's inductive approach by including additional water balance elements with non-linear storage-release functions, the forms and parameters of which are data driven. These functions and parameters are estimated using a recursive identification methodology suitable for multiple, inter-linked modeling components. The new model is applied here to intermediate scale watersheds (10^2 to 10^4 square miles) at monthly time resolution. However, the modeling concept is applicable to finer spatial and temporal scales, with additional modeling elements used to represent hydrologic process that become important at finer scales.

4.2.2 ACF Watershed Model Formulation

The model formulation is similar to that of a lumped parameter Sacramento model type, and is intended to simulate the hydrologic processes of infiltration/percolation, evapotranspiration, and surface and subsurface runoff (**Figure 4.1**).

Model inputs include precipitation and potential evapotranspiration demand (PET) averaged over the watershed area. The model includes one surface and two subsurface moisture storage layers, with water contents S_0, S_1, and S_2 respectively. Water enters the top model layer as precipitation, P, and, after some losses to surface retention, it infiltrates/percolates to the lower storage layers. Precipitation falling on impervious areas contributes immediately to runoff (Q_{Imp}). Storage layers may be depleted by evapotranspiration ET_0, ET_1, and ET_2, or runoff to the stream u_0, u_1, and u_2. Evapotranspiration depends on PET as well as storage. Runoff depends on storage through the storage-runoff functions $u_0(S_0)$, $u_1(S_1)$, and $u_2(S_2)$. Total runoff, Q, to the stream is the sum of all runoff contributions, $Q = Q_{Imp} + u_0(S_0) + u_1(S_1) + u_2(S_2)$. The infiltration/percolation functions u_{01} and u_{12} are key model elements and depend on various model variables. In addition to the evapotranspiration, storage-runoff, and infiltration/percolation functions, model parameters include storage capacities. These functions and parameters are calibrated from contemporaneous observations of precipitation, PET, and total watershed runoff. The ACF watershed models developed in this study have a monthly time resolution.

A notable difference between this and the Sacramento model formulation is the distinction of soil moisture as tension and free water. The assumption underlying the ACF model implementation is that the apportionment, storage, and release of soil moisture to and from tension and free water storage occur at time scales much faster than a month. Thus, at

monthly time resolution, tension and free water can be combined into an aggregate soil moisture storage which can adequately represent the observed storage-runoff process.

A similar argument is used to simplify the representation of the infiltration process (u_{01}) and the dynamics of the surface storage (S_0).

While on an hourly time scale, the infiltration process is controlled by the soil infiltration capacity and the availability of surface water supply, at a monthly time scale, the actual infiltration dynamics is not observable. Thus, over monthly intervals, it can be assumed that surface water (that is not retained in surface storage or does not become runoff from impervious surfaces) enters the upper sub-surface storage, provided that it is not filled to capacity.

The dynamics of the surface water storage is represented by the storage-runoff function $u_0(S_0)$. This storage begins to fill during significant precipitation events when subsurface storage is filled to capacity. While water release from this storage may develop over a period of few days, it is assumed that the storage depletion process (to runoff) will be fully completed over a period of a month without carryover effects. Thus, a simple water balance representation equating surface water storage (less evaporation) to surface runoff would be adequate. This particular assumption was tested in the ACF watersheds by using both a fully dynamic surface water element as well as the simpler water balance representation. The calibration process showed that the optimal storage-release functions $u_0(S_0)$ are nearly vertical, validating the assumption that, over a monthly time step, release from surface storage is practically instantaneous.

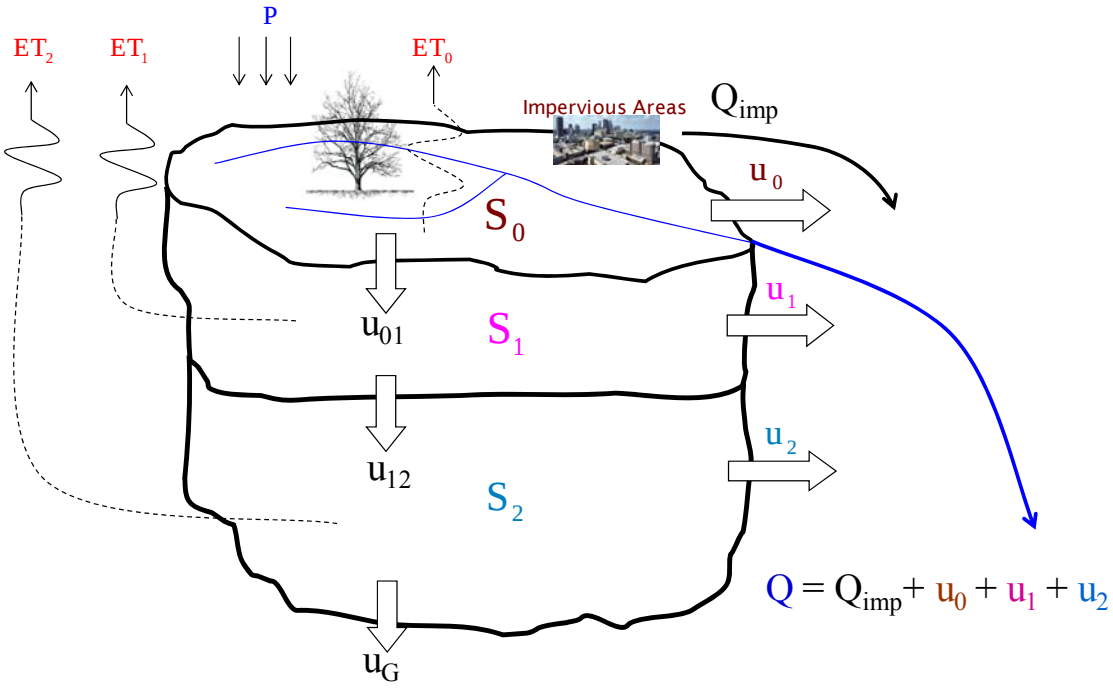

Available Observations: P, T, PET, Q, Area, Terrain, Land Cover.
Model Calibration: Storage capacities, runoff functions, and percolation functions.
Model Outputs: S_0, S_1, S_2, ET_0, ET_1, ET_2, u_0, u_1, u_2, Q.

Figure 4.1: Hydrologic Modeling System Schematic

In keeping with the previous comments and assumptions, the mathematical model formulation is as follows:

- Impervious Storage Runoff (Q_{imp}), Retention Storage (S_{ret}), and Effective Precipitation (P_{eff}):

$$Q_{imp}(k) = a_{imp}\, P(k),$$

$$S_{ret}(k) = \max\left\{ a_{ret}\, \frac{PET(k)}{\max\{PET\}}\, P(k),\, b_{ret}\, P(k) \right\},$$

$$P_{eff}(k) = P(k) - S_{ret}(k) - Q_{imp}(k),$$

where k is the monthly interval index, P(k) is the precipitation depth (averaged over the watershed area), a_{imp} is a constant coefficient; PET(k) is the potential evapotranspiration demand during month k (averaged over the watershed area), $\max\{PET\}$ is the maximum monthly PET over the simulation horizon, and a_{ret} and b_{ret} are constant coefficients.

- Evapotranspiration (ET_i, i = 0, 1, 2):

$$ET_i(k) = PET(k)\left[\frac{S_i(k)+S_i(k+1)}{2\sum_{i=0,1,2} S_i^c}\right], \quad i = 0, 1, 2,$$

where S_i^c is the capacity of storage i, i=0, 1, 2. Various other forms including proportionality and exponent coefficients were also tested for the above relationship between ET, PET, and the monthly-average storage i as a fraction of the total storage capacity. However, in all ACF watersheds, the above relationship performs best.

- Storage Dynamics (S_i, i=0, 1, 2):

(i) Storage $S_1(k+1)$ *not* constrained by capacity limit:

$$S_1(k+1) = S_1(k) + P_{eff}(k) - ET_1(k) - u_1(k) - u_{12}(k),$$

$$S_2(k+1) = S_2(k) - ET_2(k) - u_2(k) + u_{12}(k) - u_G(k),$$

$$S_0(k+1) = 0,$$

$$u_0(k) = 0.$$

(ii) Storage $S_1(k+1)$ constrained by capacity limit:

$$S_1(k+1) = S_1^c,$$

$$Q_{sat}(k) = [S_1(k) + P_{eff}(k) - ET_1(k) - u_1(k) - u_{12}(k)] - S_1^c,$$

$$S_2(k+1) = S_2(k) - ET_2(k) - u_2(k) + u_{12}(k) - u_G(k),$$

$$S_0(k+1) = 0,$$

$$u_0(k) = Q_{sat}(k) - ET_0(k).$$

Although the above dynamical relationships are expressed in monthly time steps, the actual simulation is performed at a finer resolution (e.g., daily intervals) to identify whether and when storage capacity limits are reached. This is necessary, because when subsurface storages become saturated, the form of their dynamical relationships and fluxes change.

- Storage-Runoff Functions (u_i, i=1,2):

$$u_i(k) = u_i[(S_i(k) + S_i(k+1))/2], \; i = 1, 2.$$

The functional forms of these relationships are identified as part of the model calibration process.

- Percolation Functions (u_{12} and u_G):

$$u_{12}(k) = u_{12}[S_1(k), S_2(k), P_{eff}(k), ET_1(k), ET_2(k)],$$

where the functional form of this relationship is identified as part of the model calibration process.

The deep percolation flux, u_G, is included to model any significant groundwater-surface water interaction. If such an interaction exists, its seasonal magnitude and direction is best determined by an external groundwater model.

- Total Watershed Runoff (Q):

$$Q(k) = Q_{imp}(k) + u_0(k) + u_1(k) + u_2(k).$$

4.2.3 Parameter Estimation

The parameter estimation (or model identification) process aims to identify a set of model parameters and functions such that model output matches with actual observations (total runoff Q) as best as possible. The model parameters and functions can be distinguished in two categories: The first category includes parameters and functions of structural importance that govern the dynamical model response and the interaction/linkages among its structural components and processes (i.e., soil storages and runoff). This *primary parameter set* includes:

- Total storage capacity, S^c;
- Lower soil moisture storage runoff function, $u_2(S_2)$;
- Upper soil moisture storage runoff function, $u_1(S_1)$;
- Upper and lower soil storage capacities, S_1^c and S_2^c; and
- Percolation function, $u_{12}(S_1, S_2, \ldots)$.

The second parameter category includes parameters that fine-tune model response, within the structural framework established by the primary parameters, to capture other hydrologic response aspects. This *secondary parameter set* includes:

- Impervious area runoff parameter, a_{imp};
- Retention Storage parameters, a_{ret} and b_{ret}; and
- Deep groundwater flux, $u_G(S_2)$.

This distinction is made here, because simultaneous estimation of all parameters, all too often, leads to parameter estimates assuming modeling roles for which they are not designed. The second reason for the estimation approach introduced in this work is to systematically and incrementally add processes and parameters that are necessary to explain system behavior, not based on a preconceived model design.

The estimation process is iterative and consists of *(1)* generating initial estimates of the parameters and functions, *(2)* iteratively refining the primary parameters and functions until no further improvements can be achieved, and *(3)* repeating the process for other secondary parameter values to fine-tune model performance.

4.2.3.1 Initial Parameter and Function Estimates

The estimation process begins by assuming initial parameter values for the retention storage, impervious runoff, and deep percolation terms. In this work, deep percolation (i.e., percolation to groundwater aquifers from the lower soil moisture storage) is assumed negligible, but the estimation process can also accommodate the more general case. The other terms can also be initially assumed negligible. For the initial parameter values a_{imp}, a_{ret}, and b_{ret} can be used to generate initial estimates of the impervious area runoff, Q_{imp}, retention storage S_{ret}, and effective rainfall P_{eff}:

$$Q_{imp}(k) = a_{imp}\ P(k),\ k=1,\ldots,N;$$

$$S_{ret}(k) = \max\left\{ a_{ret}\ \frac{PET(k)}{\max\{PET\}}\ P(k),\ b_{ret}\ P(k) \right\},\ k=1,\ldots,N;\ \text{and}$$

$$P_{eff}(k) = P(k) - S_{ret}(k) - Q_{imp}(k),\ k=1,\ldots,N,$$

where N is the total number of months in the historical horizon used for calibration.

Then, the storage equations become:

$$S_1(k+1) = S_1(k) + P_{eff}(k) - PET(k)\left[\frac{S_1(k) + S_1(k+1)}{2\,S^c}\right] - u_1(k) - u_{12}(k),$$

$$S_2(k+1) = S_2(k) - PET(k)\left[\frac{S_2(k) + S_2(k+1)}{2\,S^c}\right] - u_2(k) + u_{12}(k).$$

Adding the above dynamical equations results in the following aggregate soil storage equation:

$$S(k+1) = S(k) + P_{eff}(k) - PET(k)\left[\frac{S(k)+S(k+1)}{2\,S^c}\right] - u_1(k) - u_2(k),$$

where $S(k) = S_1(k) + S_2(k)$, and $u_1(k) + u_2(k) = Q - Q_{imp}$ (total runoff from soil storage). Substituting the runoff terms by the observed total runoff ($Q - Q_{imp}$), yields an aggregate storage relationship with only one unknown: the total aggregate soil storage capacity S^c. However, determining the correct S^c value is not obvious, as different S^c values (and the observed forcing of P, PET and Q) simply give rise to different storage sequences. The key to selecting the most suitable S^c value is to examine the global behavior of the storage sequence it generates and determine the one most consistent with the expected physical system response.

More specifically, the expected behavior of the hydrologic system is to have a smooth and monotonic response of runoff relative to storage. This is expected to hold particularly during periods of storage depletion when the dominant runoff contribution comes from the lower soil storage. Thus, if the observed data does not contain errors, the correct S^c value should generate a storage sequence such that when

$S(k+1) < S(k)$, $S(n+1) < S(n)$, and $[S(k+1)+S(k)]/2 < [S(n+1)+S(n)]/2$,

it should also hold that $Q(k) < Q(n)$ for all such values of k and n.

Namely, during storage depleting periods, the runoff corresponding to ranked storage values (in, say, descending order) should also adhere to the same ranking. To be sure, because of the existing data errors in the observed values of P, PET, and Q, this relationship is not expected to be perfect. But, the value of S^c that generates storages that adhere to this criterion as best as possible would represent the best S^c estimate. While this is the main idea for identifying the

initial S^c estimate, there are several quantitative criteria (that have been tested in this work) to guide this process. These will be discussed elsewhere.

An important side benefit of the above procedure is the identification of the lower storage runoff function $u_2(S_2)$. This function can be estimated by the ranked $(Q\text{-}Q_{imp})$ versus ranked S relationship corresponding top the best S^c estimate. As indicated earlier, these rankings do not include all runoff-storage paired values generated by the dynamical equation, but only those that comply with depleting storage conditions. Because the lower storage is depleted last, the basis of this relationship should be the lower part of the aggregate storage range, for example, the lower one third. This relationship can then be approximated through a suitable analytical function such as a power function:

$$u_2 = \beta_{2,1}\, S_2^{\beta_{2,2}} ,$$

where $\beta_{2,1}$ and $\beta_{2,2}$ are constant coefficients.

The previous procedure can be repeated to provide initial estimates of S_1^c and of $u_1(S_1)$. This involves substituting the newly obtained estimates of S^c and $u_2(S)$ into the aggregate storage equation and repeating the ranking process for S and $[Q\text{-}Q_{imp}\text{-}u_2(S)]$. The best value of S_1^c is that for which the ranked data exhibit an almost one to one change of Q versus S. This is because when the system is saturated, $Q\text{-}Q_{imp}$ is dominated by u_0 which equals the storage in excess of S_1^c. The ranked $[Q\text{-}Q_{imp}\text{-}u_2(S)]$ versus S relationship can then be analytically approximated to provide an initial estimate of the $u_1(S_1)$ function. As emphasized, these are only *initial* estimates to be revisited in the following stages of the estimation process.

At this stage, initial estimates of S^c, S_1^c, S_2^c $(= S^c - S_1^c)$, $u_1[S_1(k/k+1)]$, and $u_2[S_2(k/k+1)]$ have been obtained, where the notation $S_i(k/k+1)$ is used to denote the average S_i storage value over

the interval k. The last, and most crucial task in the initial estimation cycle, is to identify the percolation function u_{12}. To this end, the individual storage equations are re-instated as follows:

$$S_1(k+1) = S_1(k) + P_{eff}(k) - PET(k)\left[\frac{S_1(k/k+1)}{S^c}\right] - u_1[S_1(k/k+1)] - u_{12}(k),$$

$$S_2(k+1) = S_2(k) - PET(k)\left[\frac{S_2(k/k+1)}{S^c}\right] - u_2[S_2(k/k+1)] + u_{12}(k).$$

Consider a time step k with known initial storages $S_1(k)$ and $S_2(k)$. Assuming at first that $u_{12}=0$, the dynamical equations can be propagated to yield the end of the period storages $S_1(k+1)$ and $S_2(k+2)$. This step requires a few iterations due to the dependence of $\{ET_i, u_i, i=1,2\}$ on the end storage $S_i(k+1)$, but convergence is fast, requiring only two to three iterations. This one-step computation also provides runoff estimates $u_i[S_i(k/k+1)]$, i=1,2, which are used next to determine an optimal value for u_{12}. More specifically, this is accomplished by comparing the value of the model generated runoff, $(u_1 + u_2)$, to the observed $(Q-Q_{imp})$. If these two quantities are equal, then u_{12} is indeed zero. Otherwise, the estimation process proceeds to determine the best u_{12} such that the values of $(u_1 + u_2)$ and $(Q-Q_{imp})$ are as close as possible. This is a one-step, constrained optimization problem, where u_{12} is constrained to be within

$$0 \le u_{12} \le \min\{S_1(k), S_2^c - S_2(k)\},$$

and the storage variables are constrained to be within their applicable ranges. However, for each time step k, the solution can easily be obtained via an exhaustive, one dimensional search.

This process generates a series of u_{12} values $\{u_{12}(k), k=0, 1, 2, \ldots, N-1\}$ that are most consistent with the observed data and the other initial parameters and functions. These values are used as the basis for relating u_{12} to other system variables that would be available when the

model runs in predictive mode (i.e., when Q is not known). Various functional forms were tested in this work for all ACF watersheds. The best and most robust performance is obtained by the following relationship:

$$u_{12} = \alpha_0 + \alpha_1 P_{eff}(k) + \alpha_2 \frac{ET_1(k)}{ET_2(k)} + \alpha_3 ET_2(k) + \alpha_4 \frac{S_1(k)}{S_2(k)} + \alpha_5 S_2(k) ,$$

where α_0, α_1, α_2, α_3, α_4, and α_5 are constant regression coefficients. Furthermore, the continuing application of the model for several other Georgia basins supports the general validity of this functional form. However, all models tested use a monthly time step, and the best u_{12} form may be different for daily or sub-daily time resolutions.

After the initial estimation of the parameters and functions, the model can be run in a predictive mode, and its performance can be assessed relative to observed runoff. Various criteria can be adopted to assess the model performance including the minimization of the sum of the square error or the absolute difference between model predictions and observations, and the maximization of the Pearson and Spearman correlation (average and monthly), among others. For a more unbiased assessment, a split sample approach can be adopted where a portion of the historical record is retained for model verification purposes.

4.2.3.2 Parameter and Function Refinement

In keeping with the above, parameter and function refinement proceeds iteratively as follows:

(1) Select a_{imp}, a_{ret}, and b_{ret};

(2) Select S_0^c, S_1^c, and S_2^c, and estimate $u_2(S_2)$ from the aggregate storage model;

(3) Estimate $u_1(S_1)$ and $u_{12}(P_{eff}, ET_2, ET_1/ET_2, S_2, S_1/S_2)$ from the full model form and iterate until the model performance criterion is optimized;

(4) Repeat Steps (2) to (4) until the best performing parameter and function set $\{S_0^c, S_1^c, S_2^c, u_2(S_2), u_1(S_1)$, and $u_{12}(P_{eff}, ET_2, ET_1/ET_2, S_2, S_1/S_2)\}$ is obtained;

(5) Repeat Steps (1) to (5) until all model parameters are refined and model performance is optimized;

(6) Identify data outliers by comparing each data point (predicted minus observed value) against the error distribution of the corresponding month;

(7) Repeat Steps (1) through (7) until no model performance improvement is noted.

Step (6) was found to be useful in generating more unbiased model parameters but also in pointing out data inconsistencies needing correction. In some of the ACF watersheds, outliers occurred at a rate substantially higher than the statistically acceptable level. The parameter estimation process is computationally efficient, requiring only a few minutes on a high end personal notebook computer.

4.2.4 ACF Model Parameters and Performance

The watershed model is developed for six ACF sub-watersheds: Buford, West Point, George, Montezuma, Albany, and Woodruff-Bainbridge (**Figure 1.1**). Monthly hydro-climatic data (precipitation, temperature, potential evapotranspiration, and watershed runoff) for these watersheds are collected or calculated for the period from 1939 to 2007 (as referenced in Chapter 2). The ACF watershed models were then calibrated over this period using the procedure outlined earlier.

The results of the model calibration exercise are shown in **Table 4.1**. For all models, no retention storage term could add value to model performance. **Table 4.2** reports average global statistics for model generated and observed runoff. As shown in the table, the overall model performance is good. Most model predictions are within ±10% of the observed values. The global Pearson and Spearman correlation coefficients are all higher than 0.9. The number of data outliers is between 30 and 50, or 3% - 5% of the historical records.

Figures 4.2 through **4.13** provide a graphical comparison between observed and simulated runoff, plots of the upper and lower soil moisture storage, and comparisons between observed and model climatologies (mean and standard deviation of monthly runoff). The above tables and graphs demonstrate the validity and good simulation skill of all ACF watershed models.

4.3 Hydrologic Assessments

4.3.1 Historical Assessments

The watershed models described earlier are employed in this chapter to characterize the ACF hydrologic response under the historical climate. This assessment is based on historical climatic data for the period 1901 through 2009. This data has been pieced together from three sources: *(1)* The Climatic Research Unit and the Tyndall Center of the University of East Anglia (for precipitation and mean daily temperature from 1901 to 2002); *(2)* the Georgia Automated Environmental Monitoring Network at the University of Georgia (for daily precipitation from 2003 to 2009); and *(3)* the NCEP/NCAR reanalysis grid data set (for daily mean temperature from 2003 to 2009).

The assessments consist of running the ACF models under historical climatic forcing (of precipitation and temperature) for the 109 year period from 1901 to 2009 (in monthly steps). The model output sequences of soil moisture, evapotranspiration, and runoff are then used to assess the hydrologic watershed response. The assessment aims to *(1)* verify that the model hydrology is consistent with regional observations; *(2)* detect possible long term trends; and *(3)* create a baseline hydrologic response to be used as a comparison standard for the future climate assessments in the following section.

Figures 4.14 through **4.17** present the input (i.e., precipitation and potential evapotranspiration) and output (i.e., soil moisture, actual evapotranspiration, and runoff)

sequences of the Buford watershed assessment. For some sequences, in addition to monthly values, the graphs also present two-year moving average series to quantify inter-annual behavior.

The results support several comments and observations:

- Watershed precipitation does not show any appreciable long term trend (**Figure 4.14**). However, the two-year average precipitation is highly variable, reaching a maximum depth of 0.165 meters (in 1920) and a minimum depth of 0.085 meters (in 1986 and 2007-2008). In the most severe droughts (e.g., those in the early 1940's, 1950's, 1980's, 1998-2002, and 2006-2008), large precipitation deficits linger for several years. This model output is consistent with regional drought occurrences. The high inter-annual rainfall variability (up to 50% of normal) and persistence renders the watershed vulnerable to droughts and has critical implications for Lake Lanier at the watershed outlet. The lake is large relative to watershed inflow, and lake filling can take several years. On the other hand, high lake releases can deplete lake storage within a year. Thus, lake operation should adhere to and adapt based on the prevailing hydrologic conditions.
- Unlike precipitation, potential evapotranspiration (with its strong dependence on temperature) shows an increasing long term trend (**Figure 4.14**). Over the 109 year assessment period, the increase is approximately 9% of the early 20th century value. The inter-annual PET variability is much less than that of the precipitation. At the latitude of the Buford watershed, precipitation is consistently higher than PET. However, during droughts, when precipitation declines, PET increases and occasionally exceeds precipitation. The most pronounced such reversal occurred during the most recent drought (in 2006-2008). The ratio of annual average PET to annual average precipitation is approximately 0.71.

- Total soil moisture storage shows a declining long term trend (**Figure 4.15**) of about 4% in 109 years. This decline is solely due to the decline of the lower storage zone, while the upper storage exhibits no changing trend. The ratio of annual average S_1 to annual average P is approximately 1.08, and that of S_2 to P is 2.25. Namely, the total sub-surface storage active in the rainfall-runoff process is 3.33 times the amount of annual average precipitation.
- Actual evapotranspiration generally follows the PET trend but with a milder long term rate of increase (**Figure 4.16**). The reason for this difference is that actual evapotranspiration is also controlled by soil moisture storage, which, as indicated above, experiences a decline. The ratio of average annual evaporation to annual average precipitation is 0.58.
- Lastly, total runoff exhibits a declining trend of approximately 9% in 109 years (**Figure 4.17**). It is notable that the most recent drought (2006 to 2008) was the *worst* two-year drought on record. More specifically, the most severe two-year droughts (in order of decreasing severity) occurred in 2006-2008, 1980's, 1940's, 1950's, 1930's, 1998-2002, 1920's, and 1900's. Furthermore, the last three major droughts (1980-1988, 1998-2002, and 2006-2008) where among the most persistent. The declining trend of total runoff is due to the declining trend of the lower storage runoff. This trend implies that the watershed ability to sustain base river flows is diminishing. The runoff from the upper storage exhibits no significant trend. The ratio of total annual average runoff to annual average precipitation is 0.42, while the contributions of the individual runoff components are $(Q_{imp}+u_0)/P=0.1$, $u_1/P=0.18$, and $u_2/P=0.14$.

Figures 4.18 to **4.37** present similar assessment results for West Point, George, Montezuma, Albany, and Woodruff-Bainbridge. Each watershed has a distinct response, depending on its latitude, land cover, and soil type. Summary statistics for each watershed are reported in **Table 4.3**. Some general comments and observations follow next:

- All watersheds exhibit increasing PET and ET and declining soil moisture storage and runoff trends. These trends appear to be gaining strength in the last 30 to 40 years.
- The ratio of ET to P is generally higher in lower latitude watersheds. The watersheds are located in four distinct latitude regions: *(1)* Buford; *(2)* West Point and Montezuma; *(3)* George and Albany; and *(4)* Woodruff-Bainbridge. **Figure 4.38** depicts the average ET/P, (Total Runoff)/P, and $(Q_{imp}+u_0)/P$ for each watershed. For watersheds in lower latitudes, ET/P increases and (Total Runoff)/P decreases. Ostensibly, Woodruff-Bainbridge (W-B) is an exception to these trends. The reason for this inconsistency is the strong surface water - groundwater interaction in this region which generally results in net water gain for the surface system. The W-B watershed model does not include this interaction, and compensates for the increased watershed outflow by decreasing the evapotranspiration to precipitation ratio and increasing the runoff coefficient beyond their hydro-climatically consistent values. Additional modeling efforts are needed in this region to assess the groundwater contribution to the surface system (through groundwater investigations), represent it as u_G flux in the watershed model, and recalibrate the model parameters. This, effort will be undertaken as part of a separate study.

Figure 4.38 also includes estimates of $(Q_{imp}+u_0)/P$ by watershed. The watersheds with the highest fraction (Montezuma, West Point, and Buford) are also the most highly urbanized. Soil type also influences u_0. The southern ACF watersheds (below the fall line) have predominantly sandy soils, while the northern watershed are dominated by clay loams. As a consequence, southern watersheds are not as easily saturated, and u_0 is relatively less.

Figure 4.38 provides a summary view of how watershed hydrology changes with increasing PET. The same general, albeit more gradual, response is expected for each individual watershed as PET continues to increase. This response is seen in many of the future climate scenarios.

- Lastly, **Figure 4.39** provides summary plots of each the main hydro-climatic sequence (precipitation, PET, ET, soil moisture, and runoff) for all watersheds. The sequences are normalized by their corresponding mean to make it easier to discern temporal trends and variability range. The plots verify the observations expressed earlier with precipitation staying relative stable across the ACF watersheds, PET and ET increasing, and soil moisture and runoff decreasing. These figures show that all ACF watersheds are impacted fairly synchronously by dry and wet climate cycles, but the severity of these cycles differs for each watershed. For example the drought of 2006-2008 was the worst 2-year drought on record for the upper ACF basin (Buford, West Point, Montezuma), while the southern watersheds have experienced other more severe droughts. These features have important management implications, the most important of which is the need for adaptive reservoir management.

In concluding this section, it is important to re-iterate its most important finding: Warming temperatures of the last decades are shown to be impacting the ACF hydrology by increasing evapotranspiration and reducing soil moisture and runoff. These trends are assessed based on historical data, are consistent across the basin, and have critical long term implications for agriculture and water management.

4.3.2 Future Assessments

The future climate assessments consist of running the ACF watershed models under all A1B and A2 climate scenarios for the period from January 2000 through December 2099 (100 years) in monthly time steps. For each of the 26 future climate scenarios (i.e., 13 A1B scenarios and 13 A2 scenarios), the assessment process parallels the one described for the historical climate (previous section). Thus, the future watershed response is characterized by two sequence ensembles, one for the A1B and a second for the A2 scenarios.

Figures 4.40 and **4.41** respectively present the A1B and A2 ensembles for Buford. The figures include plots of precipitation, evapotranspiration, soil moisture, and runoff, each one of which contains 14 sequences, 13 of which pertain to future climates and one (red thick line) to the historical baseline. All sequences represent 12-month moving averages of the original monthly time series. The comparison is between the historical baseline and the future ensemble as a *whole*. For example, it can be seen on **Figures 4.40** and **4.41** that the historical storage sequence is at the top of the future climate storage ensemble in the last part of the 21st century. This is a significant conclusion indicating that Buford soil moisture will most likely become drier than its historical levels.

Because of the voluminous results, a more meaningful comparison would be to plot the data in the form of frequency curves. For Buford, these are shown on **Figures 4.42** and **4.43**. These figures lead to the following observations:

- While on average (i.e., in the vicinity of the 50% percentile), Buford precipitation is not expected to change relative to the historical baseline, the precipitation distribution is expected to "stretch" becoming wetter and drier than that of the historical climate. This assertion holds for both the A1b and A2 scenarios, with the latter stretching the distribution farther.
- Most future scenarios result in higher PET, evapotranspiration, and lower soil moisture storage. This effect is especially pronounced in dry years (those that fall below 75% of the distribution values).
- In the wettest 20% of the years, runoff is expected to be higher than historical. However, the rest of the future ensemble distributions portend drier than historical runoff conditions. Thus, the coming decades are likely to usher in more severe floods and droughts than those experienced in the historical past.

The previous results and conclusions are typical of all watersheds. However, they are based on frequency comparison with all data. To examine the potential changes on a monthly basis, box plots of the historical and future scenarios were developed for each month of the year, watershed, climate scenario type (A1B or A2), and hydrologic process (precipitation, PET, soil moisture storage, and runoff). These plots are shown on **Figures 4.44** through **4.55**. In each figure, the historical box-plots are denoted "H1 through H12" while next to them are the future scenario box-plots denoted "F1 through F12." The future box-plots include data from all 13 future scenarios, while the historical box-plots include only historical data. These figures indeed show that climate change impacts are not uniform across the months of the year. More specifically, the following observations can be made:

- Mean watershed precipitation does not show any appreciable change for all months of the year. However, the precipitation distributions for February through August are considerably extended (toward both ends) in comparison to the historical distributions. This relative change is observed on the A1B *and* the A2 scenarios, as well as all watersheds.
- Future PET exhibits higher mean and wider range than historical PET from February to September, with the largest change observed in July and August. For these two months, the future mean PET is higher than the historical PET up to 12%, while the quartile range of the future distribution exceeds that of the historical by nearly 20%.
- Future soil moisture is clearly lower than historical in June, July, August, September, and October. The change is more pronounced in the southern watersheds where the mean reduction reaches up to 15% (e.g., for Albany under A2 in October). Even more critical is the significant decline of the future low soil moisture levels (as indicators of agricultural droughts). For example the future distributions' 25% percentile is lower than the equivalent historical percentile

in all months. The summer months are particularly impacted, exhibiting a change of nearly 25 to 30% in the southern watersheds where soil moisture is critical for agriculture. The adverse implications of this finding cannot be over-emphasized for Georgia's economy.

- Future runoff is wetter (in the mean and the 75% percentile) than historical in February, March, and April; and is drier than the historical in June, July, August, and September. In the southern watersheds, the mean runoff reduction begins in February and extends through September. For the summer months, the mean reduction is 5 to 8%. The relative depletion of the lower soil moisture storage also impacts (dries up) the base river flows during droughts. The implications of these findings are critical for drought management and water resources planning.

Table 4.1: Watershed Model Parameters for the ACF Sub-basins

	Buford	West Point	George	Montezuma	Albany	Wdrff-Bnbrdge
Storage Capacity and Impervious Area Coefficient						
S^c	0.5000	0.5300	0.4950	0.3660	0.4600	0.6250
S_1^c	0.1900	0.1700	0.1800	0.1220	0.1470	0.2000
S_2^c	0.4100	0.3700	0.3700	0.2540	0.3360	0.4250
a_{imp}	0.0446	0.0480	0.0430	0.0510	0.0280	0.0220
Storage-Release Functions						
BetaPwr(2,1)	0.4133	4.5085	0.6914	0.7361	1.2038	0.2513
BetaPwr(2,2)	2.5486	5.4047	3.3248	2.5304	3.5806	2.4822
BetaPwr(1,1)	2.9347	322.5097	30.9356	4.7076	1750.2376	189.5458
BetaPwr(1,2)	2.5486	5.2126	3.8623	2.5304	5.5228	5.0231
Percolation Function						
Constant	0.0870	0.0949	0.0592	0.0514	0.0679	0.0929
ET_2	0.1325	0.1813	0.1682	0.1937	0.2536	0.3019
ET_1/ET_2	-0.2750	-0.2947	-0.2535	-0.1338	-0.2245	-0.3085
S_2	-0.1139	-0.1703	-0.0810	-0.1323	-0.1377	-0.1845
S_1/S_2	0.1950	0.2120	0.1984	0.0958	0.1600	0.2223
P_{eff}	0.3949	0.3899	0.3834	0.3509	0.4023	0.4725
ErrSTDu12	0.0218	0.0124	0.0165	0.0137	0.0157	0.0156

Table 4.2: Model Performance Measures of ACF Sub-basins

	Buford	W. Point	George	Montezuma	Albany	Wdrff-Bnbrdge
Global Average Statistics						
AvgQ	0.0553	0.0367	0.0312	0.0333	0.0282	0.0360
AvgQM	0.0517	0.0328	0.0271	0.0314	0.0254	0.0324
StDevQ	0.0320	0.0275	0.0238	0.0250	0.0238	0.0221
StDevQM	0.0323	0.0293	0.0233	0.0254	0.0230	0.0213
AvgRnkQ	382.8673	384.8062	388.0504	438.0130	384.7426	384.3796
AvgRnkQM	380.3067	384.7460	393.2741	449.2707	387.0848	384.5328
StDevRnkQ	213.9214	215.6335	212.5994	246.4978	214.0671	213.6740
StDevRnkQM	212.6924	213.1692	210.1308	242.0462	211.8834	214.2371
Global Correlation Coefficients and Error Statistics						
Pcorr	0.9312	0.9399	0.9240	0.9289	0.8586	0.9101
SpCorr	0.9210	0.9282	0.8917	0.9110	0.8446	0.9006
QRMSE/Q	0.2244	0.3433	0.3502	0.2962	0.4681	0.2713
RnkQRMSE/RnkQ	0.4469	0.4647	0.4480	0.5130	0.6104	0.4552
QAbsQError/Q	0.1813	0.2818	0.2804	0.2345	0.3638	0.2263

Table X.1: Historical ACF Hydrologic Assessment: Summary Statistics

	PET/P	ET/P	S_1/P	S_2/P	Runoff/P	u_1/P	u_2/P	(Qimp+u_0)/P
Buford	0.707	0.581	1.075	2.245	0.419	0.178	0.138	0.102
West Point	0.919	0.685	1.176	2.487	0.315	0.139	0.046	0.129
George	1.037	0.727	1.104	2.203	0.273	0.135	0.059	0.080
Montezuma	1.057	0.668	0.895	1.421	0.333	0.131	0.060	0.142
Albany	1.071	0.738	0.983	2.107	0.262	0.142	0.056	0.063
Woodruff-Bainbridge	1.006	0.664	1.230	2.341	0.335	0.143	0.121	0.071

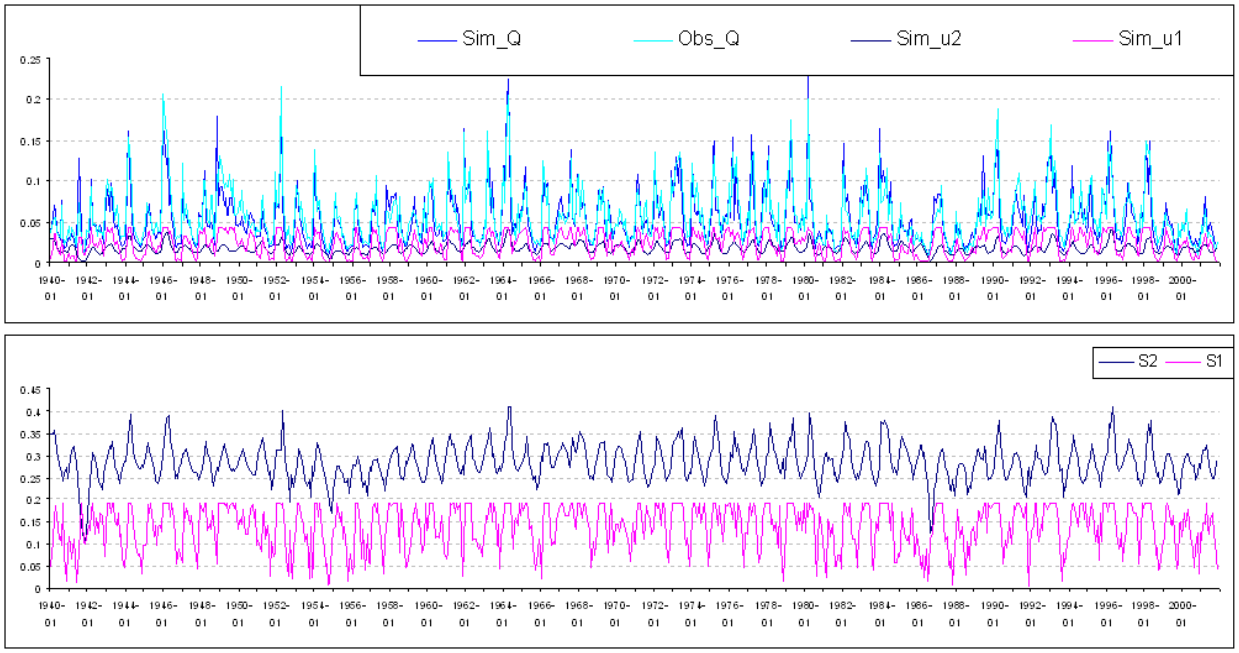

Figure 4.2: Modeled vs. Observed Flows and Storages for Buford

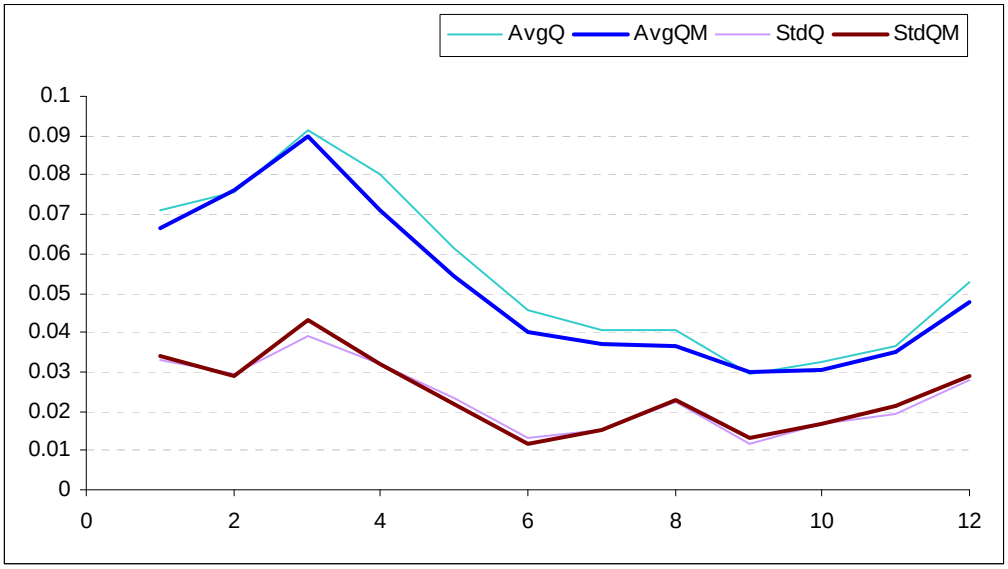

Figure 4.3: Climatology of Modeled vs. Observed Flows for Buford

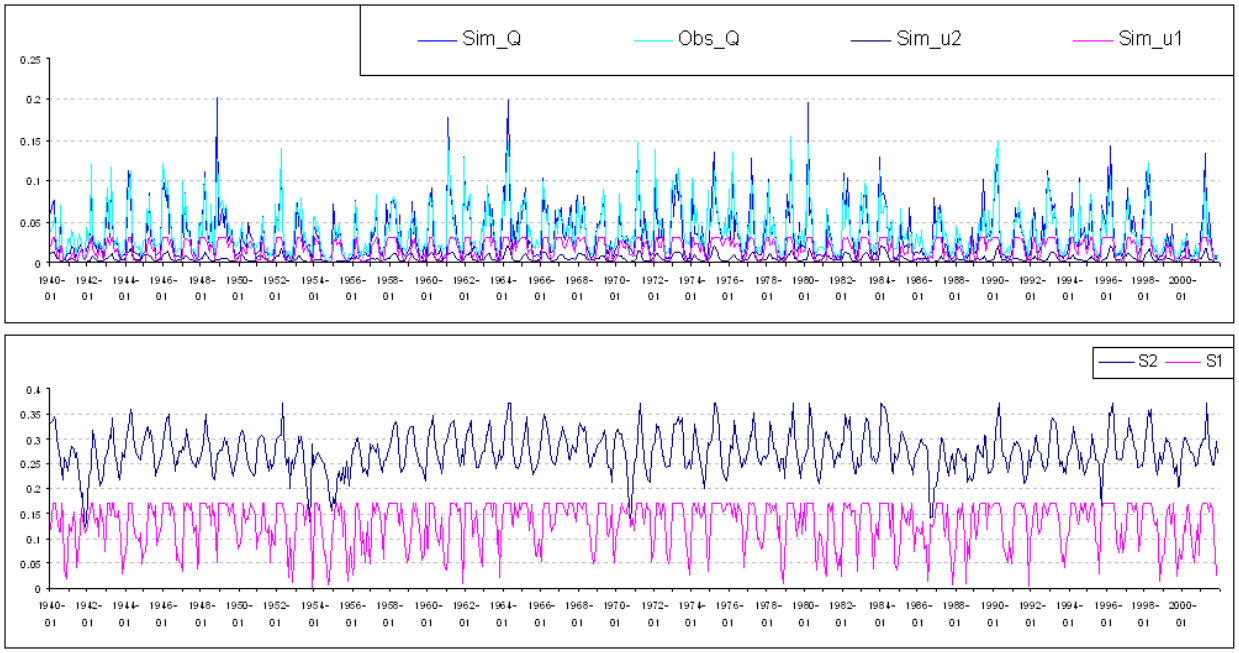

Figure 4.4: Modeled vs. Observed Flows and Storages for West Point

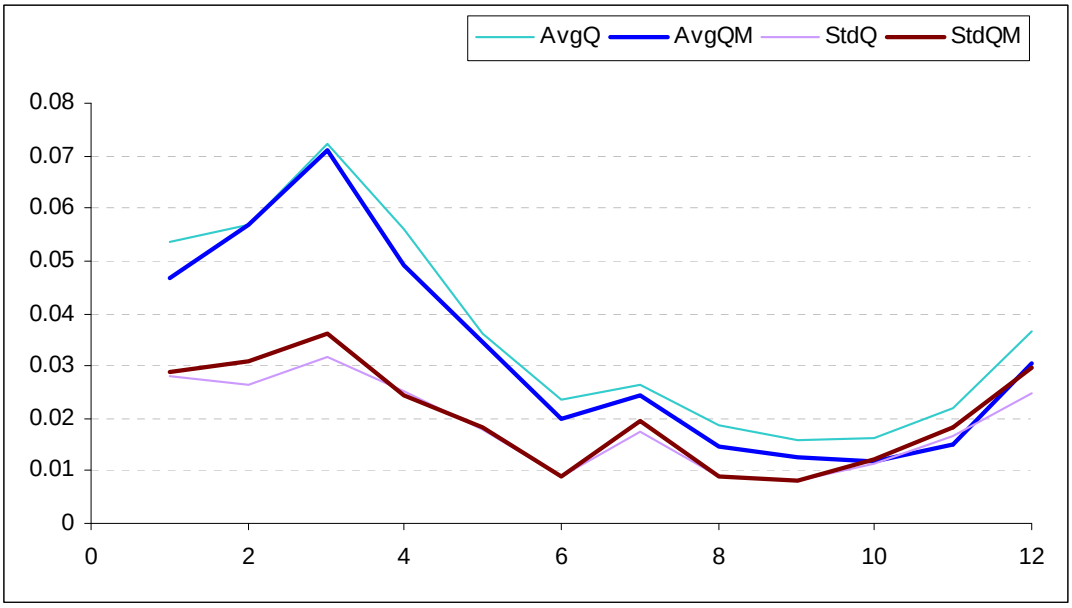

Figure 4.5: Climatology of Modeled vs. Observed Flows for West Point

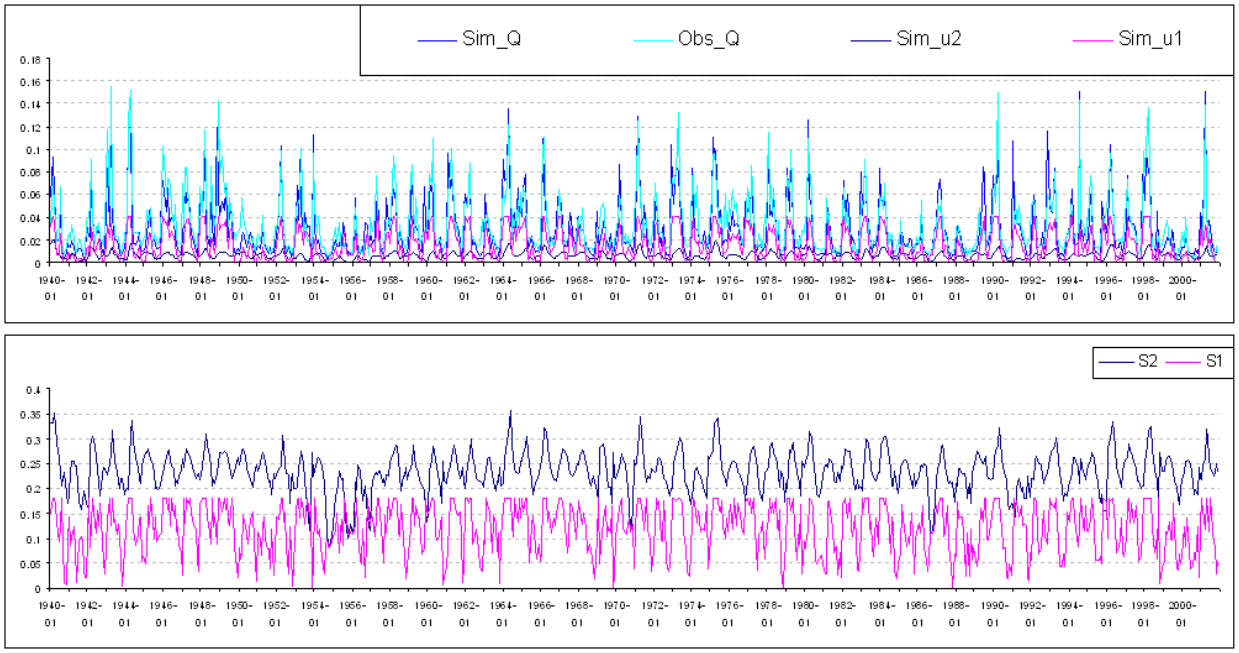

Figure 4.6: Modeled vs. Observed Flows and Storages for George

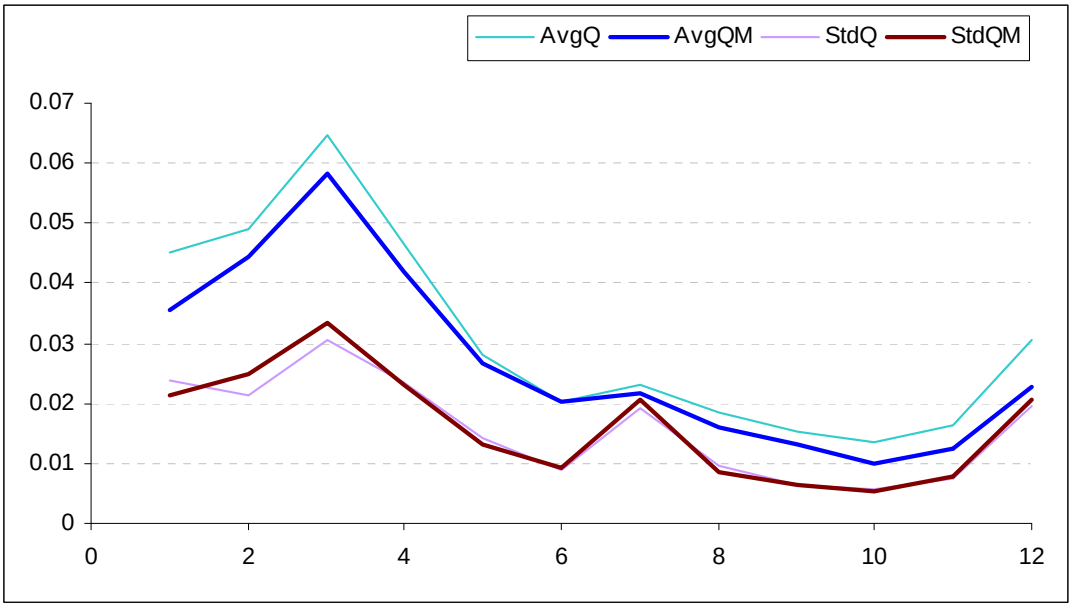

Figure 4.7: Climatology of Modeled vs. Observed Flows for George

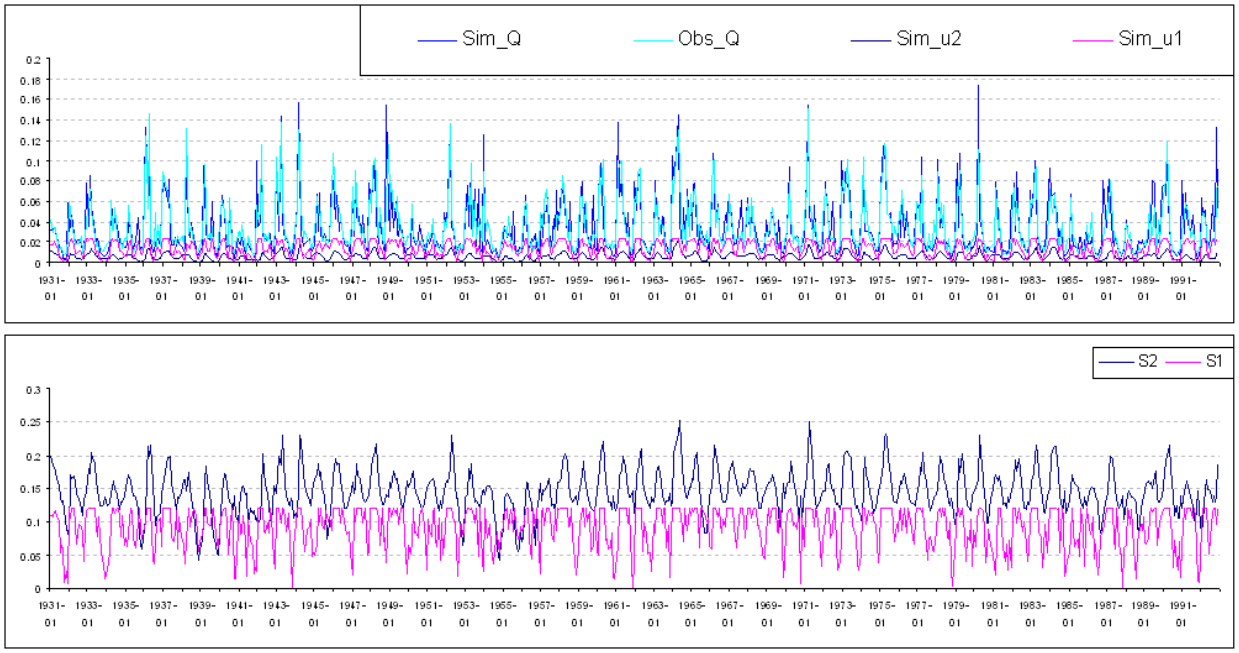

Figure 4.8: Modeled vs. Observed Flows and Storages for Montezuma

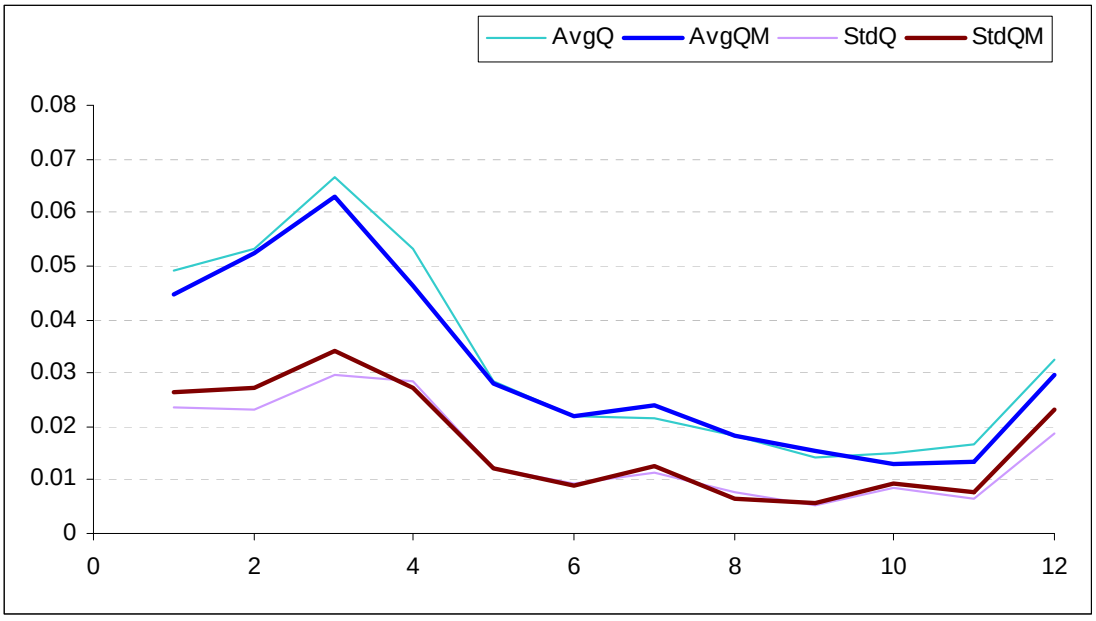

Figure 4.9: Climatology of Modeled vs. Observed Flows for Montezuma

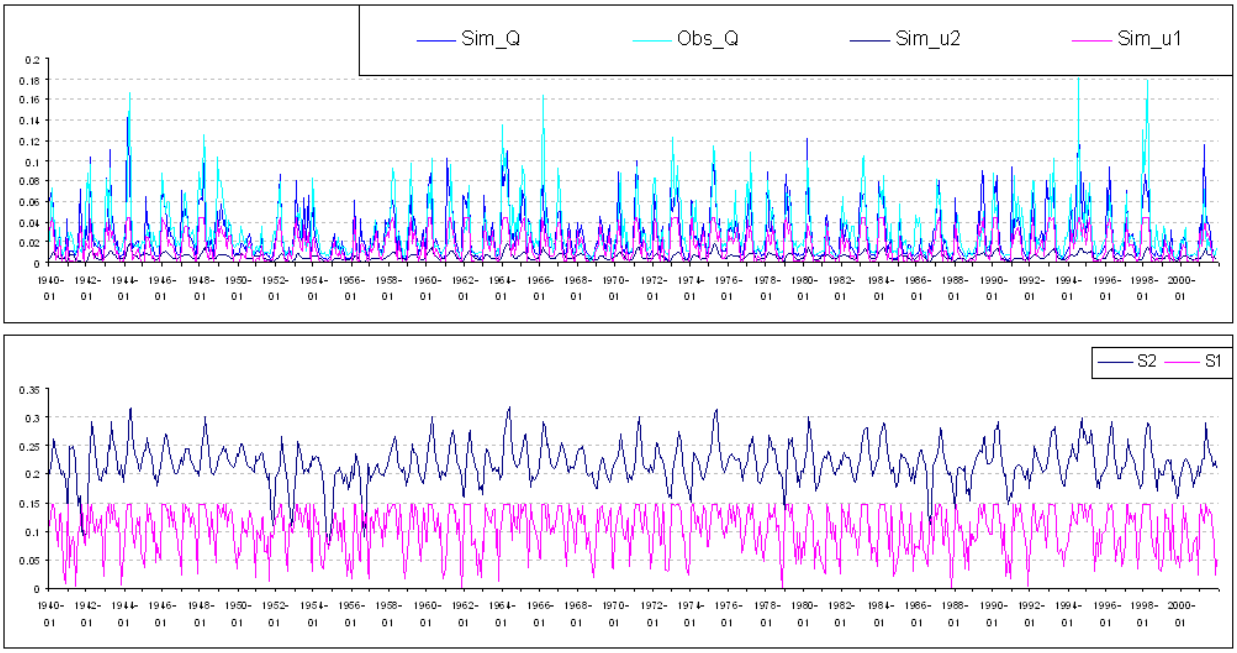

Figure 4.10: Modeled vs. Observed Flows and Storages for Albany

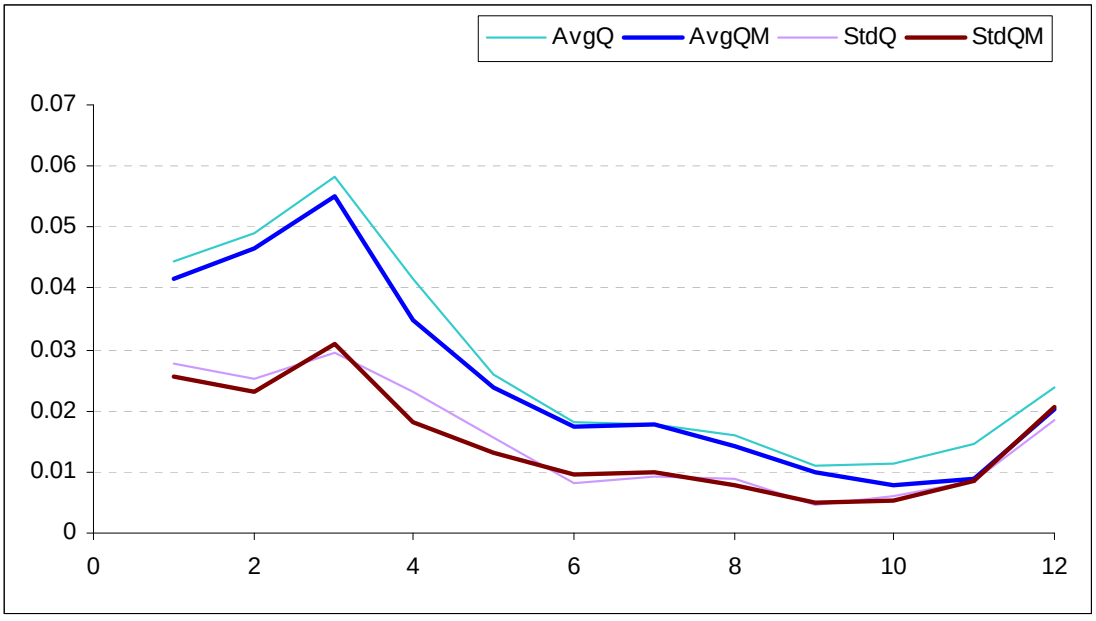

Figure 4.11: Climatology of Modeled vs. Observed Flows for Albany

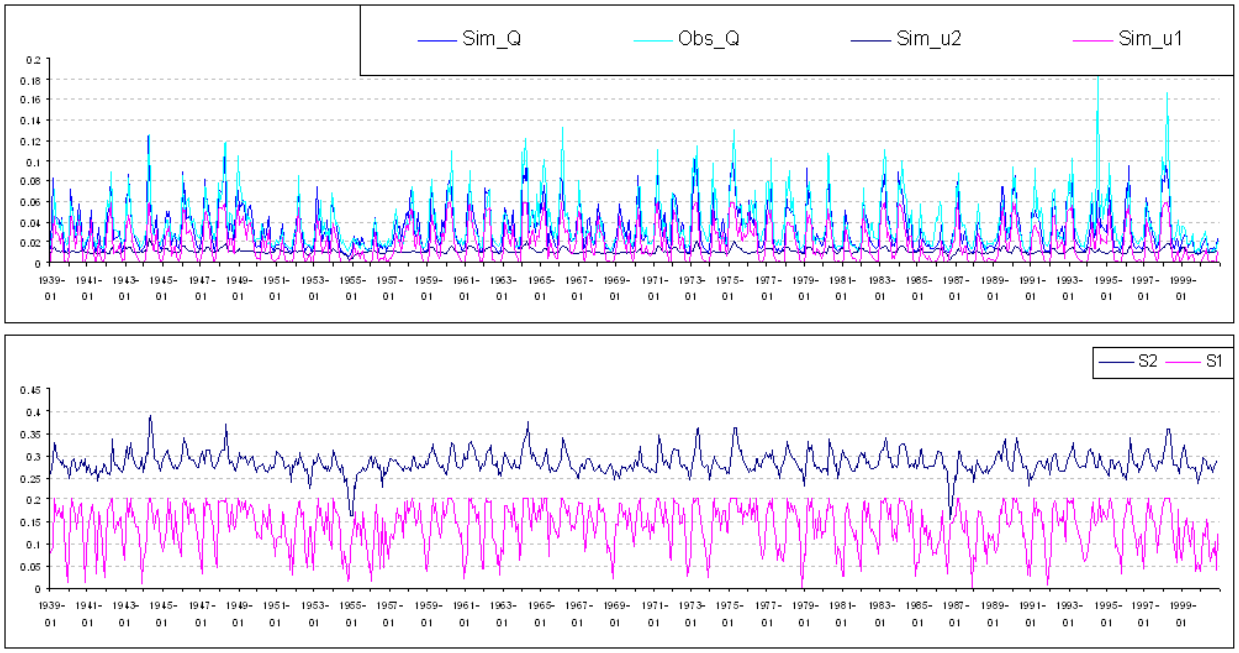

Figure 4.12: Modeled vs. Observed Flows and Storages for Woodruff-Bainbridge

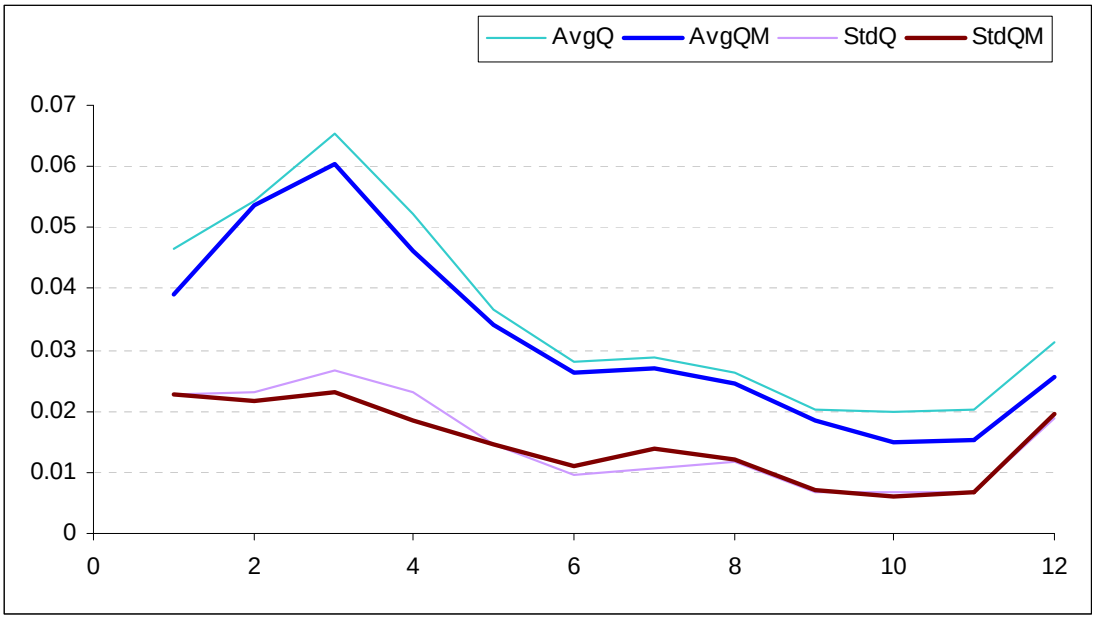

Figure 4.13: Climatology of Modeled vs. Observed Flows for Woodruff-Bainbridge

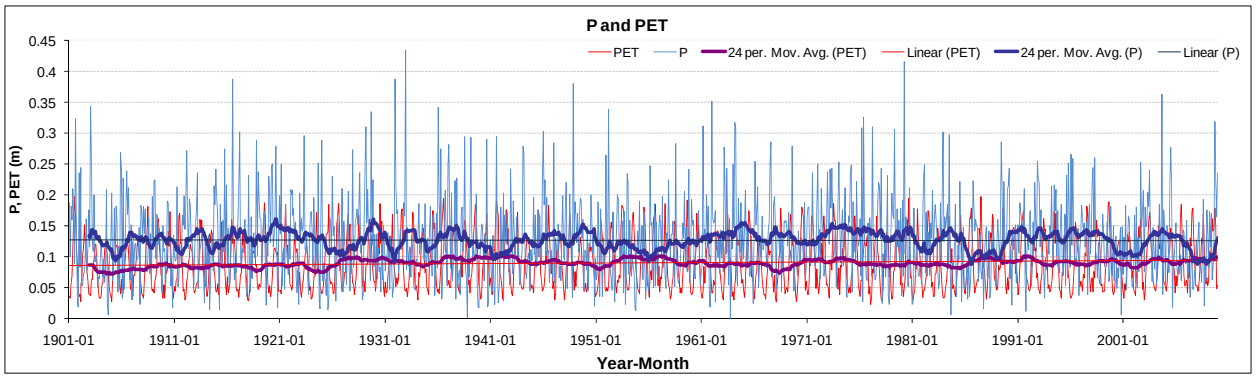

Figure 4.14: Buford Watershed Historical P and PET Sequences (1901 - 2009)

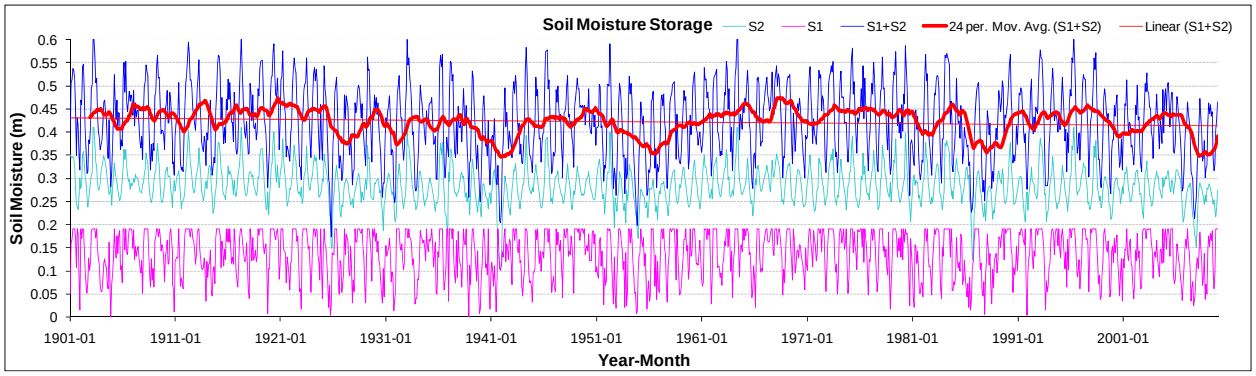

Figure 4.15: Buford Watershed Historical Soil Moisture Storage Sequences (1901 - 2009)

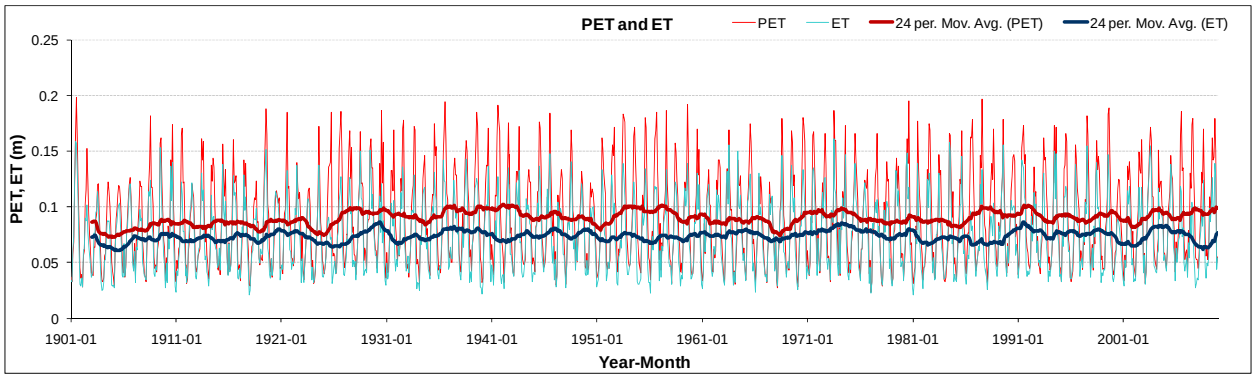

Figure 4.16: Buford Watershed Historical PET and ET Sequences (1901 - 2009)

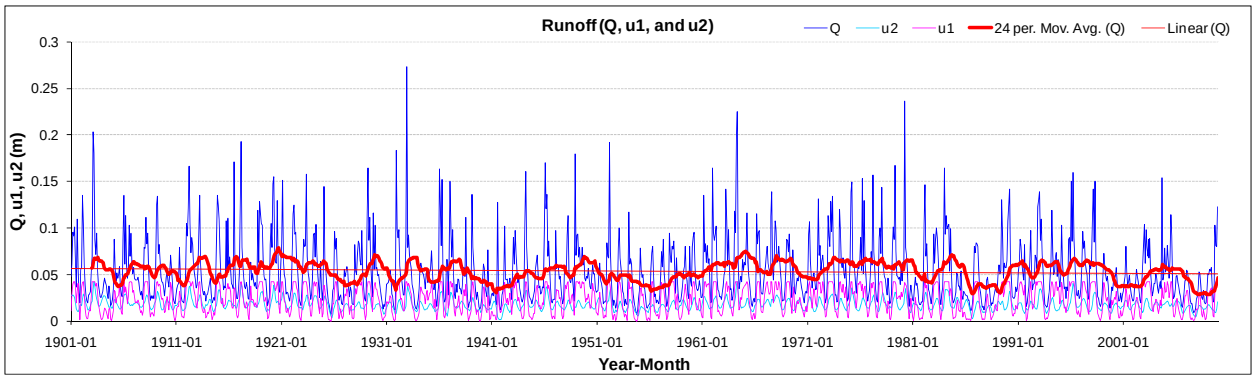

Figure 4.17: Buford Watershed Historical Runoff Sequences (1901 - 2009)

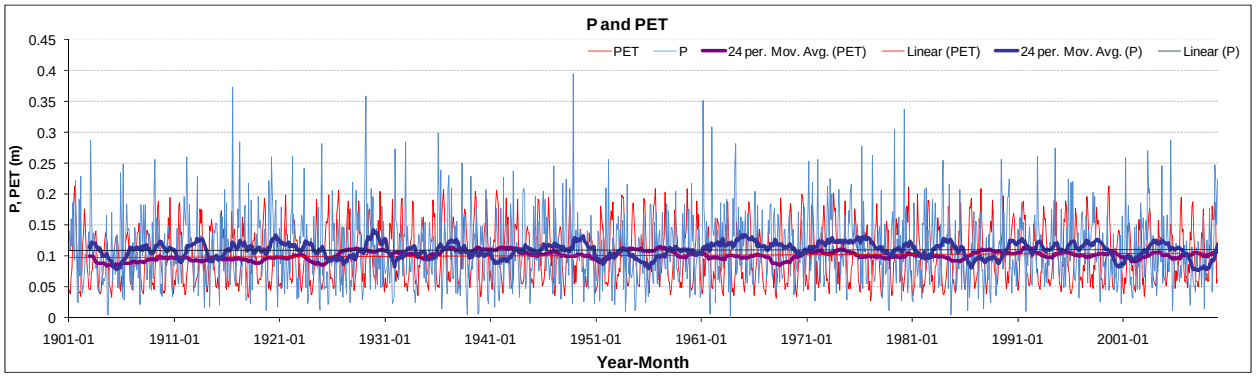

Figure 4.18: West Point Watershed Historical P and PET Sequences (1901 - 2009)

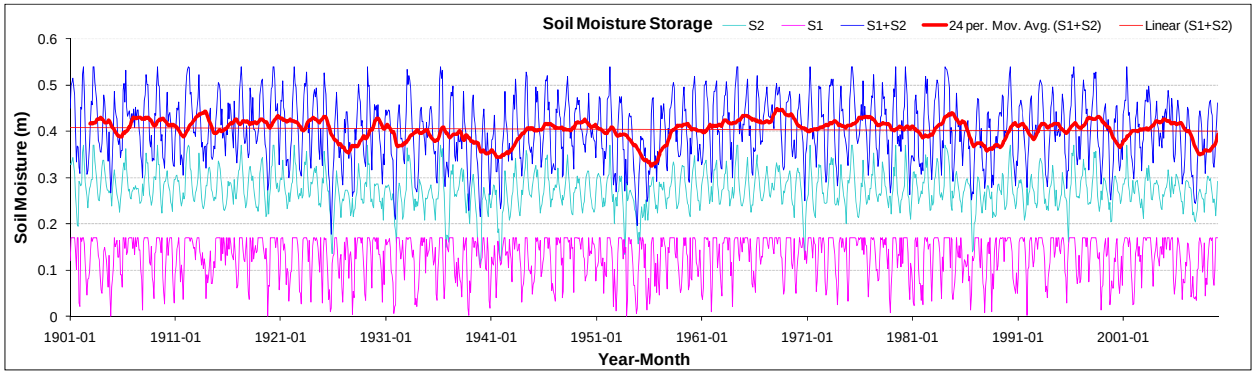

Figure 4.19: West Point Watershed Historical Soil Moisture Storage Sequences (1901 - 2009)

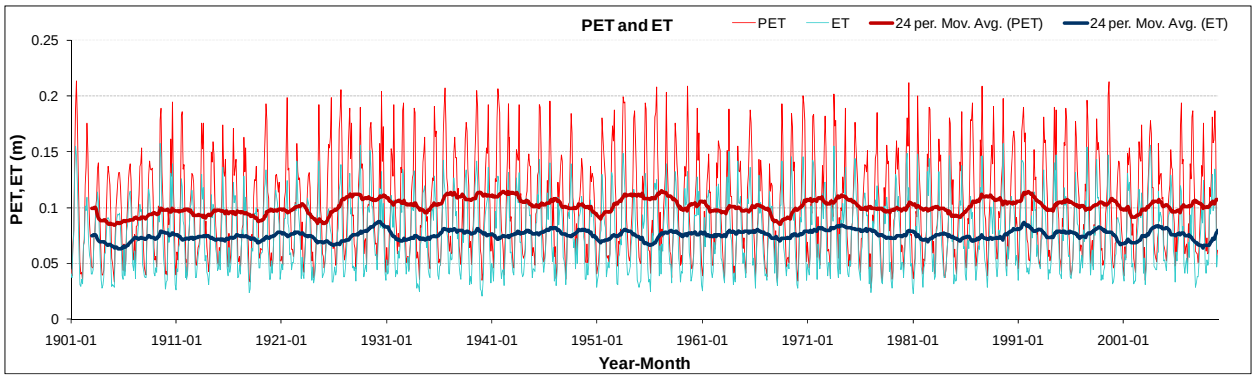

Figure 4.20: West Point Watershed Historical PET and ET Sequences (1901 - 2009)

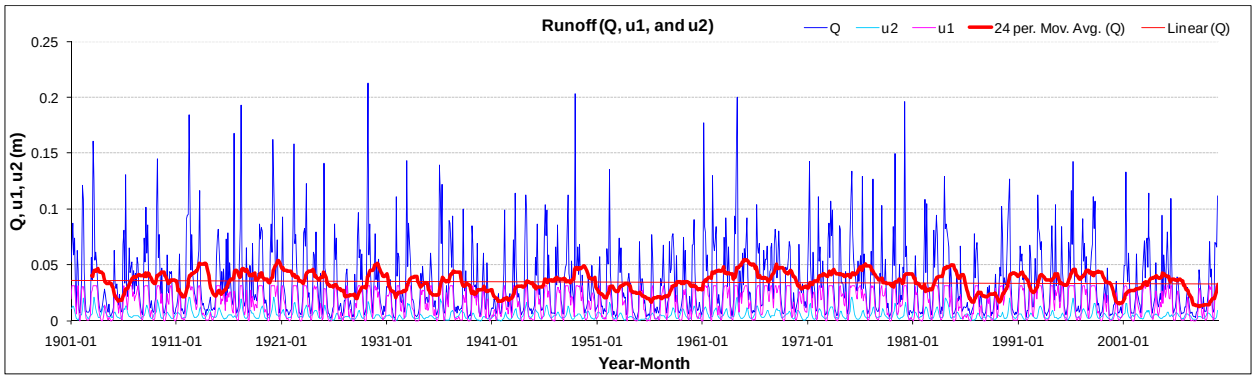

Figure 4.21: West Point Watershed Historical Runoff Sequences (1901 - 2009)

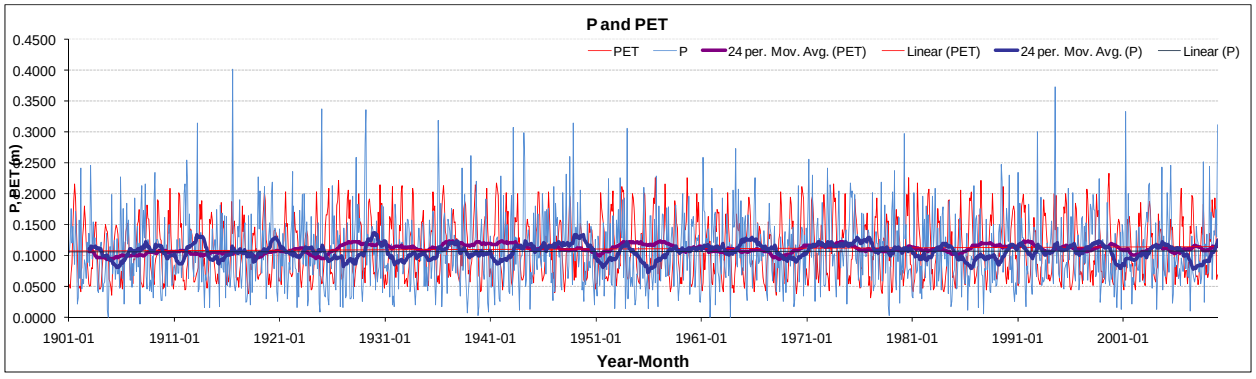

Figure 4.22: George Watershed Historical P and PET Sequences (1901 - 2009)

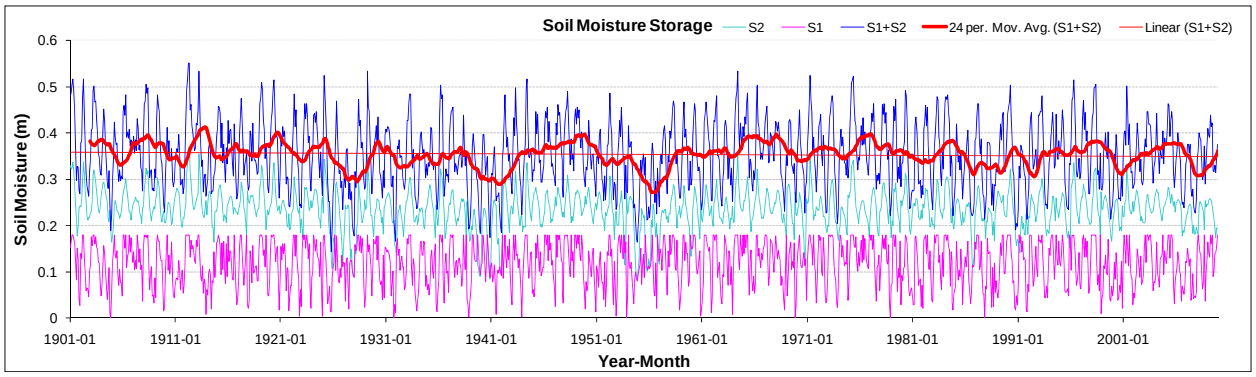

Figure 4.23: George Watershed Historical Soil Moisture Storage Sequences (1901 - 2009)

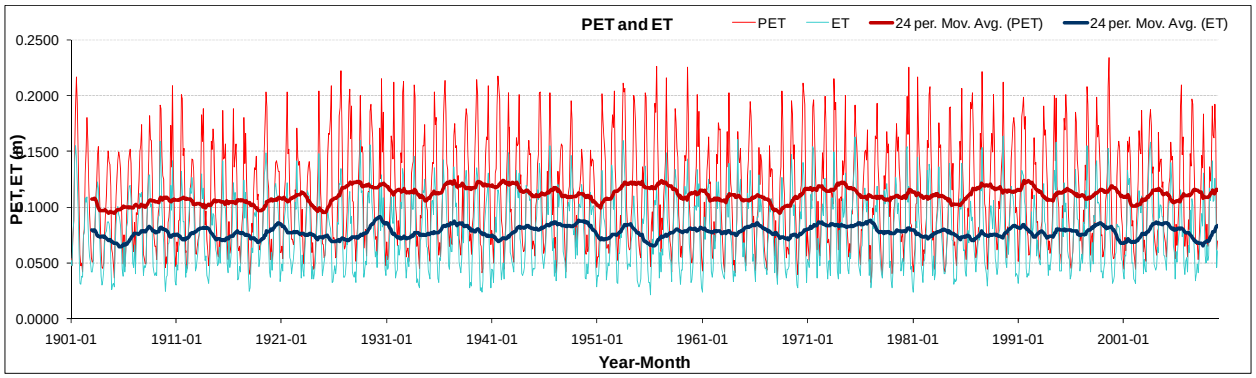

Figure 4.24: George Watershed Historical PET and ET Sequences (1901 - 2009)

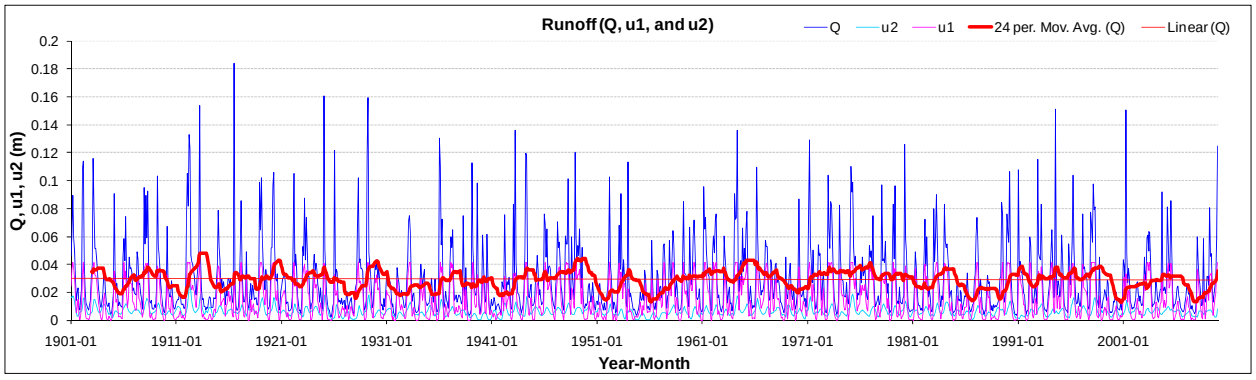

Figure 4.25: George Watershed Historical Runoff Sequences (1901 - 2009)

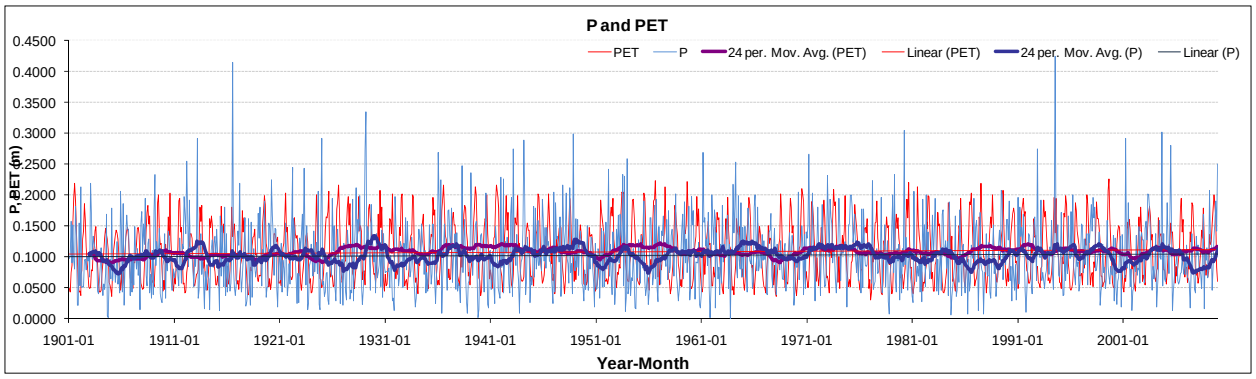

Figure 4.26: Montezuma Watershed Historical P and PET Sequences (1901 - 2009)

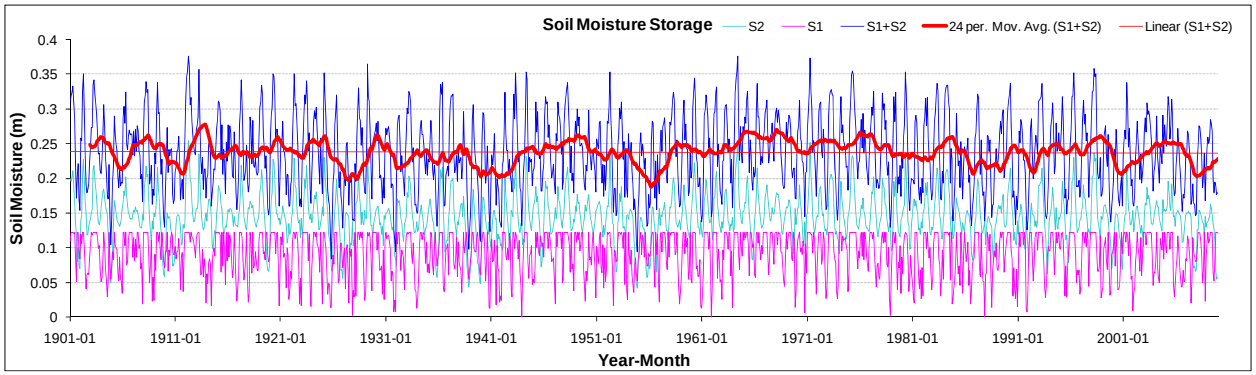

Figure 4.27: Montezuma Watershed Historical Soil Moisture Storage Sequences (1901 - 2009)

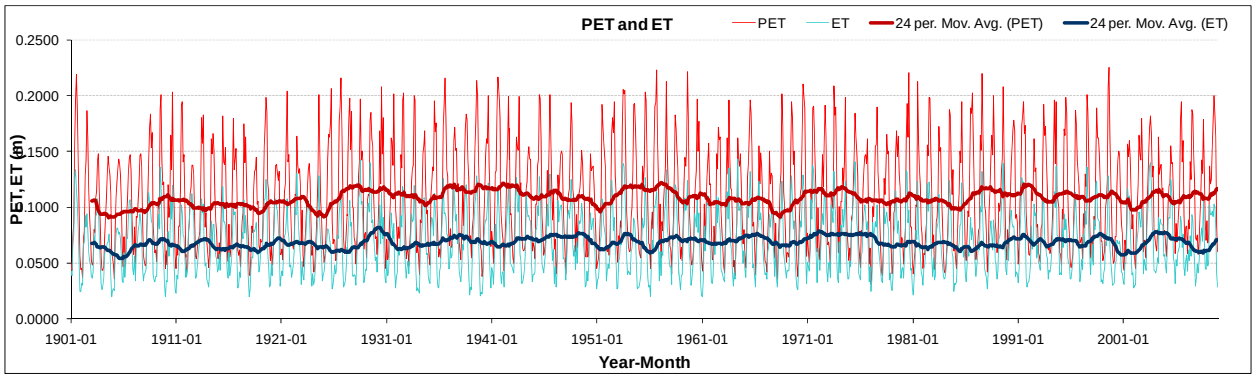

Figure 4.28: Montezuma Watershed Historical PET and ET Sequences (1901 - 2009)

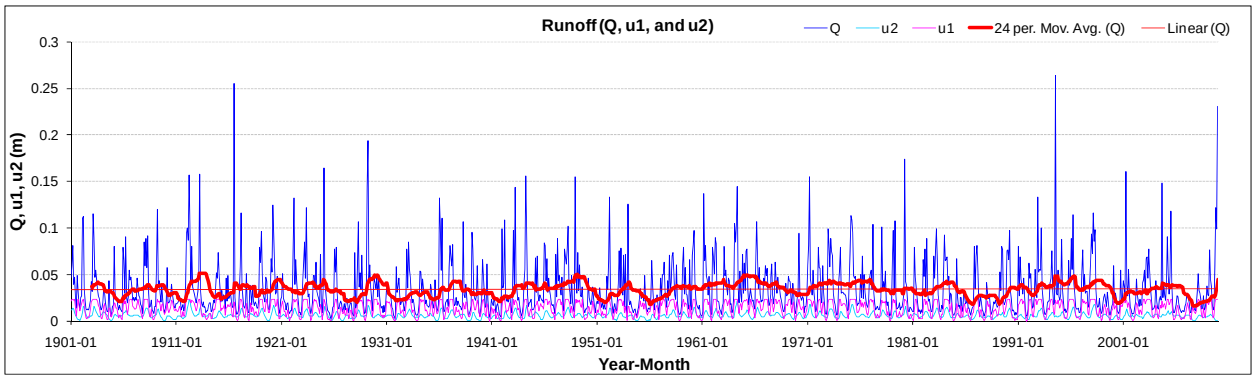

Figure 4.29: Montezuma Watershed Historical Runoff Sequences (1901 - 2009)

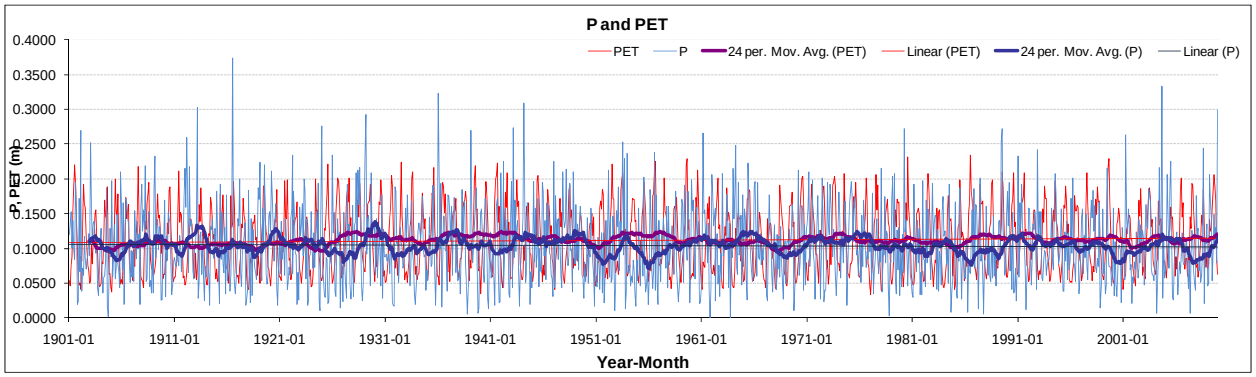

Figure 4.30: Albany Watershed Historical P and PET Sequences (1901 - 2009)

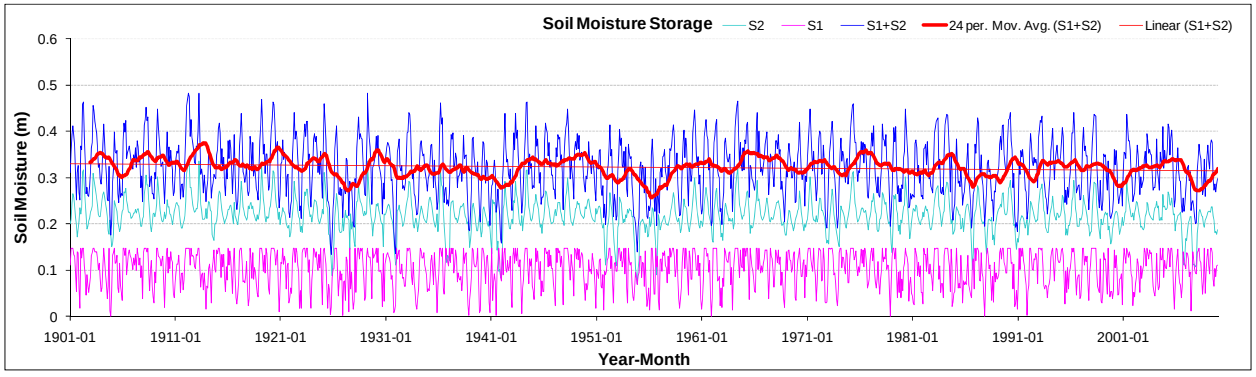

Figure 4.31: Albany Watershed Historical Soil Moisture Storage Sequences (1901 - 2009)

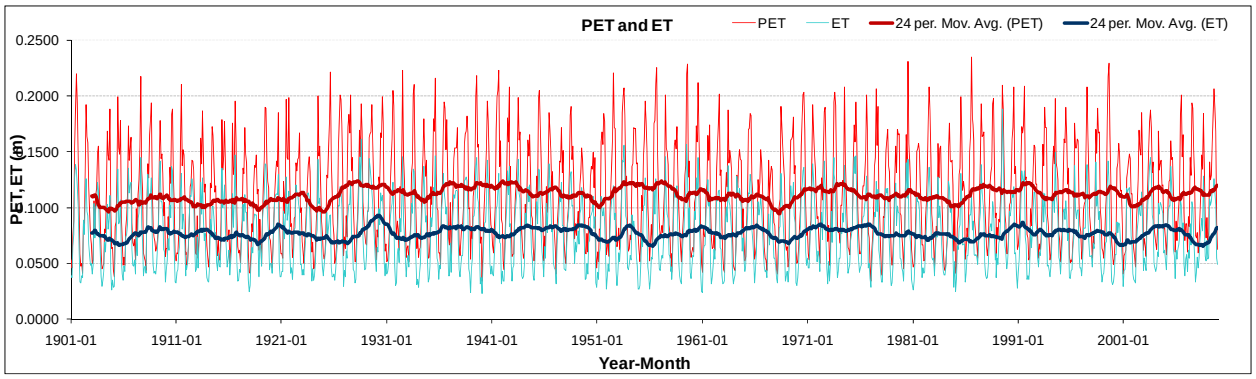

Figure 4.32: Albany Watershed Historical PET and ET Sequences (1901 - 2009)

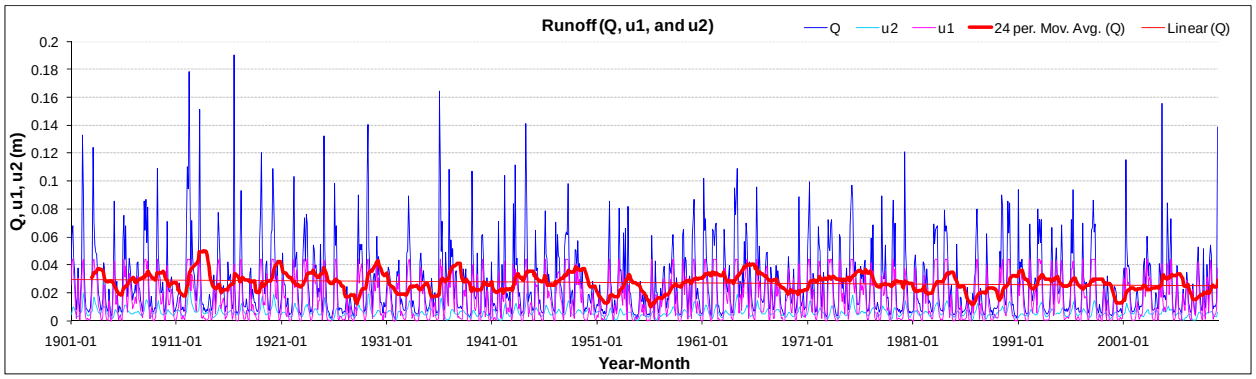

Figure 4.33: Albany Watershed Historical Runoff Sequences (1901 - 2009)

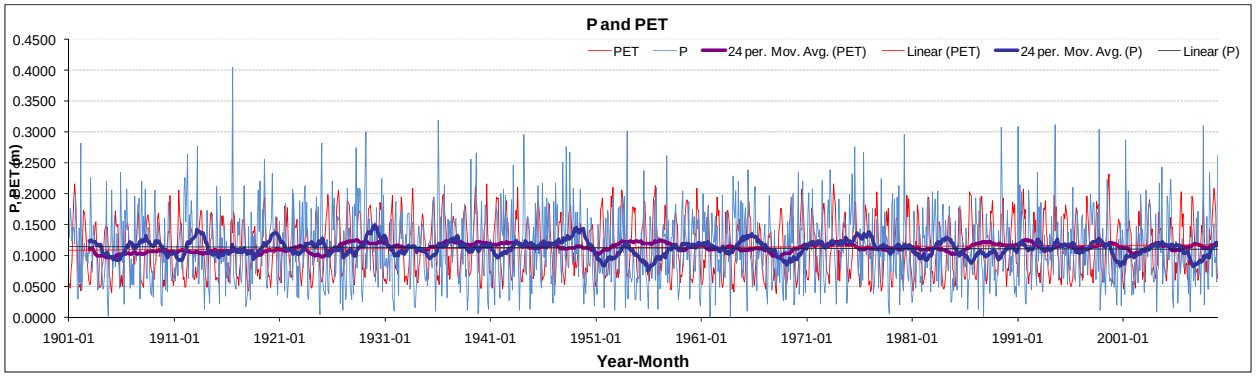

Figure 4.34: Woodruff-Bainbridge Watershed Historical P and PET Sequences (1901 - 2009)

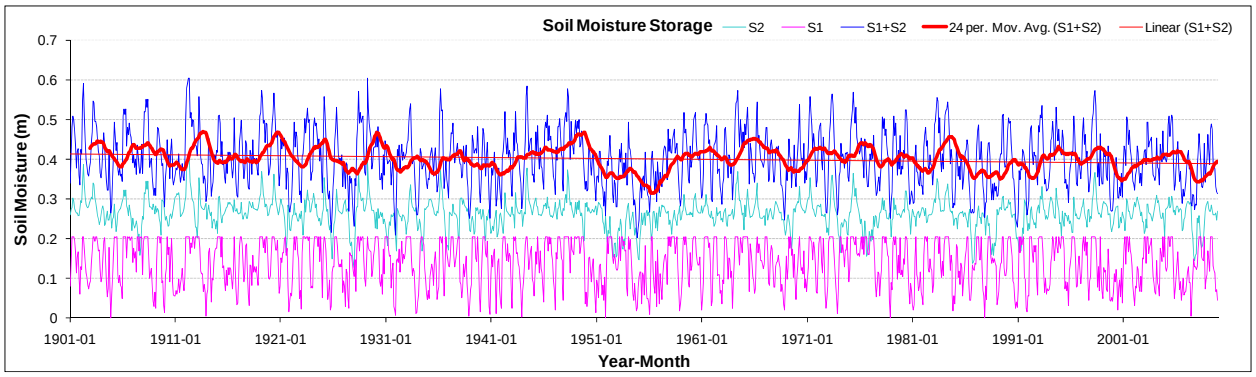

Figure 4.35: Woodruff-Bainbridge Watershed Hist. Soil Moisture Storage (1901 - 2009)

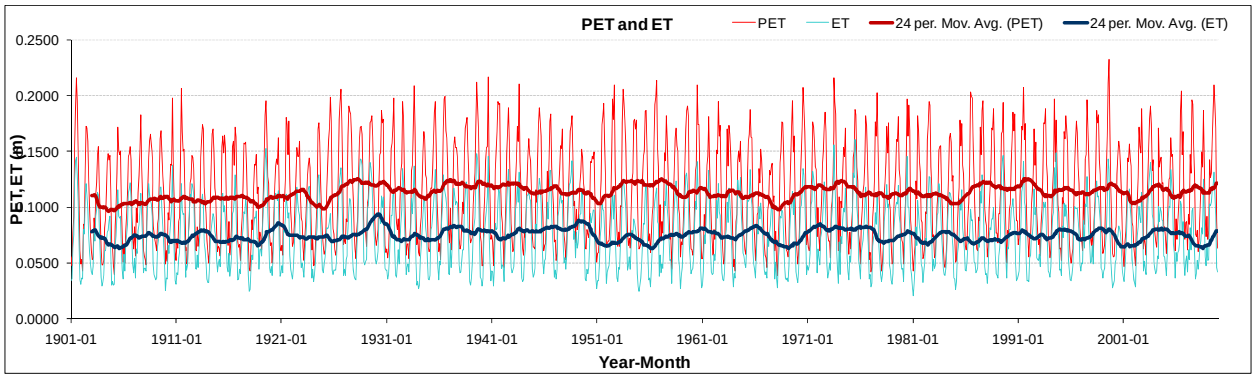

Figure 4.36: Woodruff-Bainbridge Watershed Hist. PET and ET Sequences (1901 - 2009)

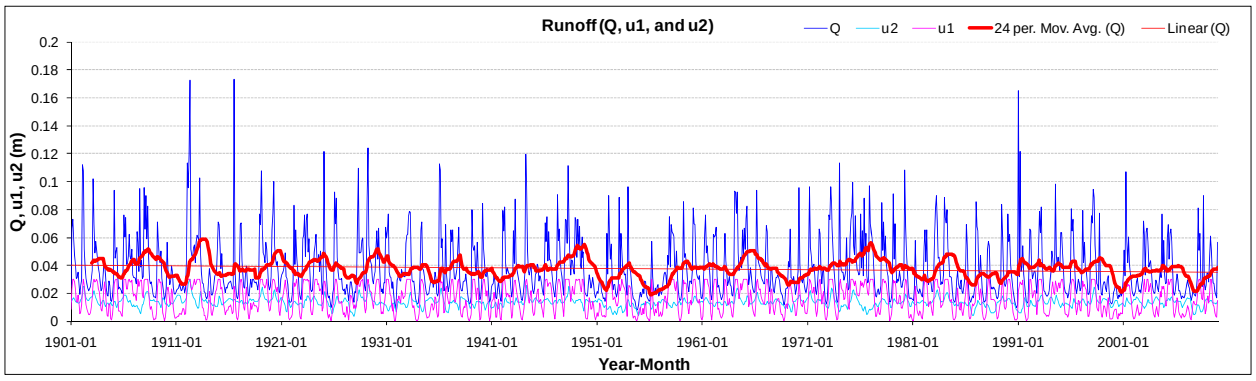

Figure 4.37: Woodruff-Bainbridge Watershed Historical Runoff Sequences (1901 - 2009)

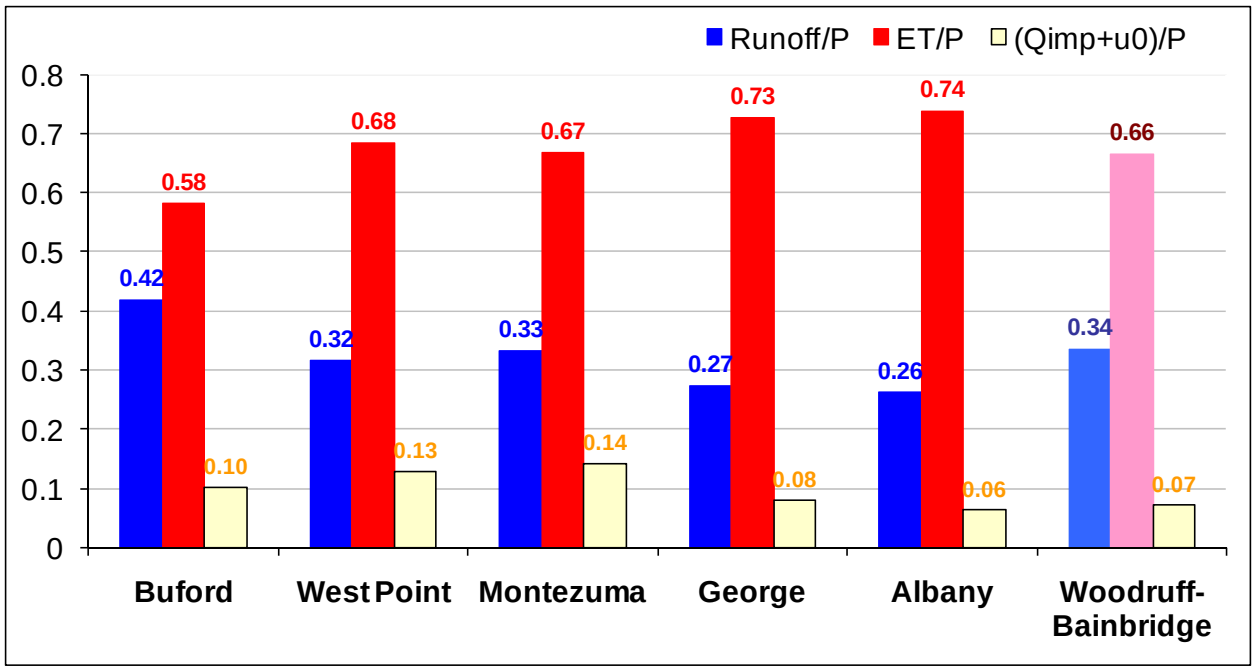

Figure 4.38: Average Hydrologic Response by Watershed (1901 - 2009)

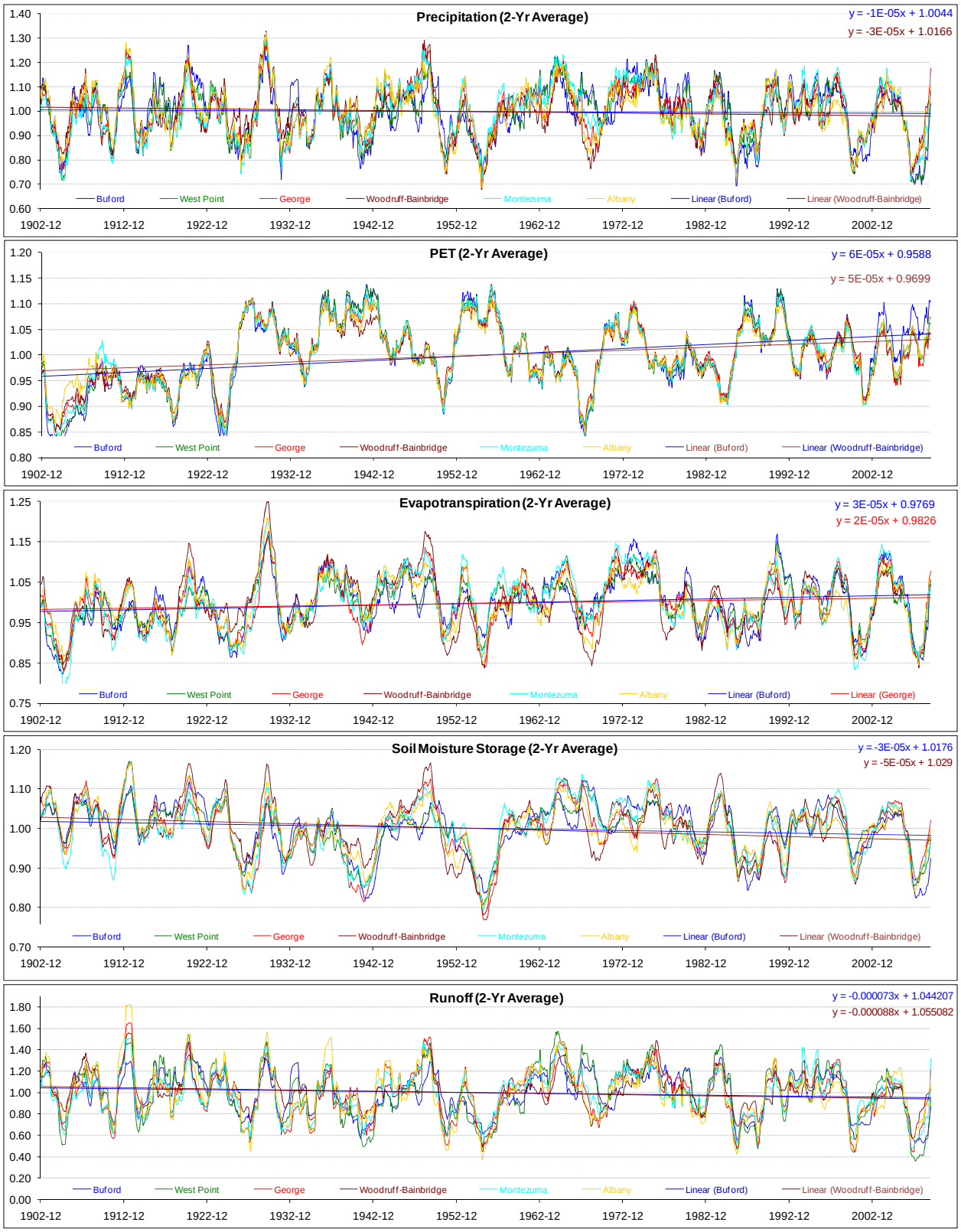

Figure 4.39: Normalized, 2Yr Average Hydrologic Response (1901 - 2009)

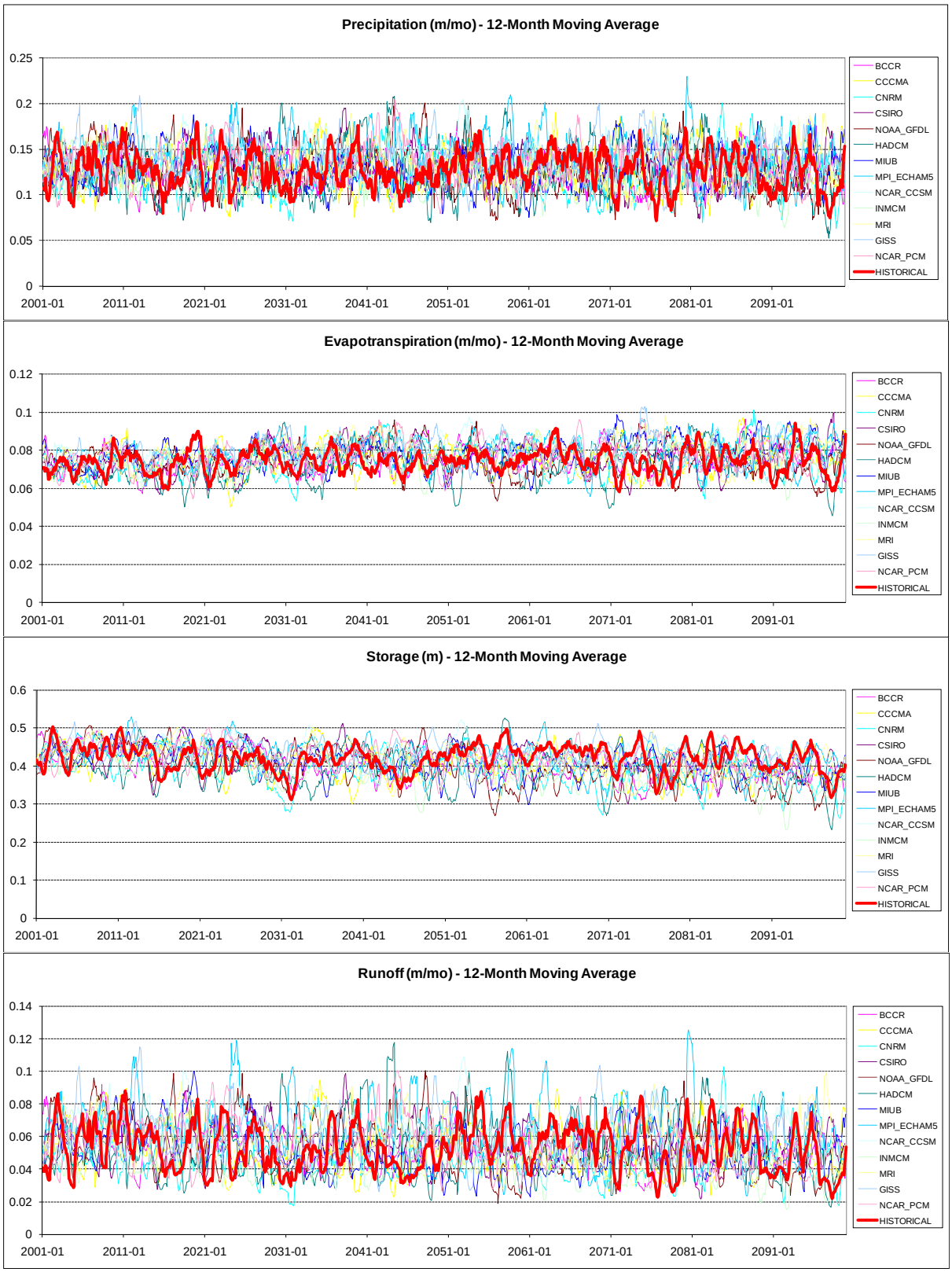

Figure 4.40: A1B Climate Scenarios (2000-2099), Buford, Sequences

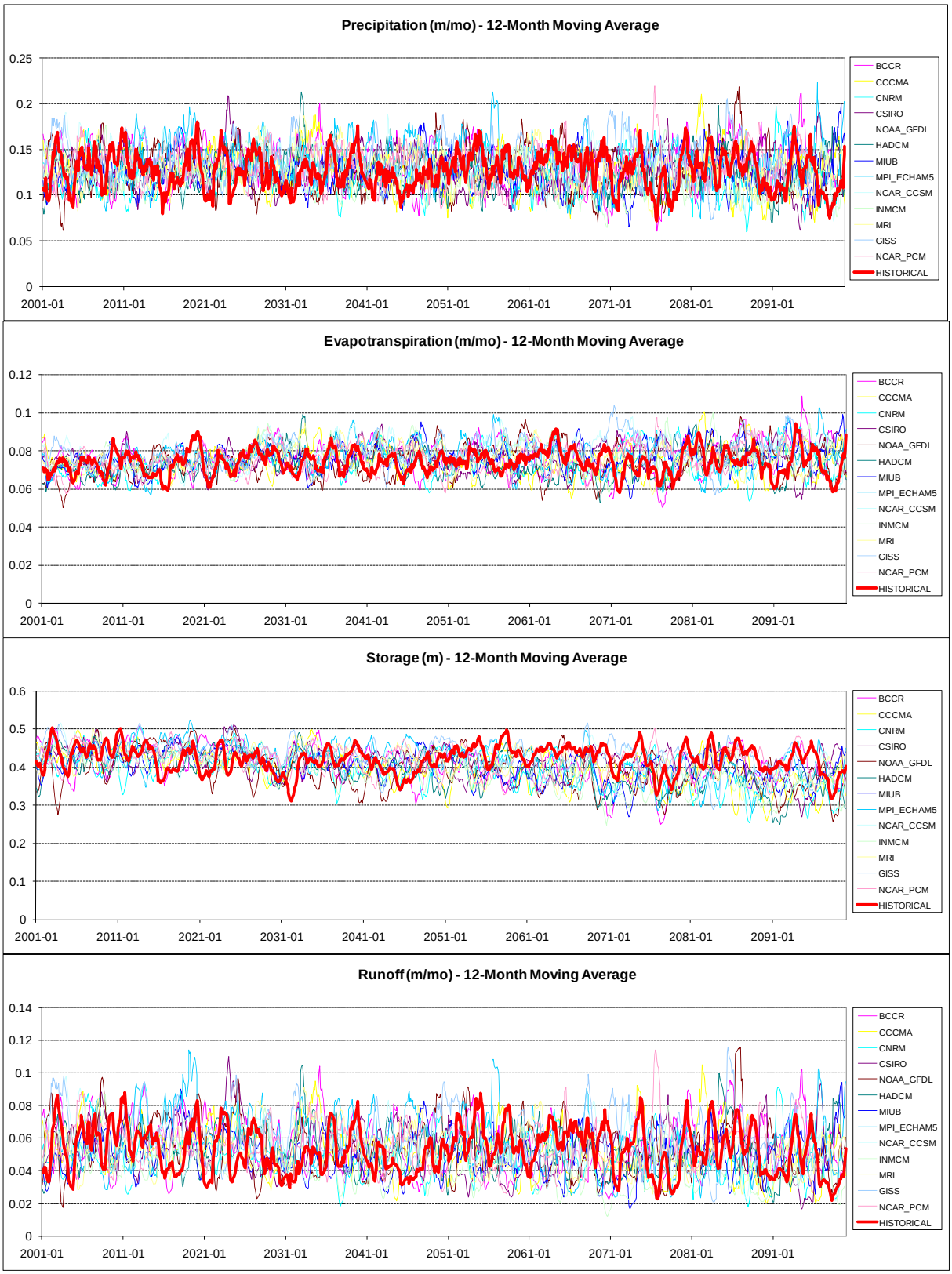

Figure 4.41: A2 Climate Scenarios (2000-2099), Buford, Sequences

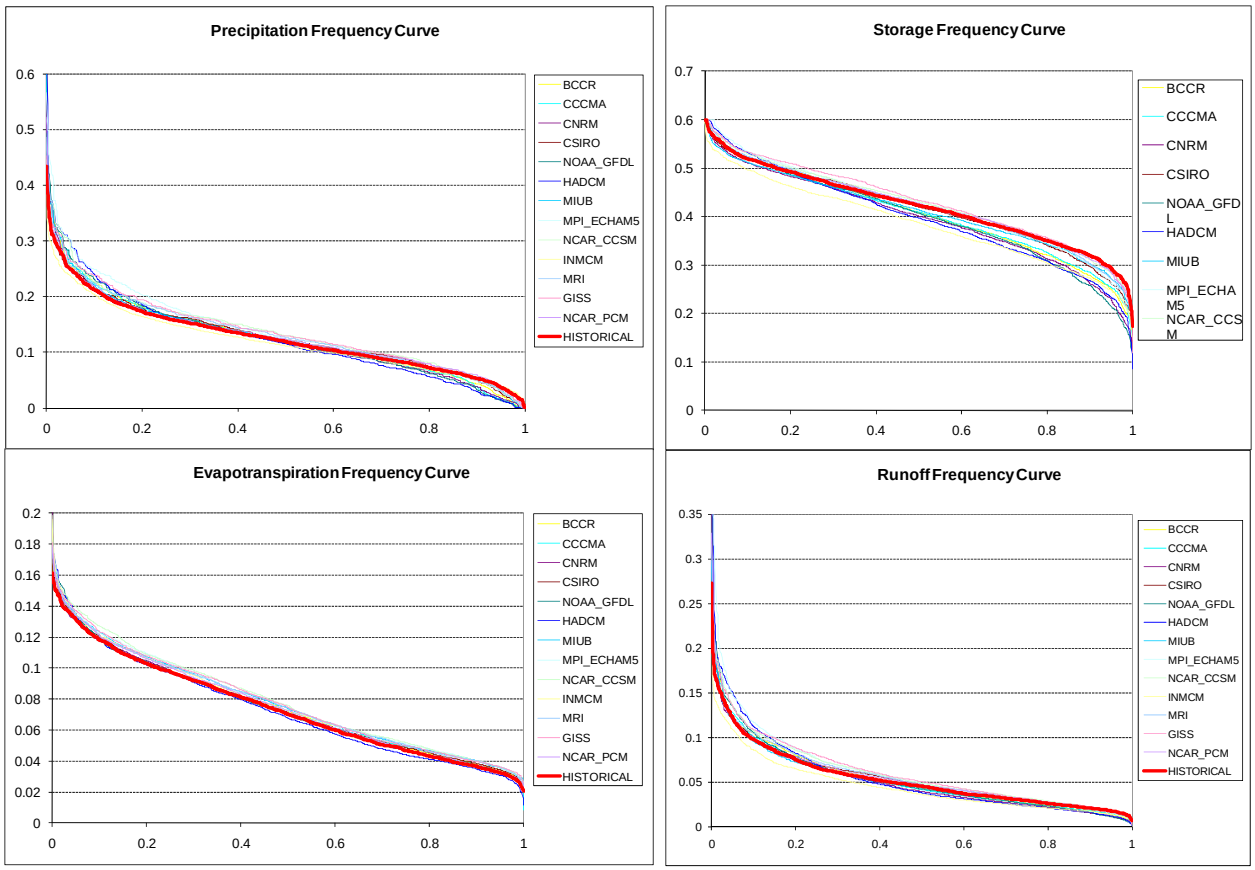

Figure 4.42: A1B Climate Scenarios (2000-2099), Buford, Frequency Curves

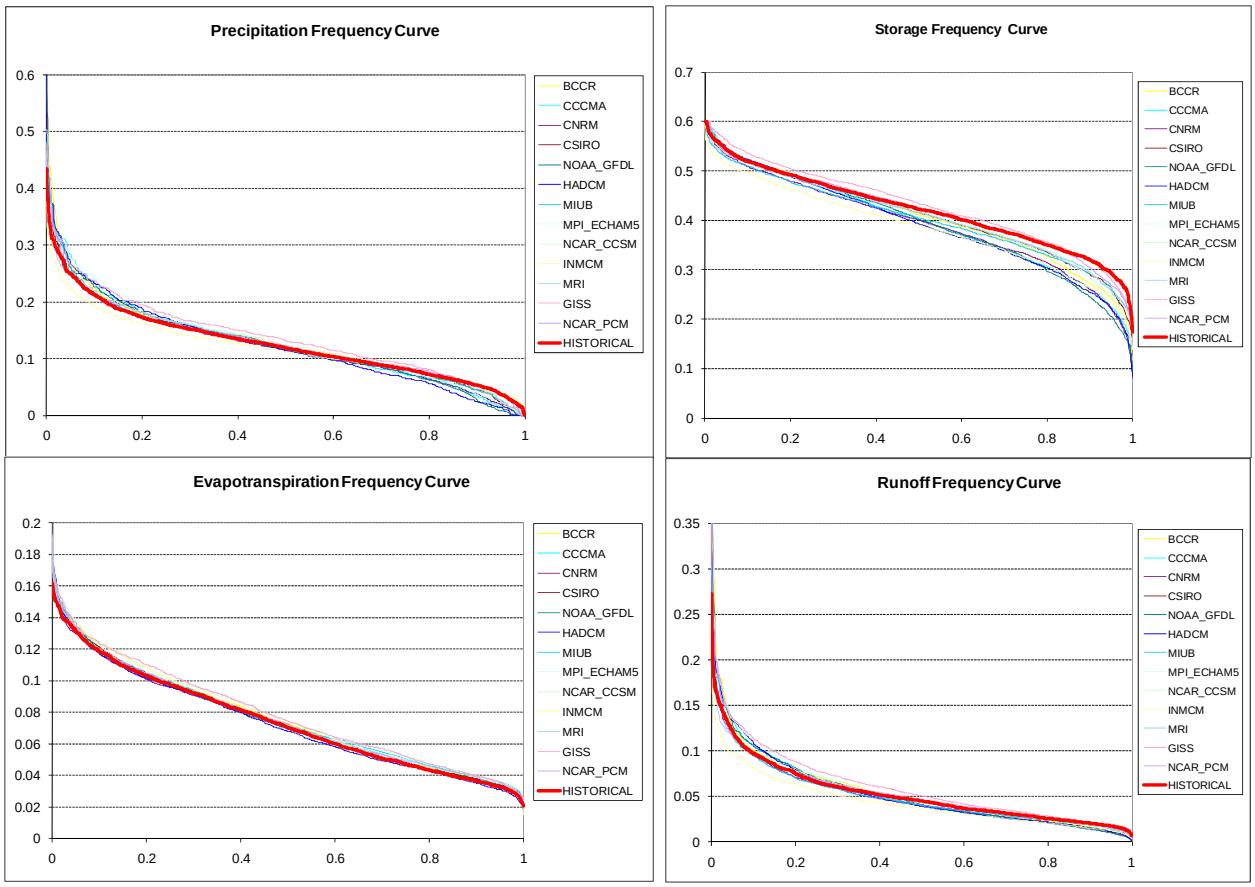

Figure 4.43: A2 Climate Scenarios (2000-2099), Buford, Frequency Curves

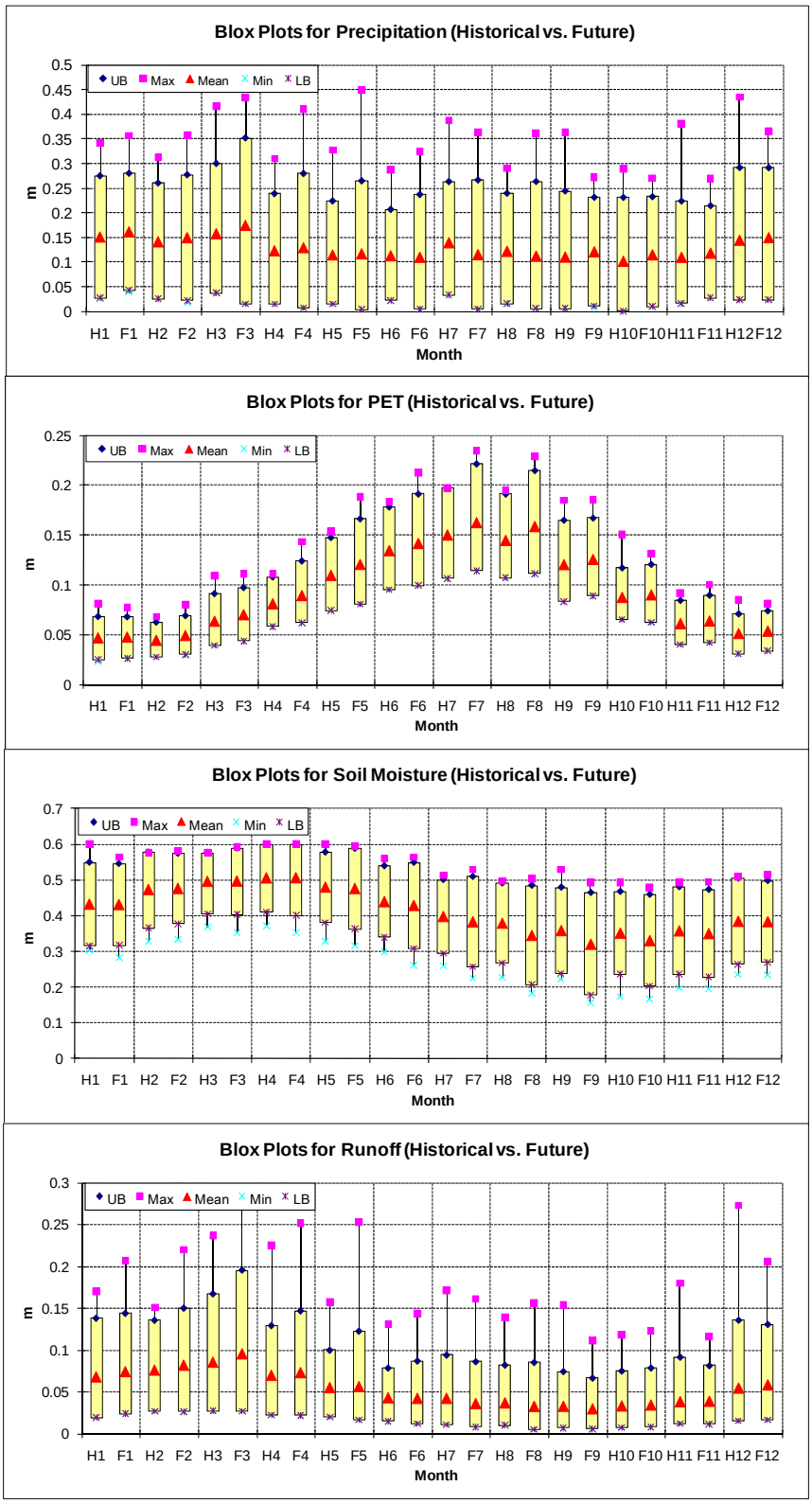

Figure 4.44: Monthly Historical vs. Future (A1B) Watershed Response, Buford

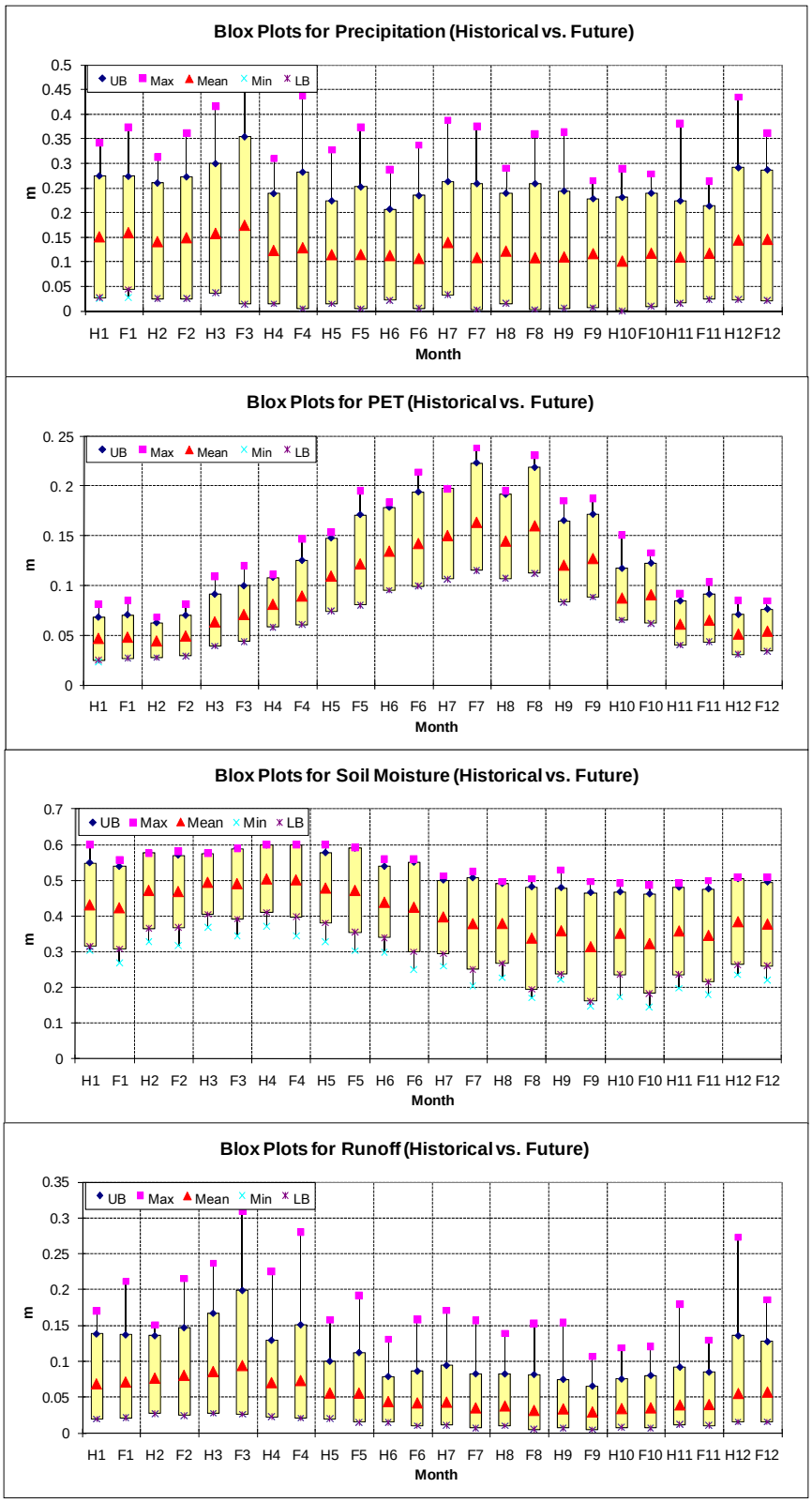

Figure 4.45: Monthly Historical vs. Future (A2) Watershed Response, Buford

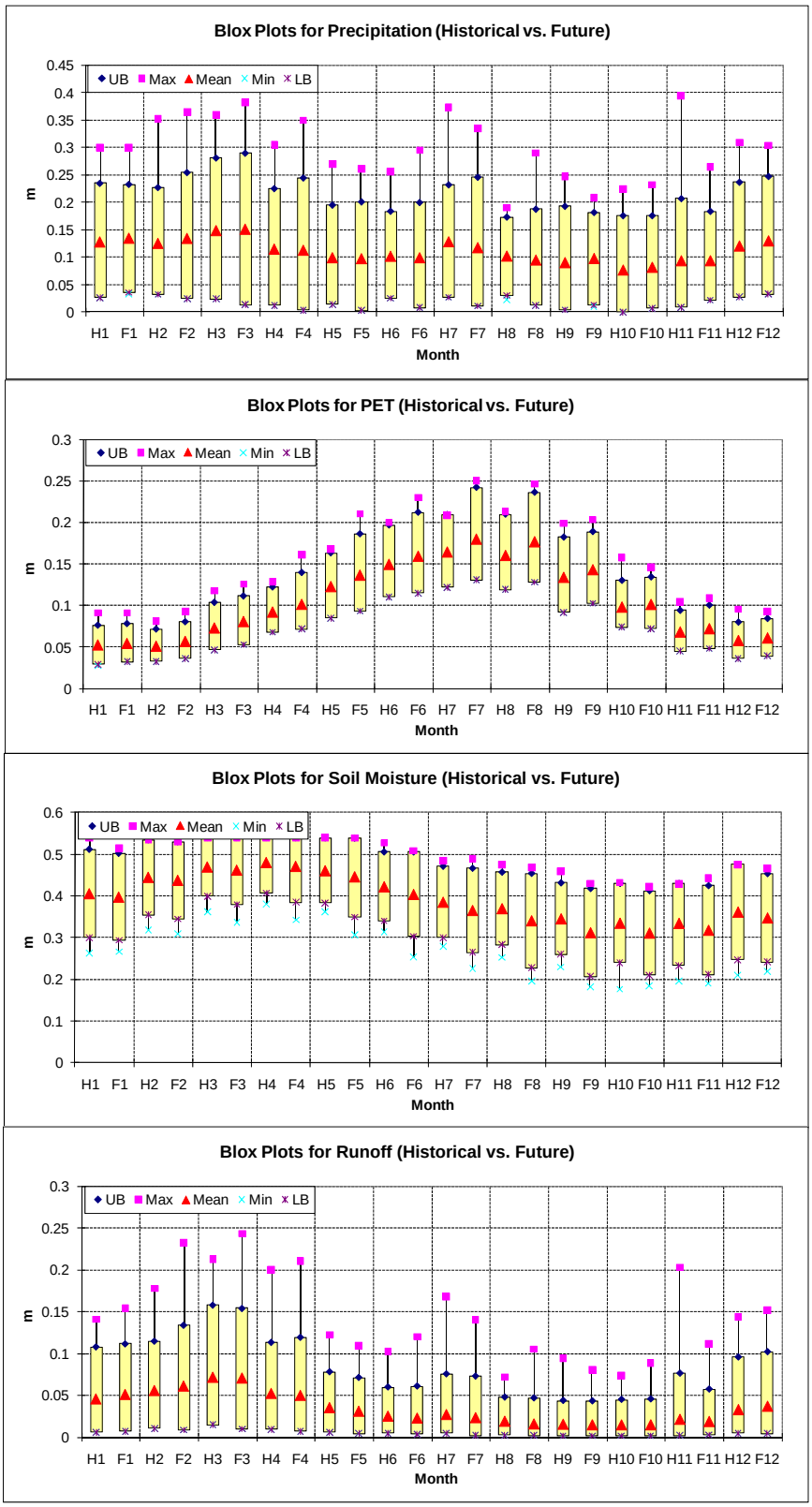

Figure 4.46: Monthly Historical vs. Future (A1B) Watershed Response, W. Point

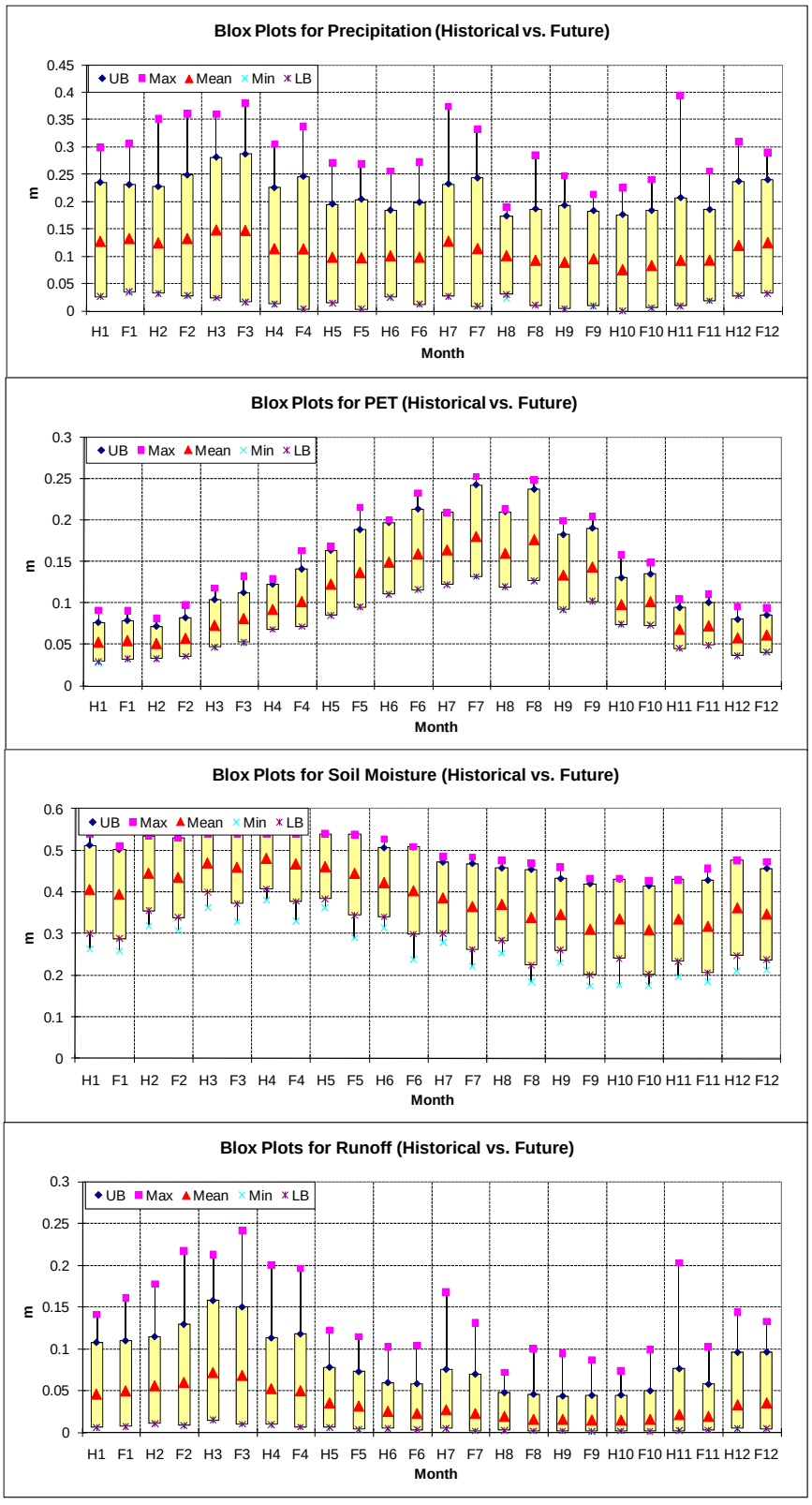

Figure 4.47: Monthly Historical vs. Future (A2) Watershed Response, W. Point

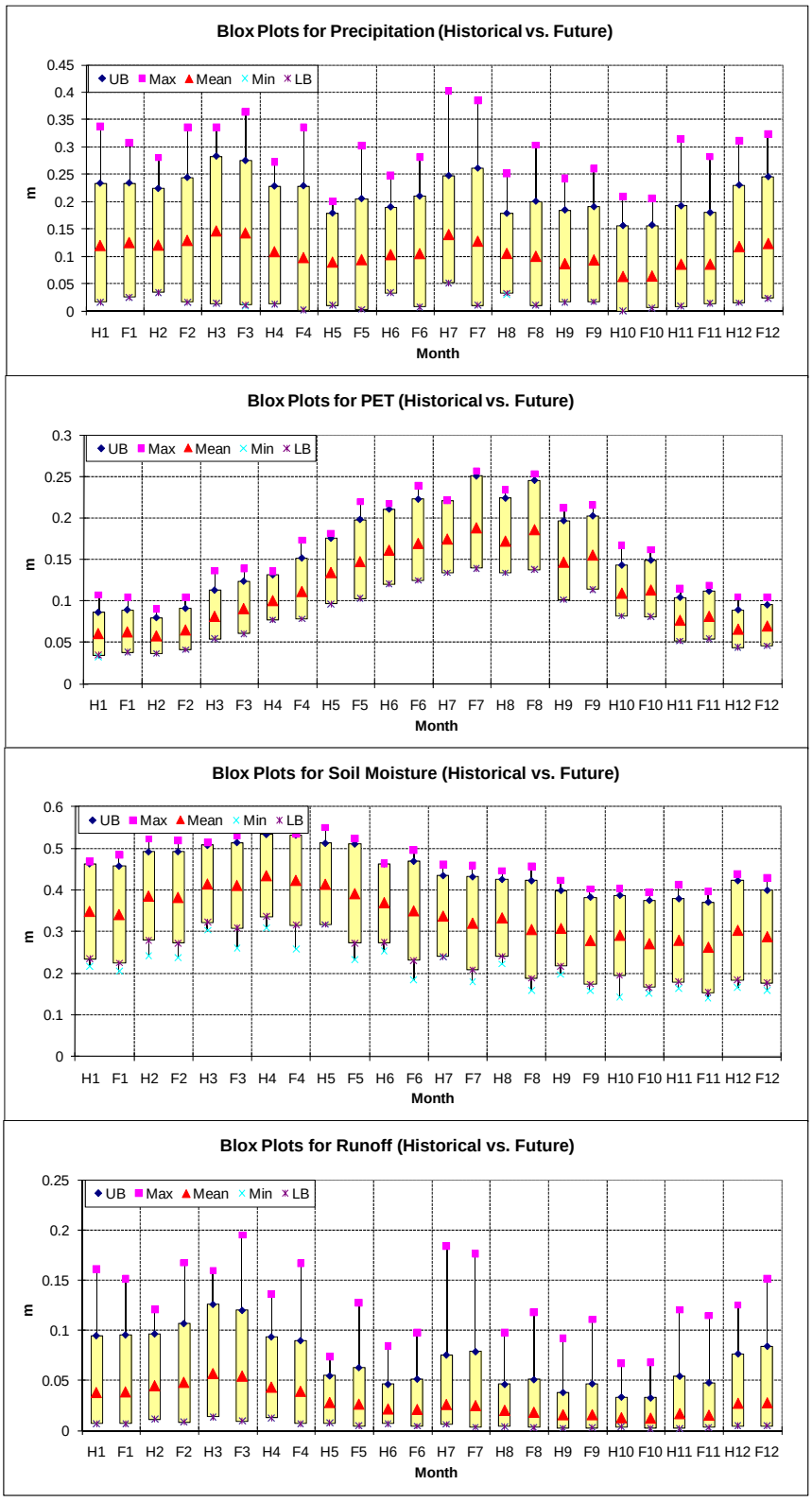

Figure 4.48: Monthly Historical vs. Future (A1B) Watershed Response, George

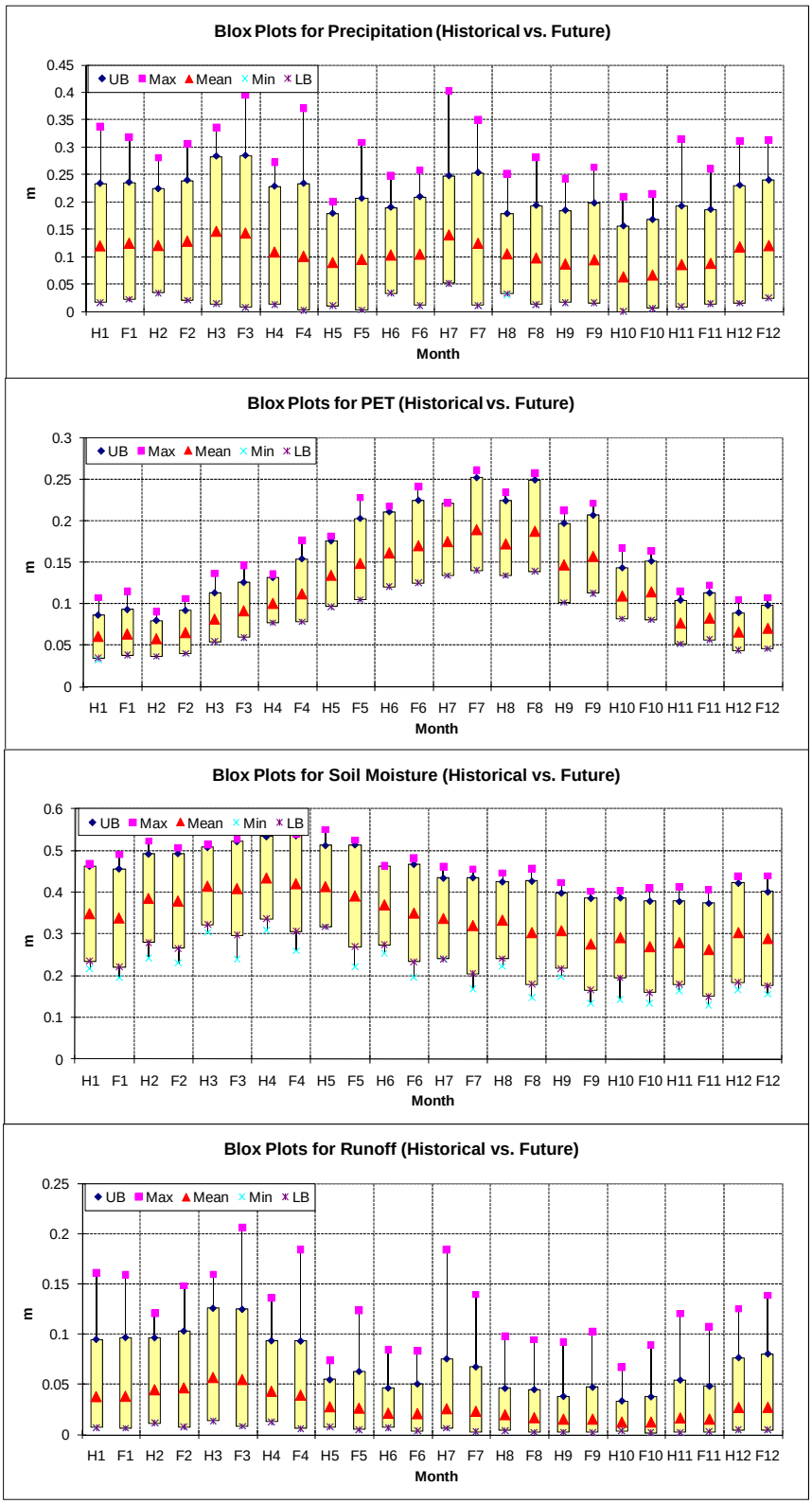

Figure 4.49: Monthly Historical vs. Future (A2) Watershed Response, George

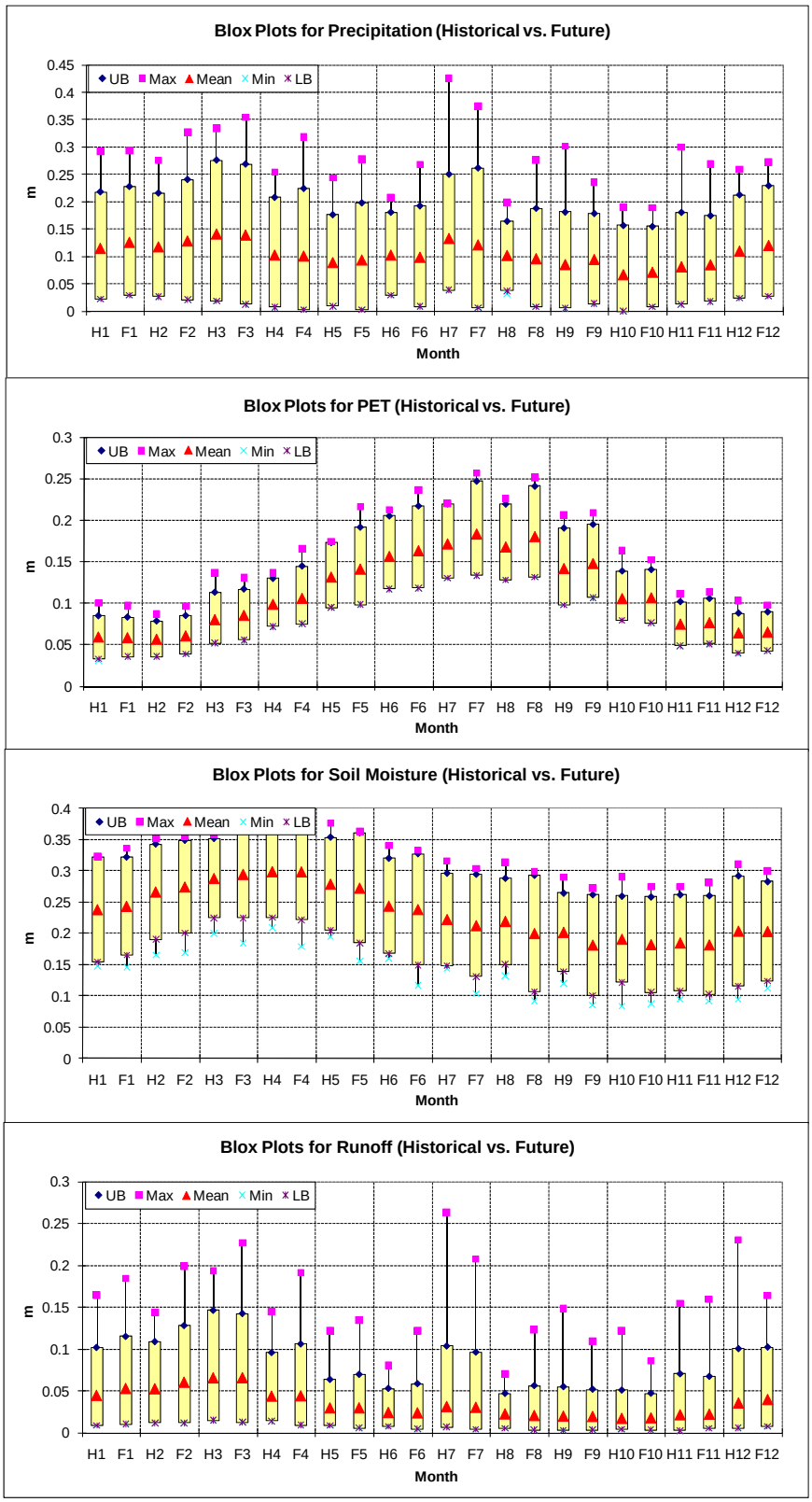

Figure 4.50: Monthly Historical vs. Future (A1B) Watershed Response, Montezuma

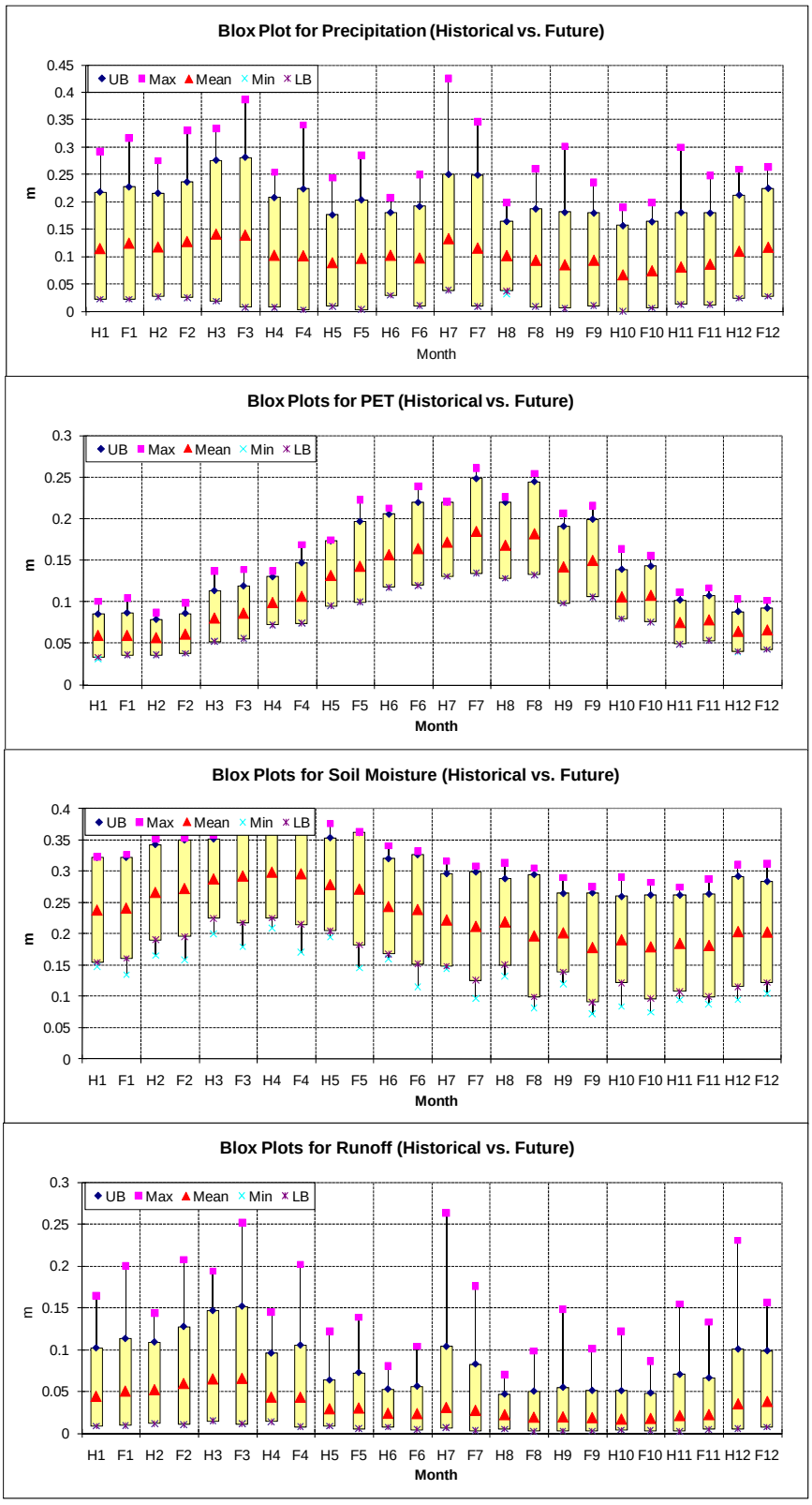

Figure 4.51: Monthly Historical vs. Future (A2) Watershed Response, Montezuma

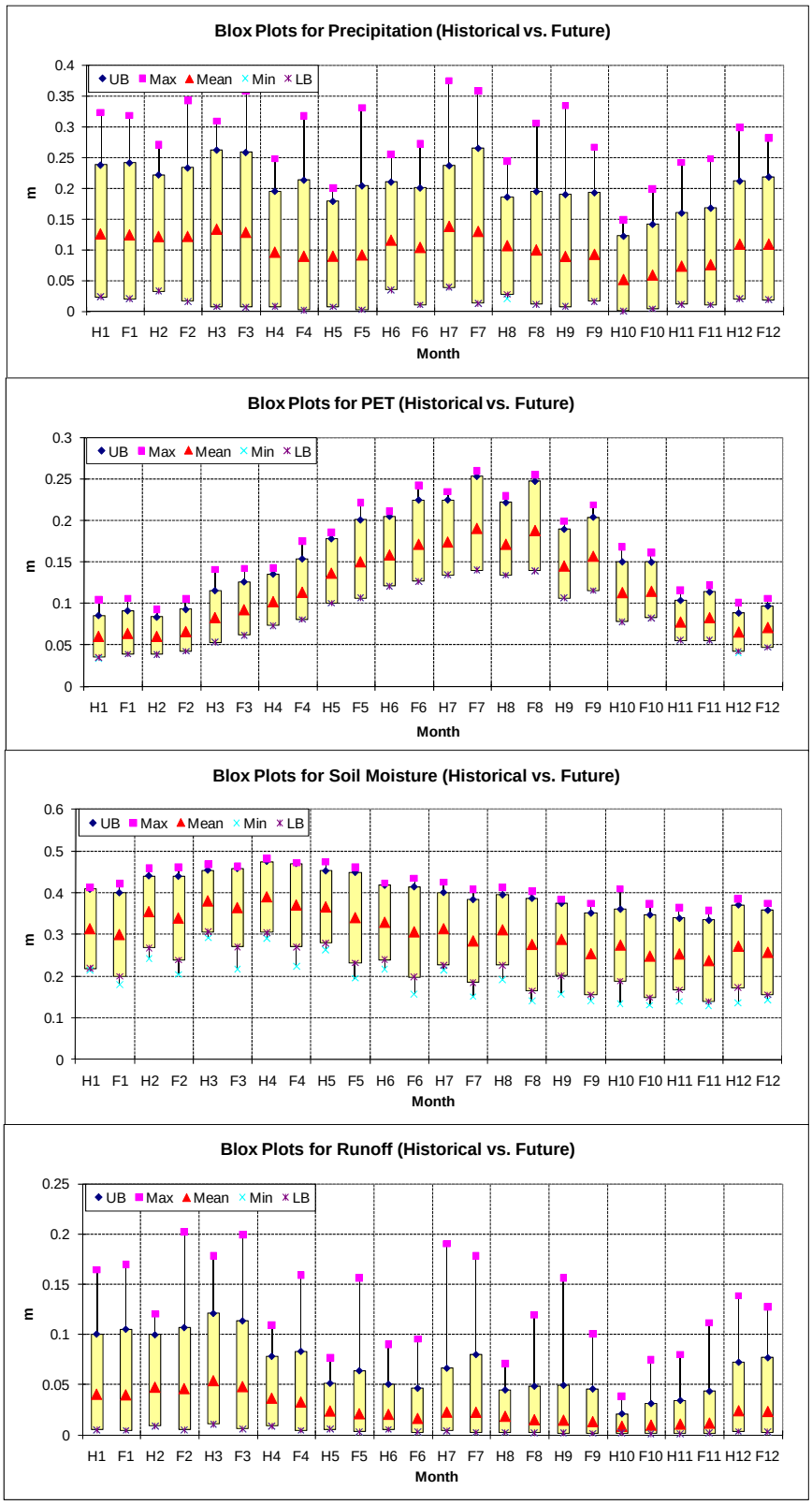

Figure 4.52: Monthly Historical vs. Future (A1B) Watershed Response, Albany

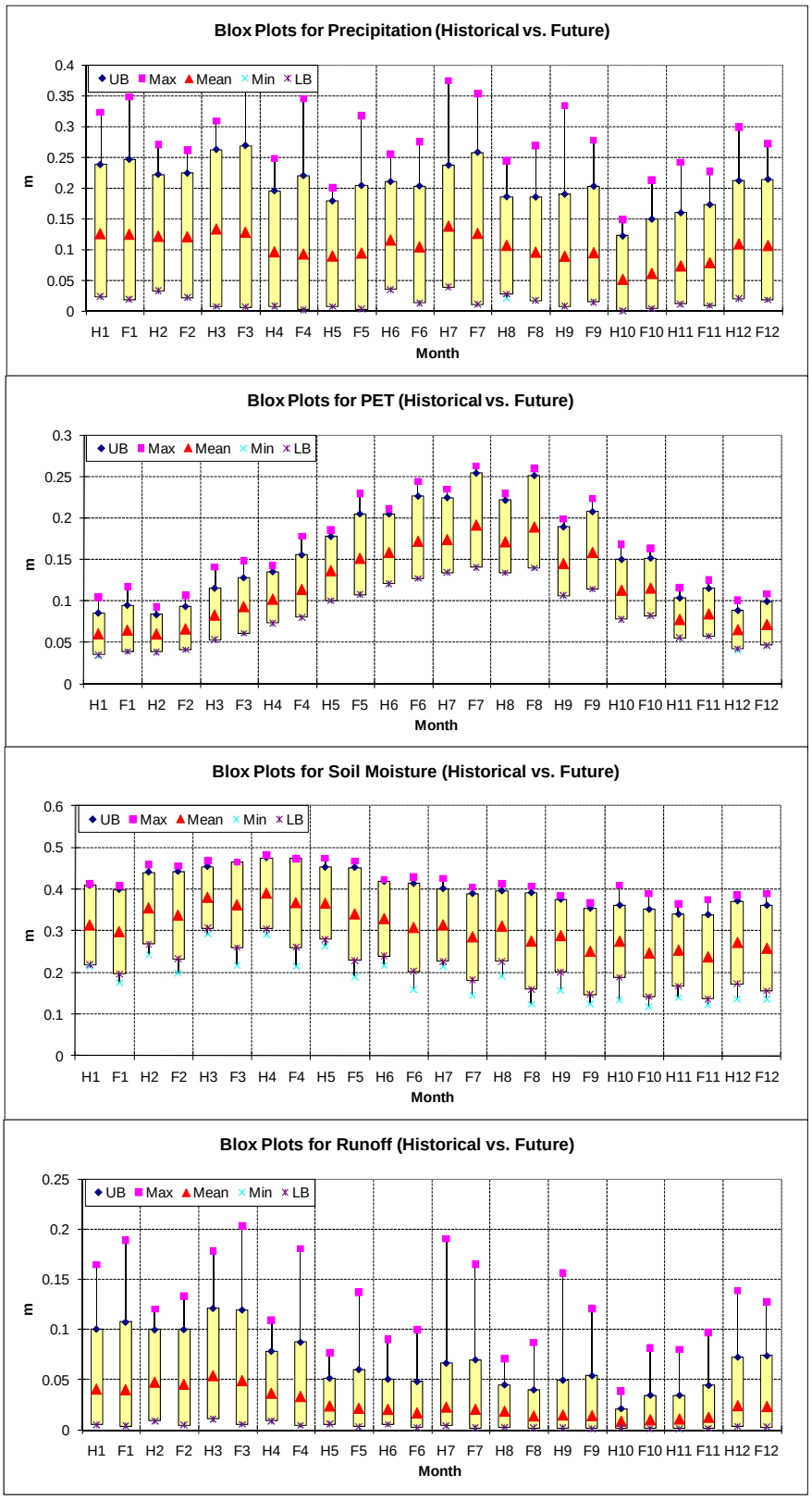

Figure 4.53: Monthly Historical vs. Future (A2) Watershed Response, Albany

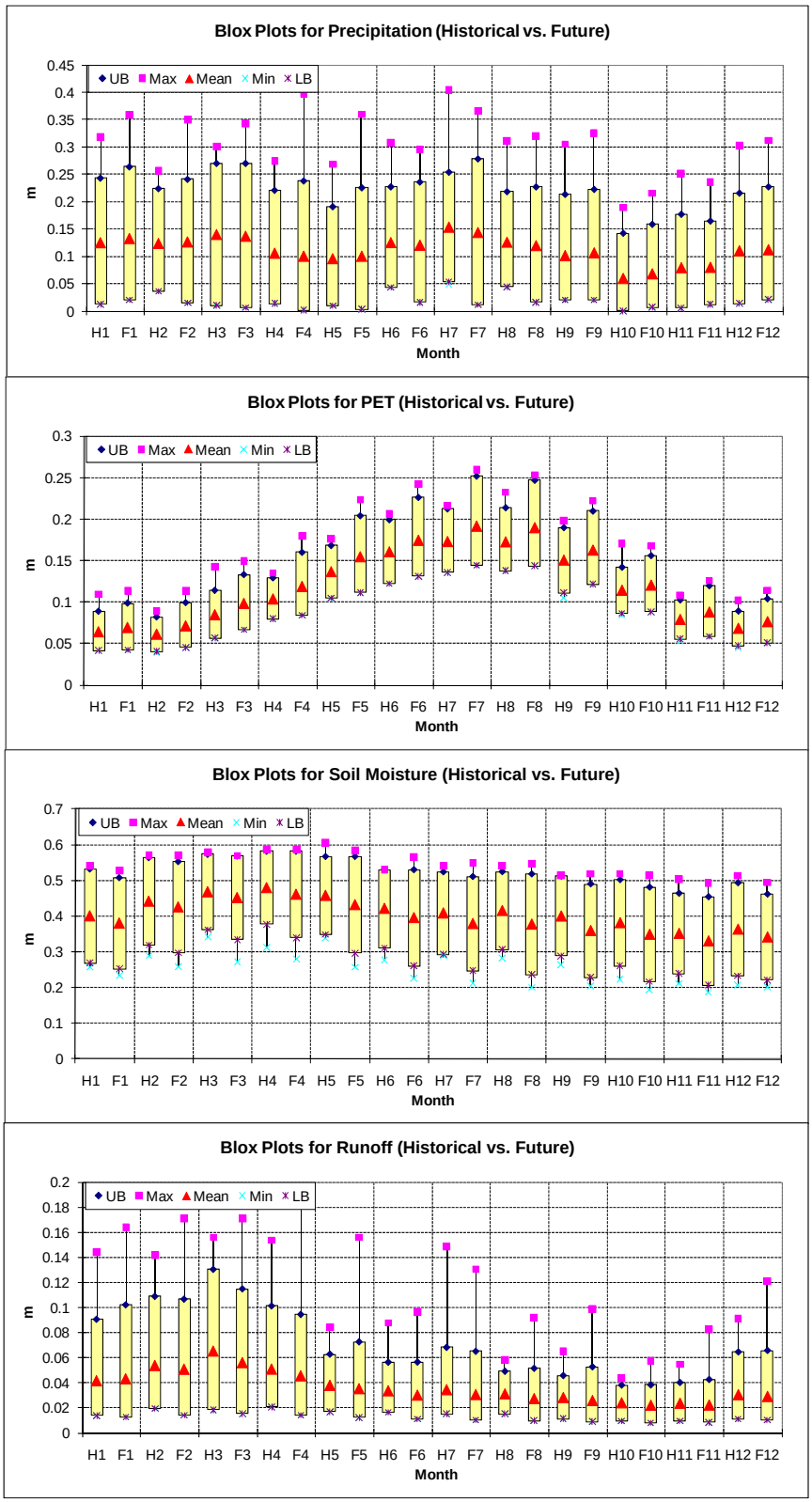

Figure 4.54: Monthly Historical vs. Future (A1B) Watershed Response, Woodruff-Bainbridge

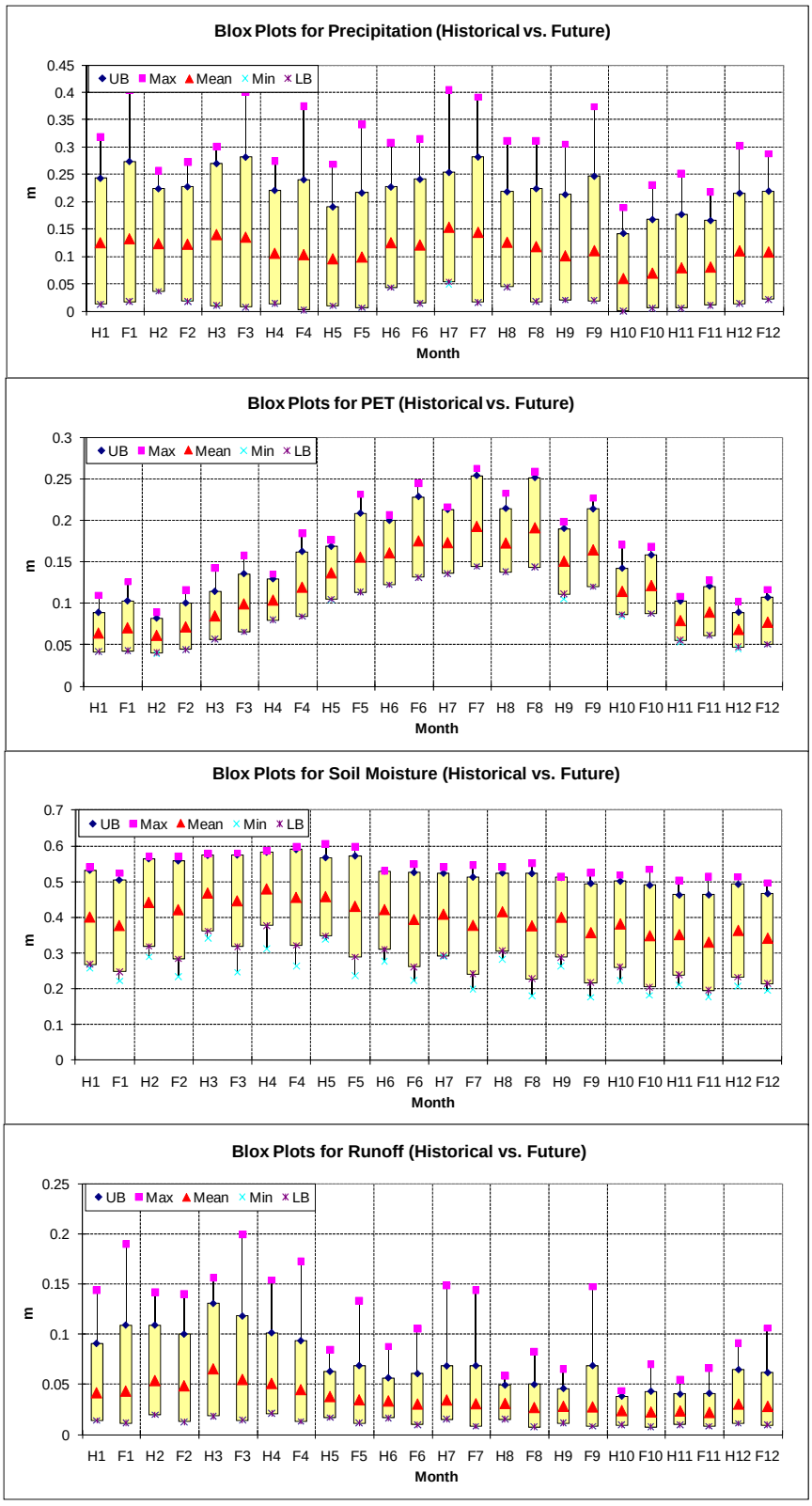

Figure 4.55: Monthly Historical vs. Future (A2) Watershed Response, Woodruff-Bainbridge

Chapter 5

Water Resources Assessments

5.1 Introduction

This chapter describes the third part of the ACF climate change assessment aiming to quantify the potential *water resources* impacts. A key input in the assessment process are the ACF watershed runoff sequences generated in the previous chapter as part of the hydrology assessment. These sequences are used to drive a water resources model that incorporates the river network, all storage projects and hydroelectric facilities, water withdrawals and returns, instream flow requirements, and management procedures. This model is fully described in Volume 2 of this report, along with its application to drought assessments. What follows in this section and in Sections 5.2 and 5.3 is a summary of the modeling framework, operational ACF requirements, and data used in the assessment described in Section 5.4.

The Apalachicola-Chattahoochee-Flint Decision Support System (ACF DSS) has been developed by GWRI to support planning and management of the ACF River Basin. It consists of databases, interfaces, and various application programs interlinked to provide meaningful and comprehensive information for policy makers and managers.

The ACF DSS uses a three modeling layer structure (**Figure 5.1**) to support decisions pertaining to various temporal scales and objectives. The three modeling layers include *(1)* turbine load dispatching (which models each turbine and hydraulic outlet and has hourly resolution over a horizon of one day), *(2)* short/mid range reservoir management (which has a daily resolution and a horizon of one month), and *(3)* long range reservoir management (which has a weekly resolution and a horizon of up to a year).

The long range management model is designed to consider long range issues such as whether water conservation strategies are appropriate for the upcoming year in view of the

hydrologic forecasts. As part of these considerations, the DSS quantifies several tradeoffs of possible interest to the management agencies and system stakeholders. These include, among others, relative water allocations to water users throughout the system (including ecosystem demands), reservoir coordination strategies and target levels, water quality constraints, and energy generation targets. This information is provided to the appropriate management agencies (planning departments) to use it as part of their decision process together with other information. After completing these deliberations, key decisions are made on monthly water supply contracts, reservoir releases, energy generation, and reservoir coordination strategies.

The short/mid range management model considers the system operation at finer time scales. The objectives addressed are more operational than planning and include flood management, water supply, and power plant scheduling. This model uses hydrologic forecasts with a daily resolution and can quantify the relative importance of, say, upstream versus downstream flooding risks, energy generation versus flood control, and other applicable tradeoffs. Such information is again provided to management agencies (operational departments) to use it within their decision processes to select the most preferable operational policy. Such policies are revised as new information on reservoir levels and flow forecasts comes in. The model is constrained by the long range decisions, unless current conditions indicate that a departure is warranted.

The real time model determines the hour by hour optimal turbine load schedules (e.g., turbine dispatching and flow regulation), which realizes all decisions made by the upper DSS models.

The three modeling layers address planning *and* management decisions. The scenario/policy assessment model addresses longer term planning issues such as changing demands, infrastructure changes (e.g., new reservoirs, water transfers, and recycling/re-use

options), potential hydro-climatic changes, and conservation/mitigation measures. The approach taken in this DSS layer is to simulate and inter-compare the system response under various inflow, demand, development, and management conditions.

Altogether, the ACF DSS provides a comprehensive modeling framework responsive to the information needs of the decision making process at all relevant time scales.

This study mainly uses the scenario assessment component to assess the impacts of various climate scenarios. However, the long range management model is embedded within the scenario assessment model. Furthermore, the long range management model uses objective function terms estimated (off-line) by lower ACF DSS levels.

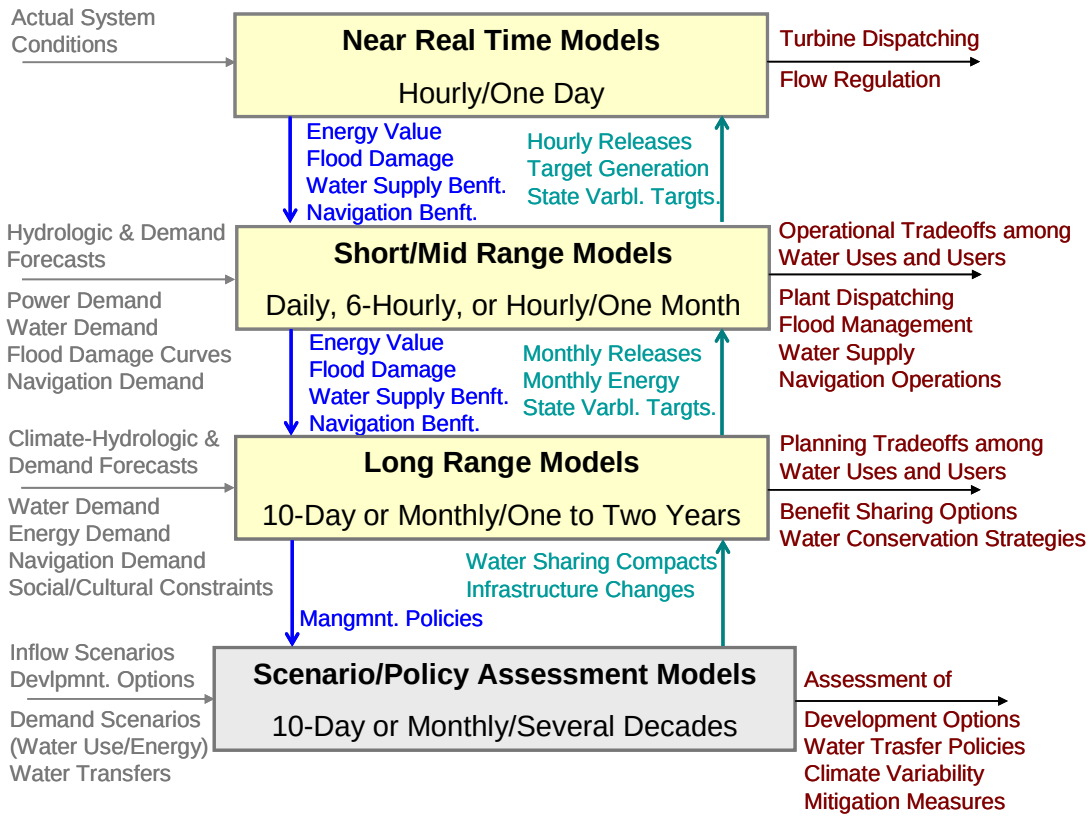

Figure 5.1: ACF DSS Modeling Framework

5.2 ACF Interim Operations Plan (IOP)

The ACF river network comprises four major federal reservoirs (Lakes Lanier, West Point, W.F. George, and J. Woodruff); five smaller private hydropower plants; and 13 river nodes where tributary inflows, water withdrawals and returns, and instream flow target requirements occur. A system schematic is shown in **Figure 5.2**. The ACF is a key southeast river basin which is expected to serve multiple water uses in three states (Alabama, Florida, and Georgia). These uses include municipal, industrial, and agricultural water supply; environmental and ecological protection; flood control; hydropower generation; thermal power cooling; navigation; and recreation. Water management responsibility lies with the US Army Corps of Engineers, who manage the federal reservoirs based on the ACF operations plan.

The recent ACF droughts have motivated a re-evaluation of the basin management procedures and led to the development of the Interim Operations Plan (IOP). The main purpose of the IOP is to support the needs of the endangered Gulf sturgeon during the spring spawn and the needs of two protected mussel species in the summer. The IOP specifies two parameters applicable to the daily releases from J. Woodruff Dam: a minimum discharge and a maximum fall rate.

Under the IOP, the minimum discharge from the Woodruff Dam is determined based on total basin inflow, month of the year, and composite basin storage. The releases are measured as a daily average flow in cfs at the Chattahoochee gage in Florida. The IOP details are presented in **Table 5.1**. The composite storage is calculated by combining the storage of Lakes Lanier, West Point, and George. The storage of each individual reservoir is distinguished in four zones. These zones are determined by the operational rule curve for each project. The basin composite storage is also distinguished in four zones. Zone 1 of the composite storage represents the combined zone 1 storage of the above-mentioned three reservoirs; the other composite storage zones are

defined similarly as shown in **Figure 5.3**. The IOP minimum Woodruff release curves for different seasons are displayed in **Figures 5.4** to 5**.6**.

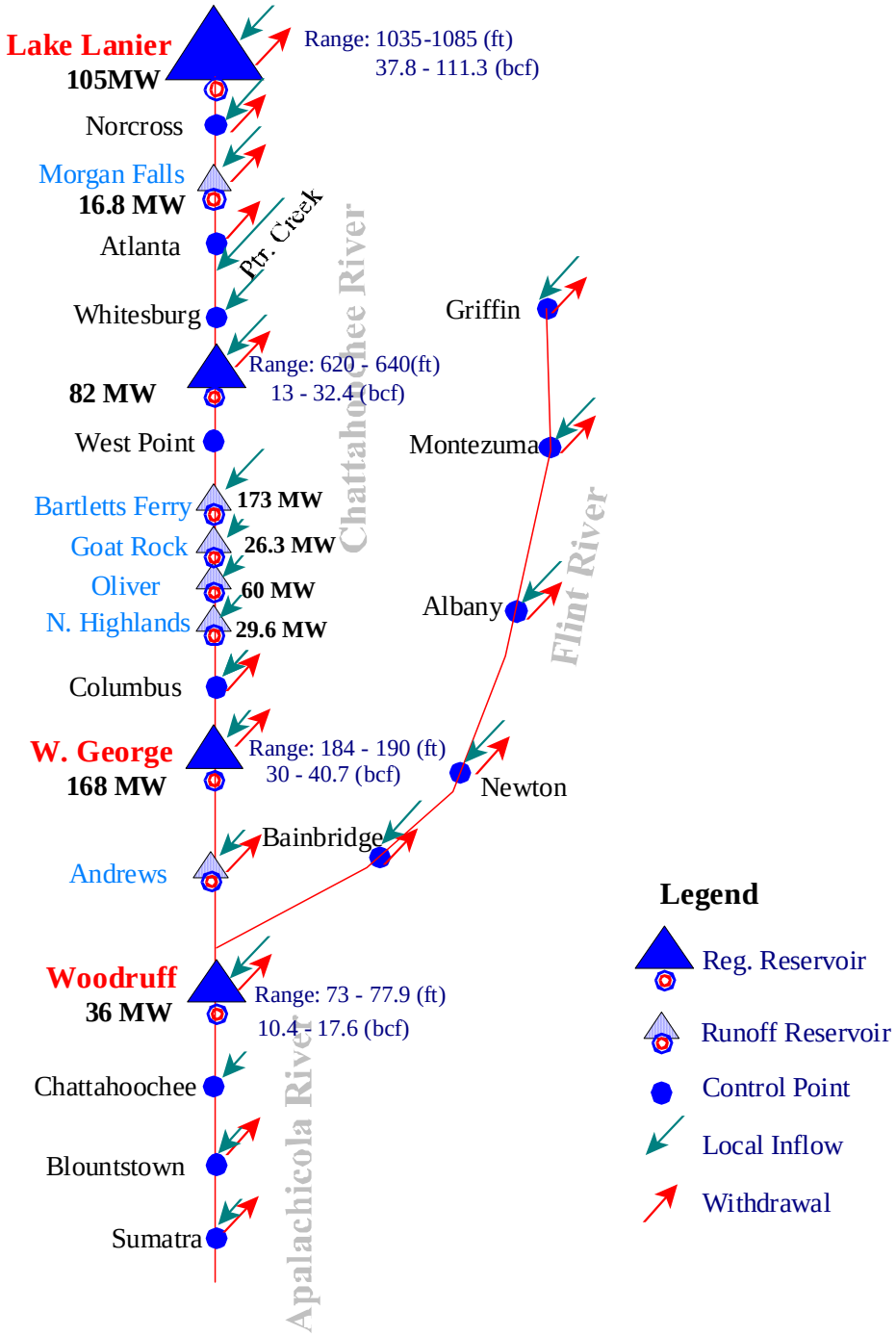

Figure 5.2: ACF Basin Schematic

The second parameter in IOP is the constraint on the fall rate of the vertical drop at the Chattahoochee gage. The fall rates are expressed in units of feet per day (ft/day), and are measured as the difference between the daily average river stage of consecutive calendar days. The maximum fall rate schedule is described in **Table 5.2**.

Table 5.1: IOP Minimum Discharge Constraints from Woodruff

Months	Composite Storage Zone	Basin Inflow (BI) (cfs)	Release (cfs)
March -May	Zones 1 and 2	>=34000	>=25000
		>=16000 and <34000	>=16000+50%*(BI-16000)
		>=5000 and <16000	>=BI
		<5000	>=5000
	Zone 3	>=39000	>=25000
		>=11000 and <39000	>=11000+50%(BI-11000)
		>=5000 and <11000	>=BI
		<5000	>=5000
June - November	Zones 1,2, and 3	>=24000	>=16000
		>=8000 and <24000	>=8000+50%(BI-8000)
		>=5000 and <8000	BI
		<5000	>=5000
December-February	Zones 1, 2, and 3	>=5000	>=5000
		<5000	>=5000
All Times	Zone 4		>=5000
All Times	Drought Zone		>=4500

Table 5.2: Maximum Fall Rate Constraints at Chattahoochee Gage

Release Range (cfs)	Max. Fall Rate (ft/day) at Chattahoochee Gage
>30000	No Restriction
>20000 and <=30000	1 to 2
>16000 and <=20000	.5 to 1
>8000 and <16000	0.25 to 0.5
<8000	<=0.25

Note: No restrictions are placed on Composite Zone 4.

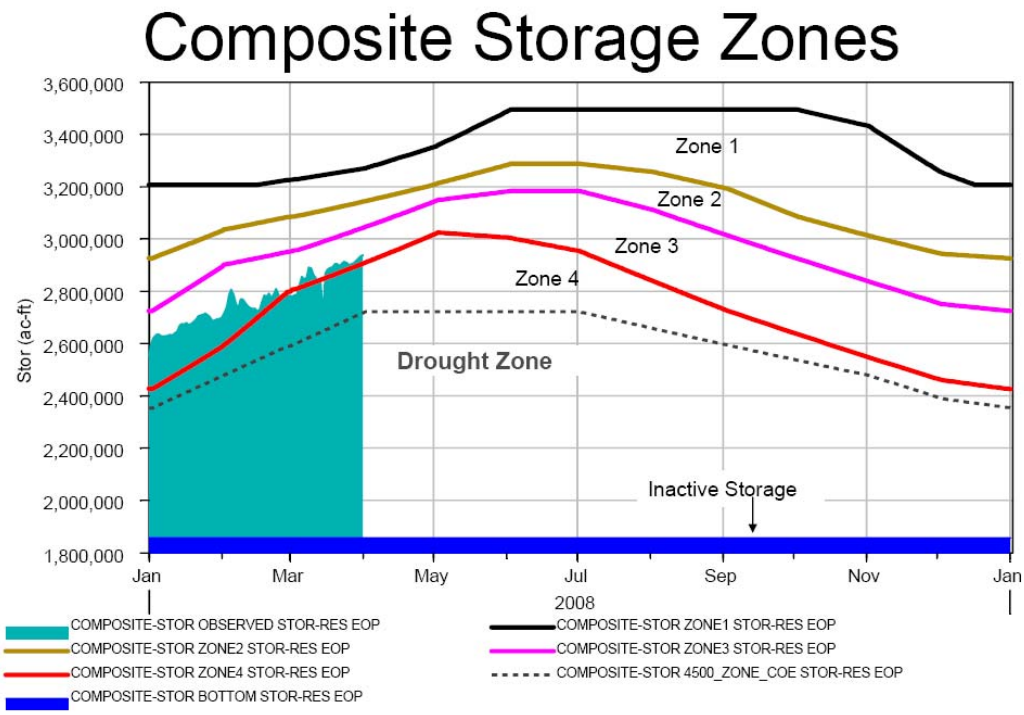

Figure 5.3: IOP Composite Reservoir Storage Zone Curves

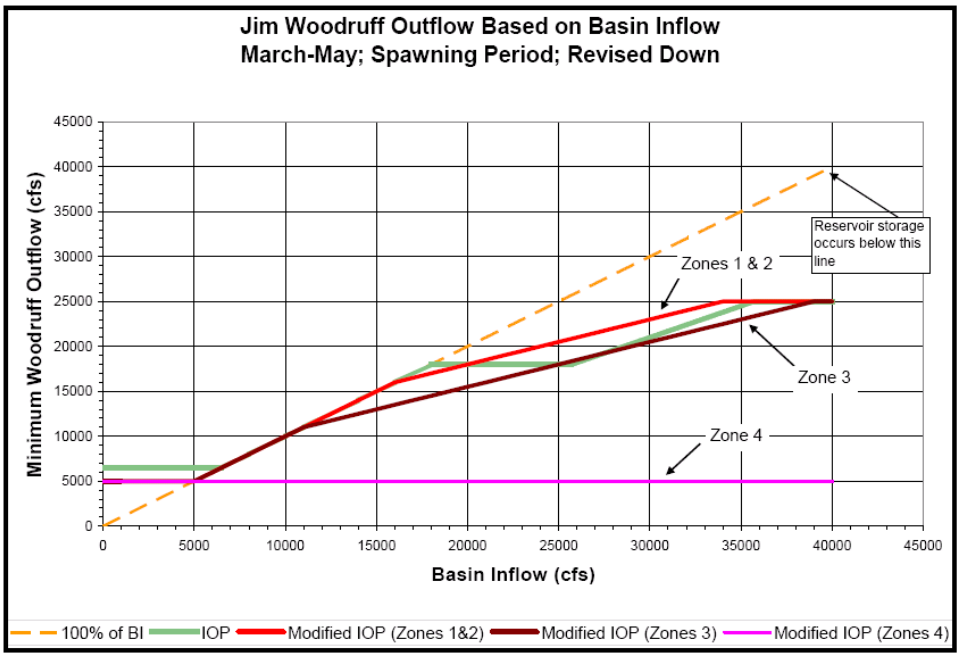

Figure 5.4: IOP Minimum Woodruff Release Curves from March to May

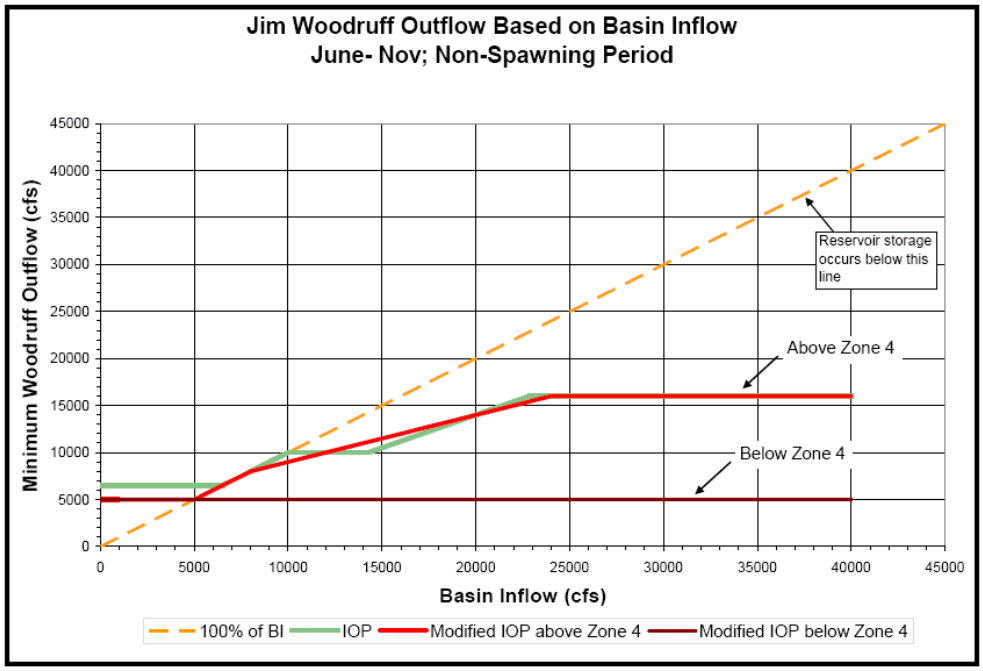

Figure 5.5: IOP Minimum Woodruff Release Curves from June to November

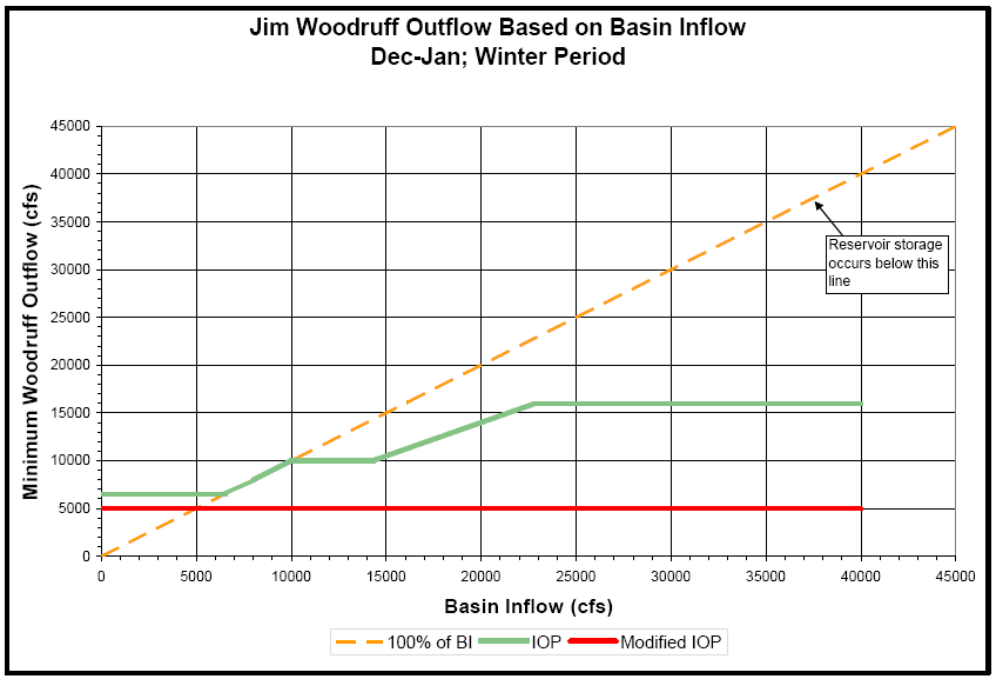

Figure 5.6: IOP Minimum Woodruff Release Curves from December to January

5.3 Water Use Data and Demand Scenarios

Current (2007) water use data was provided by the Georgia Environmental Protection Division (Georgia EPD) and is used as baseline in this assessment. The average withdrawals, returns, and net withdrawals at all locations are shown in **Figure 5.7**. The corresponding monthly distributions are listed in **Table 5.1**. It is noted that a large portion of the withdrawals from the Atlanta node is returned at Whitesburg downstream, where net withdrawals are negative.

Water demand projections are used for the future period when climate datasets are assessed. **Figure 5.8** shows the water use projections for 2050 (also provided by Georgia EPD). Compared to the current water use, significant demand growth mainly occurs in the Metro Atlanta region (Upper Chattahoochee). Water use increases in the Lower Chattahoochee and the Flint River are projected to be very mild. Thus, by 2050, the water withdrawals from the reach between Atlanta and West Point are increased to 1,258 from 722 cfs, a 172% growth. During the same period, the projected water use returns in this region are also expected to increase considerably from 381 to 951 cfs, corresponding to a 250% growth. This considerable increase of water returns is expected as a result of planned drainage and conservation infrastructure improvements. As a result, the 2050 net withdrawals (307 cfs) are expected to be lower than those in 2007 (341 cfs). The infrastructure improvements are expected to be complete by 2050 and remain in that state for some time thereafter. Based on the above, water withdrawals in the Upper Chattahoochee are assumed to grow linearly from their current (2007) levels to the 2050 targets. The same assumption is applied to the monthly water return ratio which is also assumed to be increase linearly from 2007 to 2050, remaining constant thereafter. The monthly distributions of the 2050 water demand projections are listed in **Table 5.2**.

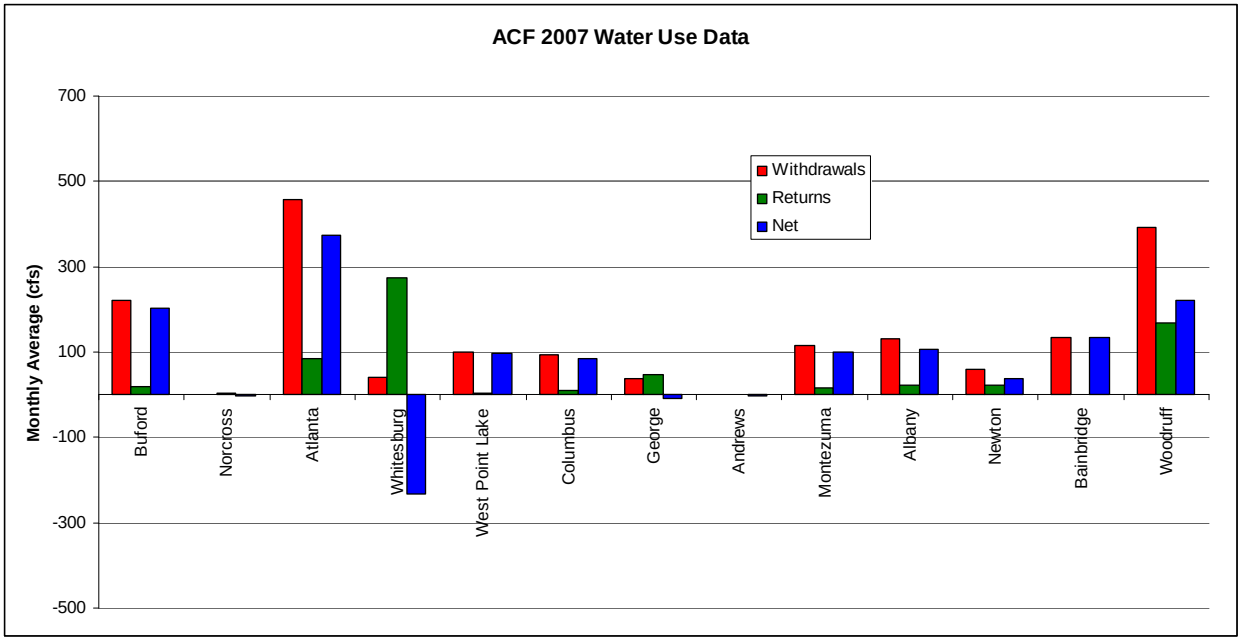

Figure 5.7: Current Water Demands

Table 5.1: ACF 2007 Monthly Water Use Distributions

	Month	Buford	Norcross	Atlanta	Whitesburg	West Point Lake	Columbus	George	Andrews	Montezuma	Albany	Newton	Bainbridge	Woodruff
Withdrawals	1	174	0	386	35	79	67	31	0	102	16	20	5	220
	2	179	0	377	30	91	72	26	0	99	27	20	6	234
	3	191	1	394	37	92	80	27	0	101	55	34	24	240
	4	207	1	438	38	97	95	35	0	113	104	40	54	297
	5	260	1	498	50	113	114	41	1	114	175	78	166	495
	6	275	1	558	50	116	111	50	2	134	217	93	226	613
	7	268	1	524	45	113	104	46	3	160	322	91	246	591
	8	270	1	539	48	114	117	53	1	148	372	91	264	602
	9	241	0	510	46	115	106	38	0	107	142	101	264	537
	10	223	0	463	37	94	90	41	0	118	37	43	156	310
	11	202	0	430	31	97	80	35	0	109	32	54	121	281
	12	180	0	388	34	94	72	34	0	95	56	45	90	281
	AVG	223	0	459	40	101	92	38	1	117	130	59	135	392
Returns	1	19	2	80	300	4	9	49	3	10	20	26	1	168
	2	23	2	81	307	5	12	55	4	11	25	27	0	166
	3	21	3	85	293	4	11	51	2	11	19	26	1	168
	4	20	3	84	287	4	10	43	0	20	31	24	1	171
	5	19	3	81	286	4	8	38	0	19	23	22	1	169
	6	21	2	83	286	4	8	45	0	19	21	24	1	170
	7	20	2	82	260	4	8	48	0	21	22	24	1	173
	8	20	2	88	269	5	9	46	0	20	21	24	1	171
	9	20	2	86	245	4	9	44	1	11	14	29	1	174
	10	22	2	88	268	4	9	45	3	15	26	0	1	173
	11	21	2	85	221	4	8	41	3	15	21	23	1	170
	12	19	2	90	263	4	8	47	3	22	27	24	1	165
	AVG	20	2	84	274	4	9	46	2	16	23	23	1	170
Net	1	155	-2	306	-265	75	59	-18	-3	92	-4	-6	4	52
	2	157	-2	296	-277	87	60	-29	-4	89	2	-7	6	68
	3	170	-2	309	-256	88	69	-24	-2	90	36	8	24	72
	4	187	-2	354	-249	93	85	-8	0	92	73	16	53	126
	5	241	-2	417	-236	109	106	3	0	95	151	55	166	326
	6	254	-1	475	-236	112	103	4	2	115	197	69	226	443
	7	248	-1	442	-215	110	96	-2	3	139	299	66	245	418
	8	249	-1	450	-221	109	109	7	1	128	352	67	263	431
	9	221	-2	424	-199	111	98	-6	-1	96	128	71	263	363
	10	201	-2	375	-231	89	81	-4	-3	104	11	43	155	136
	11	180	-2	345	-191	93	72	-6	-3	95	11	31	121	111
	12	161	-2	299	-229	90	64	-12	-3	74	29	21	89	117
	AVG	202	-2	374	-234	97	83	-8	-1	101	107	36	135	222

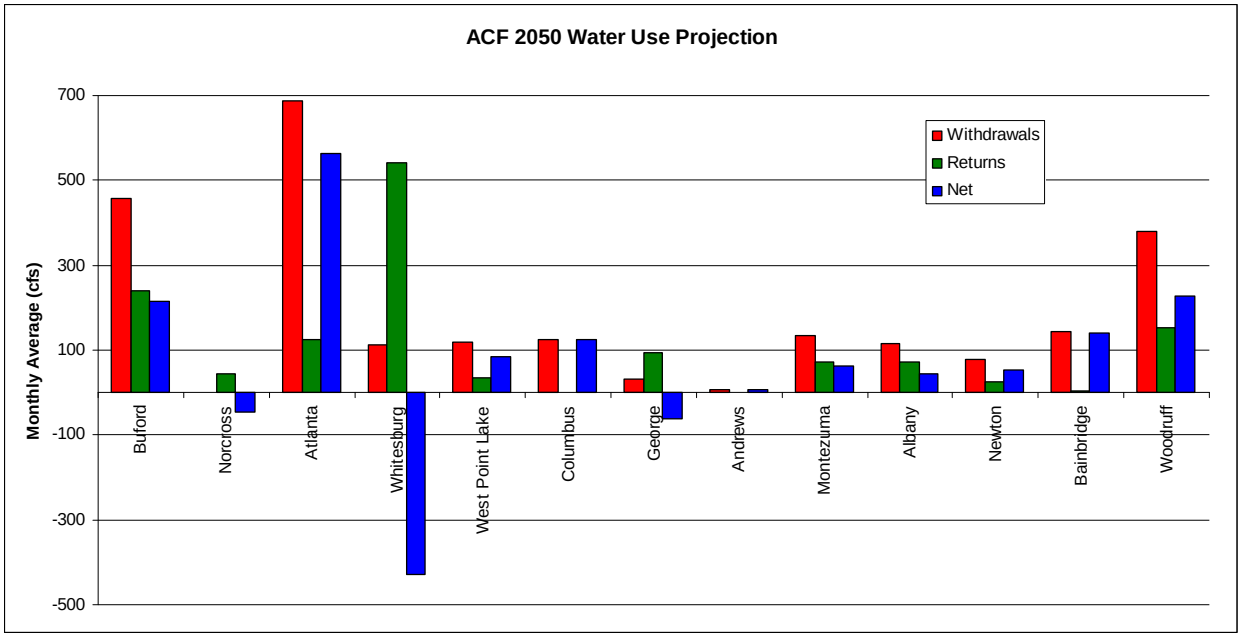

Figure 5.8: 2050 Water Use Projections

Table 5.3: 2050 Monthly Water User Projections

	Month	Buford	Norcross	Atlanta	Whitesburg	West Point Lake	Columbus	George	Andrews	Montezuma	Albany	Newton	Bainbridge	Woodruff
Withdrawals	1	357	0	581	97	91	95	23	0	113	20	20	4	219
	2	369	0	568	85	105	98	17	0	114	28	20	5	226
	3	392	0	593	103	107	111	22	0	111	35	28	19	234
	4	426	0	658	108	114	128	29	3	133	93	55	75	324
	5	537	0	747	146	133	157	41	6	155	160	84	155	415
	6	563	0	836	146	137	150	43	18	174	230	125	247	587
	7	548	0	786	134	131	141	42	22	184	282	138	306	637
	8	551	0	808	130	130	156	44	18	139	233	134	296	578
	9	494	0	764	125	135	142	34	12	127	174	127	256	489
	10	456	0	696	101	110	120	32	0	136	54	94	158	297
	11	414	0	646	87	116	107	27	0	123	42	64	117	286
	12	369	0	584	93	110	97	26	0	104	33	51	82	270
	AVG	456	0	689	113	118	125	32	7	135	115	78	143	380
Returns	1	230	34	120	592	33	2	98	0	42	65	33	2	150
	2	264	45	121	606	36	2	111	0	46	81	33	2	148
	3	246	68	127	578	32	2	103	0	48	59	32	3	154
	4	232	56	125	566	31	2	86	0	90	102	28	3	153
	5	227	52	122	564	34	2	76	0	86	76	27	2	150
	6	248	43	124	564	31	2	91	0	86	67	25	3	151
	7	235	51	123	513	29	2	97	0	98	72	23	3	154
	8	239	51	132	531	40	2	92	0	88	67	23	2	152
	9	237	38	128	483	33	2	88	0	49	44	38	2	159
	10	253	35	131	528	35	2	90	0	66	86	1	2	158
	11	246	34	127	436	32	2	82	0	66	66	21	2	153
	12	226	36	134	518	35	2	94	0	99	89	22	2	145
	AVG	240	45	126	540	33	2	92	0	72	73	26	2	152
Net	1	127	-34	461	-495	57	93	-75	0	70	-44	-13	2	70
	2	105	-45	447	-520	69	96	-93	0	68	-53	-13	4	78
	3	146	-68	466	-475	75	109	-81	0	63	-25	-4	16	80
	4	193	-56	533	-458	83	126	-57	3	43	-10	27	72	171
	5	309	-52	625	-418	100	155	-36	5	69	84	58	152	265
	6	315	-43	712	-418	105	148	-48	18	88	163	99	244	435
	7	314	-51	664	-379	102	140	-55	22	86	210	115	303	483
	8	312	-51	676	-401	90	154	-48	18	51	166	111	294	426
	9	257	-38	636	-358	102	140	-54	11	78	131	89	253	330
	10	203	-35	565	-427	75	118	-58	0	71	-32	93	156	138
	11	168	-34	519	-350	84	105	-55	0	57	-24	43	115	133
	12	143	-36	451	-425	75	95	-68	0	5	-56	29	79	125
	AVG	216	-45	563	-427	85	123	-61	6	62	42	53	141	228

5.4 Climate and Demand Change Assessments

The ACF DSS was run for all 26 inflow datasets generated from the IPCC climate scenarios. The statistics of the results were computed and compared with those of the baseline historical dataset. The baseline historical inflow dataset is from 1901 to 2009, and the future climate datasets are from 2000 to 2099.

The assessment process is as follows: For each week of the selected inflow dataset, the forecast and management models are activated first to generate optimal reservoir release sequences subject to the set of specified constraints. In identifying these release sequences, the models first priority is to meet the constraints related to water withdrawals, instream minimum flows, power generation commitments (i.e., hours of dependable power capacity), turbine and power plant load limits, IOP flow targets, and reservoir storage ranges. From the set of all feasible release sequences that meet these constraints, the DSS selects those that additionally maintain reservoir levels as high as possible and maximize long-term energy generation. Thus, optimal release sequences are those which meet the stated constraints, safeguard the system against droughts, and maximize long-term energy generation. Tradeoffs can be generated by varying the constraint levels of the various water uses and recording the relative differences in the basin response.

The forecast and control models are implemented with a 4-week control horizon and reliability level of 50%. Other control horizon and reliability values have also been used but yielded similar results. In particular, the 50% reliability was used in these runs to maintain high reservoir levels, especially in view of the existence of flood storage zones. Inflow forecasts are obtained from an embedded historical analogue model and consist of 10 inflow traces (forecast ensemble) for each reservoir. At the very start of the simulation, the elevations of the four major reservoirs are set at 1056.25 feet for Lanier, 622 feet for West Point, 185.35 feet for George, and

77.5 feet for Woodruff. The levels for the private reservoirs Morgan Fall, Bartletts Ferry, Goat Rock, Oliver, and North Highlands are equal to 866, 540, 415, 338 and 270 feet respectively, and remain constant throughout the simulation. This is a reasonable approximation in view of the limited storage capacity of these projects and their fairly constant weekly average levels. The minimum instream flows at Atlanta and Columbus are equal to 750 cfs and 1,850 cfs, respectively. The minimum flows at Chattahoochee are determined by the IOP requirement.

From the optimal release sequences generated by the model, only the first week releases are actually implemented. The system response is then simulated using the selected inflows (which are not considered known at the time of the forecast). If the optimal releases result in feasible end-of-the-week reservoir elevations, the program completes the forecast-control-simulation step, records these elevations along with the releases, instream flows, and energy generation amounts, and repeats this process at the beginning of the next week. Otherwise, appropriate release adjustments are made so that all reservoirs stay within their feasible ranges. This forecast-control-simulation process is repeated for all weeks of the selected datasets and results in a long series of simulated reservoir elevations, releases, water supply deficits, instream flow target deficits, energy generation amounts, and other quantities of interest. This data is then analyzed to develop statistics of system performance and make comparisons.

System performance criteria include reservoir drawdown frequency and severity, instream flow target violations, water supply deficits, and energy generation.

To assess the impact of future climate scenarios, a baseline case was run first. The baseline case uses the current water demand (2007) and the historical inflow record from 1901 to 2009. The baseline results indicate that the system meets all constraints throughout the period without much reservoir stress. Neither instream flow target nor water supply deficits occur. Although reservoir elevations experience significant drawdowns during the major droughts of

the 1950s, 1980s, 1998-2002, and 2006-2009, they are still able to maintain at least half of their storage capacity. The simulated reservoir elevation, river flow, water supply, and energy generation sequences are shown in **Figures 5.9** to 5**.12**.

The ACF DSS assessment process was next applied to the 26 future climate scenarios, half of which correspond to the A1B emission type and the other half to A2. Both current (2007) demands and future demands (based on 2050 projections) are applied to each dataset. All results are compared to the historical baseline using the system performance criteria mentioned earlier. More specifically, the following results (sequences and statistics) are presented for each assessment run:

- Reservoir elevation sequences and frequency curves for Lanier, West Point, George, and Woodruff;
- Instream flow deficit sequences, annual averages, and selected frequency curves for Atlanta, Whitesburg, Columbus, Andrews, and Chattahoochee (Florida);
- Water supply (net water withdrawal) sequences, deficits, and frequency curves for Lanier and Atlanta, and annual average water supply deficits for Lanier, Atlanta, West Point, George, Montezuma, Albany, Newton, and Woodruff;
- Energy generation frequency curves and annual averages for Buford, West Point, George, and Woodruff.

5.4.1 A1B Climate Scenarios with 2007 Water Demands

The simulated sequences under the A1B climate and current demand scenarios are displayed in **Figures 5.16** to **5.28**. (All runs employ 2007 water demands repeated cyclically throughout the simulation horizon.) For comparison purposes, the figures include results for all IPCC scenarios as well as the historical baseline (thick red lines). **Tables 5.3**, **5.4**, and **5.5** provide a summary of total instream flow target deficits, total water supply deficits, and annual average energy

generation for all assessment runs. **Figures 5.13**, **5.14**, and **5.15** display the table results in graphical form. The results support the following conclusions and observations:

Lake Levels: Compared to the historical baseline, the ensembles of future Lake Lanier levels and frequency curves do not show any significant bias (top plots in **Figures 5.16** and **5.17**). Namely, nearly half of the future frequency curves fall above and half below the historical baseline. However, four out of the 13 scenarios lead to full depletion of Lake Lanier. This happens in extreme droughts and occurs for only a short period of time (less than 1%) in the entire assessment horizon.

On the other hand, all other federal lakes show a clear future tendency to fall below the historical sequences (**Figures 5.16** through **5.19**). The reason for this tendency is that the majority of the future climate scenarios produce drier than the historical streamflows for all ACF watersheds except Buford, the runoff response of which remains close to the historical patterns. All federal lakes are fully depleted in four of the future scenarios.

Instream Flow Target Deficits: The driest future scenarios lead to occasional instream flow target deficits, especially toward the end of the century (**Table 5.3**, and **Figures 5.13**, **5.20**, **5.21**, and **5.22**). However, as the frequency curves for Atlanta and Chattahoochee (**Figure 5.22**) show, these violations are rather infrequent (occurring in less than 1% of the assessment horizon). The frequency curves show that the 750 cfs Atlanta flow target is violated in four scenarios, for a total of three to eleven months. Likewise, the 5,000 cfs Chattahoochee flow target is violated in the same four scenarios for a total of one to six months.

Water Supply Deficits: Similarly to the instream flow targets, water supply deficits are infrequent and happen only when system storage is fully exhausted (**Table 5.4**, and **Figures 5.14**, **5.23**, **5.24**, and **5.25**). This can be seen in **Figure 5.25** which depicts the water supply deficit frequency curves for Lanier and Atlanta where most significant violations occur. The figure shows that

deficits as high as the full water supply targets may occur, but the frequency of this is very low—one to five months in 100 years.

Energy Generation: Annual energy generation from the federal reservoirs averaged across the future scenarios is 924 GWH compared to 953 GWH of the historical baseline, corresponding to a 3% reduction (**Table 5.5** and **Figure 5.15**). The combined energy generation from the federal *and* the private reservoirs exhibits a 2.2% reduction (1,887 GWH in the future versus 1,929.5 GWH in the historical horizon).

The energy generation frequency curves (**Figures 5.26** and **5.27**) indicate that for Lanier, West Point, and George half of the thirteen future scenarios generate as much as or higher energy than the baseline in most years. However, at the very low end of the distributions (future extreme droughts), all scenarios fall below the baseline. Woodruff's response (**Figure 5.27**) is somewhat different because it receives the flows of the lower Chattahoochee as well as of the entire Flint River. The combined runoff reductions in these two sub-basins are such that future energy generation is less than the historical generation for most future scenarios and years. Furthermore, the IOP and the Woodruff release constraints (**Tables 5.1** and **5.2**) modify the low distribution end. As a result, in approximately 2.5% of the time (or in 30 months out of 100 years), Woodruff cannot generate power.

Overall, energy generation impacts are relatively small, because system storage compensates for the inflow deficits in most future climate scenarios.

Summary: Overall, the A1B climate scenarios with 2007 demands exhibit mildly adverse water resources impacts compared to the historical baseline. However, the ensemble of future climates includes droughts (as well as floods) that are more extreme than those that occurred historically. During these extreme droughts, the basin storage is unable to meet the system water supply and instream flow requirements.

5.4.2 A2 Climate Scenarios with 2007 Water Demands

Figures 5.28 to **5.39** show results from the A2 climate scenarios with current (2007) water demands.

Lake Levels: Compared to the A1B scenarios and the historical baseline, the A2 future Lake Lanier levels (as seen by the frequency curves of **Figure 5.29**) clearly shift lower. Ten out of the 13 A2 scenarios fall below the historical baseline, while eight of them experience full storage depletion in extreme droughts. Storage is depleted in about 1% of the assessment horizon, but in one case the depletion time extends to 5%.

All other federal lakes follow the same level pattern as in the A1B case (i.e., future levels are consistently lower than historical levels), albeit with more exacerbated drawdowns (**Figures 5.28** through **5.31**). This happens because A2 runoff scenarios are generally drier than A1B scenarios. Most scenarios deplete all basin storage for a cumulative period of up to 2% of the assessment horizon (24 months).

Instream Flow Target Deficits: The A2 scenarios cause more frequent instream flow target deficits than the A1B scenarios (**Table 5.3**, and **Figures 5.13**, **5.32**, **5.33**, and, especially, **5.34**). The frequency curves for Atlanta (**Figure 5.34**) show that these violations continue to be infrequent (occurring in less than 1% of the assessment horizon), except in one case where they occur 4.5% of the time (or 4.5 years). Chattahoochee flow targets are violated even more infrequently, about 1/3 the Atlanta frequency rate.

Water Supply Deficits: Similarly to the instream flow targets, water supply deficits are infrequent and happen only when system storage is fully exhausted (**Table 5.4**, and **Figures 5.14**, **5.35**, **5.36**, and, especially, **5.37**). **Table 5.4** and **Figure 5.14** show that the locations prone to water supply deficits are Lanier, Atlanta, and, to a lesser extent, Albany. **Figure 5.34** shows that water supply deficits occur for most scenarios, with a range of frequency and severity. In the worst case,

deficits range up to the full water supply target and occur for up to 2% total time (2 years). For most of the scenarios, however, violations occur for less than 0.5% of the time.

Energy Generation: Annual energy generation from the federal reservoirs averaged across the A2 scenarios is 910 GWH compared to 953 GWH of the historical baseline, corresponding to a 4.5% reduction (**Table 5.5** and **Figure 5.15**). The combined energy generation from the federal *and* the private reservoirs is 1,854 GWH compared to 1,929.5 GWH of the historical period..

The energy generation frequency curves (**Figures 5.38** and **5.39**) indicate that more than half of the future scenarios generate less energy than the historical climate throughout the frequency range. At the very extreme droughts, and for a few months, generation ceases completely. The downward shift of the energy frequency curves is more pronounced at Woodruff (**Figure 5.39**), due to the drier A2 watershed response in the lower Chattahoochee and the Flint.

Thus, A2 energy generation impacts are more significant than those of the A1B.

Summary: Overall, the A2 climate scenarios with 2007 demands exhibit more exacerbated water resources impacts compared to the A1B scenarios and the historical baseline. These impacts become critical during extreme future droughts which deplete all basin storage. The frequency with which this occurs is relatively low.

5.4.3 A1B Climate Scenarios with 2050 Water Demands

Figures 5.40 to **5.51** present the results from the A1B climate scenarios with future water demands.

Lake Levels: Compared to the historical baseline, all lakes experience lower levels under these scenarios. This is clearly seen on the frequency curves of **Figures 5.41**and **5.43.** Lake Lanier is particularly affected, with more than half of the 13 scenarios depleting its storage for a total of about 5% of the time (5 years).

Instream Flow Target Deficits: The A1B/2050 scenarios cause more frequent instream flow target deficits in the upper Chattahoochee River than either the A1B/2007 or the A2/2007 scenarios (**Table 5.3**, and **Figures 5.13**, **5.44**, and **5.46**). The frequency curves for Atlanta (**Figure 5.46**) show that these violations occur for five scenarios and reach up to 4% of the assessment horizon (or 4 years). The Lower Chattahoochee and the Flint flow targets are violated more than the baseline but less than the A2/2007 case.

Water Supply Deficits: Similarly to the instream flow targets, water supply deficits are more significant in the Upper Chattahoochee where natural inflows are deficient and demands are high (**Table 5.4**, and **Figures 5.14**, **5.47**, **5.48**, and **5.49**). **Table 5.4** and **Figure 5.14** show that the locations prone to water supply deficits are Lanier and Atlanta. **Figure 5.34** shows that water supply deficits occur for approximately half of the scenarios, with a range of up to the full water supply target and frequency up to 2% of the total time (2 years).

Energy Generation: Annual energy generation from the federal reservoirs averaged across the scenarios is 922 GWH compared to 953 GWH of the historical baseline, corresponding to a 3.2% reduction (**Table 5.5** and **Figure 5.15**). The combined energy generation from the federal *and* the private reservoirs is 1,882 GWH compared to 1,929.5 GWH of the historical period.

The energy generation frequency curves (**Figures 5.50** and **5.51**) indicate that approximately half of the future scenarios generate less energy than the historical baseline throughout the frequency range. At the extreme droughts, generation ceases completely for a few months.

Summary: Overall, the A1B climate scenarios with 2050 demands impact more adversely the Upper Chattahoochee River where natural inflows are low and demands (for Atlanta) are high. The impacts are critical during extreme future droughts which deplete Lake Lanier storage.

5.4.4 A2 Climate Scenarios with 2050 Water Demands

Figures 5.52 to **5.63** present the results of the A2 climate scenarios with future water demands.

Lake Levels: Lake drawdowns under this scenario set are more severe than all previous cases, including the historical baseline (**Figures 5.41**and **5.43)**. Lake Lanier is particularly affected, with all 13 scenarios depleting its storage for a total of up to 9% of the time (9 out of 100 years).

Instream Flow Target Deficits: Instream flow target violations are also more frequent than all previous cases. Atlanta, Whitesburg, Columbus, and Chattahoochee are impacted most (**Table 5.3**, and **Figures 5.13**, **5.56**, **5.57**, and **5.58**). The frequency curves for Atlanta (**Figure 5.58**) show that these violations occur for 11 out of 13 scenarios and reach up to 9% of the assessment horizon (or 9 years). However, the violation frequency of most scenarios is less than 2%.

Water Supply Deficits: Water supply deficits are more significant at Lanier and Atlanta (**Table 5.4**, and **Figures 5.14**, **5.59**, **5.60**, and **5.61**). **Table 5.4** and **Figure 5.61** show that water supply deficits occur in almost all scenarios, range up to the full water supply target, and occur for up to 2.5% of the total time (2.5 years).

Energy Generation: Annual energy generation from the federal reservoirs averaged across the scenarios is 905 GWH compared to 953 GWH of the historical baseline. Namely, energy generation is reduced by 5% (**Table 5.5** and **Figure 5.15**). The combined energy generation from the federal *and* the private reservoirs is 1,849 GWH compared to 1,929.5 GWH of the historical period (corresponding to a 4.2% reduction). This reduction is reflected throughout the range of the energy generation frequency curves (**Figures 5.62** and **5.63**).

Summary: Among all tested scenarios, the A2 climate scenarios with 2050 demands accrue the most severe impacts with respect to all criteria. Since climate and demand changes are likely to occur simultaneously, it is important that the ACF water resources planning process recognize and protect against the risks of both. This requires the timely adoption and implementation of

better water conservation programs, adaptive reservoir management procedures, and improved drought contingency plans that utilize hydro-climatic watershed information.

Table 5.3: Total Instream Flow Target Deficits over the Assessment Horizon (bcf)

	Atlanta	Whitesburg	Columbus	Andrews	Chattahoochee	Total
HisPeriod	0.00	0.00	0.00	0.00	0.00	0.00
A1B Scenario, Current Demands						
clmtbccrbcm2a1brun1	0.00	0.00	0.00	0.00	0.00	0.00
clmtcccmacgcm31a1brun1	0.00	0.00	0.00	0.00	0.00	0.00
clmtcnrmcm3a1brun1	11.80	14.75	6.06	3.53	5.43	41.57
clmtcsiro_mk3_0sresa1brun1	0.00	0.00	0.00	0.00	0.00	0.00
clmtgfdl_cm2_1sresa1brun1	7.77	9.74	6.65	2.09	3.61	29.86
clmtgiss_model_e_rsresa1brun2	0.00	0.00	0.00	0.00	0.00	0.00
clmthadcm3A1B	6.62	8.84	13.00	13.21	27.94	69.62
clmtinmcm3_0sresa1brun1	16.66	21.05	23.88	21.68	47.06	130.32
clmtmiub_echo_g.sresa1b	0.00	0.00	0.00	0.00	0.00	0.00
clmtmpi_echam5.sresa1b	0.00	0.00	0.00	0.00	0.00	0.00
clmtmri_cgcm2_3_2asresa1brun1	0.00	0.00	0.00	0.00	0.00	0.00
clmtncar_ccsm3_0sresa1brun2	0.00	0.00	0.00	0.00	0.00	0.00
clmtncar_pcm1sresa1brun1	0.00	0.00	0.00	0.00	0.00	0.00
Average	3.30	4.18	3.82	3.12	6.46	20.88
A2 Scenario, Current Demands						
clmtbccrbcm2a2run1	3.07	4.69	5.67	5.24	10.89	29.55
clmtcccmacgcm31a2run1	22.11	27.52	22.98	6.12	13.28	92.01
clmtcnrmcm3a2run1	7.53	10.27	10.47	12.28	23.08	63.63
clmtcsiro_mk3_0sresa2run1	4.42	4.67	0.00	0.00	0.00	9.09
clmtgfdl_cm2_1sresa2run1	6.49	9.93	5.31	0.04	1.23	23.00
clmtgiss_model_e_rsresa2run2	0.00	0.00	0.00	0.00	0.00	0.00
clmthadcm3A2	6.17	7.59	4.09	0.04	0.04	17.92
clmtinmcm3_0sresa2run1	78.94	94.45	95.67	54.25	132.09	455.40
clmtmiub_echo_g.sresa2	12.82	13.39	9.15	0.00	0.00	35.36
clmtmpi_echam5.sresa2	0.00	0.00	0.00	0.00	0.00	0.00
clmtmri_cgcm2_3_2asresa2run1	0.00	0.00	0.00	0.00	0.00	0.00
clmtncar_ccsm3_0sresa2run2	2.44	2.50	1.42	0.00	0.00	6.35
clmtncar_pcm1sresa2run1	0.00	0.00	0.00	0.00	0.00	0.00
Average	11.08	13.46	11.91	6.00	13.89	56.33
A1B Scenario, Future Demands						
clmtbccrbcm2a1brun1_futdmnd	10.03	5.64	4.23	0.00	0.00	19.90
clmtcccmacgcm31a1brun1_futdmnd	0.00	0.00	0.00	0.00	0.00	0.00
clmtcnrmcm3a1brun1_futdmnd	32.26	26.74	14.44	7.68	15.33	96.45
clmtcsiro_mk3_0sresa1brunfutdmnd	0.00	0.00	0.00	0.00	0.00	0.00
clmtgfdl_cm2_1sresa1brunfutdmnd	47.19	27.08	21.37	6.08	10.20	111.91
clmtgiss_model_e_rsresa1brunfutdmnd	0.00	0.00	0.00	0.00	0.00	0.00
clmthadcm3A1Bfutdmnd	13.22	9.53	13.89	13.66	30.43	80.72
clmtinmcm3_0sresa1brunfutdmnd	74.57	48.12	37.33	20.90	48.34	229.26
clmtmiub_echo_g.sresa1bfutdmnd	0.00	0.00	0.00	0.00	0.00	0.00
clmtmpi_echam5.sresa1bfutdmnd	0.00	0.00	0.00	0.00	0.00	0.00
clmtmri_cgcm2_3_2asresa1brunfutdmnd	0.00	0.00	0.00	0.00	0.00	0.00
clmtncar_ccsm3_0sresa1brunfutdmnd	0.00	0.00	0.00	0.00	0.00	0.00
clmtncar_pcm1sresa1brunfutdmnd	0.00	0.00	0.00	0.00	0.00	0.00
Average	13.64	9.01	7.02	3.72	8.02	41.40
A2 Scenario, Future Demands						
clmtbccrbcm2a2runfutDmnd	9.55	7.55	10.20	6.51	14.76	48.57
clmtcccmacgcm31a2run1_futdmnd	48.99	31.97	33.03	8.71	19.55	142.26
clmtcnrmcm3a2run1_futdmnd	40.22	28.92	18.95	17.36	33.55	139.00
clmtcsiro_mk3_0sresa2runfutdmnd	28.54	14.12	1.77	0.00	0.00	44.42
clmtgfdl_cm2_1sresa2runfutdmnd	16.47	11.44	7.94	0.02	1.74	37.61
clmtgiss_model_e_rsresa2runfutdmnd	0.00	0.00	0.00	0.00	0.00	0.00
clmthadcm3A2futdmnd	16.82	11.17	6.45	0.48	1.41	36.34
clmtinmcm3_0sresa2runfutdmnd	172.39	118.91	123.63	64.23	158.20	637.35
clmtmiub_echo_g.sresa2futdmnd	23.70	14.93	13.68	0.00	0.01	52.31
clmtmpi_echam5.sresa2futdmnd	3.31	1.37	0.09	0.06	0.00	4.84
clmtmri_cgcm2_3_2asresa2runfutdmnd	0.41	0.00	0.00	0.00	0.00	0.41
clmtncar_ccsm3_0sresa2runfutdmnd	13.41	8.18	4.95	0.00	0.00	26.53
clmtncar_pcm1sresa2runfutdmnd	0.00	0.00	0.00	0.00	0.00	0.00
Average	28.76	19.12	16.98	7.49	17.63	89.97

Table 5.4: Total Water Supply Deficits over the Assessment Horizon (bcf)

	Lake Lanier	Atlanta	W Point	W George	Montezuma	Albany	Newton	Woodruff	Total
HisPeriod	0.00	0.00	0.00	0.00	0.00	0.00	0.00	0.00	0.00
A1B Scenario, Current Demands									
clmtbccrbcm2a1brun1	0.00	0.00	0.00	0.00	0.00	0.44	0.15	0.00	0.58
clmtcccmacgcm31a1brun1	0.00	0.00	0.00	0.00	0.00	0.07	0.00	0.00	0.07
clmtcnrmcm3a1brun1	1.53	2.07	0.00	0.00	0.00	0.13	0.00	0.00	3.74
clmtcsiro_mk3_0sresa1brun1	0.00	0.00	0.00	0.00	0.00	0.27	0.00	0.00	0.27
clmtgfdl_cm2_1sresa1brun1	0.16	0.35	0.00	0.00	0.10	3.44	0.09	0.00	4.15
clmtgiss_model_e_rsresa1brun2	0.00	0.00	0.00	0.00	0.00	0.04	0.00	0.00	0.04
clmthadcm3A1B	1.01	1.51	0.03	0.00	0.00	0.16	0.13	0.00	2.84
clmtinmcm3_0sresa1brun1	0.42	1.64	0.16	0.00	0.00	0.14	0.00	0.00	2.36
clmtmiub_echo_g.sresa1b	0.00	0.00	0.00	0.00	0.00	0.07	0.04	0.00	0.11
clmtmpi_echam5.sresa1b	0.00	0.00	0.00	0.00	0.00	0.16	0.01	0.00	0.18
clmtmri_cgcm2_3_2asresa1brun1	0.00	0.00	0.00	0.00	0.00	0.01	0.04	0.00	0.05
clmtncar_ccsm3_0sresa1brun2	0.00	0.00	0.00	0.00	0.00	0.17	0.04	0.00	0.21
clmtncar_pcm1sresa1brun1	0.00	0.00	0.00	0.00	0.00	0.06	0.00	0.00	0.06
Average	0.24	0.43	0.01	0.00	0.01	0.40	0.04	0.00	1.13
A2 Scenario, Current Demands									
clmtbccrbcm2a2run1	0.40	0.91	0.13	0.00	0.00	1.24	0.04	0.17	2.89
clmtcccmacgcm31a2run1	0.61	2.73	0.00	0.00	0.00	1.25	0.00	0.00	4.60
clmtcnrmcm3a2run1	1.26	2.20	0.23	0.00	0.00	2.20	0.00	0.00	5.90
clmtcsiro_mk3_0sresa2run1	0.21	0.44	0.00	0.00	0.01	0.27	0.00	0.00	0.93
clmtgfdl_cm2_1sresa2run1	1.69	2.33	0.17	0.00	0.09	3.52	0.00	0.00	7.79
clmtgiss_model_e_rsresa2run2	0.00	0.00	0.00	0.00	0.00	0.36	0.24	0.00	0.60
clmthadcm3A2	1.23	2.29	0.00	0.00	0.09	1.13	0.24	0.00	4.98
clmtinmcm3_0sresa2run1	4.21	13.83	0.84	0.00	0.04	0.50	0.10	0.17	19.70
clmtmiub_echo_g.sresa2	0.03	0.88	0.00	0.00	0.00	0.17	0.04	0.00	1.12
clmtmpi_echam5.sresa2	0.00	0.00	0.00	0.00	0.00	0.64	0.04	0.00	0.67
clmtmri_cgcm2_3_2asresa2run1	0.00	0.00	0.00	0.00	0.00	0.34	0.00	0.00	0.34
clmtncar_ccsm3_0sresa2run2	0.00	0.05	0.00	0.00	0.00	0.17	0.12	0.00	0.34
clmtncar_pcm1sresa2run1	0.00	0.00	0.00	0.00	0.00	0.00	0.00	0.00	0.00
Average	0.74	1.97	0.11	0.00	0.02	0.91	0.06	0.03	3.84
A1B Scenario, Future Demands									
clmtbccrbcm2a1brun1_futdmnd	0.97	2.62	0.00	0.00	0.00	0.02	0.17	0.00	3.79
clmtcccmacgcm31a1brun1_futdmnd	0.00	0.00	0.00	0.00	0.00	0.00	0.00	0.00	0.00
clmtcnrmcm3a1brun1_futdmnd	7.33	14.86	0.00	0.00	0.00	0.00	0.00	0.00	22.19
clmtcsiro_mk3_0sresa1brunfutdmnd	0.00	0.00	0.00	0.00	0.00	0.02	0.00	0.00	0.02
clmtgfdl_cm2_1sresa1brunfutdmnd	7.77	21.51	0.10	0.00	0.00	0.64	0.09	0.00	30.11
clmtgiss_model_e_rsresa1brunfutdmnd	0.00	0.00	0.00	0.00	0.00	0.03	0.00	0.00	0.03
clmthadcm3A1Bfutdmnd	3.59	7.01	0.00	0.00	0.00	0.08	0.17	0.00	10.85
clmtinmcm3_0sresa1brunfutdmnd	4.80	31.97	0.12	0.00	0.00	0.02	0.00	0.04	36.96
clmtmiub_echo_g.sresa1bfutdmnd	0.00	0.00	0.00	0.00	0.00	0.00	0.07	0.00	0.07
clmtmpi_echam5.sresa1bfutdmnd	0.00	0.00	0.00	0.00	0.00	0.05	0.02	0.00	0.07
clmtmri_cgcm2_3_2asresa1brunfutdmnd	0.00	0.00	0.00	0.00	0.00	0.00	0.07	0.00	0.07
clmtncar_ccsm3_0sresa1brunfutdmnd	0.00	0.00	0.00	0.00	0.00	0.00	0.03	0.00	0.03
clmtncar_pcm1sresa1brunfutdmnd	0.00	0.00	0.00	0.00	0.00	0.01	0.00	0.00	0.01
Average	1.88	6.00	0.02	0.00	0.00	0.07	0.05	0.00	8.02
A2 Scenario, Future Demands									
clmtbccrbcm2a2runfutDmnd	1.07	3.14	0.00	0.00	0.00	0.18	0.07	0.14	4.60
clmtcccmacgcm31a2run1_futdmnd	6.62	27.15	0.00	0.00	0.00	0.16	0.00	0.00	33.93
clmtcnrmcm3a2run1_futdmnd	10.79	23.55	0.00	0.00	0.00	0.48	0.00	0.11	34.93
clmtcsiro_mk3_0sresa2runfutdmnd	2.29	12.89	0.00	0.00	0.00	0.02	0.00	0.00	15.20
clmtgfdl_cm2_1sresa2runfutdmnd	3.97	9.17	0.01	0.00	0.00	0.58	-0.01	0.00	13.72
clmtgiss_model_e_rsresa2runfutdmnd	0.00	0.00	0.00	0.00	0.00	0.03	0.35	0.00	0.39
clmthadcm3A2futdmnd	4.69	11.16	0.00	0.00	0.00	0.21	0.34	0.00	16.41
clmtinmcm3_0sresa2runfutdmnd	21.61	81.61	0.17	0.00	0.00	0.00	0.11	0.30	103.79
clmtmiub_echo_g.sresa2futdmnd	0.33	7.36	0.00	0.00	0.00	0.00	0.06	0.00	7.75
clmtmpi_echam5.sresa2futdmnd	0.00	0.52	0.00	0.00	0.00	0.12	0.03	0.00	0.67
clmtmri_cgcm2_3_2asresa2runfutdmnd	0.00	0.00	0.00	0.00	0.00	0.00	0.00	0.00	0.00
clmtncar_ccsm3_0sresa2runfutdmnd	2.02	6.49	0.20	0.00	0.00	0.07	0.14	0.00	8.92
clmtncar_pcm1sresa2runfutdmnd	0.00	0.00	0.00	0.00	0.00	0.00	0.00	0.00	0.00
Average	4.11	14.08	0.03	0.00	0.00	0.14	0.08	0.04	18.48

Table 5.5: Annual Average Energy Generation over the Assessment Horizon (GWH)

	Buford	West Point	W George	Woodruff	Total		Private Res.	Sys. Total
HisPeriod	170.3	190.1	395.1	197.6	953.1		976.5	1929.5
A1B Scenario, Current Demands								
clmtbccrbcm2a1brun1	168.9	179.8	371.9	179.5	900.2		941.0	1841.1
clmtcccmacgcm31a1brun1	164.0	177.2	364.6	185.3	891.1		925.9	1817.0
clmtcnrmcm3a1brun1	155.0	170.9	353.1	173.7	852.7		901.0	1753.7
clmtcsiro_mk3_0sresa1brun1	175.0	191.3	392.5	186.1	944.8		992.6	1937.4
clmtgfdl_cm2_1sresa1brun1	165.5	181.4	382.5	181.0	910.3		949.5	1859.8
clmtgiss_model_e_rsresa1brun2	196.5	211.7	433.2	188.2	1029.6		1026.1	2055.7
clmthadcm3A1B	167.4	183.2	378.6	170.8	900.1		940.4	1840.4
clmtinmcm3_0sresa1brun1	130.5	149.6	316.2	162.9	759.2		821.3	1580.5
clmtmiub_echo_g.sresa1b	165.4	182.6	373.3	190.3	911.6		945.9	1857.6
clmtmpi_echam5.sresa1b	199.1	208.5	432.6	180.9	1021.0		1048.9	2070.0
clmtmri_cgcm2_3_2asresa1brun1	182.6	192.9	392.1	183.4	951.0		987.3	1938.3
clmtncar_ccsm3_0sresa1brun2	193.1	208.3	428.4	196.8	1026.7		1054.1	2080.8
clmtncar_pcm1sresa1brun1	178.7	191.0	390.0	192.6	952.2		946.4	1898.7
Average	172.4	186.8	385.3	182.4	927.0		960.0	1887.0
A2 Scenario, Current Demands								
clmtbccrbcm2a2run1	173.9	187.5	380.7	181.3	923.5		967.5	1890.9
clmtcccmacgcm31a2run1	163.9	179.7	370.3	174.8	888.7		935.4	1824.1
clmtcnrmcm3a2run1	150.7	163.4	338.7	175.7	828.6		875.7	1704.3
clmtcsiro_mk3_0sresa2run1	168.7	188.5	396.8	185.1	939.1		974.2	1913.3
clmtgfdl_cm2_1sresa2run1	166.1	185.3	389.3	179.5	920.2		964.2	1884.4
clmtgiss_model_e_rsresa2run2	200.2	216.4	444.4	189.5	1050.5		1042.8	2093.2
clmthadcm3A2	163.8	179.6	380.6	177.2	901.1		940.2	1841.3
clmtinmcm3_0sresa2run1	125.8	150.2	318.6	163.9	758.4		817.2	1575.7
clmtmiub_echo_g.sresa2	156.7	170.7	359.3	189.7	876.4		902.1	1778.5
clmtmpi_echam5.sresa2	181.2	196.9	411.2	180.0	969.4		1005.3	1974.7
clmtmri_cgcm2_3_2asresa2run1	166.9	183.0	385.4	186.3	921.6		954.9	1876.4
clmtncar_ccsm3_0sresa2run2	172.7	184.1	378.2	190.5	925.5		956.5	1882.0
clmtncar_pcm1sresa2run1	175.9	188.4	381.1	186.6	932.0		931.5	1863.6
Average	166.7	182.6	379.6	181.6	910.4		943.7	1854.0
A1B Scenario, Future Demands								
clmtbccrbcm2a1brun1_futdmnd	162.6	179.9	371.6	180.6	894.7		940.7	1835.4
clmtcccmacgcm31a1brun1_futdmnd	157.5	177.5	364.5	186.4	885.9		927.5	1813.4
clmtcnrmcm3a1brun1_futdmnd	148.8	170.6	352.9	174.7	847.1		900.1	1747.3
clmtcsiro_mk3_0sresa1brunfutdmnd	169.1	190.8	392.0	187.2	939.0		991.7	1930.7
clmtgfdl_cm2_1sresa1brunfutdmnd	160.0	181.4	382.3	181.6	905.2		948.8	1854.0
clmtgiss_model_e_rsresa1brunfutdmnd	191.6	211.6	432.9	189.0	1025.1		1025.8	2050.9
clmthadcm3A1Bfutdmnd	162.2	183.4	378.9	171.9	896.4		941.6	1838.0
clmtinmcm3_0sresa1brunfutdmnd	124.5	149.7	316.1	163.7	753.9		819.6	1573.5
clmtmiub_echo_g.sresa1bfutdmnd	158.8	182.0	372.5	191.5	904.8		945.0	1849.8
clmtmpi_echam5.sresa1bfutdmnd	193.5	208.7	432.8	181.8	1016.7		1050.4	2067.1
clmtmri_cgcm2_3_2asresa1brunfutdmnd	177.0	192.7	391.7	184.3	945.8		986.6	1932.4
clmtncar_ccsm3_0sresa1brunfutdmnd	187.5	207.8	427.7	197.9	1020.9		1052.9	2073.8
clmtncar_pcm1sresa1brunfutdmnd	173.8	190.8	389.8	193.7	948.1		946.8	1894.9
Average	166.7	186.7	385.0	183.4	921.8		959.8	1881.6
A2 Scenario, Future Demands								
clmtbccrbcm2a2runfutDmnd	168.2	187.4	380.5	182.2	918.2		967.0	1885.2
clmtcccmacgcm31a2run1_futdmnd	157.9	180.0	370.3	175.7	883.9		936.0	1819.8
clmtcnrmcm3a2run1_futdmnd	144.9	163.9	338.8	176.5	824.1		875.7	1699.7
clmtcsiro_mk3_0sresa2runfutdmnd	163.1	188.3	396.6	186.1	934.1		974.3	1908.5
clmtgfdl_cm2_1sresa2runfutdmnd	160.2	185.5	389.2	180.5	915.4		964.8	1880.2
clmtgiss_model_e_rsresa2runfutdmnd	195.2	216.2	444.0	190.4	1045.8		1042.9	2088.7
clmthadcm3A2futdmnd	157.8	179.7	380.6	178.3	896.4		941.4	1837.8
clmtinmcm3_0sresa2runfutdmnd	120.2	150.6	319.1	164.5	754.5		817.7	1572.2
clmtmiub_echo_g.sresa2futdmnd	150.1	170.7	358.8	190.7	870.2		901.9	1772.1
clmtmpi_echam5.sresa2futdmnd	174.7	196.6	410.8	181.0	963.1		1005.2	1968.3
clmtmri_cgcm2_3_2asresa2runfutdmnd	160.3	182.5	384.6	187.4	914.8		953.4	1868.3
clmtncar_ccsm3_0sresa2runfutdmnd	166.6	183.8	377.7	191.4	919.4		955.6	1875.0
clmtncar_pcm1sresa2runfutdmnd	170.4	188.2	380.9	187.7	927.1		931.3	1858.3
Average	160.7	182.6	379.4	182.5	905.2		943.6	1848.8

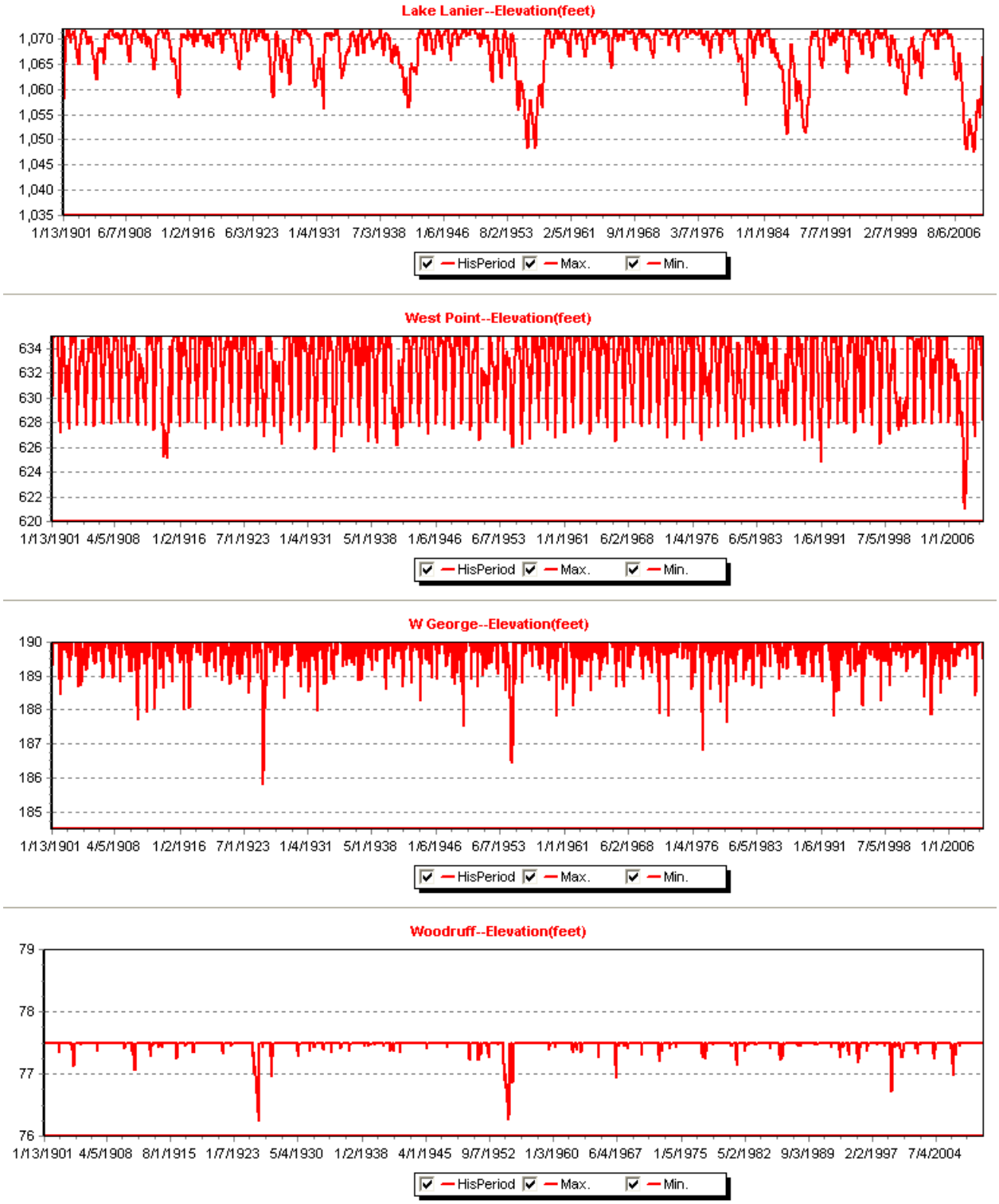

Figure 5.9: Historical Period, 2007 Demands, Reservoir Elevation Sequences

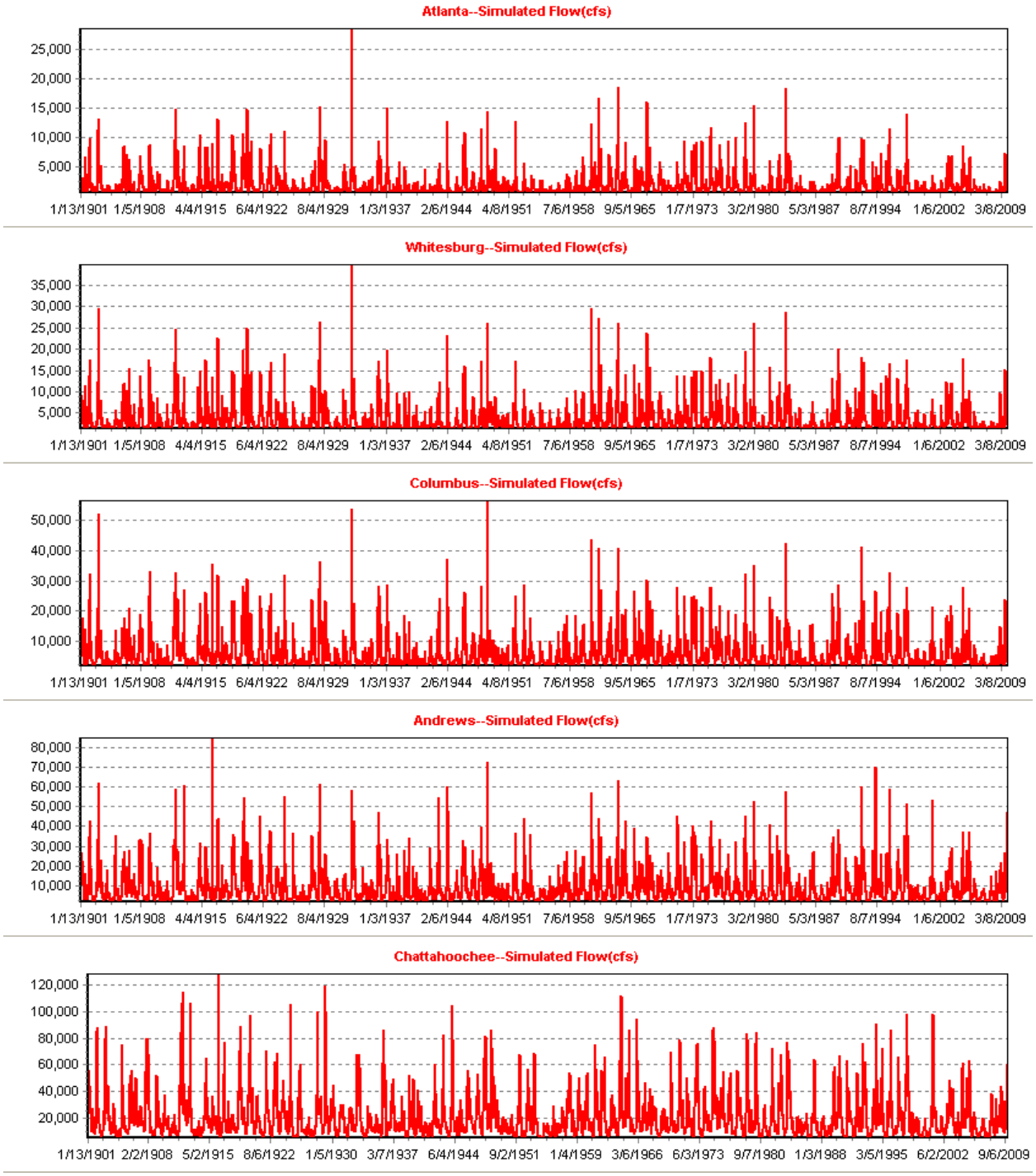

Figure 5.10: Historical Period, 2007 Demands, River Flow Sequences

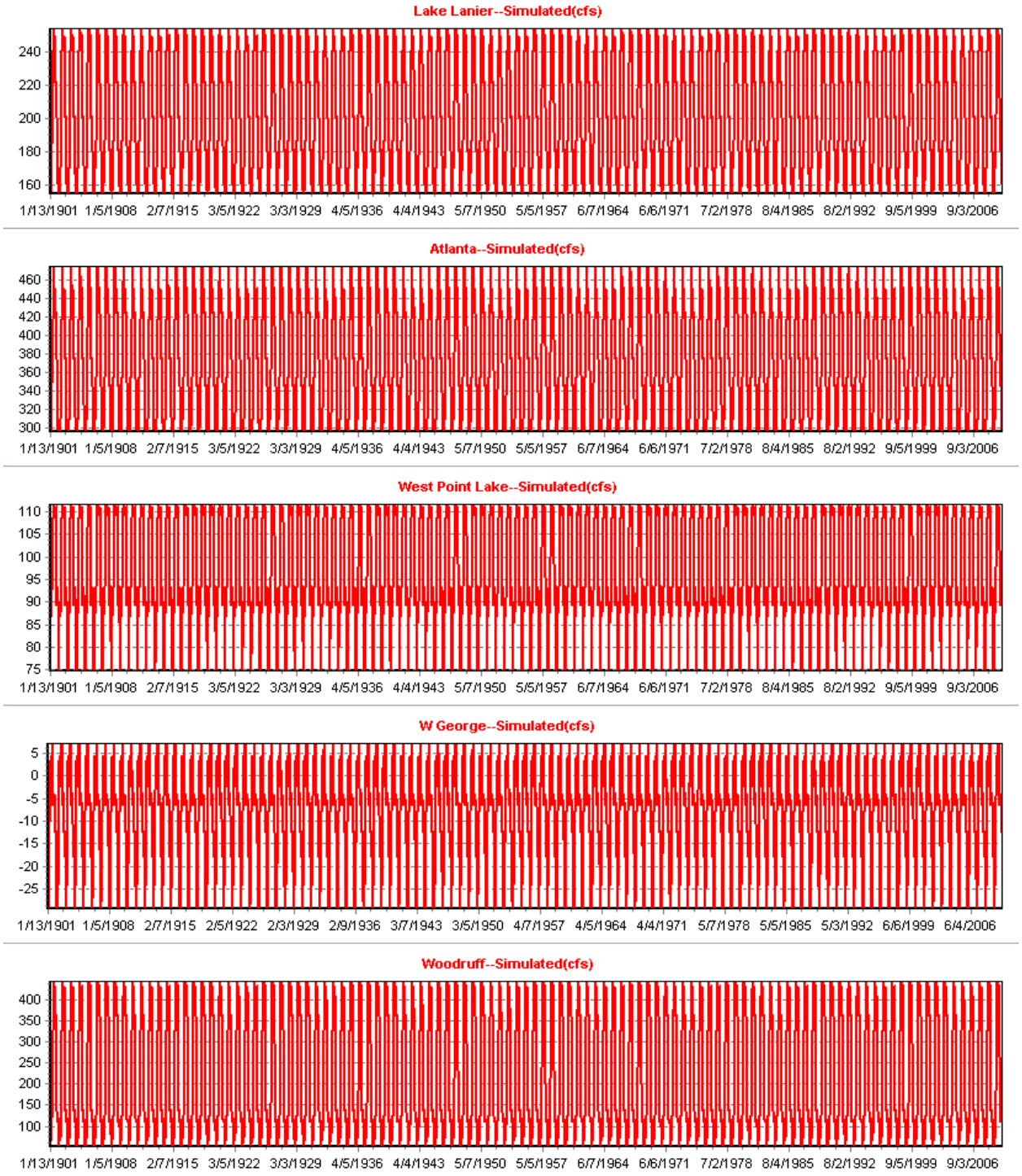

Figure 5.11: Historical Period, 2007 Demands, Water Supply Sequences

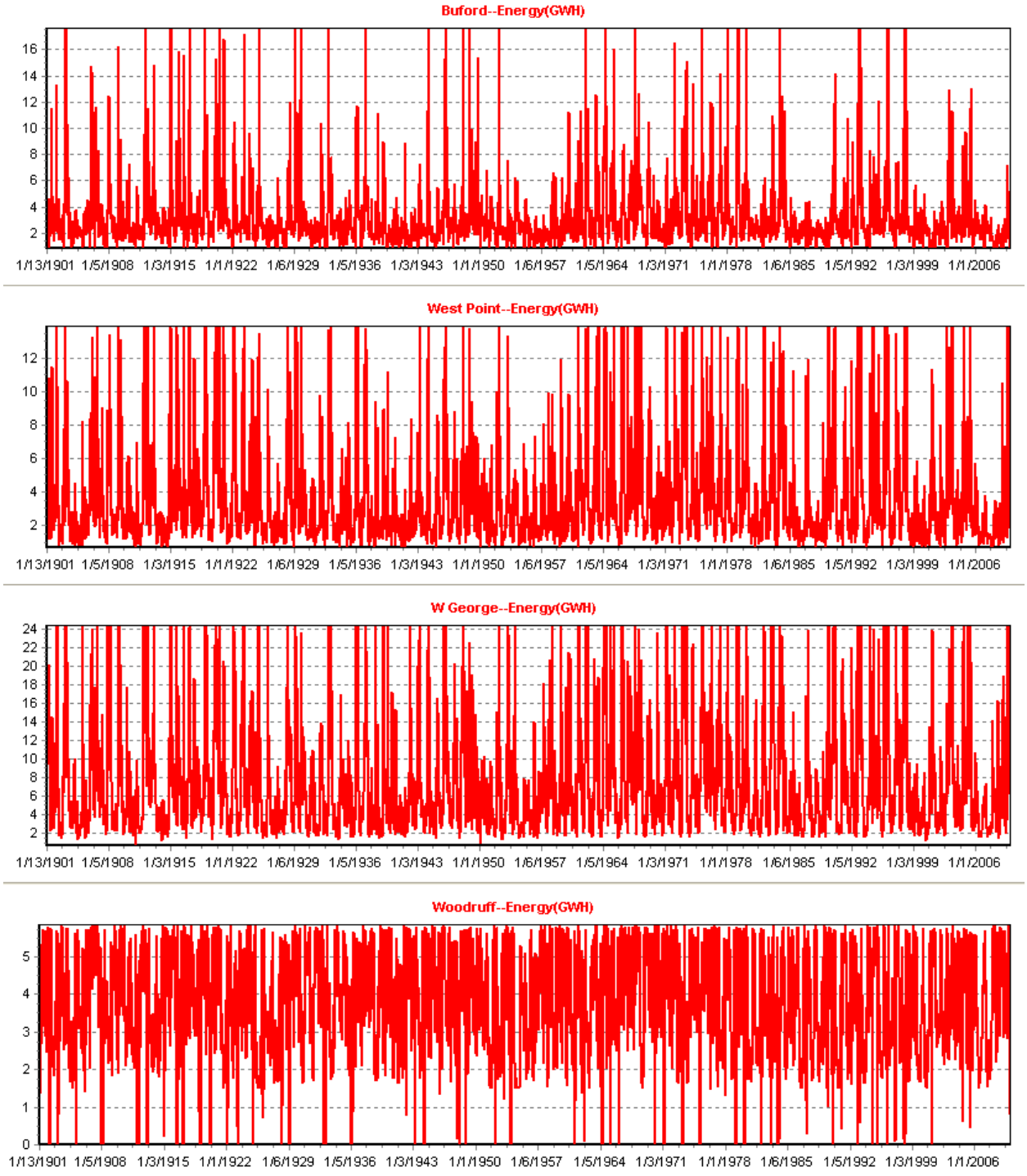

Figure 5.12: Historical Period, 2007 Demands, Energy Generation Sequences

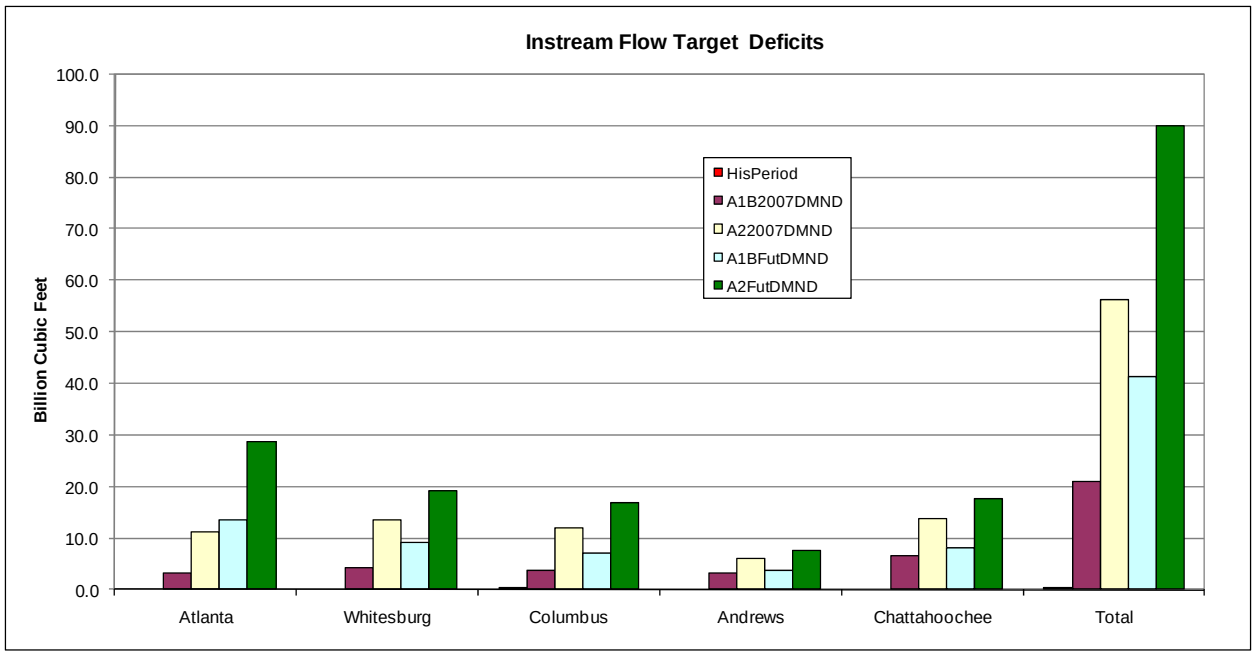

Figure 5.13: Total Instream Flow Target Deficits over the Assessment Horizon

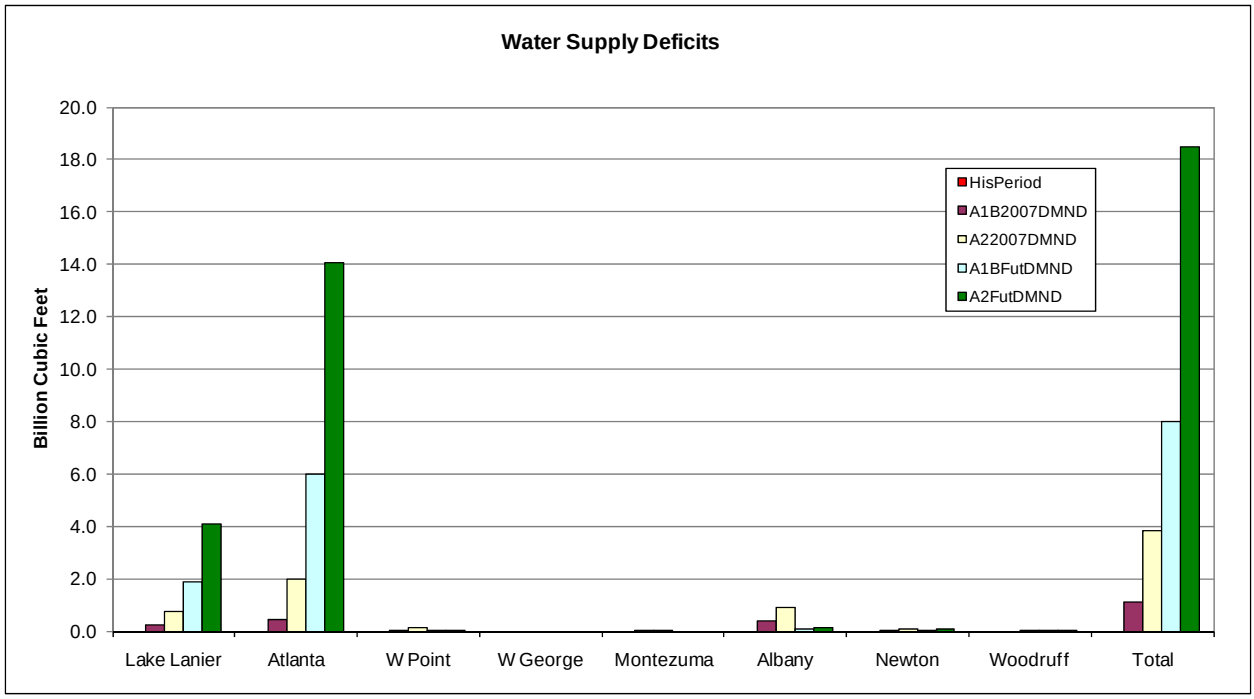

Figure 5.14: Total Water Supply Deficits over the Assessment Horizon

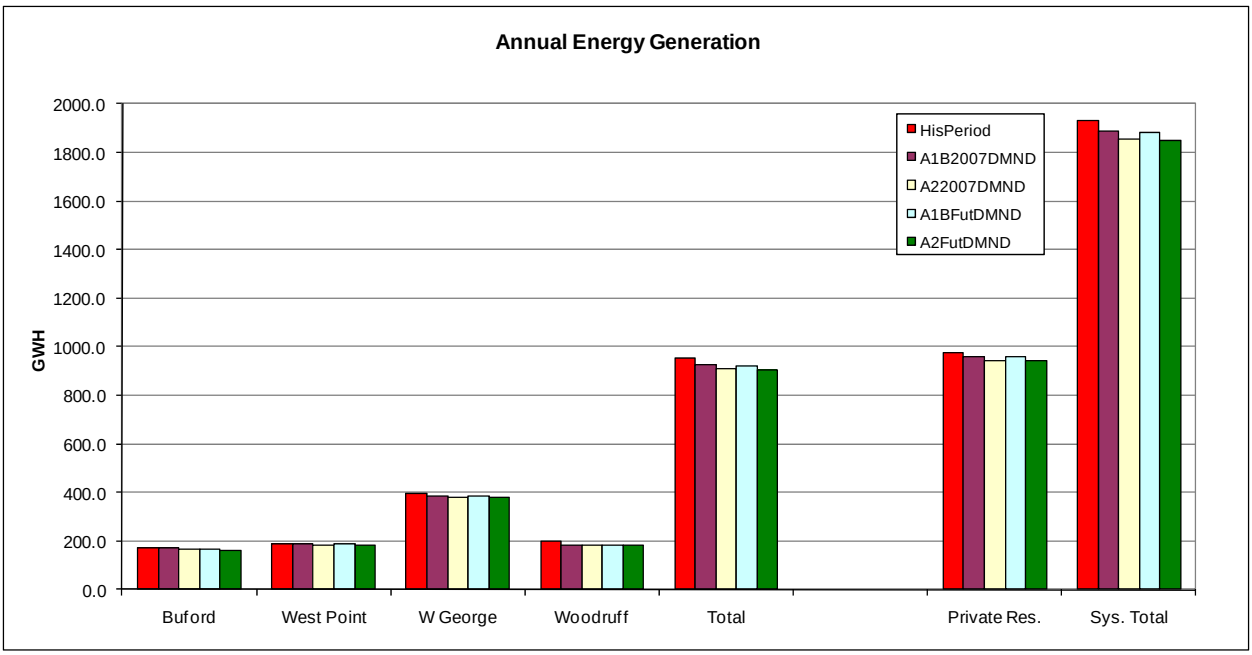

Figure 5.15: Average Annual Energy Generation over the Assessment Horizon

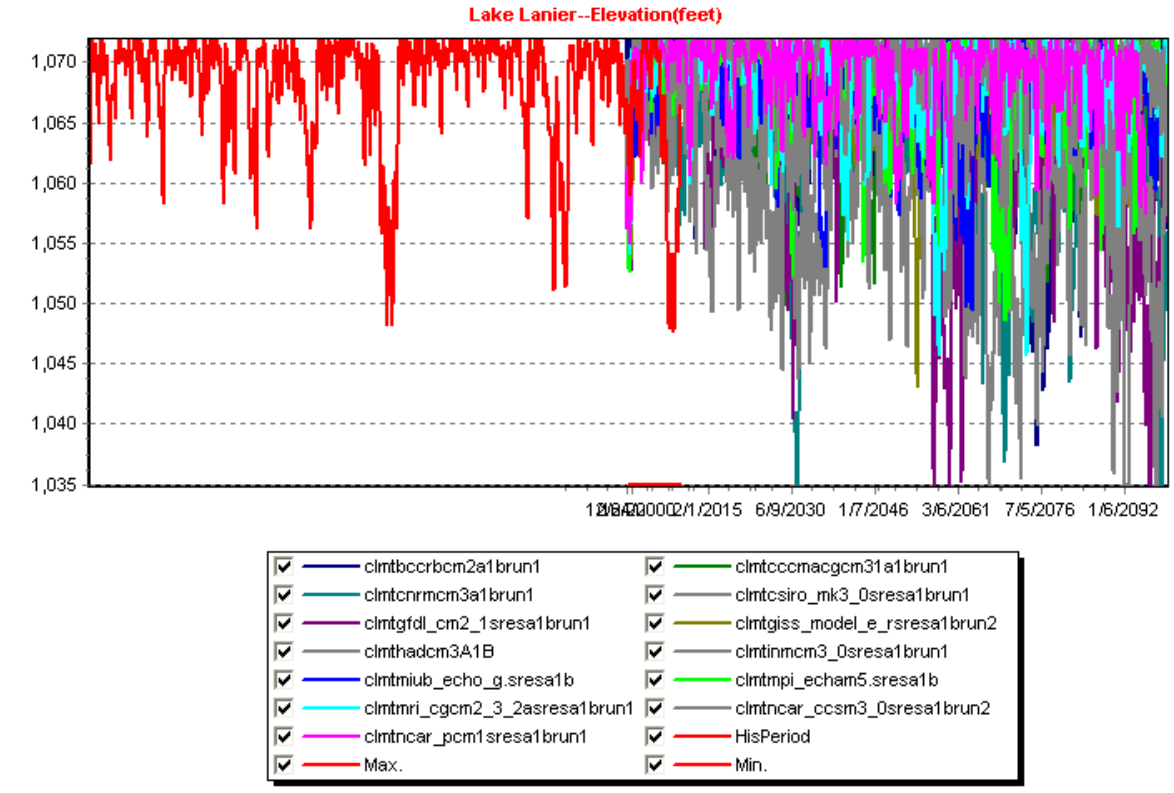

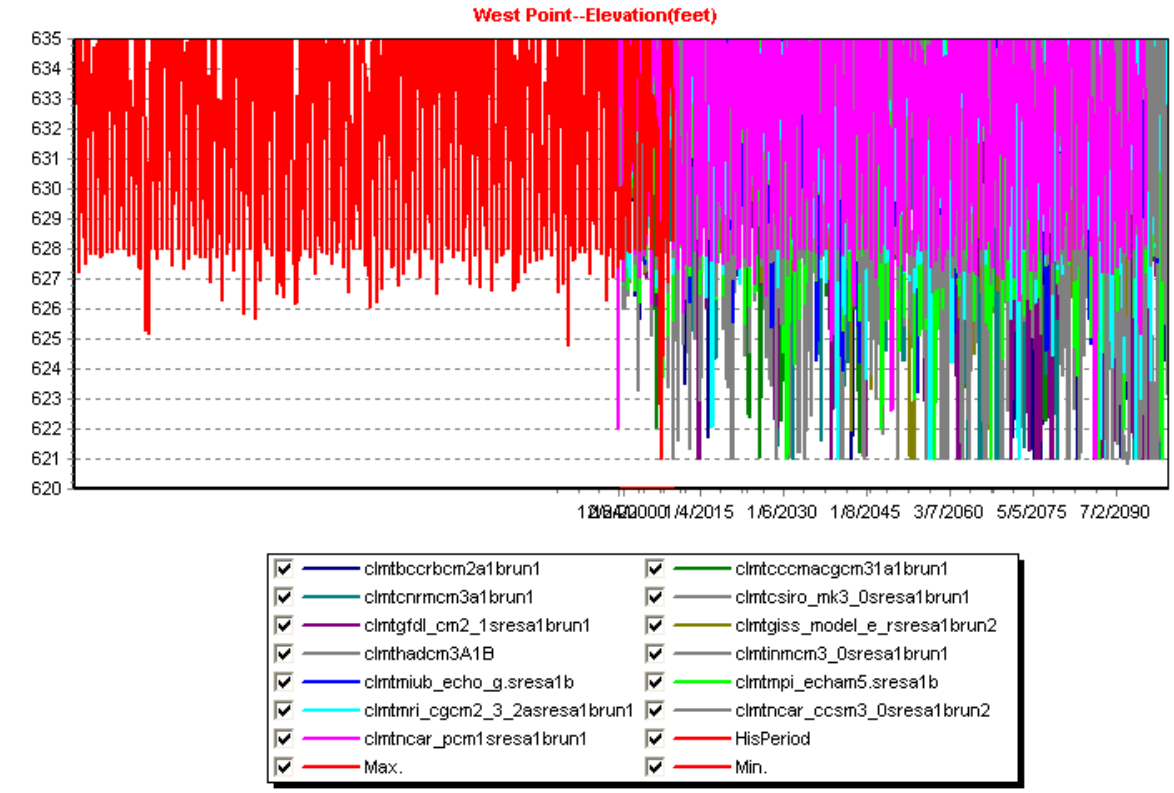

Figure 5.16: A1B, 2007 Demands, Reservoir Elevation Sequences

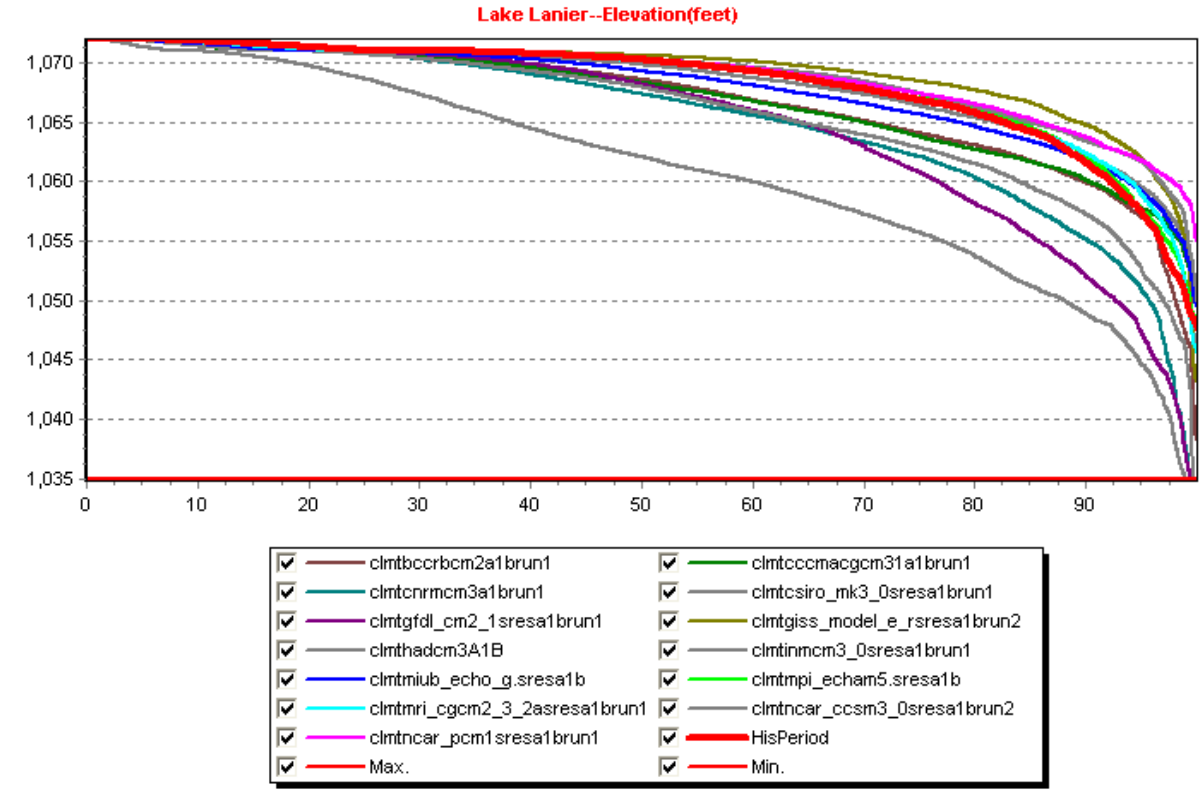

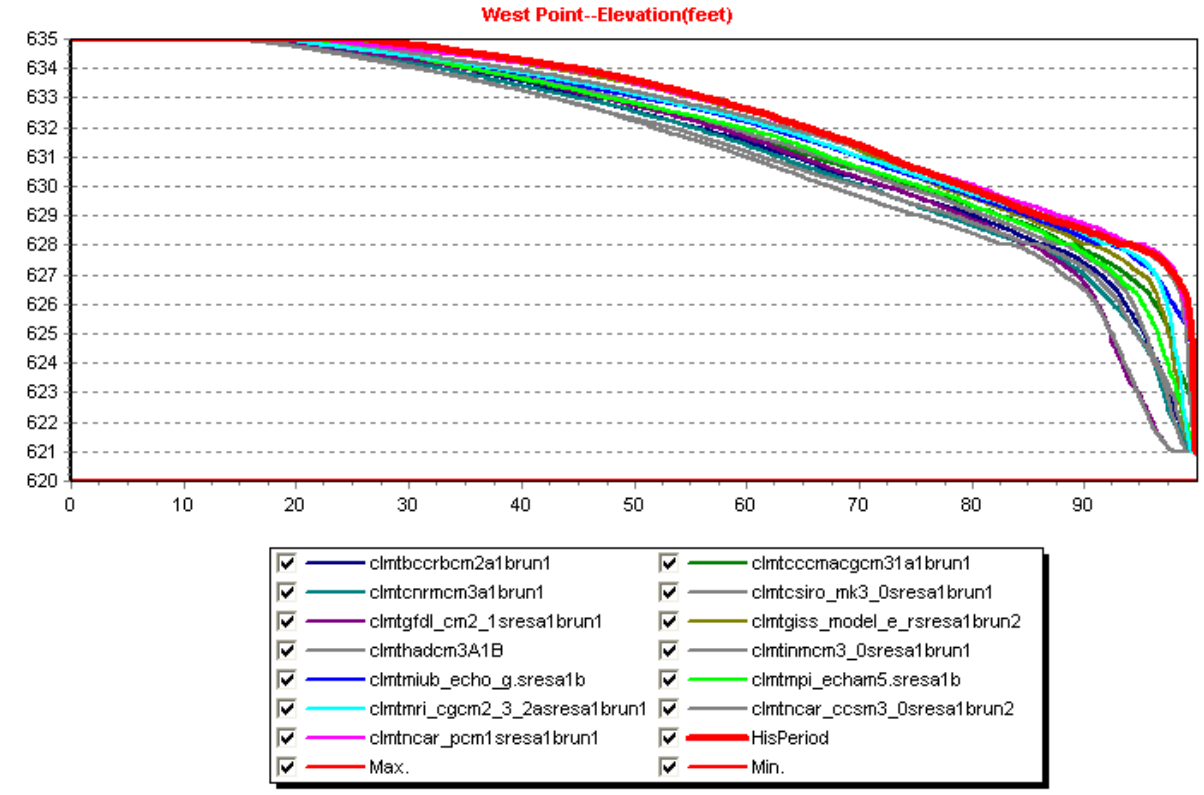

Figure 5.17: A1B, 2007 Demands, Reservoir Elevation Frequency Curves

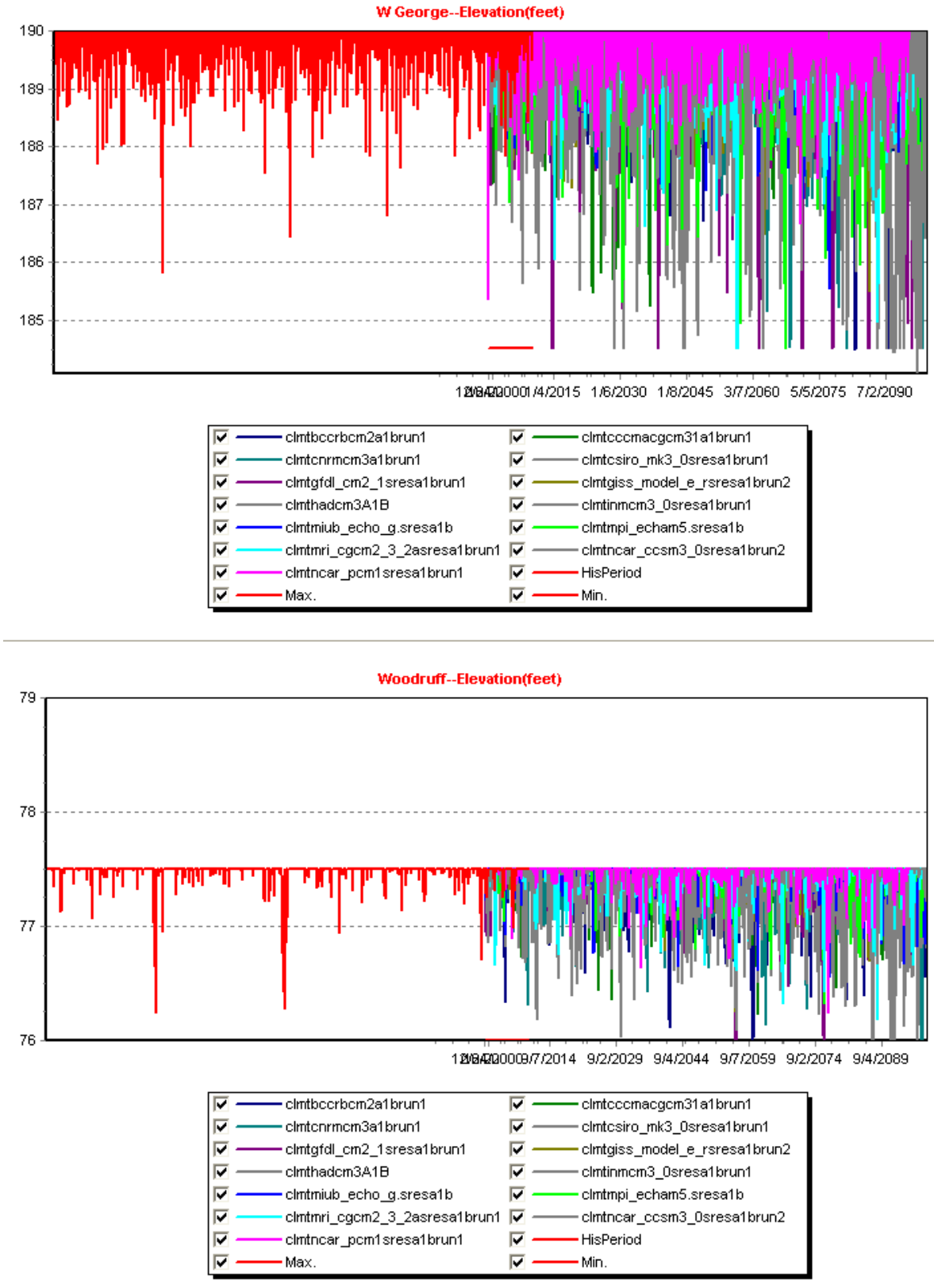

Figure 5.18: A1B, 2007 Demands, Reservoir Elevation Sequences

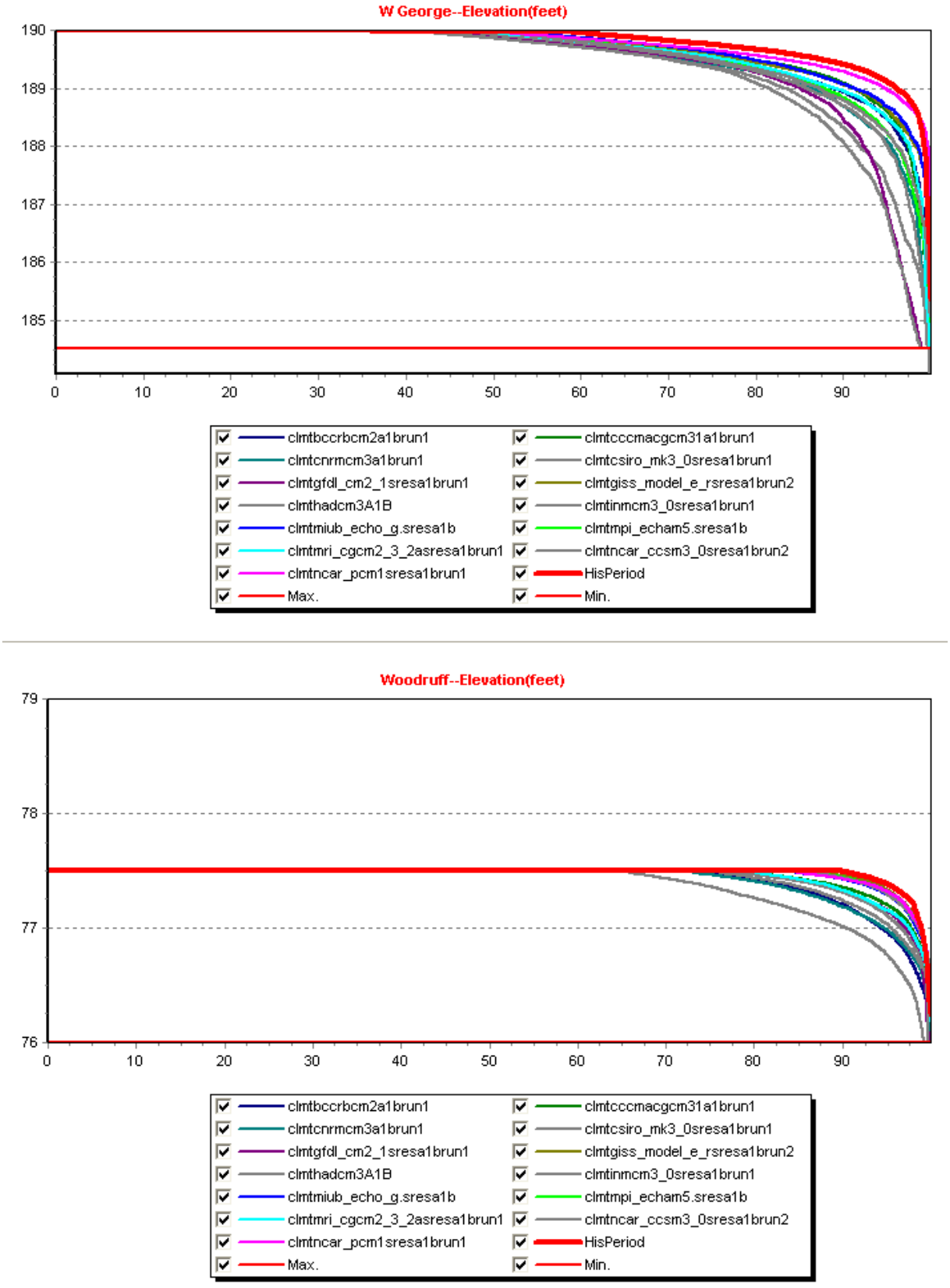

Figure 5.19: A1B, 2007 Demands, Reservoir Elevation Frequency Curves

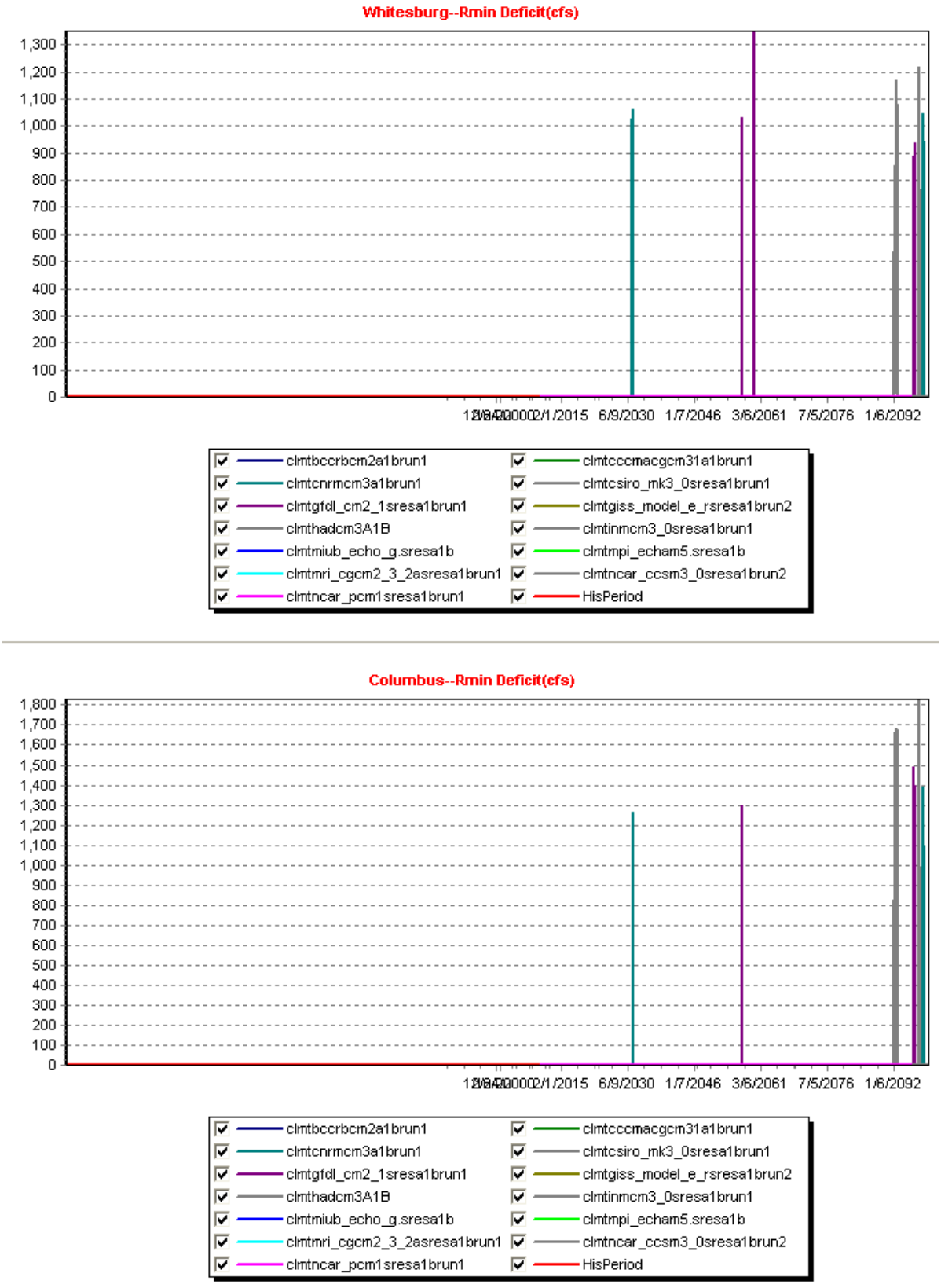

Figure 5.20: A1B, 2007 Demands, Instream Flow Deficit Sequences

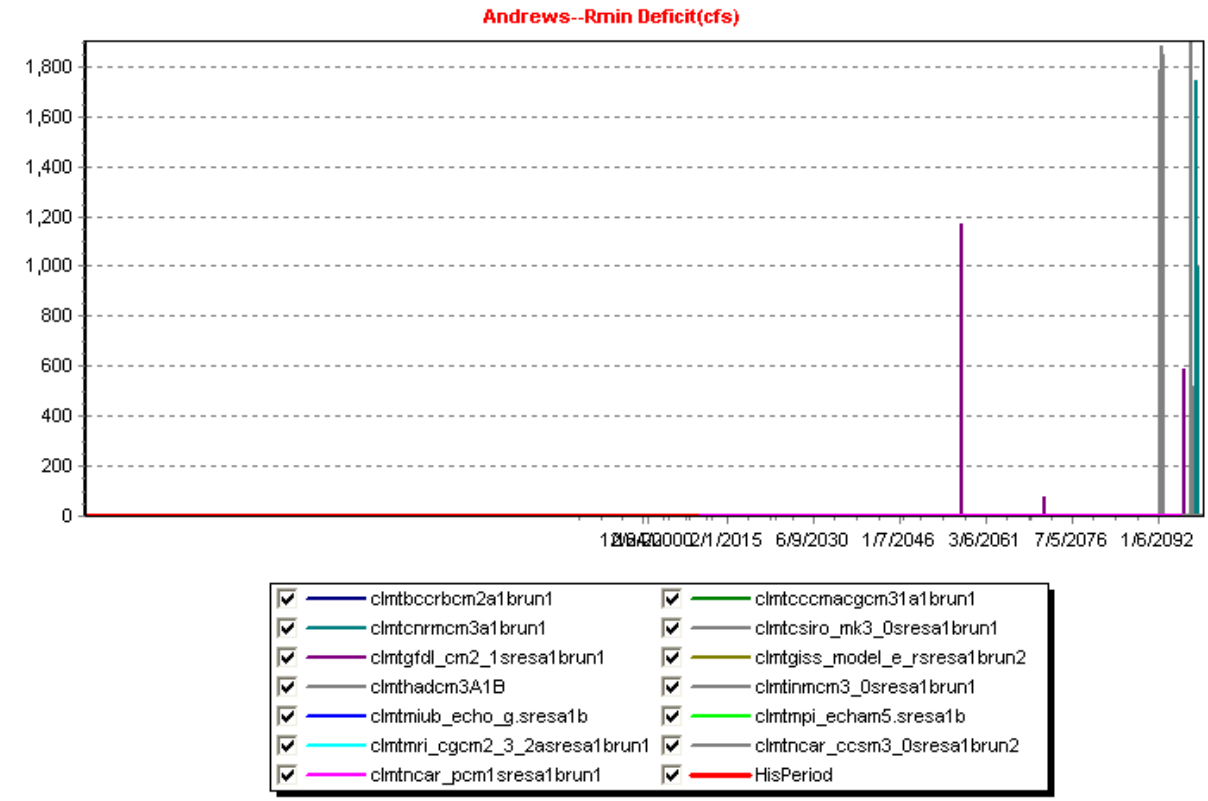

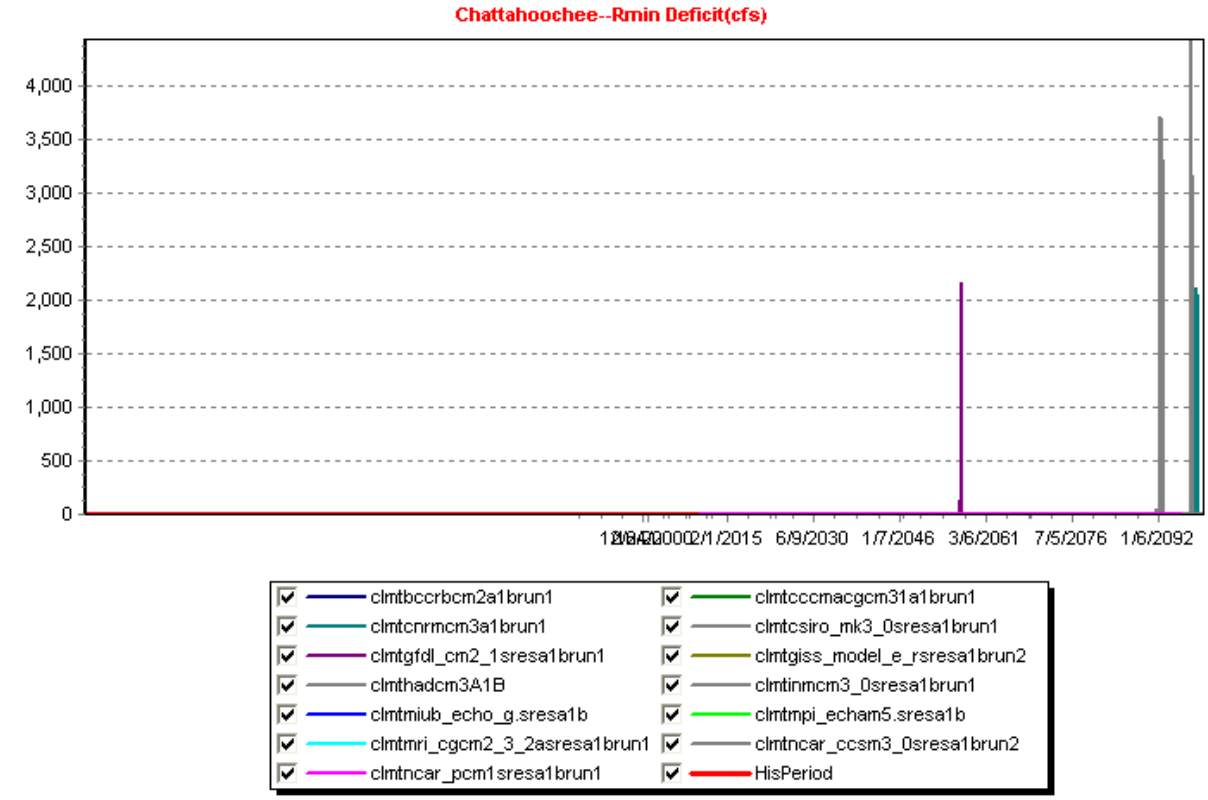

Figure 5.21: A1B, 2007 Demands, Instream Flow Deficit Sequences

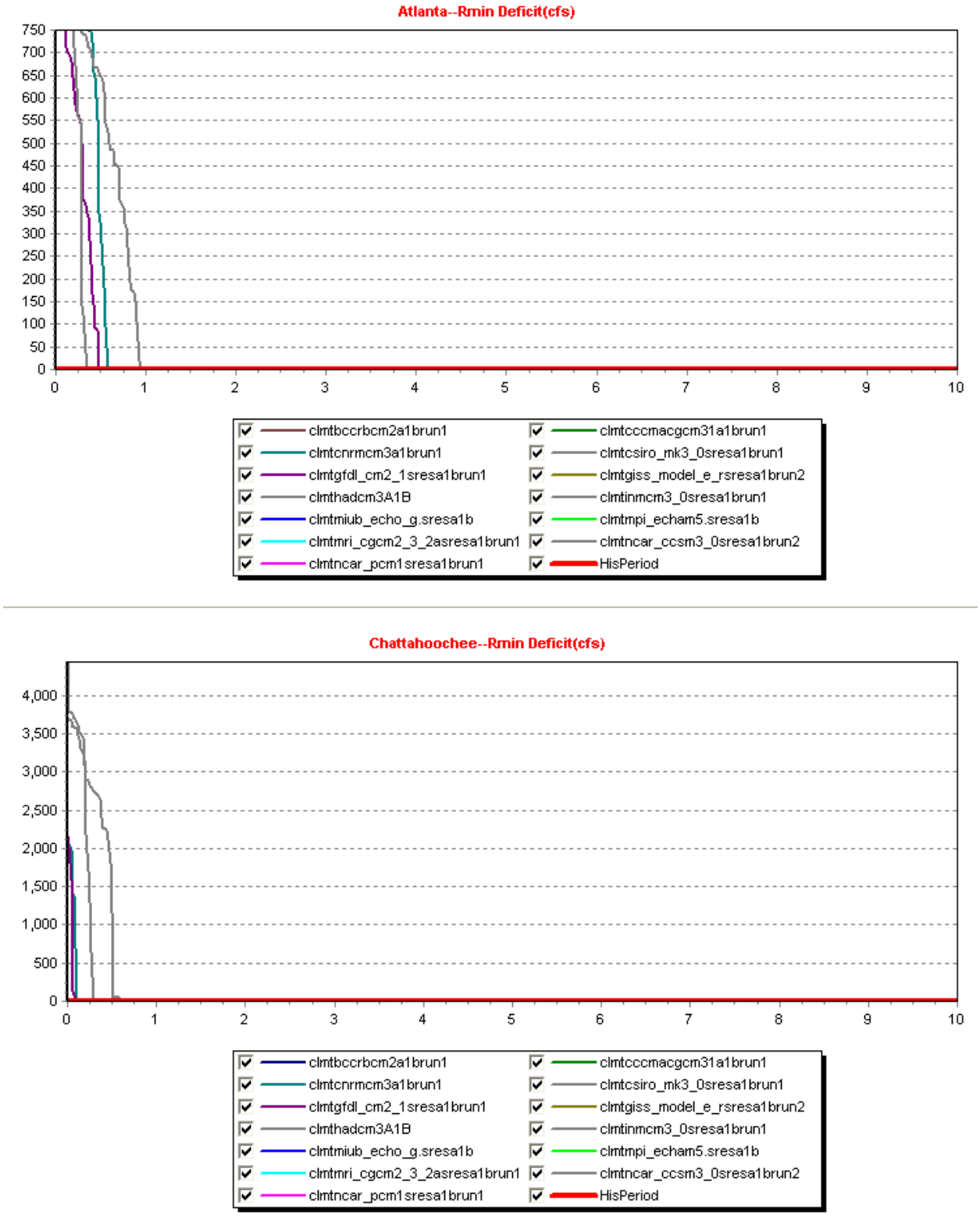

Figure 5.22: A1B, 2007 Demands, Instream Flow Deficit Frequency Curves (The horizontal axis shows frequencies up to 10%.)

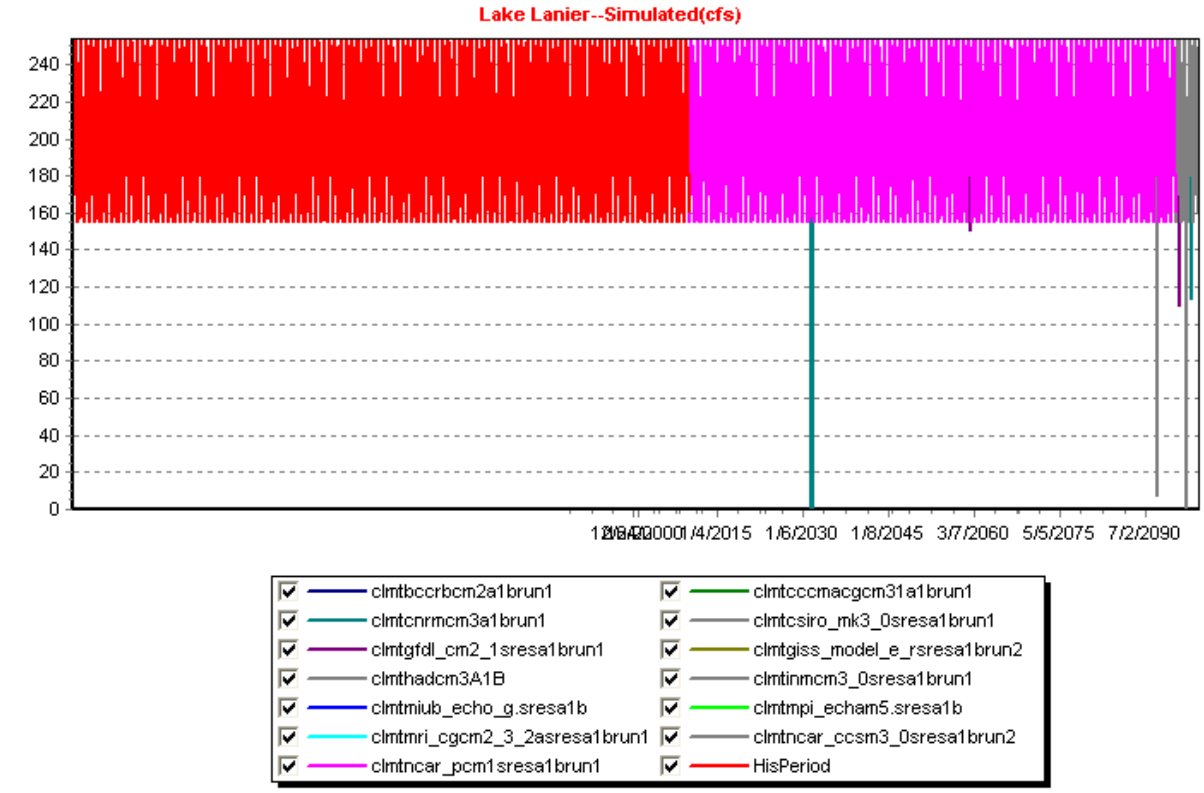

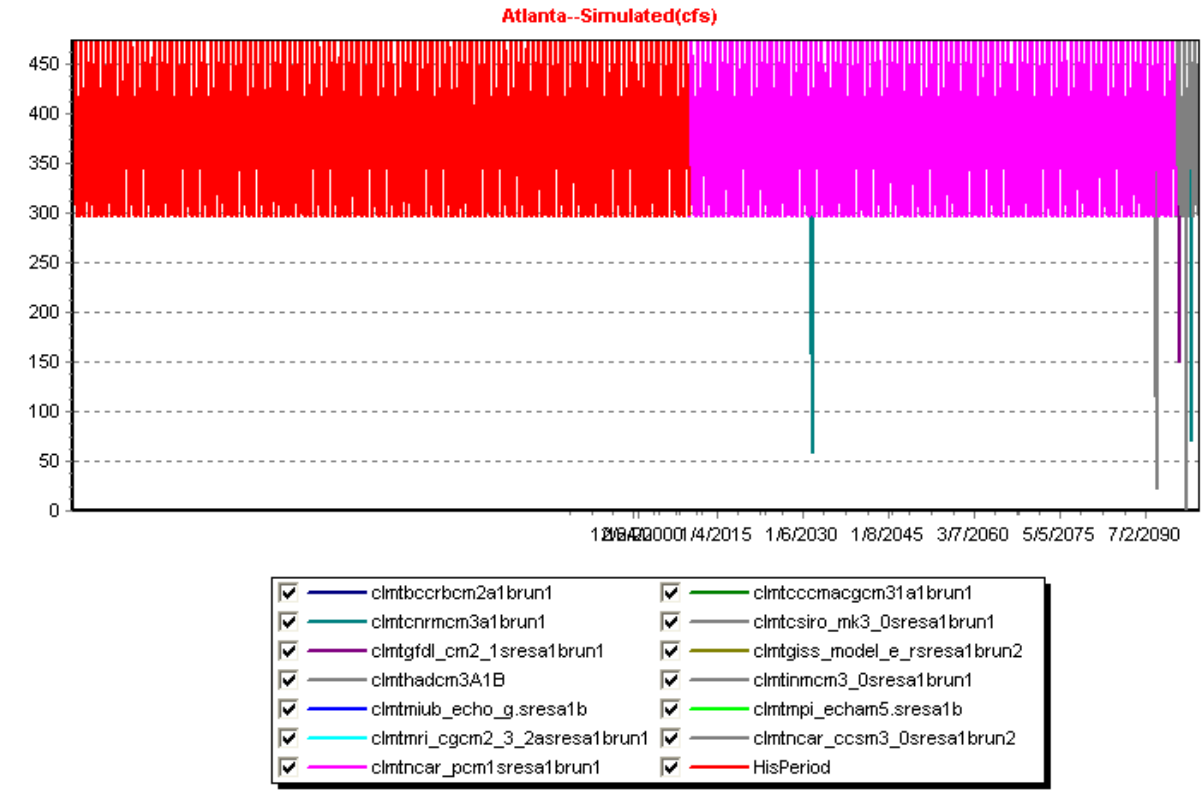

Figure 5.23: A1B, 2007 Demands, Water Supply Sequences

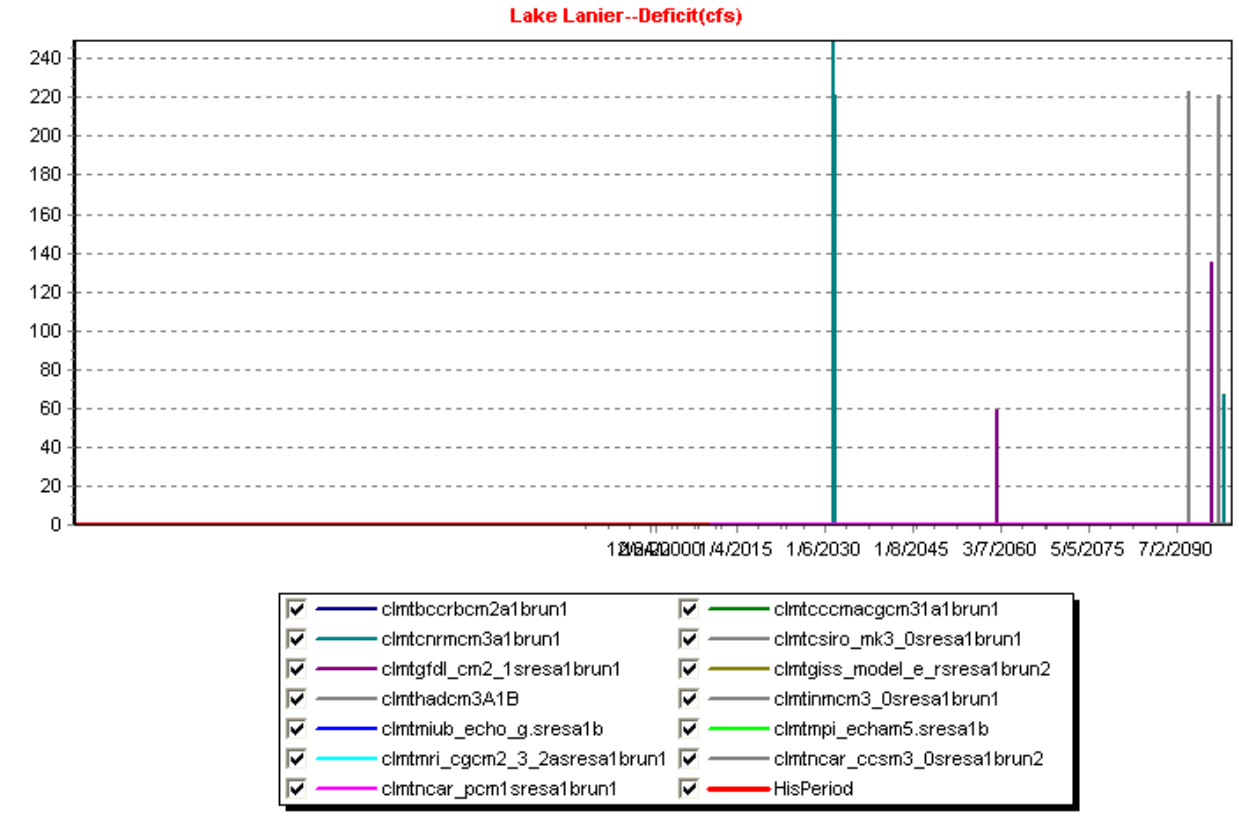

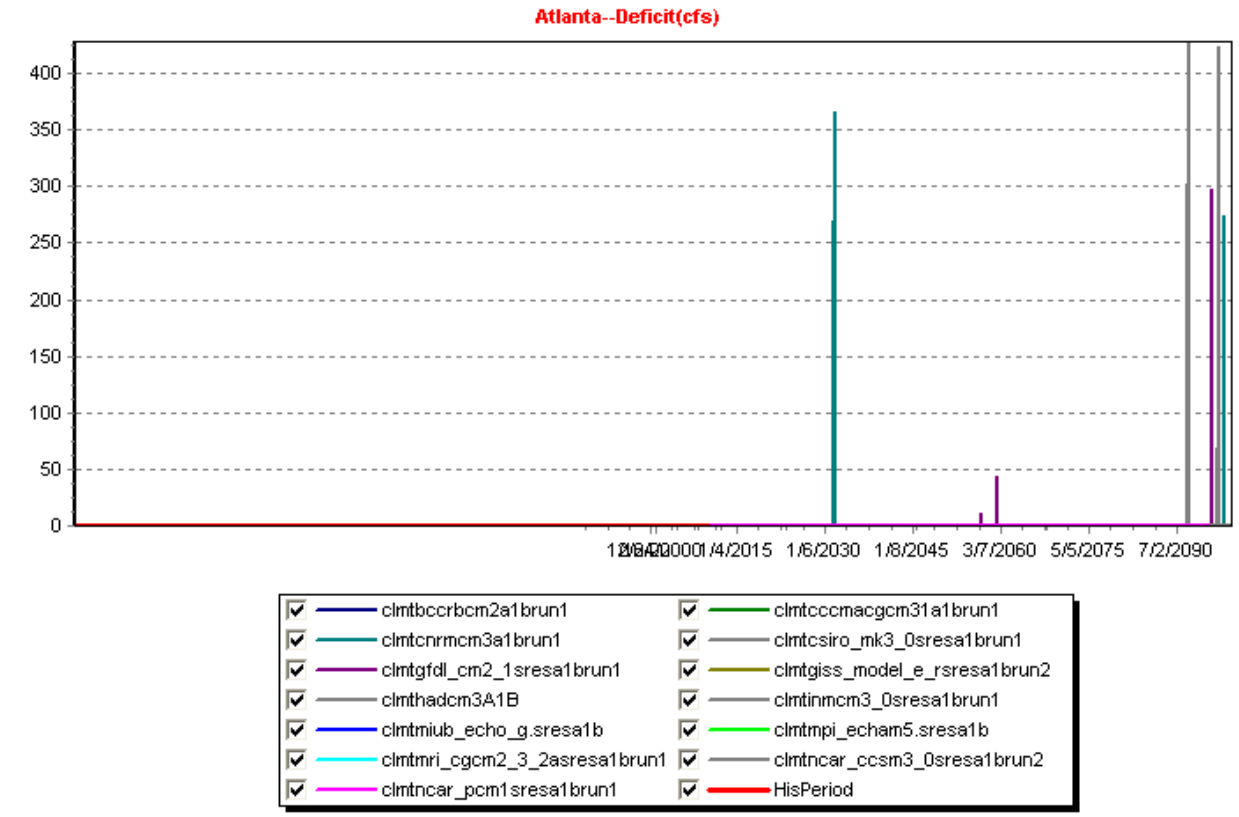

Figure 5.24: A1B, 2007 Demands, Water Supply Deficit Sequences

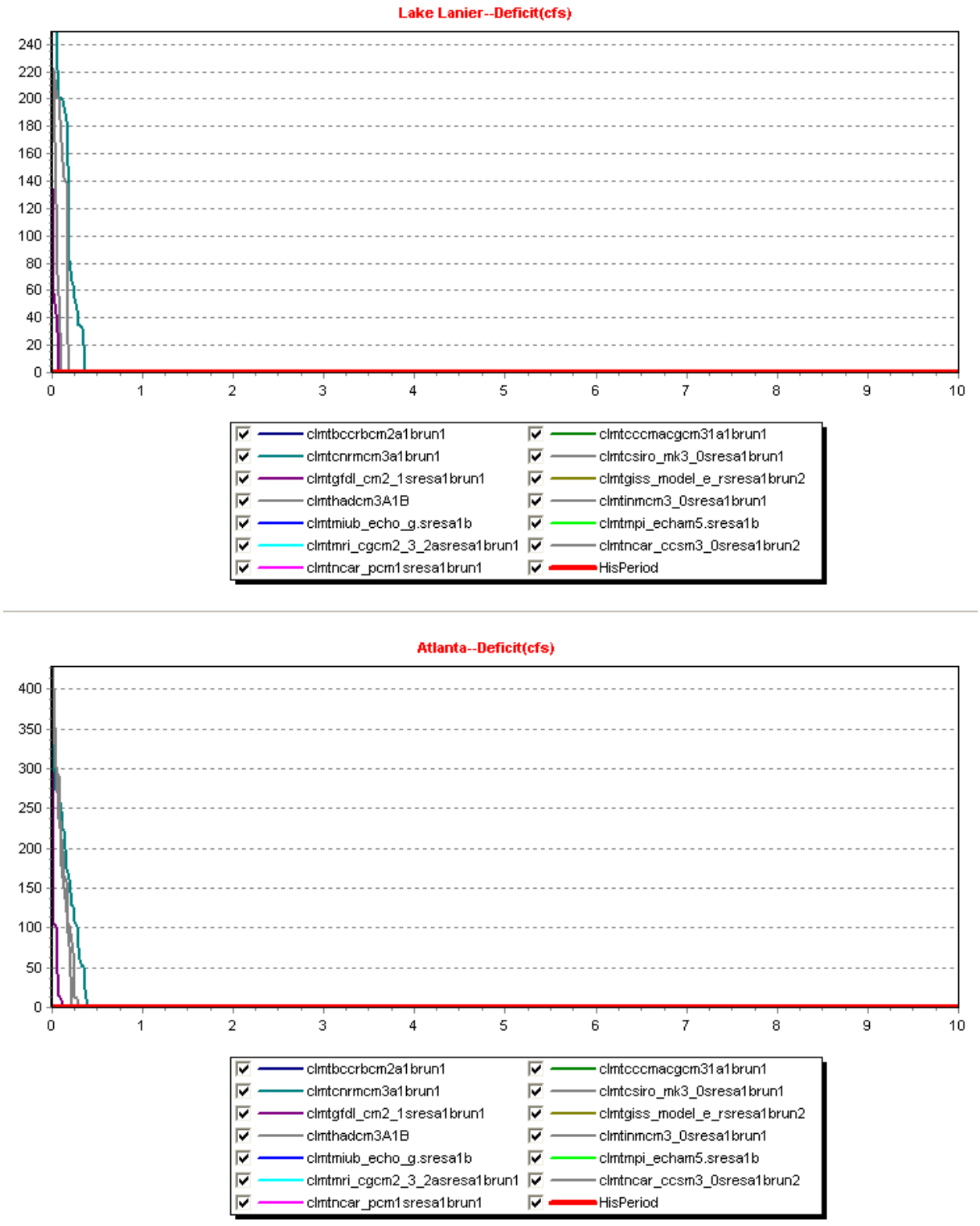

Figure 5.25: A1B, 2007 Demands, Water Supply Deficit Frequency Curves
(The horizontal axis shows frequencies up to 10%.)

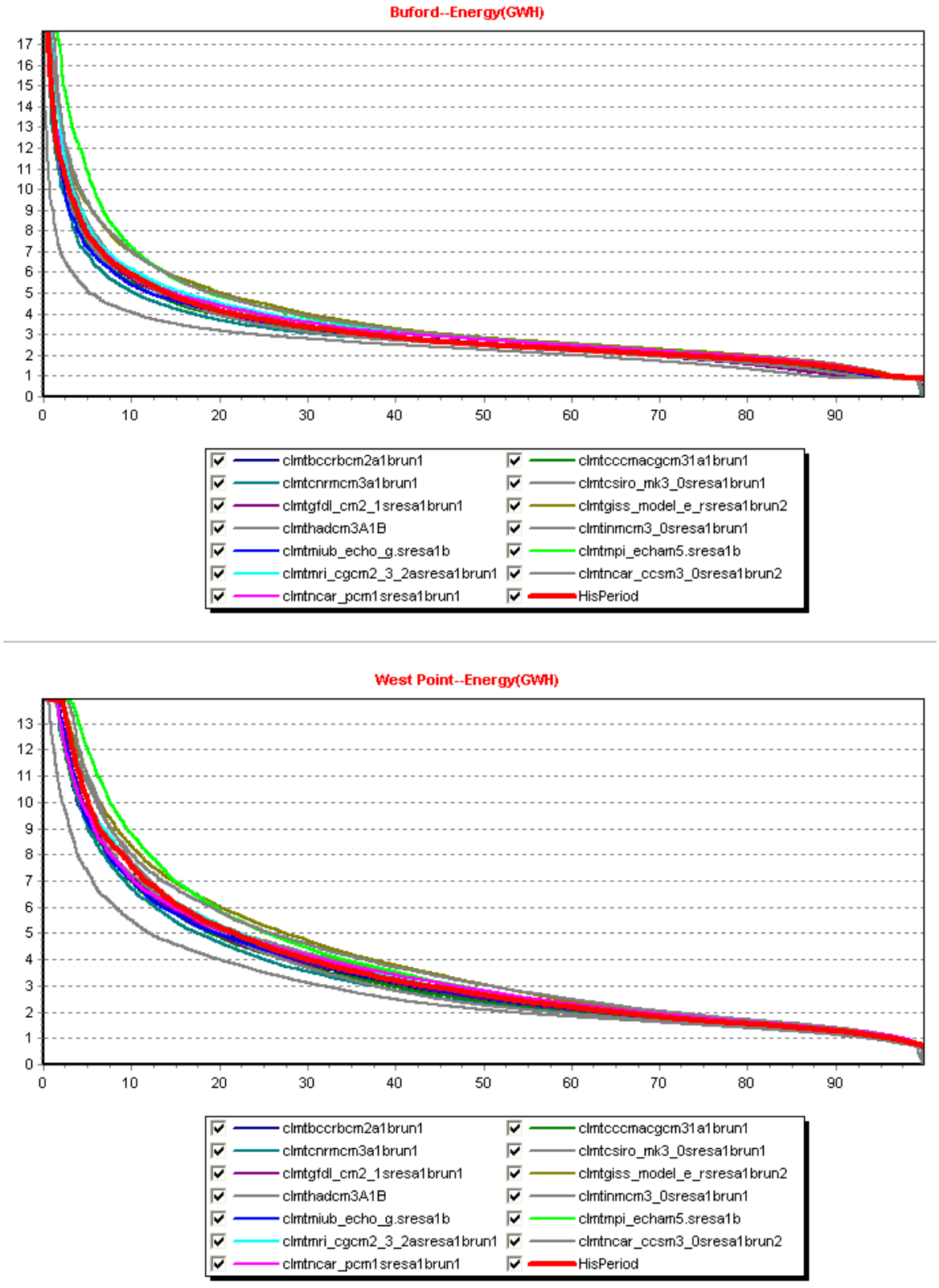

Figure 5.26: A1B, 2007 Demands, Energy Generation Frequency Curves

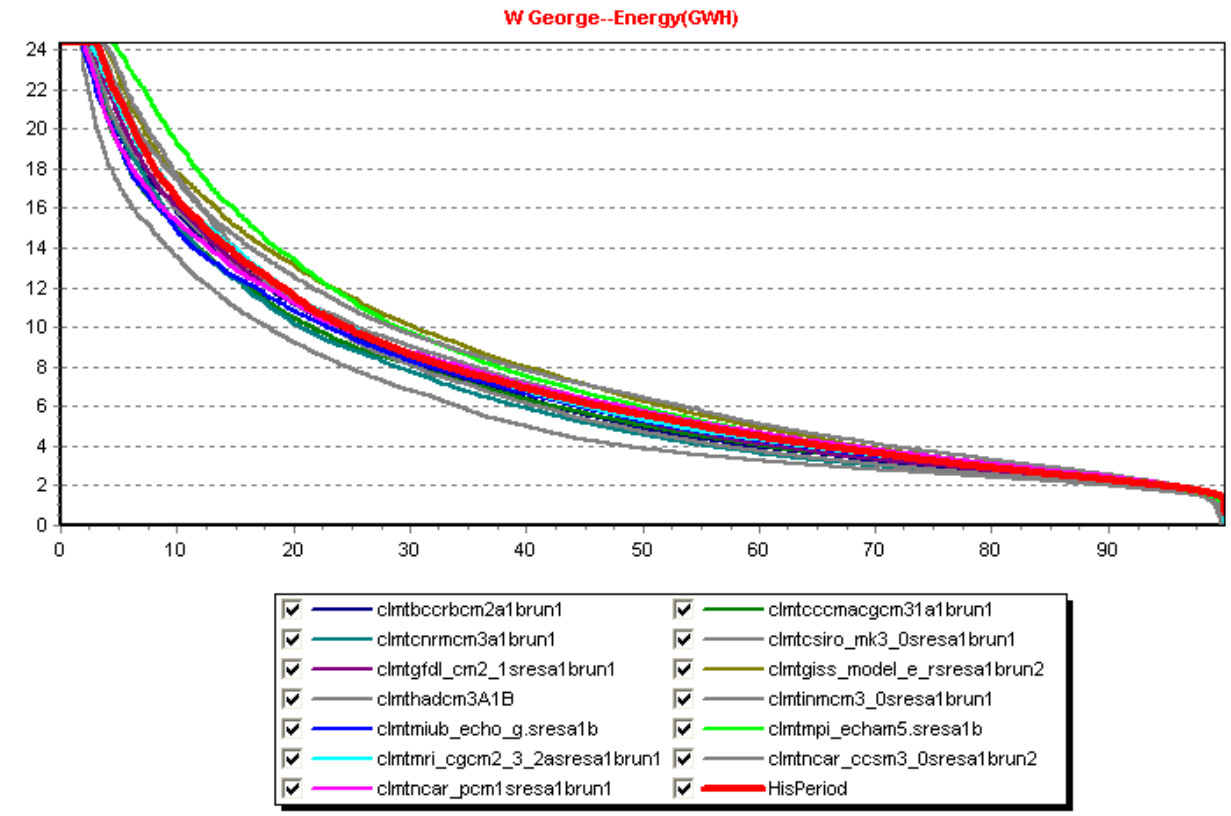

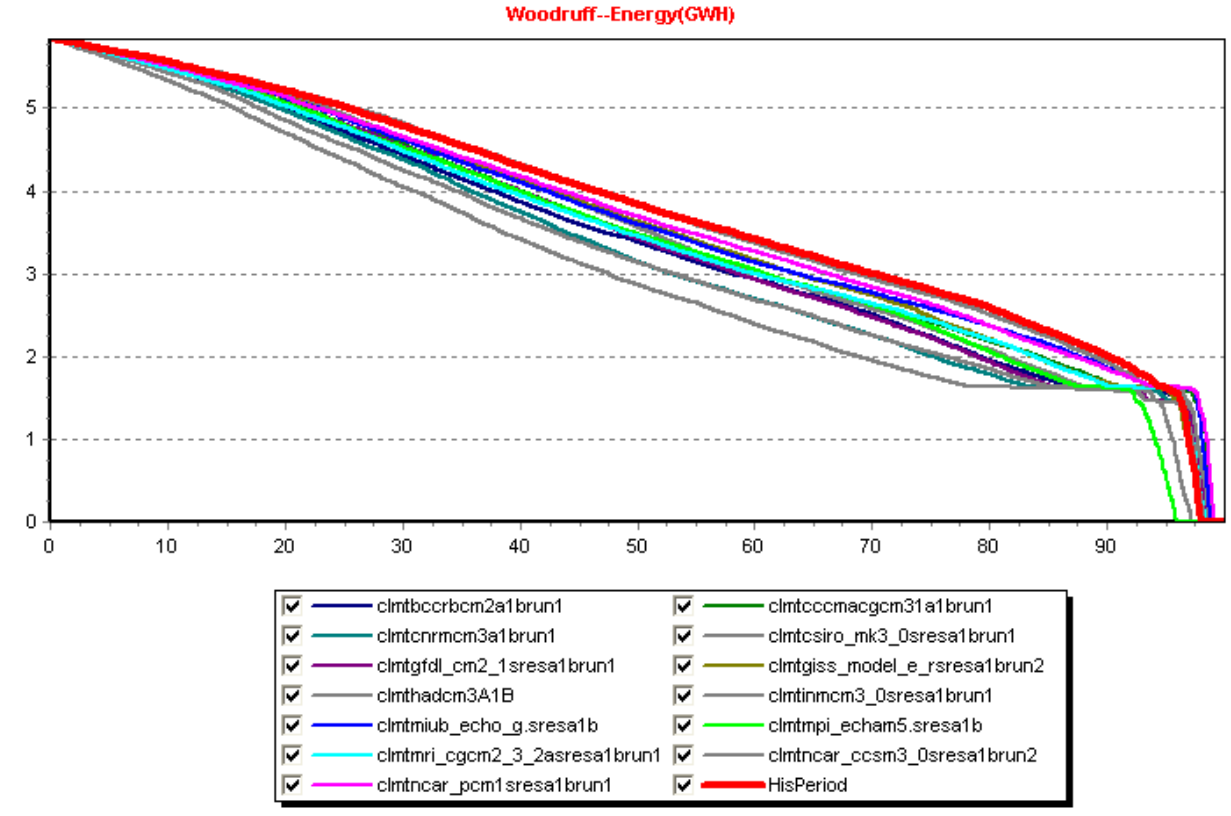

Figure 5.27: A1B, 2007 Demands, Energy Generation Frequency Curves

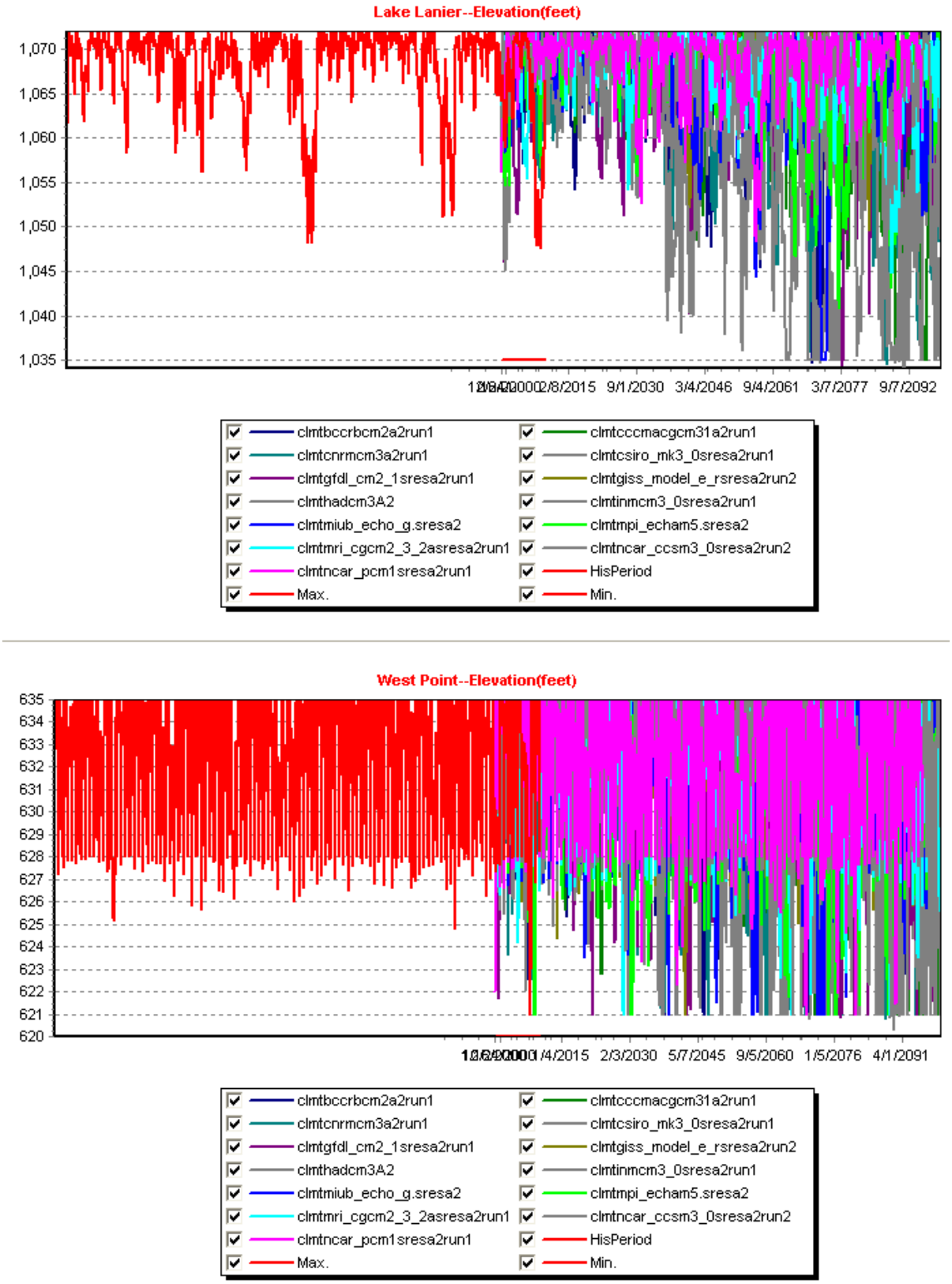

Figure 5.28: A2, 2007 Demands, Elevation Sequences

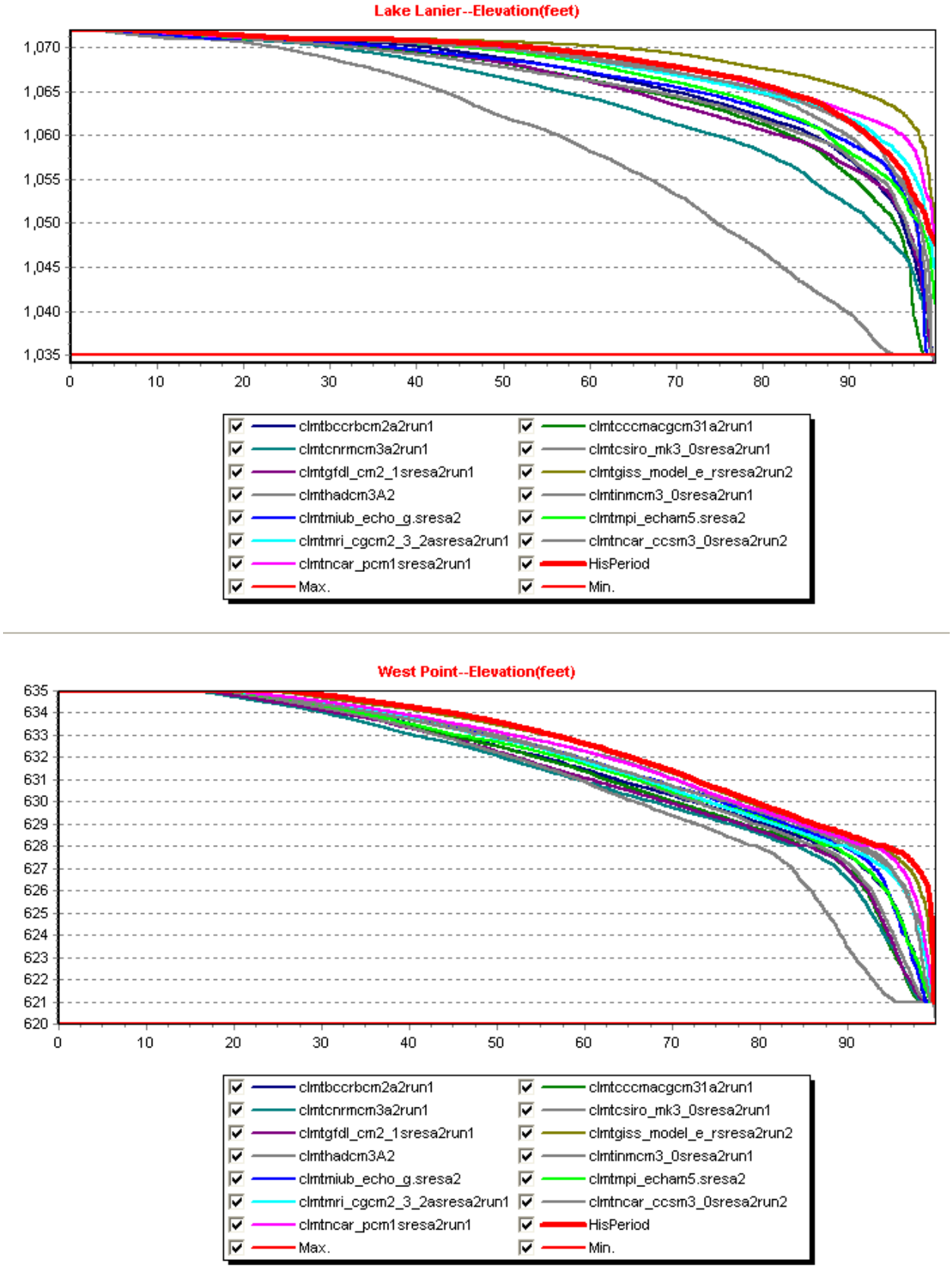

Figure 5.29: A2, 2007 Demands, Elevation Frequency Curves

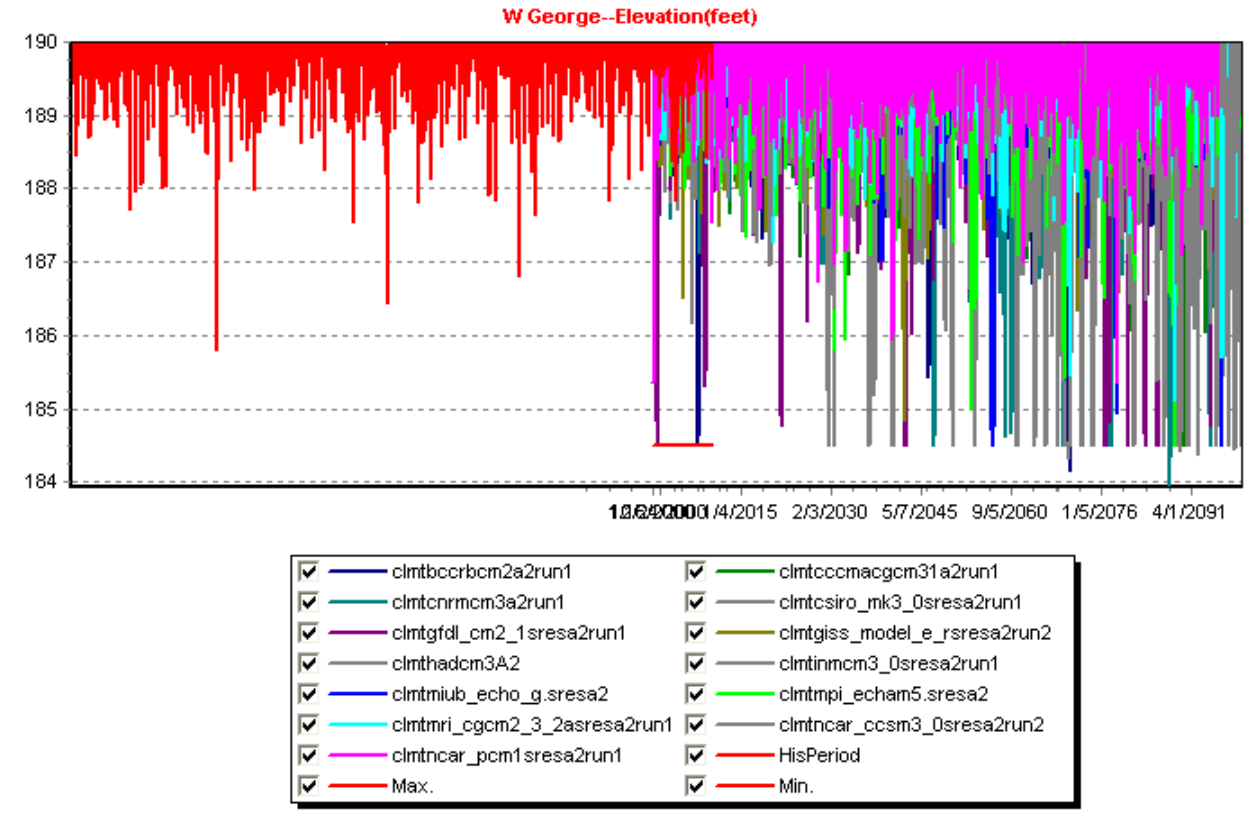

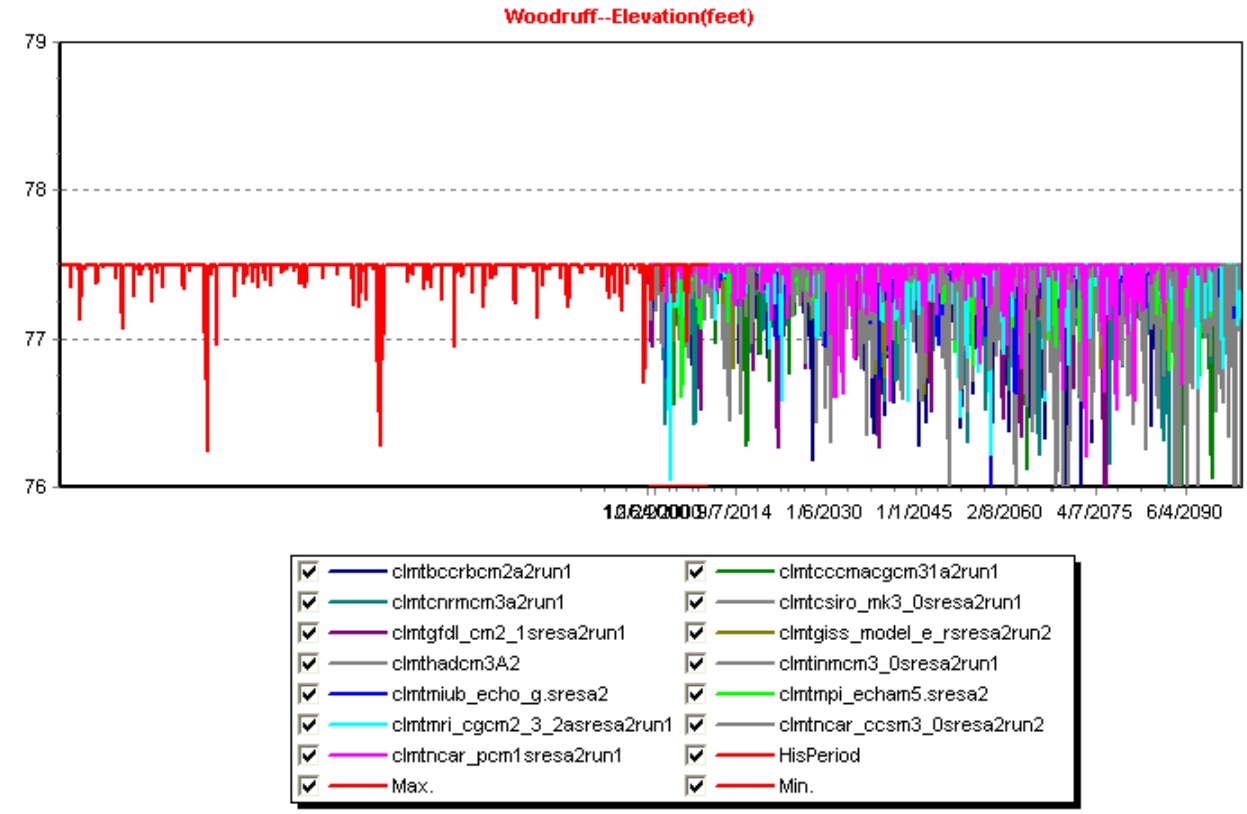

Figure 5.30: A2, 2007 Demands, Elevation Sequences

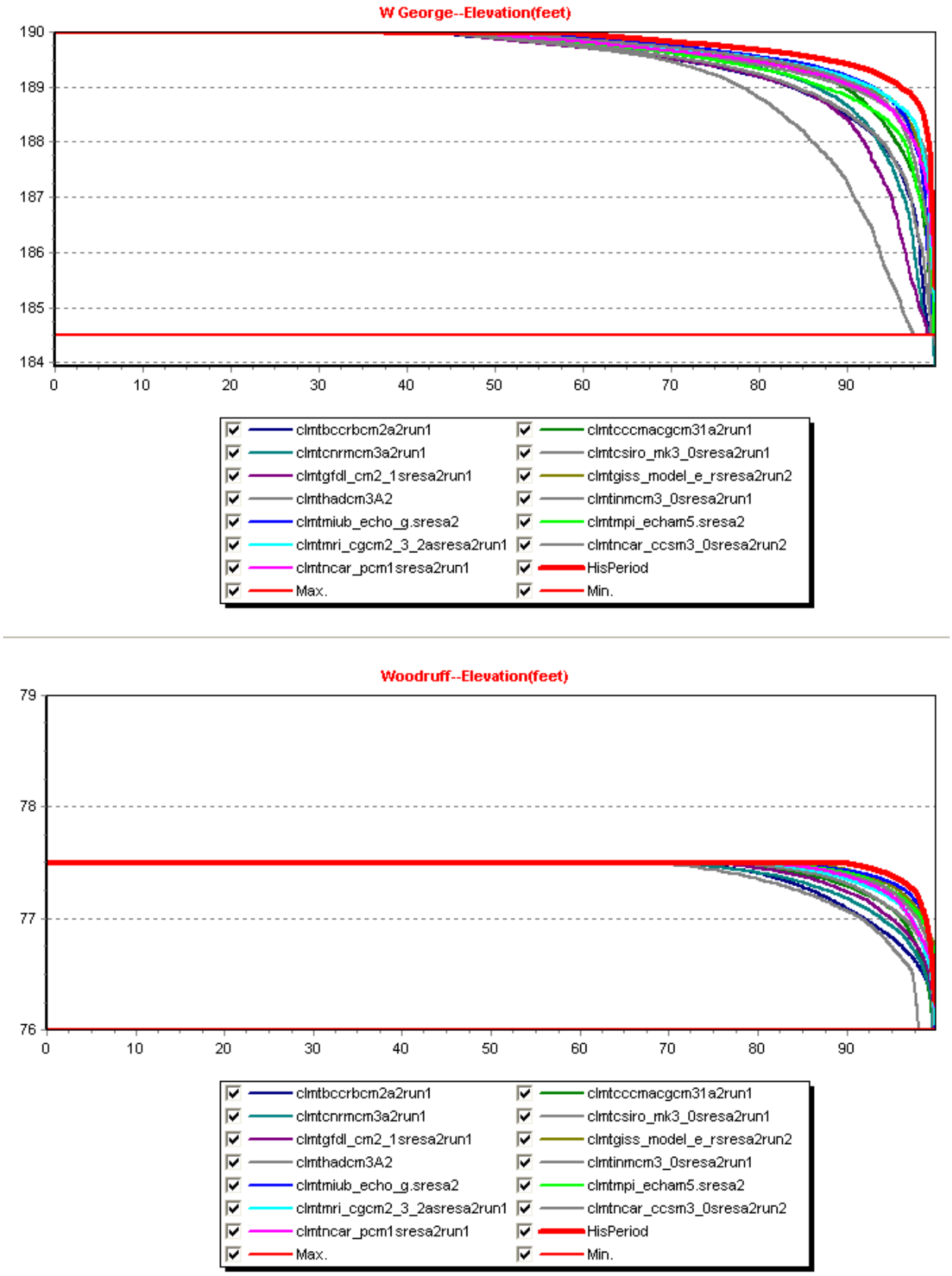

Figure 5.31: A2, 2007 Demands, Elevation Frequency Curves

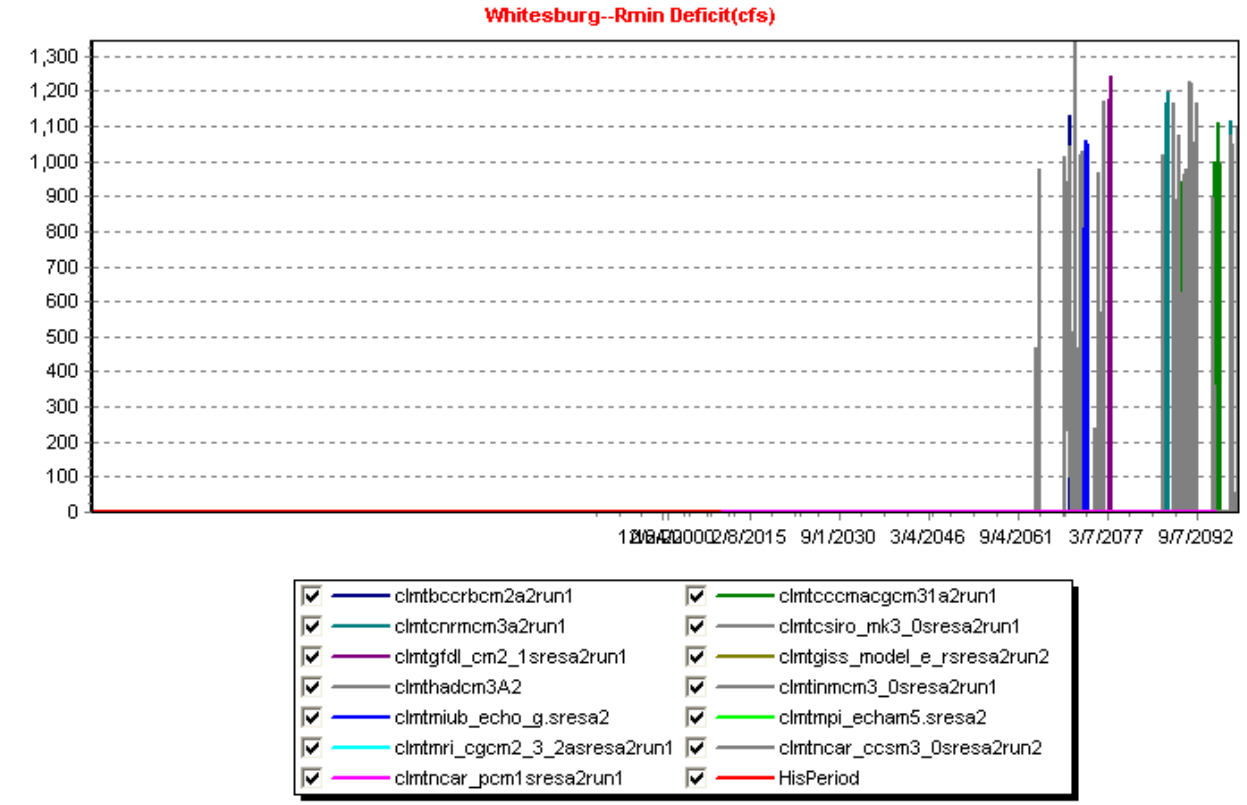

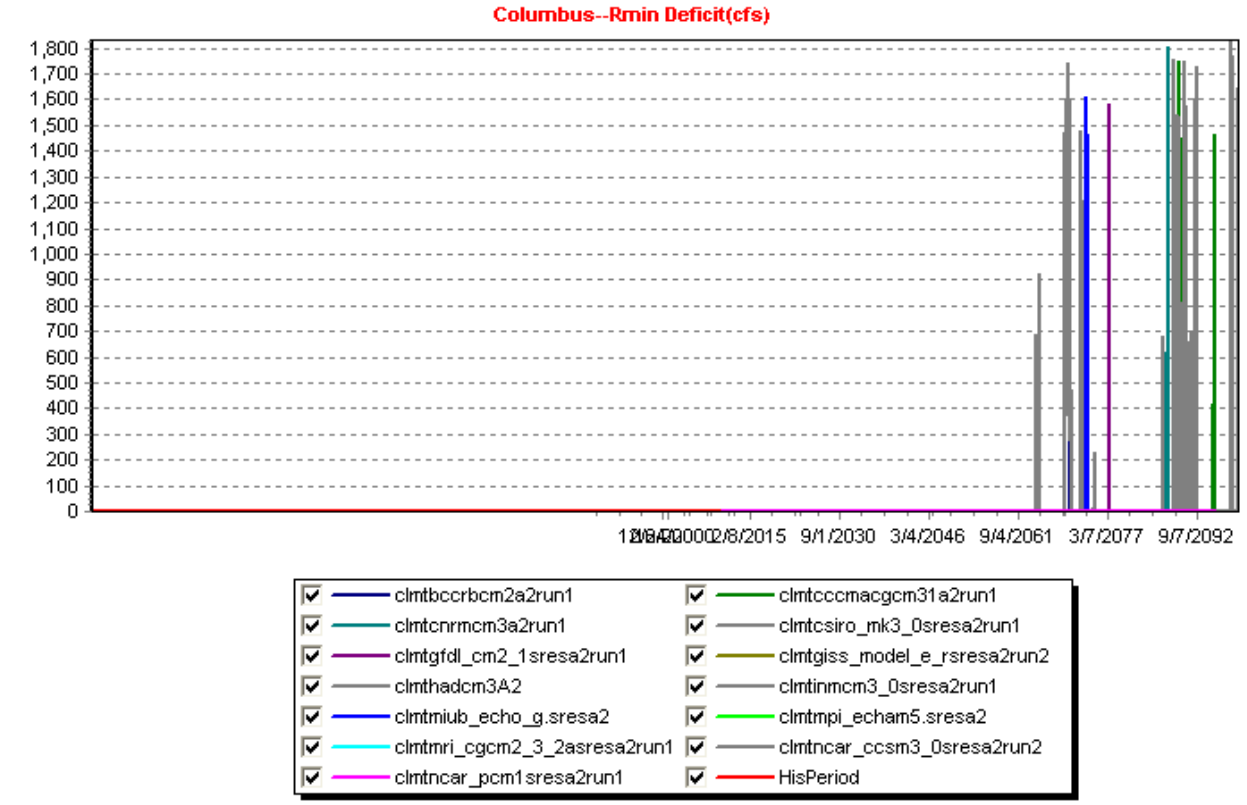

Figure 5.32: A2, 2007 Demands, Instream Flow Deficit Sequences

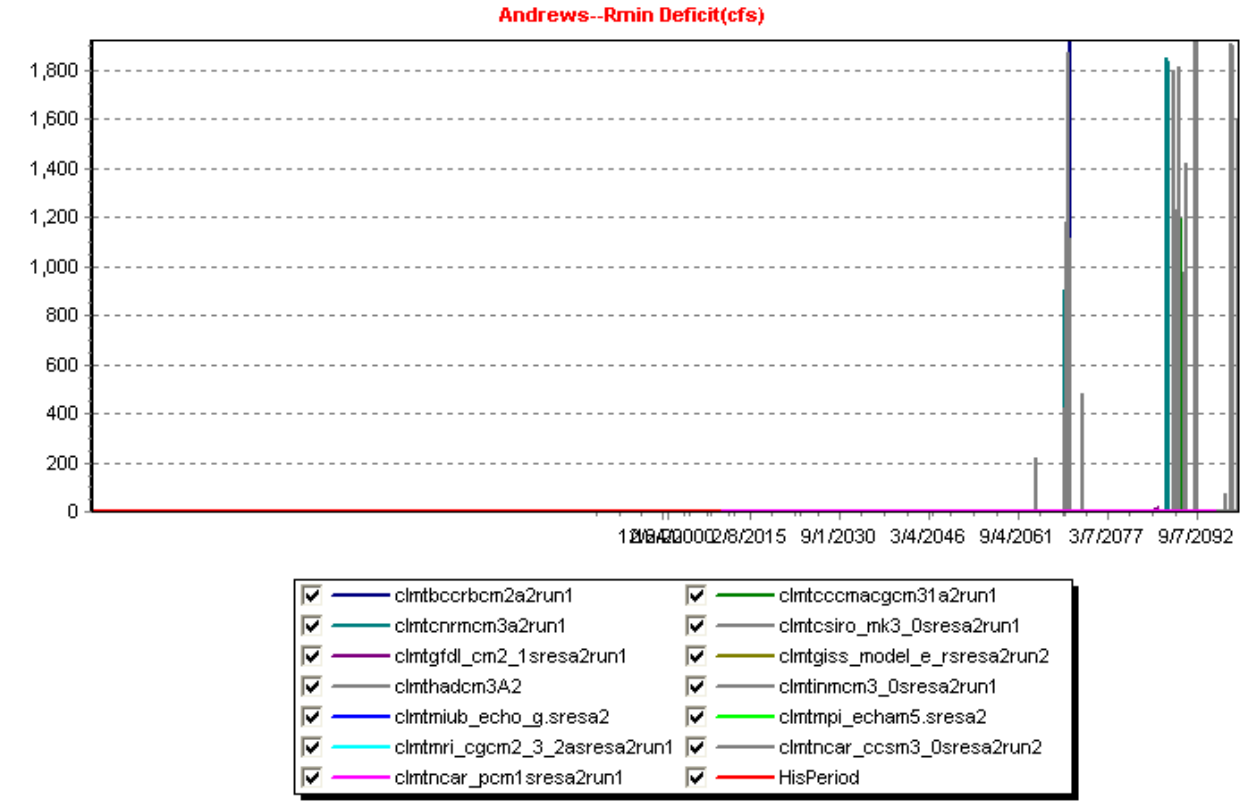

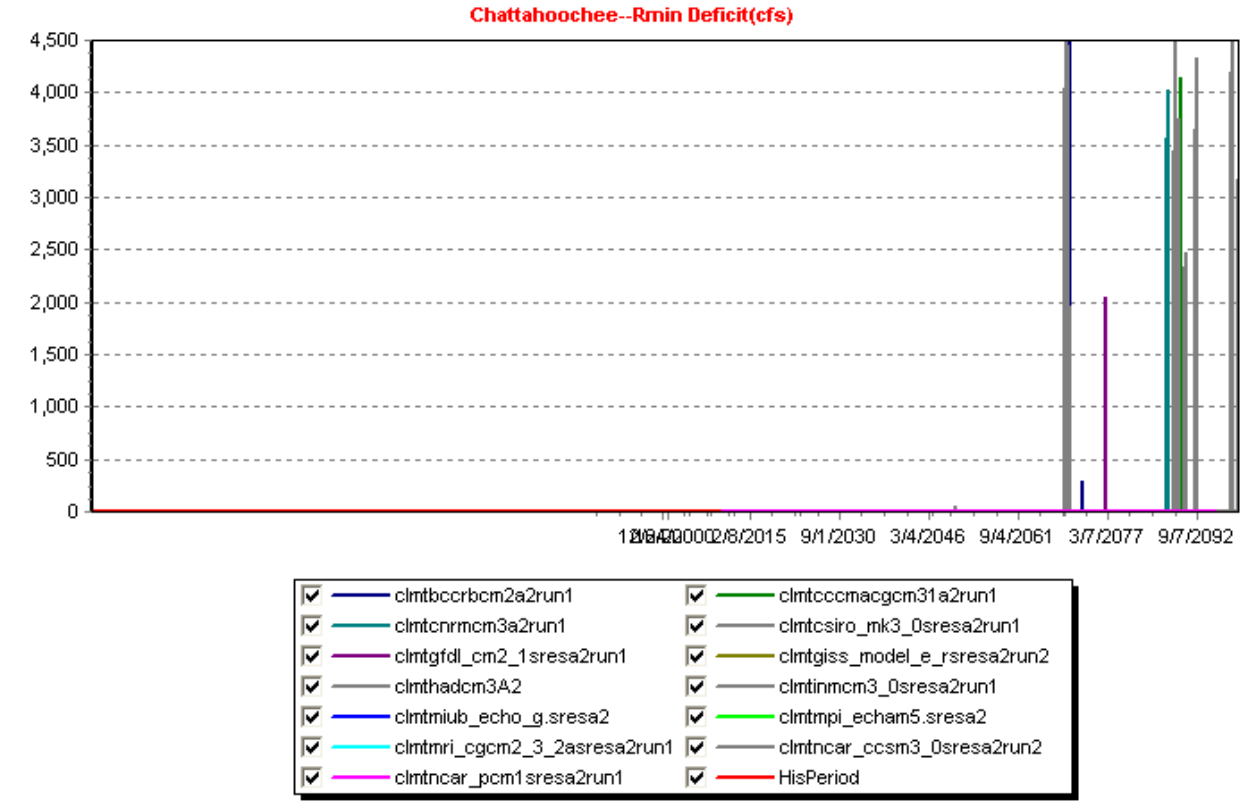

Figure 5.33: A2, 2007 Demands, Instream Flow Deficit Sequences

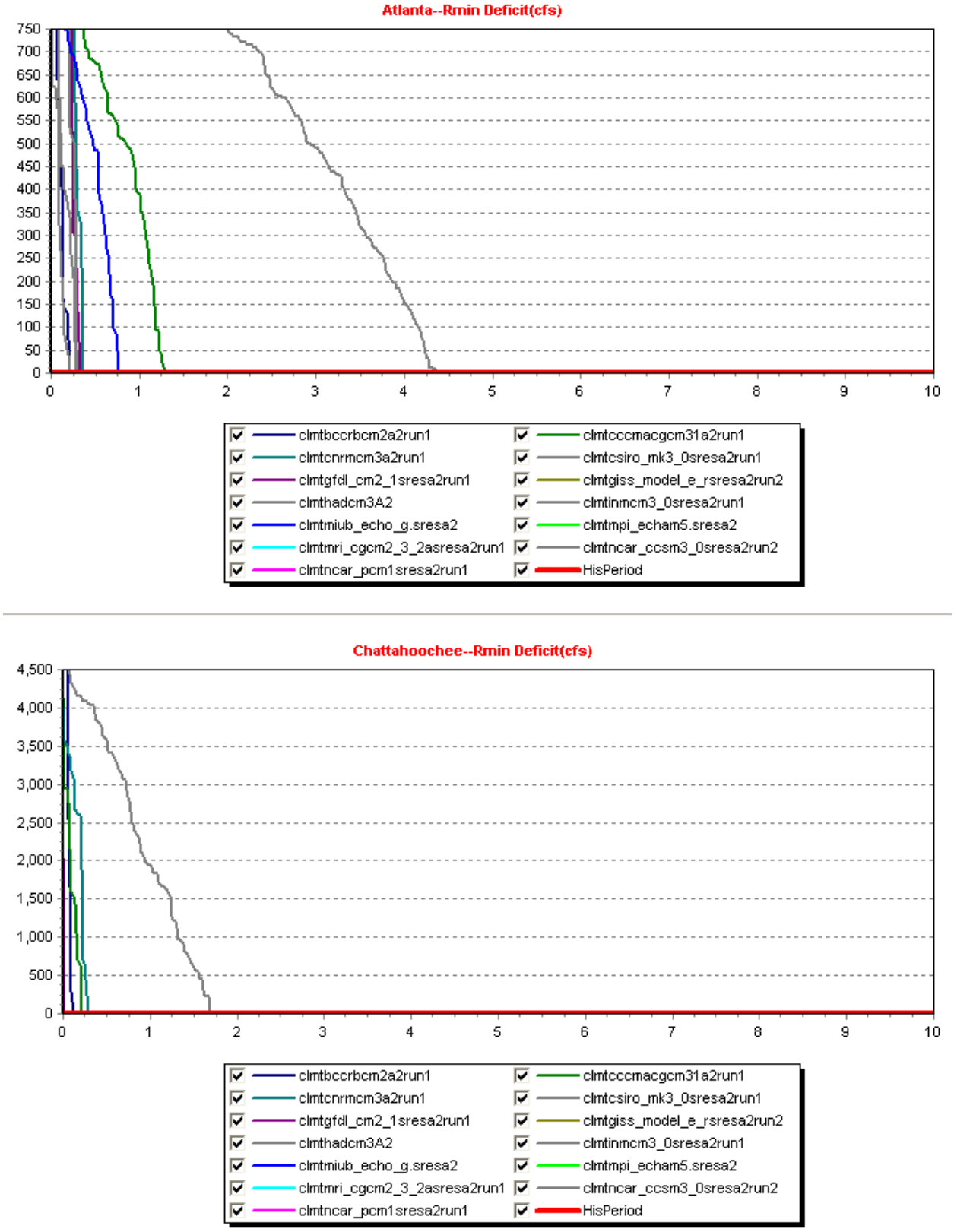

Figure 5.34: A2, 2007 Demands, Instream Flow Deficit Frequency Curves
(The horizontal axis shows frequencies up to 10%.)

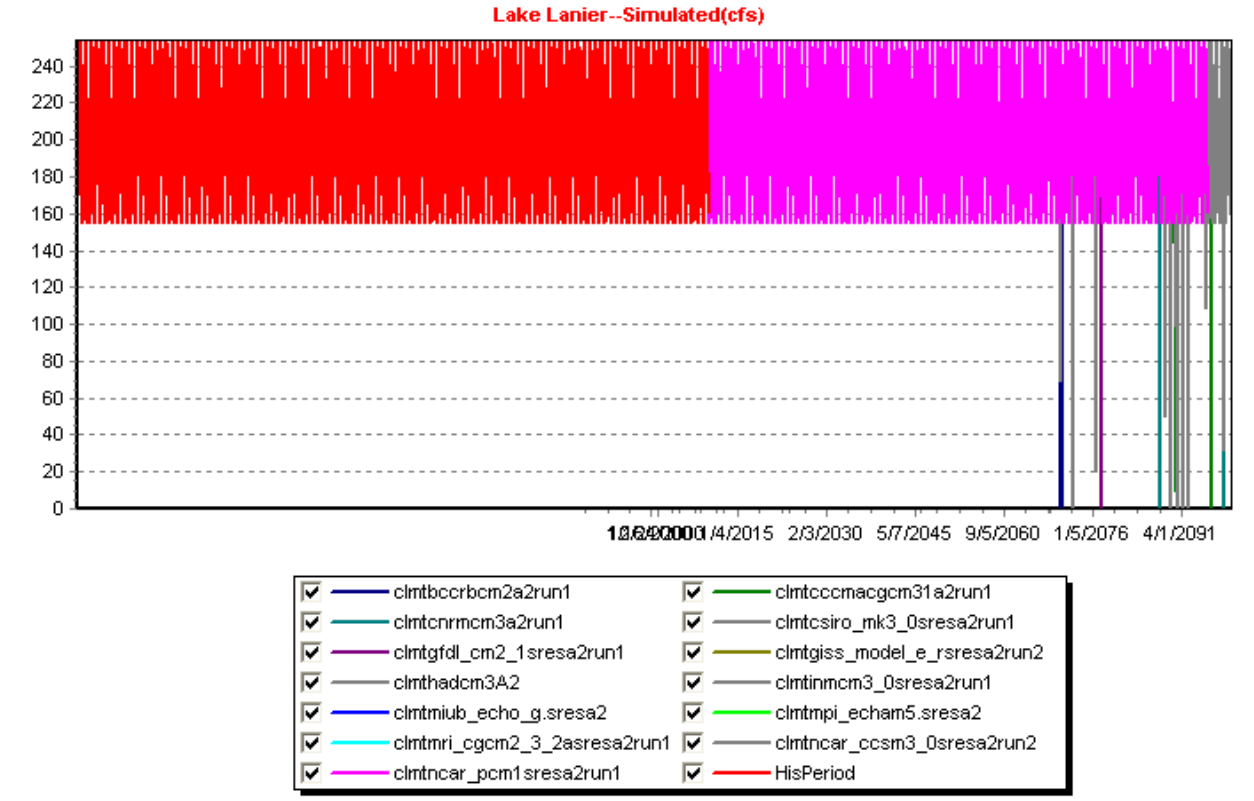

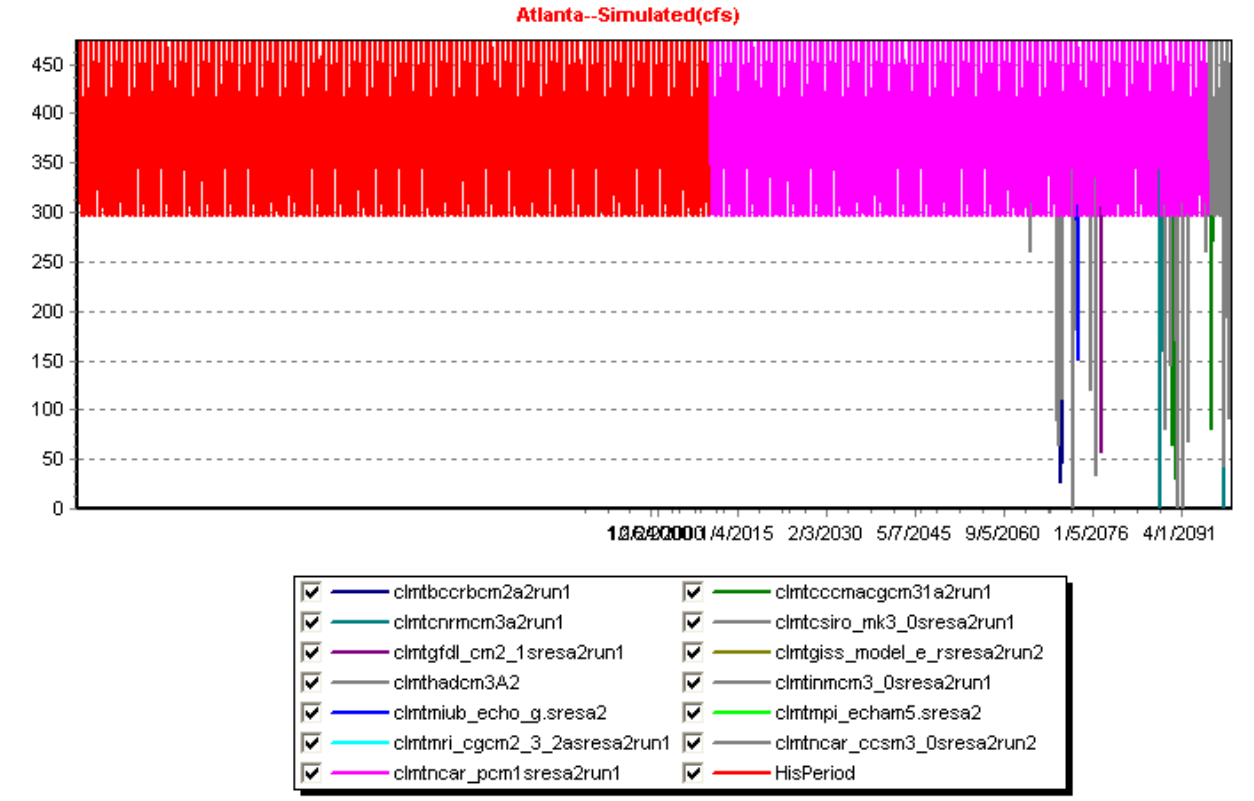

Figure 5.35: A2, 2007 Demands, Water Supply Sequences

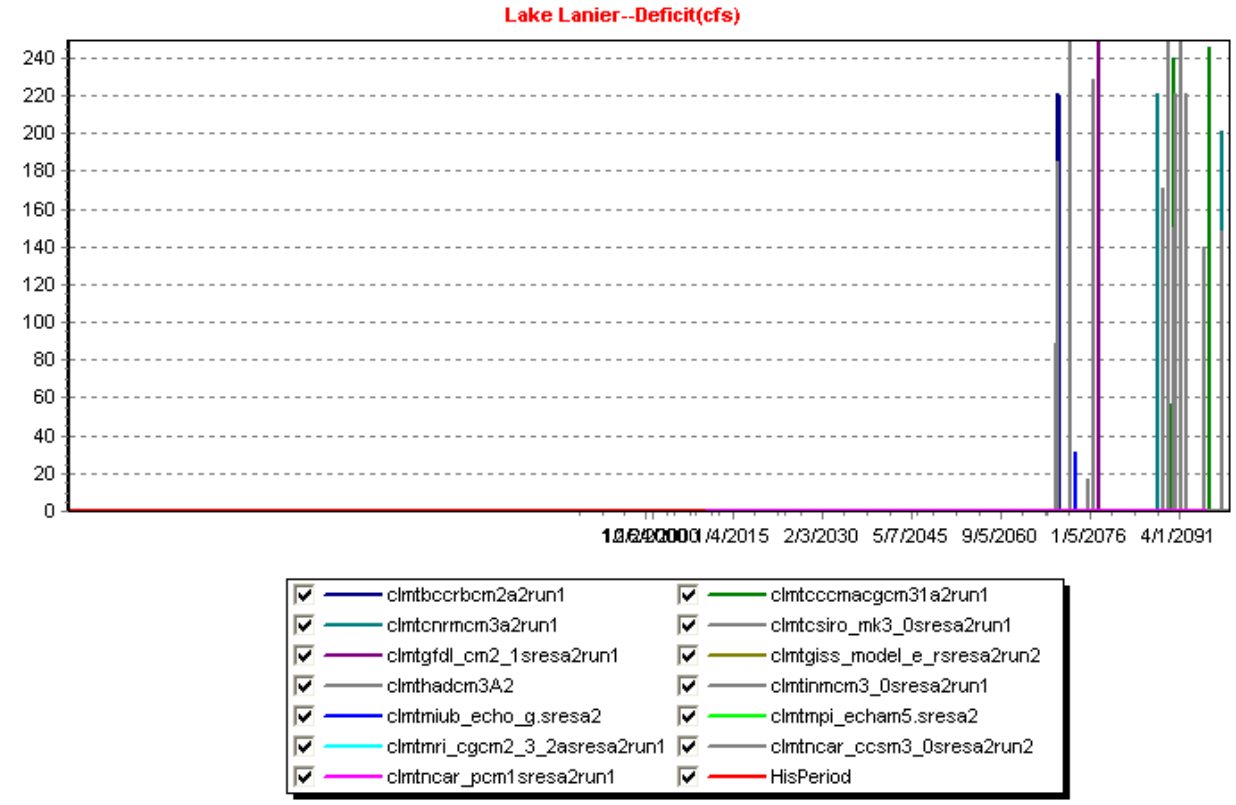

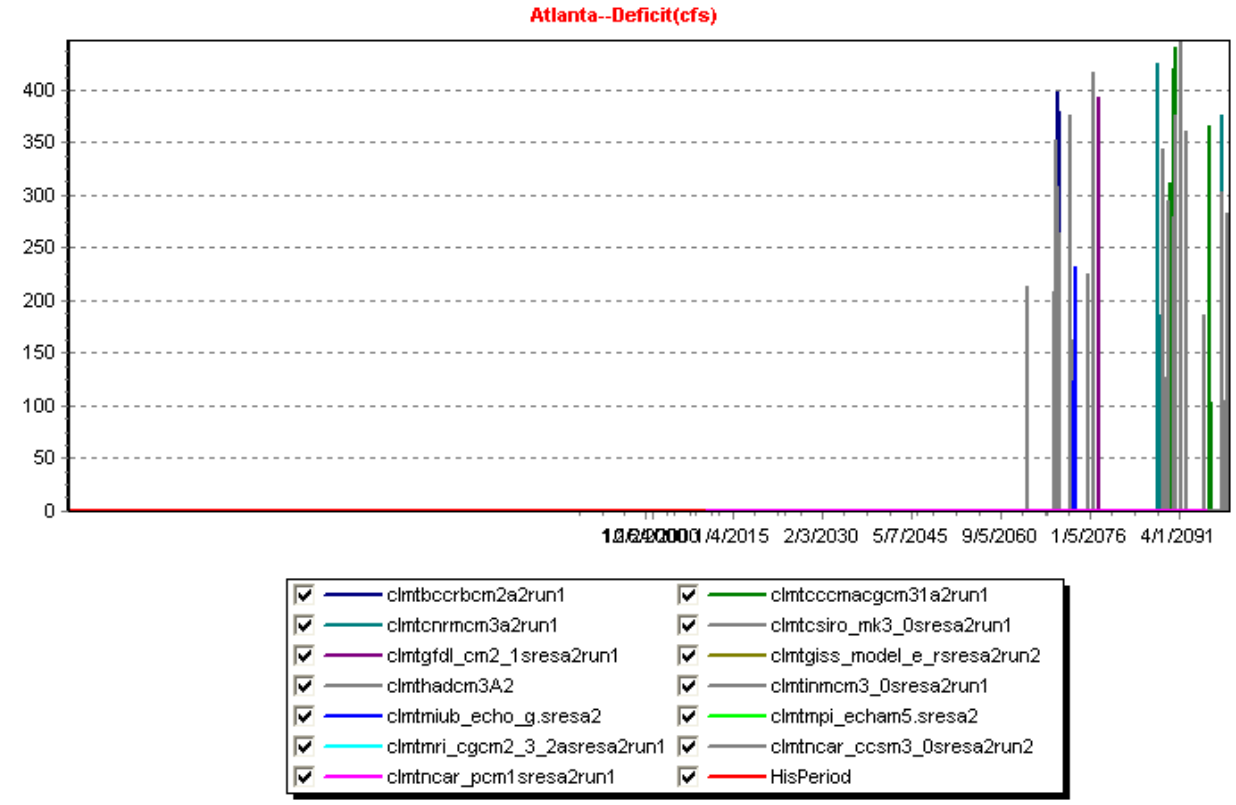

Figure 5.36: A2, 2007 Demands, Water Supply Deficit Sequences

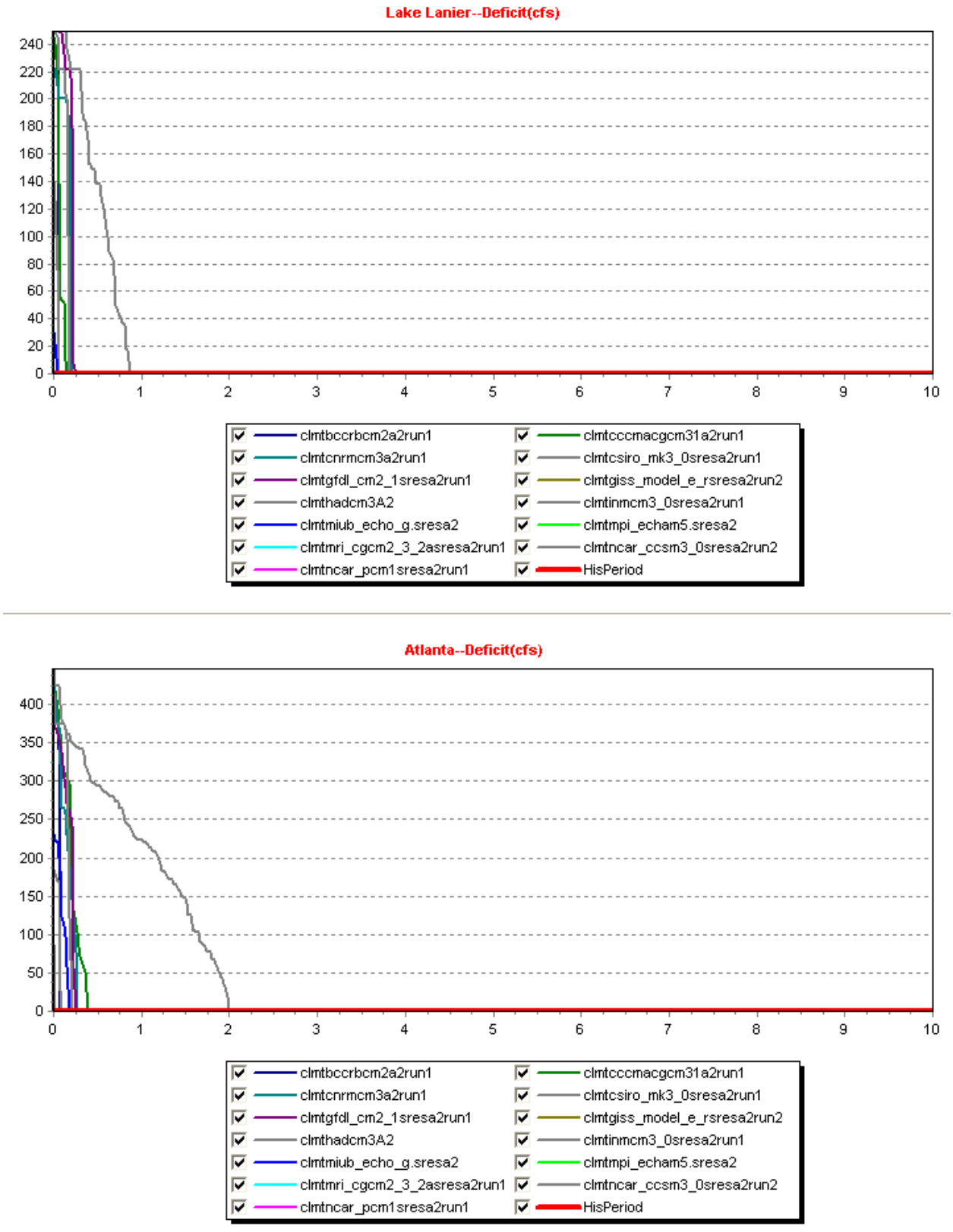

Figure 5.37: A2, 2007 Demands, Water Supply Deficit Frequency Curves
(The horizontal axis shows frequencies up to 10%.)

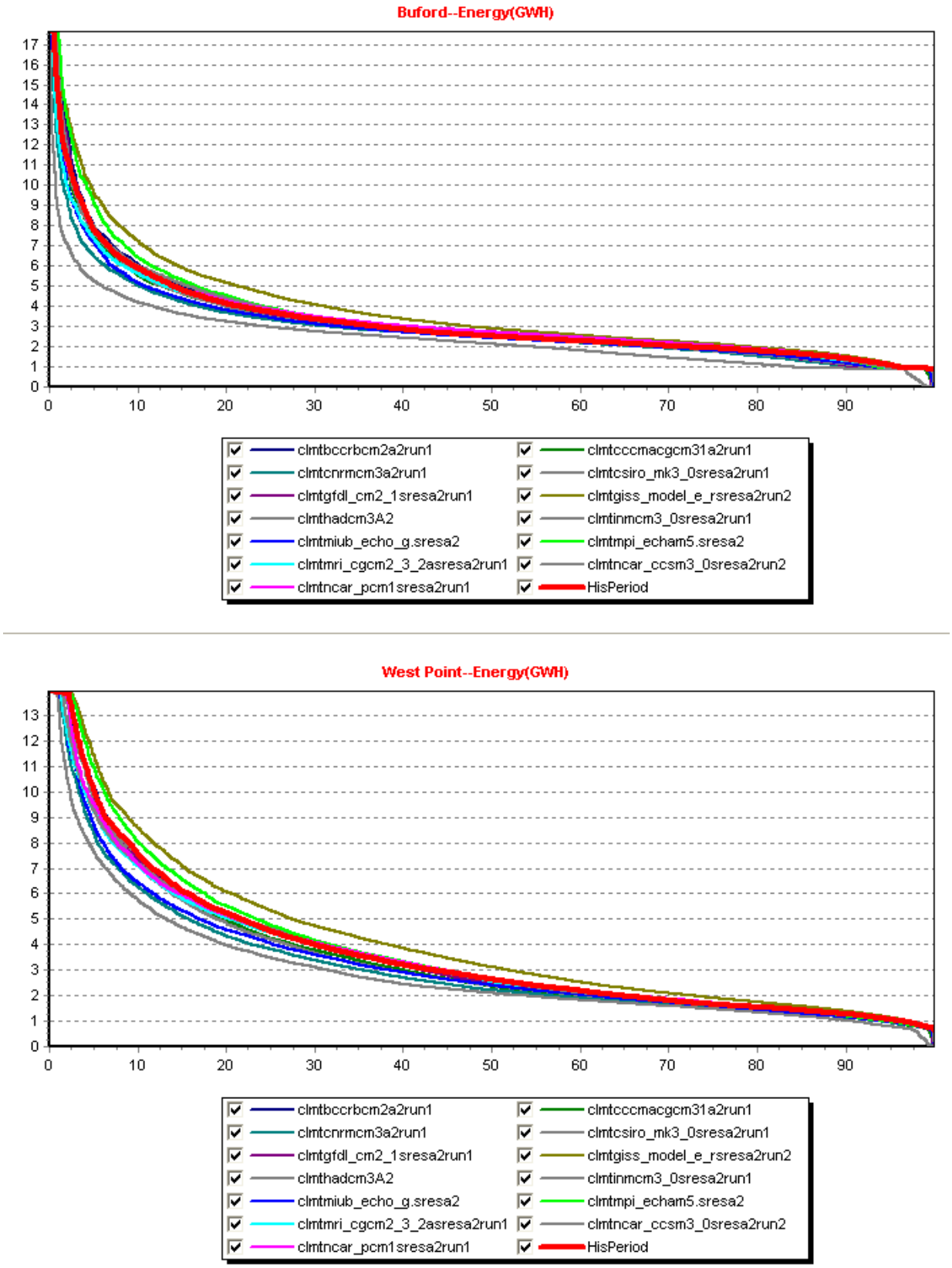

Figure 5.38: A2, 2007 Demands, Energy Generation Frequency Curves

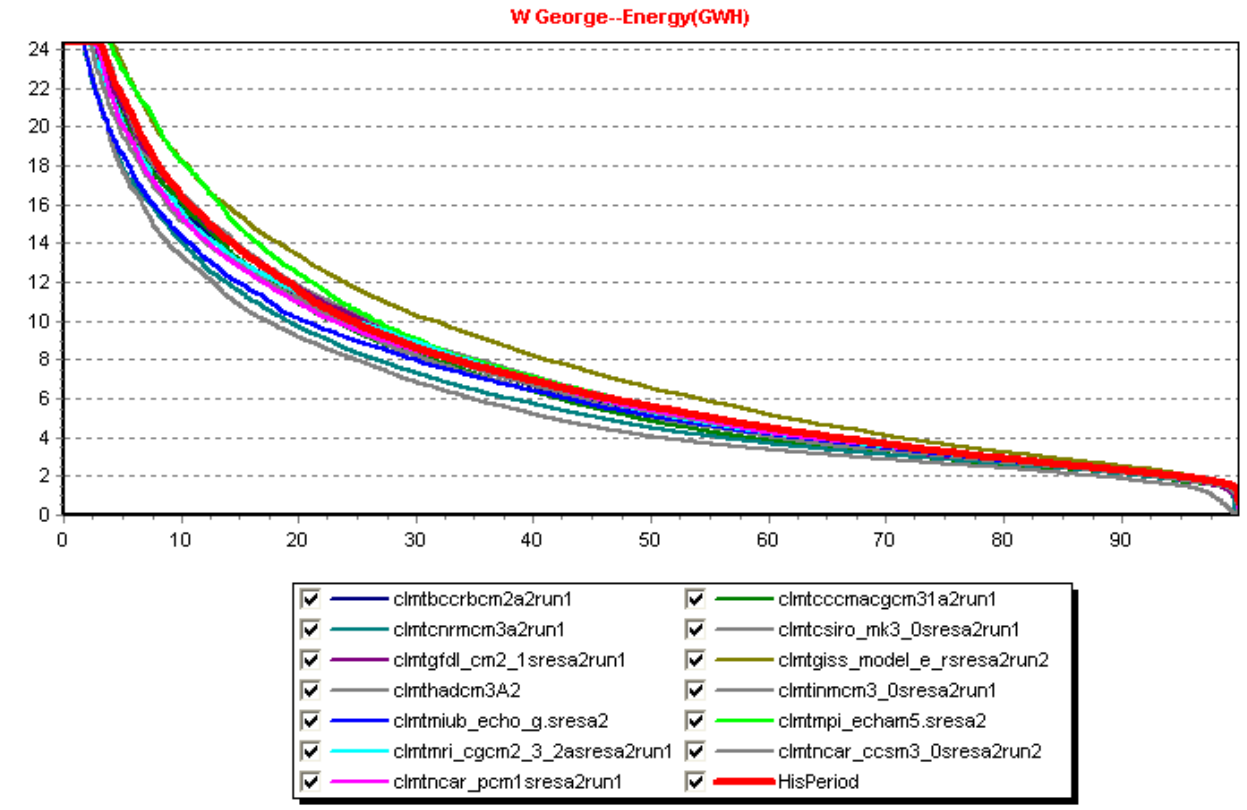

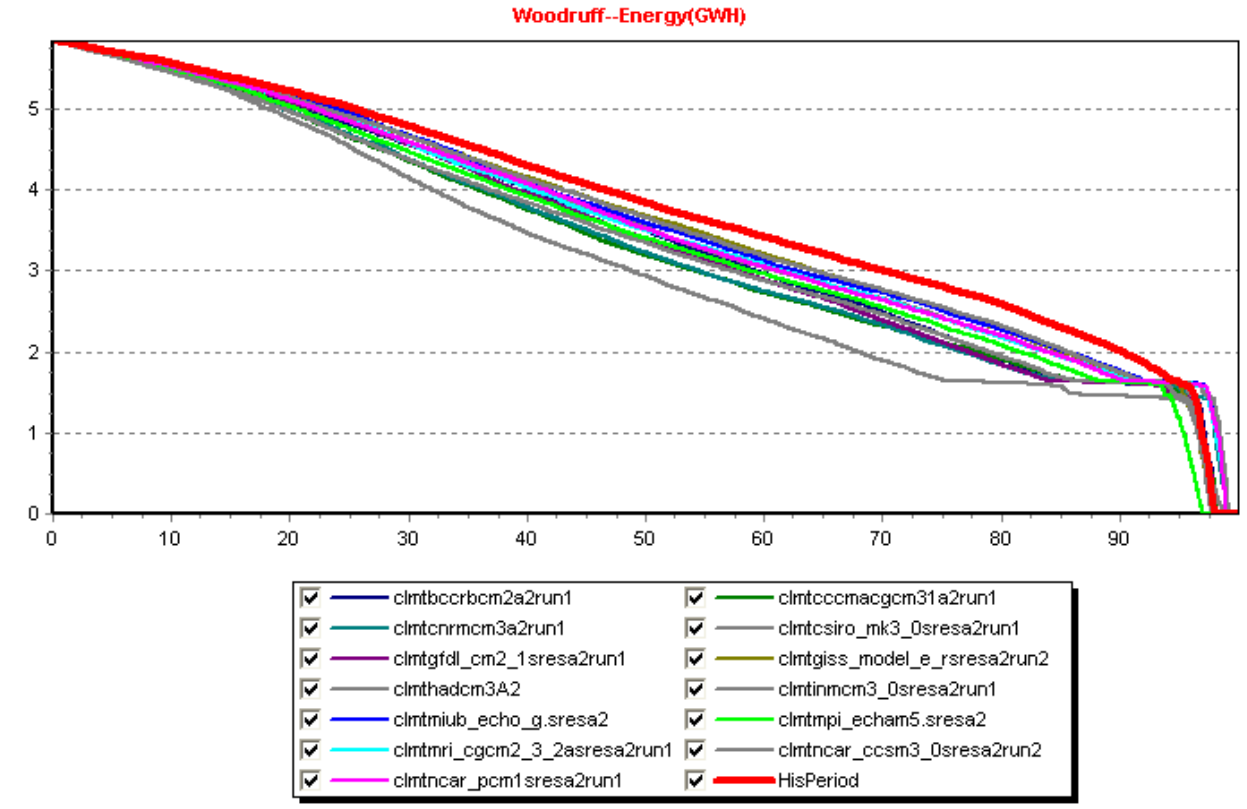

Figure 5.39: A2, 2007 Demands, Energy Generation Frequency Curves

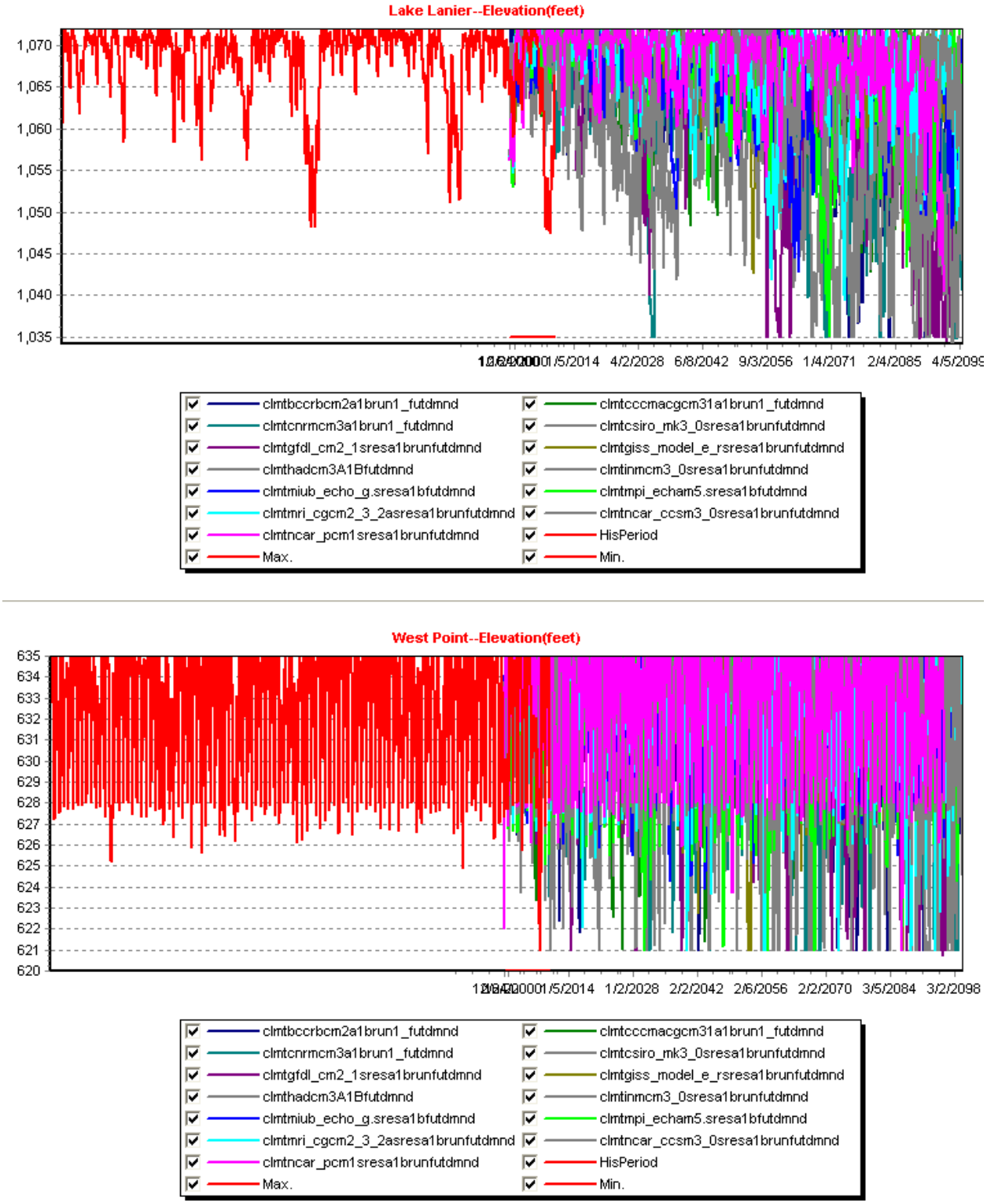

Figure 5.40: A1B, Future Demands, Reservoir Elevation Sequences

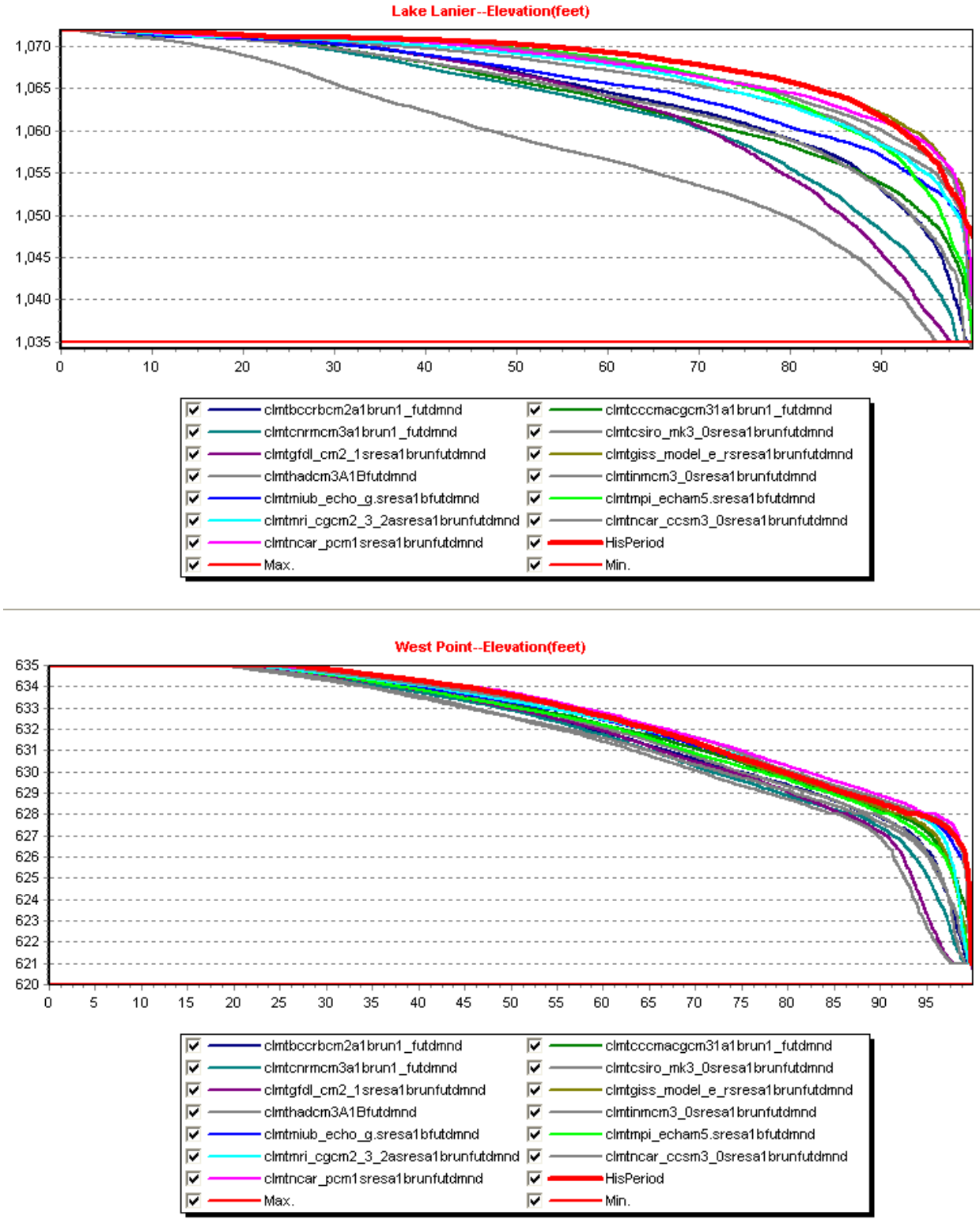

Figure 5.41: A1B, Future Demands, Reservoir Elevation Frequency Curves

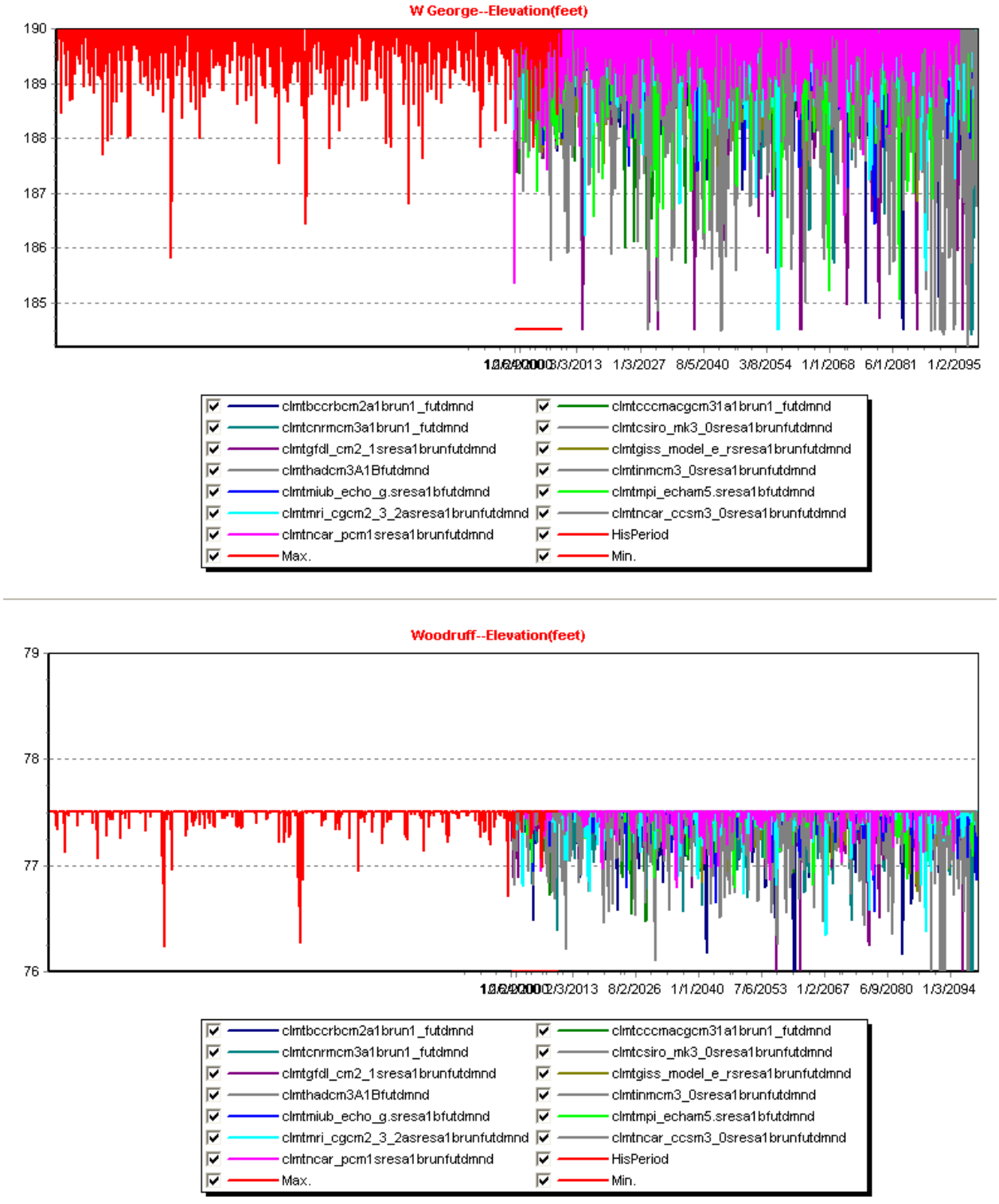

Figure 5.42: A1B, Future Demands, Reservoir Elevation Sequences

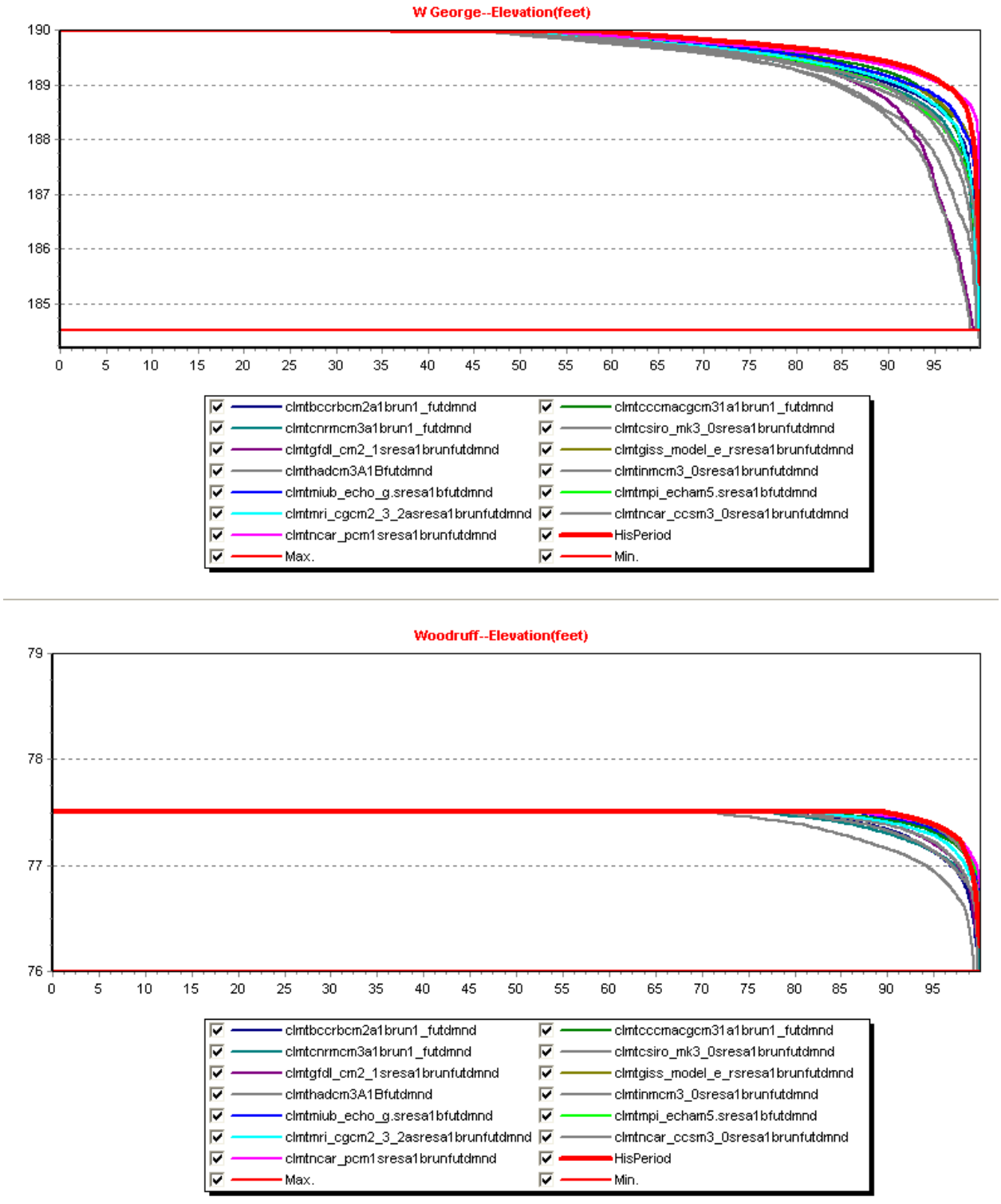

Figure 5.43: A1B, Future Demands, Reservoir Elevation Frequency Curves

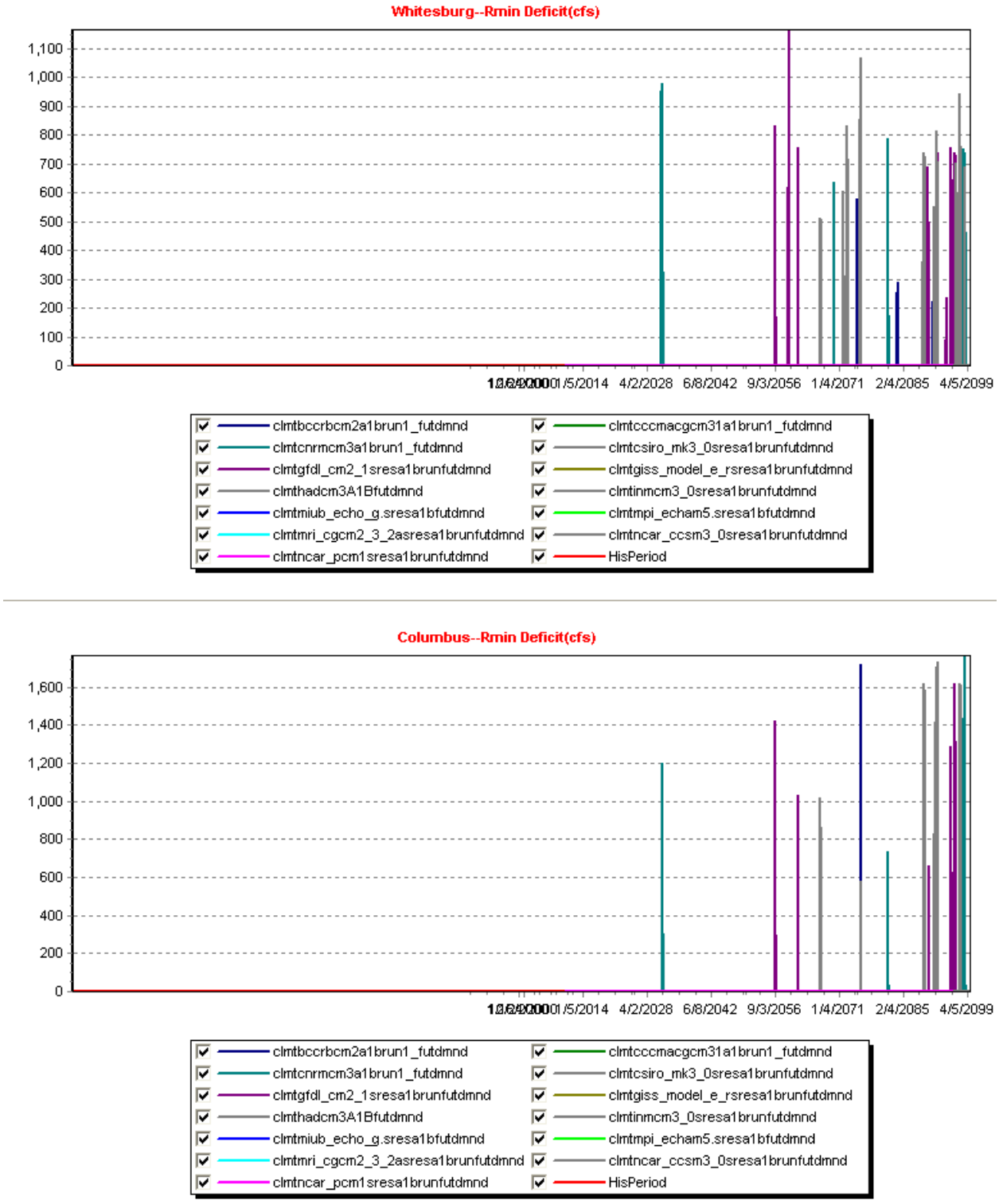

Figure 5.44: A1B, Future Demands, Instream Flow Deficit Sequences

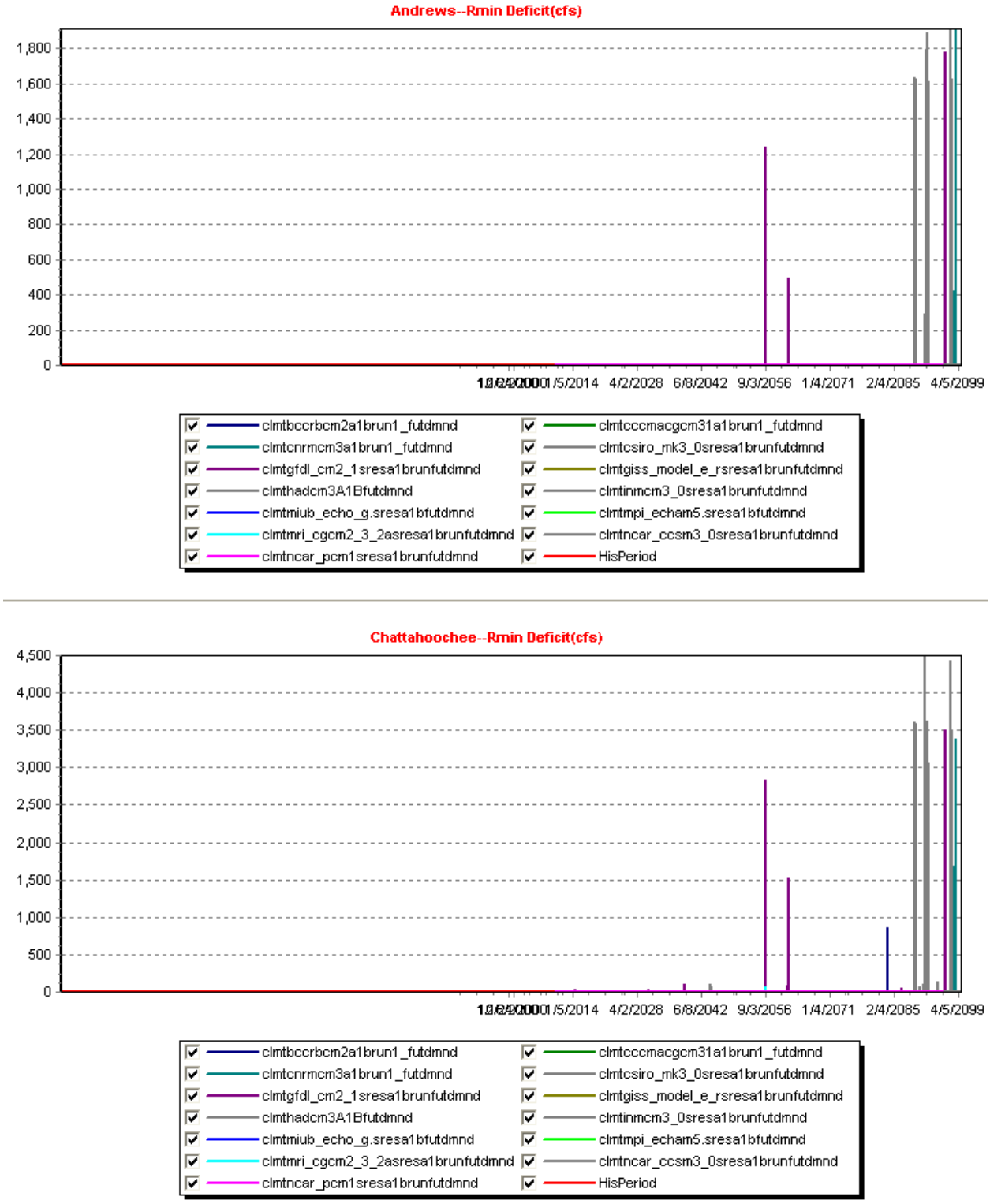

Figure 5.45: A1B, Future Demands, Instream Flow Deficit Sequences

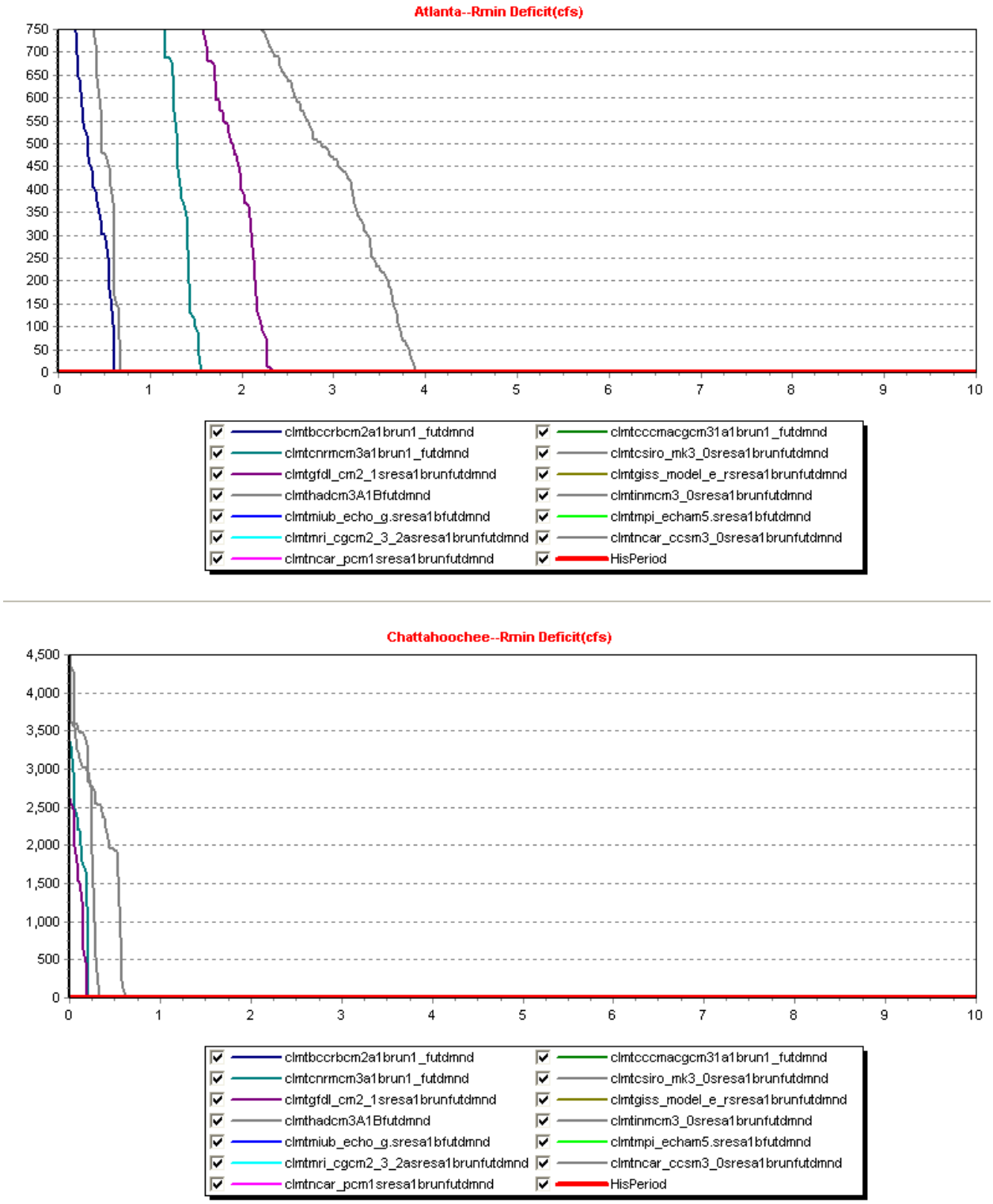

Figure 5.46: A1B, Future Demands, Instream Flow Deficit Frequency Curves (The horizontal axis shows frequencies up to 10%.)

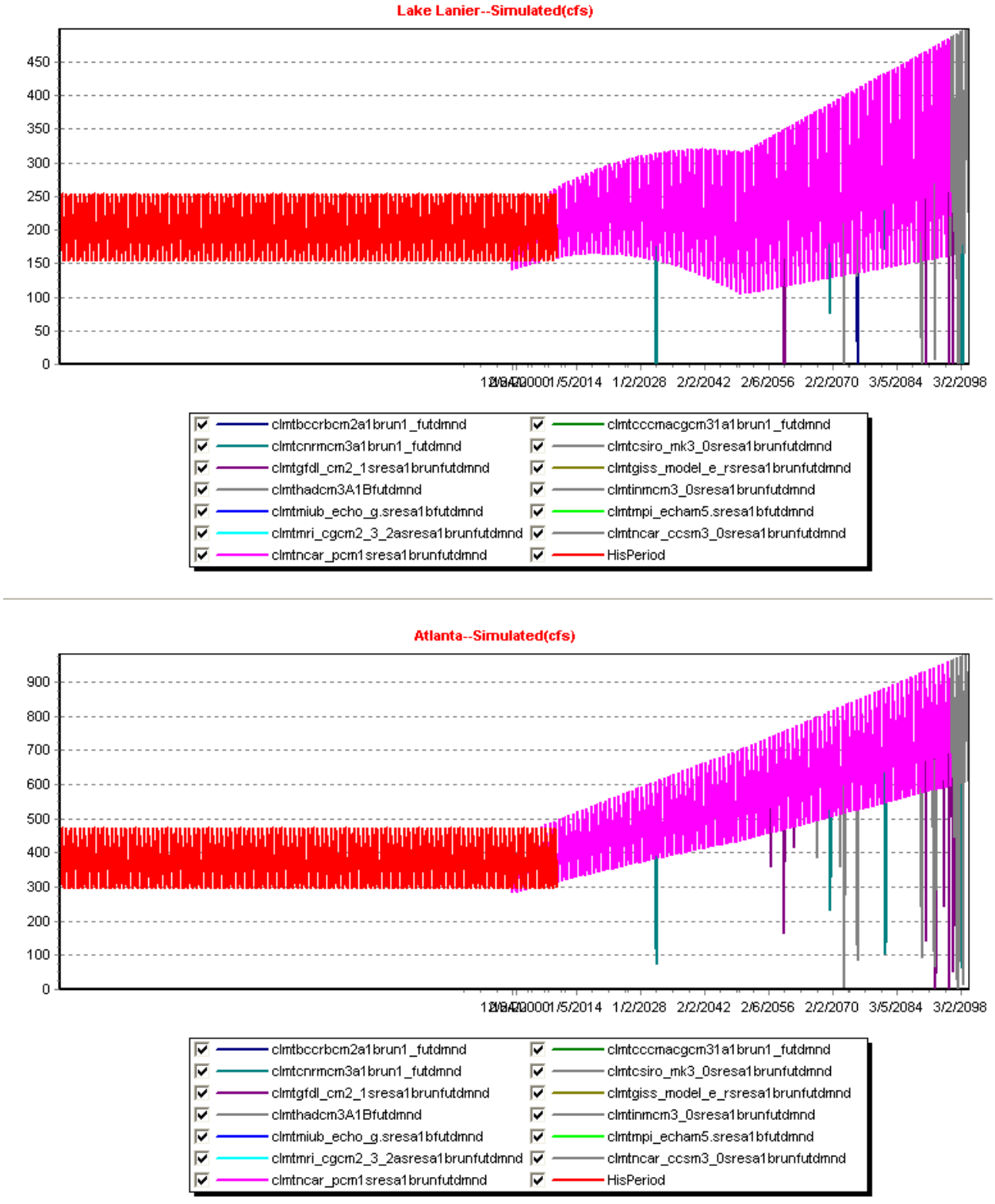

Figure 5.47: A1B, Future Demands, Water Supply Sequences

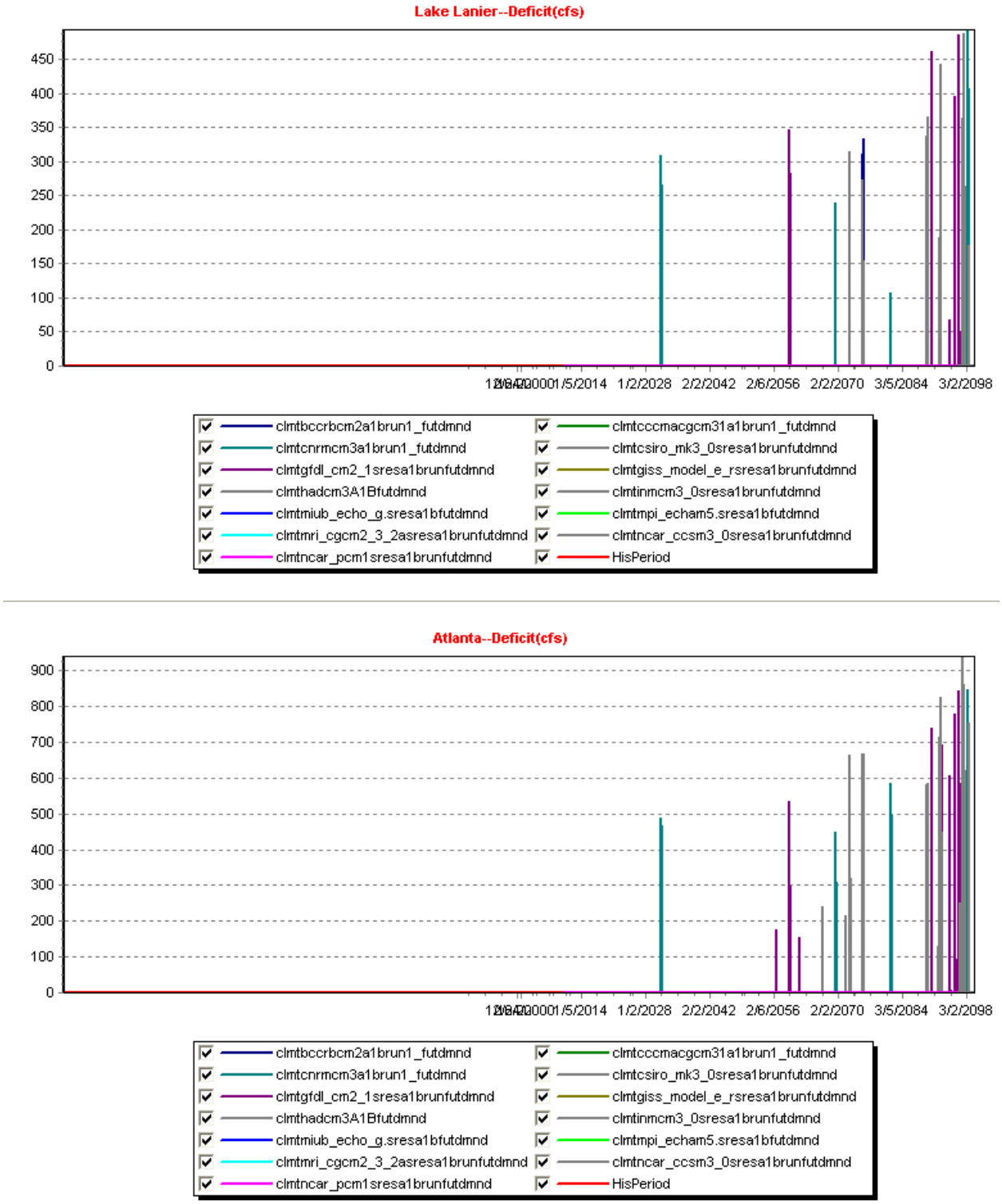

Figure 5.48: A1B, Future Demands, Water Supply Deficit Sequences

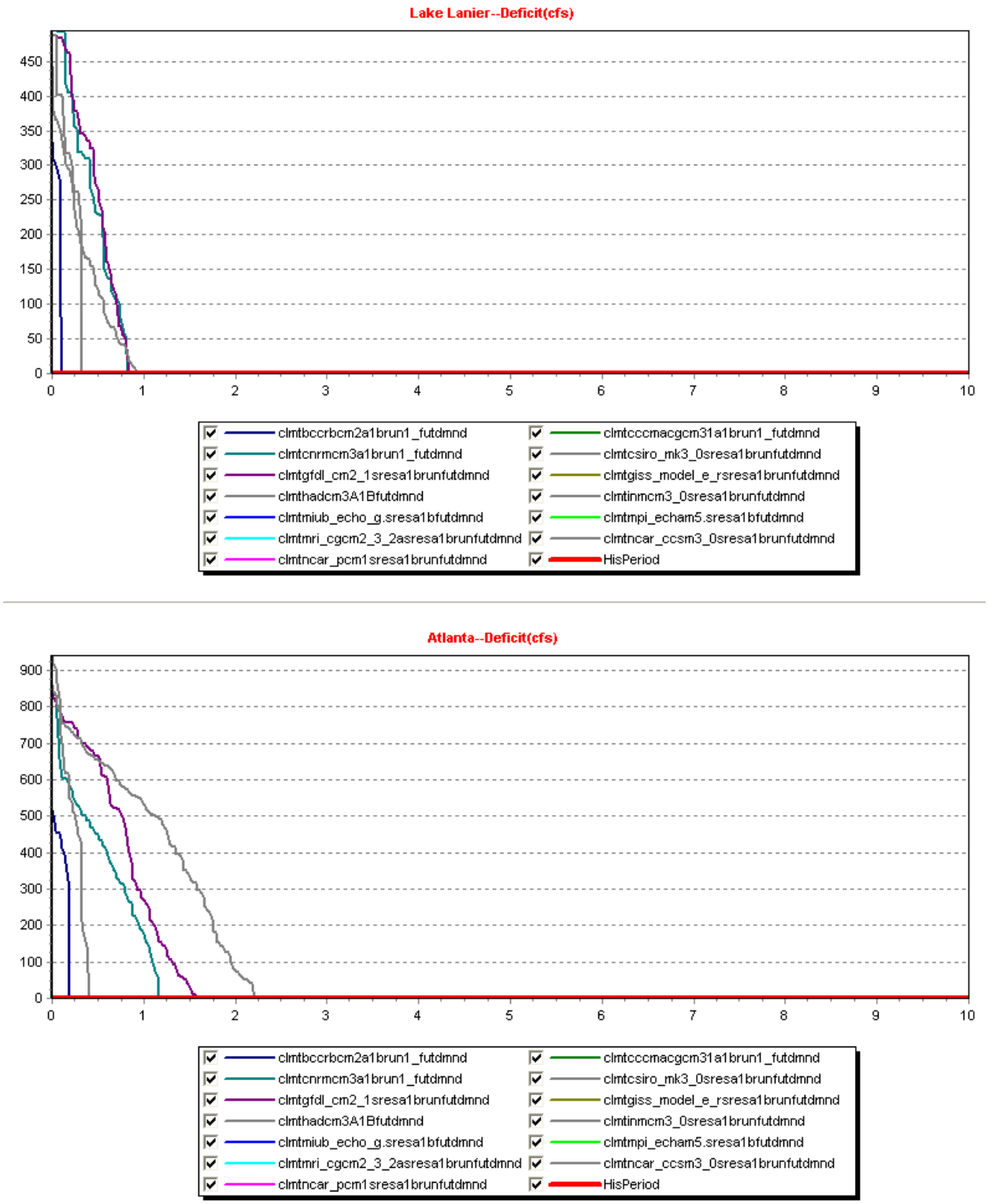

Figure 5.49: A1B, Future Demands, Water Supply Deficit Frequency Curves
(The horizontal axis shows frequencies up to 10%.)

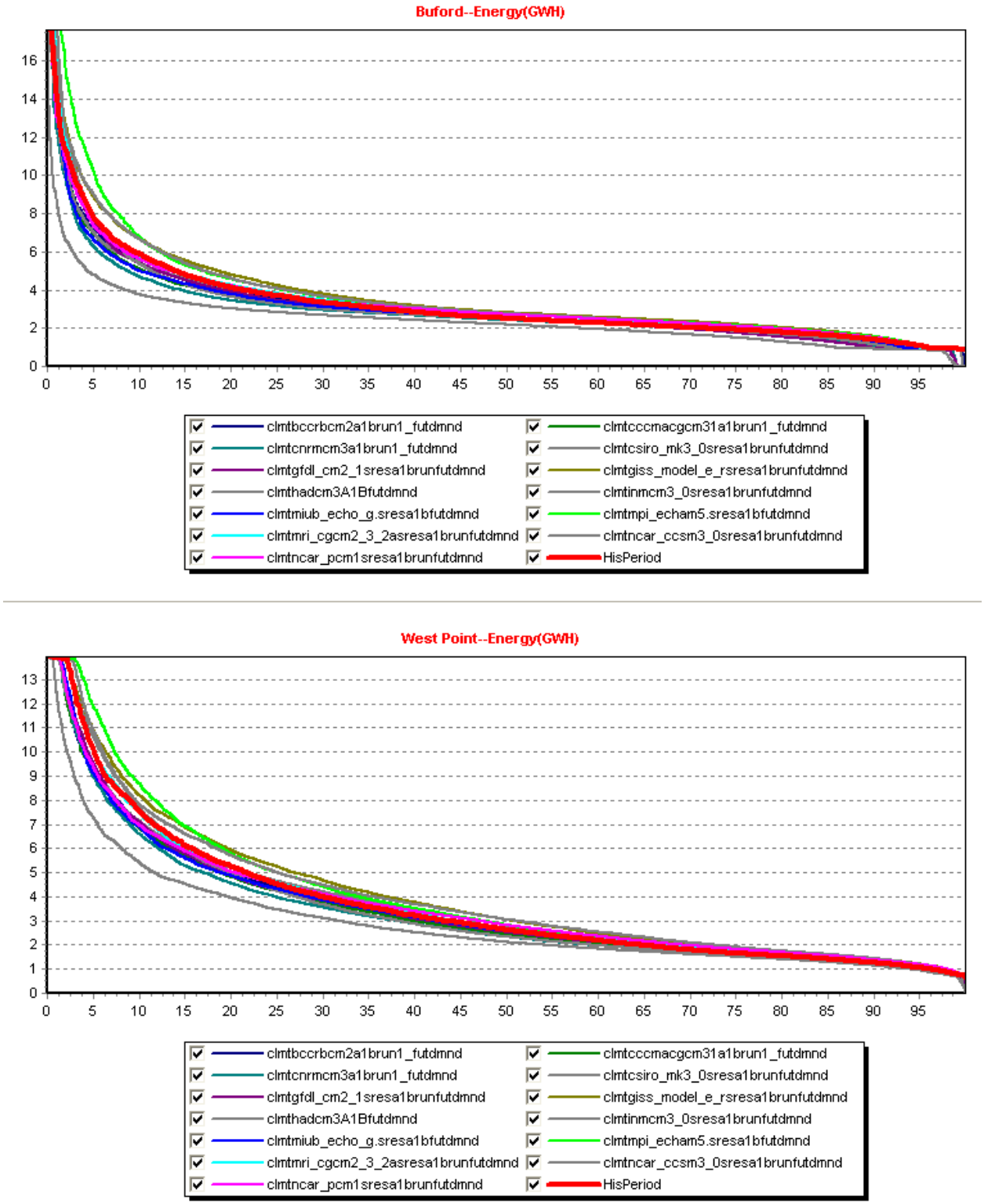

Figure 5.50: A1B, Future Demands, Energy Generation Frequency Curves

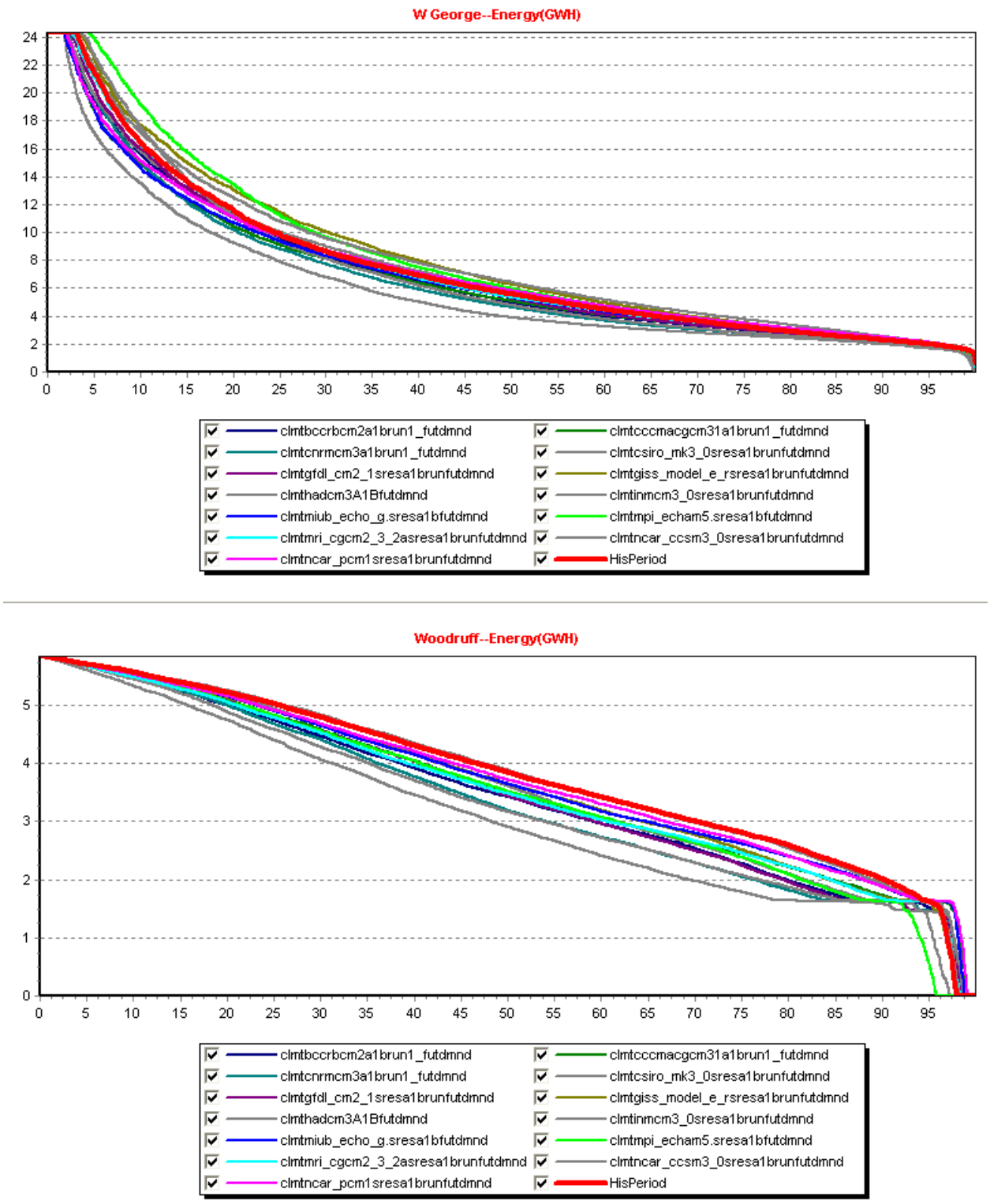

Figure 5.51: A1B, Future Demands, Energy Generation Frequency Curves

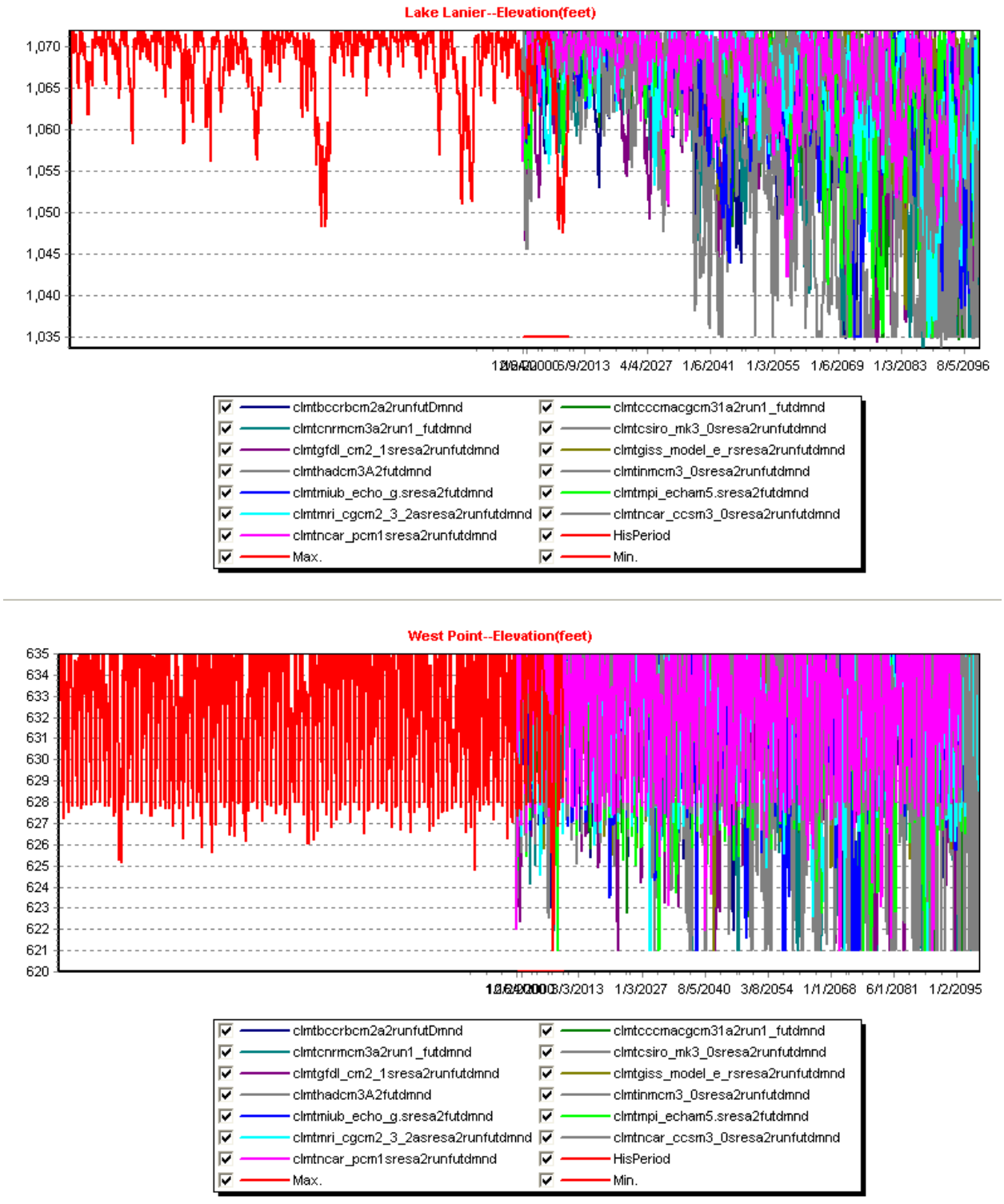

Figure 5.52: A2, Future Demands, Reservoir Elevation Sequences

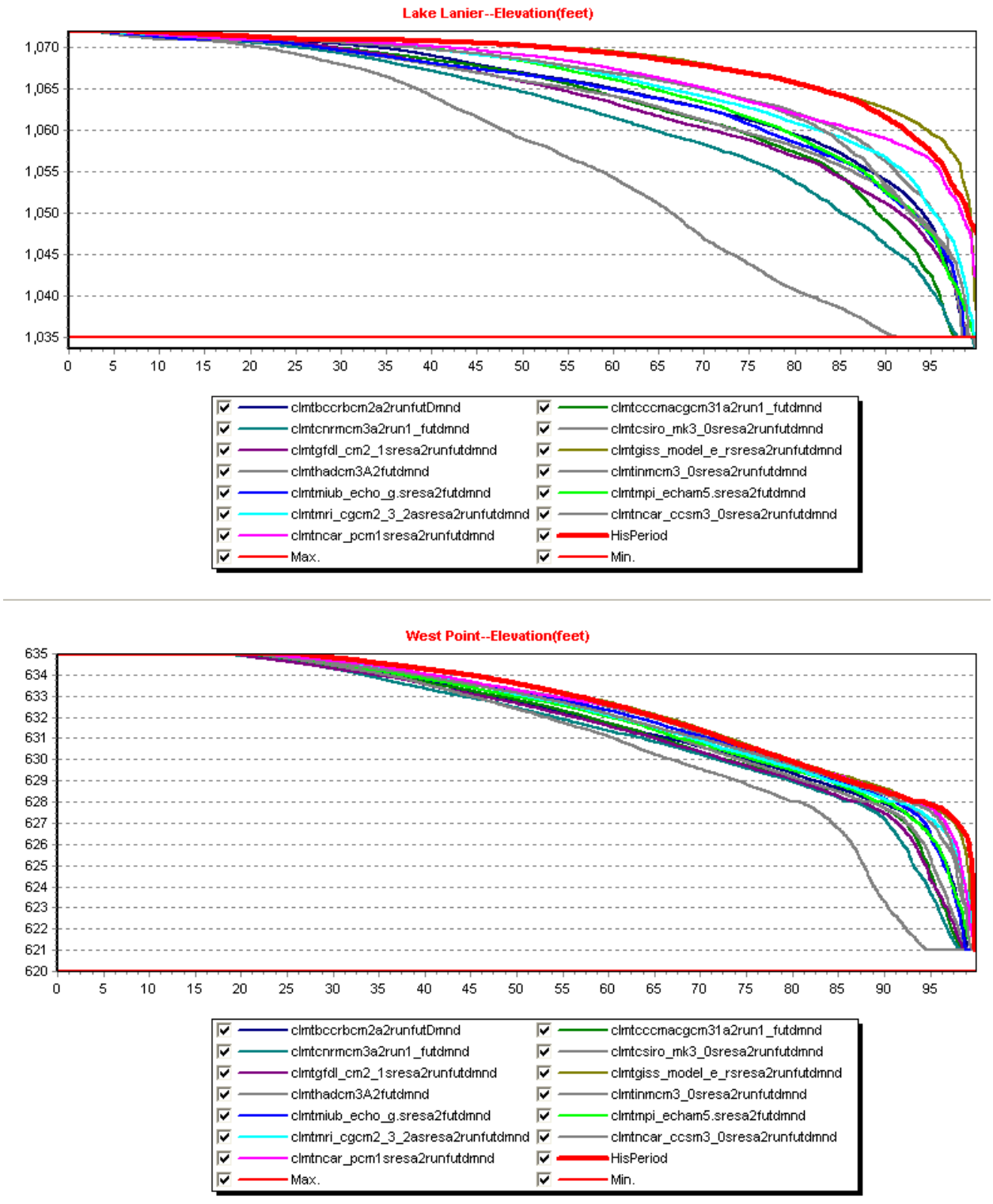

Figure 5.53: A2, Future Demands, Reservoir Elevation Frequency Curves

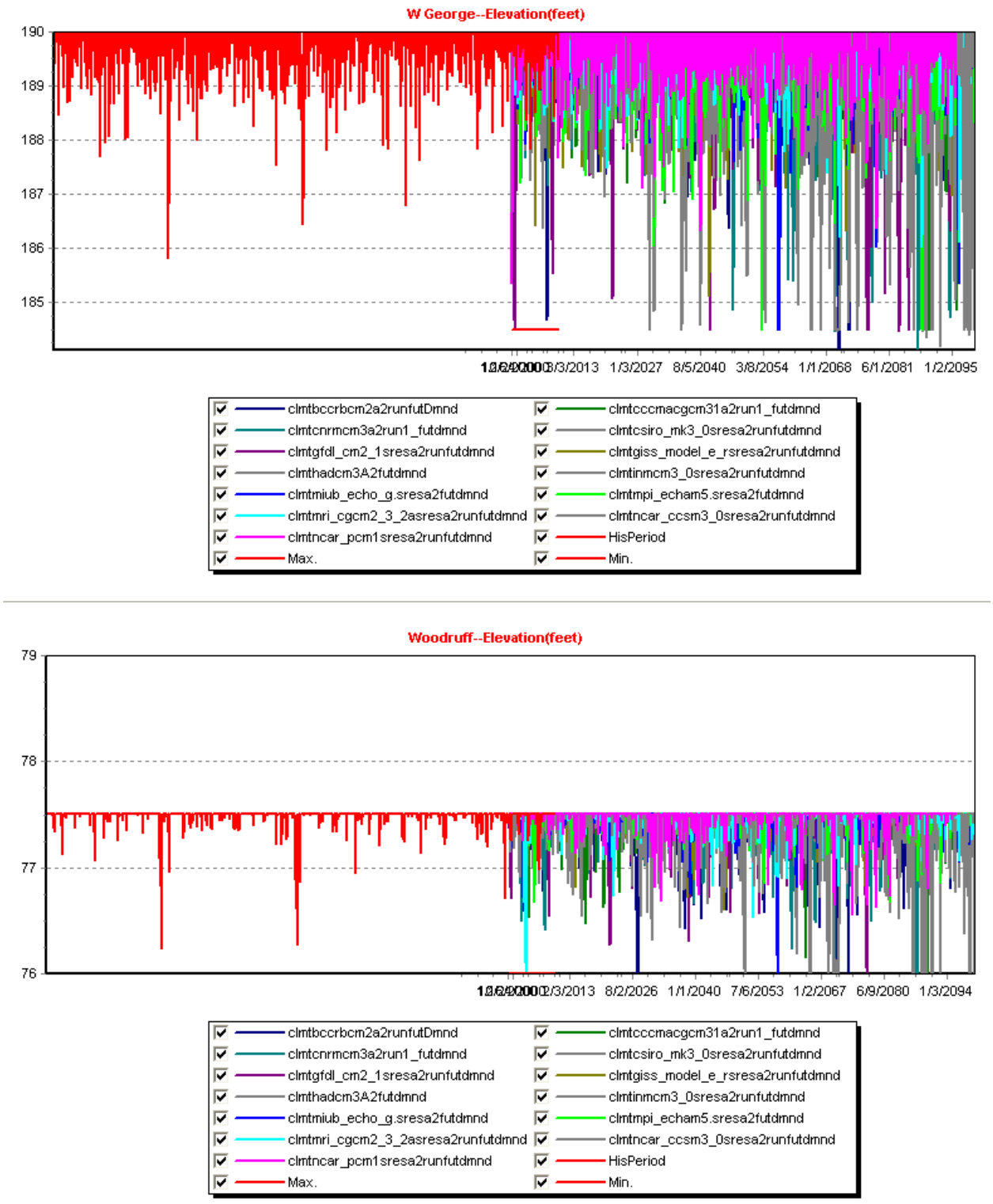

Figure 5.54: A2, Future Demands, Reservoir Elevation Sequences

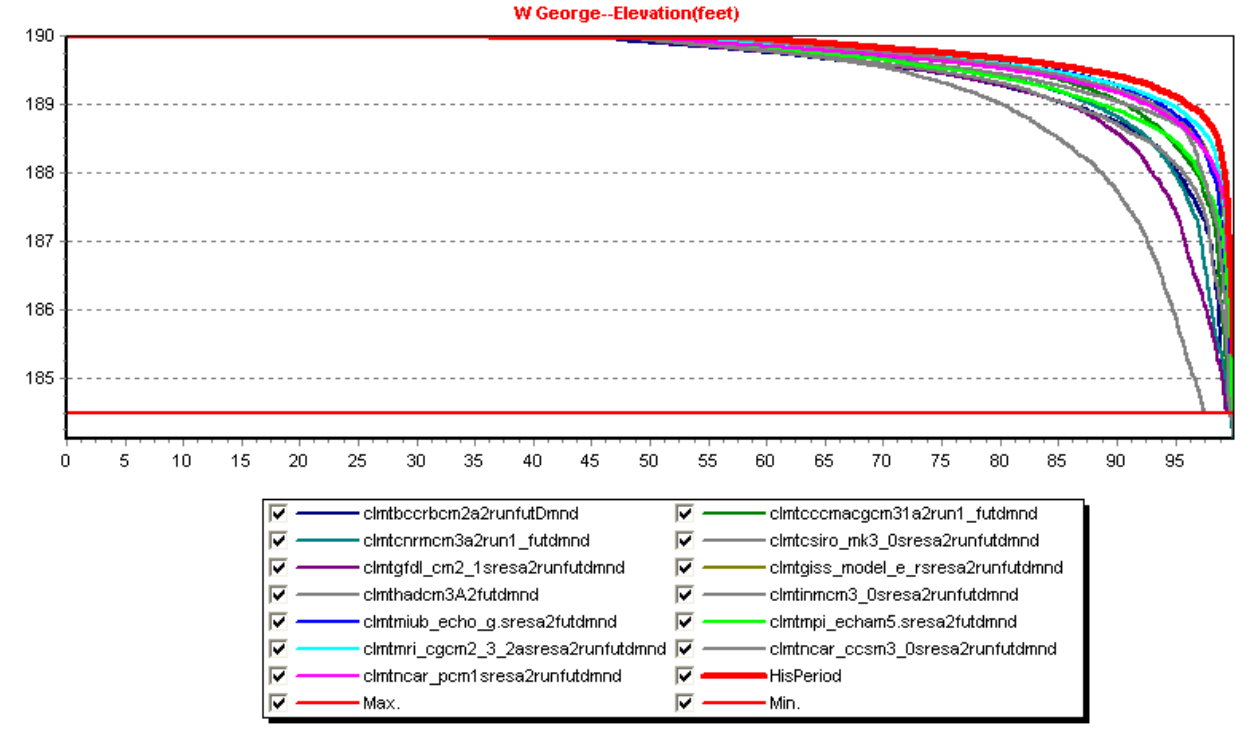

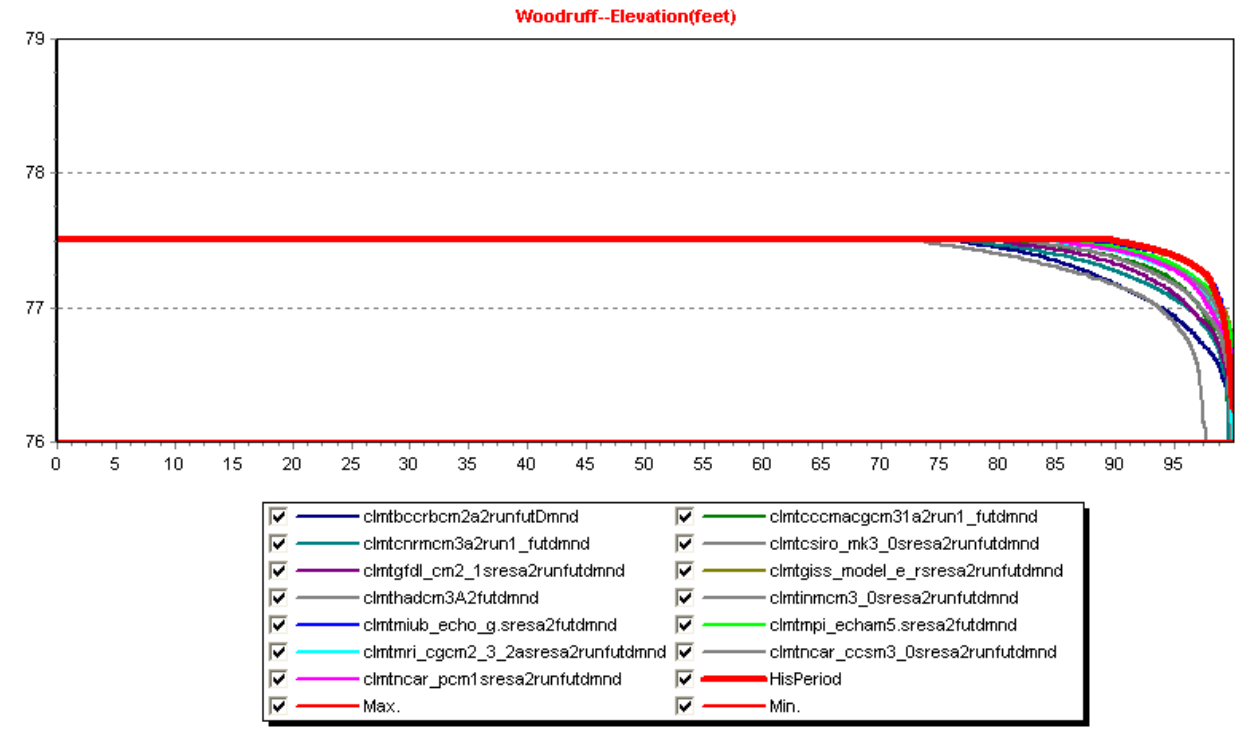

Figure 5.55: A2, Future Demands, Reservoir Elevation Frequency Curves

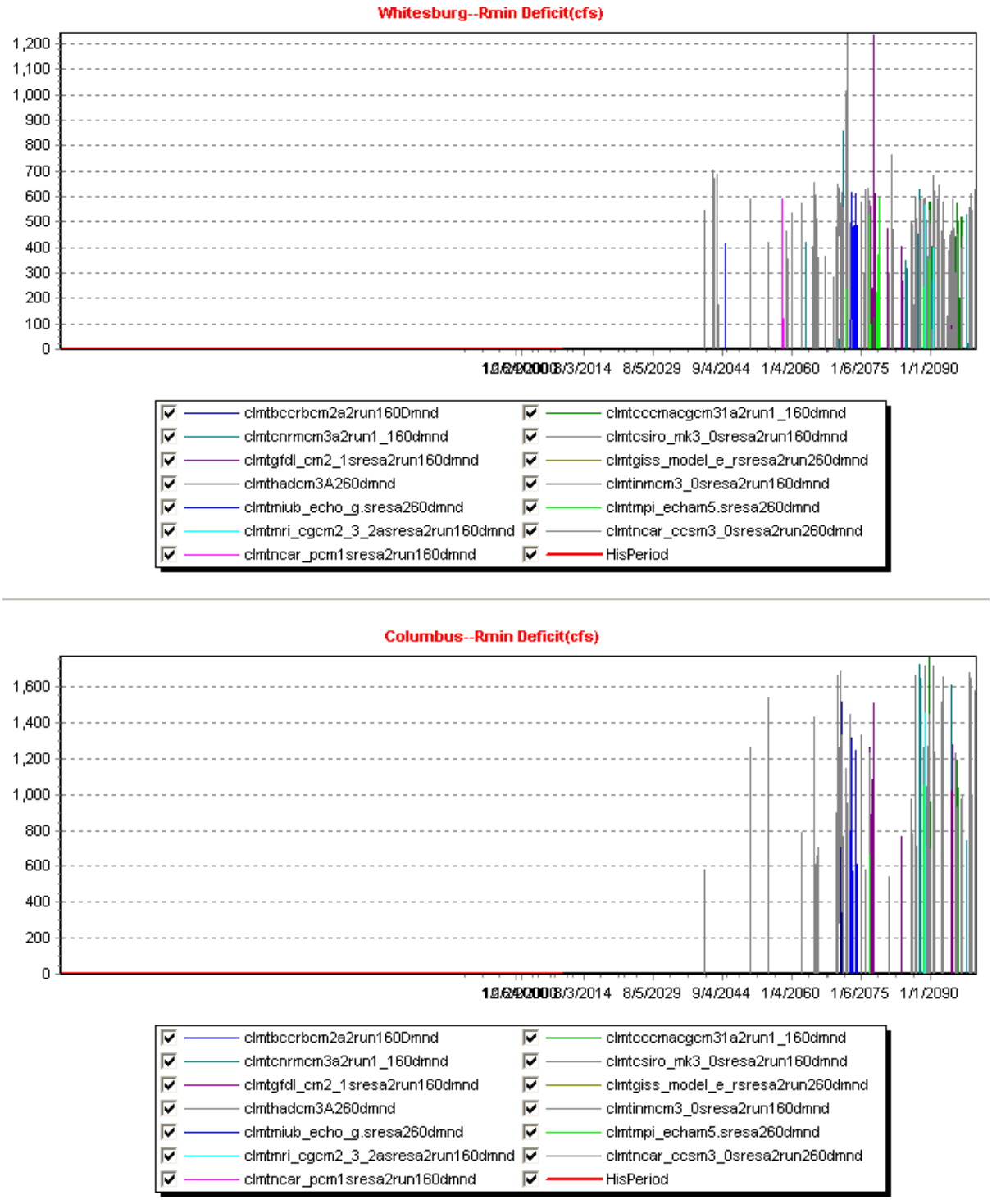

Figure 5.56: A2, Future Demands, Instream Flow Deficit Sequences

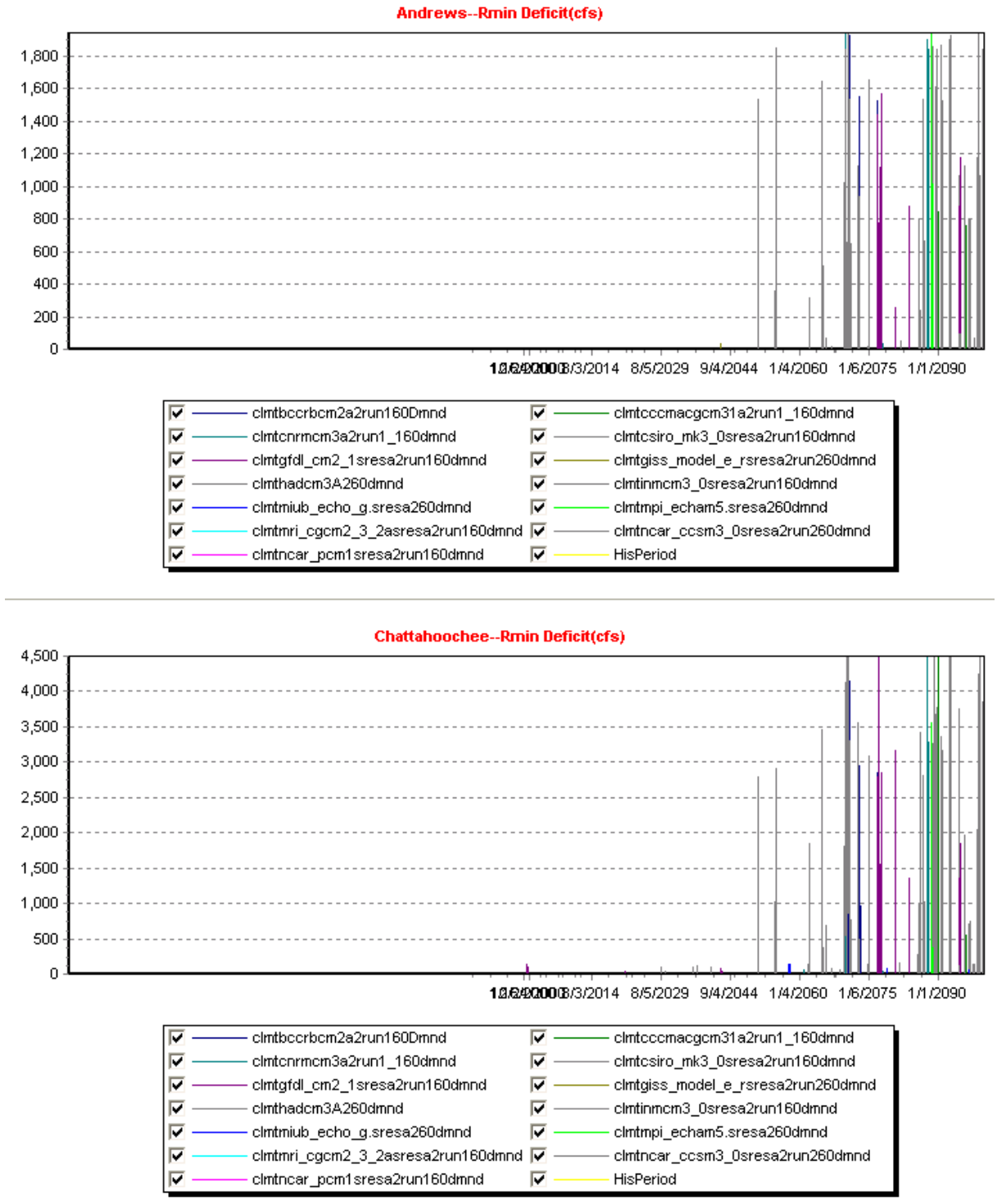

Figure 5.57: A2, Future Demands, Instream Flow Deficit Sequences

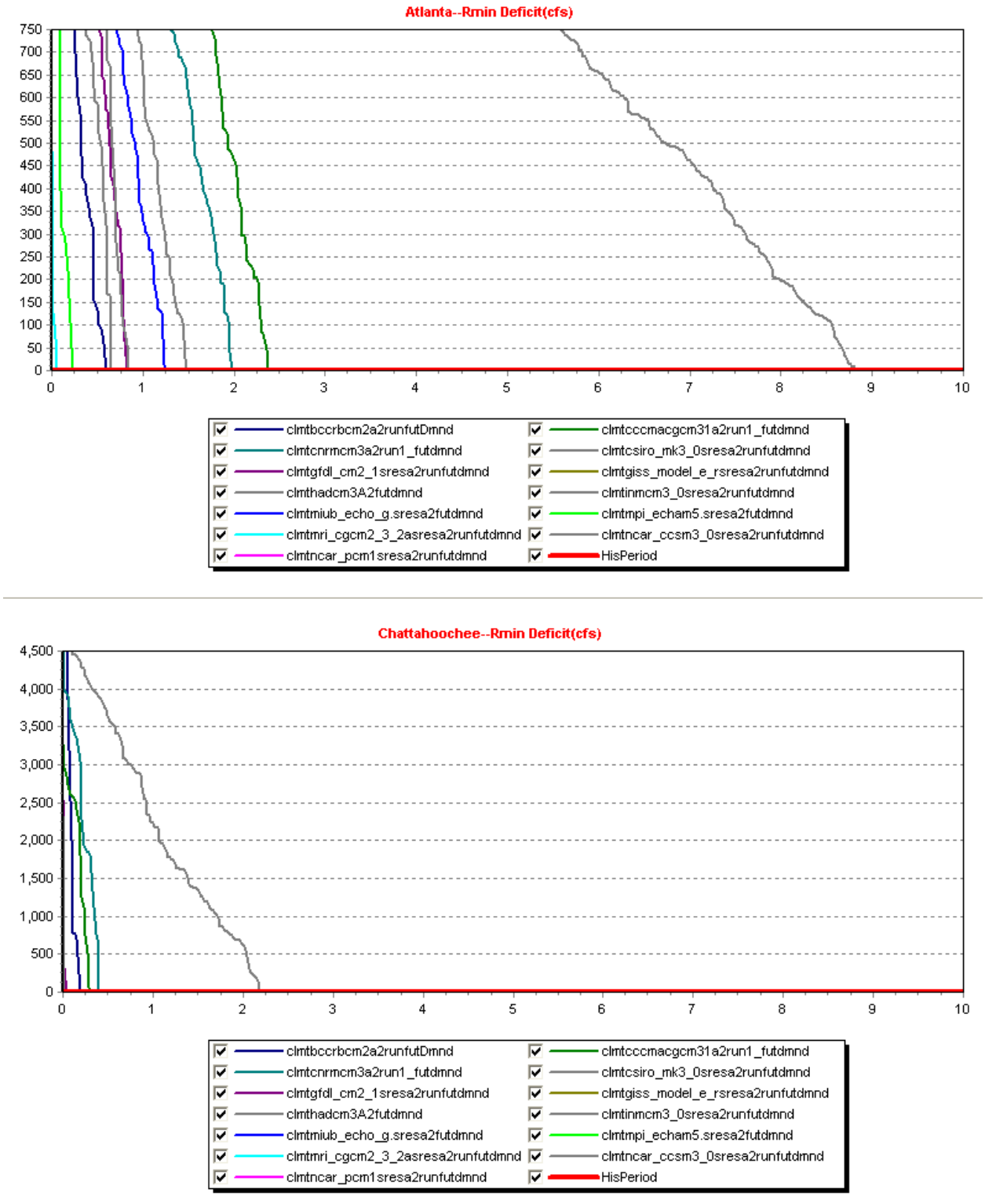

Figure 5.58: A2, Future Demands, Instream Flow Deficit Frequency Curves (The horizontal axis shows frequencies up to 10%.)

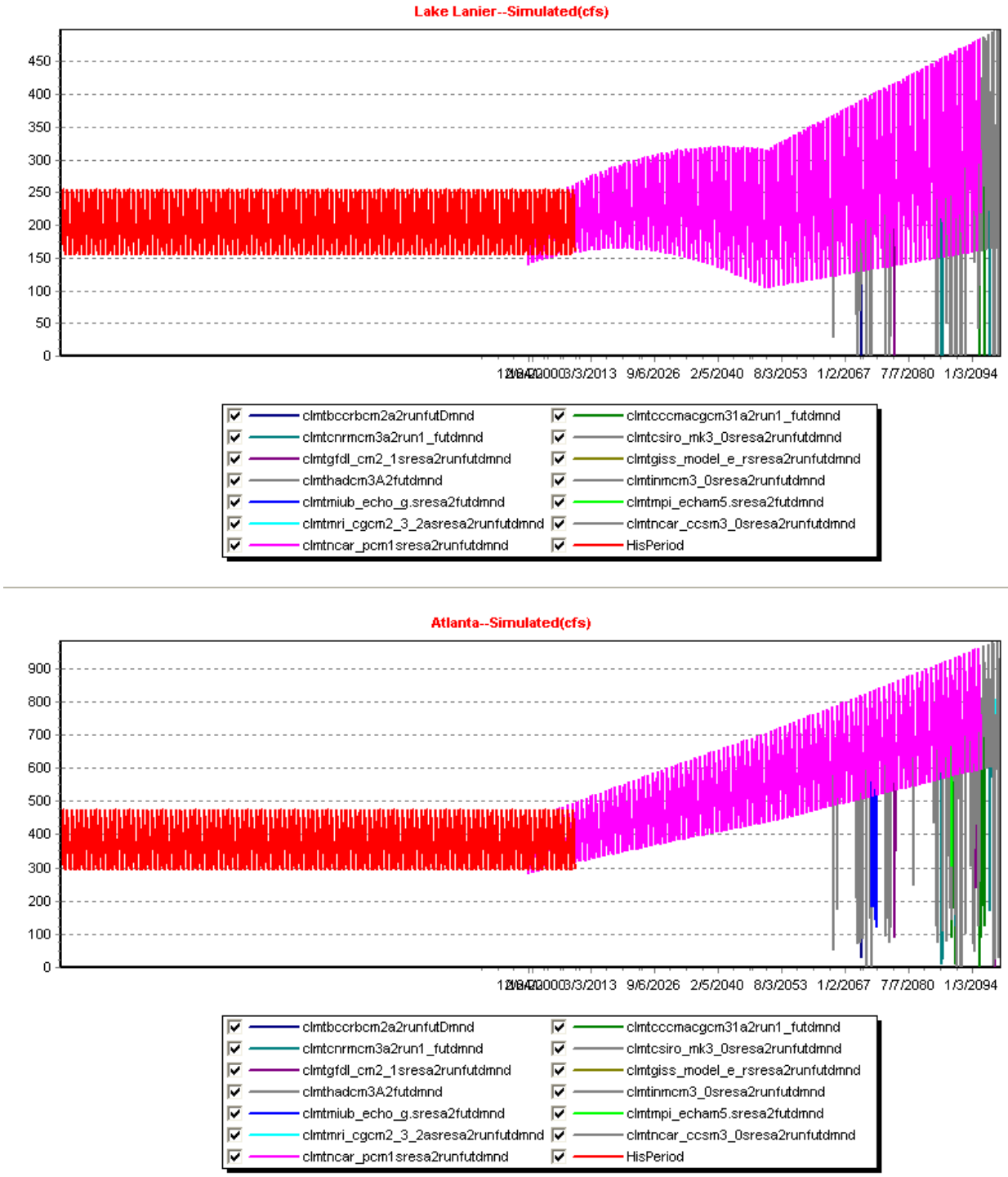

Figure 5.59: A2, Future Demands, Water Supply Sequences

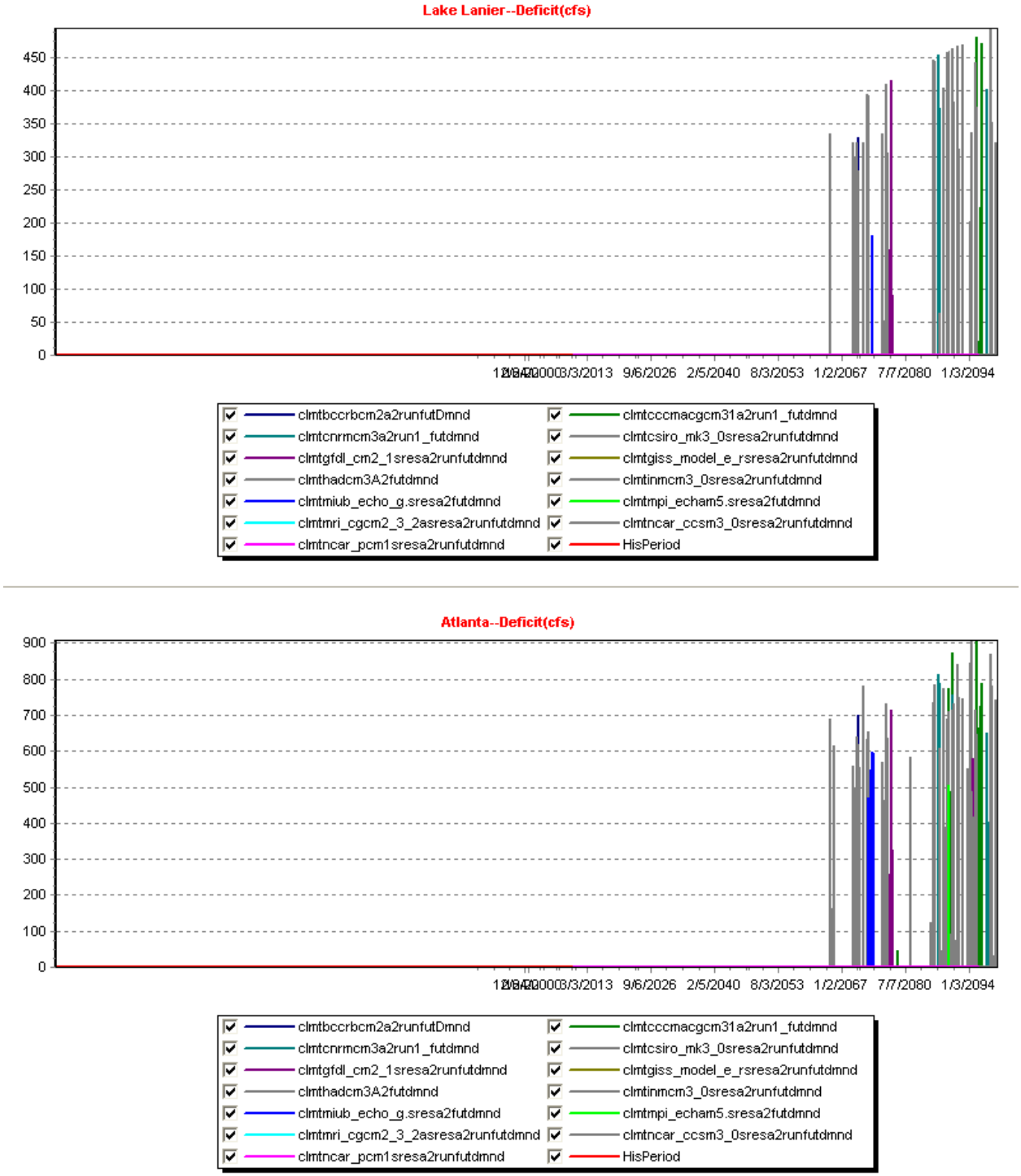

Figure 5.60: A2, Future Demands, Water Supply Deficit Sequences

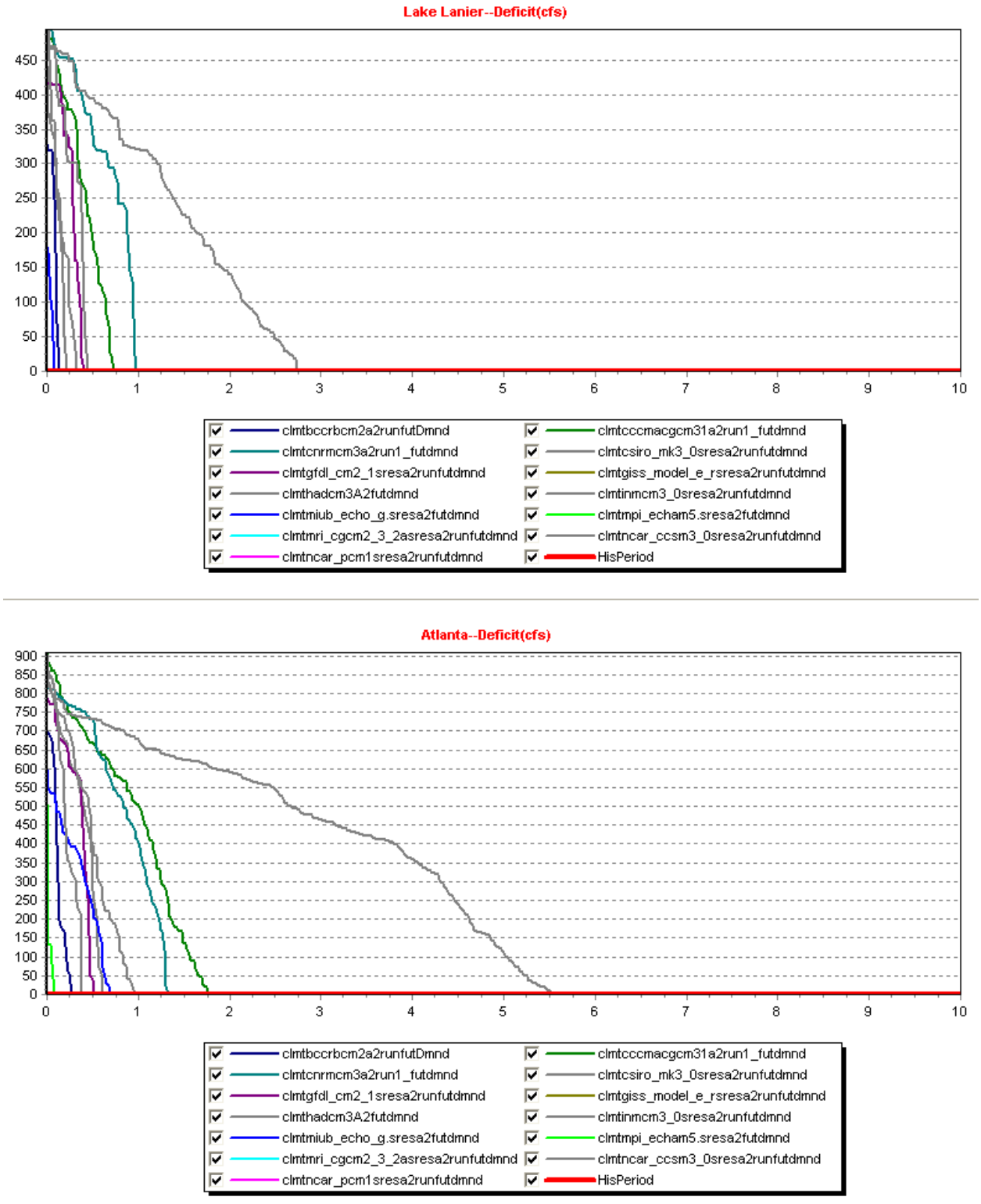

Figure 5.61: A2, Future Demands, Water Supply Deficit Frequency Curves (The horizontal axis shows frequencies up to 10%.)

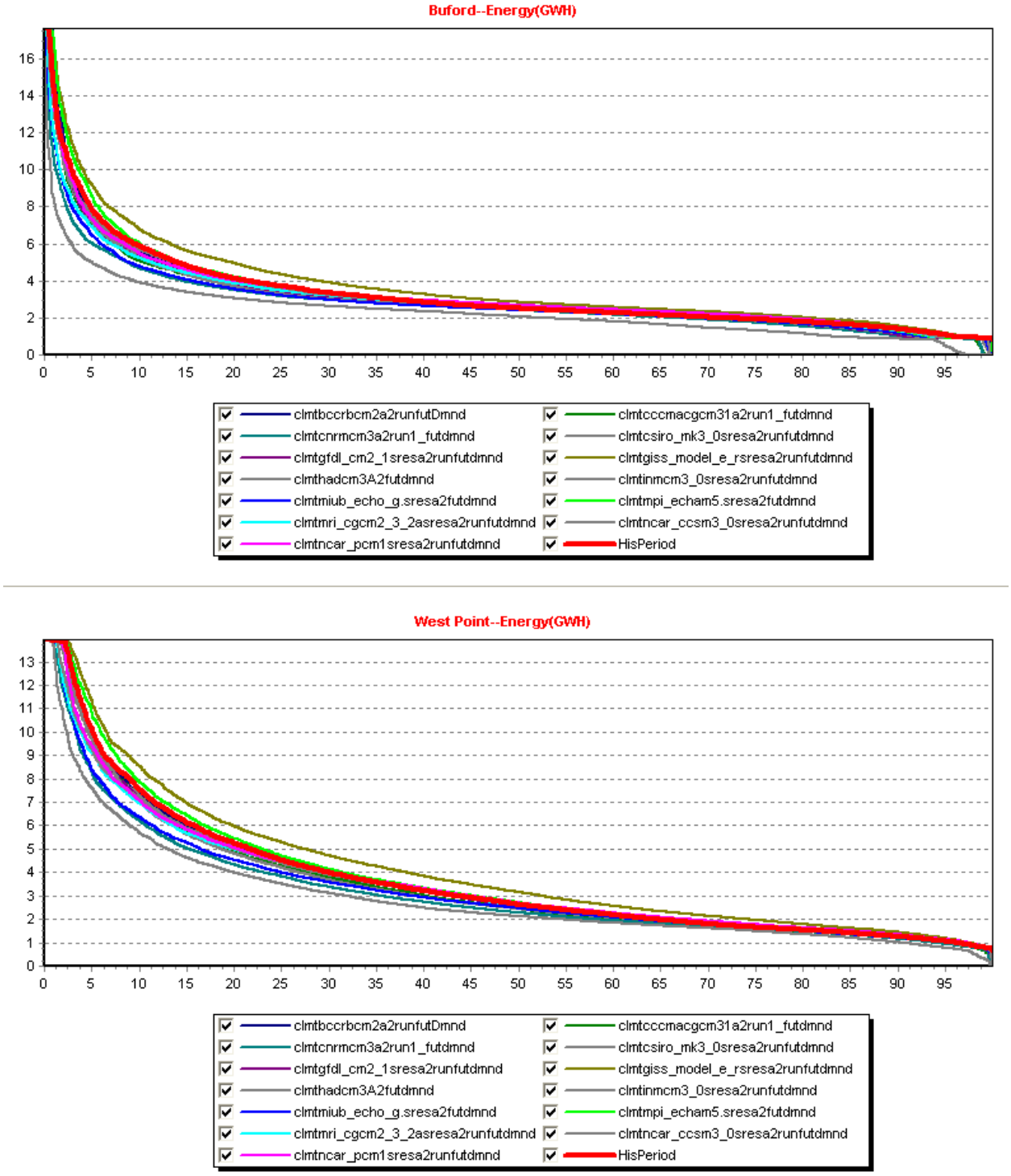

Figure 5.62: A2, Future Demands, Energy Generation Frequency Curves

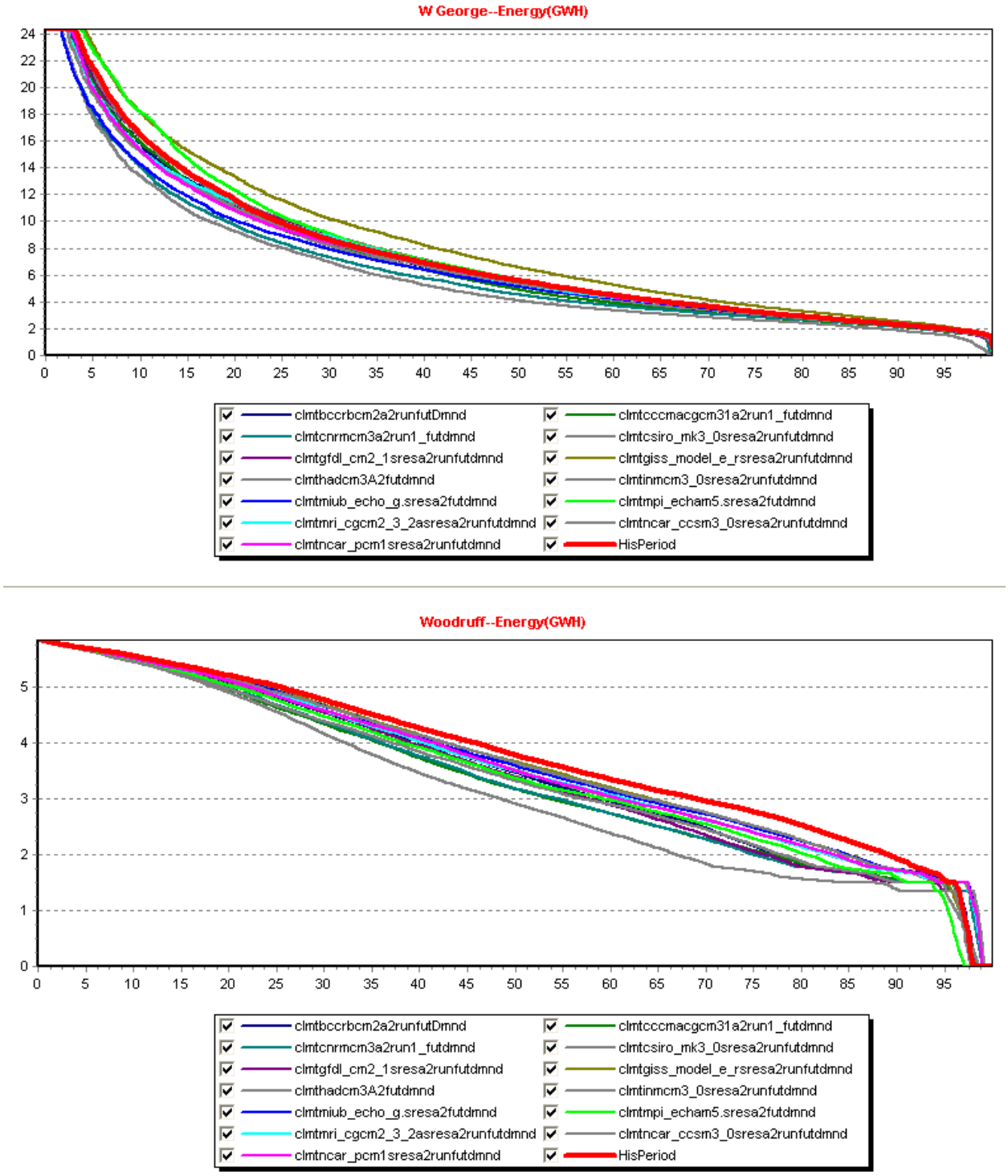

Figure 5.63: A2, Future Demands, Energy Generation Frequency Curves

Chapter 6

Conclusions and Further Research Recommendations

6.1 Conclusions

This report describes an integrated climate assessment for the Apalachicola-Chattahoochee-Flint (ACF) river basin in the southeast US. The study combines *(1)* downscaling and assessment of future precipitation and temperature scenarios for six ACF sub-watersheds, *(2)* hydrologic assessments for each sub-watershed, and *(3)* water resources assessments for the entire basin.

The study has developed and demonstrated new methods in each assessment component. These contributions include a new downscaling method (Joint Variable Statistical Downscaling; Chapter 3), a new watershed model (Chapter 4), and a new decision support system for operational reservoir management (ACF decision support system; Chapter 5 and Volume II).

The main assessment findings are summarized below:

ACF Climate and Hydrology:

- Historical ACF precipitation (1901-2009) does not exhibit any appreciable long term trend. Furthermore, assessments with 26 IPCC future climate scenarios (2000-2099) do not indicate any long term change in mean precipitation. However, the same scenarios indicate that the ACF precipitation distribution is expected to "stretch" becoming wetter and drier than that of the historical climate.
- Unlike precipitation, temperature and potential evapotranspiration (with its strong dependence on temperature) show consistently increasing historical *and* future trends.
- As a result of the increasing PET, soil moisture storage exhibits a declining trend historically as well as under future climates. This decline is solely due to the decline of the lower storage zone, while the upper storage exhibits no significant change. Declining soil moisture has

critical implications for agriculture as well as for water management (due to decline base flows).

- Lastly, watershed runoff, and thus river flow, exhibits a similar historical decline across all ACF watersheds. This average trend is expected to persist in future climates indicating that future droughts are likely to be more severe than historical droughts. At the other extreme, future wet periods are expected to be wetter than those experienced historically, signifying a higher likelihood of severe floods. However, the current study employs a monthly time step, and a proper flood risk assessment requires a daily or sub-daily resolution.

ACF Water Resources:

Water resources impacts were assessed for the A1B and A2 climate scenarios and for 2007 and future demands based on 2050 projections. The assessment criteria included reliability of water supply for municipal, industrial, and agricultural users; lake levels; environmental and ecological flow requirements; and hydropower generation.

- A1B climate scenarios with 2007 demands exhibit mildly adverse water resources impacts compared to the historical baseline. However, the ensemble of future climates includes droughts (as well as floods) that are more extreme than those that occurred historically. During these extreme droughts, the basin storage is unable to meet the system water supply and instream flow requirements.
- The A2 climate scenarios with 2007 demands exhibit more exacerbated water resources impacts compared to the A1B scenarios and the historical baseline. These impacts become critical during extreme future droughts which deplete all basin storage. The frequency with which this occurs is relatively low.

- The A1B climate scenarios with 2050 demands impact more adversely the Upper Chattahoochee River where natural inflows are low and demands (for Atlanta) are high. The impacts are critical during extreme future droughts which deplete Lake Lanier storage.
- Among all tested scenarios, the A2 climate scenarios with 2050 demands accrue the most severe impacts with respect to all criteria. Since climate and demand changes are likely to occur simultaneously, it is important that the ACF water resources planning process recognize and protect against the risks of both. This requires the timely adoption and implementation of better water conservation programs, adaptive reservoir management procedures, and improved drought contingency plans that utilize hydro-climatic watershed information.

6.2 Further Research Recommendations

Useful extensions of the current study include *(1)* revision of summer – early fall precipitation scenarios in light of future hurricane behavior; *(2)* representation of the groundwater – surface water interaction in the Woodruff – Bainbridge watershed; and *(3)* detailed climate assessments using a daily time step.

Hurricanes impact summer and early fall precipitation in the southeast US, spawning tropical storms and destructive floods. Recent studies indicate that hurricane occurrence and severity will most likely be intensified by warming sea temperatures (Bender et al., 2010). Future assessments would benefit by a more quantitative understanding of hurricane impact on summer and early fall precipitation, and would increase the value of climate model precipitation scenarios in hurricane prone areas.

The need for an accurate representation of the groundwater – surface water interaction in the lower Chattahoochee and Flint Rivers was identified and emphasized in Chapter 4. This

interaction can be quantified through numerical groundwater models, and a climate assessment can be carried out to assess the response of the groundwater system (and its changing influence on the surface hydrology) under future climate scenarios. An important element in this effort would be the accurate representation of current and future aquifer pumping which influences aquifer water table levels and determines the strength and direction of the groundwater – surface water interaction.

Lastly, daily and possibly sub-daily assessments would be necessary to quantify the climate change impacts associated with flooding. This effort would mainly require that the hydrologic models be extended and re-calibrated to account for hydrologic processes that become important at finer time scales. Two such processes include *(1)* storage and depletion of tension soil water and *(2)* channel routing. This effort is currently on-going.

References

Chapter 2

Grismer, M.E., M. Orang, R. Snyder, and R. Matyac, 2002. Pan Evaporation to Reference Evapotranspiration Conversion Methods. J. Irrigation and Drainage Engineering 128(3):180-184.

Hamon, W.R., 1963. Computation of Direct Runoff Amounts from Storm Rainfall. Int. Assoc. Sci, Hydrol. Pub. 63:52-62.

Hargreaves, G.H. and Z.A. Samani, 1985. Reference Crop Evapotranspiration From Temperature. Applied Engrg. in Agric.1(2):96-99

Juang, H.-M. H., S.-Y. Hong, and M. Kanamitsu, 1997: The NCEP Regional Spectral Model: An update. Bull. Amer. Meteor. Soc., 78, 2125–2143.

Kalnay, E., Kanamitsu, M., Kistler, R., et al., 1996. "The NCEP/NCAR 40-year reanalysis project, Bull. " Amer. Meteor. Soc., 77, 437-470.

Kundell, J. E., J.L. Meyer, K. L. Jones, G. C. Poole, C. R. Jackson, B. L. Rivenbark, E. A. Kramer, and W. Bumback. 2004. Implications of Changes in Riparian Buffer Protection for Georgia's Trout Streams. Final Report submitted to Georgia Department of Natural Resources, Environmental Protection Division.

Lu, J., G. Sun, S. McNulty, and D. M. Amatya, 2005. A Comparison of Six Potential Evapotranspiration Methods for Regional Use in the Southeastern United States. Journal of the American Water Resources Association (JAWRA) 41 (3):621-633.

Makkink, G.F., 1957. Testing the Penman Formula by Means of Lysimeters. J. Inst. of Water Eng. 11:277-288.

Penman, H.L., 1948. Natural Evaporation From Open Water, Bare Soil and Grass. Proc. Roy. Soc. London, A193:120-146.

Priestley, C.H.B. and R.J. Taylor, 1972. On the Assessment of Surface Heat Flux and Evaporation Using Large Scale Parameters. Mon. Weath. Rev. 100:81-92.

Turc, L., 1961. Evaluation de besoins en eau d'irrigation, ET potentielle, Ann. Agron. 12:13-49.

Chapter 3

Conway, D., (1998). "Recent Climate Variability and Future Climate Change Scenarios for Great Britain." Progress in Physical Geography 22.3: 350-74.

Drignei, D., (2009). "A Kriging Approach to the Analysis of Climate Model Experiments." Journal of Agricultural Biological and Environmental Statistics 14.1: 99-114.

Flato, G. M., Boer, G. J., Lee, W. G., McFarlane, N. A., Ramsden, D., Reader, M. C., and Weaver, A. J., (2000). "The Canadian Centre for Climate Modelling and Analysis Global Coupled Model and Its Climate." Climate Dynamics 16.6: 451-67.

Fowler, H. J., S. Blenkinsop, and C. Tebaldi, (2007). "Linking Climate Change Modelling to Impacts Studies: Recent Advances in Downscaling Techniques for Hydrological Modelling." International Journal of Climatology 27.12: 1547-78.

Georgakakos, A. P., Yao, H., Mullusky M. G., and Georgakakos, K. P., (1998). "Impacts of Climate Variability on the Operational Forecast and Management of the Upper Des Moines River Basin." Water Resources Research 34.4: 799-821.

Gissila, T., Black, E., Grimes, D. I. F., and Slingo, J. M., (2004). "Seasonal Forecasting of the Ethiopian Summer Rains." International Journal of Climatology 24.11: 1345-58.

Hidalgo, H. G., Dettinger, M. D., and Cayan, D. R. (2008). "Downscaling with constructed analogues: daily precipitation and temperature fields over the United States." Report No. CEC-500-2007-123, California Energy Commission, Sacramento, CA, 48 pp.

Huth, R., (1999). "Statistical Downscaling in Central Europe: Evaluation of Methods and Potential Predictors." Climate Research 13.2: 91-101.

IPCC, 2007: Climate Change (2007). The Physical Science Basis. Contribution of Working Group I to the Fourth Assessment Report of the Intergovernmental Panel on Climate Change [Solomon, S., D. Qin, M. Manning, Z. Chen, M. Marquis, K.B. Averyt, M. Tignor and H.L. Miller (eds.)]. Cambridge University Press, Cambridge, United Kingdom and New York, NY, USA, 996 pp.

Nakicenovic N, Swart R (eds). (2000). Special Report on Emissions Scenarios. A Special Report of Working Group III of the Intergovernmental Panel on Climate Change. Cambridge University Press: Cambridge, UK and New York. 570 p.

Lettenmaier, D. P., and D. Rind, (1992). "Hydrological Aspects of Global Climate Change - Preface." Journal of Geophysical Research-Atmospheres 97.D3: 2675-76.

Maurer, E. P., Wood, A. W., Adam, J. C., Lettenmaier, D. P., and Nijssen, B., (2002). "A Long-Term Hydrologically Based Dataset of Land Surface Fluxes and States for the Conterminous United States." Journal of Climate 15.22: 3237-51.

Maurer, E. P., (2007). "Uncertainty in Hydrologic Impacts of Climate Change in the Sierra Nevada, California, under Two Emissions Scenarios." Climatic Change 82.3-4: 309-25.

Maurer, E.P. and H.G. Hidalgo (2008) "Utility of daily vs. monthly large-scale climate data: an intercomparison of two statistical downscaling methods." Hydrology and Earth System Sciences Vol. 12, 551-563.

Mearns, L. O., F. Giorgi, P. Whetton, D. Pabon, M. Hulme, and M. Lal, (2003a). "Guidelines for Use of Climate Scenarios Developed from Regional Climate Model Experiments." Data Distribution Center of the Intergovernmental Panel on Climate Change.

Mearns, L. O., F. Giorgi, L. McDaniel and C. Shields, (2003b). "Climate Scenarios for the Southeastern US Based on Gcm and Regional Model Simulations." Climatic Change 60.1-2: 7-35.

Miller, N. L., Jinwon Kim, and Robert K. HartmanJohn Farrara, (1999). "Downscaled Climate and Streamflow Study of the Southwestern United States." Journal of the American Water Resources Association 35.6: 1525-37.

Mitchell, T. D., and M. Hulme, (1999). "Predicting Regional Climate Change: Living with Uncertainty." Progress in Physical Geography 23.1 (1999): 57-78.

Mitchell, T. D., and P. D. Jones, (2005). "An Improved Method of Constructing a Database of Monthly Climate Observations and Associated High-Resolution Grids." International Journal of Climatology 25.6: 693-712.

Mujumdar, P. P., and S. Ghosh, (2008). "Modeling Gcm and Scenario Uncertainty Using a Possibilistic Approach: Application to the Mahanadi River, India." Water Resources Research 44.6.

Oberhuber, J. M., (1993). "Simulation of the Atlantic Circulation with a Coupled Sea Ice-Mixed Layer-Isopycnic General-Circulation Model .2. Model Experiment." Journal of Physical Oceanography 23.5: 830-45.

Randel, D.A. and Wood, R. A., 2007: Climate models and their evaluation. In: Climate Change 2007: The Physical Basis. (Solomon et al., eds.) Cambridge University Press:Cambridge. pp. 589-662.

Roeckner, E., J. M. Oberhuber, A. Bacher, M. Christoph and I. Kirchner, (1996). "Enso Variability and Atmospheric Response in a Global Coupled Atmosphere-Ocean GCM." Climate Dynamics 12.11: 737-54.

Shepard, D.S. (1984). "Computer mapping: The SYMAP interpolation algorithm, in Spatial Statistics and Models.", edited by G.L. Gaile and C.J. Willmott, pp. 133 145, D. Reidel, Norwell, Mass.

Stamm, J. F., E. F. Wood, and D. P. Lettenmaier, (1994). "Sensitivity of a Gcm Simulation of Global Climate to the Representation of Land-Surface Hydrology." Journal of Climate 7.8 (1994): 1218-39.

Tebaldi, C., Smith, Richard L, Nychka, Doug, and Mearns, Linda O., (2005). "Quantifying Uncertainty in Projections of Regional Climate Change: A Bayesian Approach to the Analysis of Multimodel Ensembles." Journal of Climate 18.10: 1524-40.

Vrac, M., M. Stein, and K. Hayhoe, (2007). "Statistical Downscaling of Precipitation through Nonhomogeneous Stochastic Weather Typing." Climate Research 34.3: 169-84.

Wilby, R. L., and T. M. L. Wigley, (1997). "Downscaling General Circulation Model Output: A Review of Methods and Limitations." Progress in Physical Geography 21.4: 530-48.

Wilby, R. L., Charles, S.P., Zorita, E., Timbal, B., Whetton, P., and Mearns, L.O. (2004). "Guidelines for use of climate scenarios developed from statistical downscaling methods", Data Distribution Center of the Intergovernmental Panel on Climate Change.

Wilks, D. S., and R. L. Wilby, (1999). "The Weather Generation Game: A Review of Stochastic Weather Models." Progress in Physical Geography 23.3: 329-57.

Wood, A. W., L. R. Leung, V. Sridhar and D. P. Lettenmaier, (2004). "Hydrologic Implications of Dynamical and Statistical Approaches to Downscaling Climate Model Outputs." Climatic Change 62.1-3: 189-216.

Xu, C. Y., (1999). "From Gcms to River Flow: A Review of Downscaling Methods and Hydrologic Modelling Approaches." Progress in Physical Geography 23.2: 229-49.

Xue, Y. K., Vasic, Ratko, Janjic, Zavisa, Mesinger, Fedor, and Mitchell, Kenneth E, (2007). "Assessment of Dynamic Downscaling of the Continental Us Regional Climate Using the Eta/Ssib Regional Climate Model." Journal of Climate 20.16: 4172-93.

Chapter 4

Amorocho, J., (1963) Measures of the linearity of hydrologic systems, J. Geophys. Res., 68(8), 2237–2249.

Amorocho, J., (1967) The nonlinear prediction problem in the study of the runoff cycle, Water Resour. Res., 3(3), 861–880.

Apostolopoulos, T. K., and K. P. Georgakakos, (1997) Parallel Computation for Streamflow Prediction with Distributed Hydrologic Models, Journal of Hydrology, 197(1-4), 1-24.

Arnold, J. G., and N. Fohrer, (2005) Swat2000: Current Capabilities and Research Opportunities in Applied Watershed Modelling, Hydrological Processes, 19(3), 563-72.

Botter, G. , Porporato, A. , Rodriguez-Iturbe, I. , and Rinaldo, A., (2009) Nonlinear Storage-discharge Relations and Catchment Streamflow Regimes, Water Resources Research, 45.

Brutsaert, W., (2005) Hydrology: An Introduction, Cambridge Univ. Press, New York.

Carpenter, T. M., and K. P. Georgakakos, (2004) Continuous Streamflow Simulation with the HRCDHM Distributed Hydrologic Model, Journal of Hydrology 298.1-4, 61-79.

Conway, D., (1998) Recent Climate Variability and Future Climate Change Scenarios for Great Britain, Progress in Physical Geography, 22(3), 350-74.

Duan, Q. Y., S. Sorooshian, and V. K. Gupta, (1994) Optimal Use of the Sce-Ua Global Optimization Method for Calibrating Watershed Models, Journal of Hydrology 158(3-4), 265-84.

Duan, Q. Y., et al., (2007) Multi-Model Ensemble Hydrologic Prediction Using Bayesian Model Averaging, Advances in Water Resources, 30(5), 1371-86.

Georgakakos, K. P., and O. W. Baumer, (1996) Measurement and utilization of on-site soil moisture data, Journal of Hydrology, 184(1-2), 131-152

Gupta, H. V., S. Sorooshian, and P. O. Yapo, (1996) Toward Improved Calibration of Hydrologic Models: Multiple and Noncommensurable Measures of Information, Water Resources Research 34(4), 751-63.

Kirchner, J.W., (2009) Catchments as Simple Dynamical Systems: Catchment Characterization, Rainfall-runoff Modeling, and Doing Hydrology Backward, Water Resources Research, 45.

Kirchner, J.W., (2006) Getting the right answers for the right reasons: Linking measurements, analyses, and models to advance the science of hydrology, Water Resources Research, 42.

Koren, V., Reed, S., Smith, M., Zhang, Z., Seo, D. J., (2004) Hydrology Laboratory Research Modeling System (Hl-Rms) of the Us National Weather Service, Journal of Hydrology, 291(3-4), 297-318.

Lettenmaier, D. P., and D. Rind, (1992) Hydrological Aspects of Global Climate Change - Preface, Journal of Geophysical Research-Atmospheres, 97(D3), 2675-76.

Liang, X., Lettennmaier, Dennis P., Wood, Eric F., Burges, and Stephen J., (1994) A simple hydrologically based model of land surface water and energy fluxes for general circulation models, Journal of Geophysical Research, 99(D7), 14415-14428

Maurer, E. P., (2007) Uncertainty in Hydrologic Impacts of Climate Change in the Sierra Nevada, California, under Two Emissions Scenarios, Climatic Change, 82(3-4), 309-25.

Mishra, A., H. Takeshi, W. Abdelhadi, A. Tada, and H. Tanakamaru, (2003) Recession flow analysis of the Blue Nile River, Hydrol. Processes, 17, 2825– 2835.

Mohseni, O., and H. G. Stefan, (1998) A monthly streamflow model, Water Resources Research, 34(5), 1287-1298

Stamm, J. F., E. F. Wood, and D. P. Lettenmaier, (1994) Sensitivity of a Gcm Simulation of Global Climate to the Representation of Land-Surface Hydrology, Journal of Climate 7(8), 1218-39.

Thornthwaite, C.W., (1948) An approach toward a rational classification of climate,Geogr. Rev. 38(1),55–94.

Thornthwaite, C. W. and Mather, J. R., (1955) The water balance, Publ. Climatol. Lab. Climatol. Dresel Inst. Technol. 8(8), 1–104.

Vieux, B. E., (2001) Distributed hydrologic modeling using GIS, First Edition, Kluwer Academic Press, Water and Science Technology Series, 38.

Wagener, T., et al., (2009) Multiobjective Sensitivity Analysis to Understand the Information Content in Streamflow Observations for Distributed Watershed Modeling, Water Resources Research, 45.

Wittenberg, H., (1999) Baseflow recession and recharge as nonlinear storage processes, Hydrol. Processes, 13, 715– 726.

Wood, A. W., et al., (2004) Hydrologic Implications of Dynamical and Statistical Approaches to Downscaling Climate Model Outputs, Climatic Change 62(1-3), 189-216.

Wood, E. F., Lettenmaier, D. P., and Zartarian, V. G., (1992) A land-surface hydrology parameterization with subgrid variability for general circulation models, J. Geophys. Res., 97, 2717-2728.

Xu, C.Y. and Vandewiele, G. L., (1995) Parsimonious monthly rainfallrunoff models for humid basins with different input requirements, Adv. Water Resour. 18, 39–48.

Yapo, P. O., H. V. Gupta, and S. Sorooshian, (1998) Multi-Objective Global Optimization for Hydrologic Models, Journal of Hydrology, 204(1-4), 83-97.

Young P.C., (1993) Time variable and state dependent modelling of nonstationary and nonlinear time series, In Developments in Time Series Analysis, Subba Rao T (ed.). Chapman and Hall: 374–413.

Young P.C., (1998) Data-based mechanistic modelling of environmental, ecological, economic and engineering systems, Environmental Modelling and Software 13: 105–122.

Young P.C. (1999) Data-based mechanistic modelling, generalised sensitivity and dominant mode analysis, Computer Physics Communications 115: 1–17.

Young, P.C., (2003) Top-down and data-based mechanistic modelling of rainfall-flow dynamics at the catchment scale, Hydrol. Processes, 17, 2195– 2217.

Chapter 6

Bender, M.A., Knutson, T.R., Tuleya R.E., Sirutis, J.J., Vecchi, G.A., Garner, S.T., and Held I.M., 2010, “Modeled Impact of Anthropogenic Warming on the Frequency of Intense Atlantic Hurricanes,” Science, 327, 454-458.

Appendix A

GCM Seasonal Climatology Results

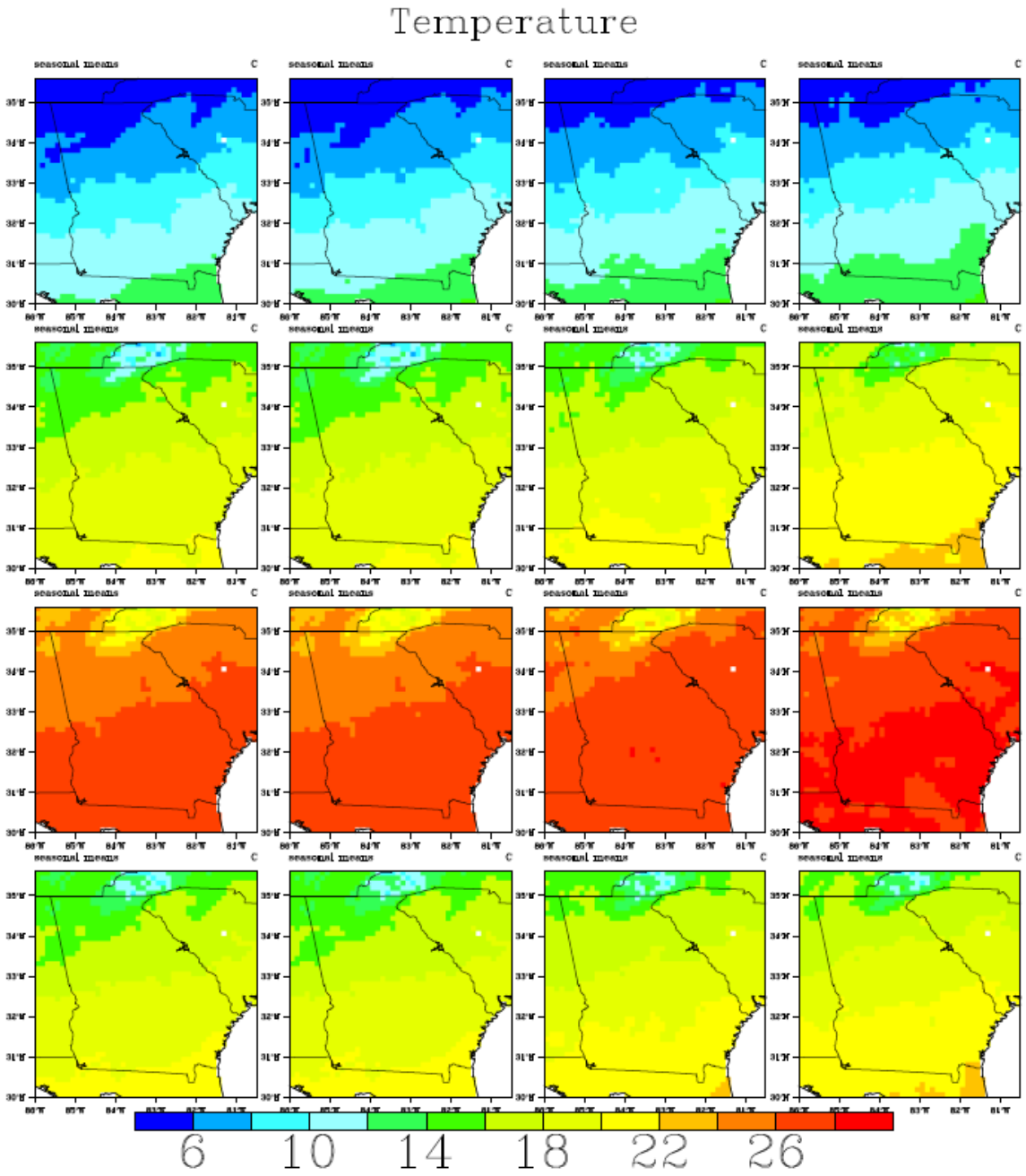

Figure A.1: Spatial temperature distributions over the ACF basin and the southeast US. Monthly temperature fields are aggregated by season (DJF, MAM, JJA, SON). The columns depict observations for the period 01/1950 - 12/1999 (Column 1); JVSD downscaled data using input from the 20CM3 experiment for the period 01/1950 - 12/1999 (Column 2); JVSD downscaled data using input from the CGCM3.1-run1 A1B Scenario for the period 01/2000-12/2049 (Column 3); and JVSD downscaled data using input from the CGCM3.1-run1A1B Scenario for the period 01/2050-12/2099 (Column 4).

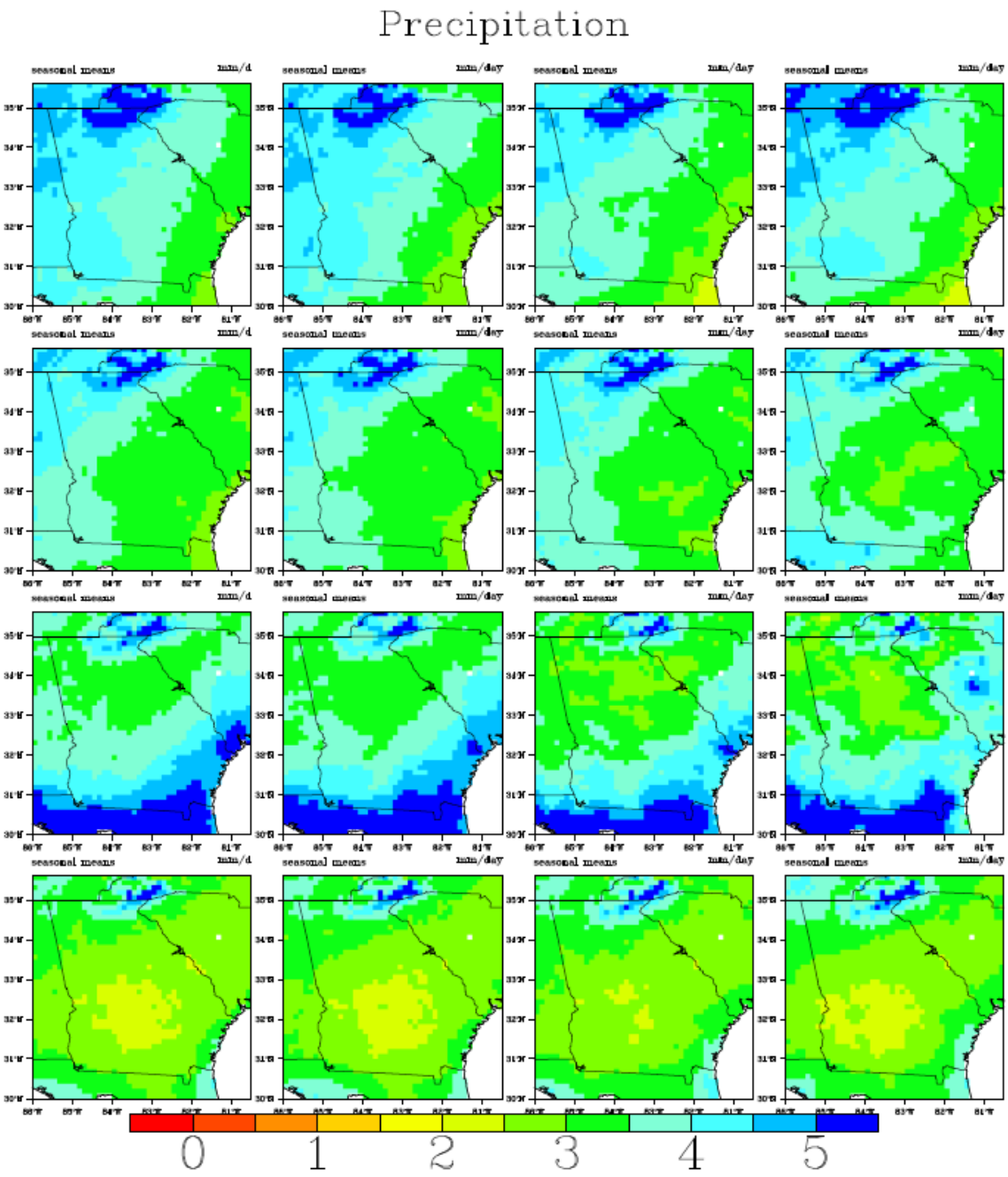

Figure A.2: Spatial precipitation distributions over the ACF basin and the southeast US. Monthly precipitation fields are aggregated by season (DJF, MAM, JJA, SON). The columns depict observations for the period 01/1950 - 12/1999 (Column 1); JVSD downscaled data using input from the 20CM3 experiment for the period 01/1950 - 12/1999 (Column 2); JVSD downscaled data using input from the CGCM3.1-run1A1B Scenario for the period 01/2000-12/2049 (Column 3); and JVSD downscaled data using input from the CGCM3.1-run1 A1B Scenario for the period 01/2050-12/2099 (Column 4).

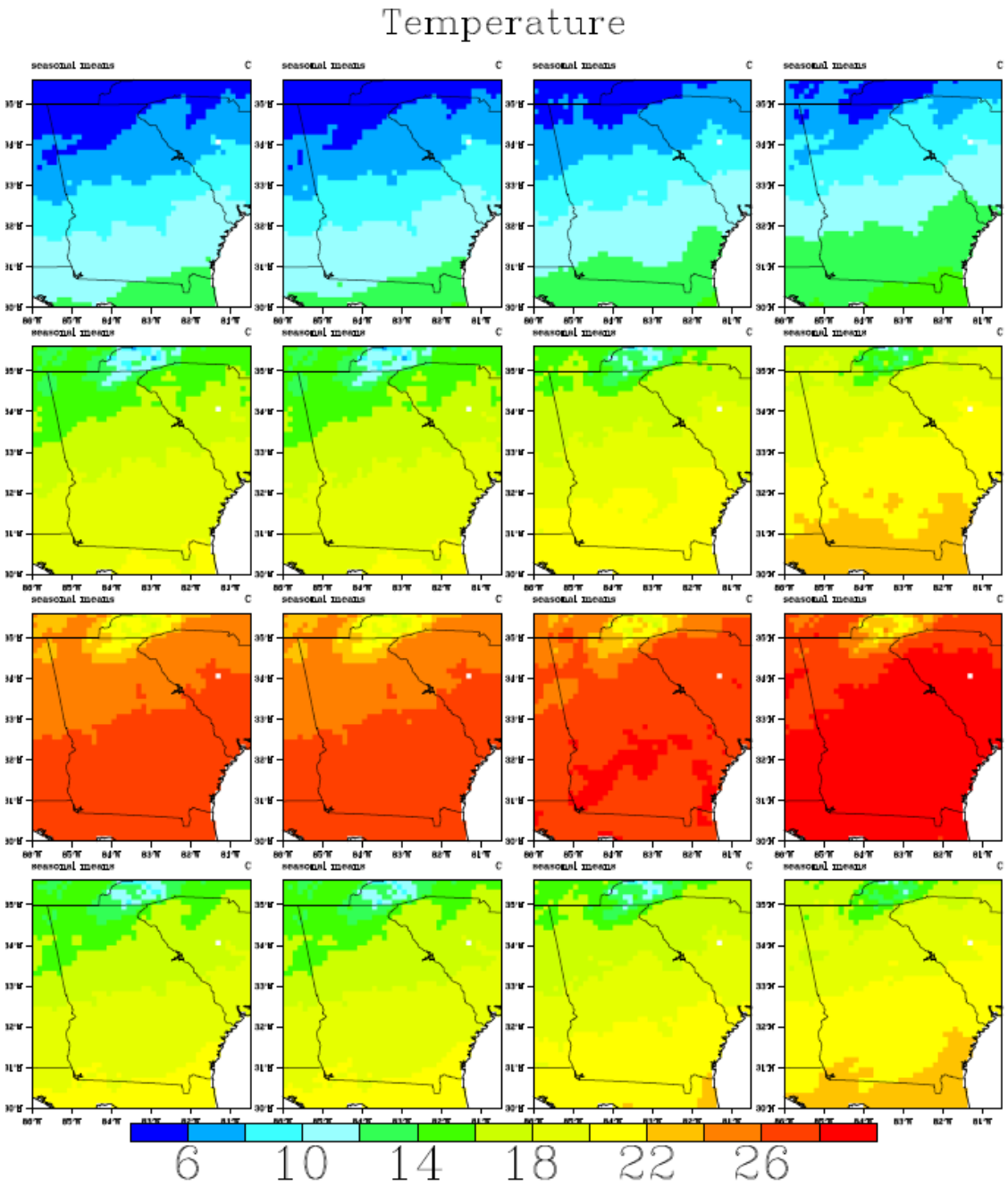

Figure A.3: Spatial temperature distributions over the ACF basin and the southeast US. Monthly temperature fields are aggregated by season (DJF, MAM, JJA, SON). The columns depict observations for the period 01/1950 - 12/1999 (Column 1); JVSD downscaled data using input from the 20CM3 experiment for the period 01/1950 - 12/1999 (Column 2); JVSD downscaled data using input from the CGCM3.1-run1A2 Scenario for the period 01/2000-12/2049 (Column 3); and JVSD downscaled data using input from the CGCM3.1-run1A2 Scenario for the period 01/2050-12/2099 (Column 4).

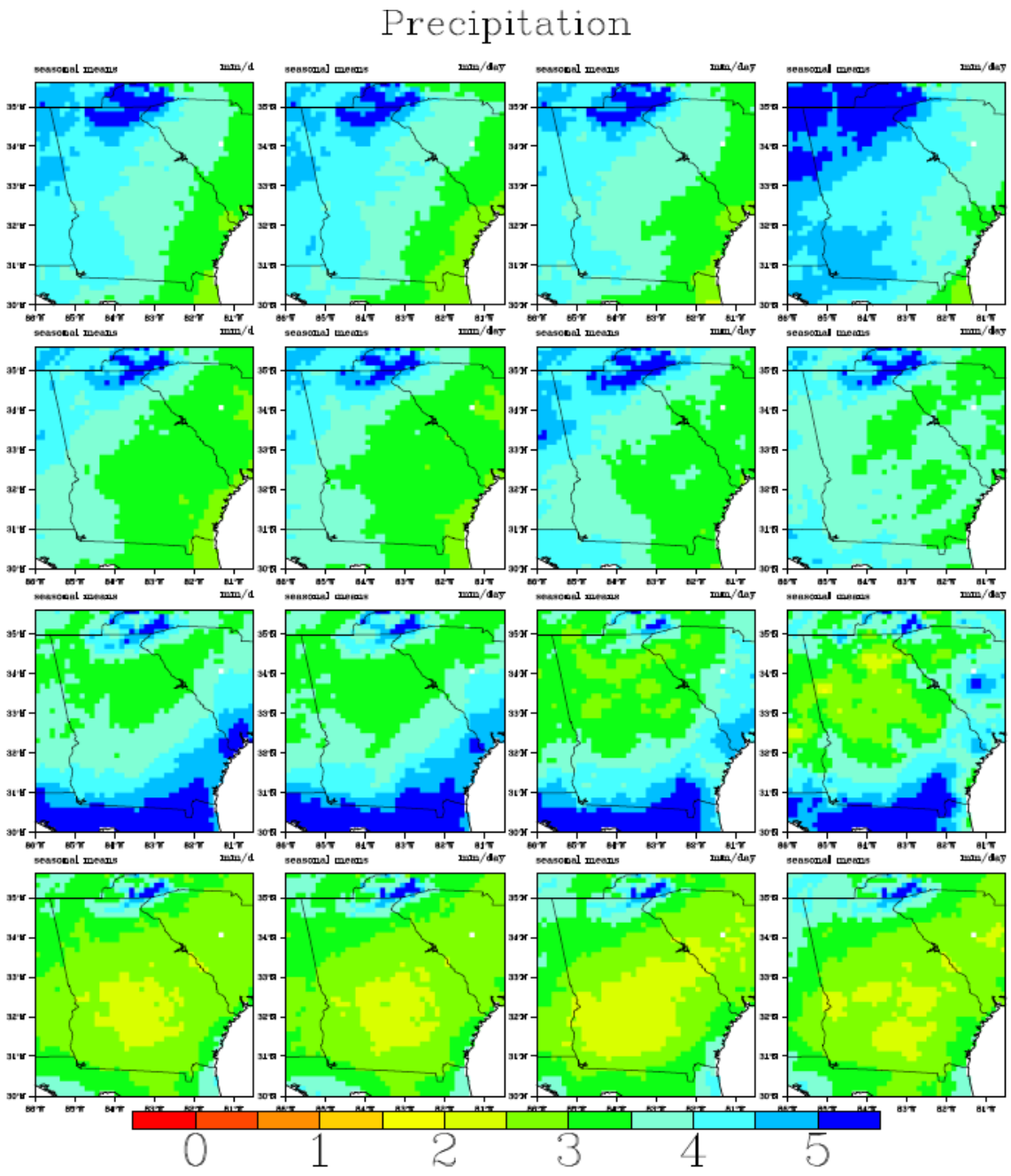

Figure A.4: Spatial precipitation distributions over the ACF basin and the southeast US. Monthly precipitation fields are aggregated by season (DJF, MAM, JJA, SON). The columns depict observations for the period 01/1950 - 12/1999 (Column 1); JVSD downscaled data using input from the 20CM3 experiment for the period 01/1950 - 12/1999 (Column 2); JVSD downscaled data using input from the CGCM3.1-run1A2 Scenario for the period 01/2000-12/2049 (Column 3); and JVSD downscaled data using input from the CGCM3.1-run1A2 Scenario for the period 01/2050-12/2099 (Column 4).

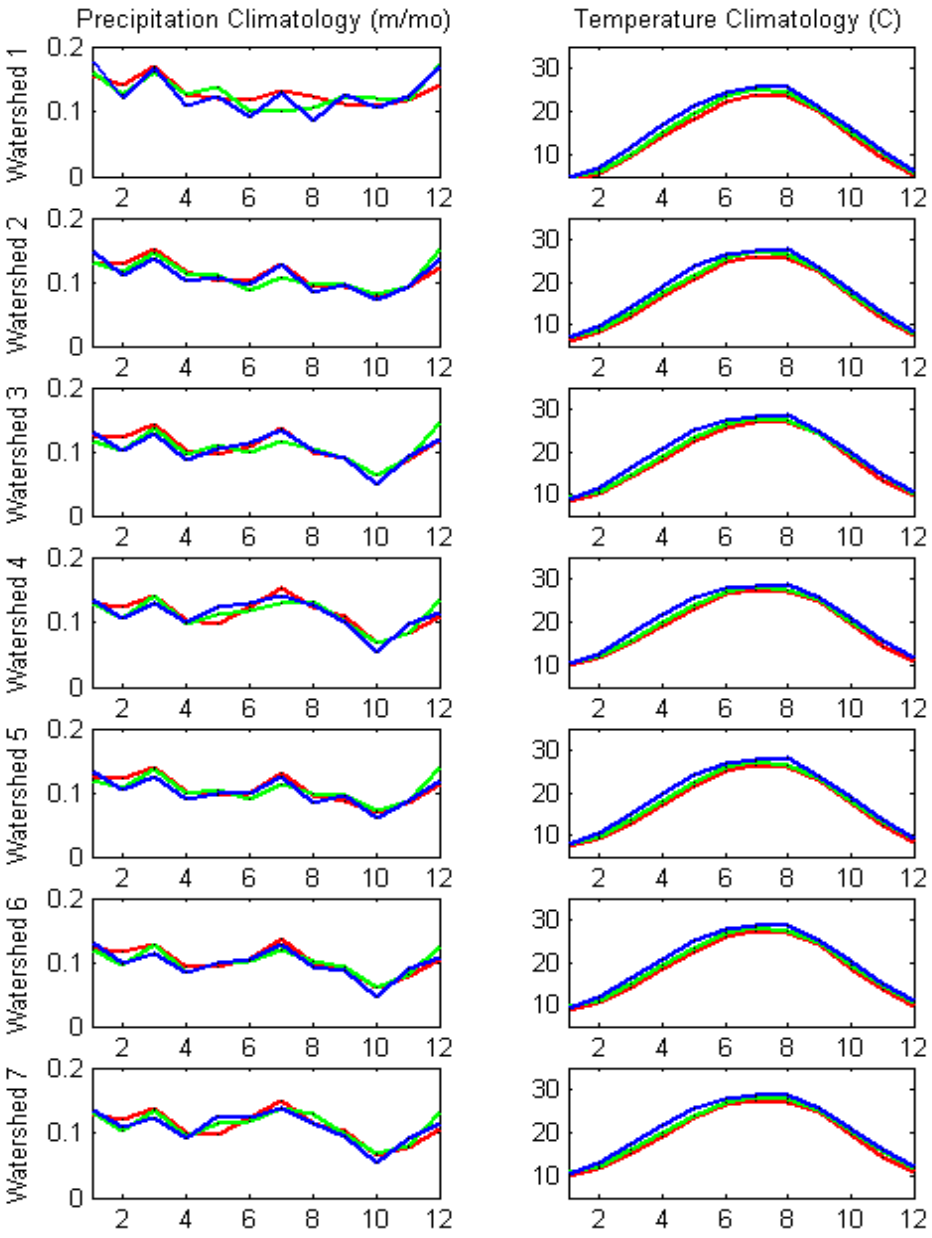

Figure A.5a: Climatologies of spatially aggregated precipitation and temperature for seven ACF watersheds: *(1)* Buford, *(2)* West Point, *(3)* George, *(4)* Woodruff, *(5)* Montezuma, *(6)* Albany, and *(7)* Bainbridge; Lines in Red–Observations (1950-1999); Green–JVSD downscaled (2000-2049); Blue–JVSD downscaled (2050-2099) under CGCM3.1-run1 A1B Scenarios.

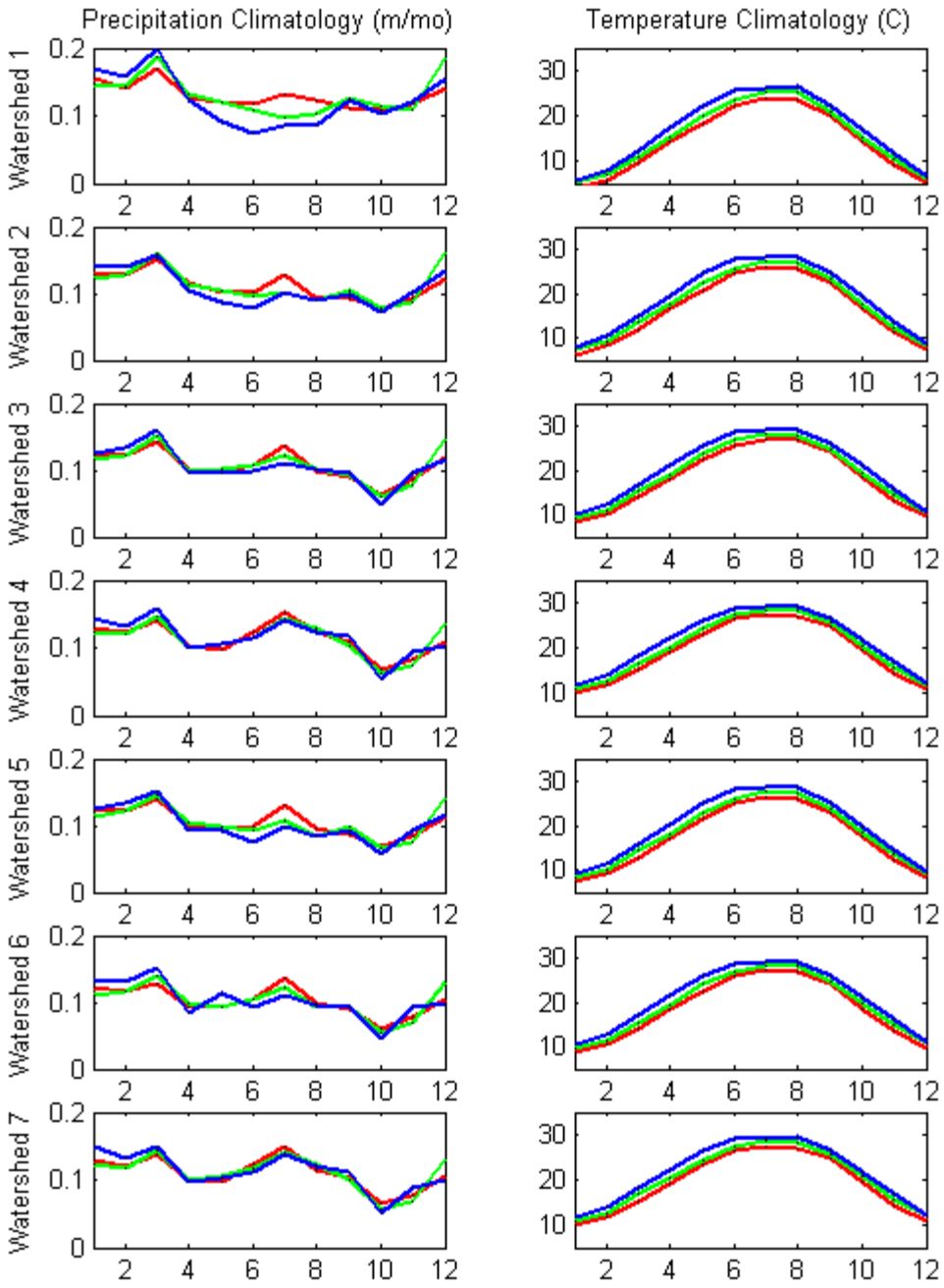

Figure A.5b: Climatologies of spatially aggregated precipitation and temperature for seven ACF watersheds: *(1)* Buford, *(2)* West Point, *(3)* George, *(4)* Woodruff, *(5)* Montezuma, *(6)* Albany, and *(7)* Bainbridge; Lines in Red–Observations (1950-1999); Green–JVSD downscaled (2000-2049); Blue–JVSD downscaled (2050-2099) under CGCM3.1-run1 A2 Scenarios.

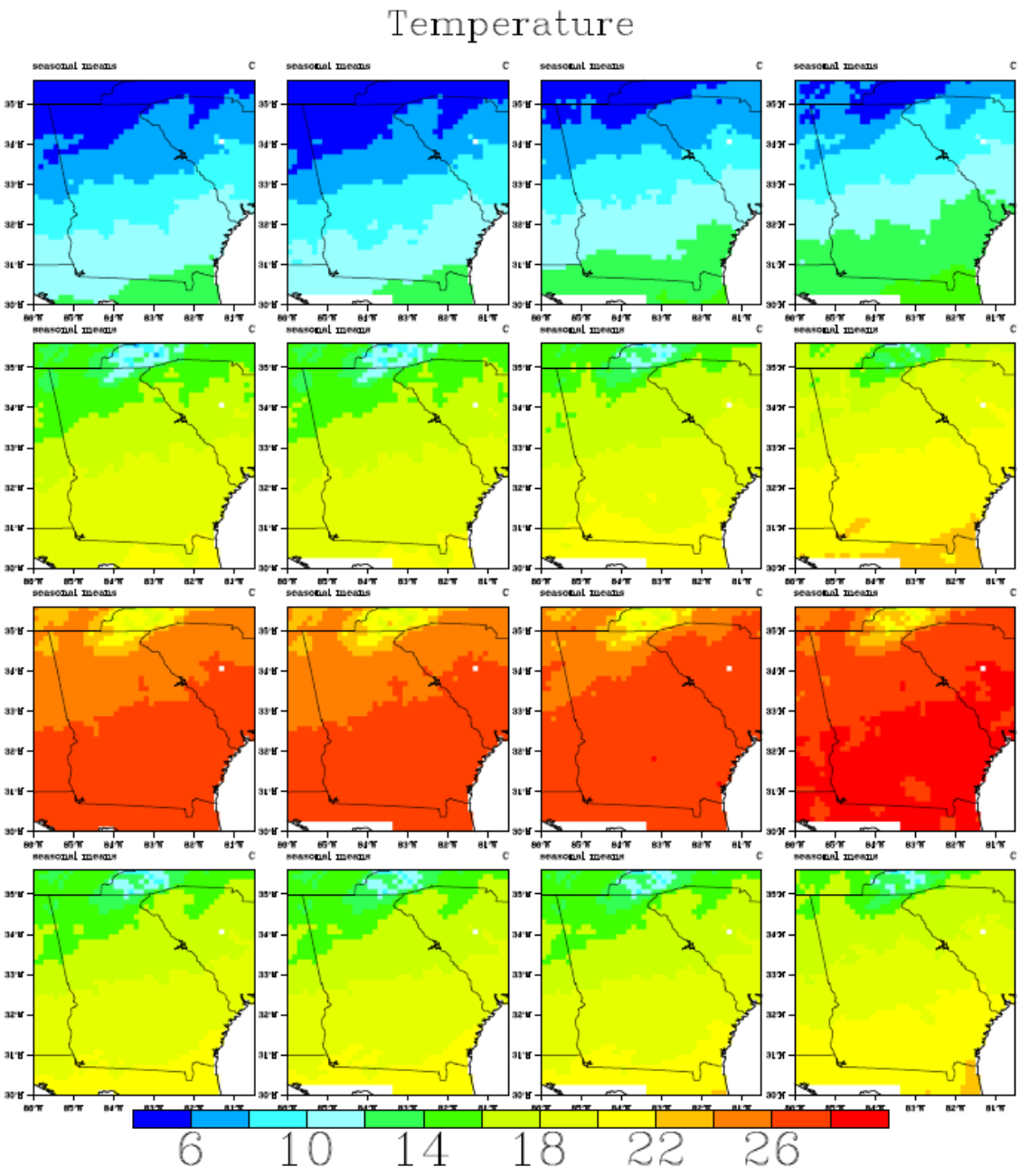

Figure A.6: Spatial temperature distributions over the ACF basin and the southeast US. Monthly temperature fields are aggregated by season (DJF, MAM, JJA, SON). The columns depict observations for the period 01/1950 - 12/1999 (Column 1); JVSD downscaled data using input from the 20CM3 experiment for the period 01/1950 - 12/1999 (Column 2); JVSD downscaled data using input from the BCCR BCM2.0 -run1 A1B Scenario for the period 01/2000-12/2049 (Column 3); and JVSD downscaled data using input from the BCCR BCM2.0 -run1 A1B Scenario for the period 01/2050-12/2099 (Column 4).

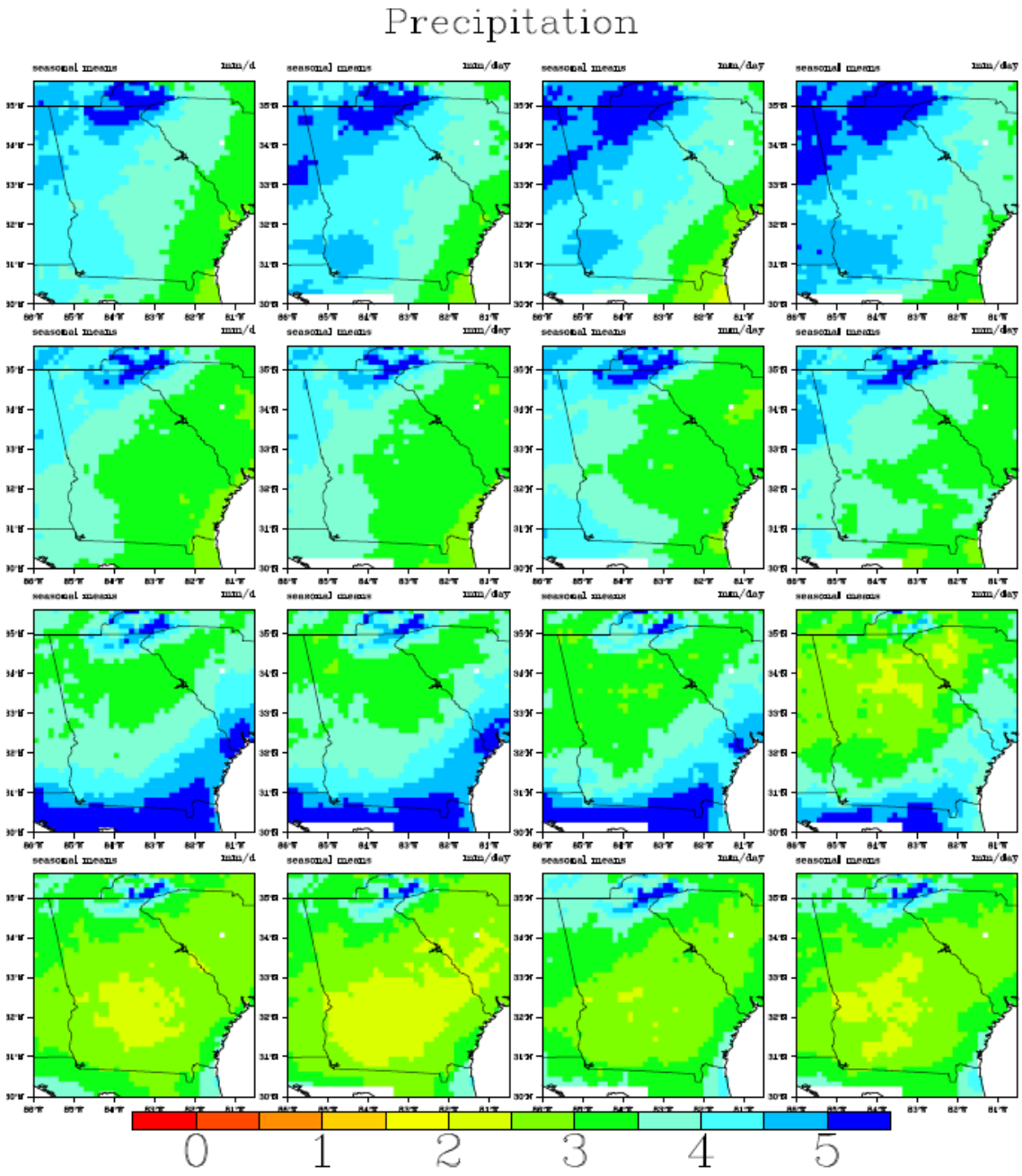

Figure A.7: Spatial precipitation distributions over the ACF basin and the southeast US. Monthly precipitation fields are aggregated by season (DJF, MAM, JJA, SON). The columns depict observations for the period 01/1950 - 12/1999 (Column 1); JVSD downscaled data using input from the 20CM3 experiment for the period 01/1950 - 12/1999 (Column 2); JVSD downscaled data using input from the BCCR BCM2.0 -run1A1B Scenario for the period 01/2000-12/2049 (Column 3); and JVSD downscaled data using input from the BCCR BCM2.0 - run1 A1B Scenario for the period 01/2050-12/2099 (Column 4).

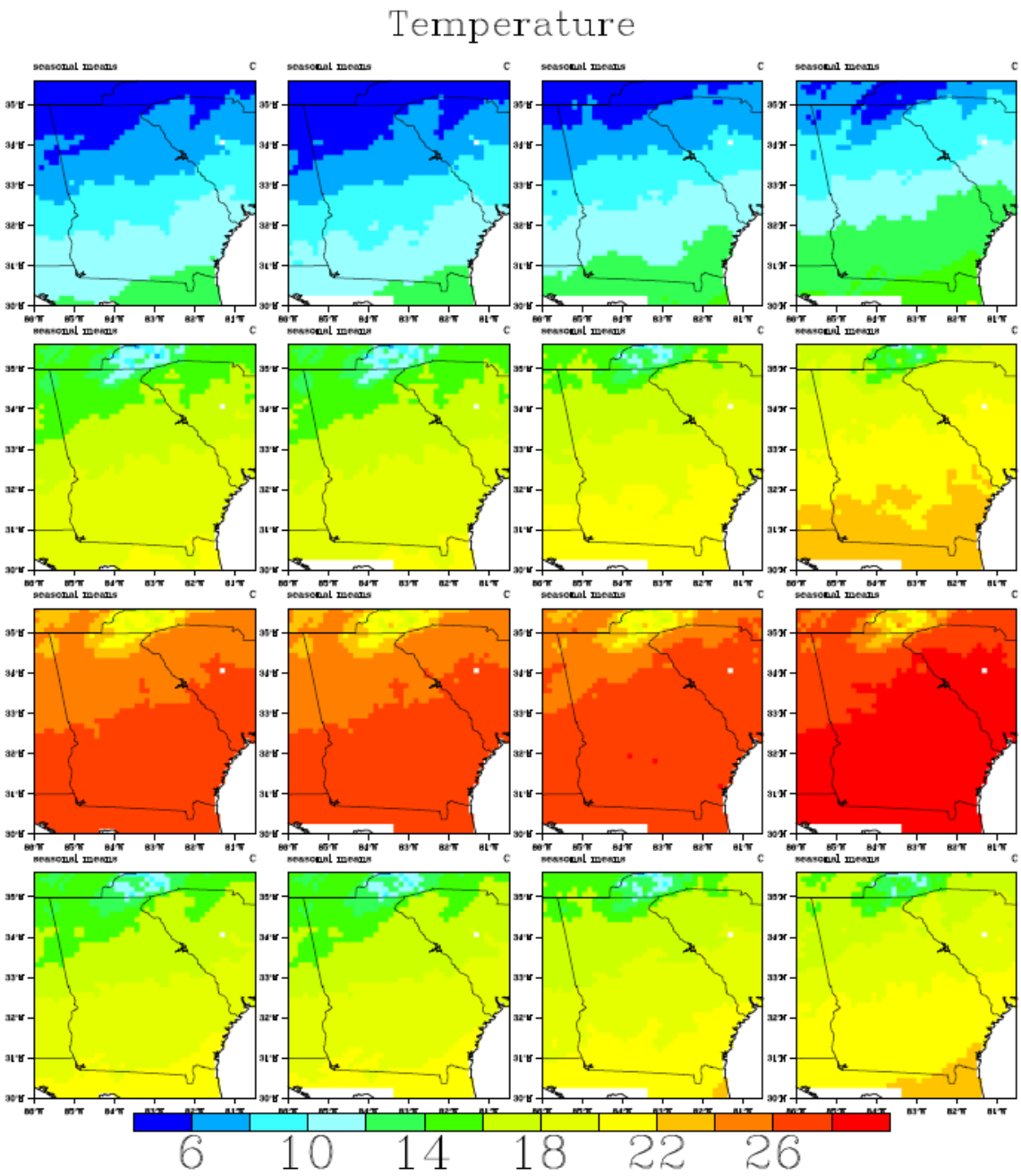

Figure A.8: Spatial temperature distributions over the ACF basin and the southeast US. Monthly temperature fields are aggregated by season (DJF, MAM, JJA, SON). The columns depict observations for the period 01/1950 - 12/1999 (Column 1); JVSD downscaled data using input from the 20CM3 experiment for the period 01/1950 - 12/1999 (Column 2); JVSD downscaled data using input from the BCCR BCM2.0 -run1A2 Scenario for the period 01/2000-12/2049 (Column 3); and JVSD downscaled data using input from the BCCR BCM2.0 -run1A2 Scenario for the period 01/2050-12/2099 (Column 4).

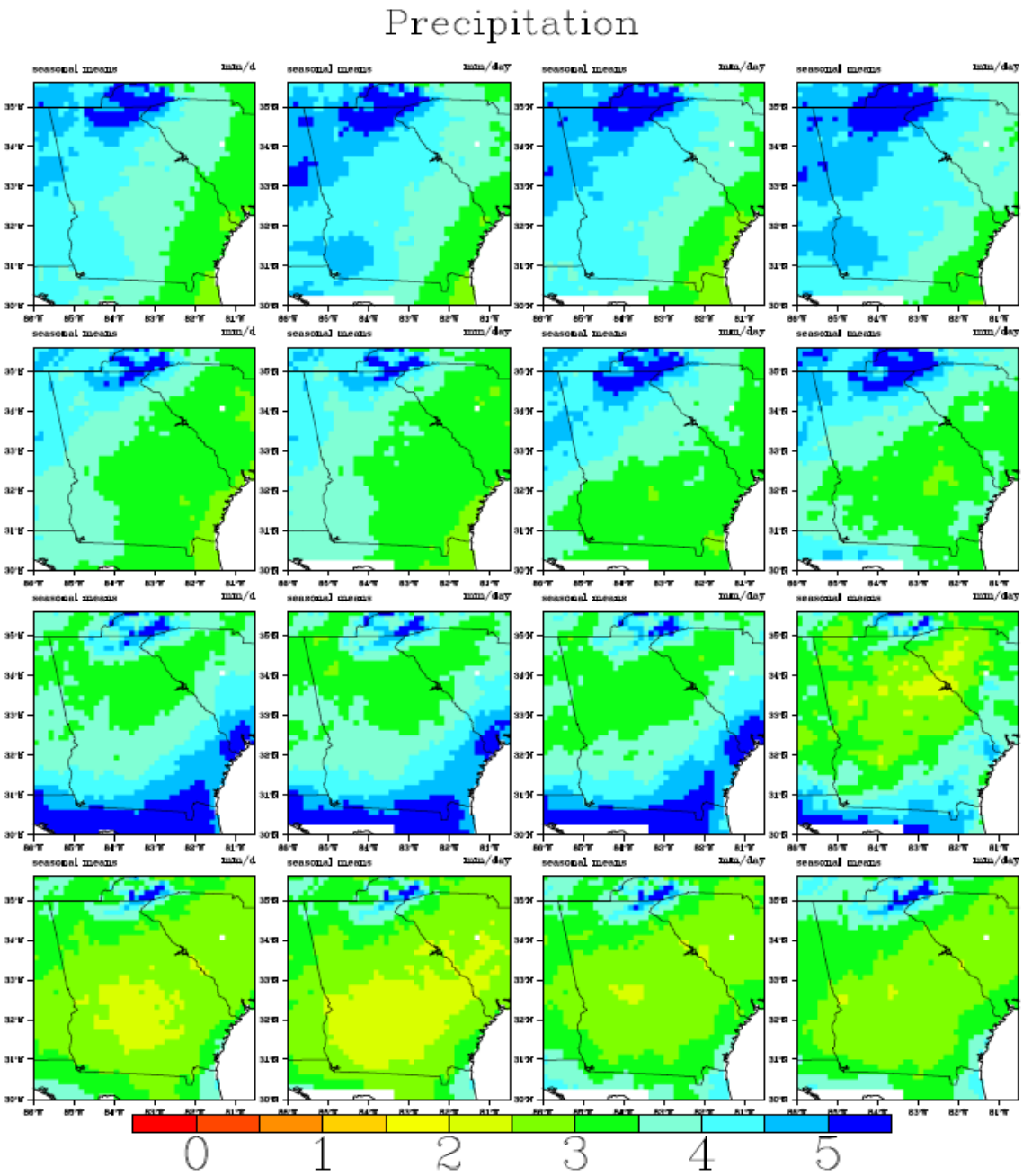

Figure A.9: Spatial precipitation distributions over the ACF basin and the southeast US. Monthly precipitation fields are aggregated by season (DJF, MAM, JJA, SON). The columns depict observations for the period 01/1950 - 12/1999 (Column 1); JVSD downscaled data using input from the 20CM3 experiment for the period 01/1950 - 12/1999 (Column 2); JVSD downscaled data using input from the BCCR BCM2.0 -run1A2 Scenario for the period 01/2000-12/2049 (Column 3); and JVSD downscaled data using input from the BCCR BCM2.0 -run1A2 Scenario for the period 01/2050-12/2099 (Column 4).

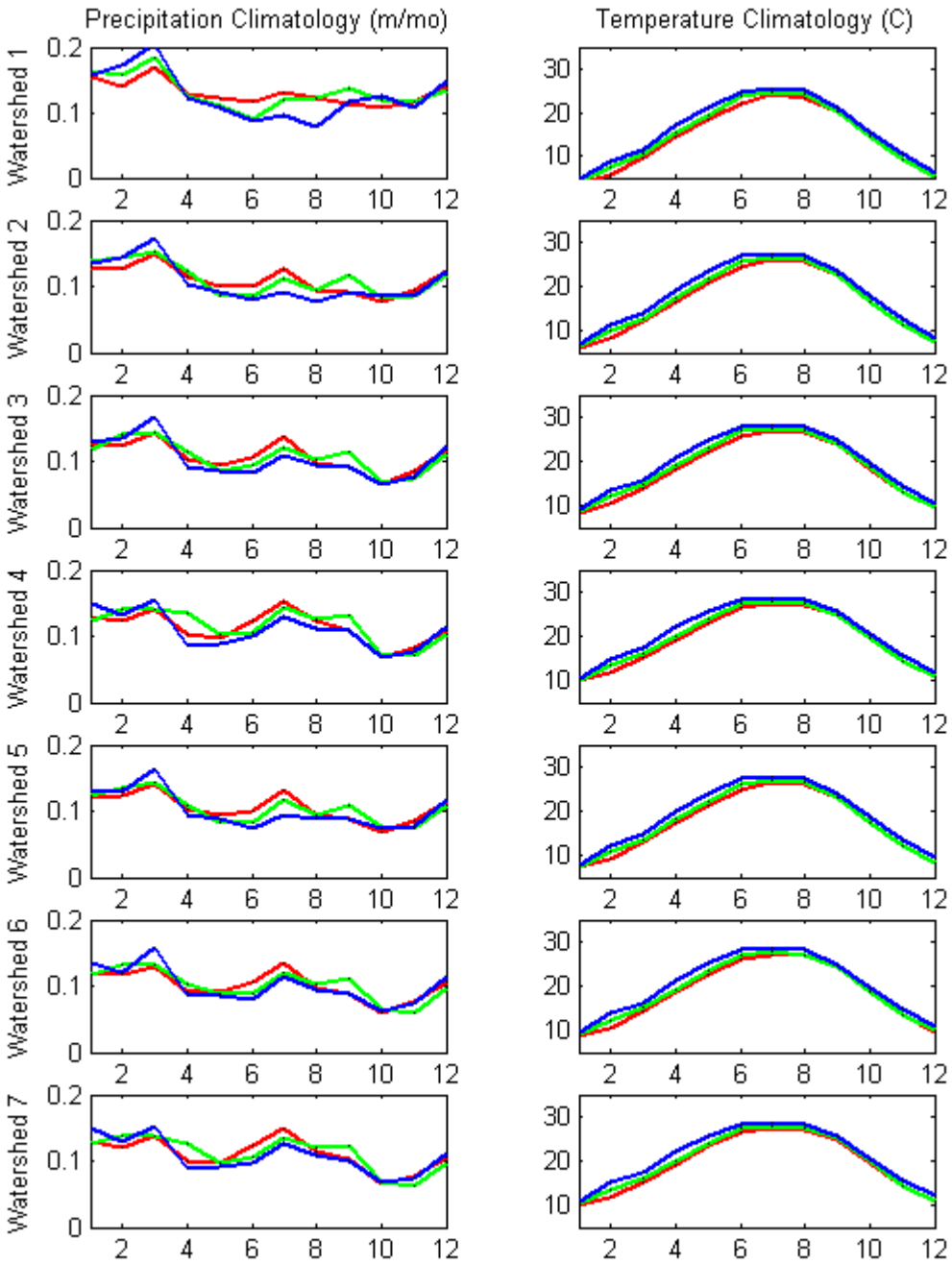

Figure A.10a: Climatologies of spatially aggregated precipitation and temperature for seven ACF watersheds: *(1)* Buford, *(2)* West Point, *(3)* George, *(4)* Woodruff, *(5)* Montezuma, *(6)* Albany, and *(7)* Bainbridge; Lines in Red–Observations (1950-1999); Green–JVSD downscaled (2000- 2049); Blue–JVSD downscaled (2050-2099) under BCCR BCM2.0 -run1 A1B Scenarios.

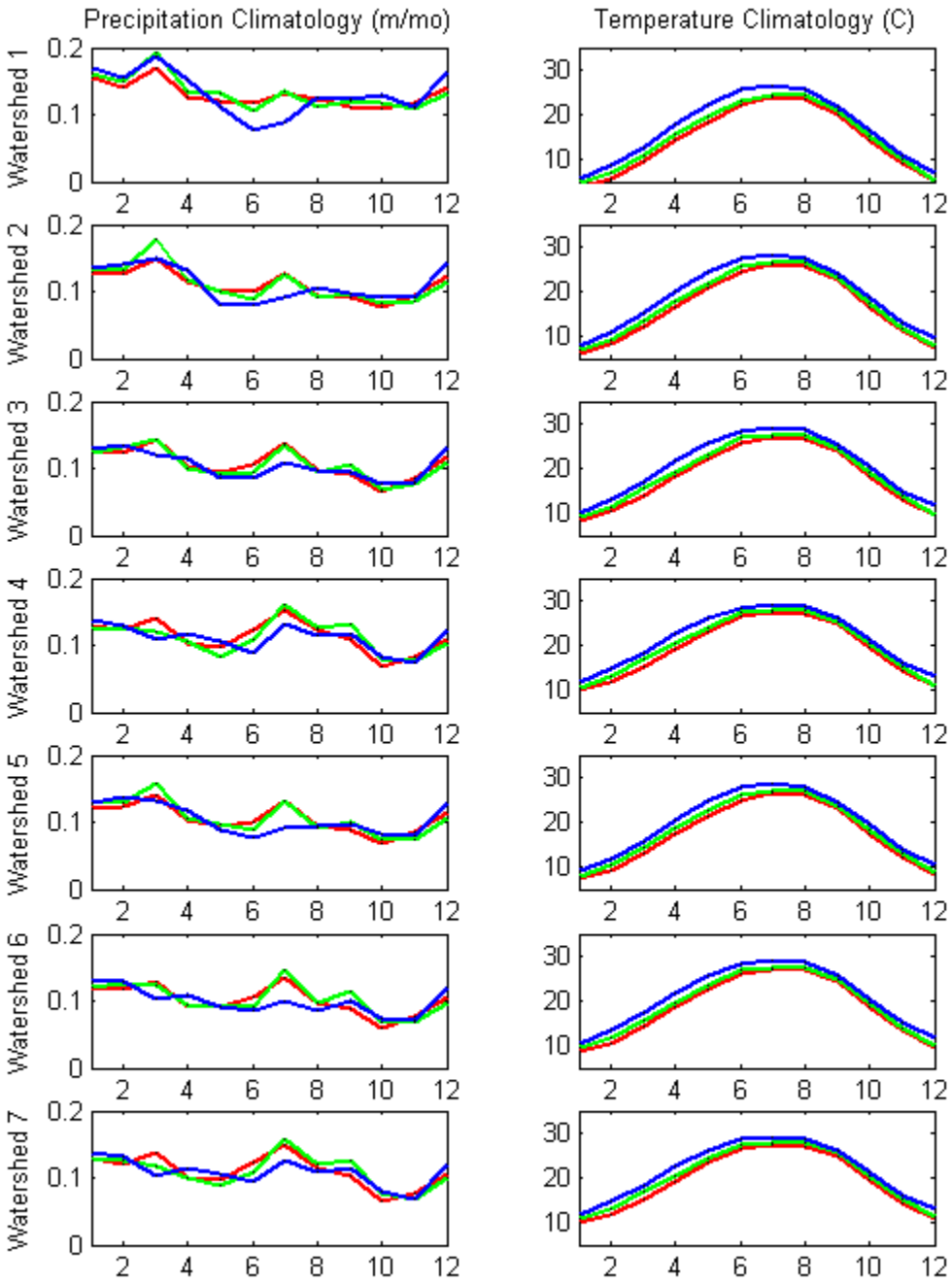

Figure A.10b: Climatologies of spatially aggregated precipitation and temperature for seven ACF watersheds: *(1)* Buford, *(2)* West Point, *(3)* George, *(4)* Woodruff, *(5)* Montezuma, *(6)* Albany, and *(7)* Bainbridge; Lines in Red–Observations (1950-1999); Green–JVSD downscaled (2000- 2049); Blue–JVSD downscaled (2050-2099) under BCCR BCM2.0 -run1 A2 Scenarios.

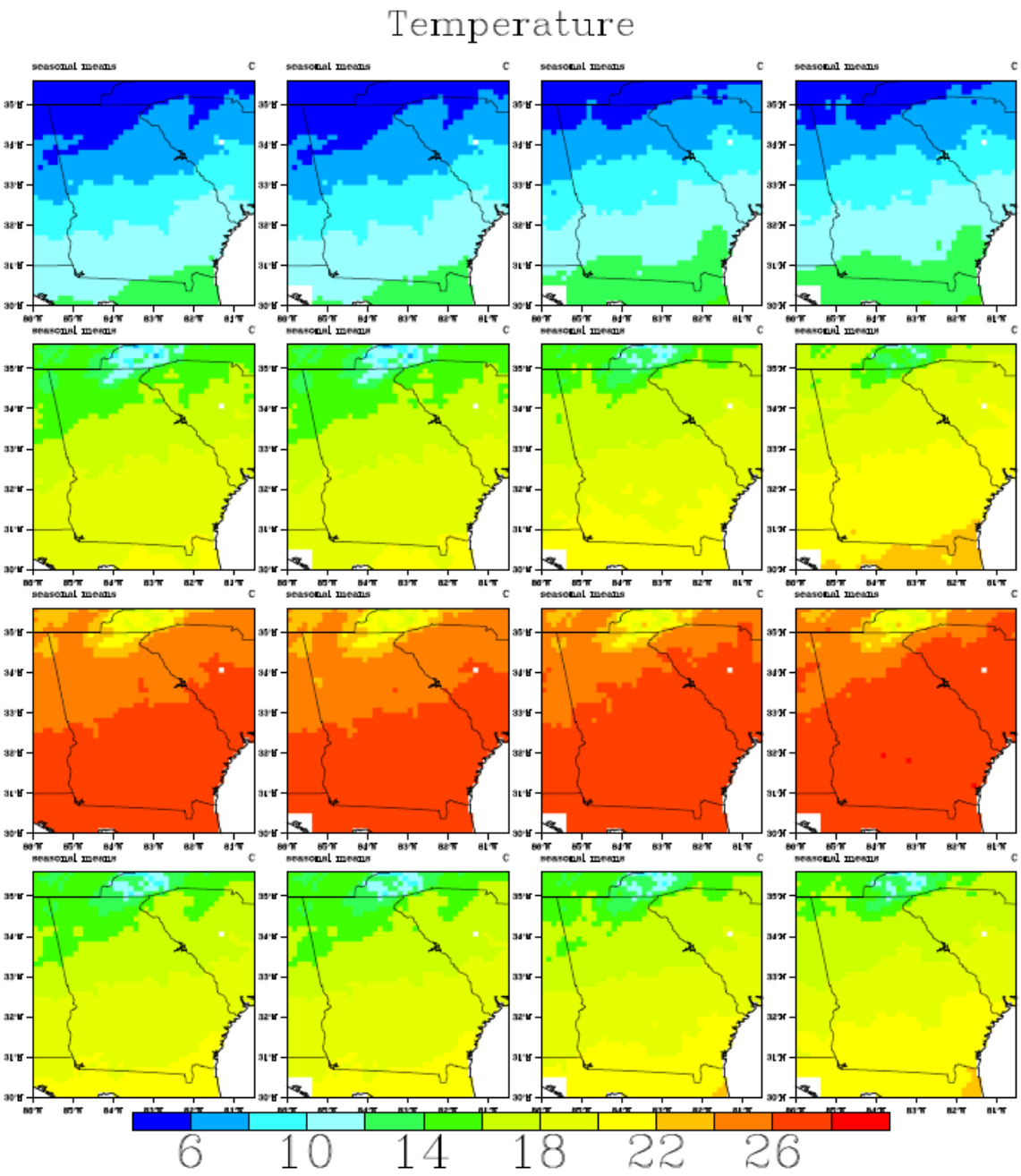

Figure A.11: Spatial temperature distributions over the ACF basin and the southeast US. Monthly temperature fields are aggregated by season (DJF, MAM, JJA, SON). The columns depict observations for the period 01/1950 - 12/1999 (Column 1); JVSD downscaled data using input from the 20CM3 experiment for the period 01/1950 - 12/1999 (Column 2); JVSD downscaled data using input from the NCAR_CCSM3.0 -run2 A1B Scenario for the period 01/2000-12/2049 (Column 3); and JVSD downscaled data using input from the NCAR_CCSM3.0 -run2 A1B Scenario for the period 01/2050-12/2099 (Column 4).

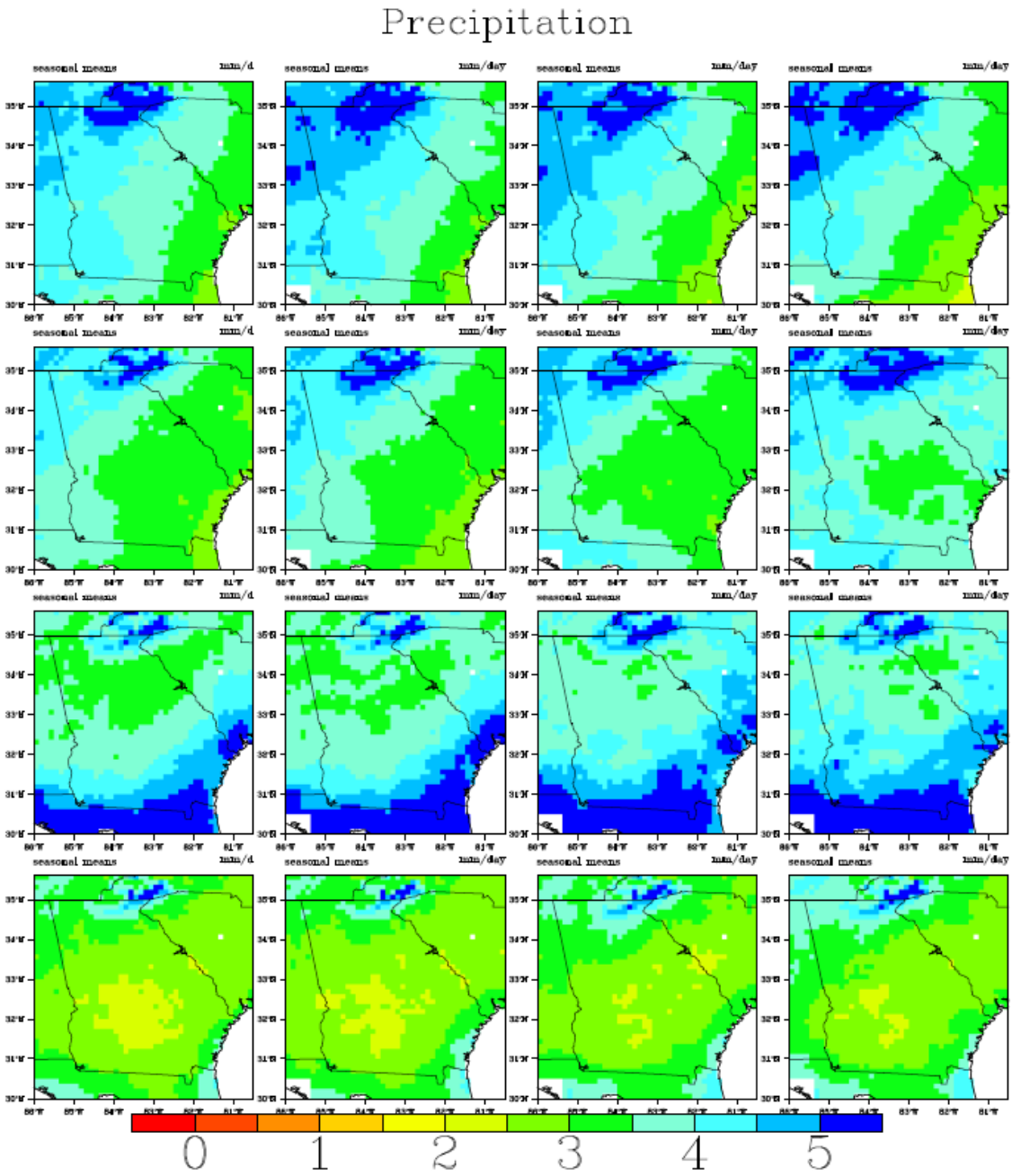

Figure A.12: Spatial precipitation distributions over the ACF basin and the southeast US. Monthly precipitation fields are aggregated by season (DJF, MAM, JJA, SON). The columns depict observations for the period 01/1950 - 12/1999 (Column 1); JVSD downscaled data using input from the 20CM3 experiment for the period 01/1950 - 12/1999 (Column 2); JVSD downscaled data using input from the NCAR_CCSM3.0 -run2A1B Scenario for the period 01/2000-12/2049 (Column 3); and JVSD downscaled data using input from the NCAR_CCSM3.0 -run2 A1B Scenario for the period 01/2050-12/2099 (Column 4).

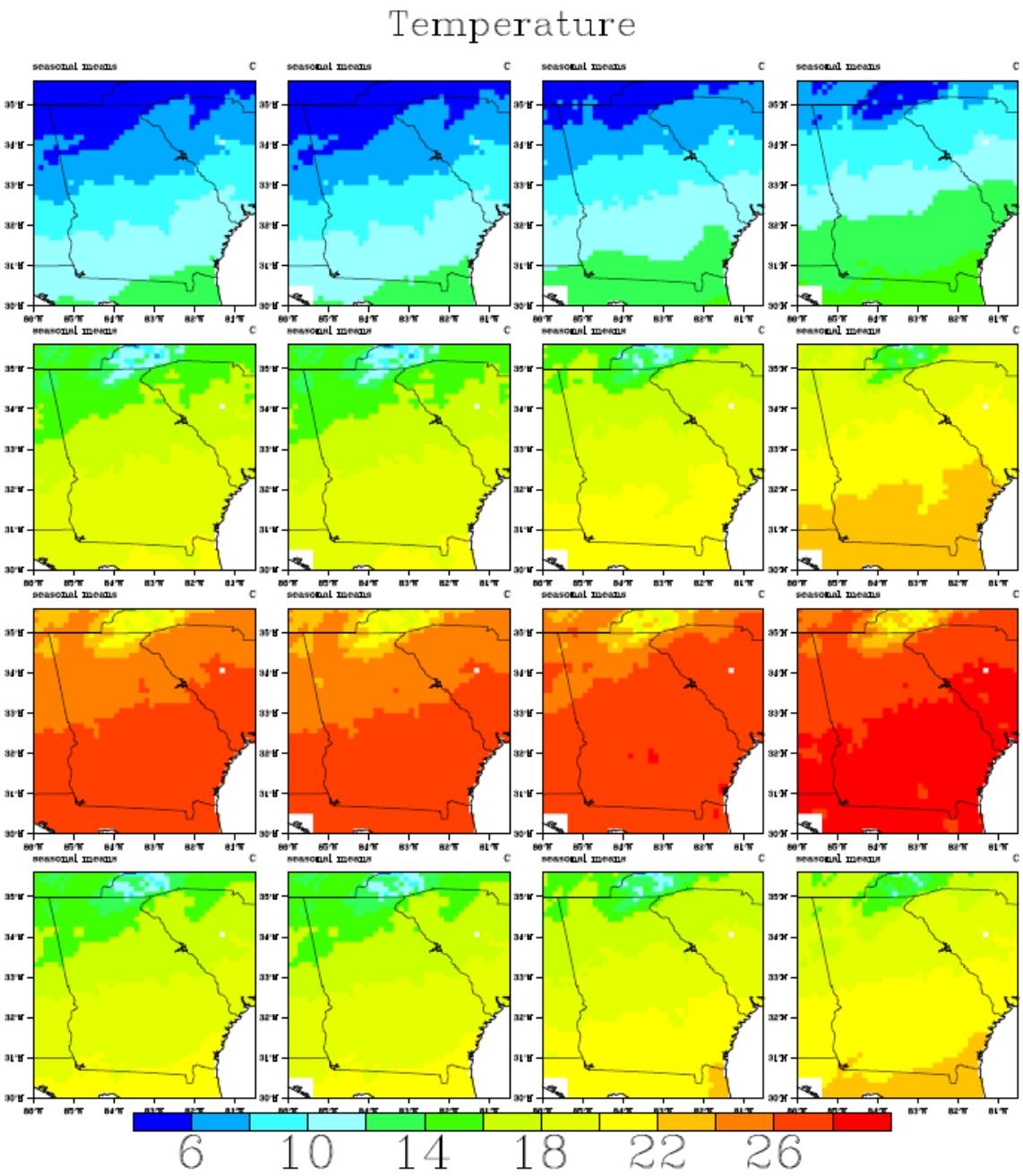

Figure A.13: Spatial temperature distributions over the ACF basin and the southeast US. Monthly temperature fields are aggregated by season (DJF, MAM, JJA, SON). The columns depict observations for the period 01/1950 - 12/1999 (Column 1); JVSD downscaled data using input from the 20CM3 experiment for the period 01/1950 - 12/1999 (Column 2); JVSD downscaled data using input from the NCAR_CCSM3.0 -run2A2 Scenario for the period 01/2000-12/2049 (Column 3); and JVSD downscaled data using input from the NCAR_CCSM3.0 -run2A2 Scenario for the period 01/2050-12/2099 (Column 4).

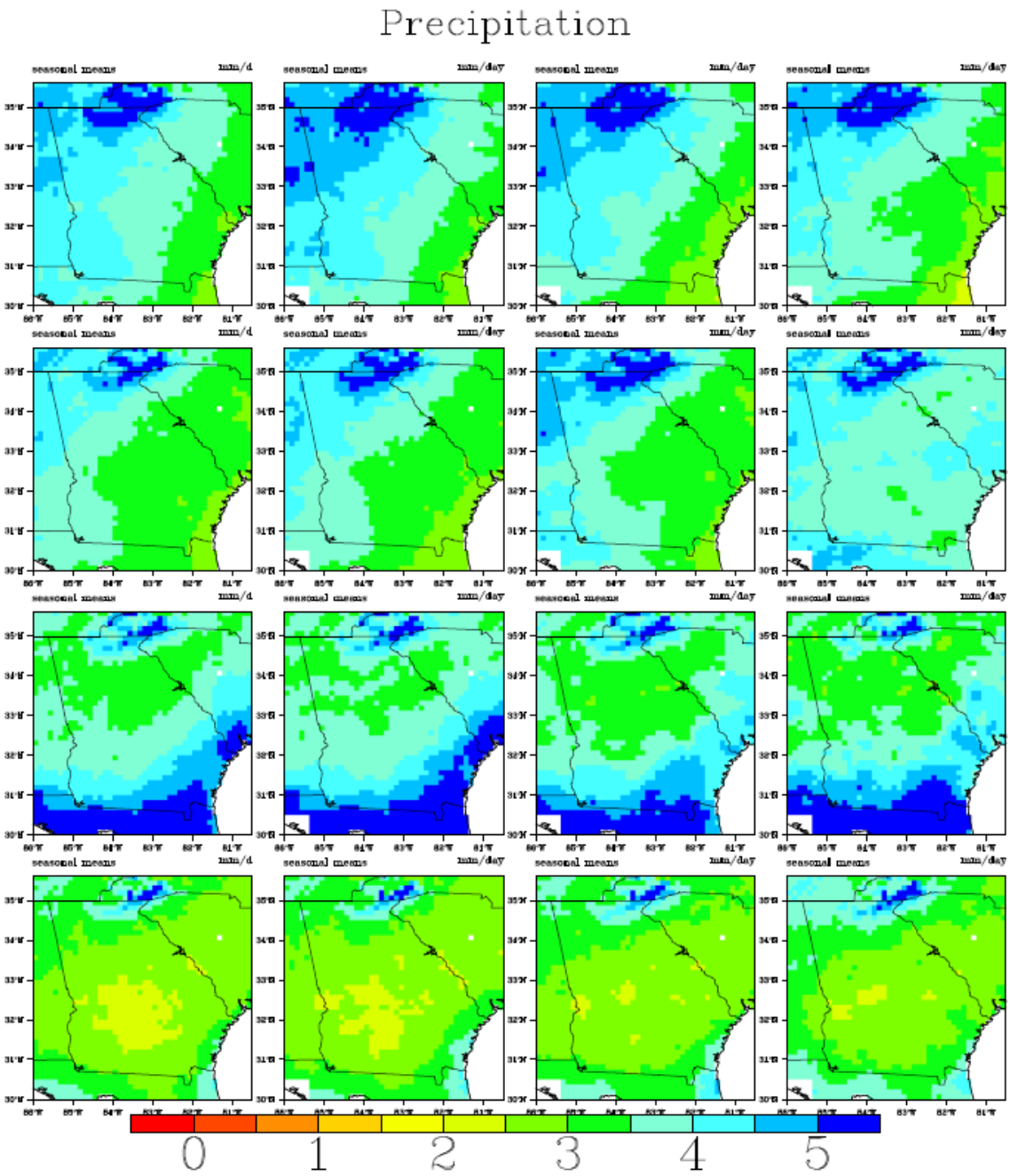

Figure A.14: Spatial precipitation distributions over the ACF basin and the southeast US. Monthly precipitation fields are aggregated by season (DJF, MAM, JJA, SON). The columns depict observations for the period 01/1950 - 12/1999 (Column 1); JVSD downscaled data using input from the 20CM3 experiment for the period 01/1950 - 12/1999 (Column 2); JVSD downscaled data using input from the NCAR_CCSM3.0 -run2A2 Scenario for the period 01/2000-12/2049 (Column 3); and JVSD downscaled data using input from the NCAR_CCSM3.0 -run2A2 Scenario for the period 01/2050-12/2099 (Column 4).

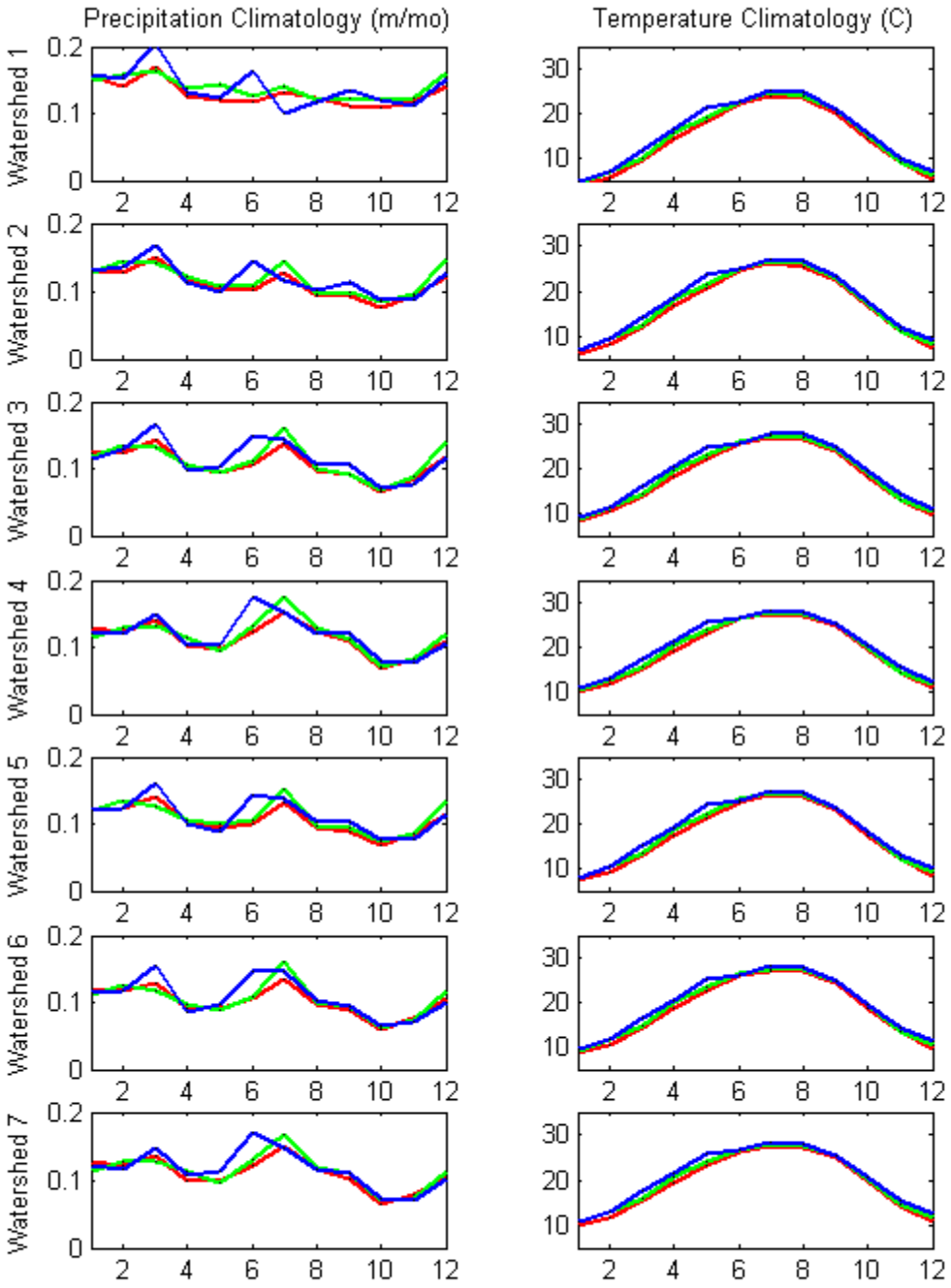

Figure A.15a: Climatologies of spatially aggregated precipitation and temperature for seven ACF watersheds: *(1)* Buford, *(2)* West Point, *(3)* George, *(4)* Woodruff, *(5)* Montezuma, *(6)* Albany, and *(7)* Bainbridge; Lines in Red–Observations (1950-1999); Green–JVSD downscaled (2000- 2049); Blue–JVSD downscaled (2050-2099) under NCAR_CCSM3.0 -run2 A1B Scenarios.

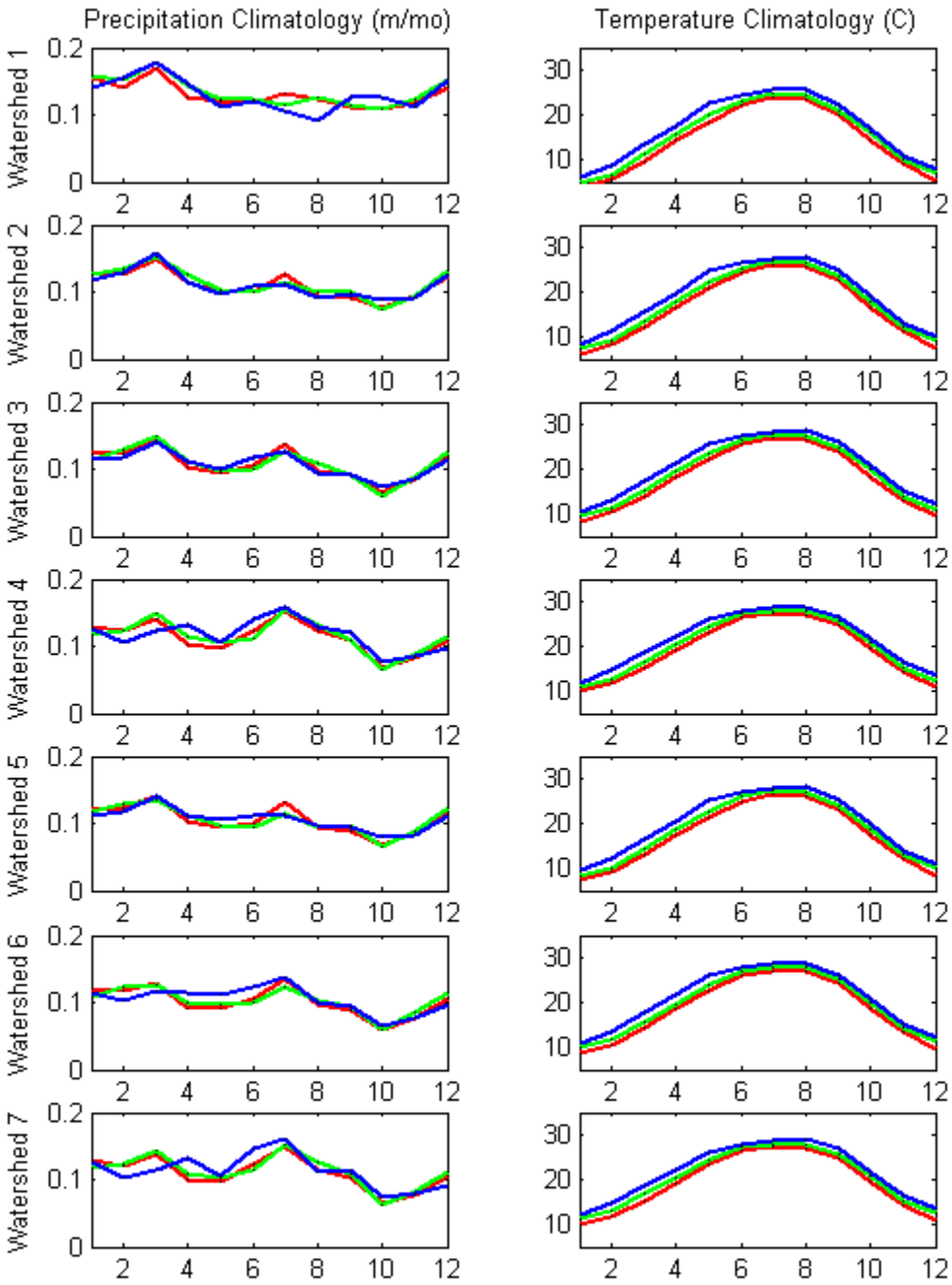

Figure A.15b: Climatologies of spatially aggregated precipitation and temperature for seven ACF watersheds: *(1)* Buford, *(2)* West Point, *(3)* George, *(4)* Woodruff, *(5)* Montezuma, *(6)* Albany, and *(7)* Bainbridge; Lines in Red–Observations (1950-1999); Green–JVSD downscaled (2000- 2049); Blue–JVSD downscaled (2050-2099) under NCAR_CCSM3.0 -run2 A2 Scenarios.

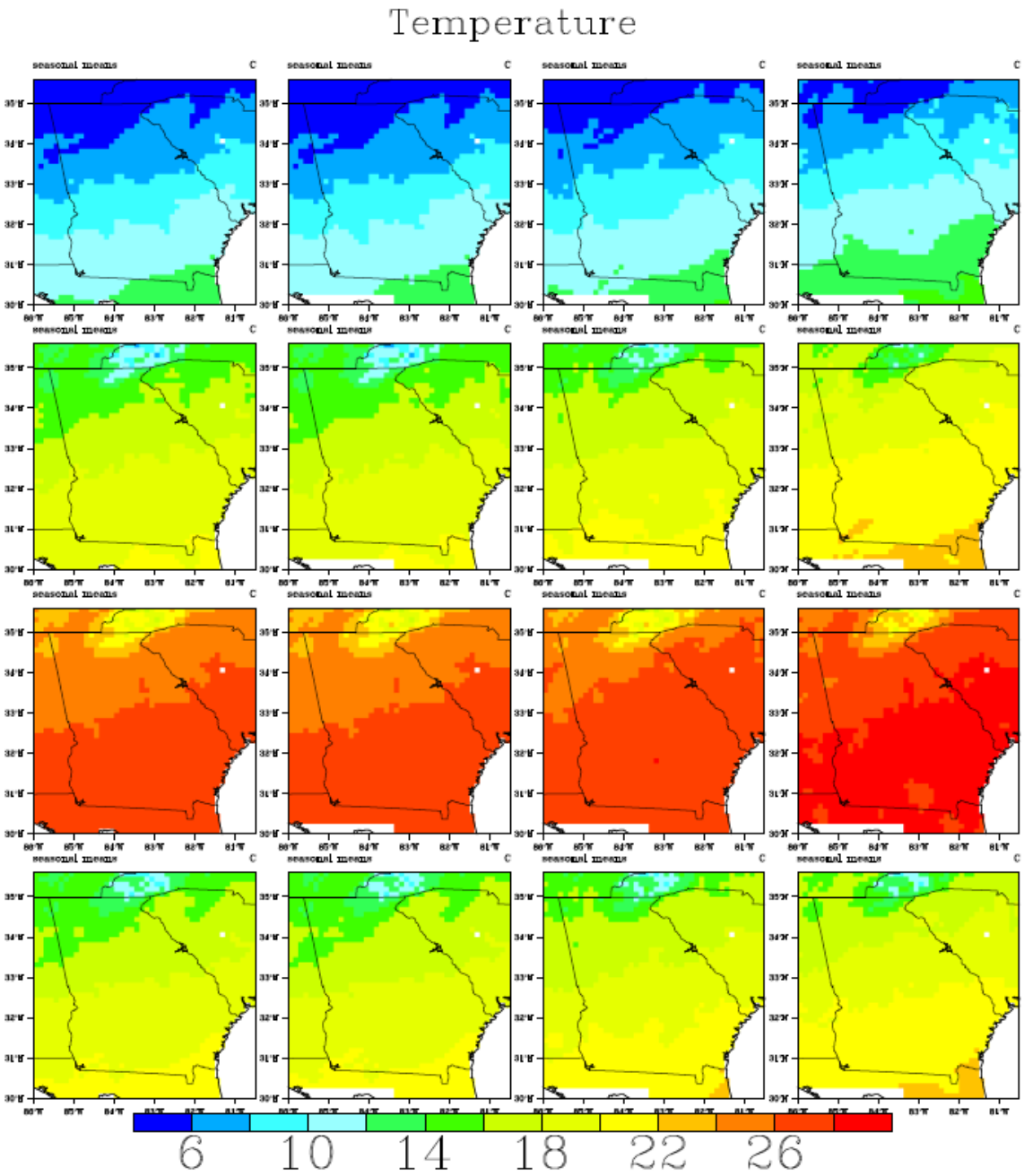

Figure A.16: Spatial temperature distributions over the ACF basin and the southeast US. Monthly temperature fields are aggregated by season (DJF, MAM, JJA, SON). The columns depict observations for the period 01/1950 - 12/1999 (Column 1); JVSD downscaled data using input from the 20CM3 experiment for the period 01/1950 - 12/1999 (Column 2); JVSD downscaled data using input from the CNRM CM3 -run1 A1B Scenario for the period 01/2000-12/2049 (Column 3); and JVSD downscaled data using input from the CNRM CM3 -run1 A1B Scenario for the period 01/2050-12/2099 (Column 4).

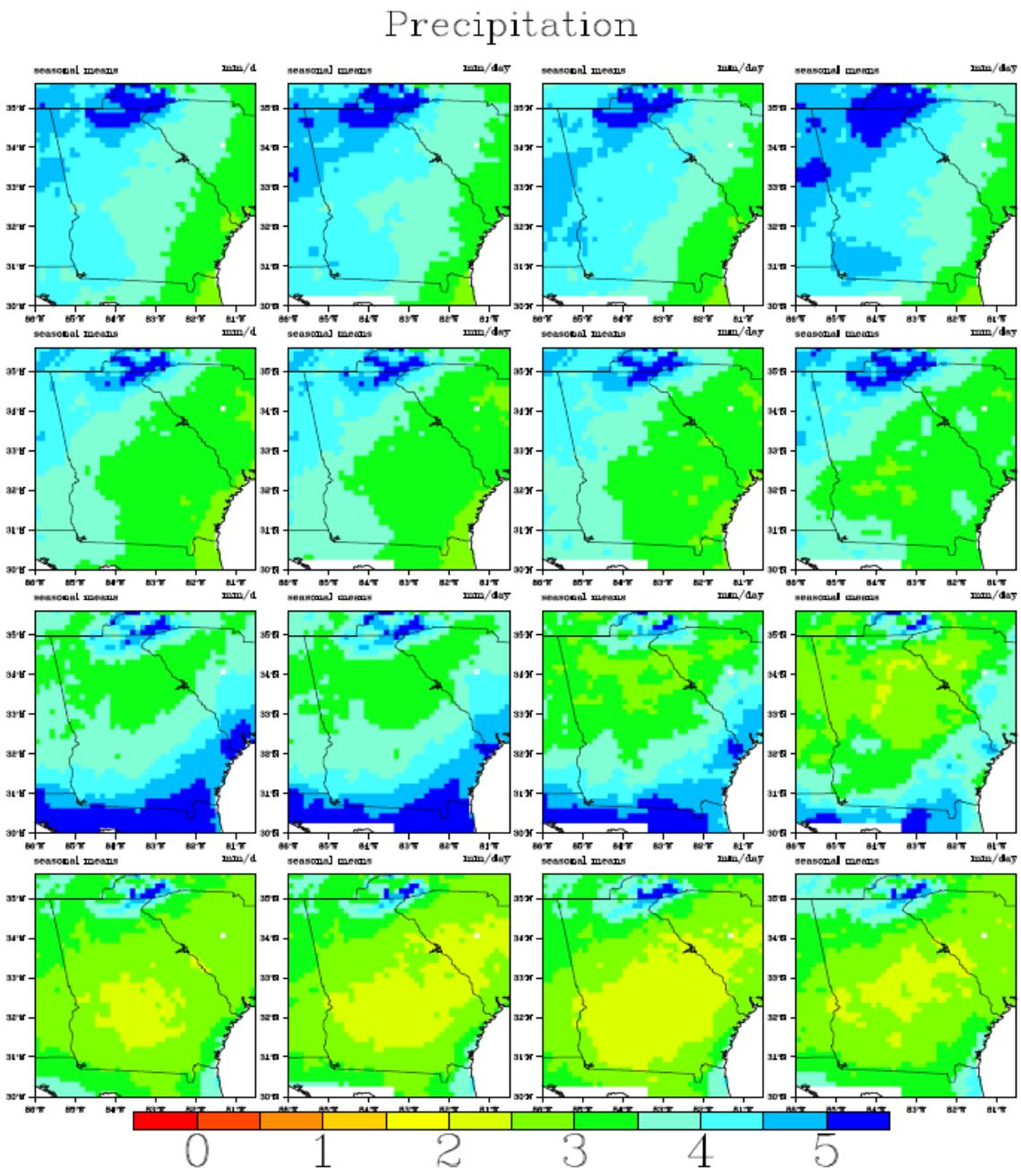

Figure A.17: Spatial precipitation distributions over the ACF basin and the southeast US. Monthly precipitation fields are aggregated by season (DJF, MAM, JJA, SON). The columns depict observations for the period 01/1950 - 12/1999 (Column 1); JVSD downscaled data using input from the 20CM3 experiment for the period 01/1950 - 12/1999 (Column 2); JVSD downscaled data using input from the CNRM CM3 -run1A1B Scenario for the period 01/2000-12/2049 (Column 3); and JVSD downscaled data using input from the CNRM CM3 -run1 A1B Scenario for the period 01/2050-12/2099 (Column 4).

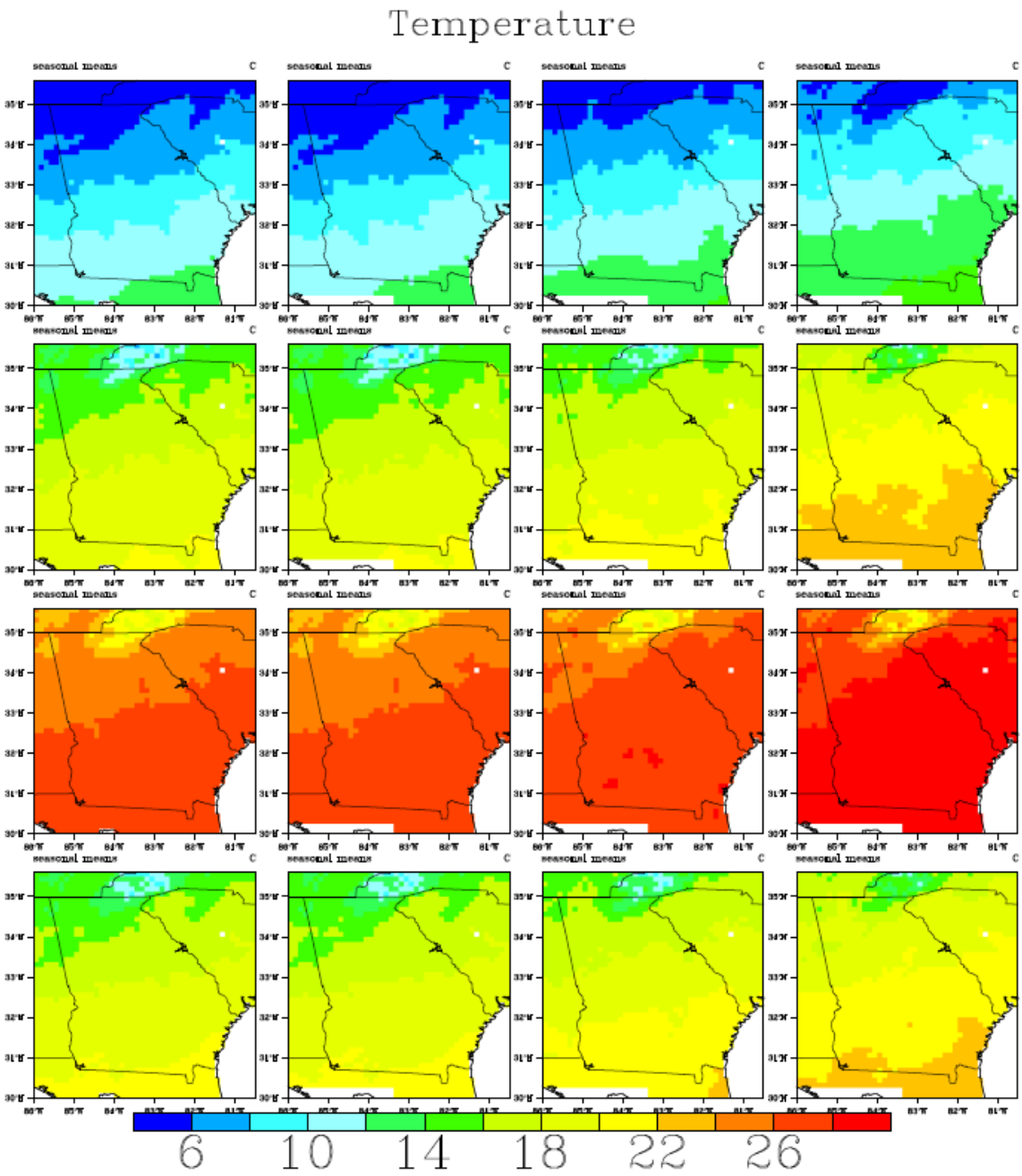

Figure A.18: Spatial temperature distributions over the ACF basin and the southeast US. Monthly temperature fields are aggregated by season (DJF, MAM, JJA, SON). The columns depict observations for the period 01/1950 - 12/1999 (Column 1); JVSD downscaled data using input from the 20CM3 experiment for the period 01/1950 - 12/1999 (Column 2); JVSD downscaled data using input from the CNRM CM3 -run1A2 Scenario for the period 01/2000-12/2049 (Column 3); and JVSD downscaled data using input from the CNRM CM3 -run1A2 Scenario for the period 01/2050-12/2099 (Column 4).

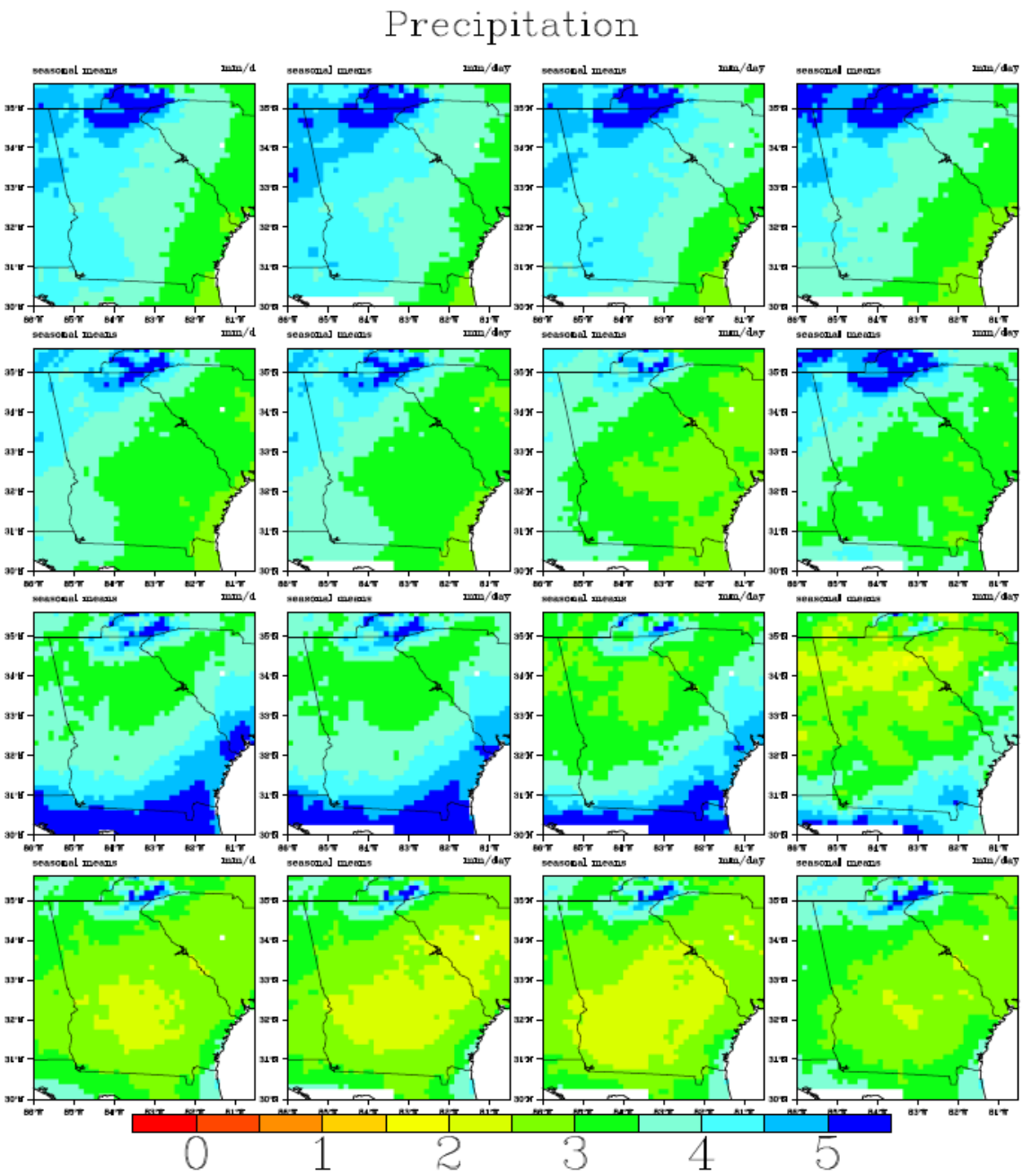

Figure A.19: Spatial precipitation distributions over the ACF basin and the southeast US. Monthly precipitation fields are aggregated by season (DJF, MAM, JJA, SON). The columns depict observations for the period 01/1950 - 12/1999 (Column 1); JVSD downscaled data using input from the 20CM3 experiment for the period 01/1950 - 12/1999 (Column 2); JVSD downscaled data using input from the CNRM CM3 -run1A2 Scenario for the period 01/2000-12/2049 (Column 3); and JVSD downscaled data using input from the CNRM CM3 -run1A2 Scenario for the period 01/2050-12/2099 (Column 4).

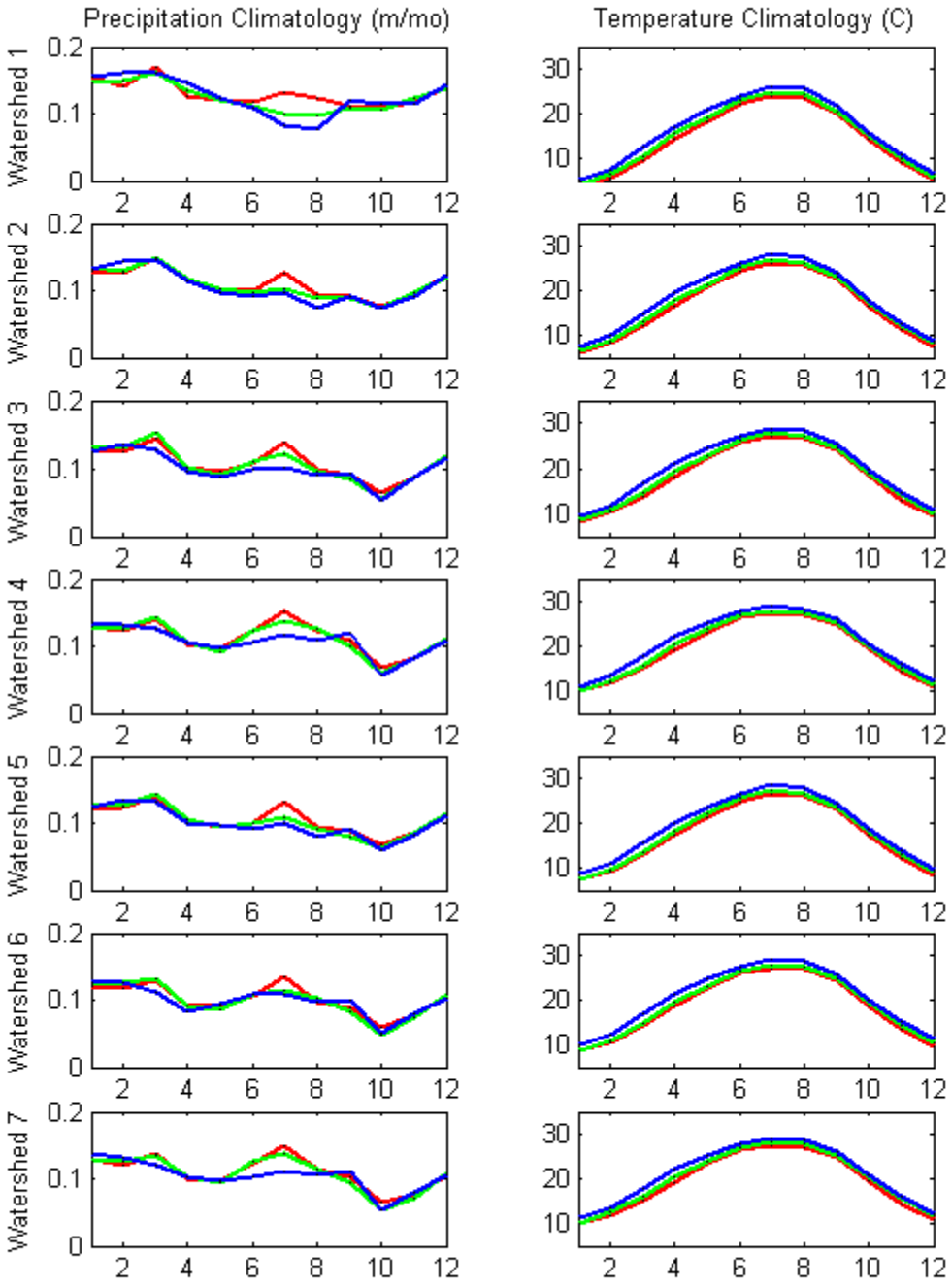

Figure A.20a: Climatologies of spatially aggregated precipitation and temperature for seven ACF watersheds: *(1)* Buford, *(2)* West Point, *(3)* George, *(4)* Woodruff, *(5)* Montezuma, *(6)* Albany, and *(7)* Bainbridge; Lines in Red–Observations (1950-1999); Green–JVSD downscaled (2000- 2049); Blue–JVSD downscaled (2050-2099) under CNRM CM3 -run1 A1B Scenarios.

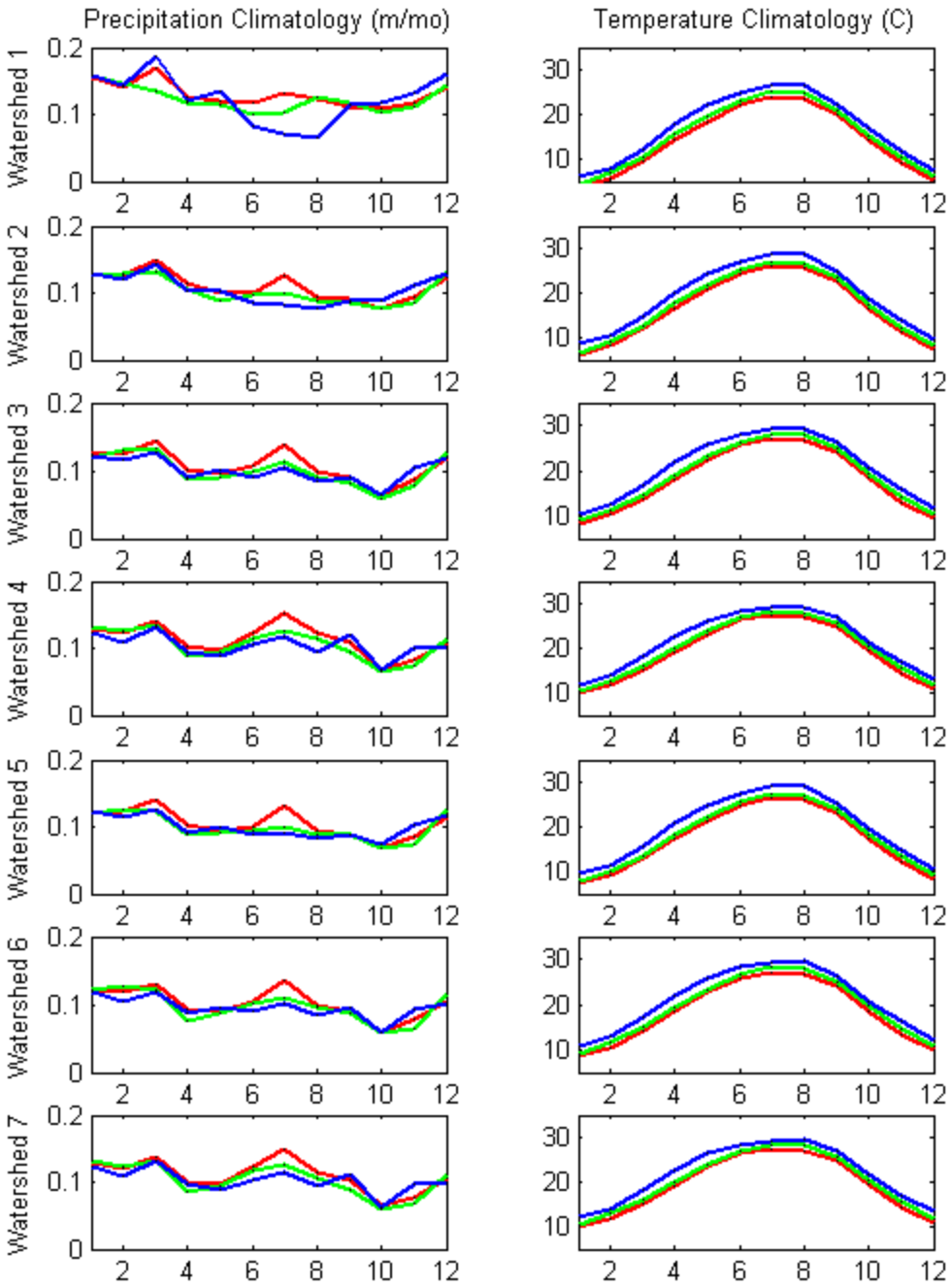

Figure A.20b: Climatologies of spatially aggregated precipitation and temperature for seven ACF watersheds: *(1)* Buford, *(2)* West Point, *(3)* George, *(4)* Woodruff, *(5)* Montezuma, *(6)* Albany, and *(7)* Bainbridge; Lines in Red–Observations (1950-1999); Green–JVSD downscaled (2000- 2049); Blue–JVSD downscaled (2050-2099) under CNRM CM3 -run1 A2 Scenarios.

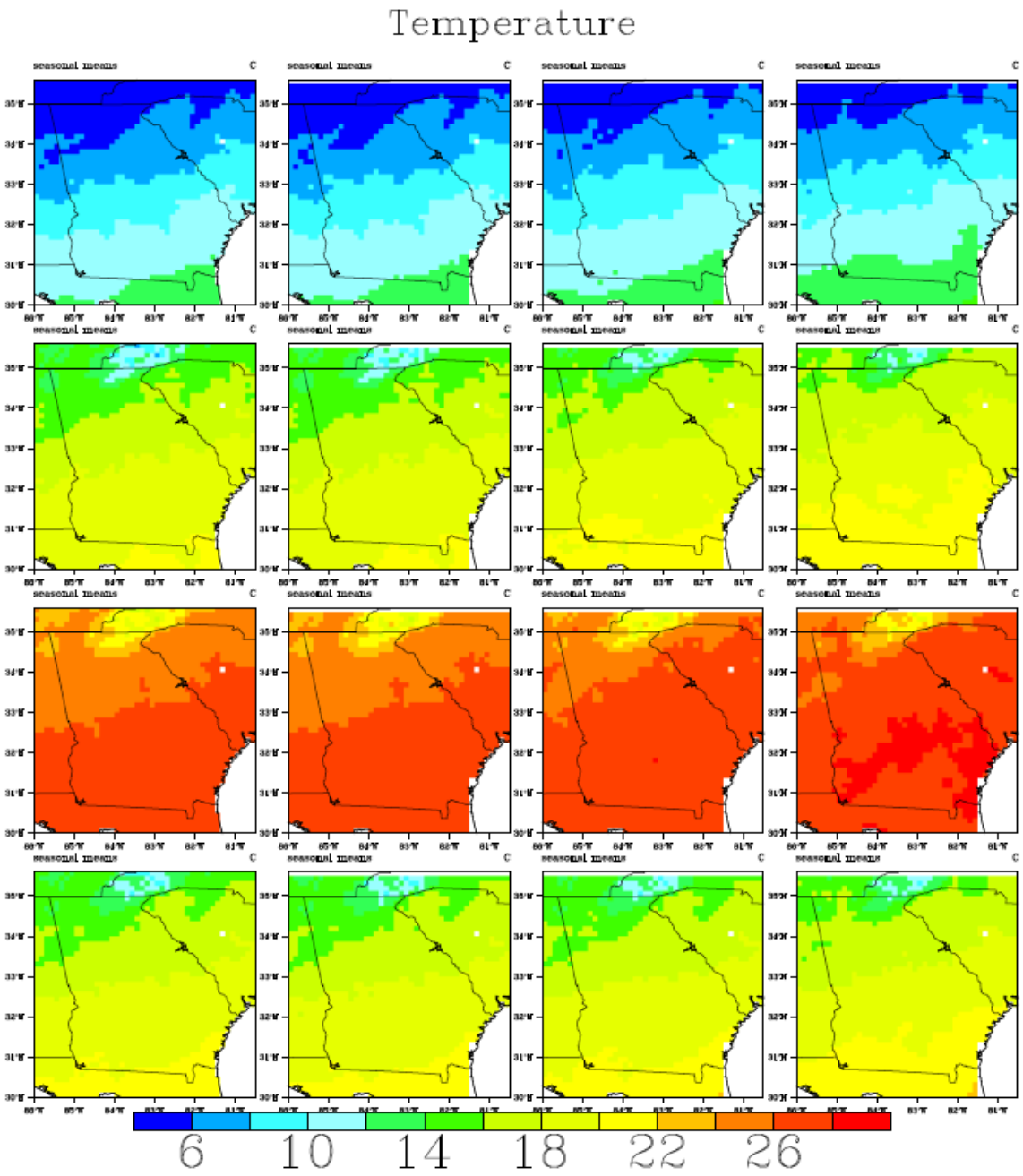

Figure A.21: Spatial temperature distributions over the ACF basin and the southeast US. Monthly temperature fields are aggregated by season (DJF, MAM, JJA, SON). The columns depict observations for the period 01/1950 - 12/1999 (Column 1); JVSD downscaled data using input from the 20CM3 experiment for the period 01/1950 - 12/1999 (Column 2); JVSD downscaled data using input from the CSIRO MK3.0 -run1 A1B Scenario for the period 01/2000-12/2049 (Column 3); and JVSD downscaled data using input from the CSIRO MK3.0 - run1 A1B Scenario for the period 01/2050-12/2099 (Column 4).

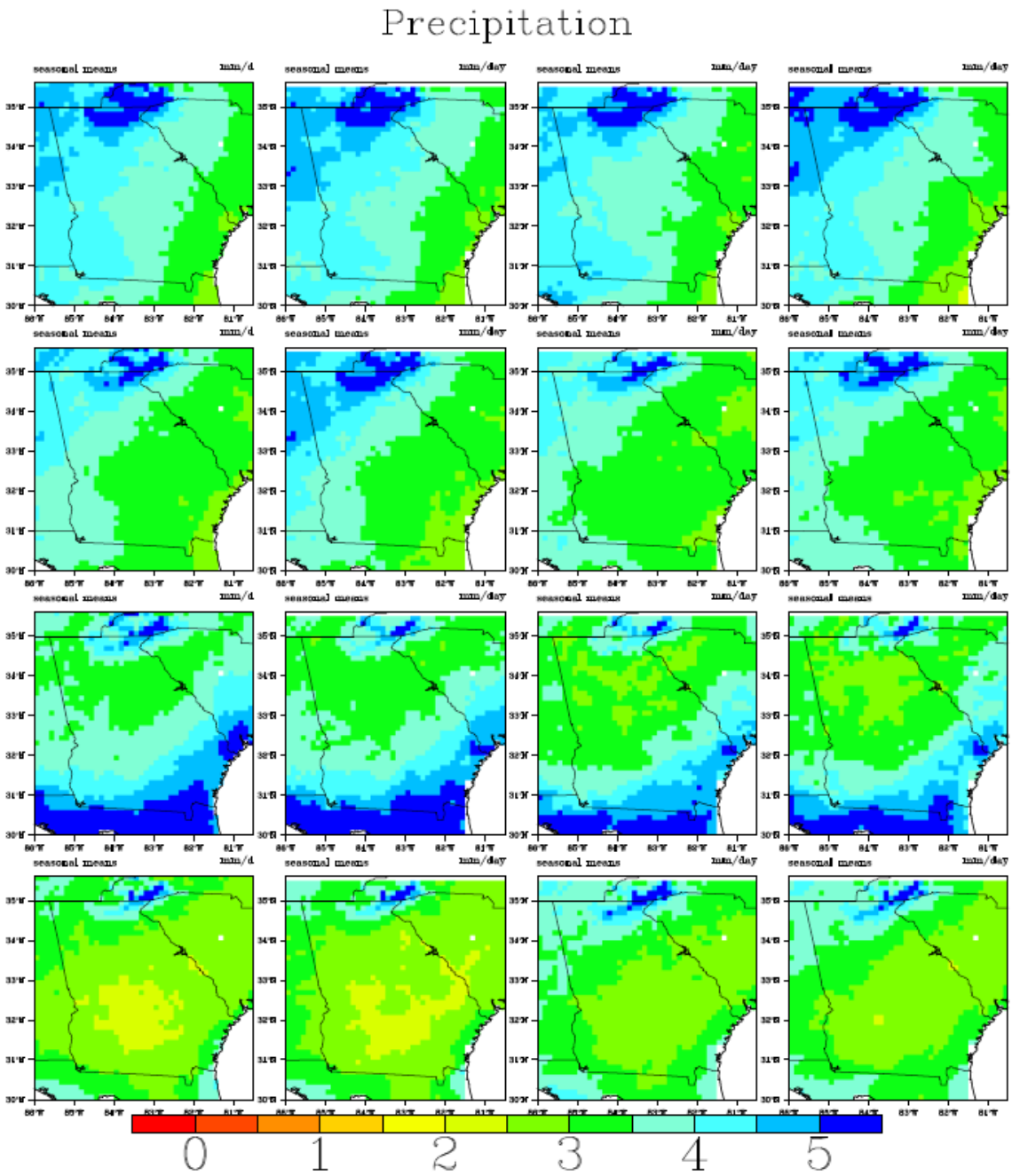

Figure A.22: Spatial precipitation distributions over the ACF basin and the southeast US. Monthly precipitation fields are aggregated by season (DJF, MAM, JJA, SON). The columns depict observations for the period 01/1950 - 12/1999 (Column 1); JVSD downscaled data using input from the 20CM3 experiment for the period 01/1950 - 12/1999 (Column 2); JVSD downscaled data using input from the CSIRO MK3.0 -run1A1B Scenario for the period 01/2000-12/2049 (Column 3); and JVSD downscaled data using input from the CSIRO MK3.0 -run1 A1B Scenario for the period 01/2050-12/2099 (Column 4).

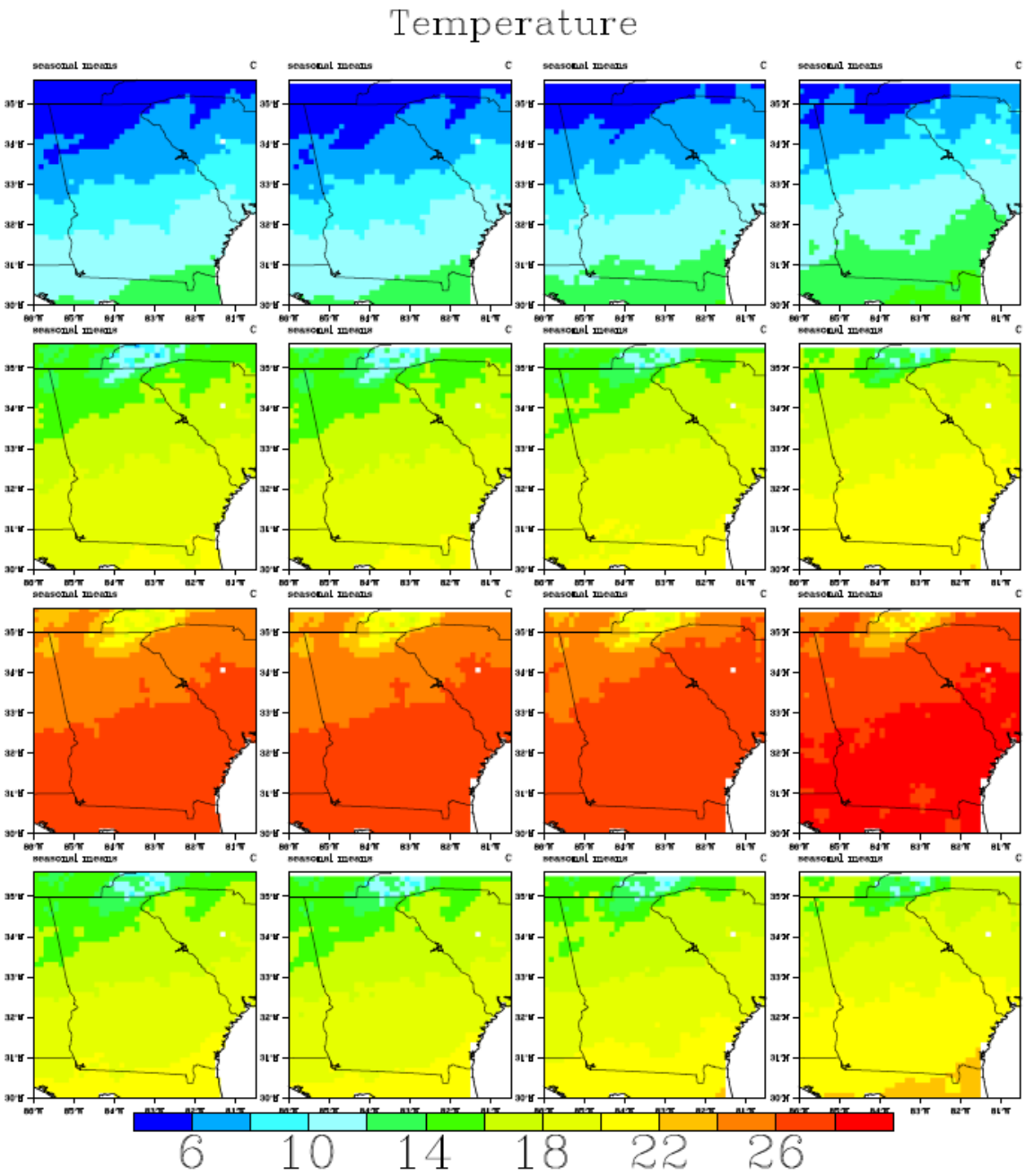

Figure A.23: Spatial temperature distributions over the ACF basin and the southeast US. Monthly temperature fields are aggregated by season (DJF, MAM, JJA, SON). The columns depict observations for the period 01/1950 - 12/1999 (Column 1); JVSD downscaled data using input from the 20CM3 experiment for the period 01/1950 - 12/1999 (Column 2); JVSD downscaled data using input from the CSIRO MK3.0 -run1A2 Scenario for the period 01/2000-12/2049 (Column 3); and JVSD downscaled data using input from the CSIRO MK3.0 -run1A2 Scenario for the period 01/2050-12/2099 (Column 4).

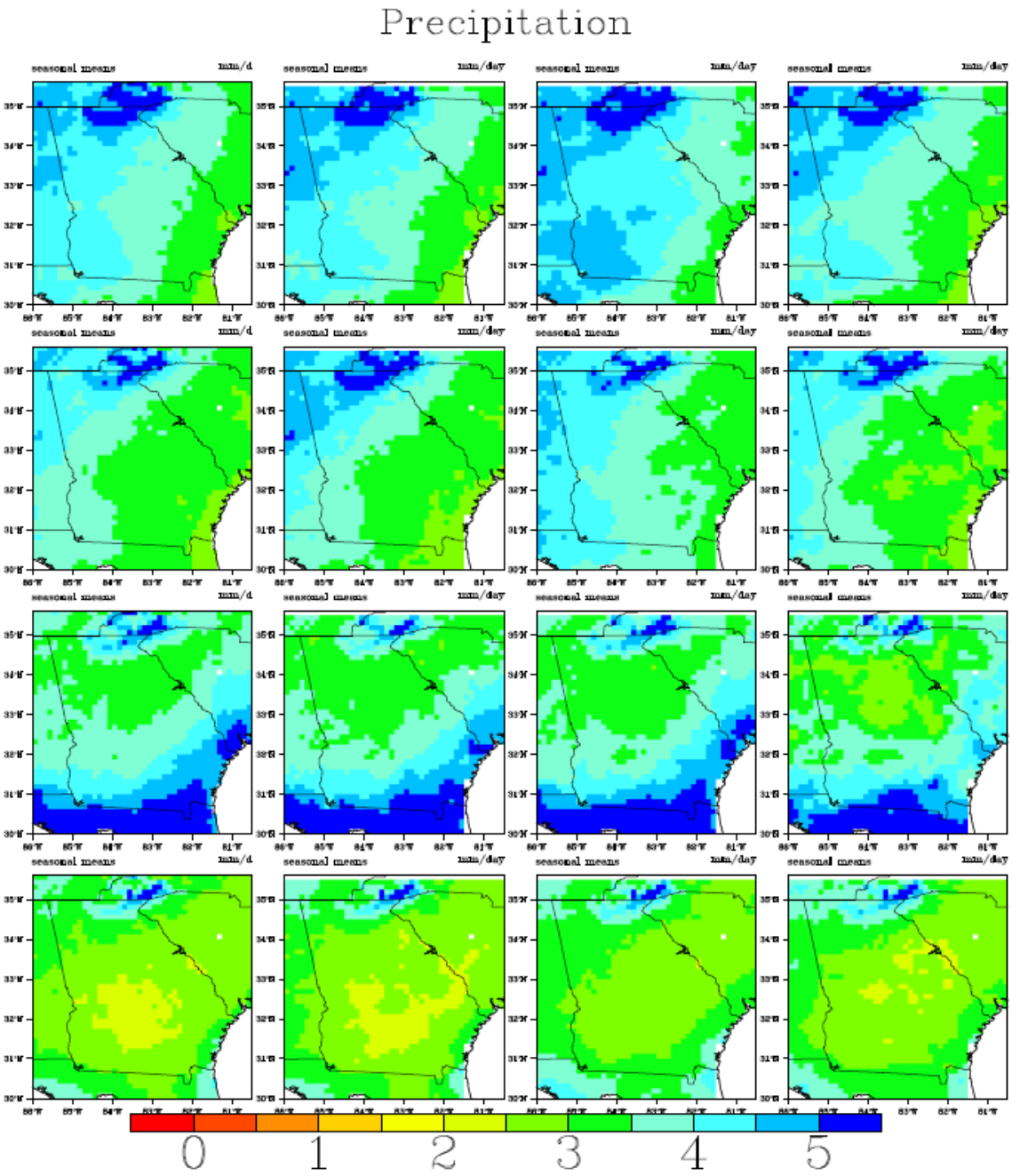

Figure A.24: Spatial precipitation distributions over the ACF basin and the southeast US. Monthly precipitation fields are aggregated by season (DJF, MAM, JJA, SON). The columns depict observations for the period 01/1950 - 12/1999 (Column 1); JVSD downscaled data using input from the 20CM3 experiment for the period 01/1950 - 12/1999 (Column 2); JVSD downscaled data using input from the CSIRO MK3.0 -run1A2 Scenario for the period 01/2000-12/2049 (Column 3); and JVSD downscaled data using input from the CSIRO MK3.0 -run1A2 Scenario for the period 01/2050-12/2099 (Column 4).

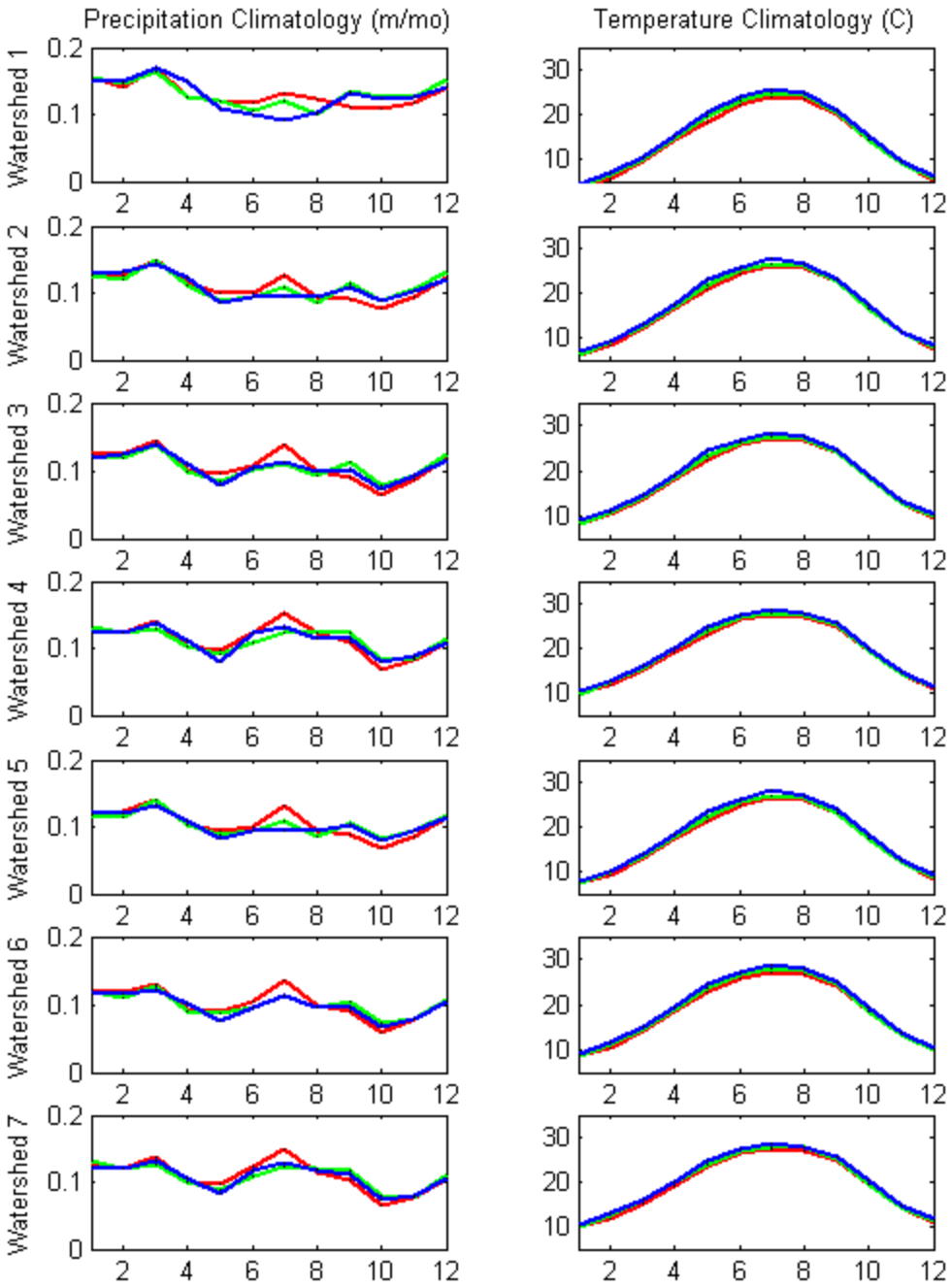

Figure A.25a: Climatologies of spatially aggregated precipitation and temperature for seven ACF watersheds: *(1)* Buford, *(2)* West Point, *(3)* George, *(4)* Woodruff, *(5)* Montezuma, *(6)* Albany, and *(7)* Bainbridge; Lines in Red–Observations (1950-1999); Green–JVSD downscaled (2000- 2049); Blue–JVSD downscaled (2050-2099) under CSIRO MK3.0 -run1 A1B Scenarios.

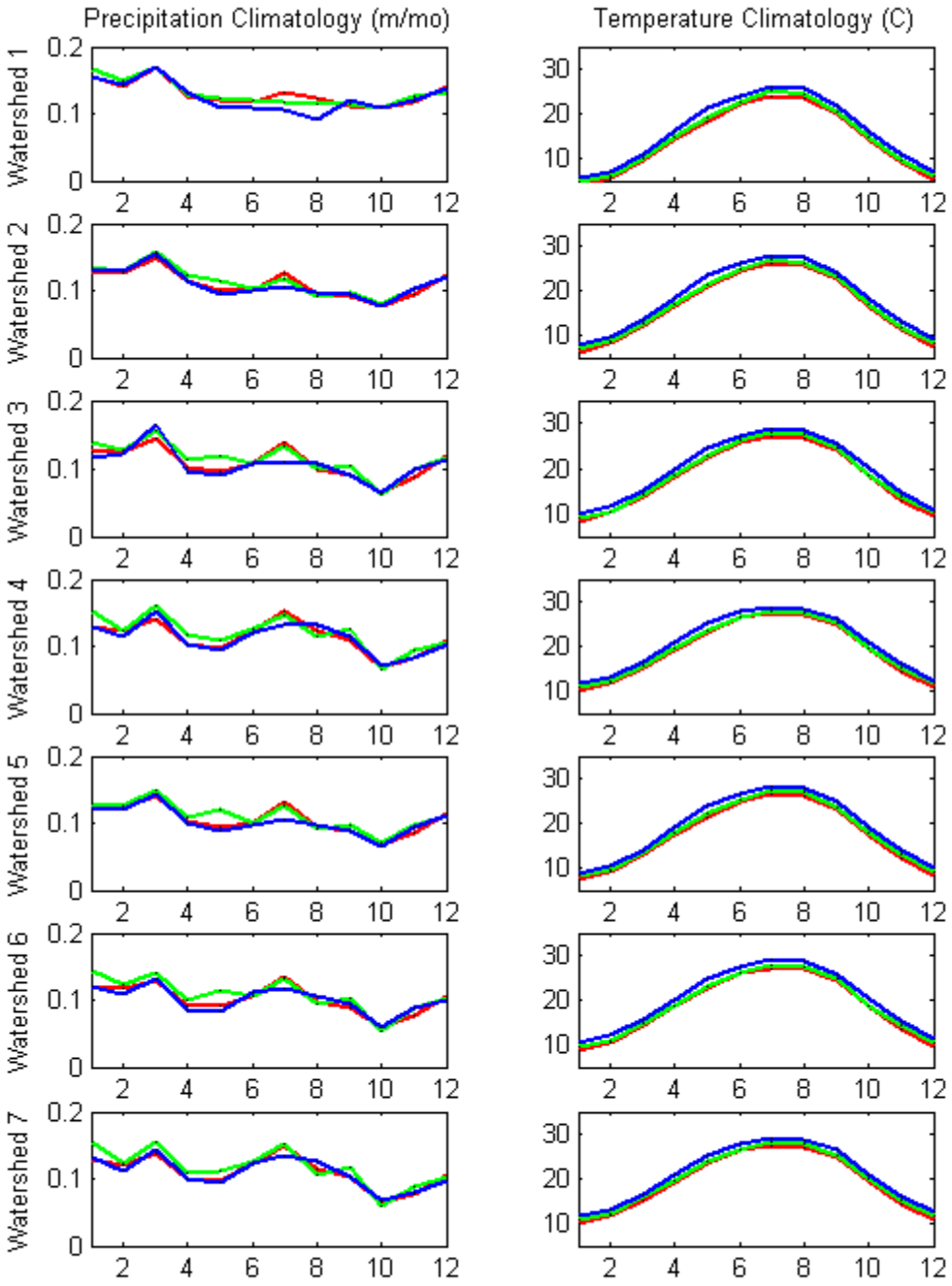

Figure A.25b: Climatologies of spatially aggregated precipitation and temperature for seven ACF watersheds: *(1)* Buford, *(2)* West Point, *(3)* George, *(4)* Woodruff, *(5)* Montezuma, *(6)* Albany, and *(7)* Bainbridge; Lines in Red–Observations (1950-1999); Green–JVSD downscaled (2000- 2049); Blue–JVSD downscaled (2050-2099) under CSIRO MK3.0 -run1 A2 Scenarios.

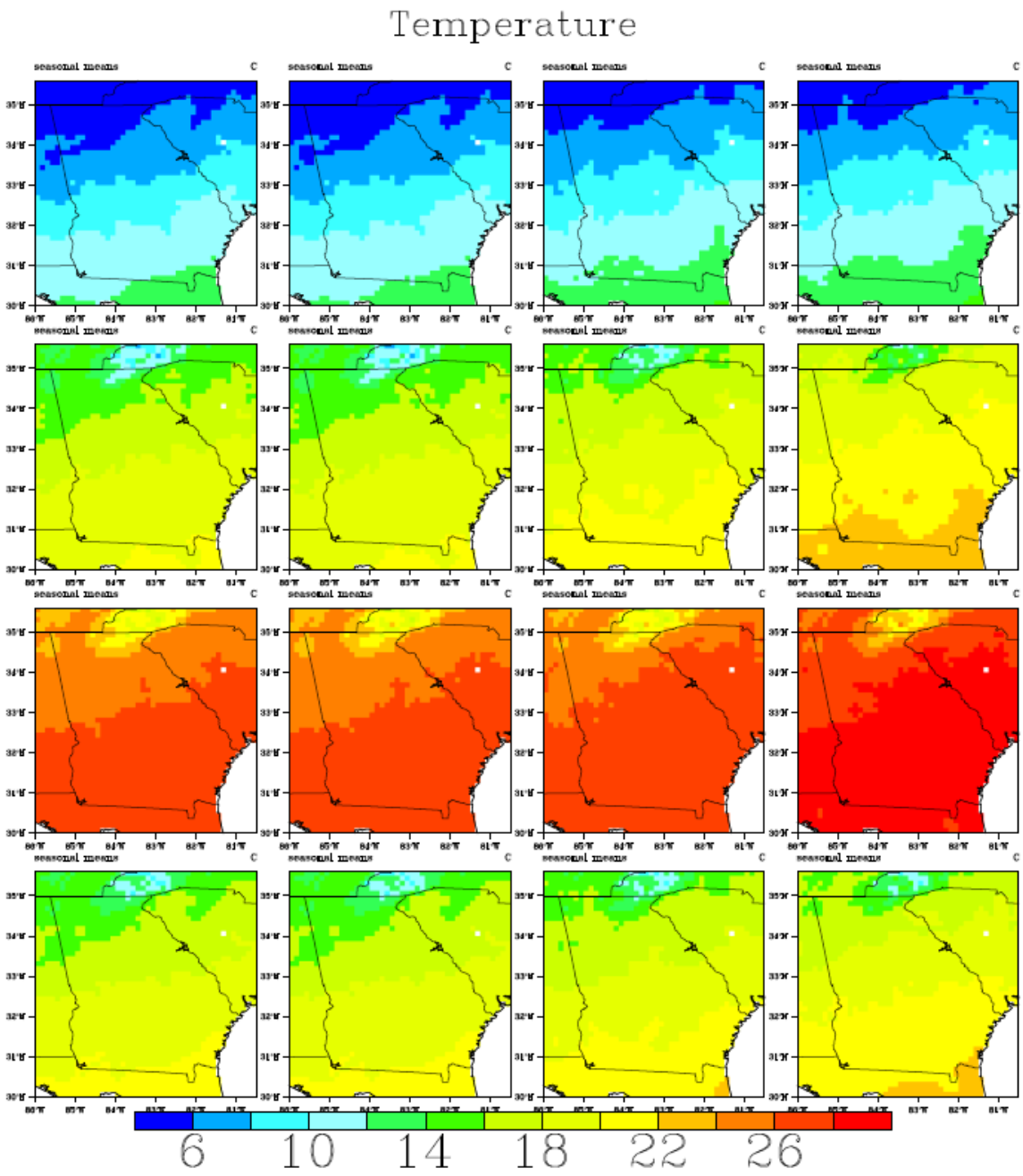

Figure A.26: Spatial temperature distributions over the ACF basin and the southeast US. Monthly temperature fields are aggregated by season (DJF, MAM, JJA, SON). The columns depict observations for the period 01/1950 - 12/1999 (Column 1); JVSD downscaled data using input from the 20CM3 experiment for the period 01/1950 - 12/1999 (Column 2); JVSD downscaled data using input from the GFDL CM2.1 -run1 A1B Scenario for the period 01/2000-12/2049 (Column 3); and JVSD downscaled data using input from the GFDL CM2.1 -run1 A1B Scenario for the period 01/2050-12/2099 (Column 4).

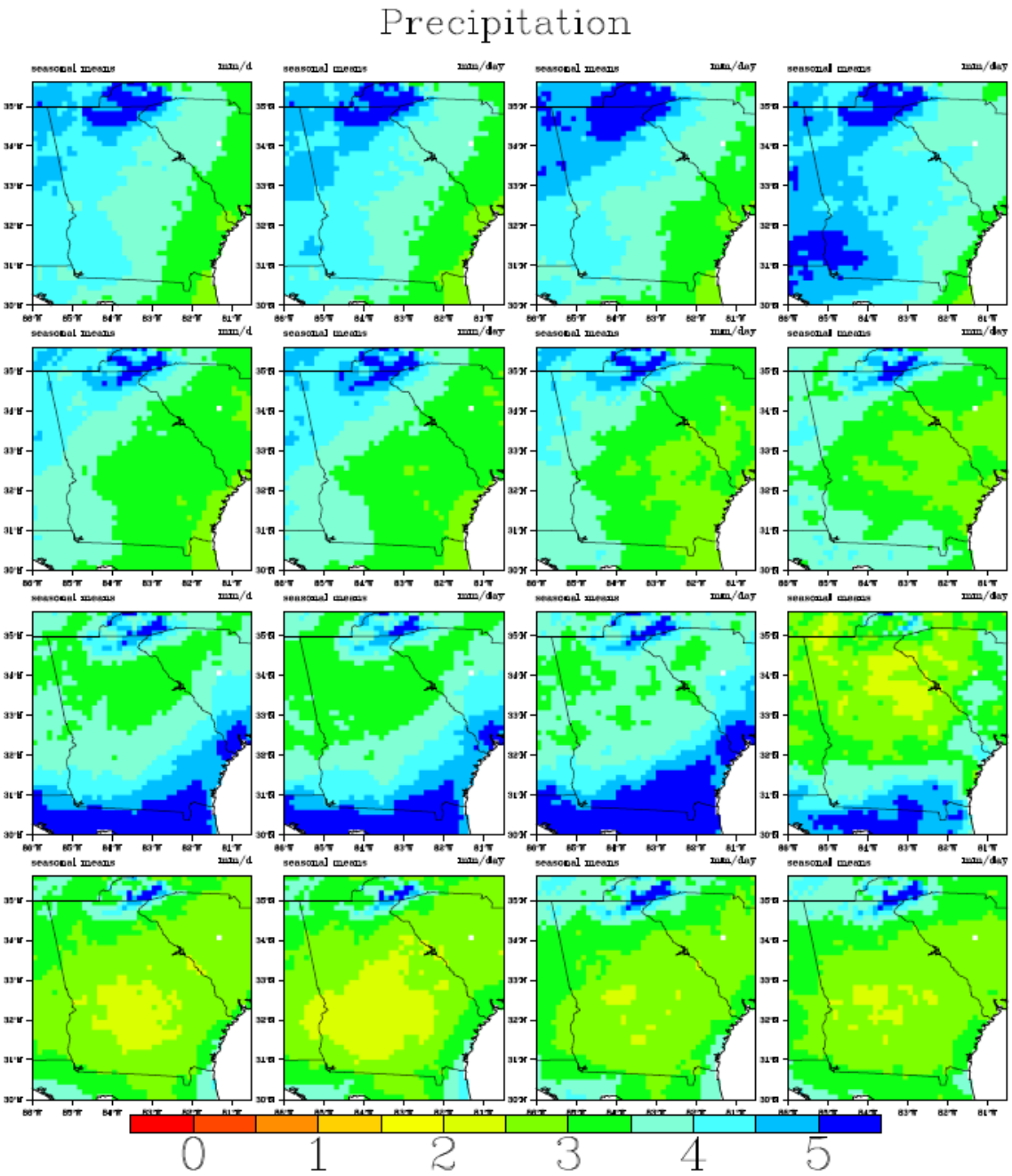

Figure A.27: Spatial precipitation distributions over the ACF basin and the southeast US. Monthly precipitation fields are aggregated by season (DJF, MAM, JJA, SON). The columns depict observations for the period 01/1950 - 12/1999 (Column 1); JVSD downscaled data using input from the 20CM3 experiment for the period 01/1950 - 12/1999 (Column 2); JVSD downscaled data using input from the GFDL CM2.1 -run1A1B Scenario for the period 01/2000-12/2049 (Column 3); and JVSD downscaled data using input from the GFDL CM2.1 -run1 A1B Scenario for the period 01/2050-12/2099 (Column 4).

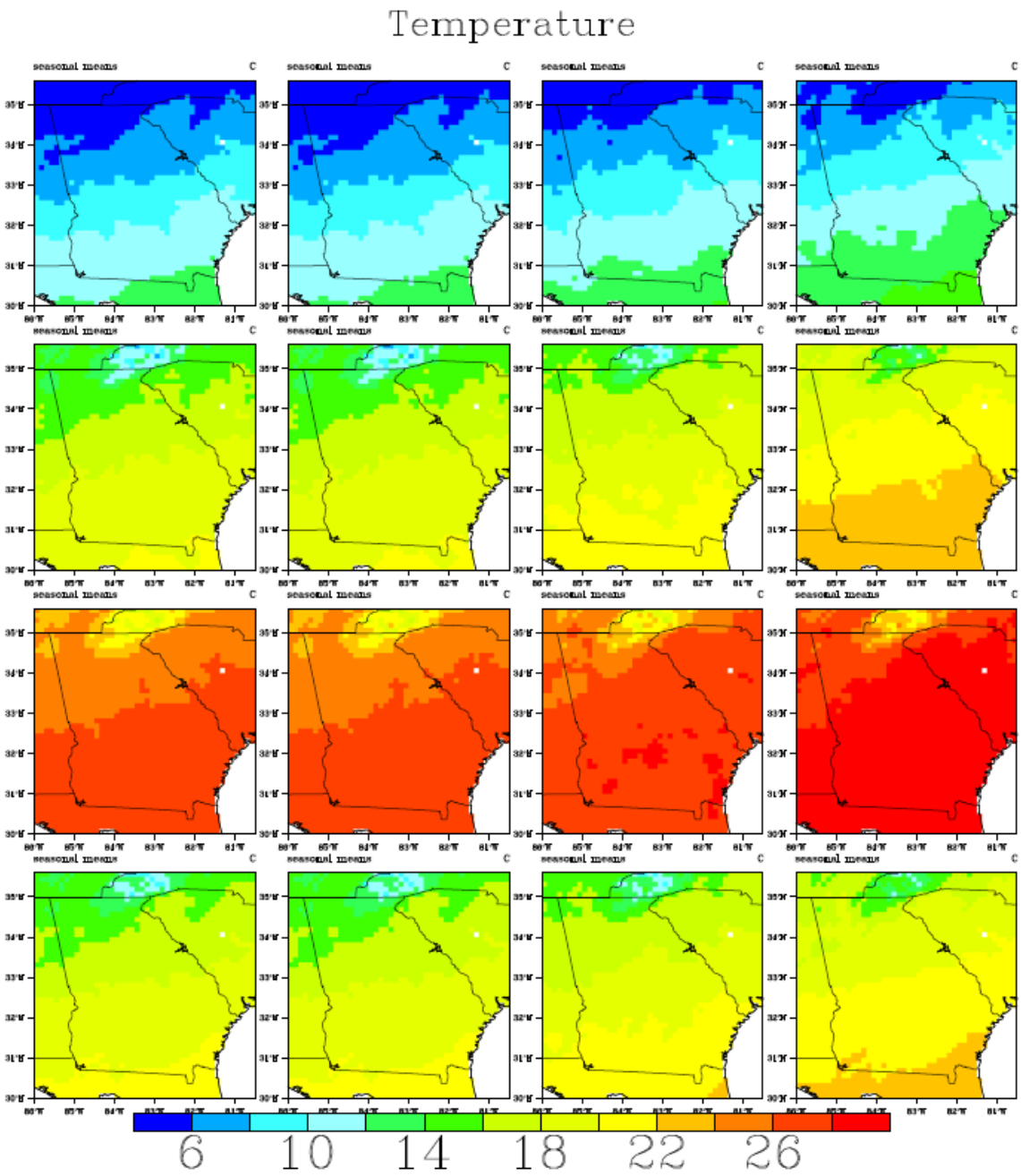

Figure A.28: Spatial temperature distributions over the ACF basin and the southeast US. Monthly temperature fields are aggregated by season (DJF, MAM, JJA, SON). The columns depict observations for the period 01/1950 - 12/1999 (Column 1); JVSD downscaled data using input from the 20CM3 experiment for the period 01/1950 - 12/1999 (Column 2); JVSD downscaled data using input from the GFDL CM2.1 -run1A2 Scenario for the period 01/2000-12/2049 (Column 3); and JVSD downscaled data using input from the GFDL CM2.1 -run1A2 Scenario for the period 01/2050-12/2099 (Column 4).

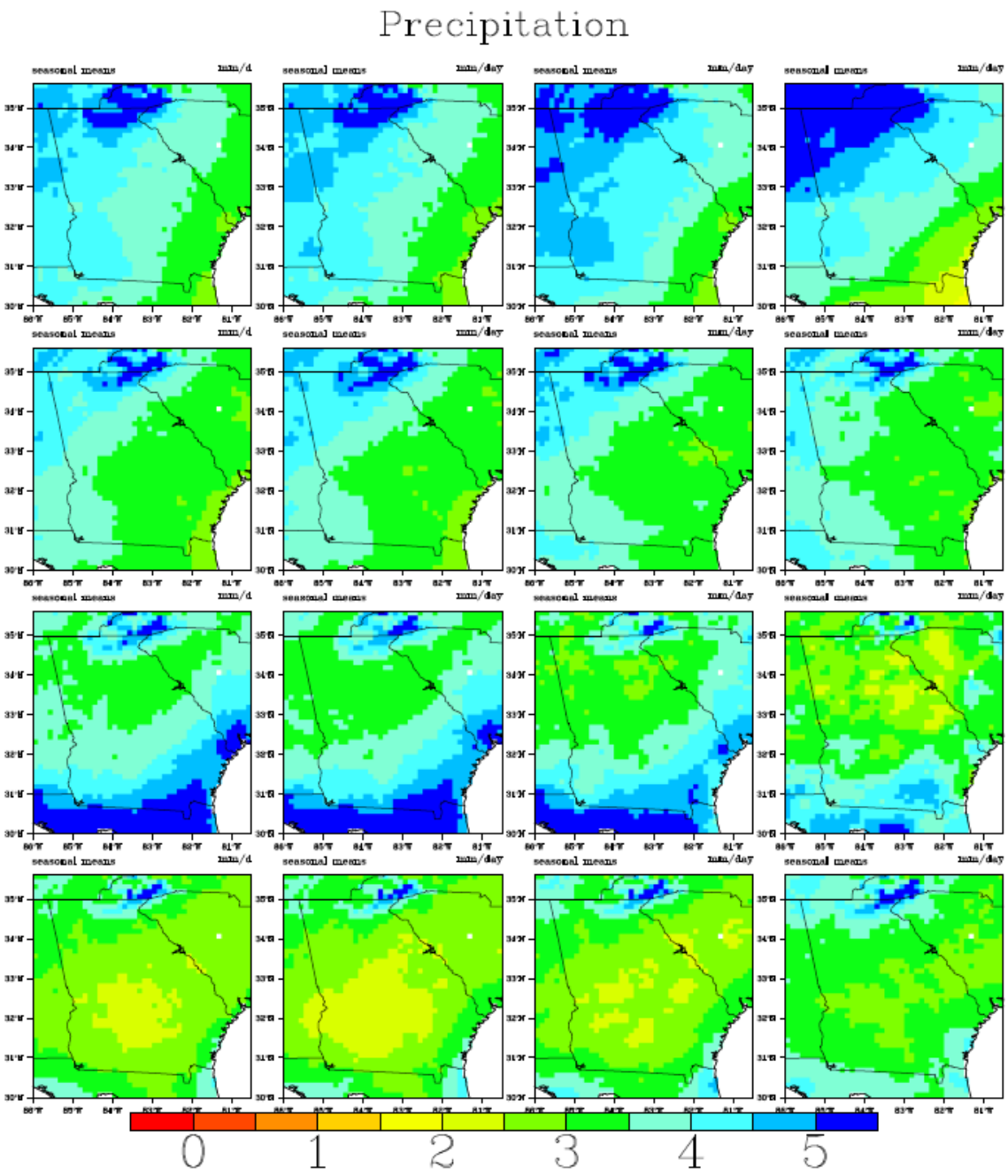

Figure A.29: Spatial precipitation distributions over the ACF basin and the southeast US. Monthly precipitation fields are aggregated by season (DJF, MAM, JJA, SON). The columns depict observations for the period 01/1950 - 12/1999 (Column 1); JVSD downscaled data using input from the 20CM3 experiment for the period 01/1950 - 12/1999 (Column 2); JVSD downscaled data using input from the GFDL CM2.1 -run1A2 Scenario for the period 01/2000-12/2049 (Column 3); and JVSD downscaled data using input from the GFDL CM2.1 -run1A2 Scenario for the period 01/2050-12/2099 (Column 4).

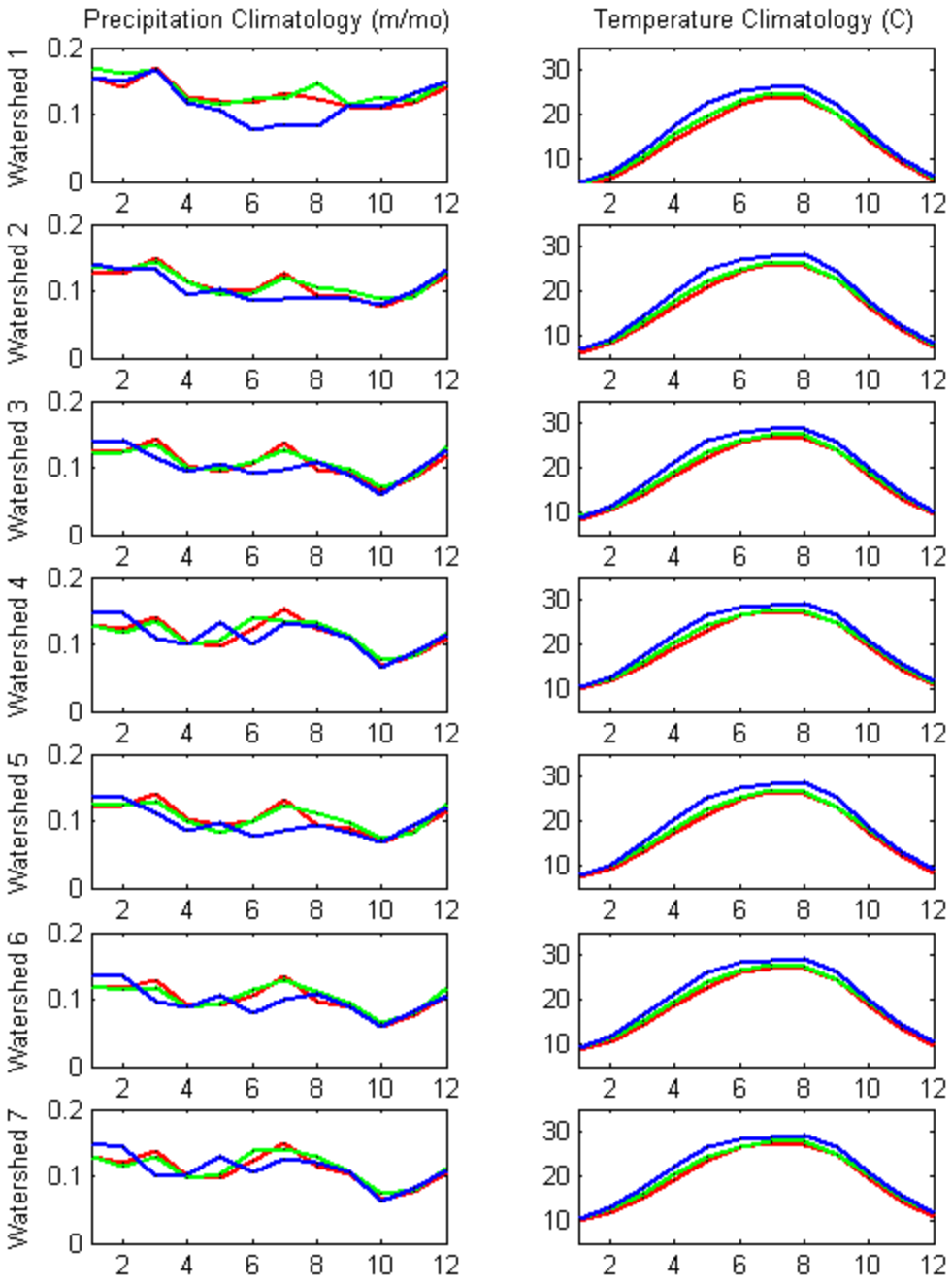

Figure A.30a: Climatologies of spatially aggregated precipitation and temperature for seven ACF watersheds: *(1)* Buford, *(2)* West Point, *(3)* George, *(4)* Woodruff, *(5)* Montezuma, *(6)* Albany, and *(7)* Bainbridge; Lines in Red–Observations (1950-1999); Green–JVSD downscaled (2000- 2049); Blue–JVSD downscaled (2050-2099) under GFDL CM2.1 -run1 A1B Scenarios.

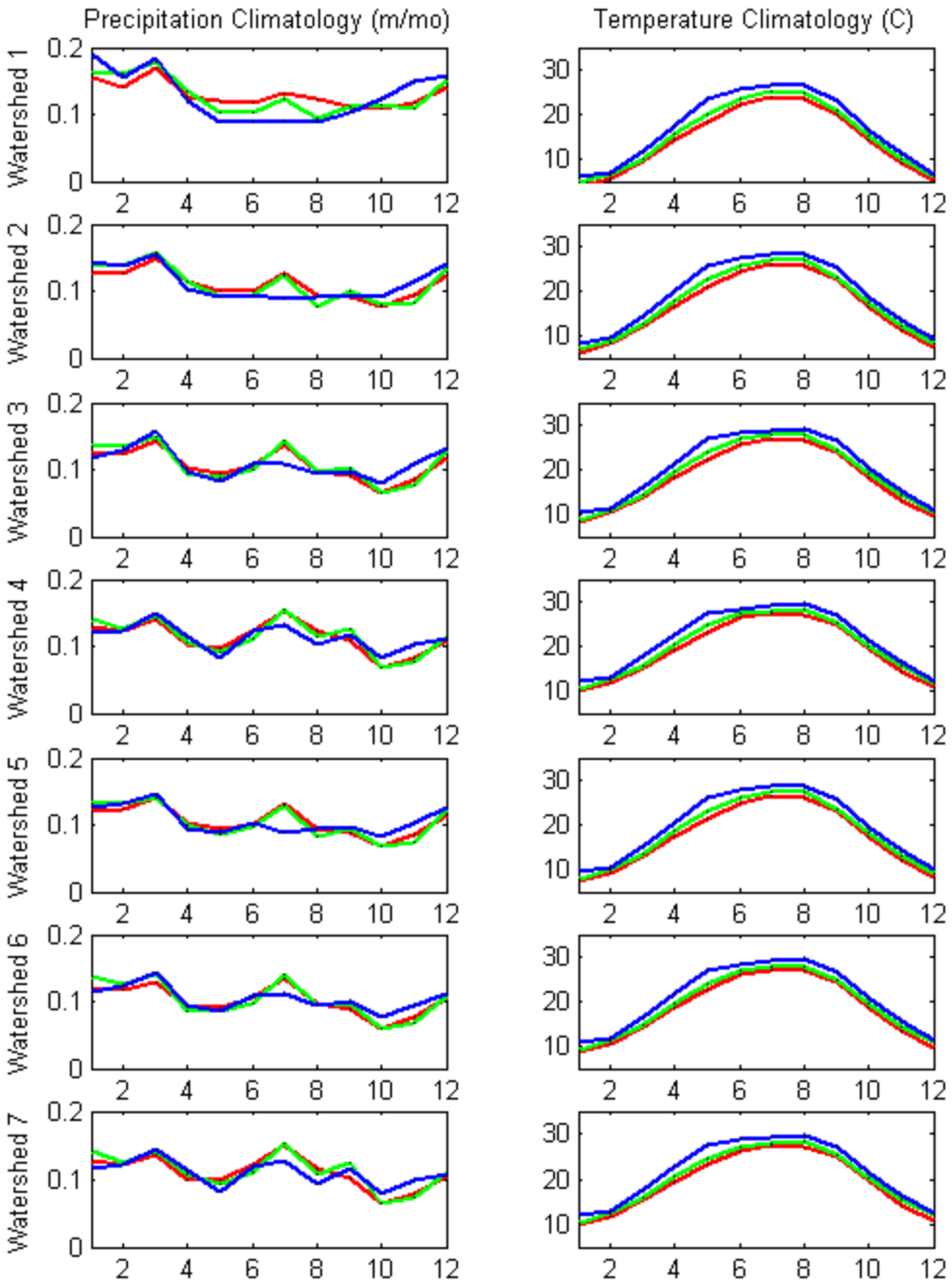

Figure A.30b: Climatologies of spatially aggregated precipitation and temperature for seven ACF watersheds: *(1)* Buford, *(2)* West Point, *(3)* George, *(4)* Woodruff, *(5)* Montezuma, *(6)* Albany, and *(7)* Bainbridge; Lines in Red–Observations (1950-1999); Green–JVSD downscaled (2000- 2049); Blue–JVSD downscaled (2050-2099) under GFDL CM2.1 -run1 A2 Scenarios.

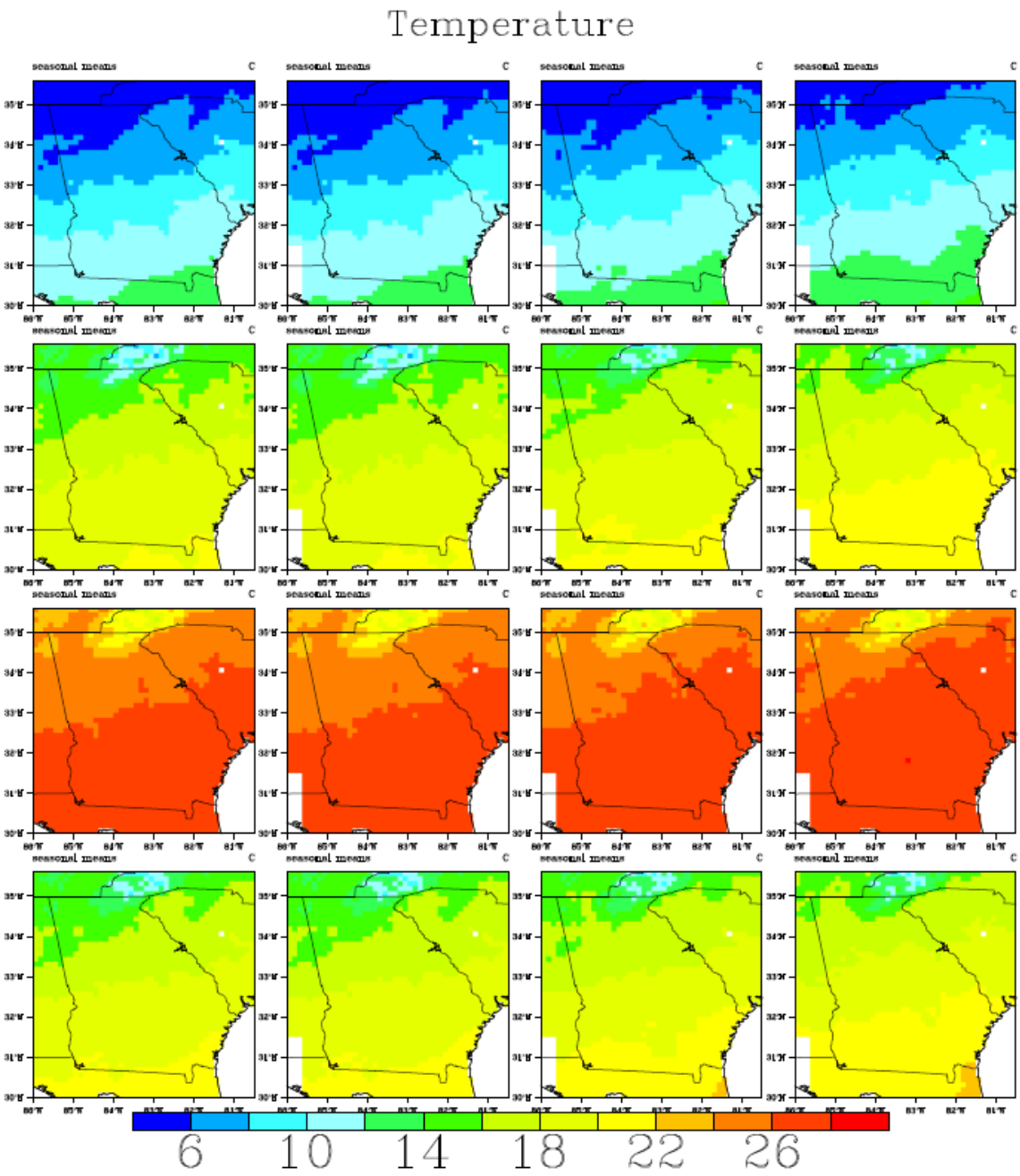

Figure A.31: Spatial temperature distributions over the ACF basin and the southeast US. Monthly temperature fields are aggregated by season (DJF, MAM, JJA, SON). The columns depict observations for the period 01/1950 - 12/1999 (Column 1); JVSD downscaled data using input from the 20CM3 experiment for the period 01/1950 - 12/1999 (Column 2); JVSD downscaled data using input from the GISS ER -run2 A1B Scenario for the period 01/2000-12/2049 (Column 3); and JVSD downscaled data using input from the GISS ER -run2 A1B Scenario for the period 01/2050-12/2099 (Column 4).

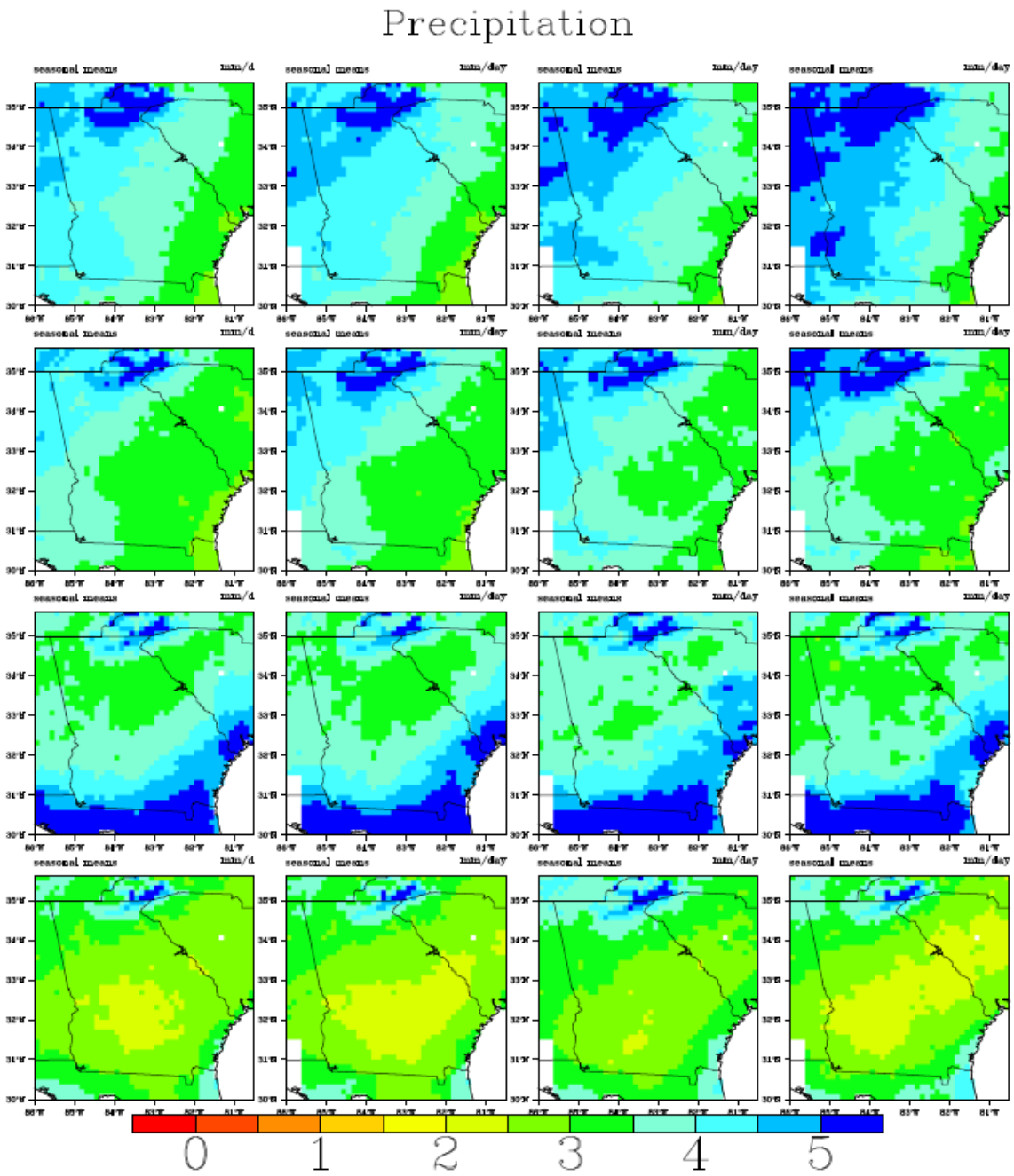

Figure A.32: Spatial precipitation distributions over the ACF basin and the southeast US. Monthly precipitation fields are aggregated by season (DJF, MAM, JJA, SON). The columns depict observations for the period 01/1950 - 12/1999 (Column 1); JVSD downscaled data using input from the 20CM3 experiment for the period 01/1950 - 12/1999 (Column 2); JVSD downscaled data using input from the GISS ER -run2A1B Scenario for the period 01/2000-12/2049 (Column 3); and JVSD downscaled data using input from the GISS ER -run2 A1B Scenario for the period 01/2050-12/2099 (Column 4).

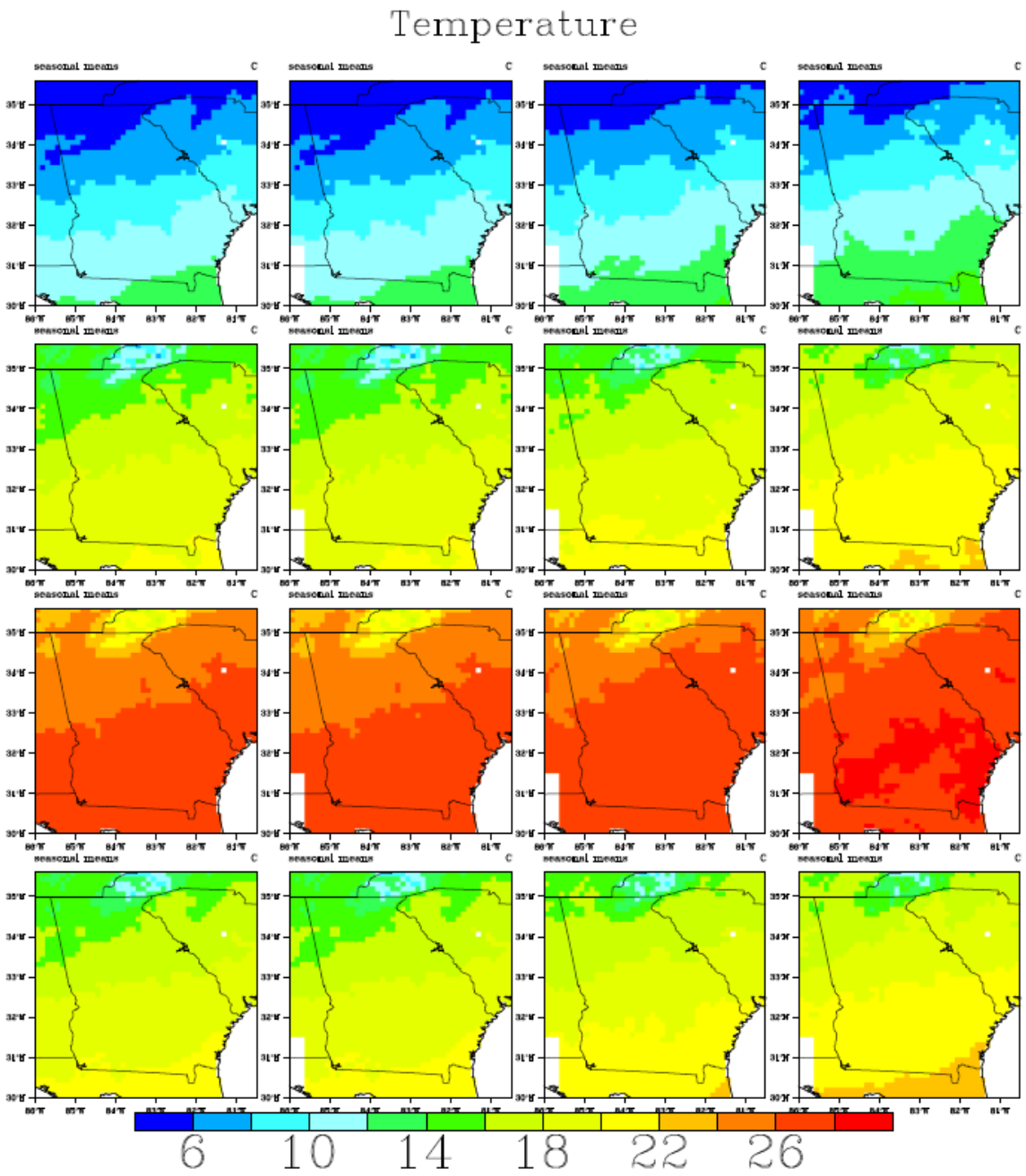

Figure A.33: Spatial temperature distributions over the ACF basin and the southeast US. Monthly temperature fields are aggregated by season (DJF, MAM, JJA, SON). The columns depict observations for the period 01/1950 - 12/1999 (Column 1); JVSD downscaled data using input from the 20CM3 experiment for the period 01/1950 - 12/1999 (Column 2); JVSD downscaled data using input from the GISS ER -run2A2 Scenario for the period 01/2000-12/2049 (Column 3); and JVSD downscaled data using input from the GISS ER -run2A2 Scenario for the period 01/2050-12/2099 (Column 4).

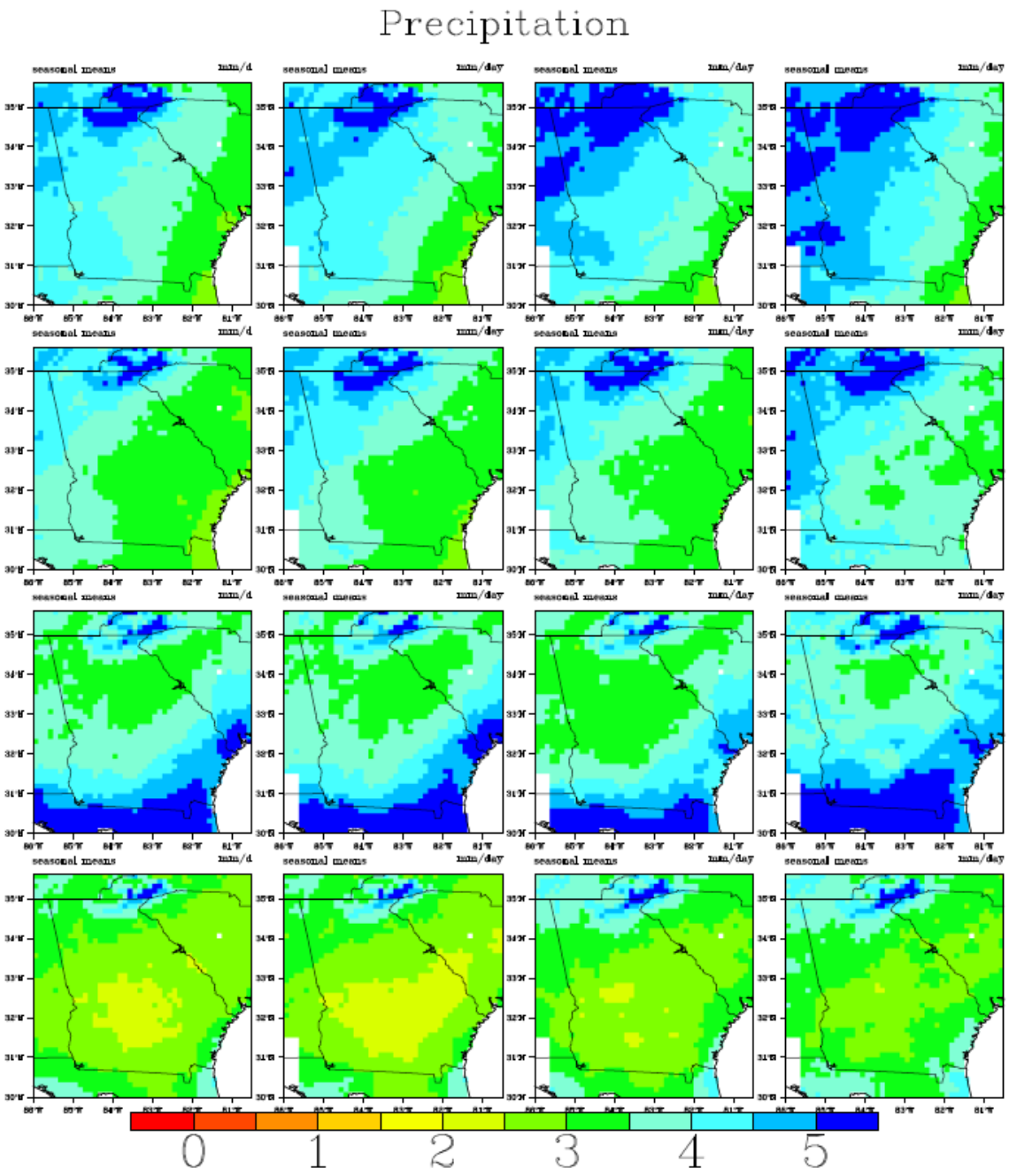

Figure A.34: Spatial precipitation distributions over the ACF basin and the southeast US. Monthly precipitation fields are aggregated by season (DJF, MAM, JJA, SON). The columns depict observations for the period 01/1950 - 12/1999 (Column 1); JVSD downscaled data using input from the 20CM3 experiment for the period 01/1950 - 12/1999 (Column 2); JVSD downscaled data using input from the GISS ER -run2A2 Scenario for the period 01/2000-12/2049 (Column 3); and JVSD downscaled data using input from the GISS ER -run2A2 Scenario for the period 01/2050-12/2099 (Column 4).

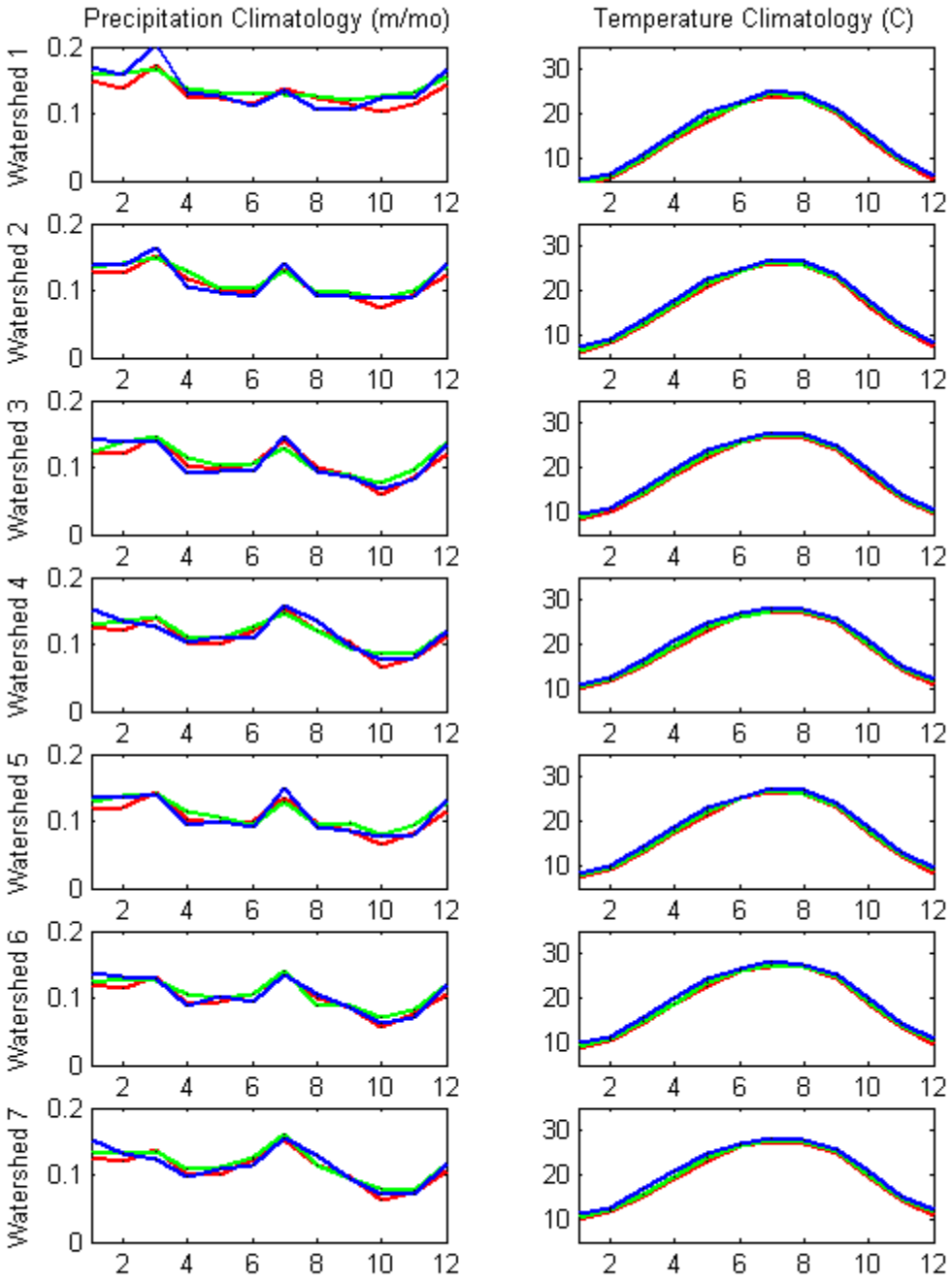

Figure A.35a: Climatologies of spatially aggregated precipitation and temperature for seven ACF watersheds: *(1)* Buford, *(2)* West Point, *(3)* George, *(4)* Woodruff, *(5)* Montezuma, *(6)* Albany, and *(7)* Bainbridge; Lines in Red–Observations (1950-1999); Green–JVSD downscaled (2000- 2049); Blue–JVSD downscaled (2050-2099) under GISS ER -run2 A1B Scenarios.

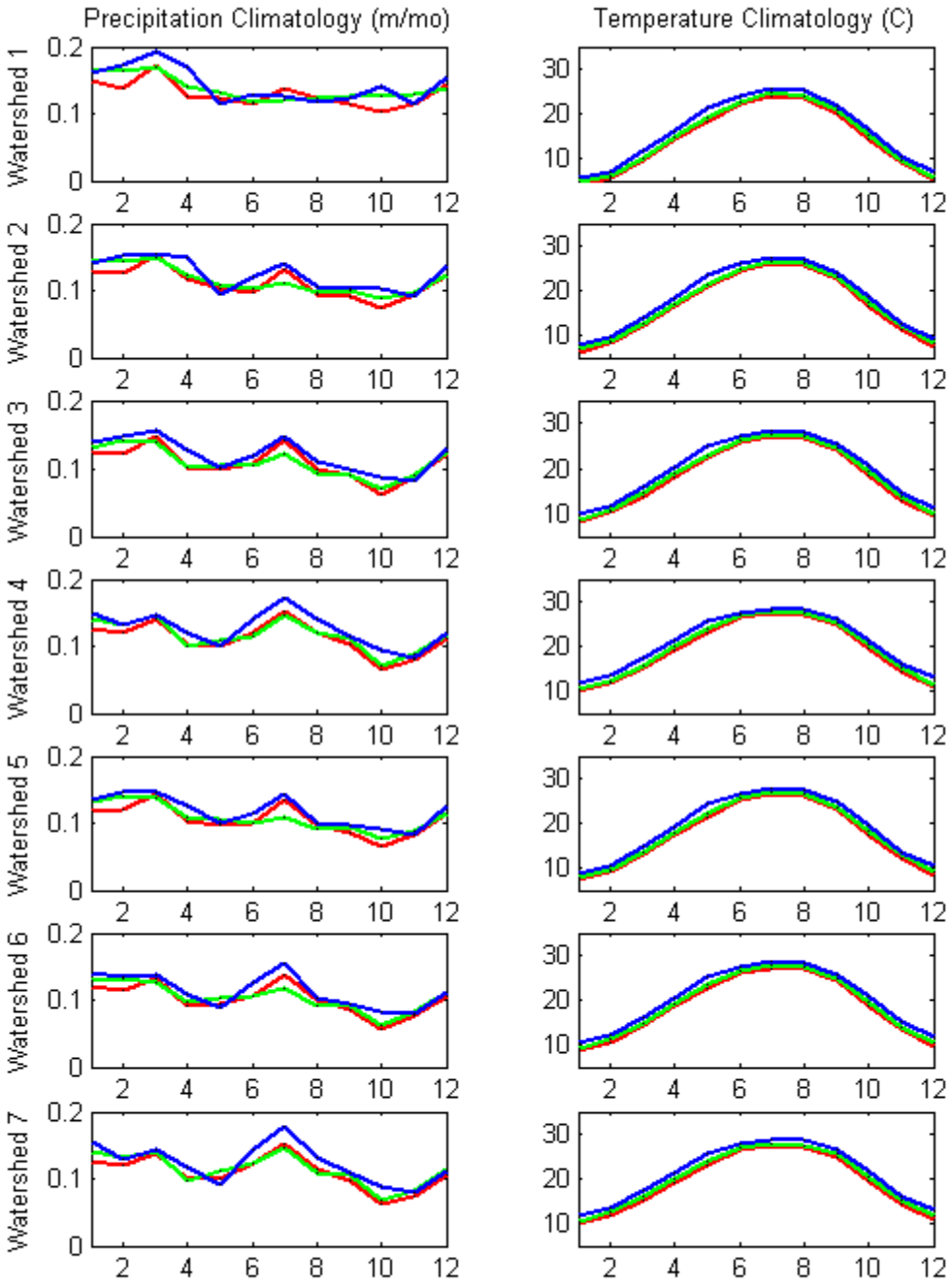

Figure A.35b: Climatologies of spatially aggregated precipitation and temperature for seven ACF watersheds: *(1)* Buford, *(2)* West Point, *(3)* George, *(4)* Woodruff, *(5)* Montezuma, *(6)* Albany, and *(7)* Bainbridge; Lines in Red–Observations (1950-1999); Green–JVSD downscaled (2000- 2049); Blue–JVSD downscaled (2050-2099) under GISS ER -run2 A2 Scenarios.

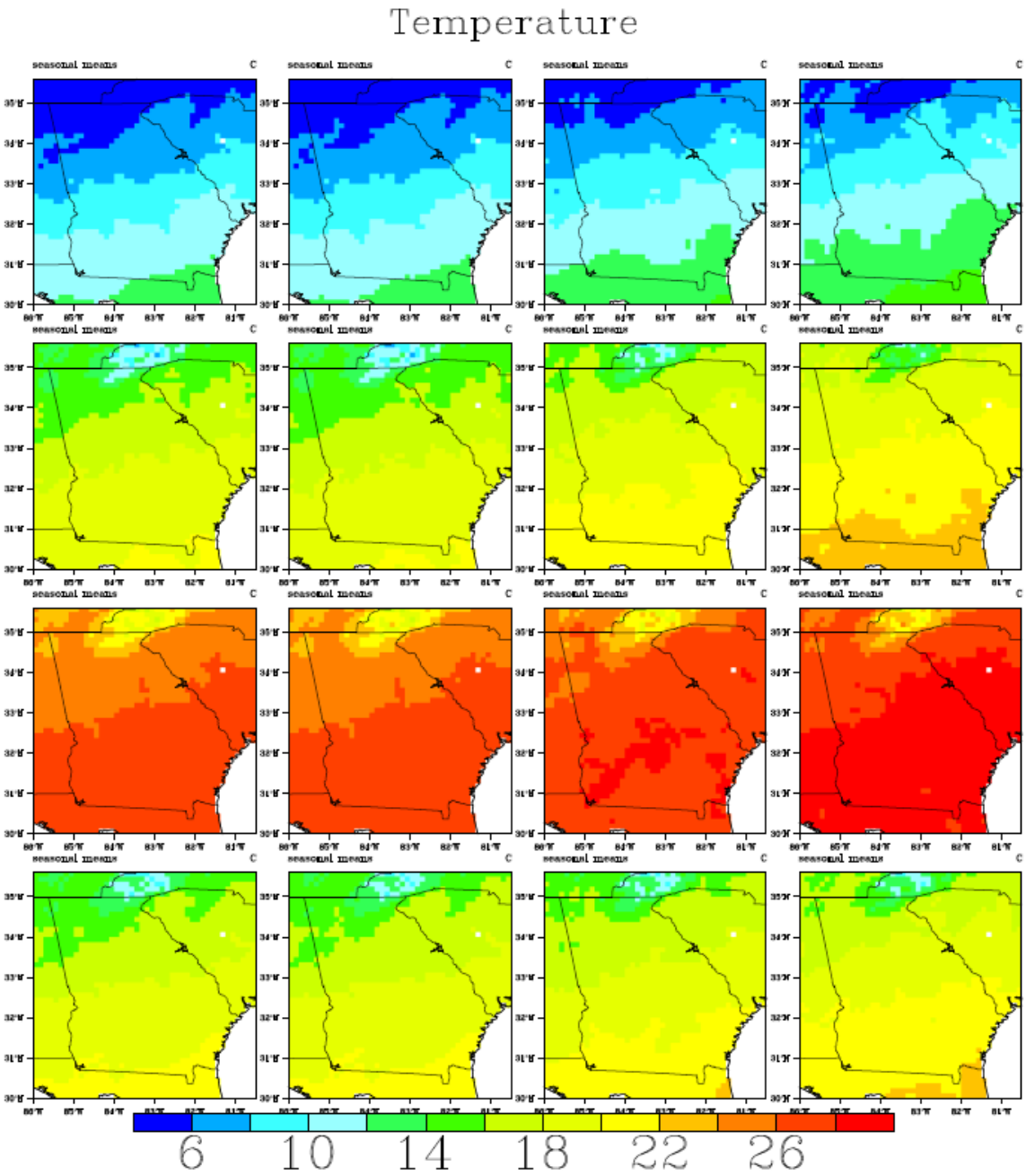

Figure A.36: Spatial temperature distributions over the ACF basin and the southeast US. Monthly temperature fields are aggregated by season (DJF, MAM, JJA, SON). The columns depict observations for the period 01/1950 - 12/1999 (Column 1); JVSD downscaled data using input from the 20CM3 experiment for the period 01/1950 - 12/1999 (Column 2); JVSD downscaled data using input from the UKMO HADCM3 -run1 A1B Scenario for the period 01/2000-12/2049 (Column 3); and JVSD downscaled data using input from the UKMO HADCM3 -run1 A1B Scenario for the period 01/2050-12/2099 (Column 4).

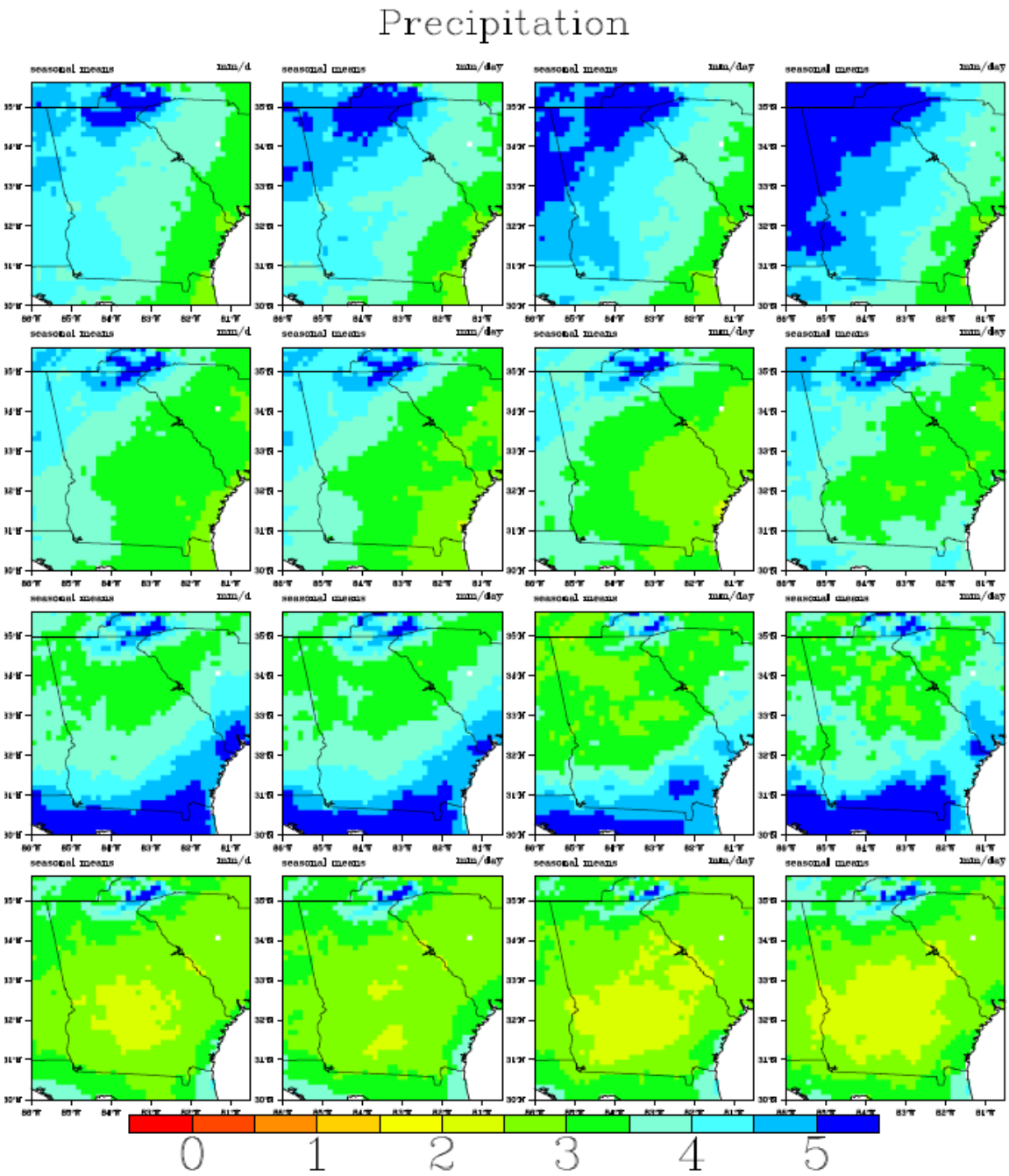

Figure A.37: Spatial precipitation distributions over the ACF basin and the southeast US. Monthly precipitation fields are aggregated by season (DJF, MAM, JJA, SON). The columns depict observations for the period 01/1950 - 12/1999 (Column 1); JVSD downscaled data using input from the 20CM3 experiment for the period 01/1950 - 12/1999 (Column 2); JVSD downscaled data using input from the UKMO HADCM3 -run1A1B Scenario for the period 01/2000-12/2049 (Column 3); and JVSD downscaled data using input from the UKMO HADCM3 -run1 A1B Scenario for the period 01/2050-12/2099 (Column 4).

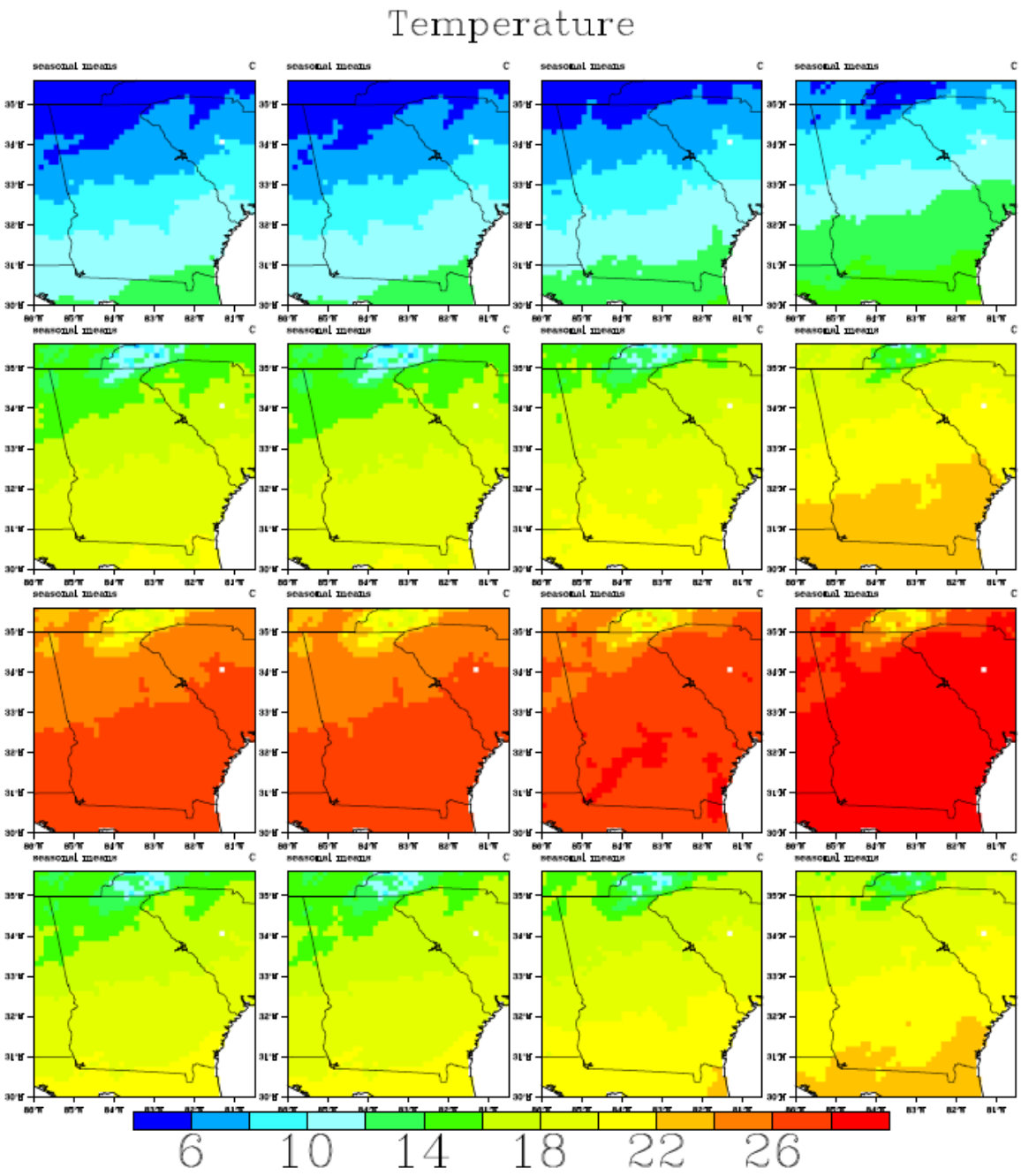

Figure A.38: Spatial temperature distributions over the ACF basin and the southeast US. Monthly temperature fields are aggregated by season (DJF, MAM, JJA, SON). The columns depict observations for the period 01/1950 - 12/1999 (Column 1); JVSD downscaled data using input from the 20CM3 experiment for the period 01/1950 - 12/1999 (Column 2); JVSD downscaled data using input from the UKMO HADCM3 -run1A2 Scenario for the period 01/2000-12/2049 (Column 3); and JVSD downscaled data using input from the UKMO HADCM3 -run1A2 Scenario for the period 01/2050-12/2099 (Column 4).

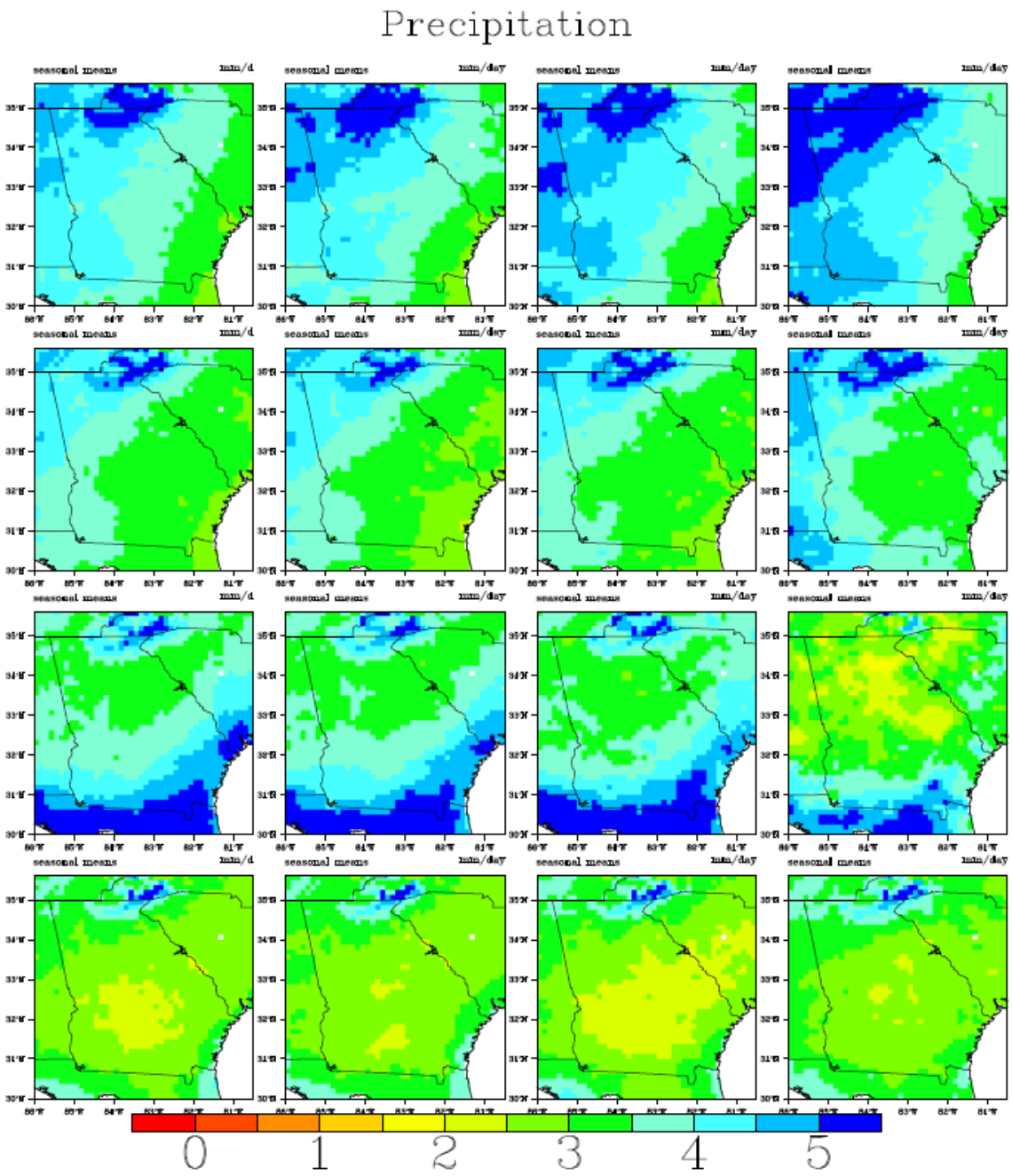

Figure A.39: Spatial precipitation distributions over the ACF basin and the southeast US. Monthly precipitation fields are aggregated by season (DJF, MAM, JJA, SON). The columns depict observations for the period 01/1950 - 12/1999 (Column 1); JVSD downscaled data using input from the 20CM3 experiment for the period 01/1950 - 12/1999 (Column 2); JVSD downscaled data using input from the UKMO HADCM3 -run1A2 Scenario for the period 01/2000-12/2049 (Column 3); and JVSD downscaled data using input from the UKMO HADCM3 -run1A2 Scenario for the period 01/2050-12/2099 (Column 4).

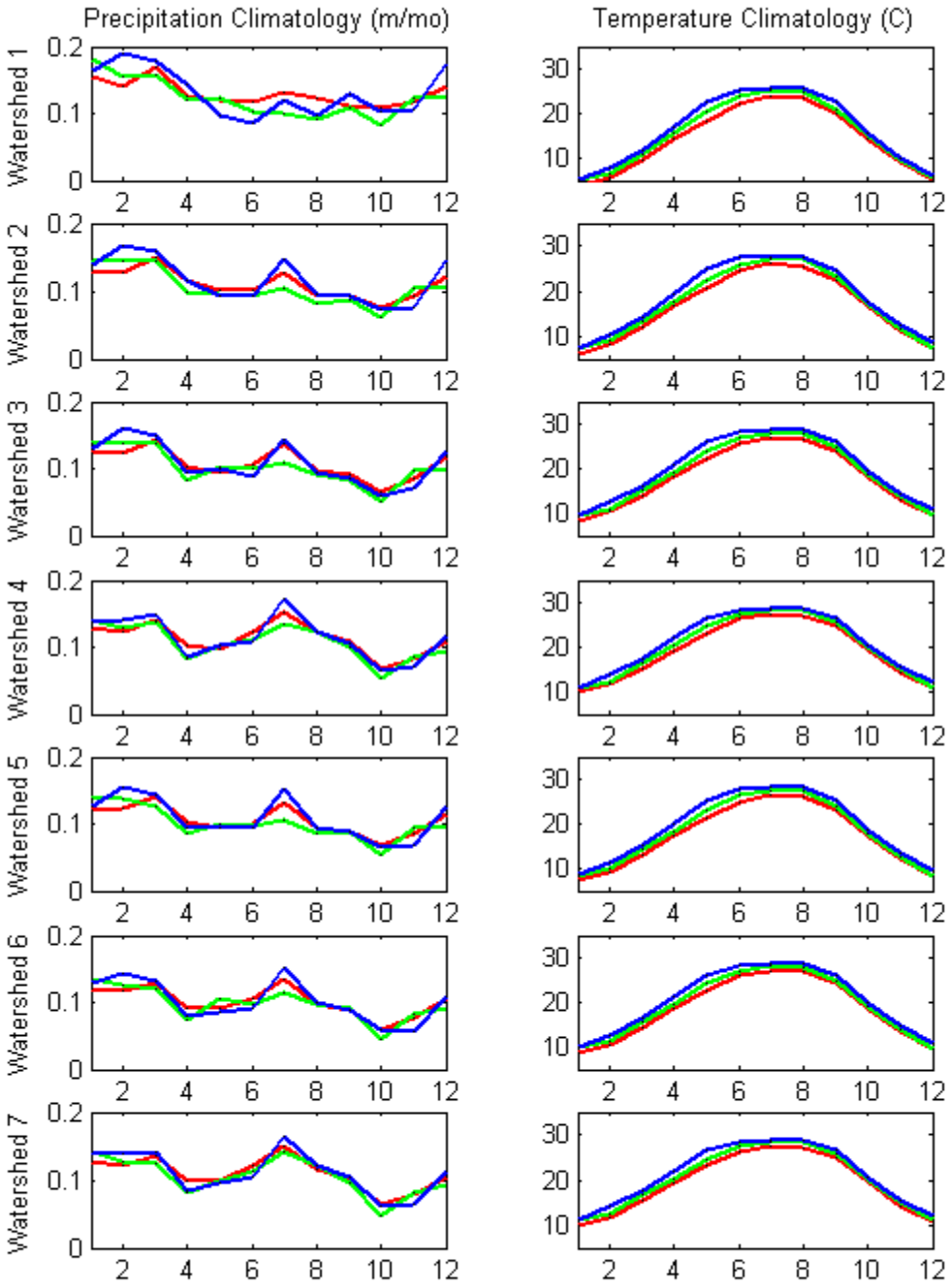

Figure A.40a: Climatologies of spatially aggregated precipitation and temperature for seven ACF watersheds: *(1)* Buford, *(2)* West Point, *(3)* George, *(4)* Woodruff, *(5)* Montezuma, *(6)* Albany, and *(7)* Bainbridge; Lines in Red–Observations (1950-1999); Green–JVSD downscaled (2000- 2049); Blue–JVSD downscaled (2050-2099) under UKMO HADCM3 -run1 A1B Scenarios.

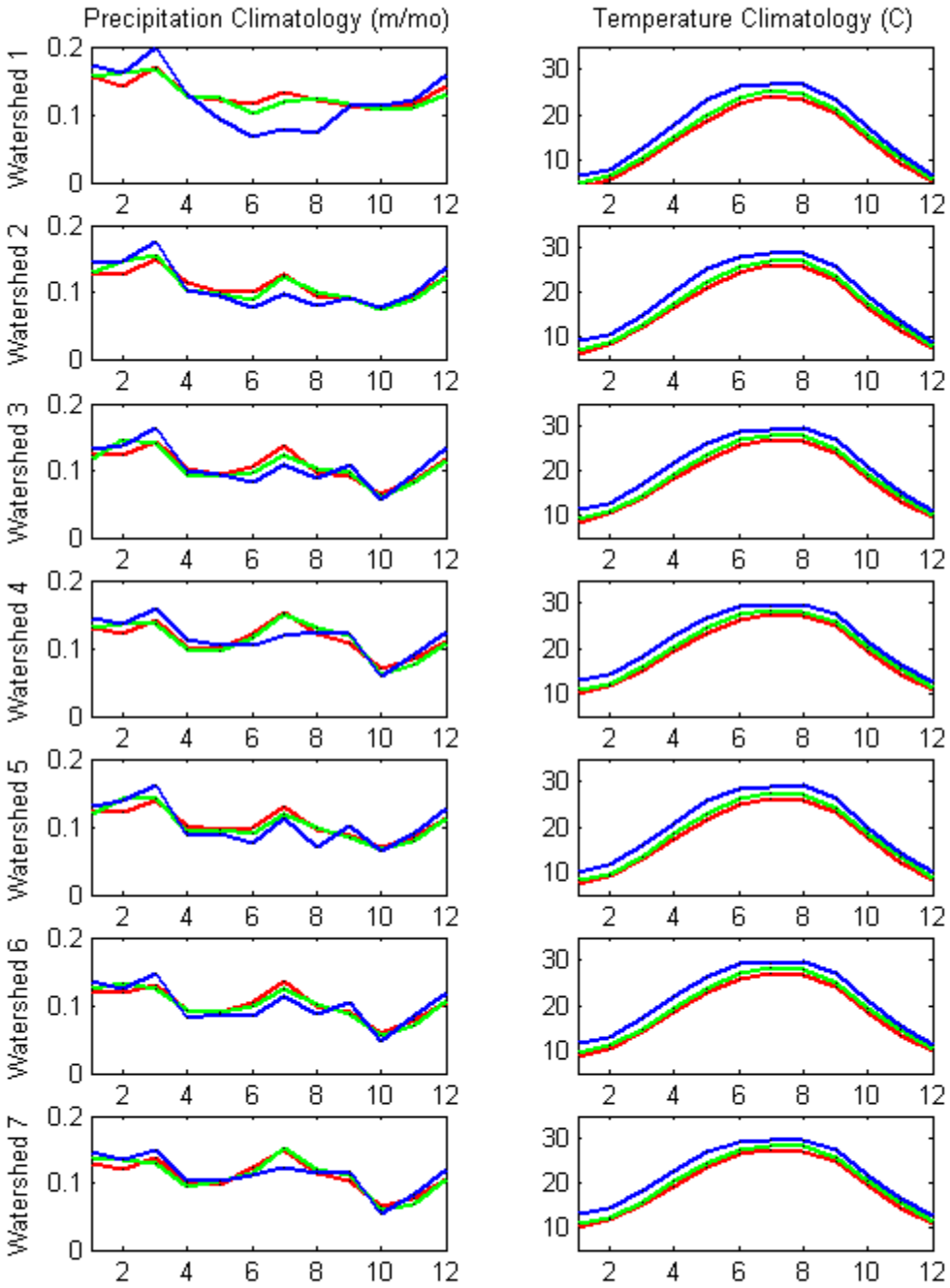

Figure A.40b: Climatologies of spatially aggregated precipitation and temperature for seven ACF watersheds: *(1)* Buford, *(2)* West Point, *(3)* George, *(4)* Woodruff, *(5)* Montezuma, *(6)* Albany, and *(7)* Bainbridge; Lines in Red–Observations (1950-1999); Green–JVSD downscaled (2000- 2049); Blue–JVSD downscaled (2050-2099) under UKMO HADCM3 -run1 A2 Scenarios.

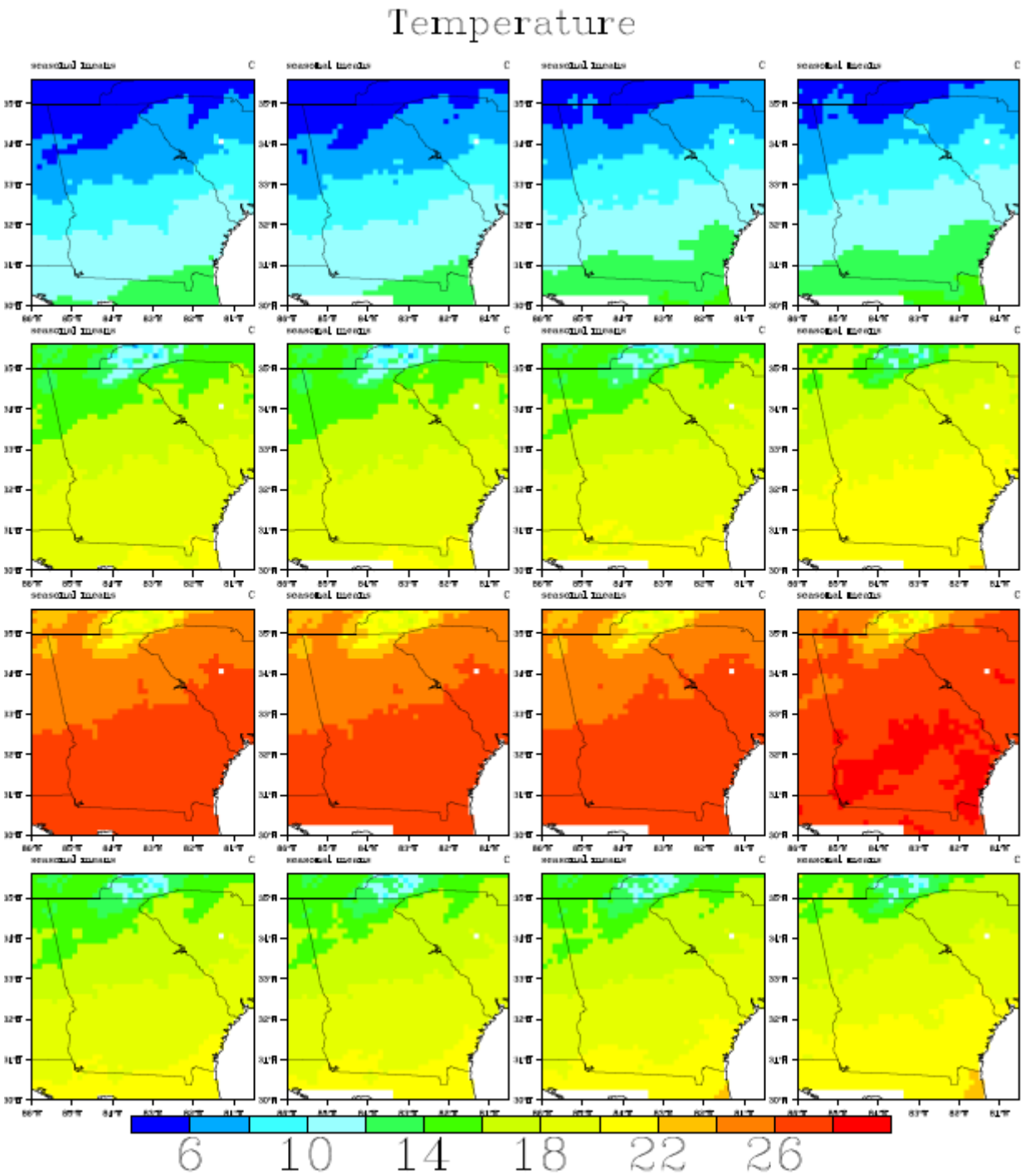

Figure A.41: Spatial temperature distributions over the ACF basin and the southeast US. Monthly temperature fields are aggregated by season (DJF, MAM, JJA, SON). The columns depict observations for the period 01/1950 - 12/1999 (Column 1); JVSD downscaled data using input from the 20CM3 experiment for the period 01/1950 - 12/1999 (Column 2); JVSD downscaled data using input from the INMCM3.0 -run1 A1B Scenario for the period 01/2000-12/2049 (Column 3); and JVSD downscaled data using input from the INMCM3.0 -run1 A1B Scenario for the period 01/2050-12/2099 (Column 4).

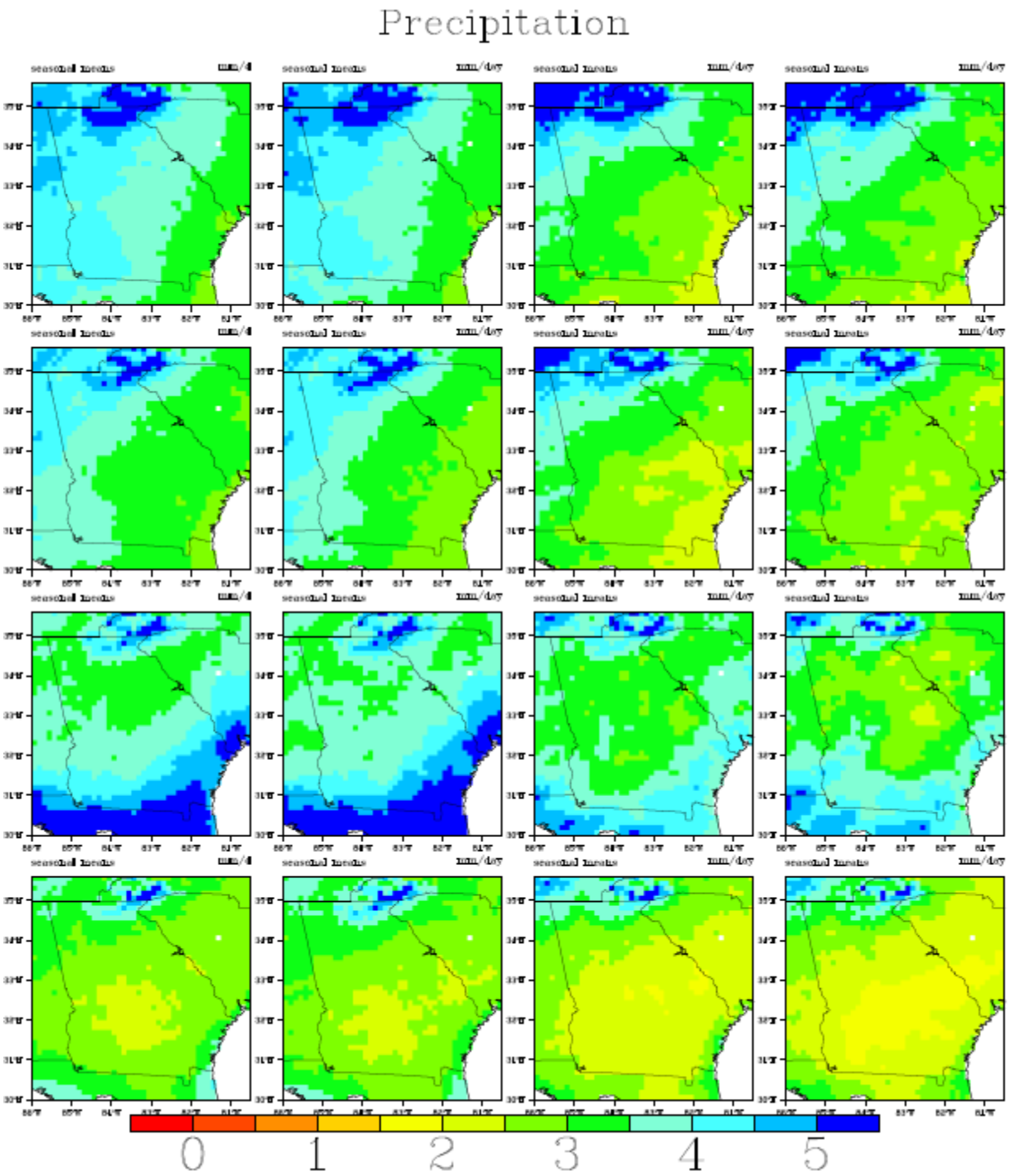

Figure A.42: Spatial precipitation distributions over the ACF basin and the southeast US. Monthly precipitation fields are aggregated by season (DJF, MAM, JJA, SON). The columns depict observations for the period 01/1950 - 12/1999 (Column 1); JVSD downscaled data using input from the 20CM3 experiment for the period 01/1950 - 12/1999 (Column 2); JVSD downscaled data using input from the INMCM3.0 -run1A1B Scenario for the period 01/2000-12/2049 (Column 3); and JVSD downscaled data using input from the INMCM3.0 -run1 A1B Scenario for the period 01/2050-12/2099 (Column 4).

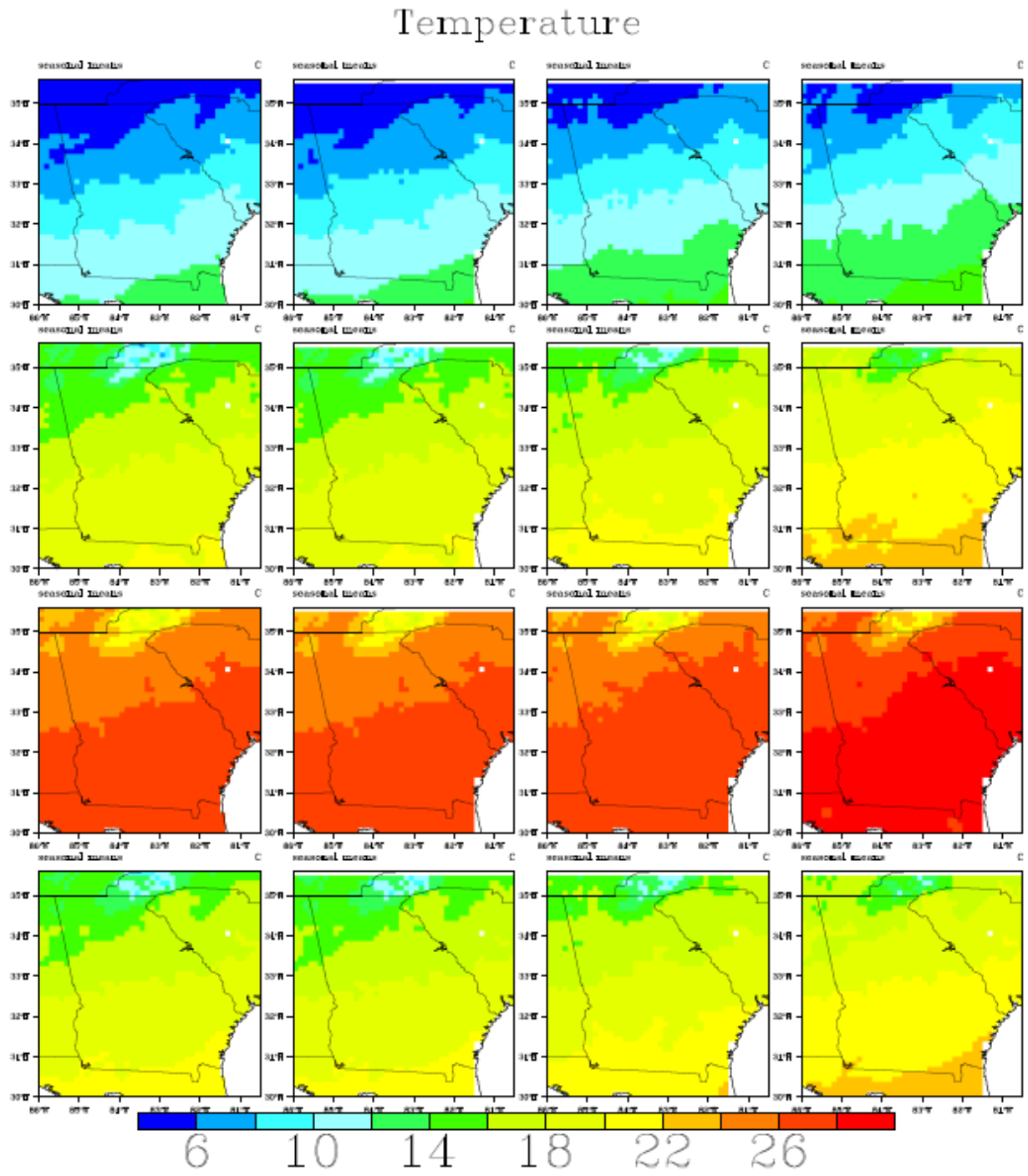

Figure A.43: Spatial temperature distributions over the ACF basin and the southeast US. Monthly temperature fields are aggregated by season (DJF, MAM, JJA, SON). The columns depict observations for the period 01/1950 - 12/1999 (Column 1); JVSD downscaled data using input from the 20CM3 experiment for the period 01/1950 - 12/1999 (Column 2); JVSD downscaled data using input from the INMCM3.0 -run1A2 Scenario for the period 01/2000-12/2049 (Column 3); and JVSD downscaled data using input from the INMCM3.0 -run1A2 Scenario for the period 01/2050-12/2099 (Column 4).

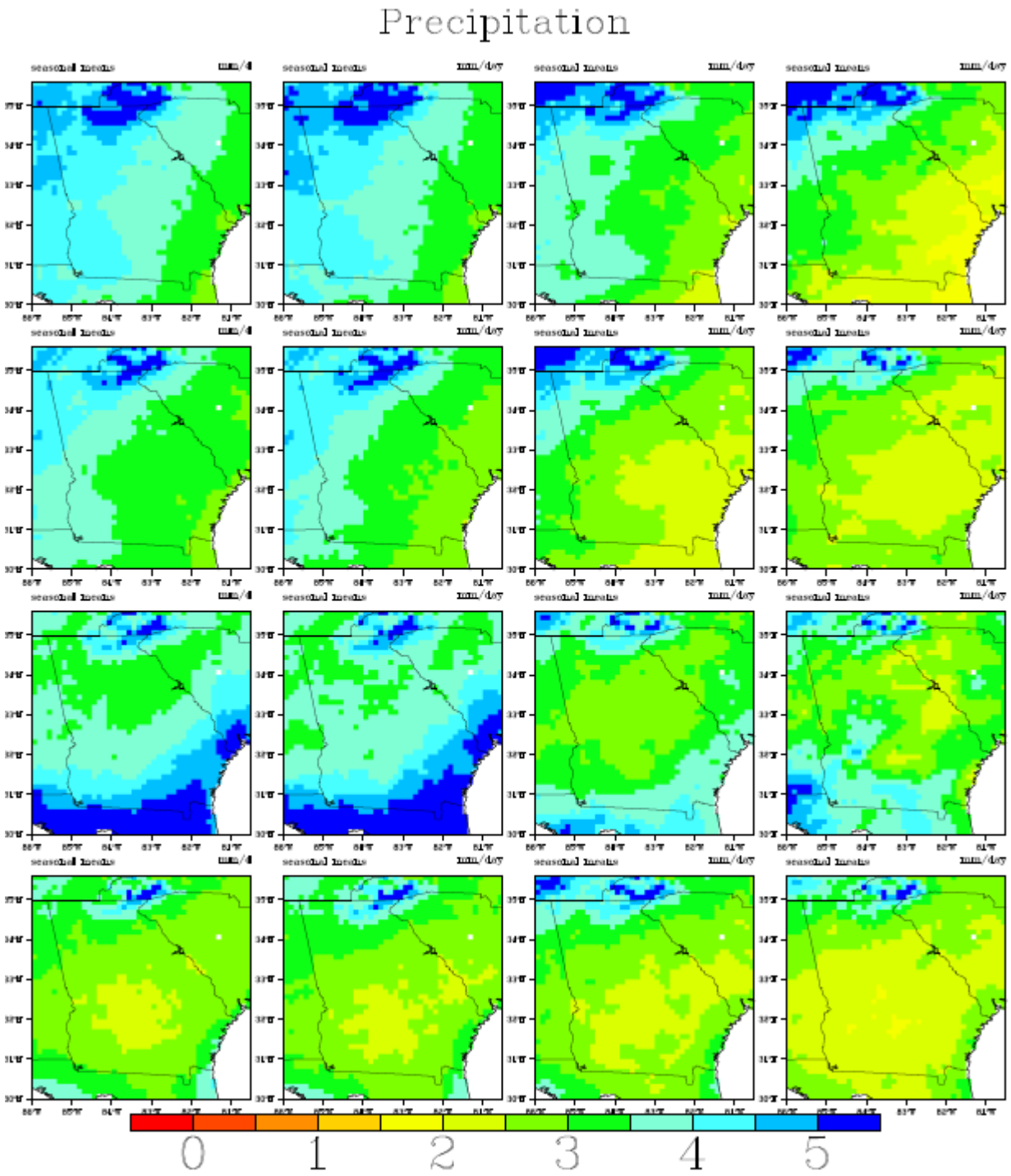

Figure A.44: Spatial precipitation distributions over the ACF basin and the southeast US. Monthly precipitation fields are aggregated by season (DJF, MAM, JJA, SON). The columns depict observations for the period 01/1950 - 12/1999 (Column 1); JVSD downscaled data using input from the 20CM3 experiment for the period 01/1950 - 12/1999 (Column 2); JVSD downscaled data using input from the INMCM3.0 -run1A2 Scenario for the period 01/2000-12/2049 (Column 3); and JVSD downscaled data using input from the INMCM3.0 -run1A2 Scenario for the period 01/2050-12/2099 (Column 4).

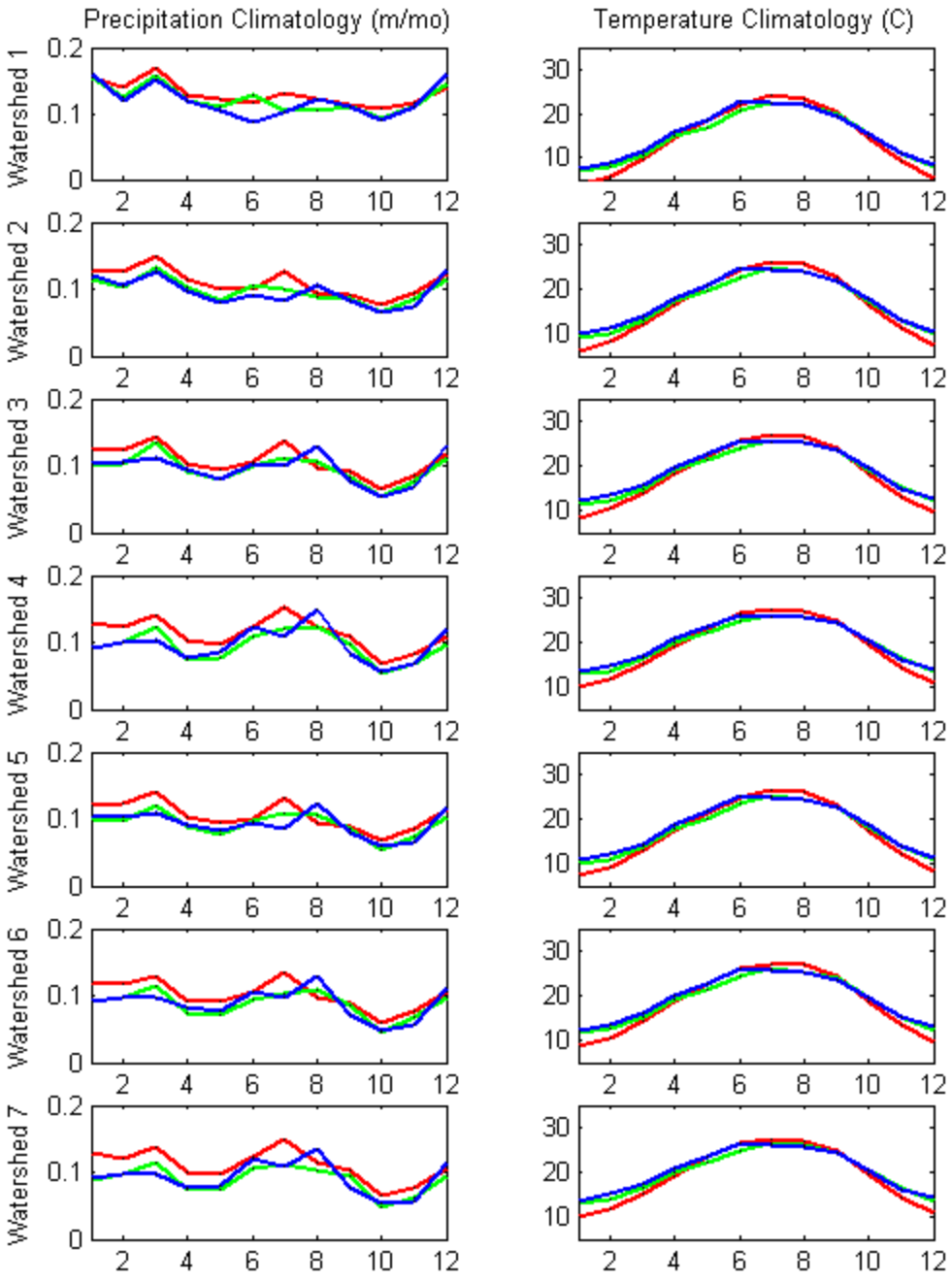

Figure A.45a: Climatologies of spatially aggregated precipitation and temperature for seven ACF watersheds: *(1)* Buford, *(2)* West Point, *(3)* George, *(4)* Woodruff, *(5)* Montezuma, *(6)* Albany, and *(7)* Bainbridge; Lines in Red–Observations (1950-1999); Green–JVSD downscaled (2000- 2049); Blue–JVSD downscaled (2050-2099) under INMCM3.0 -run1 A1B Scenarios.

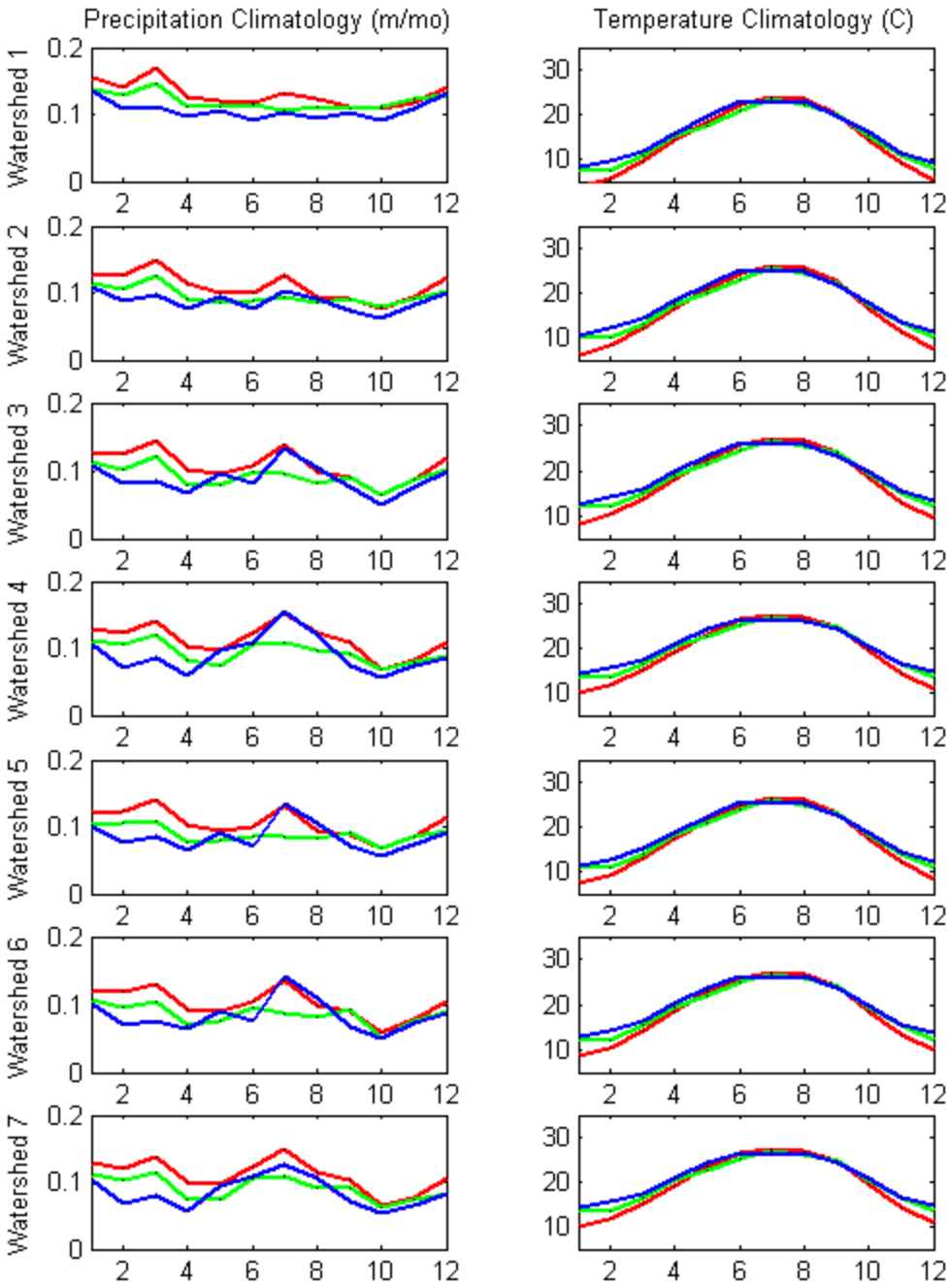

Figure A.45b: Climatologies of spatially aggregated precipitation and temperature for seven ACF watersheds: *(1)* Buford, *(2)* West Point, *(3)* George, *(4)* Woodruff, *(5)* Montezuma, *(6)* Albany, and *(7)* Bainbridge; Lines in Red–Observations (1950-1999); Green–JVSD downscaled (2000- 2049); Blue–JVSD downscaled (2050-2099) under INMCM3.0 -run1 A2 Scenarios.

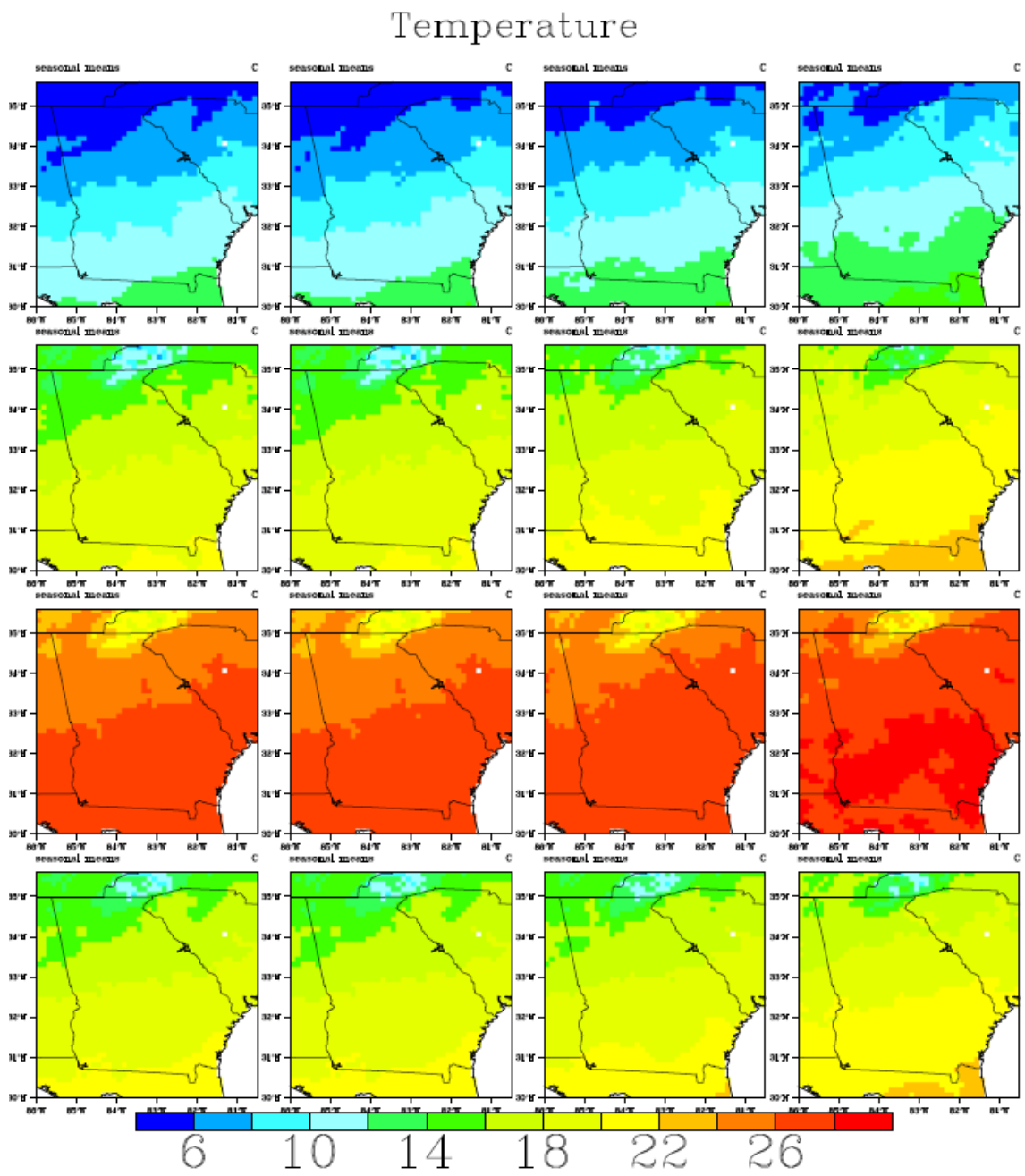

Figure A.46 Spatial temperature distributions over the ACF basin and the southeast US. Monthly temperature fields are aggregated by season (DJF, MAM, JJA, SON). The columns depict observations for the period 01/1950 - 12/1999 (Column 1); JVSD downscaled data using input from the 20CM3 experiment for the period 01/1950 - 12/1999 (Column 2); JVSD downscaled data using input from the MIUB ECHO_G -run1 A1B Scenario for the period 01/2000-12/2049 (Column 3); and JVSD downscaled data using input from the MIUB ECHO_G -run1 A1B Scenario for the period 01/2050-12/2099 (Column 4).

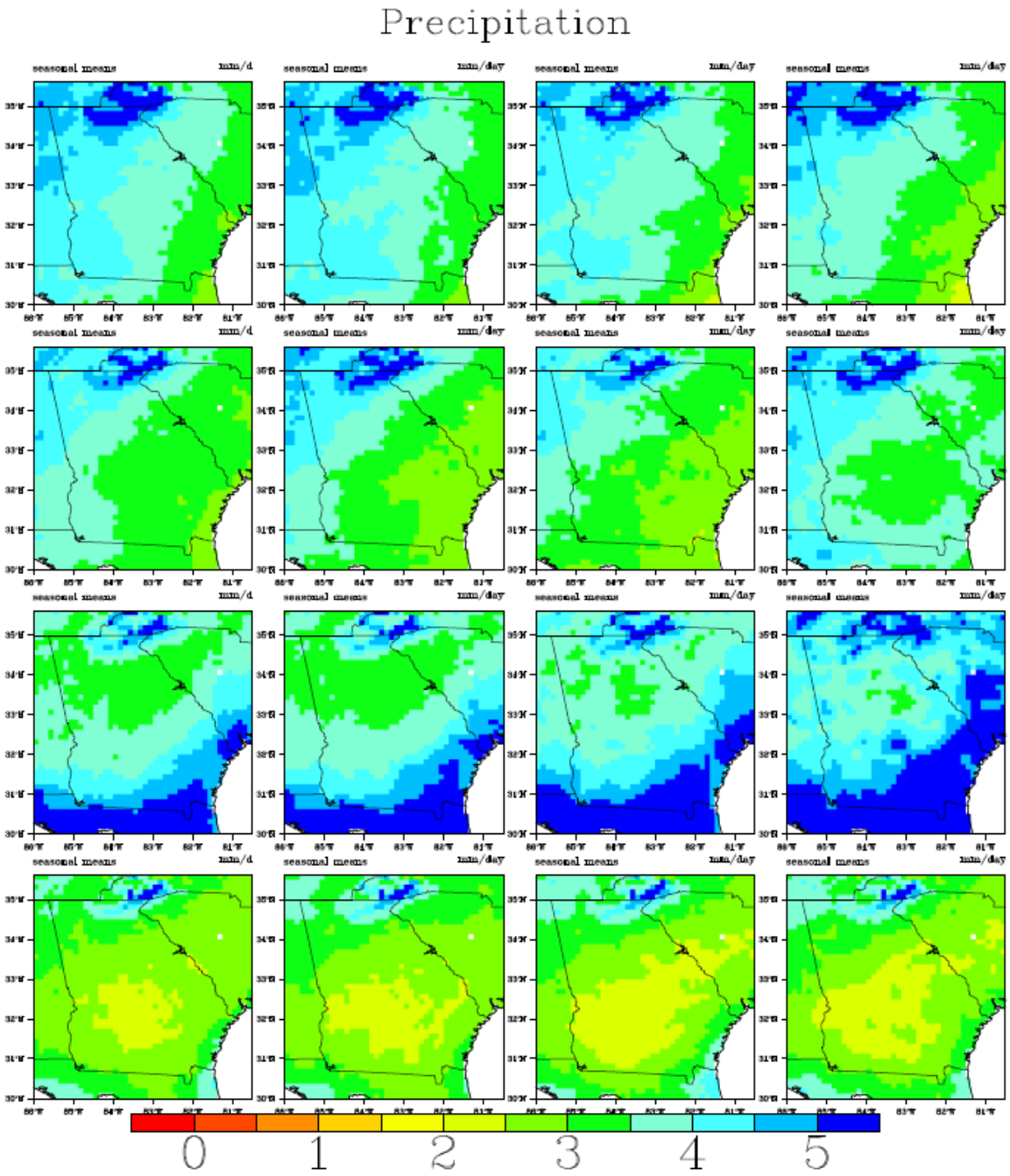

Figure A.47 Spatial precipitation distributions over the ACF basin and the southeast US. Monthly precipitation fields are aggregated by season (DJF, MAM, JJA, SON). The columns depict observations for the period 01/1950 - 12/1999 (Column 1); JVSD downscaled data using input from the 20CM3 experiment for the period 01/1950 - 12/1999 (Column 2); JVSD downscaled data using input from the MIUB ECHO_G -run1A1B Scenario for the period 01/2000-12/2049 (Column 3); and JVSD downscaled data using input from the MIUB ECHO_G -run1 A1B Scenario for the period 01/2050-12/2099 (Column 4).

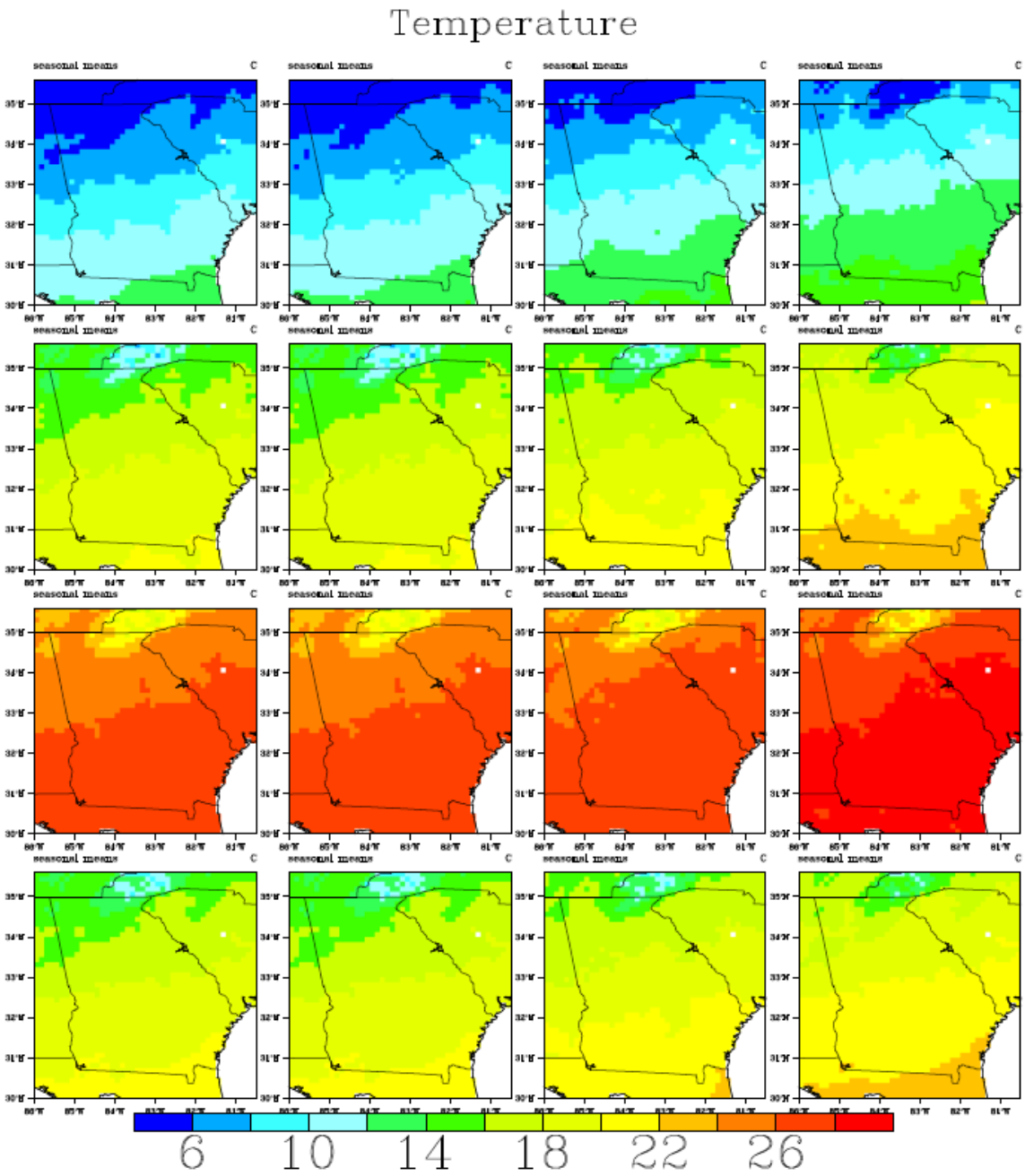

Figure A.48 Spatial temperature distributions over the ACF basin and the southeast US. Monthly temperature fields are aggregated by season (DJF, MAM, JJA, SON). The columns depict observations for the period 01/1950 - 12/1999 (Column 1); JVSD downscaled data using input from the 20CM3 experiment for the period 01/1950 - 12/1999 (Column 2); JVSD downscaled data using input from the MIUB ECHO_G -run1A2 Scenario for the period 01/2000-12/2049 (Column 3); and JVSD downscaled data using input from the MIUB ECHO_G -run1A2 Scenario for the period 01/2050-12/2099 (Column 4).

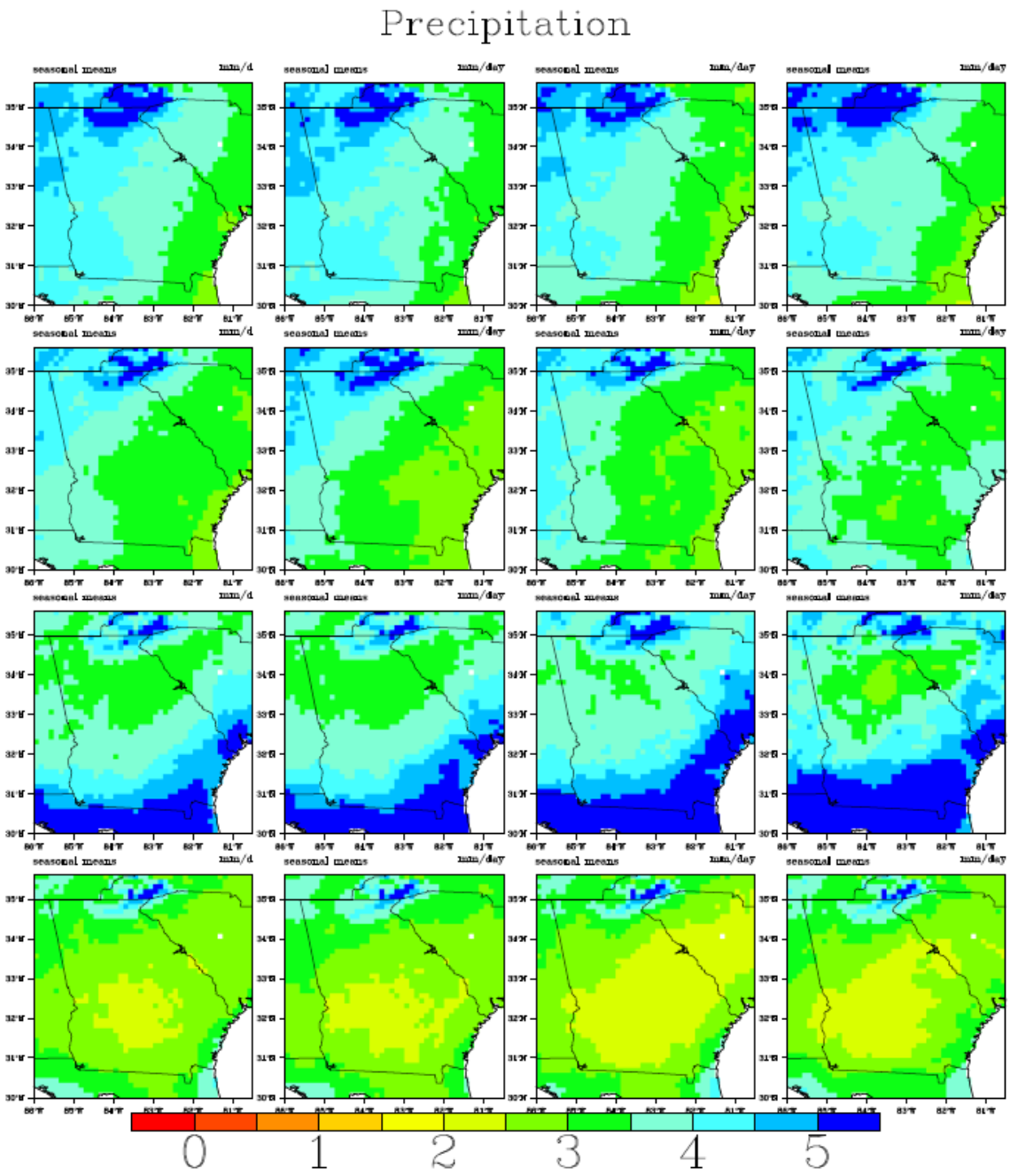

Figure A.49 Spatial precipitation distributions over the ACF basin and the southeast US. Monthly precipitation fields are aggregated by season (DJF, MAM, JJA, SON). The columns depict observations for the period 01/1950 - 12/1999 (Column 1); JVSD downscaled data using input from the 20CM3 experiment for the period 01/1950 - 12/1999 (Column 2); JVSD downscaled data using input from the MIUB ECHO_G -run1A2 Scenario for the period 01/2000-12/2049 (Column 3); and JVSD downscaled data using input from the MIUB ECHO_G -run1A2 Scenario for the period 01/2050-12/2099 (Column 4).

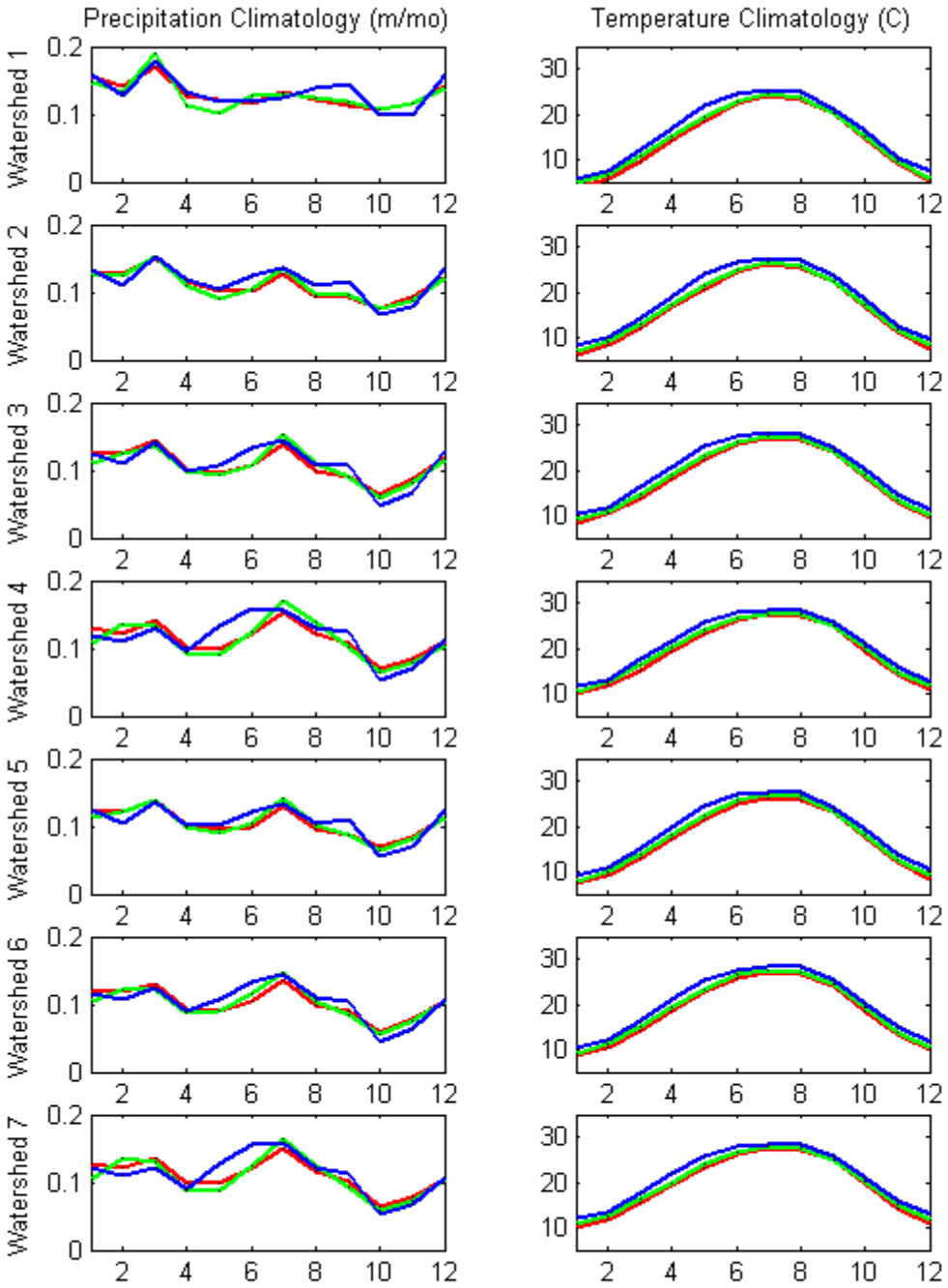

Figure A.50: Climatologies of spatially aggregated precipitation and temperature for seven ACF watersheds: *(1)* Buford, *(2)* West Point, *(3)* George, *(4)* Woodruff, *(5)* Montezuma, *(6)* Albany, and *(7)* Bainbridge; Lines in Red–Observations (1950-1999); Green–JVSD downscaled (2000-2049); Blue–JVSD downscaled (2050-2099) under MIUB ECHO_G -run1 A1B Scenarios.

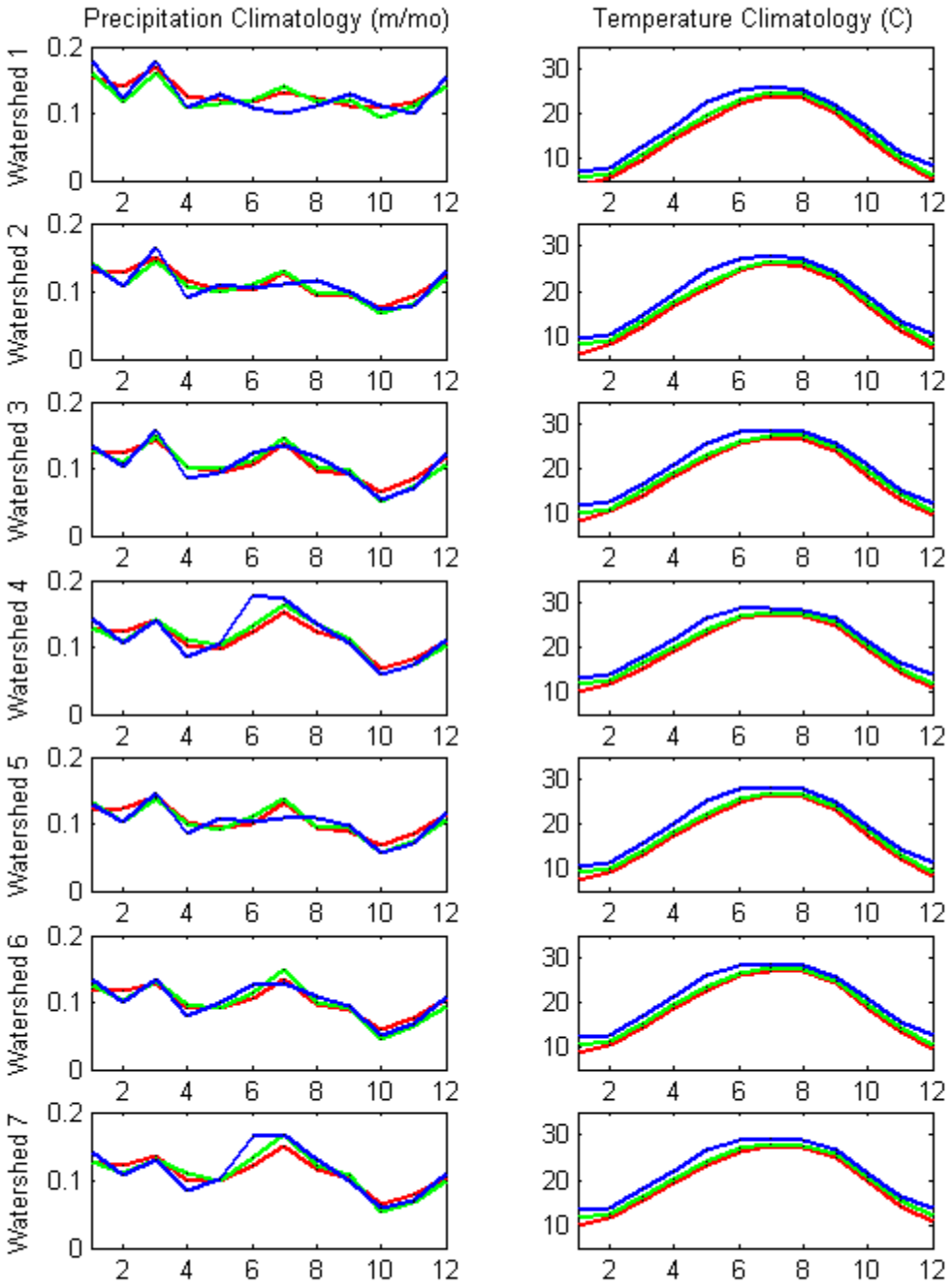

Figure A.50: Climatologies of spatially aggregated precipitation and temperature for seven ACF watersheds: *(1)* Buford, *(2)* West Point, *(3)* George, *(4)* Woodruff, *(5)* Montezuma, *(6)* Albany, and *(7)* Bainbridge; Lines in Red–Observations (1950-1999); Green–JVSD downscaled (2000-2049); Blue–JVSD downscaled (2050-2099) under MIUB ECHO_G -run1 A2 Scenarios.

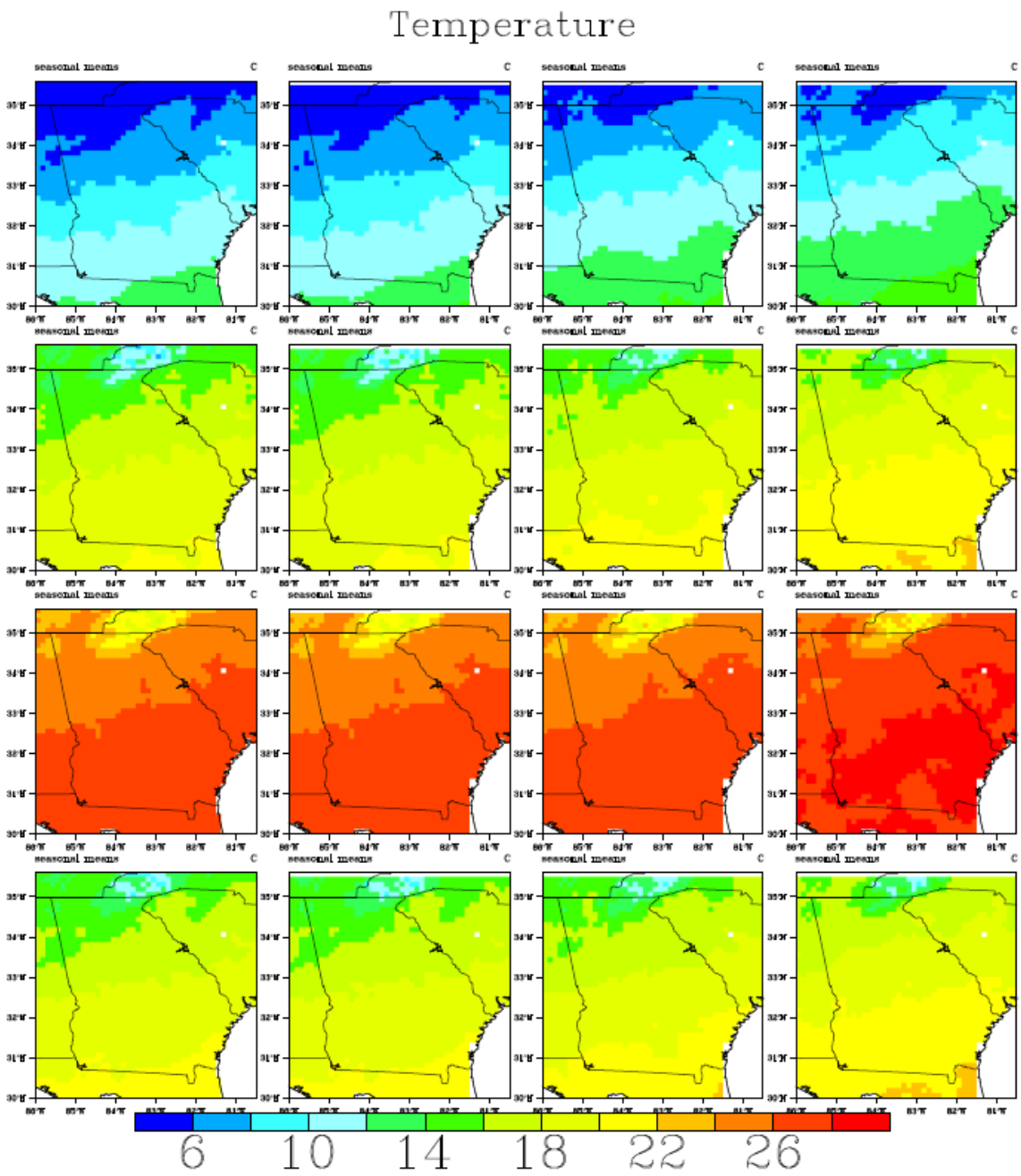

Figure A.51: Spatial temperature distributions over the ACF basin and the southeast US. Monthly temperature fields are aggregated by season (DJF, MAM, JJA, SON). The columns depict observations for the period 01/1950 - 12/1999 (Column 1); JVSD downscaled data using input from the 20CM3 experiment for the period 01/1950 - 12/1999 (Column 2); JVSD downscaled data using input from the MPI ECHAM5 -run1 A1B Scenario for the period 01/2000-12/2049 (Column 3); and JVSD downscaled data using input from the MPI ECHAM5 - run1 A1B Scenario for the period 01/2050-12/2099 (Column 4).

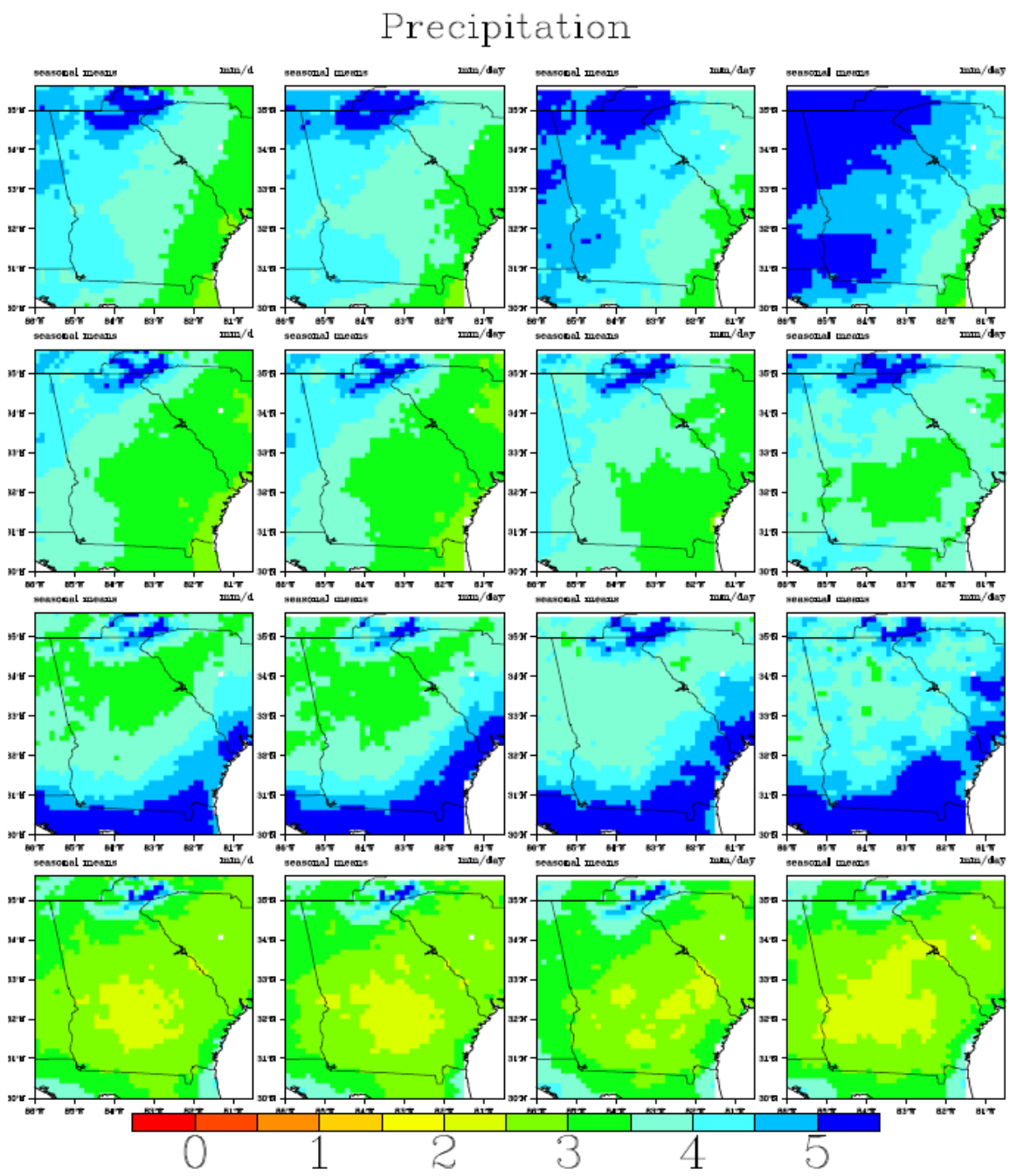

Figure A.52: Spatial precipitation distributions over the ACF basin and the southeast US. Monthly precipitation fields are aggregated by season (DJF, MAM, JJA, SON). The columns depict observations for the period 01/1950 - 12/1999 (Column 1); JVSD downscaled data using input from the 20CM3 experiment for the period 01/1950 - 12/1999 (Column 2); JVSD downscaled data using input from the MPI ECHAM5 -run1A1B Scenario for the period 01/2000-12/2049 (Column 3); and JVSD downscaled data using input from the MPI ECHAM5 - run1 A1B Scenario for the period 01/2050-12/2099 (Column 4).

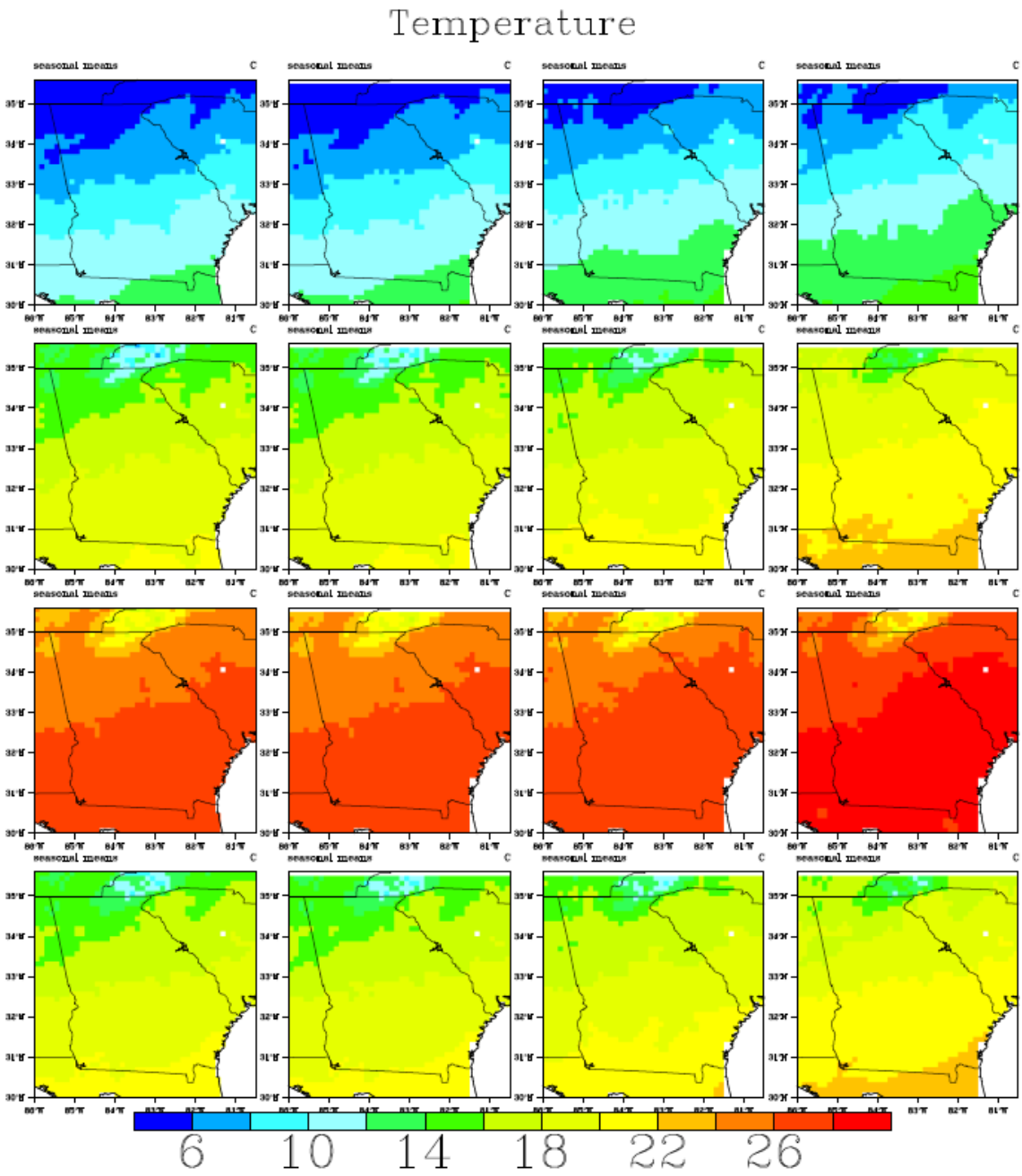

Figure A.53: Spatial temperature distributions over the ACF basin and the southeast US. Monthly temperature fields are aggregated by season (DJF, MAM, JJA, SON). The columns depict observations for the period 01/1950 - 12/1999 (Column 1); JVSD downscaled data using input from the 20CM3 experiment for the period 01/1950 - 12/1999 (Column 2); JVSD downscaled data using input from the MPI ECHAM5 -run1A2 Scenario for the period 01/2000-12/2049 (Column 3); and JVSD downscaled data using input from the MPI ECHAM5 -run1A2 Scenario for the period 01/2050-12/2099 (Column 4).

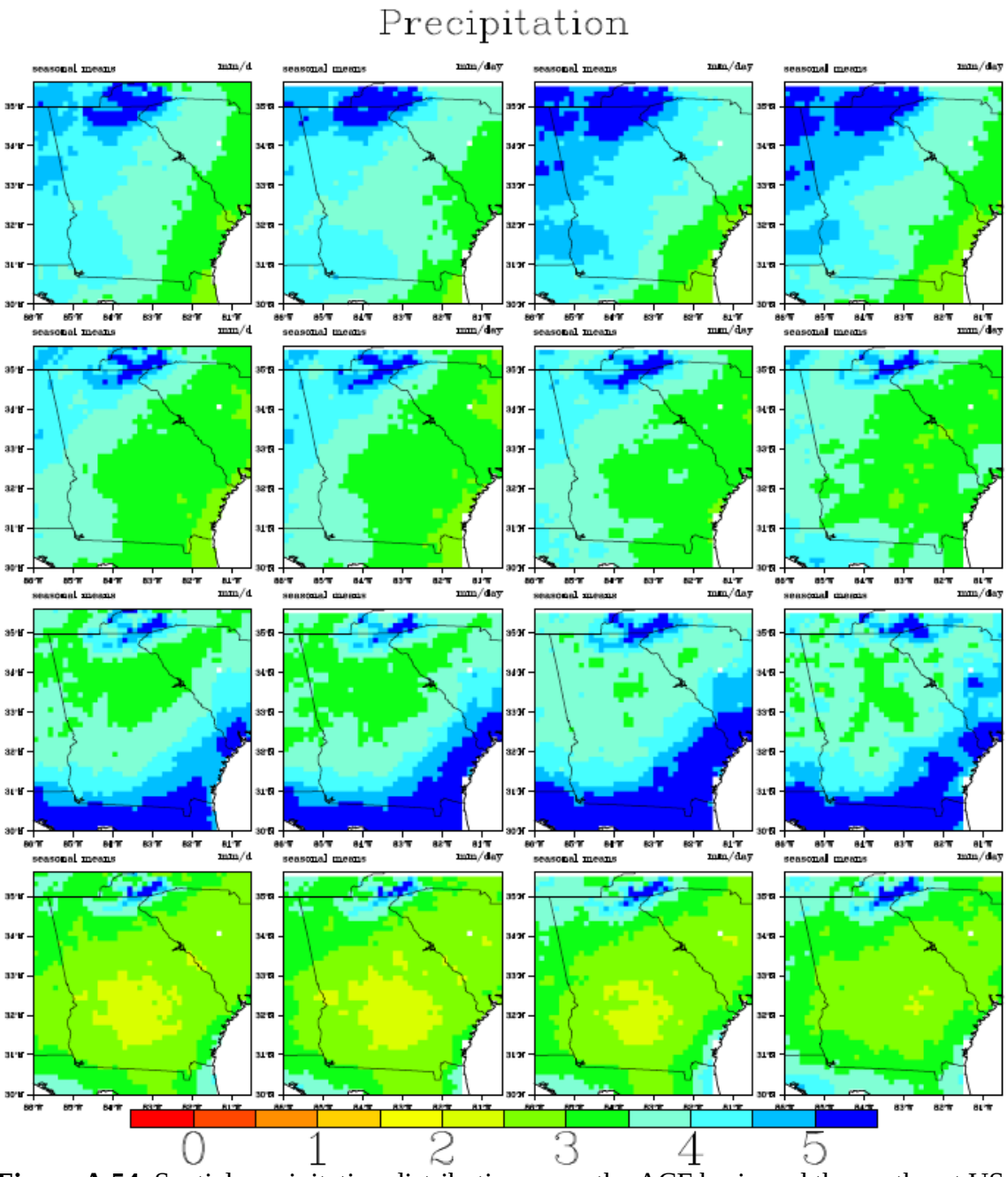

Figure A.54: Spatial precipitation distributions over the ACF basin and the southeast US. Monthly precipitation fields are aggregated by season (DJF, MAM, JJA, SON). The columns depict observations for the period 01/1950 - 12/1999 (Column 1); JVSD downscaled data using input from the 20CM3 experiment for the period 01/1950 - 12/1999 (Column 2); JVSD downscaled data using input from the MPI ECHAM5 -run1A2 Scenario for the period 01/2000-12/2049 (Column 3); and JVSD downscaled data using input from the MPI ECHAM5 -run1A2 Scenario for the period 01/2050-12/2099 (Column 4).

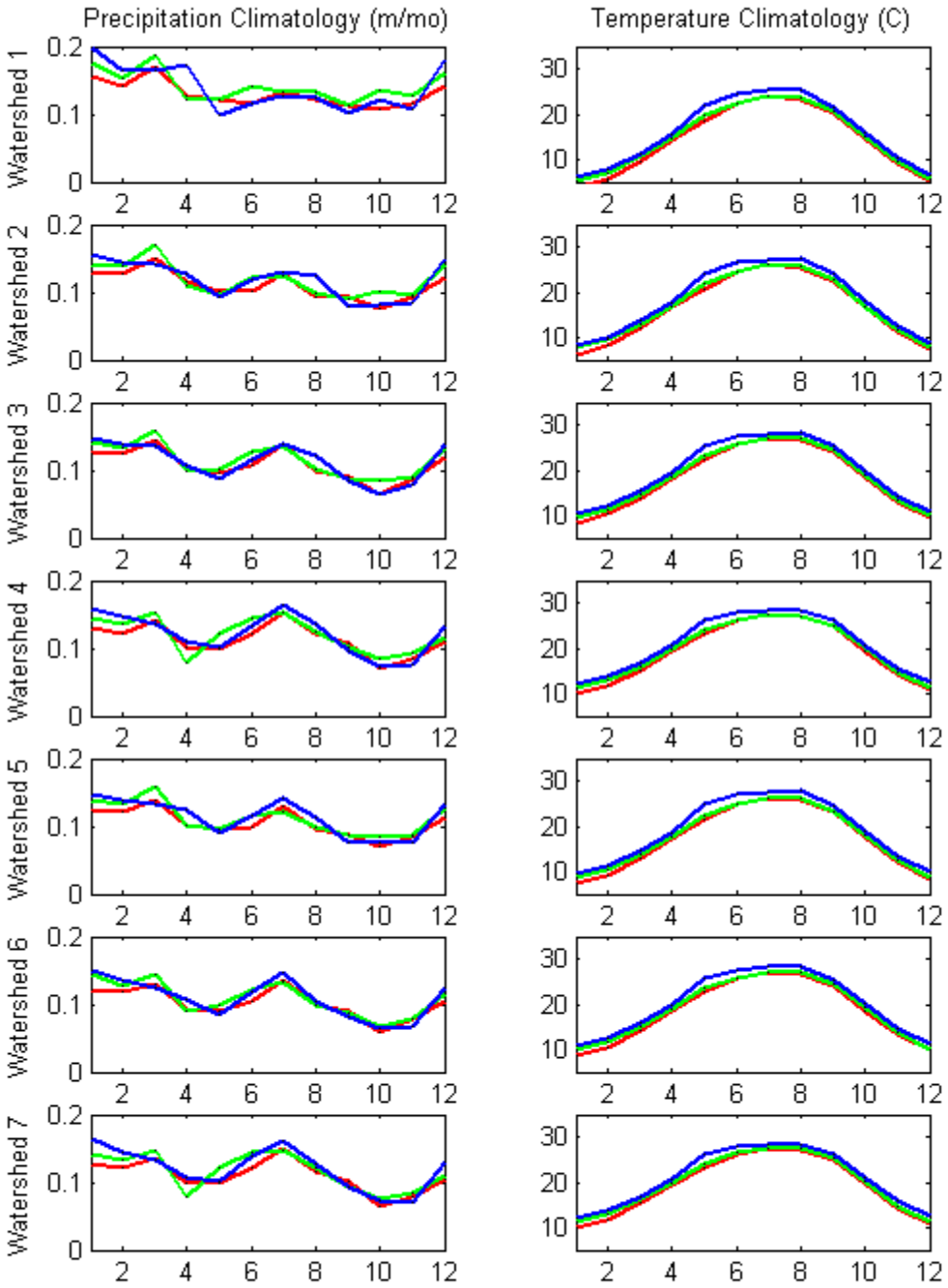

Figure A.55a: Climatologies of spatially aggregated precipitation and temperature for seven ACF watersheds: *(1)* Buford, *(2)* West Point, *(3)* George, *(4)* Woodruff, *(5)* Montezuma, *(6)* Albany, and *(7)* Bainbridge; Lines in Red–Observations (1950-1999); Green–JVSD downscaled (2000- 2049); Blue–JVSD downscaled (2050-2099) under MPI ECHAM5 -run1 A1B Scenarios.

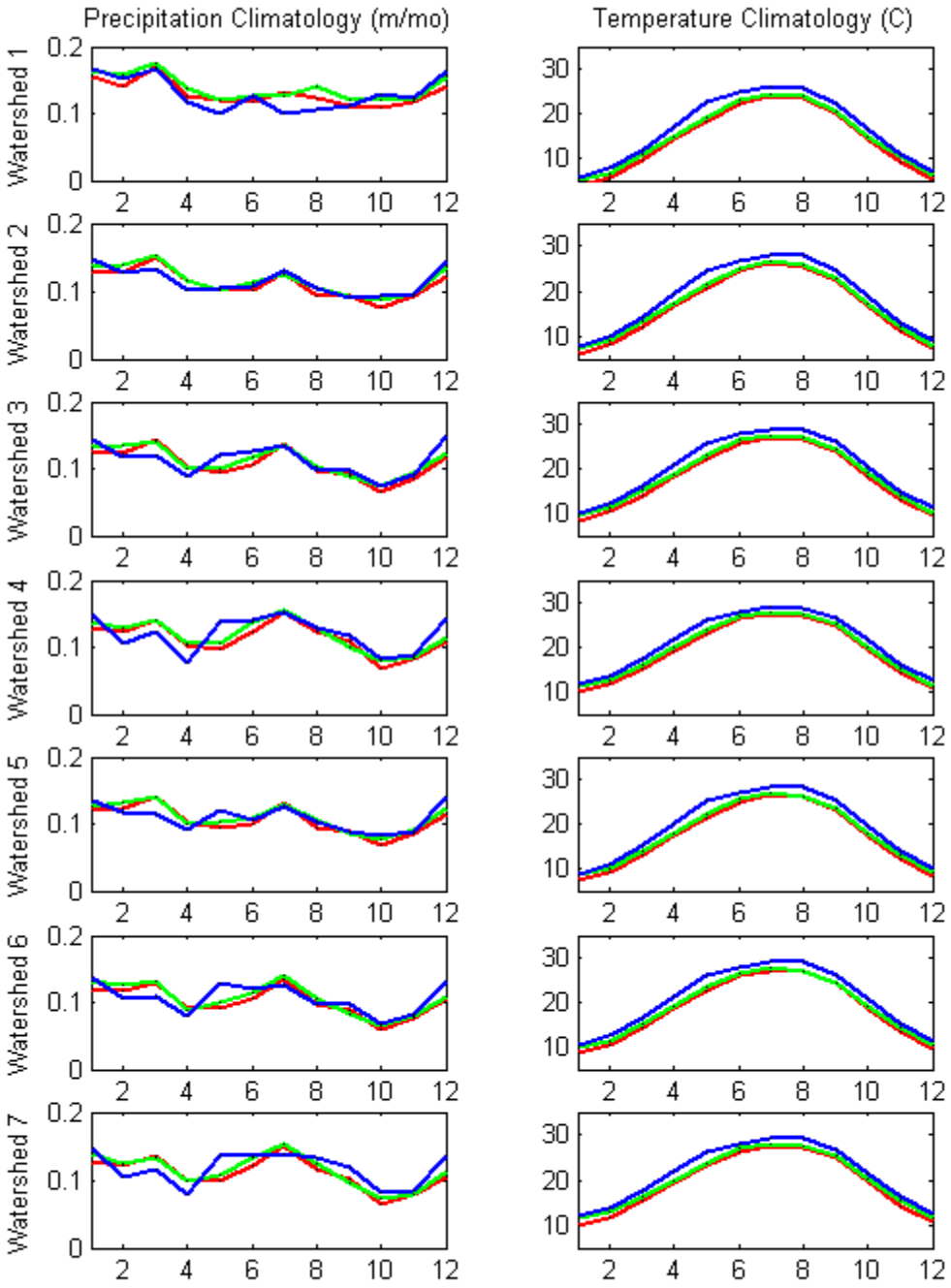

Figure A.55b: Climatologies of spatially aggregated precipitation and temperature for seven ACF watersheds: *(1)* Buford, *(2)* West Point, *(3)* George, *(4)* Woodruff, *(5)* Montezuma, *(6)* Albany, and *(7)* Bainbridge; Lines in Red–Observations (1950-1999); Green–JVSD downscaled (2000- 2049); Blue–JVSD downscaled (2050-2099) under MPI ECHAM5 -run1 A2 Scenarios.

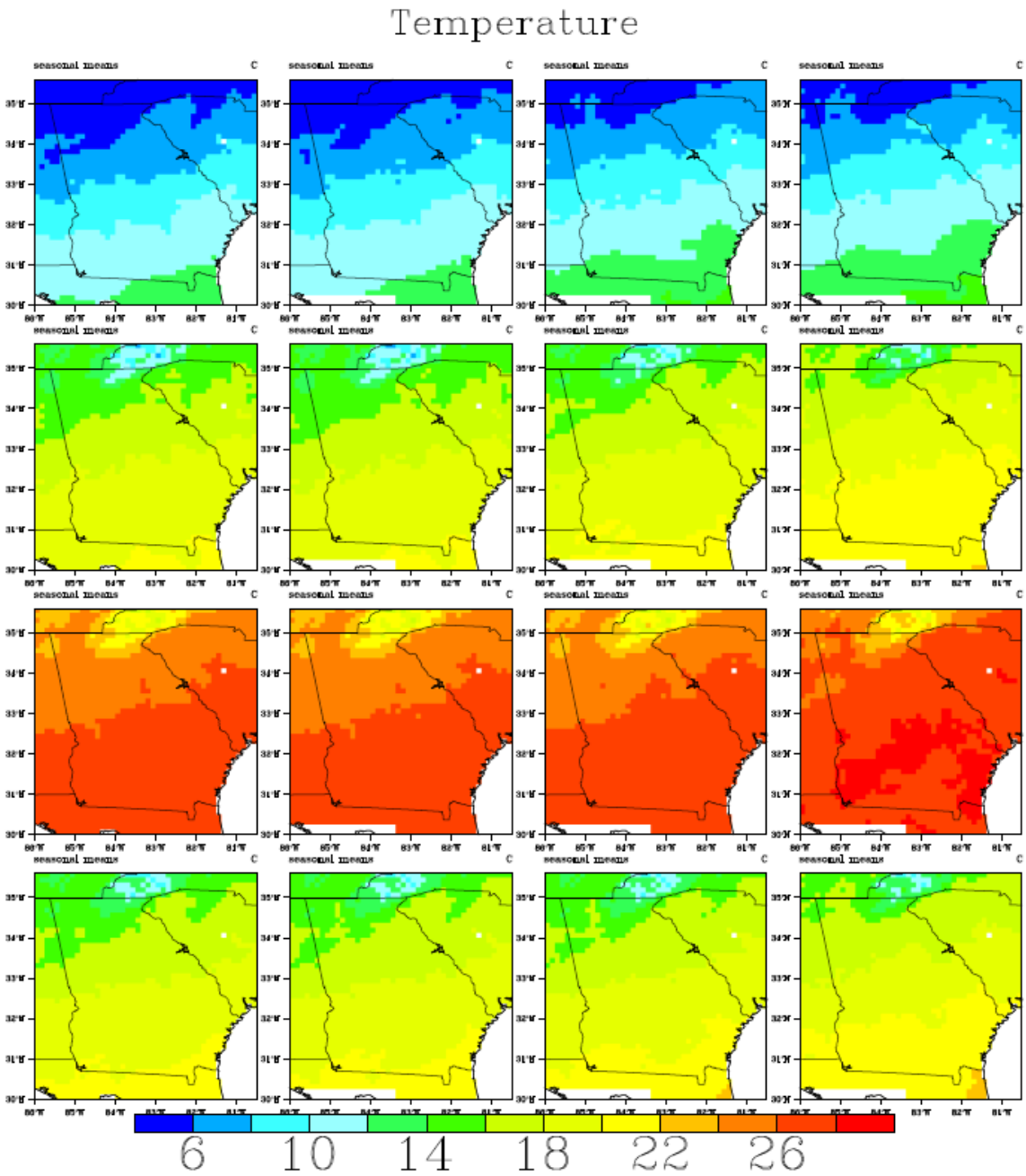

Figure A.56: Spatial temperature distributions over the ACF basin and the southeast US. Monthly temperature fields are aggregated by season (DJF, MAM, JJA, SON). The columns depict observations for the period 01/1950 - 12/1999 (Column 1); JVSD downscaled data using input from the 20CM3 experiment for the period 01/1950 - 12/1999 (Column 2); JVSD downscaled data using input from the MRI CGCM2.3.2A -run1 A1B Scenario for the period 01/2000-12/2049 (Column 3); and JVSD downscaled data using input from the MRI CGCM2.3.2A -run1 A1B Scenario for the period 01/2050-12/2099 (Column 4).

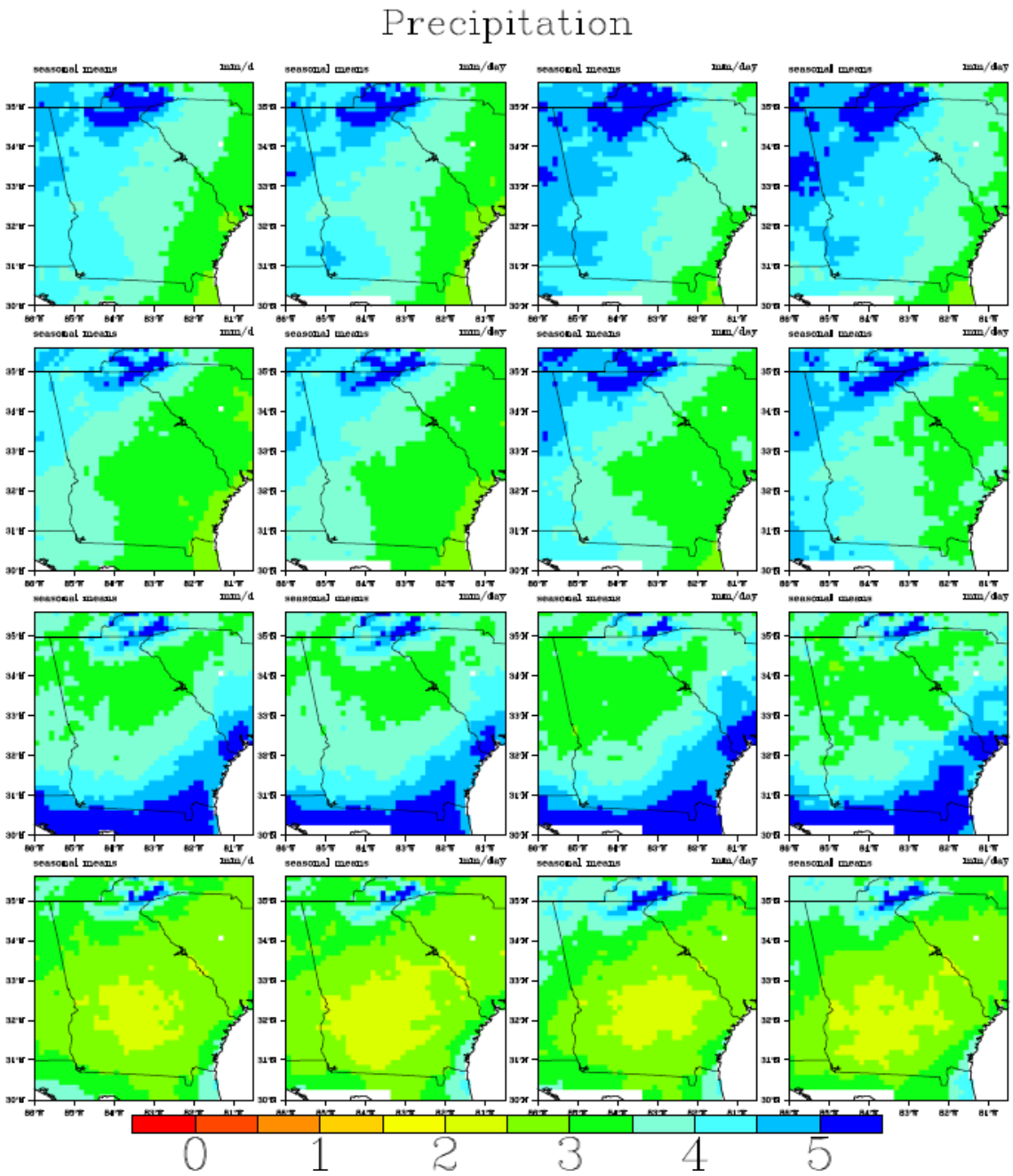

Figure A.57: Spatial precipitation distributions over the ACF basin and the southeast US. Monthly precipitation fields are aggregated by season (DJF, MAM, JJA, SON). The columns depict observations for the period 01/1950 - 12/1999 (Column 1); JVSD downscaled data using input from the 20CM3 experiment for the period 01/1950 - 12/1999 (Column 2); JVSD downscaled data using input from the MRI CGCM2.3.2A -run1A1B Scenario for the period 01/2000-12/2049 (Column 3); and JVSD downscaled data using input from the MRI CGCM2.3.2A -run1 A1B Scenario for the period 01/2050-12/2099 (Column 4).

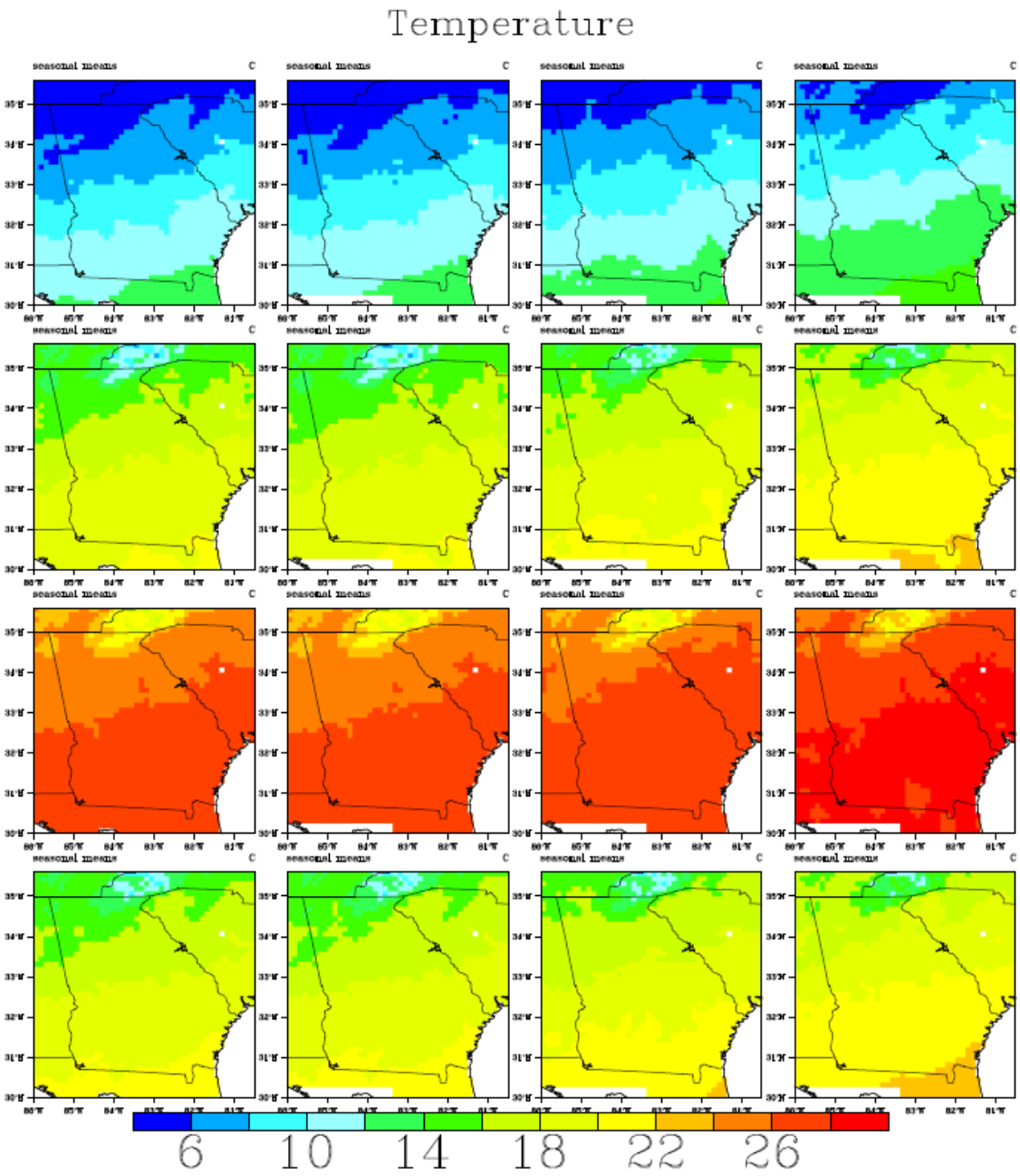

Figure A.58: Spatial temperature distributions over the ACF basin and the southeast US. Monthly temperature fields are aggregated by season (DJF, MAM, JJA, SON). The columns depict observations for the period 01/1950 - 12/1999 (Column 1); JVSD downscaled data using input from the 20CM3 experiment for the period 01/1950 - 12/1999 (Column 2); JVSD downscaled data using input from the MRI CGCM2.3.2A -run1A2 Scenario for the period 01/2000-12/2049 (Column 3); and JVSD downscaled data using input from the MRI CGCM2.3.2A -run1A2 Scenario for the period 01/2050-12/2099 (Column 4).

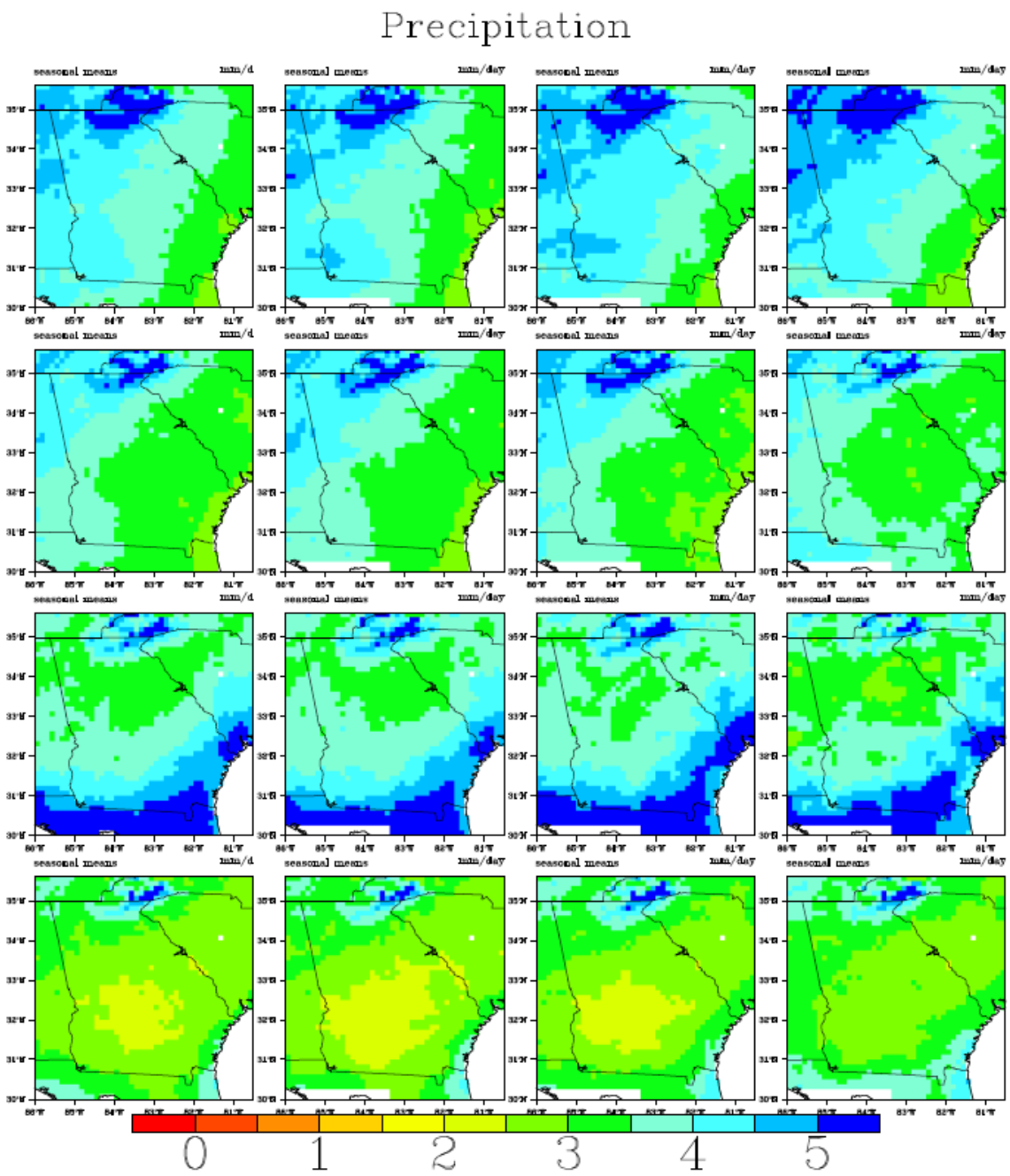

Figure A.59: Spatial precipitation distributions over the ACF basin and the southeast US. Monthly precipitation fields are aggregated by season (DJF, MAM, JJA, SON). The columns depict observations for the period 01/1950 - 12/1999 (Column 1); JVSD downscaled data using input from the 20CM3 experiment for the period 01/1950 - 12/1999 (Column 2); JVSD downscaled data using input from the MRI CGCM2.3.2A -run1A2 Scenario for the period 01/2000-12/2049 (Column 3); and JVSD downscaled data using input from the MRI CGCM2.3.2A -run1A2 Scenario for the period 01/2050-12/2099 (Column 4).

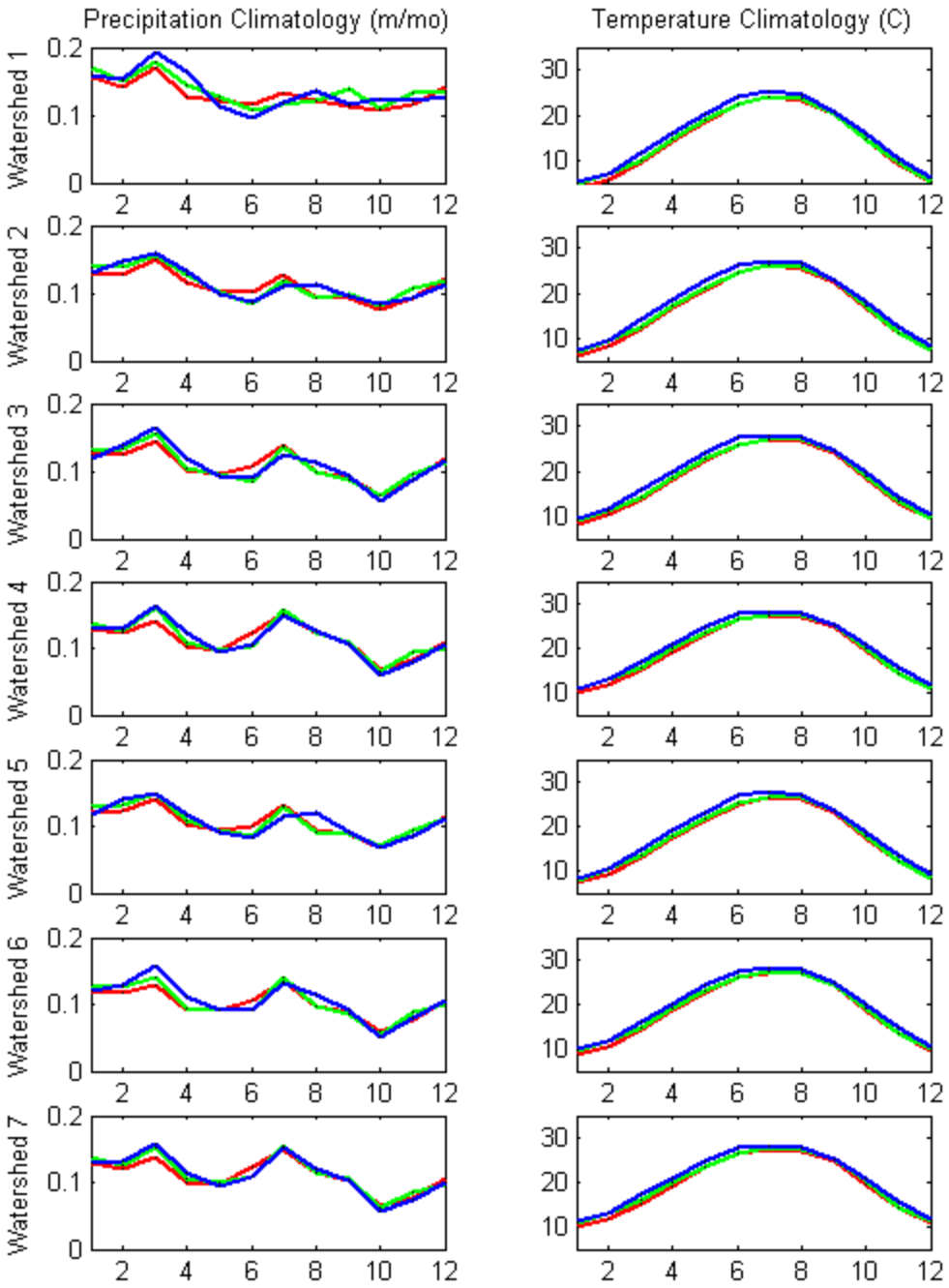

Figure A.60a: Climatologies of spatially aggregated precipitation and temperature for seven ACF watersheds: *(1)* Buford, *(2)* West Point, *(3)* George, *(4)* Woodruff, *(5)* Montezuma, *(6)* Albany, and *(7)* Bainbridge; Lines in Red–Observations (1950-1999); Green–JVSD downscaled (2000- 2049); Blue–JVSD downscaled (2050-2099) under MRI CGCM2.3.2A -run1 A1B Scenarios.

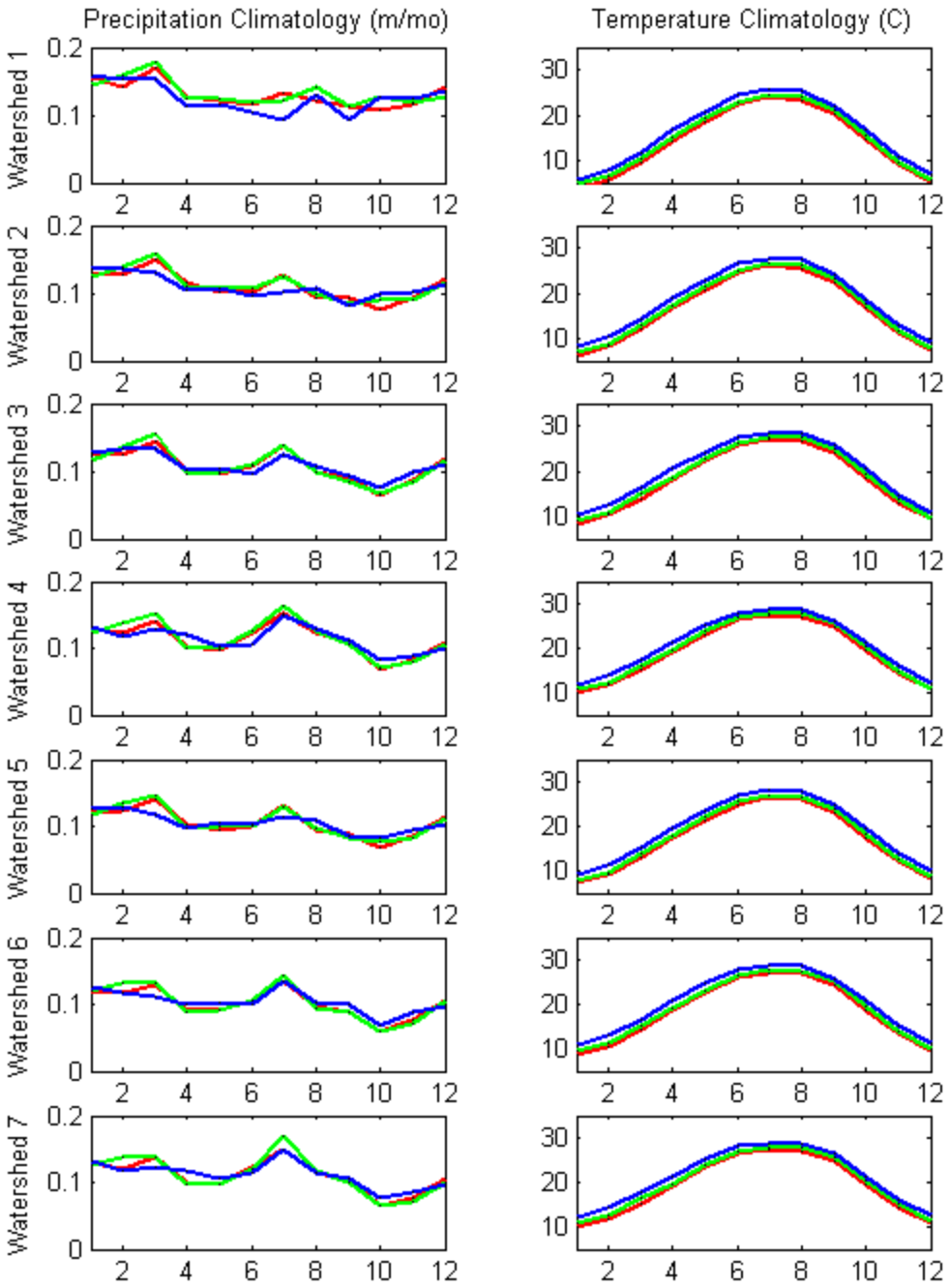

Figure A.60b: Climatologies of spatially aggregated precipitation and temperature for seven ACF watersheds: *(1)* Buford, *(2)* West Point, *(3)* George, *(4)* Woodruff, *(5)* Montezuma, *(6)* Albany, and *(7)* Bainbridge; Lines in Red–Observations (1950-1999); Green–JVSD downscaled (2000- 2049); Blue–JVSD downscaled (2050-2099) under MRI CGCM2.3.2A -run1 A2 Scenarios.

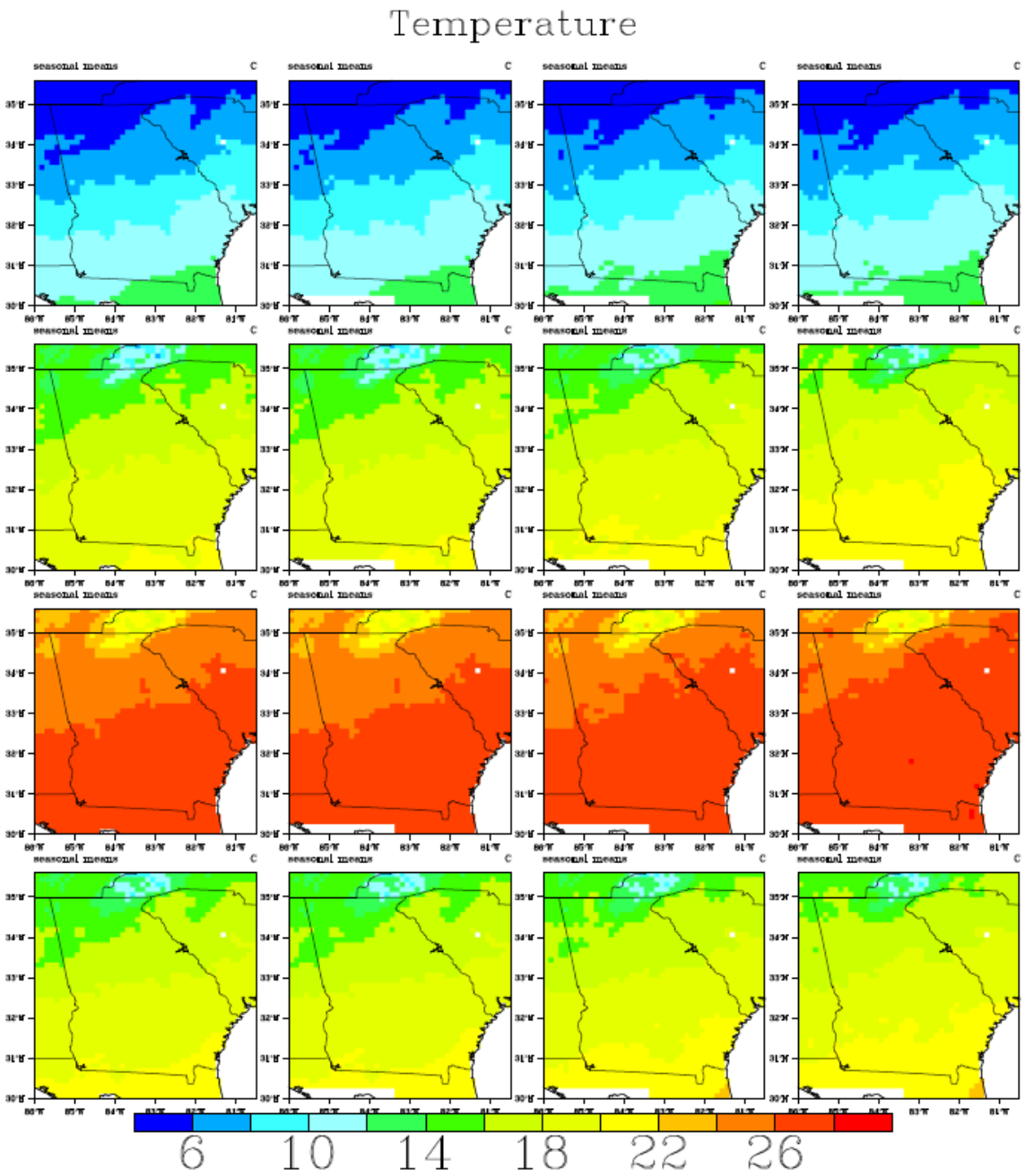

Figure A.61: Spatial temperature distributions over the ACF basin and the southeast US. Monthly temperature fields are aggregated by season (DJF, MAM, JJA, SON). The columns depict observations for the period 01/1950 - 12/1999 (Column 1); JVSD downscaled data using input from the 20CM3 experiment for the period 01/1950 - 12/1999 (Column 2); JVSD downscaled data using input from the NCAR PCM1 -run1 A1B Scenario for the period 01/2000-12/2049 (Column 3); and JVSD downscaled data using input from the NCAR PCM1 -run1 A1B Scenario for the period 01/2050-12/2099 (Column 4).

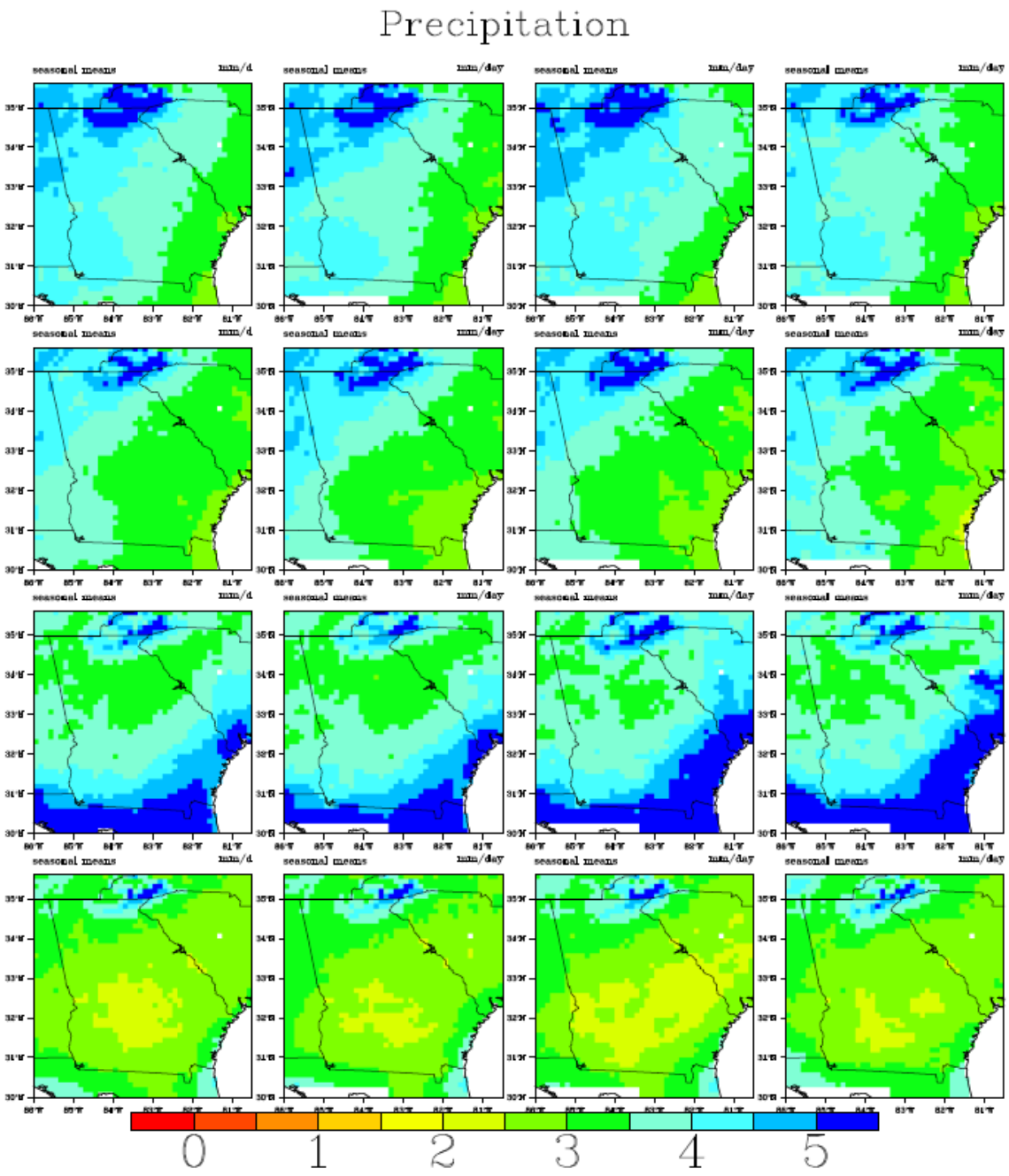

Figure A.62: Spatial precipitation distributions over the ACF basin and the southeast US. Monthly precipitation fields are aggregated by season (DJF, MAM, JJA, SON). The columns depict observations for the period 01/1950 - 12/1999 (Column 1); JVSD downscaled data using input from the 20CM3 experiment for the period 01/1950 - 12/1999 (Column 2); JVSD downscaled data using input from the NCAR PCM1 -run1A1B Scenario for the period 01/2000-12/2049 (Column 3); and JVSD downscaled data using input from the NCAR PCM1 -run1 A1B Scenario for the period 01/2050-12/2099 (Column 4).

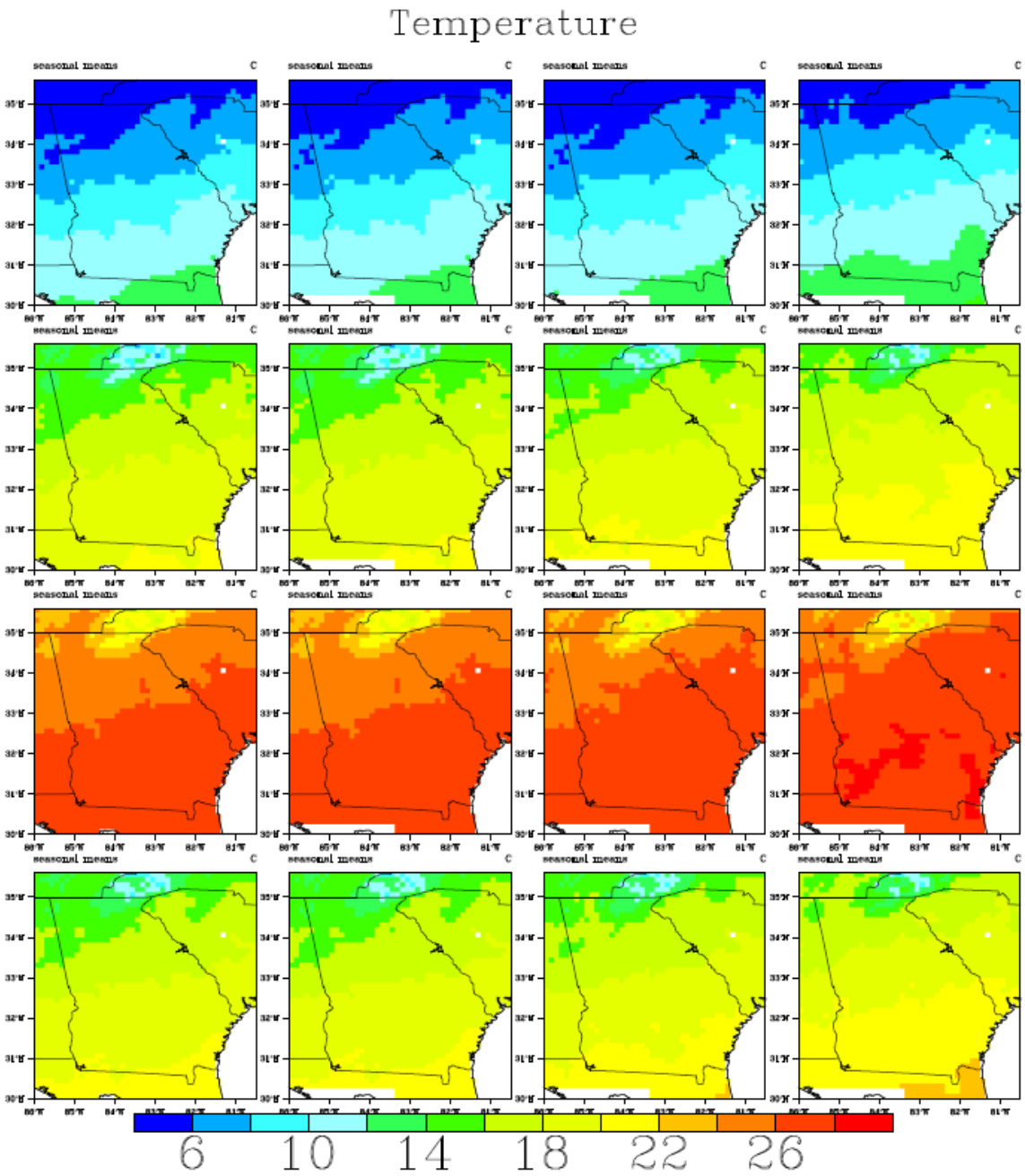

Figure A.63: Spatial temperature distributions over the ACF basin and the southeast US. Monthly temperature fields are aggregated by season (DJF, MAM, JJA, SON). The columns depict observations for the period 01/1950 - 12/1999 (Column 1); JVSD downscaled data using input from the 20CM3 experiment for the period 01/1950 - 12/1999 (Column 2); JVSD downscaled data using input from the NCAR PCM1 -run1A2 Scenario for the period 01/2000-12/2049 (Column 3); and JVSD downscaled data using input from the NCAR PCM1 -run1A2 Scenario for the period 01/2050-12/2099 (Column 4).

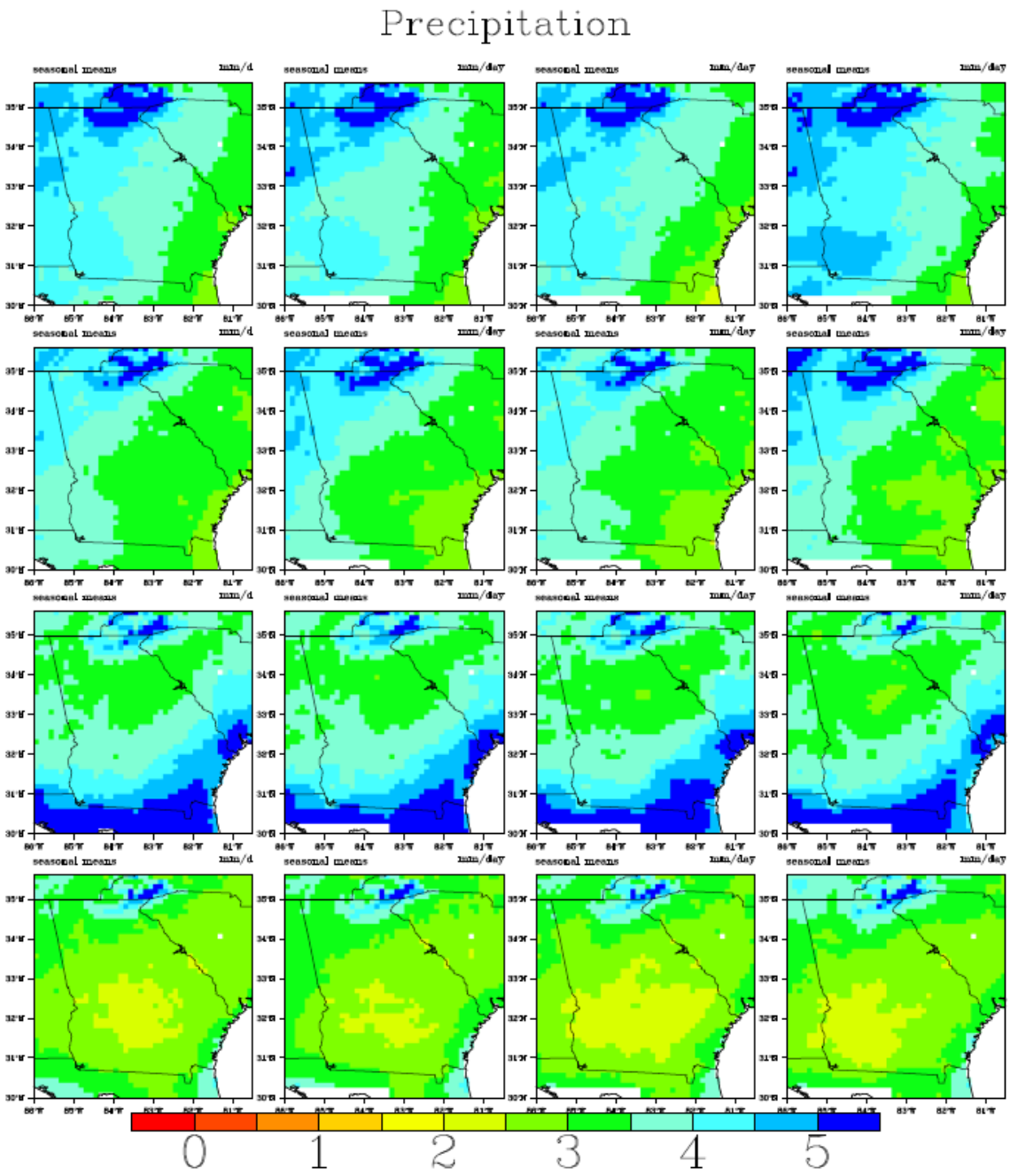

Figure A.64: Spatial precipitation distributions over the ACF basin and the southeast US. Monthly precipitation fields are aggregated by season (DJF, MAM, JJA, SON). The columns depict observations for the period 01/1950 - 12/1999 (Column 1); JVSD downscaled data using input from the 20CM3 experiment for the period 01/1950 - 12/1999 (Column 2); JVSD downscaled data using input from the NCAR PCM1 -run1A2 Scenario for the period 01/2000-12/2049 (Column 3); and JVSD downscaled data using input from the NCAR PCM1 -run1A2 Scenario for the period 01/2050-12/2099 (Column 4).

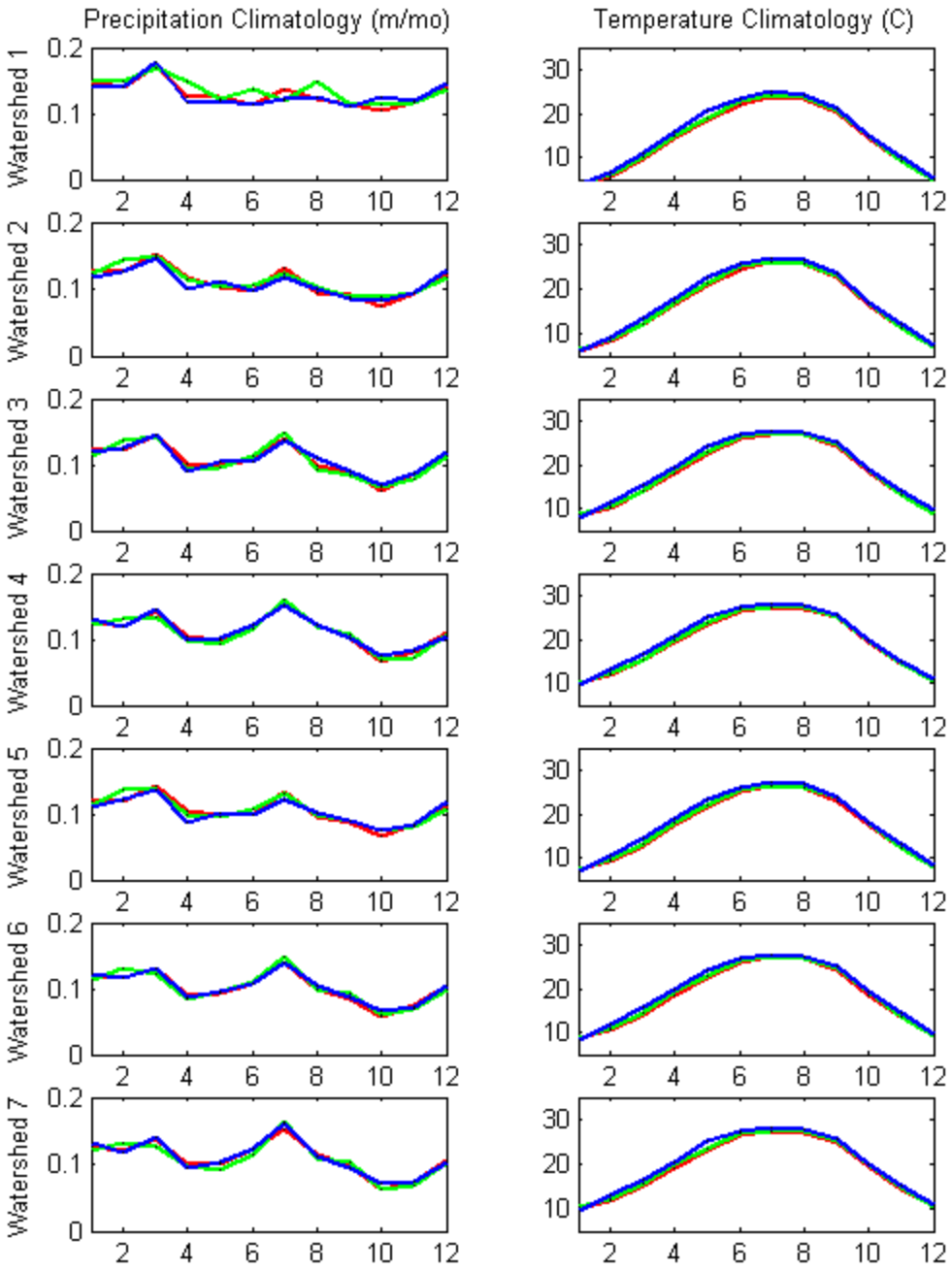

Figure A.65a: Climatologies of spatially aggregated precipitation and temperature for seven ACF watersheds: *(1)* Buford, *(2)* West Point, *(3)* George, *(4)* Woodruff, *(5)* Montezuma, *(6)* Albany, and *(7)* Bainbridge; Lines in Red–Observations (1950-1999); Green–JVSD downscaled (2000- 2049); Blue–JVSD downscaled (2050-2099) under NCAR PCM1 -run1 A1B Scenarios.

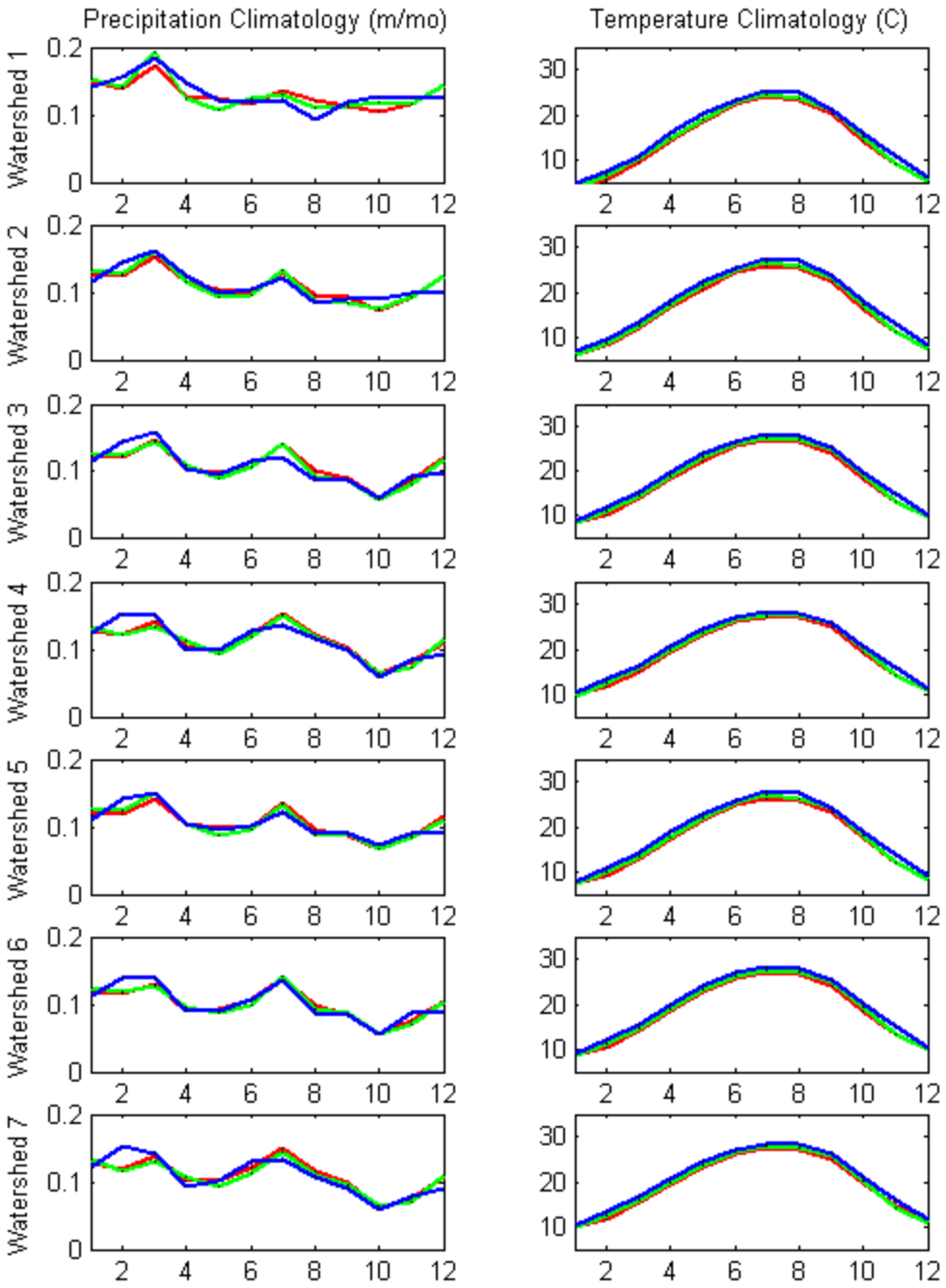

Figure A.65b: Climatologies of spatially aggregated precipitation and temperature for seven ACF watersheds: *(1)* Buford, *(2)* West Point, *(3)* George, *(4)* Woodruff, *(5)* Montezuma, *(6)* Albany, and *(7)* Bainbridge; Lines in Red–Observations (1950-1999); Green–JVSD downscaled (2000- 2049); Blue–JVSD downscaled (2050-2099) under NCAR PCM1 -run1 A2 Scenarios.